

DOT/FAA/TC-15/63

Federal Aviation Administration
William J. Hughes Technical Center
Aviation Research Division
Atlantic City International Airport
New Jersey 08405

A Quantitative Assessment of Conventional and Advanced Nondestructive Inspection Techniques for Detecting Flaws in Composite Honeycomb Aircraft Structures

December 2016

Final Report

This document is available to the U.S. public
through the National Technical Information
Services (NTIS), Springfield, Virginia 22161.

This document is also available from the
Federal Aviation Administration William J. Hughes
Technical Center at actlibrary.tc.faa.gov.



U.S. Department of Transportation
Federal Aviation Administration

NOTICE

This document is disseminated under the sponsorship of the U.S. Department of Transportation in the interest of information exchange. The U.S. Government assumes no liability for the contents or use thereof. The U.S. Government does not endorse products or manufacturers. Trade or manufacturers' names appear herein solely because they are considered essential to the objective of this report. The findings and conclusions in this report are those of the author(s) and do not necessarily represent the views of the funding agency. This document does not constitute FAA policy. Consult the FAA sponsoring organization listed on the Technical Documentation page as to its use.

This report is available at the Federal Aviation Administration William J. Hughes Technical Center's Full-Text Technical Reports page: actlibrary.tc.faa.gov in Adobe Acrobat portable document format (PDF).

Technical Report Documentation Page

1. Report No. DOT/FAA/TC-15/63		2. Government Accession No.		3. Recipient's Catalog No.	
4. Title and Subtitle A QUANTITATIVE ASSESSMENT OF CONVENTIONAL AND ADVANCED NONDESTRUCTIVE INSPECTION TECHNIQUES FOR DETECTING FLAWS IN COMPOSITE HONEYCOMB AIRCRAFT STRUCTURES				5. Report Date December 2016	
				6. Performing Organization Code	
7. Author(s) Dennis P. Roach				8. Performing Organization Report No.	
9. Performing Organization Name and Address Sandia National Laboratories FAA Airworthiness Assurance Center Box 5800 MS-0615 Albuquerque, NM 87185				10. Work Unit No. (TRAIS)	
12. Sponsoring Agency Name and Address FAA National Headquarters 950 L'Enfant Plaza N SW 950 L'Enfant Plaza Washington, DC 20024				13. Type of Report and Period Covered Final Report	
				14. Sponsoring Agency Code AIR-100	
15. Supplementary Notes The Federal Aviation Administration William J. Hughes Technical Center Aviation Research Division Technical Monitor was David Westlund.					
16. Abstract The aircraft industry continues to increase its use of composite materials. This is most noteworthy in the area of principle structural elements. The extreme damage tolerance and high strength-to-weight ratio of composites have motivated designers to expand the role of fiberglass and carbon graphite in aircraft structures. This has placed greater emphasis on the development of improved nondestructive inspection (NDI) methods that are more reliable and sensitive than conventional NDI. The FAA Airworthiness Assurance NDI Validation Center (AANC) at Sandia Laboratories has been pursuing this goal via a host of studies on inspection of composite structures. Through the FAA-AANC's participation in the Commercial Aircraft Composite Repair Committee Inspection Task Group, this team has been investigating the need for improved inspections of composite structures. The majority of composite honeycomb structure inspections are performed visually and supplemented by tap test methods. Tap testing, which uses a human-detected change in acoustic response to locate flaws, and more sophisticated NDI methods such as ultrasonics or thermography have been applied to an increasing number of applications to detect voids, disbonds, and delaminations in adhesively bonded composite aircraft parts. Low frequency bond testing and mechanical impedance analysis tests are often used to inspect thicker laminates. A probability of detection experiment was completed to assess the performance of both conventional and advanced NDI techniques. A series of composite honeycomb specimens with statistically relevant flaw profiles was inspected using both human tap test equipment and new inspection techniques, which have recently been introduced to automate and improve composite NDI. Industry-wide performance curves have been produced to establish: 1) how well current inspection techniques are able to reliably find flaws in composite honeycomb structure, and 2) the degree of improvements possible through the integration of more advanced NDI techniques and procedures. This study compared the results from a wide array of NDI methods, and identified limitations and optimum applications for specific inspection methods while producing key recommendations for improving the performance of NDI.					
17. Key Words Nondestructive inspection, honeycomb composites, solid laminate composites, probability of detection, disbonds, delaminations, impact, aircraft			18. Distribution Statement This document is available to the U.S. public through the National Technical Information Service (NTIS), Springfield, VA 22161. This document is also available from the Federal Aviation Administration William J. Hughes Technical Center at actlibrary.tc.faa.gov.		
19. Security Classif. (of this report) Unclassified		20. Security Classif. (of this page) Unclassified		21. No. of Pages 350	
				22. Price	

ACKNOWLEDGEMENTS

This program is sponsored by the Federal Aviation Administration (FAA) William J. Hughes Technical Center under the direction of the technical monitor David Westlund. The approach used in this effort was formulated in concert with the Commercial Aircraft Composite Repair Committee (CACRC) Inspection Task Group, which consisted of the team members listed below, whose contributions are gratefully acknowledged.

Gerry Doetkott, Northwest Airlines
Alex Melton, Delta Air Lines
Richard Watkins, Delta Air Lines
Tom Dreher, Rolls Royce
Robert Stevens, United Airlines
Bruce Garbett, Airbus Industries
John Hewitt, Airbus Industries
Jim Hofer, Boeing
Jeff Kollgaard, Boeing
Glae McDonald, US Airways
Eric Bartoletti, American Airlines
Kirk Rackow, Sandia Labs AANC
Dennis Roach, Sandia Labs AANC

The author would like to recognize the data acquisition support provided by others at Sandia National Laboratories AANC, including Phil Walkington, Tony DeLong, Joe Dimambro, and Ciji Nelson. Special thanks go to Kirk Rackow (retired Sandia National Laboratories) who played a critical role in the development and implementation of this experiment. FAA oversight and extensive guidance for this effort was provided by David Westlund and Dave Galella, FAA Project Managers, and Rusty Jones, FAA Senior Technical Specialist in Nondestructive Inspection (NDI) and Composites. David Hsu and Dan Barnard of Iowa State University provided many useful ideas on tap testing and appropriate performance testing. Thanks also to David Caulkins and his colleagues in the Sandia National Laboratories composite shop for their assistance in test specimen fabrication.

Advanced NDI tests were supported by Laser Technology Inc. (shearography), Honeywell (laser velocimetry Structural Anomaly Mapping), Imperium Inc. (ultrasonic imaging Acoustocam), Iowa State University (Computer-aided tap tester and air-coupled ultrasonics), Boeing (Mobile Automated Scanner in MIA and Resonance mode), Thermal Wave Imaging (thermography), Sonatest (Rapidscan linear array ultrasonics), Southern Research Institute (ultrasonic spectroscopy), Lockheed Martin (laser ultrasonics), Evisive (microwave), GMA Industries (terahertz ultrasonic imaging), NDT Solutions Inc. (FlawInspecta phased array ultrasonics), QUEST Integrated (induction thermography), and Digiray (digital x-ray laminography).

Finally, the author would like to thank the following airlines and maintenance facilities for participating in this experiment: Delta Air Lines (four facilities), United Airlines (three facilities), American Airlines (two facilities), Aloha Airlines, Alaska Airlines, US Airways, British Airways, KLM Airlines, Air France, FedEx (two facilities), SR Technics, GKN Westland Aerospace, and FLS Aerospace Manchester.

Sandia National Laboratories is a multi-program laboratory managed and operated by Sandia Corporation, a wholly owned subsidiary of Lockheed Martin Corporation, for the U.S. Department of Energy's National Nuclear Security Administration under contract DE-AC04-94AL85000.

TABLE OF CONTENTS

	Page
EXECUTIVE SUMMARY	xxiv
1. INTRODUCTION AND BACKGROUND	1
1.1 Overview of Composite Honeycomb Flaw Detection Experiment	1
1.1.1 Description of CHE:	2
1.1.2 Results Obtained From CHE	3
1.2 Increasing Use of Composites in Aircraft Structures	4
1.3 Background on In-Service Inspection Needs for Composite Structures	9
1.4 Damage Tolerance Approach to Establish Inspection Intervals	9
1.4.1 Inspection intervals:	12
2. PURPOSE OF COMPOSITE HONEYCOMB FLAW DETECTION EXPERIMENT	13
2.1 OEM Guidelines for Inspecting Composite Honeycomb Structures	19
3. CONVENTIONAL INSPECTION METHODS FOR COMPOSITE HONEYCOMB STRUCTURE	22
3.1 Bond Testing	23
3.2 Manual Mechanical Tap Testing	25
3.3 Automated/Instrumented Mechanical Tap Testing	29
3.4 Low Frequency Bond Testing	32
3.5 High Frequency Bond Testing – Resonance Mode	33
3.6 Mechanical Impedance Analysis	34
3.7 Ultrasonic Inspection Methods	36
3.7.1 A-scan Mode:	36
3.7.2 B-scan Mode	38
3.7.3 C-scan Mode—Use of UT Scanning Technology	39
4. ADVANCED COMPOSITE HONEYCOMB INSPECTION TECHNIQUES	42
4.1 Instrumented and Automated Tap Test Devices	43
4.1.1 Woodpecker	46
4.1.2 Rapid Damage Detection Device	47
4.1.3 Computer-Aided Tap Test Device	48

4.2	Pulsed Thermography	53
4.2.1	Thermal Wave Imaging EchoTherm Thermography Inspection System	55
4.3	Line Scanning Thermography	61
4.3.1	MISTRAS Line Scan Thermography Inspection System	63
4.4	Lock-In Thermography	64
4.4.1	MoviTHERM Lock-In Thermography System	66
4.5	Shearography	67
4.5.1	Laser Technology Inc. LTI-5200 System	69
4.5.2	Dantec Dynamics Q-810 Laser Shearography System	72
4.6	Mobile Automated Scanner in Resonance and Mia Modes	74
4.7	Microwave	76
4.8	Structural Anomaly Mapping System	80
4.9	Phased Array and Linear Array Ultrasonics	84
4.9.1	Boeing MAUS FlawInspecta Linear Array UT System and the Diagnostic Sonar FlawInspecta PA-UT System	87
4.10	Air-Coupled Ultrasonics	90
4.11	Laser Ultrasonics	96
4.11.1	LUS deployment	96
4.11.2	iPhoton LUS (iPLUS)	99
4.12	Laminography	101
5.	COMPOSITE HONEYCOMB FLAW DETECTION EXPERIMENT DESIGN	106
5.1	Experiment Design Criteria	109
5.2	Experiment Test Specimen Design	110
6.	COMPOSITE HONEYCOMB FLAW DETECTION EXPERIMENT IMPLEMENTATION	123
7.	RESULTS FROM COMPOSITE HONEYCOMB FLAW DETECTION EXPERIMENT	134
8.	CONCLUSIONS AND RECOMMENDATIONS	278
9.	REFERENCES	284

APPENDIX A— EXPERIMENT BRIEFING AND INFORMATION PACKET

APPENDIX B—EXPERIMENT OBSERVATIONS

APPENDIX C—DISTRIBUTION LIST FOR DOT DOCUMENT

LIST OF FIGURES

Figure	Page
1 Typical construction of composite sandwich structures	4
2 Use of composite structures on Airbus 320 series aircraft	5
3 Major composite structures on A380 aircraft	6
4 Summary of composite structures on Boeing 787 aircraft	6
5 Summary of composite structures on Cessna Citation III aircraft and conventional NDI methods used to inspect them	7
6 Production of an all-composite fuselage section	7
7 Summary of advanced composite applications on A380 primary structures	8
8 Residual strength curve	11
9 Crack growth curve showing time available for fracture control	11
10 Probability of flaw detection versus flaw size	12
11 Effect of circumstances on probability of detection	13
12 Expansion in use of composite materials in aircraft construction	14
13 Sample sources of damage to composite structures	16
14 Sample damage from ground service vehicle impact	16
15 Sample damage from ground operations	17
16 Sample damage from impacts during flight	17
17 Sample damage from lightning strike	18
18 Sources of in-service damage to composite structures	18
19 Probability of impact energy as a function of take-off speed (based on runway debris collected from four U.K. military air bases)	19
20 Effects of impact on composite structures	20
21 Example of external impact creating minor surface demarcation but significant internal damage	20
22 Comparison between visible and backside damage (crushed core and backside fiber fracture) in honeycomb structures	21
23 Tap test inspections of composite aircraft structure	22
24 Evolution of the tap test method in nondestructive testing	25
25 Mechanical tap hammer specified by Airbus	26
26 Mechanical tap hammer specified by Boeing	27

27	Samples of homemade tappers used in the field including modification to Woodpecker device (addition of wood piece) to ensure that automated tap is perpendicular to the surface being inspected	27
28	General test pattern used for mechanical impact inspections	28
29	Detailed view of test pattern used for mechanical impact inspections	28
30	Sample composite honeycomb damage to be detected with mechanical tap test	29
31	Comparison of the surface stiffness deduced from the tap test with the stiffness measured in a static load test	30
32	Force versus time history for various tapping forces in a good region and a damaged region on a composite honeycomb panel	31
33	Instrumented tap test devices: DTH and Woodpecker	32
34	S-9 Sondicator low frequency bond test device	33
35	Olympus BondMaster device operating in HFBT/resonance test mode	34
36	Mechanical impedance analysis inspection with V-95 device	35
37	Schematic of pulse-echo ultrasonic inspection and A-scan signal showing reflection of UT waves at assorted interfaces	38
38	A-scan waveform from bonded and disbonded portions of a composite structure	39
39	Schematic of C-scan setup for pulse-echo ultrasonic inspection	40
40	MAUS automated ultrasonic scanning system	41
41	Sample ultrasonic signals generated from: structure without damage and structure with damage	41
42	Sample C-scan produced by an automated ultrasonic scanning device	42
43	Tapping head	44
44	Determination of the impact duration, τ , from an accelerometer output and a photograph of an oscilloscope trace with a $\tau = 968 \mu\text{s}$	44
45	Sample force pulses	45
46	Fourier transform of the impulse	45
47	Three examples of instrumented tap test devices: Woodpecker, RD ³ , and CATT	46
48	Woodpecker automated tap test device	47
49	RD ³ automated tap test device	48
50	Manual deployment of CATT device	48
51	Manual tap probe and hand-deployed cart for semi-automated scanning using CATT system	49
52	CATT system being deployed by Iowa State University developers on honeycomb flaw detection experiment test panels	49

53	Close-up of CATT tapper and transfer of data from computer to grading sheets	49
54	CATT C-scan tap test image of surface contact stiffness of a composite honeycomb sandwich panel containing engineered defects	51
55	Sample CATT C-scan of a 6-ply fiberglass test panel with flaw template overlay showing hits and misses	51
56	Two-dimensional and three-dimensional C-scan images produced from a CATT inspection of a B767 elevator	52
57	Assembled CATT tap test image of the inner and outer surfaces of a composite rudder recovered from an aircraft accident	52
58	Principle of active pulsed thermography	54
59	Laboratory thermal wave imaging system inspecting composite flaw detection panels and a portable field system inspecting an aircraft fuselage	54
60	Comparison of IR cameras for thermography inspection	55
61	TWI system equipment and inspection of aircraft	56
62	Sample thermography image showing a disbond in an aluminum fuselage tear strap structure	57
63	FLIR A40 uncooled camera inspecting the honeycomb test panels and a sample IR image from a fiberglass panel	57
64	Thermography image produced from inspection of composite laminate panel with flaw profile as shown in drawing on the right	58
65	Sample thermography images showing damage in composite structures with comparisons from three different IR cameras on 3-ply carbon honeycomb panel (all flaws identified by all cameras)	59
66	Sequence of thermal wave images from DC-9 composite doubler inspection	60
67	Examples of thermal images generated after scanning a composite structure using the LST technique	61
68	Setup of LST where IR camera and heat source move in tandem through the surface to be inspected	62
69	Panel showing the observation gate selection with respect to the heat deposition location	62
70	MISTRAS LST system—crawler used on composites	63
71	MISTRAS LST system—small area scanner	64
72	Results produced by MISTRAS LST system on a 32-ply panel with substructure elements	64
73	Equipment setup used for typical lock-in thermography inspection	66
74	MoviTHERM lock-in thermography with halogen heat lamp being used as the excitation source	67

75	Results produced by lock-in thermography on a 32-ply panel with substructure elements	67
76	LTI-5200 portable shearography system with camera on test specimen	68
77	Basic principles of shearography	69
78	Composite rudder inspection using LTI-5200 portable vacuum shearography system	70
79	Schematic of shearography inspection for near-side and far-side disbond detection	70
80	Near-side and far-side disbonds detected by LTI-5200 shearography system in A310 composite rudder	71
81	Close-up view of LTI-5200 shearography image showing flaws in a composite honeycomb structure and a sample shearography result for 6-ply fiberglass panel showing near-side and far-side flaw imaging	71
82	LTI-5200 shearographic inspection image of a scarfed repair to a honeycomb structure with anomaly indications in the repair plies	72
83	Shearography image produced from inspection of composite laminate panel (0.11" thick skin) with flaw profile as shown in drawing	72
84	Q-810 laser shearography system	73
85	Test specimen and Q-810 shearography image of wrinkles in a composite laminate	73
86	MAUS inspections on aircraft fuselage section	74
87	MAUS system operating on an aircraft fuselage with sample C-scan image produced from resonance inspection on a 6-ply carbon skin honeycomb panel	75
88	MAUS MIA inspections on honeycomb panel with sample C-scan image produced	76
89	X and Y scans of a composite honeycomb panel produced by the MAUS inspection system deployed in resonance mode	76
90	Configuration of microwave inspection system on a laboratory scan table	77
91	Basic equipment setup for microwave inspection	78
92	Microwave C-scan of a fiberglass boom structure showing the presence of interply delaminations	79
93	Microwave inspection results for fiberglass and carbon skin honeycomb panels with engineered flaws (skins bonded to Nomex honeycomb)	79
94	Sample microwave inspection results for 3-ply and 12-ply fiberglass panels with delamination, disbonds, potted core, and core splice	80
95	Schematic showing the principle of the SAM inspection method	81
96	SAM laser Doppler velocimetry camera and acoustic excitation device; composite test specimen in the background	82
97	SAM system inspecting composite honeycomb panels and transfer of scan data onto experiment grading sheets	82

98	Frequency response plots produced during the application of the SAM inspection system on an engine cowling	83
99	SAM system inspecting an engine cowling and sample image showing flaws	83
100	Sample image produced by SAM system showing flaws in a fiberglass composite honeycomb structure	84
101	PA-UT deployed in rolling wheel mechanism and contained in a single probe housing	85
102	Schematic showing the operation of an ultrasonic array that allows for the generation and acquisition of multiple UT signals	85
103	Olympus OmniScan device with a 16:128 phased array transducer	86
104	Amplitude and time of flight data produced by OmniScan inspection of composite laminate aircraft panel with flaw profile as shown	86
105	C-Scan images produced by OmniScan PA-UT inspection of 20-ply composite laminate feedback panel with the flaw profile as shown	87
106	Diagnostic sonar FlawInspecta PA-UT inspection system	88
107	FlawInspecta linear array UT system deployed on MAUS V scanner platform—linear array UT probe includes a delay line shoe	88
108	Composite honeycomb reference standard and sample FlawInspecta results—3-ply carbon skin with 1" thick core	89
109	Sample result from FlawInspecta PA-UT system on 6-ply carbon specimen	89
110	C-scan images produced by FlawInspecta MAUS V linear array UT system on a 32-ply composite laminate feedback panel with the flaw profile as shown	90
111	Schematic of air-coupled ultrasonic inspection of panel in through-transmission mode	92
112	Equipment setup for air-coupled ultrasonic inspections of composite honeycomb panels shown in background	92
113	AC-UT applied to a composite panel test specimen in both through-transmission mode and one-sided pitch/catch mode	93
114	AC-UT TTU test setup on fiberglass skin and foam core test specimen	94
115	AC-UT TTU C-scan image produced by 120 kHz inspection of composite foam core test specimen	94
116	AC-UT TTU C-scan showing disbonds in skin-to-core bondline of a composite honeycomb panel	95
117	Sample C-scan data produced by AC-UT method on composite honeycomb test specimen	95
118	Schematic of laser UT system operation	96
119	Comparison of conventional and laser UT interrogation of components	98
120	Schematic of laser UT method and deployment in gantry system and rail system	98

121	Inspection of a part using the iPLUS scan head and articulating robot	99
122	iPLUS laser-ultrasonic scan of a 16-ply composite laminate with impact damage	100
123	iPLUS laser-ultrasonic inspection of 0.111" thick composite laminate test specimen; photo on right shows the layout of the engineered flaws	100
124	iPLUS laser-ultrasonic image of a composite part containing an inclusion as highlighted	101
125	Sample results from laser UT inspection of 3-ply fiberglass panel	101
126	Schematic of the reverse geometry laminography concept	102
127	Use of array of detectors and scanning beam to produce images of layers within the part being inspected	103
128	Images highlighting the sensitivity of laminography and ability to produce slices for improved detail recognition	103
129	Comparison of normal X-ray with laminography images showing ability of laminography to detect damage in a 4" thick Lucite part	104
130	Laminography slices of machined honeycomb core that simulate a disbond in the fiberglass skin-to-core bond line	105
131	Laminography slices of interply delaminations in a 3-ply fiberglass honeycomb panel	105
132	Laminography test setup and sample image showing all flaws detected in 3-ply fiberglass panel	106
133	Test specimens used in composite honeycomb flaw detection experiment	107
134	Schematic of composite honeycomb NDI reference standards showing construction and flaw profiles	108
135	Cross-section of honeycomb reference standard design	108
136	Impactors and impactor drop-table apparatus used to produce damaged area on test panels	111
137	Sample results from calibration shots used to determine energy levels needed to produce damage in composite honeycomb panels without producing surface demarcations	112
138	Pyramid pattern matrix crack produced by impact of composite skin	112
139	Cross-section of sample impact damage in composite honeycomb experiment panels showing crushed core but no skin deformation	112
140	Engineering drawing to evaluate honeycomb reference standard design and fabrication	116
141	Construction of pillow insert for delamination flaws	117
142	Process for creating potted honeycomb core areas	118

143	TTU inspection of honeycomb panel—assessment of methods to engineer repeatable flaws	119
144	TTU C-scan showing signal attenuation produced by inserts; tests on 6-ply fiberglass laminate	119
145	TTU C-scan showing signal attenuation produced by inserts; tests on 6-ply fiberglass laminate	120
146	Specimen characterization—TTU C-scan of honeycomb test panel used to verify fabrication and location of engineered flaws	121
147	Experiment instructions being provided to supplement the written experimenter briefing and information packet	124
148	During inspections, each panel was supported around its perimeter by a foam frame to provide uniform boundary conditions	126
149	Samples of homemade tappers used in the field and modification to Woodpecker device to ensure that automated tap is perpendicular to the surface	126
150	Sample tap testing at maintenance depots and alternative tappers identified in study	127
151	Airline and aircraft maintenance depot participants in composite honeycomb flaw detection experiment	128
152	Advanced NDI companies that participated in composite honeycomb flaw detection experiment	128
153	Sample implementation of experiment in Alaska Airlines' hangar environment	129
154	CHE being implemented at American Airlines' maintenance facility	129
155	Typical experiment setup with separate inspector— Airbus facility hosting multiple airlines	130
156	Inspectors completing inspections and marking flaw detections on the test specimens—clockwise from upper right: Airbus tap hammer, Boeing tap hammer, DTH, LFBT, Woodpecker, and MIA	131
157	Honeycomb panel with sample grid markings used by inspector during inspection of panel along with flaw markings within the grid	132
158	Schematic showing the grading categories comparing experimenter flaw calls with actual flaw information	133
159	Probability of detection curves showing the performance of multiple NDI devices for a single type of test specimen: 6-ply carbon	137
160	Probability of detection curves for flaw detection performance of a single device (Woodpecker) over the range of test specimen types	137
161	Probability of detection curves quantifying inspection improvements possible through the application of advanced NDI techniques	140
162	Sample effect of inspection time on flaw detection performance (example for Boeing tap hammer on 3-ply fiberglass)	141

163	Individual and cumulative PoD curve comparisons along with tabulated values for the Airbus tap hammer deployed on 3-ply carbon test specimen set	145
164	Individual and cumulative PoD curve comparisons along with tabulated values for the Airbus tap hammer deployed on 3-ply fiberglass test specimen set	146
165	Individual and cumulative PoD curve comparisons along with tabulated values for the Airbus tap hammer deployed on 6-ply carbon test specimen set	147
166	Individual and cumulative PoD curve comparisons along with tabulated values for the Airbus tap hammer deployed on 6-ply fiberglass test specimen set	148
167	Individual and cumulative PoD curve comparisons along with tabulated values for the Airbus tap hammer deployed on 9-ply carbon test specimen set	149
168	Individual and cumulative PoD curve comparisons along with tabulated values for the Airbus tap hammer deployed on 9-ply fiberglass test specimen set	150
169	Individual and cumulative PoD curve comparisons along with tabulated values for the Boeing tap hammer deployed on 3-ply carbon test specimen set	151
170	Individual and cumulative PoD curve comparisons along with tabulated values for the Boeing tap hammer deployed on 3-ply fiberglass test specimen set	152
171	Individual and cumulative PoD curve comparisons along with tabulated values for the Boeing tap hammer deployed on 6-ply carbon test specimen set	153
172	Individual and cumulative PoD curve comparisons along with tabulated values for the Boeing tap hammer deployed on 6-ply fiberglass test specimen set	154
173	Individual and cumulative PoD curve comparisons along with tabulated values for the Boeing tap hammer deployed on 9-ply carbon test specimen set	155
174	Individual and cumulative PoD curve comparisons along with tabulated values for the Boeing tap hammer deployed on 9-ply fiberglass test specimen set	156
175	Individual and cumulative PoD curve comparisons along with tabulated values for LFBT deployed on 3-ply carbon test specimen set	157
176	Individual and cumulative PoD curve comparisons along with tabulated values for LFBT deployed on 3-ply fiberglass test specimen set	158
177	Individual and cumulative PoD curve comparisons along with tabulated values for LFBT deployed on 6-ply carbon test specimen set	159
178	Individual and cumulative PoD curve comparisons along with tabulated values for LFBT deployed on 6-ply fiberglass test specimen set	160
179	Individual and cumulative PoD curve comparisons along with tabulated values for LFBT deployed on 9-ply carbon test specimen set	161
180	Individual and cumulative PoD curve comparisons along with tabulated values for LFBT deployed on 9-ply fiberglass test specimen set	162
181	Individual and cumulative PoD curve comparisons along with tabulated values for MIA deployed on 3-ply carbon test specimen set	163

182	Individual and cumulative PoD curve comparisons along with tabulated values for MIA deployed on 3-ply fiberglass test specimen set	164
183	Individual and cumulative PoD curve comparisons along with tabulated values for MIA deployed on 6-ply carbon test specimen set	165
184	Individual and cumulative PoD curve comparisons along with tabulated values for MIA deployed on 6-ply fiberglass test specimen set	166
185	Individual and cumulative PoD curve comparisons along with tabulated values for MIA deployed on 9-ply carbon test specimen set	167
186	Individual and cumulative PoD curve comparisons along with tabulated values for MIA deployed on 9-ply fiberglass test specimen set	168
187	Individual and cumulative PoD curve comparisons along with tabulated values for WichiTech DTH deployed on 3-ply carbon test specimen set	169
188	Individual and cumulative PoD curve comparisons along with tabulated values for WichiTech DTH deployed on 3-ply fiberglass test specimen set	170
189	Individual and cumulative PoD curve comparisons along with tabulated values for WichiTech DTH deployed on 6-ply carbon test specimen set	171
190	Individual and cumulative PoD curve comparisons along with tabulated values for WichiTech DTH deployed on 6-ply fiberglass test specimen set	172
191	Individual and cumulative PoD curve comparisons along with tabulated values for WichiTech DTH deployed on 9-ply carbon test specimen set	173
192	Individual and cumulative PoD curve comparisons along with tabulated values for WichiTech DTH deployed on 9-ply fiberglass test specimen set	174
193	Individual and cumulative PoD curve comparisons along with tabulated values for Woodpecker deployed on 3-ply carbon test specimen set	175
194	Individual and cumulative PoD curve comparisons along with tabulated values for Woodpecker deployed on 3-ply fiberglass test specimen set	176
195	Individual and cumulative PoD curve comparisons along with tabulated values for Woodpecker deployed on 6-ply carbon test specimen set	177
196	Individual and cumulative PoD curve comparisons along with tabulated values for Woodpecker deployed on 6-ply fiberglass test specimen set	178
197	Individual and cumulative PoD curve comparisons along with tabulated values for Woodpecker deployed on 9-ply carbon test specimen set	179
198	Individual and cumulative PoD curve comparisons along with tabulated values for Woodpecker deployed on 9-ply fiberglass test specimen set	180
199	Comparison showing level of PoD improvement when single performance outlier is removed from the calculation—Airbus tap hammer, 6-ply fiberglass	181
200	Comparison showing level of PoD improvement when performance outliers are removed from the calculation—Airbus tap hammer, 9-ply fiberglass	181

201	Comparison showing level of PoD improvement when single performance outlier is removed from the calculation—LFBT, 6-ply fiberglass	182
202	Comparison showing level of PoD improvement when single performance outlier is removed from the calculation—LFBT, 9-ply fiberglass	182
203	Cumulative PoD curve with 95% confidence bound— Airbus tap hammer, 3-ply carbon	183
204	Cumulative PoD curve with 95% confidence bound— Airbus tap hammer, 3-ply fiberglass	183
205	Cumulative PoD curve with 95% confidence bound— Airbus tap hammer, 6-ply carbon	184
206	Cumulative PoD curve with 95% confidence bound— Airbus tap hammer, 6-ply fiberglass	184
207	Cumulative PoD curve with 95% confidence bound— Airbus tap hammer, 9-ply carbon	185
208	Cumulative PoD curve with 95% confidence bound— Airbus tap hammer, 9-ply fiberglass	185
209	Cumulative PoD curve with 95% confidence bound— Boeing tap hammer, 3-ply carbon	186
210	Cumulative PoD curve with 95% confidence bound— Boeing tap hammer, 3-ply Fiberglass	186
211	Cumulative PoD curve with 95% confidence bound— Boeing tap hammer, 6-ply carbon	187
212	Cumulative PoD curve with 95% confidence bound— Boeing tap hammer, 6-ply fiberglass	187
213	Cumulative PoD curve with 95% confidence bound— Boeing tap hammer, 9-ply carbon	188
214	Cumulative PoD curve with 95% confidence bound— Boeing tap hammer, 9-ply fiberglass	188
215	Cumulative PoD curve with 95% confidence bound—LFBT, 3-ply carbon	189
216	Cumulative PoD curve with 95% confidence bound—LFBT, 3-ply fiberglass	189
217	Cumulative PoD curve with 95% confidence bound—LFBT, 6-ply carbon	190
218	Cumulative PoD curve with 95% confidence bound—LFBT, 6-ply fiberglass	190
219	Cumulative PoD curve with 95% confidence bound—LFBT, 9-ply carbon	191
220	Cumulative PoD curve with 95% confidence bound—LFBT, 9-ply fiberglass	191
221	Cumulative PoD curve with 95% confidence bound—MIA, 3-ply carbon	192
222	Cumulative PoD curve with 95% confidence bound—MIA, 3-ply fiberglass	192
223	Cumulative PoD curve with 95% confidence bound—MIA, 6-ply carbon	193

224	Cumulative PoD curve with 95% confidence bound—MIA, 6-ply fiberglass	193
225	Cumulative PoD curve with 95% confidence bound—MIA, 9-ply carbon	194
226	Cumulative PoD curve with 95% confidence bound—MIA, 9-ply fiberglass	194
227	Cumulative PoD curve with 95% confidence bound— WichiTech DTH, 3-ply carbon	195
228	Cumulative PoD curve with 95% confidence bound— WichiTech DTH, 3-ply fiberglass	195
229	Cumulative PoD curve with 95% confidence bound— WichiTech DTH, 6-ply carbon	196
230	Cumulative PoD curve with 95% confidence bound— WichiTech DTH, 6-ply fiberglass	196
231	Cumulative PoD curve with 95% confidence bound— WichiTech DTH, 9-ply carbon	197
232	Cumulative PoD curve with 95% confidence bound— WichiTech DTH, 9-ply fiberglass	197
233	Cumulative PoD curve with 95% confidence bound— Woodpecker, 3-ply carbon	198
234	Cumulative PoD curve with 95% confidence bound— Woodpecker, 3-ply fiberglass	198
235	Cumulative PoD curve with 95% confidence bound— Woodpecker, 6-ply carbon	199
236	Cumulative PoD curve with 95% confidence bound— Woodpecker, 6-ply fiberglass	199
237	Cumulative PoD curve with 95% confidence bound— Woodpecker, 9-ply carbon	200
238	Cumulative PoD curve with 95% confidence bound— Woodpecker, 9-ply fiberglass	200
239	Individual PoD curve comparisons along with tabulated values for advanced inspection methods on 3-ply carbon (Tier 1 results)	201
240	Individual PoD curve comparisons along with tabulated values for advanced inspection methods on 3-ply carbon (Tier 2 results)	202
241	Individual PoD curve comparisons along with tabulated values for advanced inspection methods on 3-ply fiberglass (Tier 1 results)	203
242	Individual PoD curve comparisons along with tabulated values for advanced inspection methods on 3-ply fiberglass (Tier 2 results)	204
243	Individual PoD curve comparisons along with tabulated values for advanced inspection methods on 6-ply carbon (Tier 1 results)	205
244	Individual PoD curve comparisons along with tabulated values for advanced inspection methods on 6-ply carbon (Tier 2 results)	206
245	Individual PoD curve comparisons along with tabulated values for advanced inspection methods on 6-ply fiberglass (Tier 1 results)	207
246	Individual PoD curve comparisons along with tabulated values for advanced inspection methods on 6-ply fiberglass (Tier 2 results)	208

247	Individual PoD curve comparisons along with tabulated values for advanced inspection methods on 9-ply carbon (Tier 1 results)	209
248	Individual PoD curve comparisons along with tabulated values for advanced inspection methods on 9-ply carbon (Tier 2 results)	210
249	Individual PoD curve comparisons along with tabulated values for advanced inspection methods on 9-ply fiberglass (Tier 1 results)	211
250	Individual PoD curve comparisons along with tabulated values for advanced inspection methods on 9-ply fiberglass (Tier 2 results)	212
251	Cumulative PoD curve comparisons along with tabulated values of all conventional NDI devices on 3-ply carbon (average results for all inspectors)	213
252	Cumulative PoD curve comparisons along with tabulated values of all conventional NDI devices on 3-ply fiberglass (average results for all inspectors)	214
253	Cumulative PoD curve comparisons along with tabulated values of all conventional NDI devices on 6-ply carbon (average results for all inspectors)	215
254	Cumulative PoD curve comparisons along with tabulated values of all conventional NDI devices on 6-ply fiberglass (average results for all inspectors)	216
255	Cumulative PoD curve comparisons along with tabulated values of all conventional NDI devices on 9-ply carbon (average results for all inspectors)	217
256	Cumulative PoD curve comparisons along with tabulated values of all conventional NDI devices on 9-ply fiberglass (average results for all inspectors)	218
257	Comparison of all mechanical tap test devices on 3-ply carbon	219
258	Comparison of all mechanical tap test devices on 3-ply fiberglass	219
259	Comparison of all mechanical tap test devices on 6-ply carbon	220
260	Comparison of all mechanical tap test devices on 6-ply fiberglass	220
261	Comparison of all mechanical tap test devices on 9-ply carbon	221
262	Comparison of all mechanical tap test devices on 9-ply fiberglass	221
263	Cumulative PoD curves for Airbus tap hammer along with tabulated values on all panel types (average results for all inspectors)	222
264	Cumulative PoD curves for Boeing tap hammer along with tabulated values on all panel types (average results for all inspectors)	223
265	Cumulative PoD curves for LFBT along with tabulated values on all panel types (average results for all inspectors)	224
266	Cumulative PoD curves for MIA along with tabulated values on all panel types (average results for all inspectors)	225
267	Cumulative PoD curves for WichiTech DTH along with tabulated values on all panel types (average results for all inspectors)	226

268	Cumulative PoD curves for Woodpecker along with tabulated values on all panel types (average results for all inspectors)	227
269	PoD curve comparisons for CATT along with tabulated values on all panel types	228
270	PoD curve comparisons for MAUS Resonance 1 inspections along with tabulated values on all panel types (results shown for resonance experimenter #1 only)	229
271	PoD curve comparisons for SAM inspections along with tabulated values on all panel types	230
272	PoD curve comparisons for shearography inspections along with tabulated values on all panel types	231
273	PoD curve comparisons for thermography inspections along with tabulated values on all panel types	232
274	PoD curve comparisons for MAUS IV MIA inspections along with tabulated values on all panel types	233
275	PoD curve comparisons for AC-UT inspections (TTU mode) along with tabulated values on all panel types	234
276	PoD curve comparisons for laminography inspections along with tabulated values on all panel types	235
277	PoD curve comparisons for microwave inspections along with tabulated values on all panel types	236
278	PoD curve comparisons for FlawInspecta UT array along with tabulated values on all panel types	237
279	PoD curve comparisons for laminography showing the improvement when impact and edge (inspection image overlap) flaws are removed from PoD calculation on 6-ply carbon	238
280	PoD curve comparisons for laminography showing the improvement when impact and edge (inspection image overlap) flaws are removed from PoD calculation on 6-ply fiberglass	238
281	PoD curve comparisons for laminography showing the improvement when impact and edge (inspection image overlap) flaws are removed from PoD calculation on 9-ply carbon	239
282	PoD curve comparisons for laminography showing the improvement when impact and edge (inspection image overlap) flaws are removed from POD calculation on 9-ply fiberglass	239
283	PoD curve comparisons along with tabulated values for laser-ultrasonic inspections with exception that includes removing flaws located in center area of specimen from PoD calculations on 3-ply fiberglass	240
284	PoD curve comparisons along with tabulated values for advanced inspection methods and best performing conventional method on 3-ply carbon	241

285	PoD curve comparisons along with tabulated values for advanced inspection methods and best performing conventional method on 3-ply fiberglass	242
286	PoD curve comparisons along with tabulated values for advanced inspection methods and best performing conventional method on 6-ply carbon	243
287	PoD curve comparisons along with tabulated values for advanced inspection methods and best performing conventional method on 6-ply fiberglass	244
288	PoD curve comparisons along with tabulated values for advanced inspection methods and best performing conventional method on 9-ply carbon	245
289	PoD curve comparisons along with tabulated values for advanced inspection methods and best performing conventional method on 9-ply fiberglass	246
290	Scatter diagram showing effect of inspection time on PoD values for 3-ply panels	257
291	Scatter diagram showing effect of inspection time on PoD values for 6-ply panels	258
292	Scatter diagram showing effect of inspection time on PoD values for 9-ply panels	259
293	Scatter diagram showing effect of inspection time on false calls for 3-ply panels	260
294	Scatter diagram showing effect of inspection time on false calls for 6-ply panels	261
295	Scatter diagram showing effect of inspection time on false calls for 9-ply panels	262
296	Scatter diagram showing the effect of the number of false calls on PoD values for 3-ply panels	263
297	Scatter diagram showing the effect of the number of false calls on PoD values for 6-ply panels	264
298	Scatter diagram showing the effect of the number of false calls on PoD values for 9-ply panels	265

LIST OF TABLES

Table	Page
1. Inspection methods applied to the composite honeycomb flaw-detection experiment	24
2. Digital tap test results from Mitsui Woodpecker comparing flaw detection in Nomex and fiberglass cores	113
3. Digital tap test results from Mitsui Woodpecker showing relative stiffness values for different cores	114
4. Test specimen matrix for composite honeycomb flaw-detection study	115
5. Sample S/N data from various flaws demonstrating the viability of each flaw for use in the composite honeycomb flaw detection experiment	122
6. Inspectors' NDI experience level for conventional methods	135
7. Advanced NDI methods deployed on composite honeycomb flaw-detection experiment	135
8. Summary of overall flaw detection for 6-ply fiberglass construction — PoD levels along with false calls and ability to correctly size flaws	139
9. Inspection summary—description of all figures and tables showing the variables captured in the results	143
10. Average inspection times per 18" x 18" panel and max/min times for 3-ply panels —conventional NDI methods	247
11. Average inspection times per 18" x 18" panel and max/min times for 6-ply panels —conventional NDI methods	248
12. Average inspection times per 18" x 18" panel and max/min times for 9-ply panels —conventional NDI methods	248
13. Average inspection times per 18" x 18" panel and max/min times for all panels—advanced NDI methods (times shown in minutes)	249
14. Summary of individual and average false calls for all inspectors and false call averages per inspection method and panel type—conventional NDI	250
15. Average number of false calls produced by conventional NDI devices on carbon and fiberglass specimens	252
16. False calls generated by advanced inspection techniques (arranged by panel type)	252
17. Backside flaw detection for all inspectors and average backside flaws detected per inspection method and panel type—conventional NDI	253
18. Summary of average backside flaw detection for conventional inspection techniques listed by panel type	255
19. Backside flaw detection for advanced inspection techniques by panel type (note: AC-UT was executed in through-transmission mode)	256

20.	Summary of all NDI performance for 3-ply carbon and fiberglass test specimens —flaw sizing, overall 90% PoD levels, and false calls	266
21.	Summary of all NDI performance for 6-ply carbon and fiberglass test specimens —flaw sizing, overall 90% PoD levels, and false calls	268
22.	Summary of all NDI performance for 9-ply carbon and fiberglass test specimens —flaw sizing, overall 90% PoD levels, and false calls	270
23.	Summary of all NDI flaw-detection capability for 3-ply carbon and fiberglass test specimens—overall flaw detection, highest detection (by individual inspector), lowest detection (by individual inspector), overall 90% PoD levels, and false calls	272
24.	Summary of all NDI flaw-detection capability for 6-ply carbon and fiberglass test specimens—overall flaw detection, highest detection (by individual inspector), lowest detection (by individual inspector), overall 90% PoD levels, and false calls	274
25.	Summary of all NDI flaw-detection capability for 9-ply carbon and fiberglass test specimens—overall flaw detection, highest detection (by individual inspector), lowest detection (by individual inspector), overall 90% PoD levels, and false calls	276

LIST OF ACRONYMS

AANC	Airworthiness Assurance NDI Validation Center
AC	Advisory circular
ARP	Aerospace recommended practice
AC-UT	Air-coupled ultrasonic testing
CACRC-ITG	Commercial Aircraft Composite Repair Committee Inspection Task Group
CATT	Computer-aided tap tester
CCD	Charge-coupled device
CHE	Composite Honeycomb Flaw Detection Experiment
DTA	Damage tolerance analysis
DTH	Digital tap hammer
FWC	Full waveform capture
HFBT	High frequency bond testing
iPLUS	iPhoton laser ultrasonic system™
IR	Infrared
LFBT	Low frequency bond testing
LST	Line Scan Thermography™
LUS	Laser ultrasonics
MAUS	Mobile Automated Scanner
MIA	Mechanical impedance analysis
MRO	Maintenance and repair organizations
NDI	Nondestructive inspection
NDT	Nondestructive test
NDTM	Nondestructive testing manuals
OEM	Original equipment manufacturer
PA-UT	Phased array ultrasonic
PE-UT	Pulse-echo ultrasonic
PoD	Probability of detection
QMI	Quality Material Inspection
RD ³	Rapid Damage Detection Device
RF	Radio frequency
RGX	Reverse Geometry X-ray®
S/N	Signal-to-noise
SAM	Structural Anomaly Mapping
TTU	Through-transmission ultrasonic
TWI	Thermal Wave Imaging
UT	Ultrasonic testing
WFD	Widespread fatigue damage

EXECUTIVE SUMMARY

The aircraft industry continues to increase its use of composite materials. This is most noteworthy in the area of principle structural elements. The extreme damage tolerance and high strength-to-weight ratio of composites have motivated designers to expand the role of fiberglass and carbon graphite in aircraft structures. This has placed greater emphasis on the development of improved nondestructive inspection (NDI) methods that are more reliable and sensitive than conventional NDI. The Federal Aviation Administration's (FAA) Airworthiness Assurance NDI Validation Center (AANC) at Sandia Laboratories has been pursuing this goal via a host of studies on inspection of composite structures. Through the FAA-AANC's participation in the Commercial Aircraft Composite Repair Committee Inspection Task Group, this team has been investigating the need for improved inspections of composite structures.

The majority of composite honeycomb structure inspections are performed visually and supplemented by tap test methods. Tap testing, which uses a human-detected change in acoustic response to locate flaws, and more sophisticated NDI methods such as ultrasonics or thermography have been applied to an increasing number of applications to detect voids, disbonds, and delaminations in adhesively bonded composite aircraft parts. Low frequency bond testing and mechanical impedance analysis tests are often used to inspect thicker laminates. A probability of detection experiment was completed to assess the performance of both conventional and advanced NDI techniques.

A series of composite honeycomb specimens with statistically relevant flaw profiles was inspected using both human tap test equipment and new inspection techniques, which have recently been introduced to automate and improve composite NDI. Industry-wide performance curves have been produced to establish: 1) how well current inspection techniques are able to reliably find flaws in composite honeycomb structure, and 2) the degree of improvements possible through the integration of more advanced NDI techniques and procedures. This study compared the results from a wide array of NDI methods, and identified limitations and optimum applications for specific inspection methods while producing key recommendations for improving the performance of NDI.

1. INTRODUCTION AND BACKGROUND

1.1 OVERVIEW OF COMPOSITE HONEYCOMB FLAW DETECTION EXPERIMENT

In 1991, the FAA established an Airworthiness Assurance NDI Validation Center (AANC) at Sandia National Laboratories. Its primary mission is to support technology development, validation, and transfer to industry to enhance airworthiness and improve the aircraft maintenance practices of the commercial aviation industry. The rapidly increasing use of composites on commercial airplanes coupled with the potential for economic savings associated with their use in aircraft structures means that the demand for composite materials technology will continue to increase. Inspecting these composite structures is a critical element in assuring their continued airworthiness. The FAA-AANC at Sandia National Laboratories, in conjunction with the Commercial Aircraft Composite Repair Committee Inspection Task Group (CACRC-ITG), completed a study to assess conventional and advanced inspection methods as applied to flaw detection in honeycomb composite structures.

Aircraft reliability is a critical concern that is receiving increased attention in today's aviation industry. More sophisticated methods and enhanced training of maintenance personnel are being deployed in an effort to increase aircraft safety as well as aircraft availability. To safely extend the operational life of their aircraft, operators may need to perform additional inspections. Nondestructive inspection (NDI) becomes critical when addressing widespread fatigue damage (WFD) for which requirements may call for the detection of exceedingly small damage. As composite materials are increasingly used in principal structural elements, the application of NDI methods suited for composite and bonded structures becomes more important. The evolution of advanced NDI methods produces a number of inspection options that can enhance sensitivity, improve reliability, minimize human factors concerns, and even reduce operating costs.

The aircraft industry continues to increase its use of composite materials. This is most noteworthy in the area of principle structural elements. The extreme damage tolerance and high strength-to-weight ratio of composites have motivated designers to expand the role of fiberglass and carbon graphite in aircraft structures. This has placed greater emphasis on the development of improved NDI methods that are more reliable and sensitive than conventional NDI and the optimization of current inspection practices. The FAA-AANC has been pursuing this goal via a host of studies addressing the inspection of composite structures. The FAA-AANC, in collaboration with the CACRC-ITG, have been investigating the performance of conventional inspection methods and determining the need for improved inspections of composite structures.

The majority of composite honeycomb structure inspections are performed visually and supplemented by tap test methods. Tap testing, which uses a human-detected change in acoustic response to locate flaws, and more sophisticated NDI methods (e.g., ultrasonics or thermography), has been applied to an increasing number of applications to detect voids, disbonds, and delaminations in adhesively bonded composite aircraft parts. Low-frequency bond testing and mechanical impedance analysis tests are often used to inspect thicker laminates.

The FAA-ANNC conducted the Composite Honeycomb Flaw Detection Experiment (CHE) to assess flaw detection in composite honeycomb aircraft structures using both conventional and advanced NDI techniques. The CHE involves the use of a set of composite honeycomb test

specimens containing engineered flaws that were shipped to airlines and third-party maintenance depots for the purpose of acquiring flaw detection data from aviation industry inspectors. A series of composite honeycomb specimens with statistically relevant flaw profiles was inspected using both human tap test equipment and new inspection techniques that have recently been introduced to automate and improve composite NDI. The majority of the testing was in the form of blind probability of detection (PoD) studies, whereas other portions of the testing determined signal-to-noise ratios from which flaw detection could be inferred. The primary factors affecting inspections were incorporated into this study, including composite materials and construction type, flaw profiles (e.g., voids, heat damage, disbonds, delaminations, and impact damage), mechanical interactions (e.g., impact and audible response), subsurface damage, and environmental conditions. The critical phase of this effort used airline personnel to study PoD performance in the field and to formulate improvements to conventional inspection practices. Industry-wide performance curves have been produced to establish: 1) how well current inspection techniques are able to reliably find flaws in composite honeycomb structure, and 2) the degree of improvements possible through the integration of more advanced NDI techniques and procedures.

The conventional composite inspection techniques studied were: Boeing and Airbus manual tap hammers, low frequency bond testing (LFBT), high frequency bond testing (resonance), through-transmission ultrasonics (TTU), and mechanical impedance analysis (MIA). In addition, 18 different advanced NDI methods were evaluated in these experiments, including: Mitsui Woodpecker automated tap hammer, WichiTech Digital Tap Hammer (DTH), computer-aided tap tester (CATT), thermography (pulsed and induction), pulse-echo ultrasonic testing (UT), air-coupled UT, MAUS C-scanning in MIA and resonance mode, laser UT, shearography, microwave, Structural Anomaly Mapping (SAM), UT linear array, digital acoustic video, laminography, terahertz imaging, and BaNDIcoot resonance scanning.

The CACRC-ITG completed an effort to develop solid laminate and honeycomb NDI reference standards [1] to aid the uniform and optimum application of aircraft NDI techniques. As a follow-on activity, the CACRC-ITG completed a multiyear study to assess flaw detection capabilities in composite honeycomb structure. This document summarizes the experiment purpose, the test variables included in the CHE study, the experiment planning issues, the set of test specimen designs, and a comprehensive set of results from the conventional and advanced NDI methods evaluated in this experiment.

1.1.1 Description of CHE:

The test articles for this experiment were modeled after the general range of construction scenarios found on commercial aircraft. A set of 44 composite honeycomb test specimens containing engineered and natural flaws were manufactured. Flaws of various size, shape, and type were randomly located across the specimen footprints. Details of the specimen construction are as follows:

- Skin type: carbon graphite and fiberglass
- Skin thickness: panels have three-, six-, and nine-ply skins
- Core: 1" thick Nomex[®] core

- Paint: all panels are painted as per current aircraft specifications

The flaw types included in the test specimens are:

- Interply delaminations (pillow inserts).
- Machined core disbonds simulating the presence of an air gap.
- Pillow insert disbonds simulating tight contact but no adhesive strength (kissing disbond).
- Naturally formed impact damage (e.g., crushed core, disbonds, delaminations, and broken fibers).

One critical technical challenge required a parallel research effort to determine how to produce representative flaws in composite honeycomb structure. During the experiment, each blind inspection was preceded by inspections on appropriate reference standards supplied by the experiment monitors. The inspectors were given information on the manufactured flaws present in the reference standards and allowed to use these specimens to ensure the proper operation of their equipment.

Over the course of several years, the CHE traveled to airlines, third-party maintenance depots, and aircraft manufacturers to acquire flaw detection data. The experiment was deployed in a hangar to provide a representative inspection environment, including impediments such as poor lighting and noise distractions. The experiment required approximately two to three days of each inspector's time. In general, inspectors were asked to locate and size hidden flaws in the test specimens. After a sufficient number of inspectors completed the experiment, industry-wide performance curves were established to determine how well current inspection techniques are able to reliably find flaws in composite laminate structure. A total of 75 inspectors from 22 airlines as well as maintenance and repair organizations located around the world participated in the experiment. Inspector feedback on performance provided excellent training for the experimenter, whereas their results produced a valuable baseline of how well the industry is able to inspect composite structures (e.g., flaw hits/misses, false calls, flaw sizing, effects of construction scenarios, and effects of environment). The test program was intended to evaluate the technical capability of the inspection procedures and equipment (i.e., NDI method). Key insights regarding measures to improve inspection performance were obtained. The results are published in this report as industry-wide performance measures, and all links to specific aircraft maintenance depots have been permanently removed. These blind tests produced statistically valid PoD curves that are representative of the industry as a whole. Furthermore, results from the 18 advanced NDI methods allowed the team to quantify the degree of inspection improvements possible via the application of more sophisticated inspection methods and procedures. The experiment results also allowed the team to determine which NDI methods possess unique capabilities to satisfy specific inspection requirements.

1.1.2 Results Obtained From CHE

Each inspection technique was evaluated using the following performance attributes: 1) accuracy and sensitivity; 2) data analysis capabilities; 3) versatility; 4) portability; 5) complexity; 6) human factors; and 7) inspection time. The most important of these parameters was the quantitative metrics, as they are objective standards that can be numerically counted. Accuracy is

the ability to detect flaws reliably and correctly in composite structures and repairs without overcalling (false calls). Sensitivity is the extent to which the inspection system responds to flaws as a function of size, type, and location in the structure (e.g., proximity to repair edges, and underlying or adjacent structural elements). Each inspector's flaw calls were used to identify hits (calls with any amount of overlap between the call and the solution), misses (no call for an area of a known flaw), false calls (call with no overlap of a flaw), and the degree of overlap between experimenter calls and actual flaw areas. Typical results include PoD curves, tabulated flaw detection and false call data, and scatter charts relating accuracy in delineating flaw size and shape. All of the data were sorted by the attributes of the structure being inspected. For example, some PoD curves compare conventional inspection methods for a particular construction type of honeycomb panel. Another set of PoD curves may compare the results from several advanced NDI methods with those obtained from one of the better-performing conventional methods.

1.2 INCREASING USE OF COMPOSITES IN AIRCRAFT STRUCTURES

Composite materials are increasingly becoming the material of choice for aircraft designers because of their global benefits. Engineers estimate that building comparable fuselages with aluminum would take thousands of components and fasteners and require extensive tooling and dozens of technicians. An aircraft would weigh approximately 20% more and consume more fuel. Through the use of composite technology construction, engineers can cut the number of parts in an assembly in half. This results in significant cost savings. Other benefits of composite technology include lower acquisition costs; lower operating costs; and improved maintainability, reliability, and durability. Figure 1 shows a typical composite honeycomb construction with laminate skins, produced from fiberglass, carbon, or other epoxy-impregnated materials, bonded to a honeycomb core using an adhesive film. The laminate skins may be pre-cured prior to the secondary honeycomb bonding process. The skins may also be co-cured where the various plies in the skins are cured simultaneously with the adhesive layer between the skins and the core.

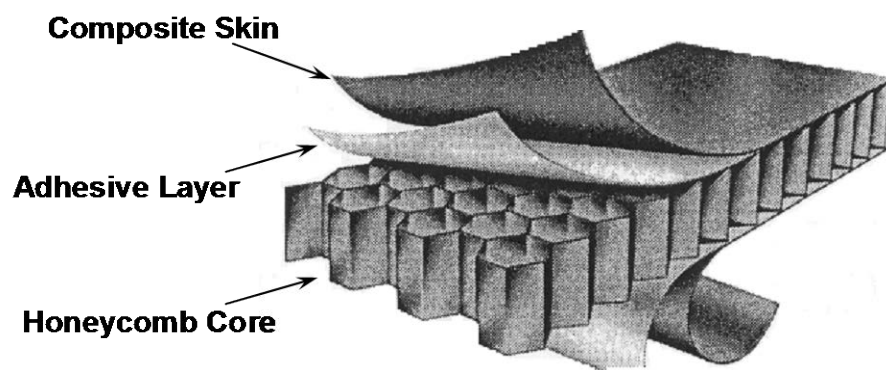


Figure 1. Typical construction of composite sandwich structures

New transport and commuter category aircraft, such as the Boeing 787 and the Airbus A350, are being produced with a majority of their structure composed of composite materials. Typical damage encountered in composite structures includes: 1) disbonds and delaminations stemming from normal flight loads; 2) fluid ingress; 3) impact damage; 4) lightning strikes; 5) deterioration from contact with fluids, such as paint strippers or hydraulic fluids; and 6) extreme heat and

ultraviolet exposure. Each of these elements can produce hidden damage that may be difficult to visually detect yet are significantly detrimental to the strength of the structure.

References 1–3 describe a successful effort to develop an industry-wide set of composite reference standards. The standards are being used in NDI equipment calibration for damage assessment and post-repair inspection of commercial aircraft composites. Final review of these honeycomb and solid laminate standards was completed, and several aircraft manufacturers have already adopted these standards into their maintenance manuals. The activity described herein complements the composite reference standard development effort. The purpose of this experiment was to assess the ability of conventional and emerging NDI techniques to inspect for flaws in representative composite structures. The experiment established the sensitivities and limitations of applicable NDI methods. Other observations accumulated during the test program will allow for inspection improvements via optimized procedures and practices.

Figures 2–5 depict the increasing use of composite materials in aircraft manufacture and highlight the wide range of composite structures on commercial aircraft. The photos in figures 6 and 7 show several finished composite aircraft components. They underscore the degree of complexity associated with these structures and the size of components that are being fabricated from composites.

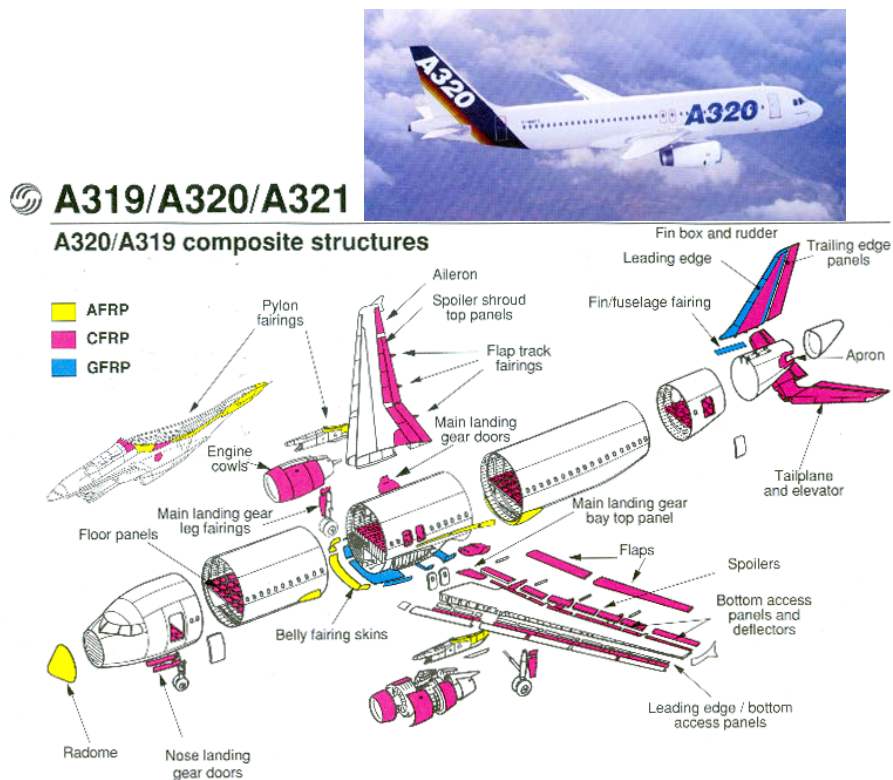


Figure 2. Use of composite structures on Airbus 320 series aircraft

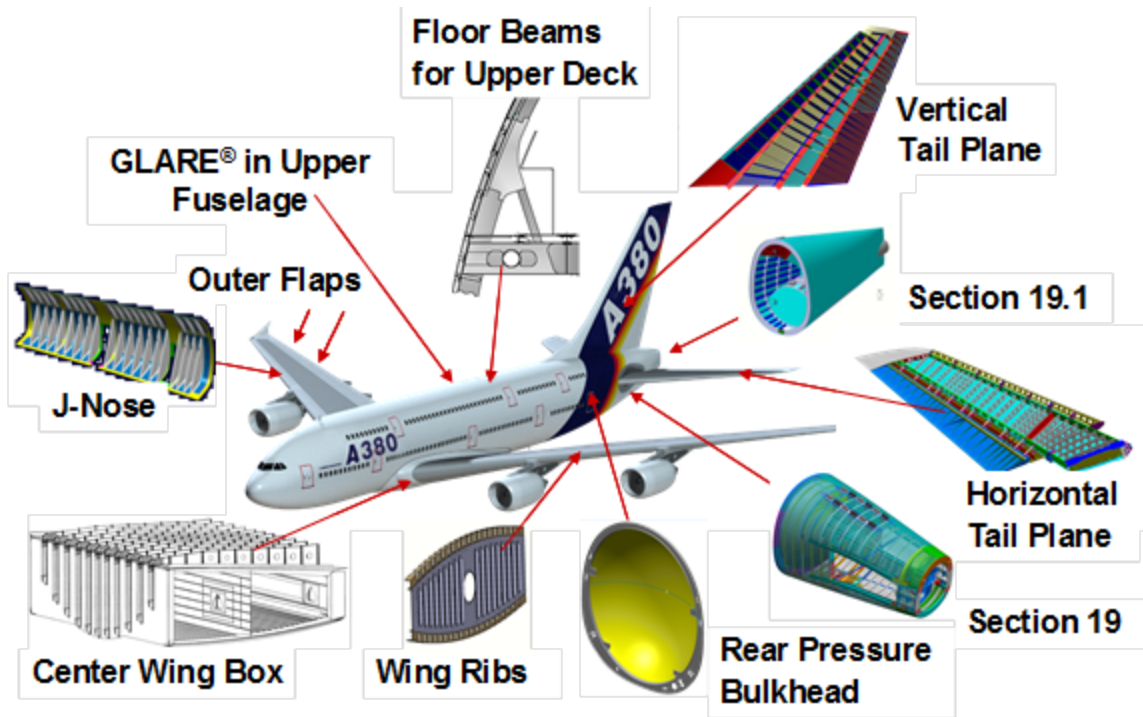


Figure 3. Major composite structures on A380 aircraft

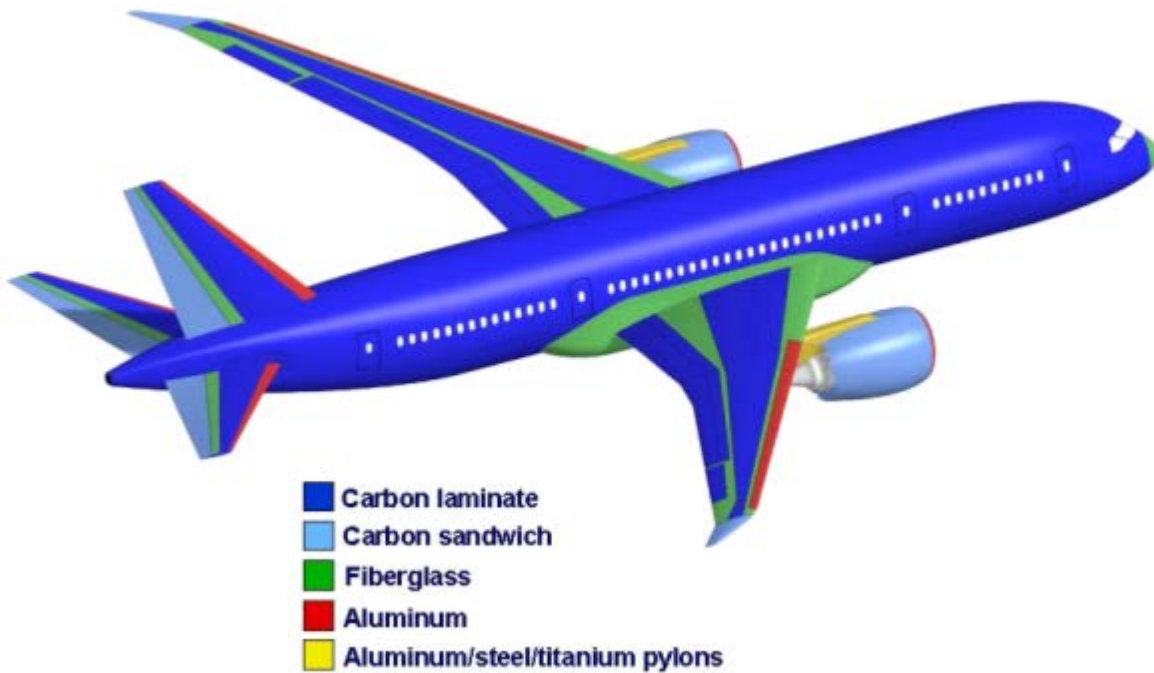








Figure 4. Summary of composite structures on Boeing 787 aircraft

	MIA or pitch-catch
	Pitch-catch
	Resonance
	Resonance
	N/A
	MIA or pitch-catch
	Pitch-catch

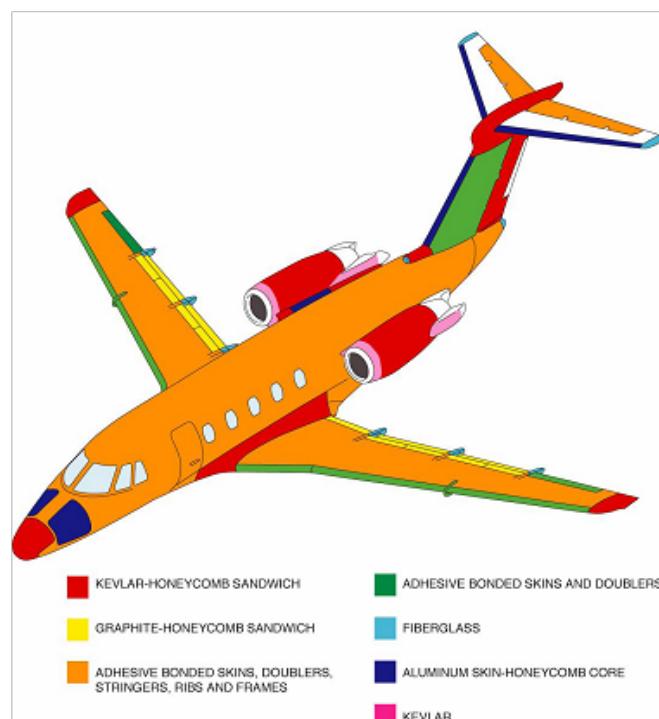


Figure 5. Summary of composite structures on Cessna Citation III aircraft and conventional NDI methods used to inspect them



Figure 6. Production of an all-composite fuselage section



Figure 7. Summary of advanced composite applications on A380 primary structures

1.3 BACKGROUND ON IN-SERVICE INSPECTION NEEDS FOR COMPOSITE STRUCTURES

Composites have many advantages pertaining to their use as aircraft structural materials. These advantages include their high specific strength and stiffness, resistance to damage by fatigue loading, and resistance to corrosion. In addition, new analyses, operational experience, and aircraft safe-life extension programs may produce additional NDI requirements. The expanded use of composite structures, coupled with difficulties associated with damage tolerance analysis (DTA) of composites, create a greater need for NDI methods that can effectively identify degradation and damage in composite structures. This must be balanced with the need for simple, low-cost NDI methods for detecting damage in composite structures and repair configurations. Recent developments in advanced NDI techniques have produced a number of new inspection options. Many of these methods can be categorized as wide-area techniques that produce two-dimensional flaw maps of the structure. New inspection techniques available today or in the immediate future hold promise for reducing the direct maintenance costs while improving the capacity for detecting damage. Improved NDI techniques could also help detect damage in its early stages, thus, improving safety and reducing the costs associated with the restoration of a larger affected area.

The reliability, safety, and availability of aircraft can be improved, if deemed necessary, through the application of more sophisticated NDI methods and with enhanced procedures and improved training of maintenance personnel. This study compared the results from a wide array of NDI methods, and identified limitations and optimum applications for specific inspection methods. Reference 4 previously addressed the application of conventional pulse-echo UT NDI methods to establish an aviation industry performance baseline for flaw detection capability.

1.4 DAMAGE TOLERANCE APPROACH TO ESTABLISH INSPECTION INTERVALS

Today's transport category aircraft were designed using the damage tolerance approach, such that they can meet continuing structural airworthiness requirements for an indefinite period. This approach is predicated on the use of an effective inspection and corrective maintenance program that effectively ensures structural integrity over the life of the aircraft. Damage tolerance is the attribute of the structure that permits it to retain its required residual strength without detrimental structural deformation for a period of use after the structure has sustained a given level of fatigue, corrosion, and accidental or discrete source damage. The maintenance program may be adjusted to reflect real-time operational experience and analytical findings through the use of modern analysis tools, testing, and trends assessment of historical operation. Effective maintenance programs can ensure that airplane structures continue to meet the required ultimate strength, fatigue, and damage tolerance requirements.

Inspection requirements (sensitivity and inspection intervals) are driven by DTA. However, the multiple plies of composite material, composite lamina (anisotropic) response characteristics, and adhesive layers make the analysis quite complex and hinder the calculation of an exact DTA. It is difficult to determine the effects of flaw size and the point at which a flaw size/location becomes critical. This is especially true of disbond, delamination, and porosity flaws. Thus, an increased emphasis is placed on quantifying the probability that a flaw of a particular size and

location will be detected by a piece of NDI equipment. In any surveillance of aircraft structure, there are three main aspects to the inspection requirements:

1. The DTA that determines the flaw onset and growth data (especially critical flaw size information)
2. The sensitivity, accuracy, and repeatability of NDI techniques, which, in concert with the DTA, establishes the minimum inspection intervals
3. The impediments with which the NDI techniques must contend while achieving the required level of sensitivity.

In addition to this report, detailed discussions on damage tolerance assessments for composite materials are presented in references 5–9.

Damage tolerance is the ability of an aircraft structure to sustain damage, without catastrophic failure, until such time that the component can be repaired or replaced. The U.S. Federal Aviation Requirements (i.e., Title 14 Code of Federal Regulations Part 25) specify that the residual strength shall not fall below limit load, P_L , which is the load anticipated to occur once in the life of an aircraft. This establishes the minimum permissible residual strength, $\sigma_p = \sigma_L$. To varying degrees, the strength of composite doubler repairs is affected by crack, disbond, and delamination flaws. The residual strength as a function of flaw size can be calculated using fracture mechanics concepts. Figure 8 shows a sample residual strength diagram. The residual strength curve is used to relate this minimum permissible residual strength, σ_p , to a maximum permissible flaw size, a_p .

A damage control plan is needed to safely address any possible flaws that may develop in a structure. NDI is the tool used to implement the damage control plan. Once the maximum permissible flaw size is determined, the additional information needed to properly apply NDI is the flaw growth versus time or number of cycles. Figure 9 contains a flaw growth curve. The first item of note is the total time, or cycles, required to reach a_p . A second parameter of note is a_d , which is the minimum detectable flaw size. A flaw smaller than a_d would likely be undetected and, thus, inspections performed in the time frame prior to n_d would be of little value. The time, or number of cycles, associated with the bounding parameters a_d and a_p is set forth by the flaw growth curve and establishes $H(\text{inspection})$. Safety is maintained by providing at least two inspections during $H(\text{inspection})$ to ensure flaw detection between a_d and a_p .

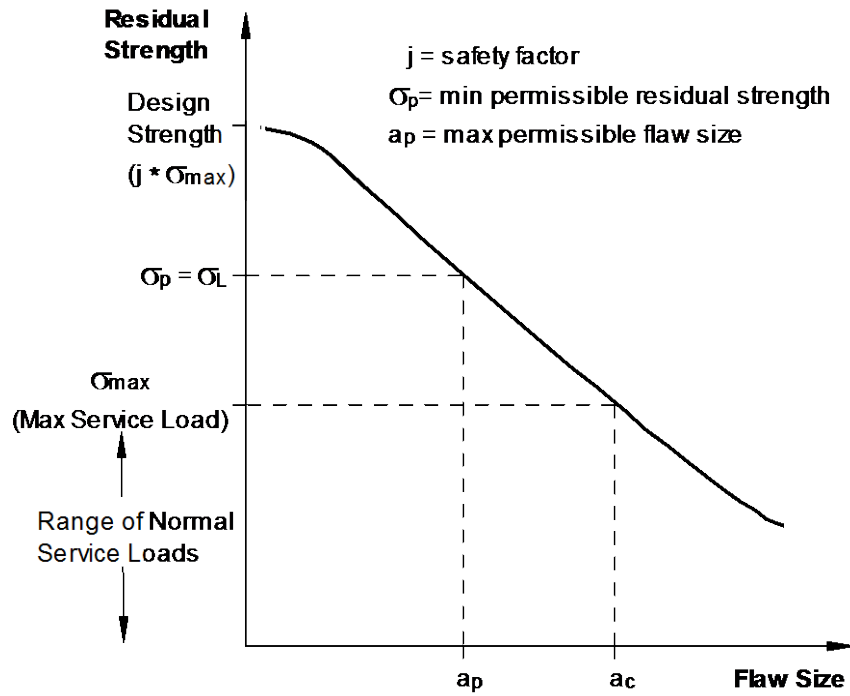


Figure 8. Residual strength curve

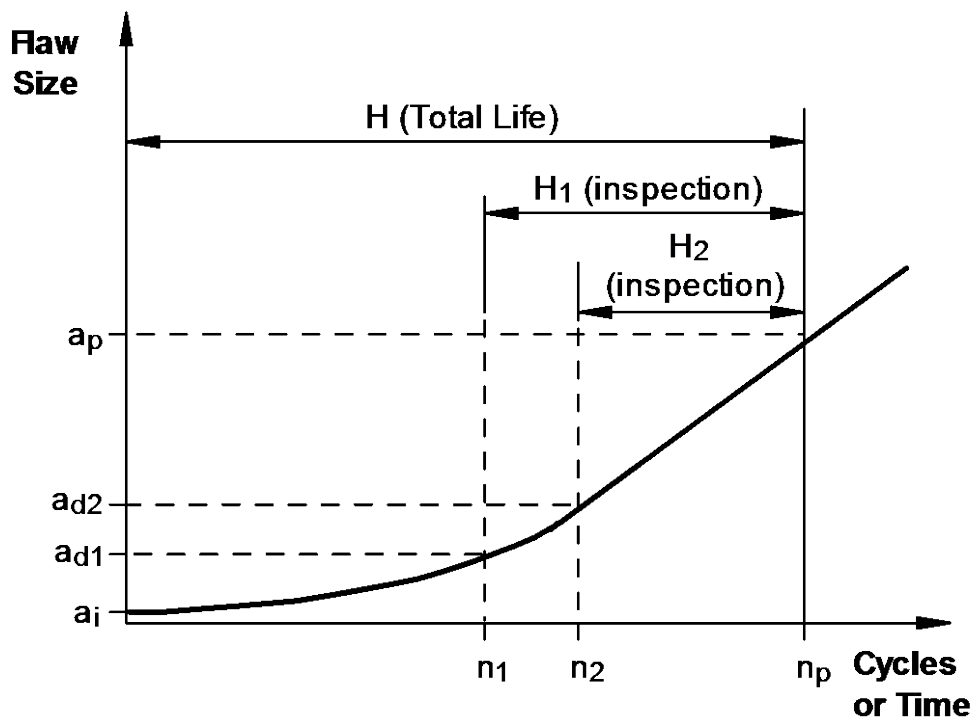


Figure 9. Crack growth curve showing time available for fracture control

1.4.1 Inspection intervals:

An important NDI feature highlighted by figure 9 is the large effect that NDI sensitivity has on the required inspection interval. Two sample flaw detection levels, $a_d(1)$ and $a_d(2)$, are shown along with their corresponding intervals, n_{I1} and n_{I2} . Because of the gradual slope of the flaw growth curve in this region, it can be seen that the inspection interval $H_1(\text{inspection})$ can be much larger than $H_2(\text{inspection})$ if NDI can produce just a slightly better flaw detection capability. As the detectable flaw size provides the basis for the inspection interval, it is essential that quantitative measures of flaw detection are performed for each NDI technique applied to the structure of interest. This quantitative measure is represented by a PoD curve such as the one shown in figure 10. Regardless of the flaw size, the PoD never quite reaches 1 (100% PoD). Inspection sensitivity requirements normally ask for a 90–95% POD at a_p . For any given inspection task, the PoD is affected by many factors, such as the skill and experience of the inspector, accessibility to the structure, exposure of the inspection surface, and confounding attributes (e.g., underlying structure or the presence of fasteners). Thus, the effects of circumstances on PoD must be accounted for in any NDI application and associated damage control plan. Figure 11 shows how increasingly difficult circumstances can degrade the PoD of an NDI technique.

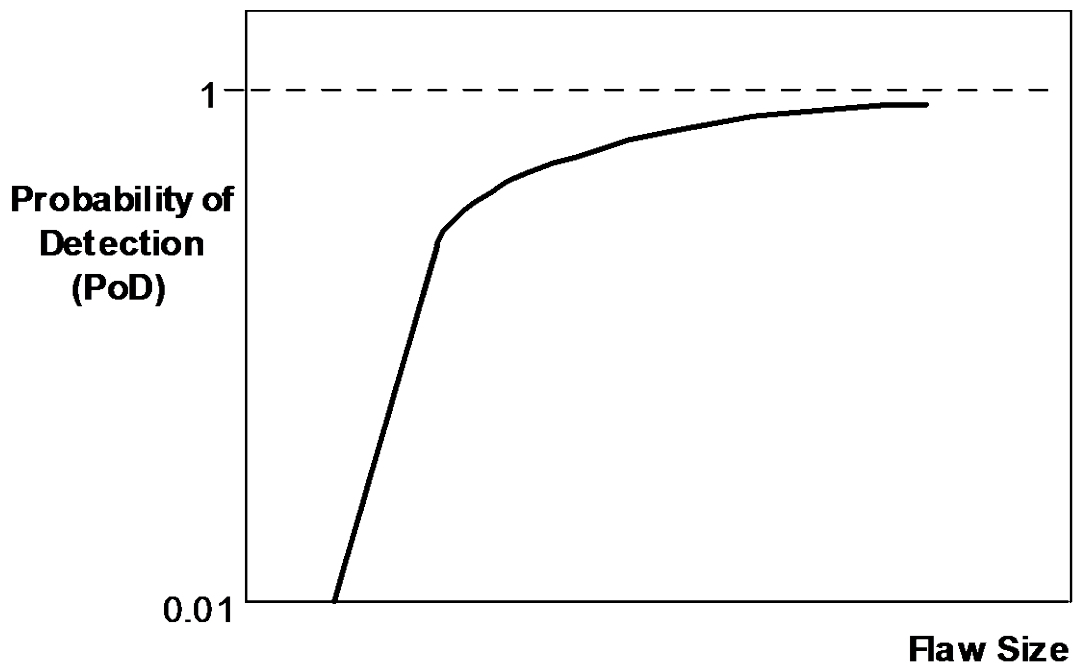


Figure 10. Probability of flaw detection versus flaw size

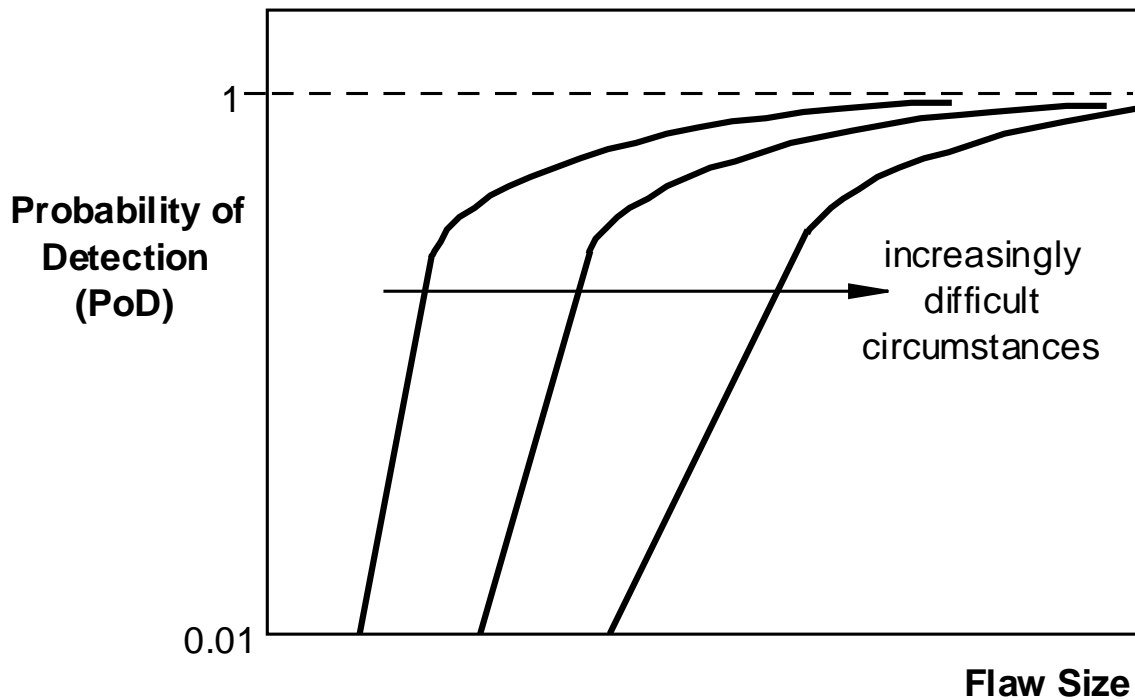


Figure 11. Effect of circumstances on probability of detection

2. PURPOSE OF COMPOSITE HONEYCOMB FLAW DETECTION EXPERIMENT

Composites have many advantages for use as aircraft structural materials, including their high specific strength and stiffness, resistance to damage by fatigue loading, light weight, and resistance to corrosion. The percentage of composite materials used on new aircraft continues to rise, most noteworthy in the area of principle structural elements. This expanded use, coupled with difficulties associated with DTA of composites, create a greater need for NDI methods that can effectively identify degradation and damage in composite structures. This must be balanced with the need in both the commercial and military aircraft industries for simple, low-cost nondestructive test (NDT) methods for detecting damage in composite structures and repair configurations.

The rapidly increasing use of composites on commercial airplanes coupled with the potential for economic savings associated with their use means that the demand for composite materials technology will continue to increase. Inspecting these composite structures is a critical element in assuring their continued airworthiness. Many composite honeycomb structure inspections are performed by tap test methods that use a human-detected change in acoustic response to locate flaws. More sophisticated NDI methods could be applied to improve the damage detection in adhesively bonded composite aircraft parts. Towards that end, the CACRC-ITG, chaired by the FAA-AANC at Sandia Laboratories, completed a study to assess current inspection capabilities and the need for improved inspections of composite structures. The use of more advanced NDI to supplement or substitute for existing inspections can be introduced through new original equipment manufacturer (OEM) requirements.

The primary motivation for this program is to address the extensive and increasing use of composites on commercial aircraft and the associated increase in the array of NDI methods used to inspect them. Figure 12 shows how the use of composite materials has risen dramatically over the last decade. The end result of this experiment is an assessment of the NDI flaw detection capability in composite honeycomb structures, along with insights that can be used to improve the performance of composite inspection methods.

Goal—use airline inspectors to establish industry-wide NDI performance curves that quantify:

- How well current inspection techniques are able to reliably find flaws in composite honeycomb structure.
- The degree of improvements possible through the integration of more advanced NDI techniques and procedures.

The related goals include: improve composite laminate inspection procedures and performance, and develop structured comparisons between results from handheld inspection equipment and automated scanning systems. Overall, the results from this study will provide input and recommendations to the FAA regarding guidance (e.g., Advisory Circulars) that can enhance the composite inspection process. Thus, this study is driven by a desire to improve aircraft safety. Airlines and OEMs can use these results to guide NDI deployment and training, define what flaws/damage can be reliably found by inspectors, and reduce the human factors issues to produce improved NDI performance in the field.

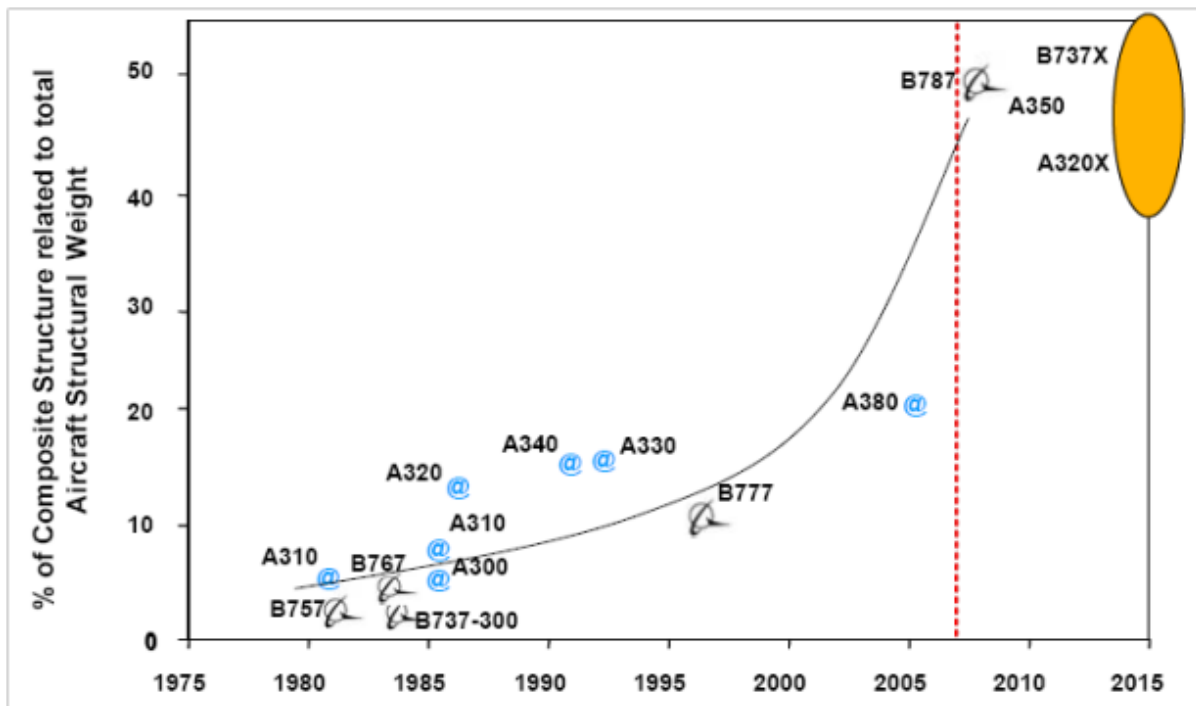


Figure 12. Expansion in use of composite materials in aircraft construction

The primary sources of damage to composite structures are:

- Normal and abnormal flight loads.
- Fluid contamination and ingress.
- Surface coating removal/erosion.
- Impact (in-flight and on the ground).
hail, birds, tools, runway debris, tire separation, and ground handling equipment
- Lightning strikes.
- Heat and ultraviolet light exposure.
- Corrosion effects from adjacent metals in conductive joints (carbon materials)
- Maintenance errors.

Sample damage found in composite structures is shown in figures 13–18. Information from one airline report indicates an average of eight composite damage events per aircraft, with 87% of those stemming from impact. Figure 19 shows data relating the probability of an aircraft being impacted by runway debris alone. The data indicate probability of impact that reaches the 25–30% range. The costs associated with the repair of such impact damage averages \$200,000 per aircraft. Another report indicates that fuselage damage is incurred every 1,000 flights in wide body aircraft and every 4,600 flights in narrow body aircraft.

The inspection challenges associated with the composite damage described above include:

- Subsurface delaminations and disbands.
- Hidden, subsurface damage.
- Small amounts of moisture.
- Cluster of damage where each individual damage point is quite small.
- Heat damage that affects resin matrix.
- Weak bonds (manufacturing or environmentally induced).

Impact damage can be especially hard to detect because this damage mode often produces subsurface damage while leaving no external surface demarcations or visual clues. Figures 20–22 describe the physics behind this impact damage scenario and include photos of this type of “blind” damage in both solid laminate and honeycomb structure. For example, hailstorm damage can produce subsurface interply delaminations, whereas low-velocity, high-mass impacts (e.g., ground handling equipment) can produce substructure damage (e.g., stringer-to-skin disbonds, frame fracture), both of which can be challenging to detect.



Figure 13. Sample sources of damage to composite structures



**Ground Service
Vehicles**



Figure 14. Sample damage from ground service vehicle impact



Towing and
Docking Damage

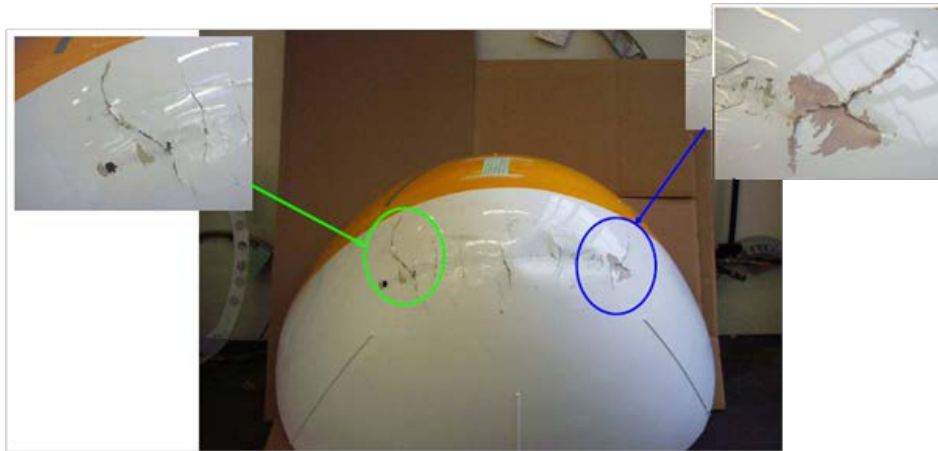
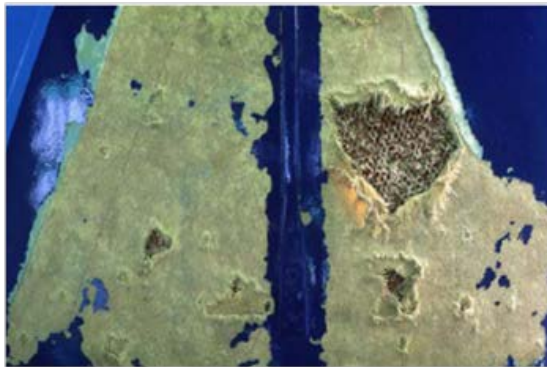


Figure 15. Sample damage from ground operations



Hailstorm Damage



Bird Strike



Figure 16. Sample damage from impacts during flight



Figure 17. Sample damage from lightning strike

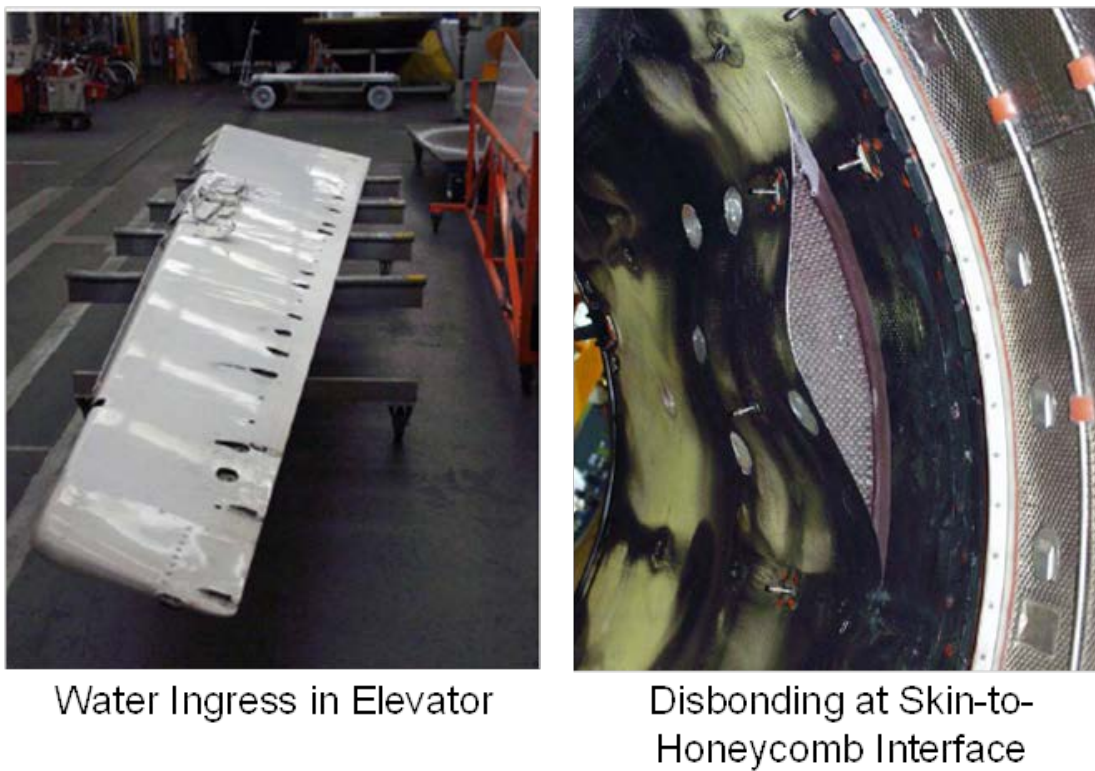


Figure 18. Sources of in-service damage to composite structures

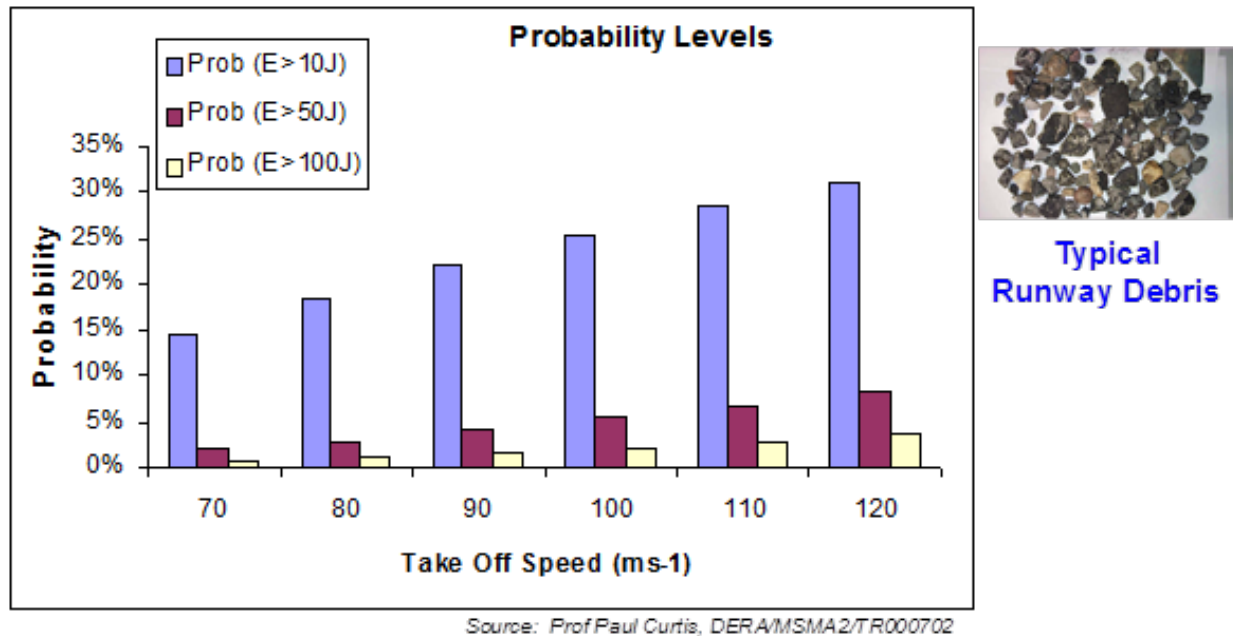


Figure 19. Probability of impact energy as a function of take-off speed (based on runway debris collected from four U.K. military air bases)

2.1 OEM GUIDELINES FOR INSPECTING COMPOSITE HONEYCOMB STRUCTURES

The nondestructive testing manuals (NDTM) produced by the OEMs (e.g., Boeing, Airbus, Embraer, and Bombardier) describe the inspection techniques developed for the detection of composite damage before they reach critical levels [10, 11]. The procedures described in the NDTM provide step-by-step instructions on how to apply each inspection method. These procedures are developed through maintenance engineering experience, comparisons with similar installations on service equipment, and engineering evaluation. They are refined and changed as required during the service life of the equipment by a continuous evaluation of the performance of the equipment, the results of scheduled inspections, and through study of failure data.

The inspection requirements are stated in such a manner as to establish what is to be inspected, what inspection conditions are needed, what NDI method(s) are to be used, and how the methods are to be deployed. However, it must be emphasized that the reliability of the inspection results depends on the proper application of the NDI method by trained, experienced, and proficient inspectors. For example, interpretations of radiographs and the readout of other nondestructive testing equipment, such as ultrasonic and eddy current, require much skill and must be performed only by trained and experienced personnel. The operator must have training in both the basic theory and the practical application of the NDT methods he is using and a good working knowledge of aircraft structure. The inspectors must understand the failure characteristics of the composite structures and be aware of limitations and capabilities of the nondestructive testing methods they are using [10–12].

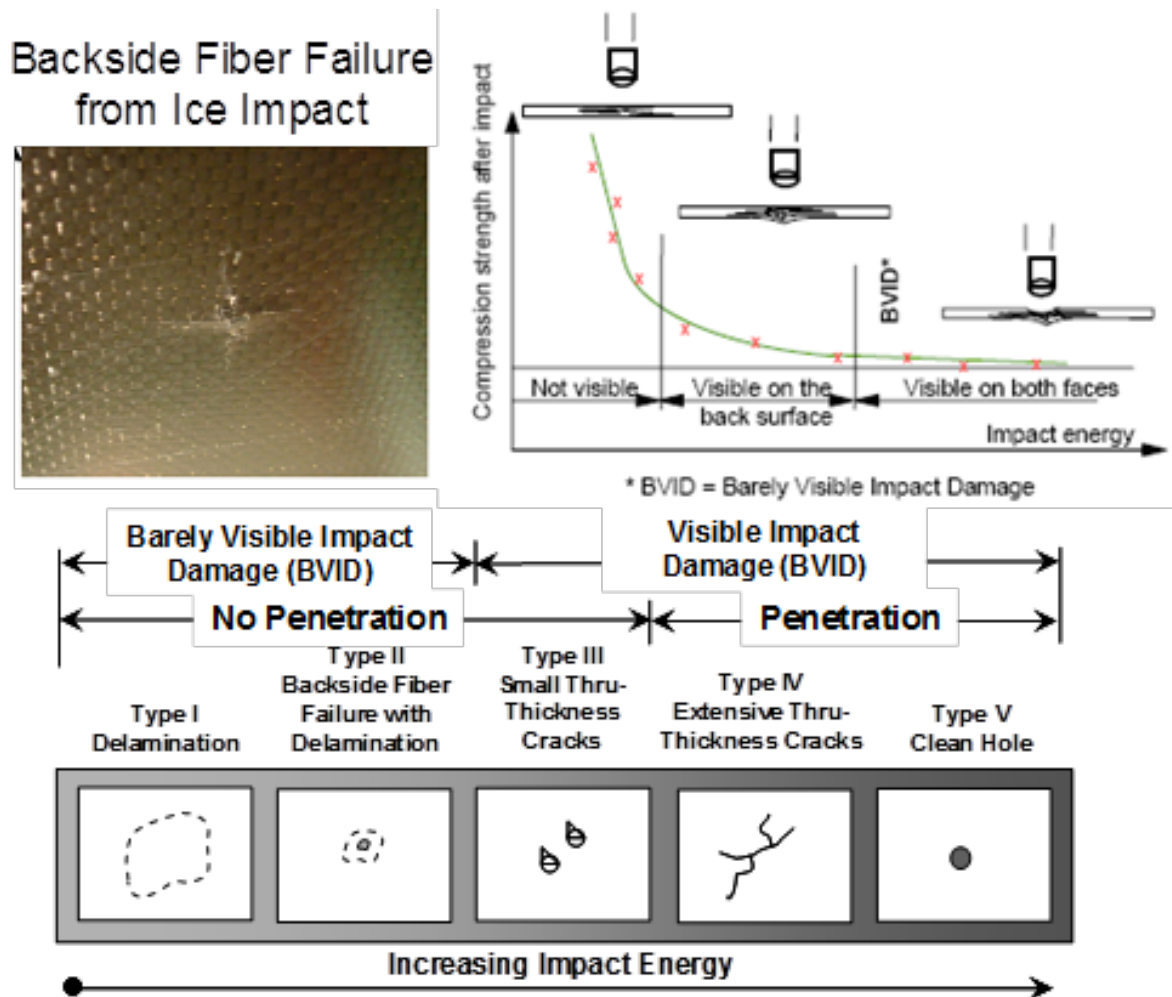


Figure 20. Effects of impact on composite structures

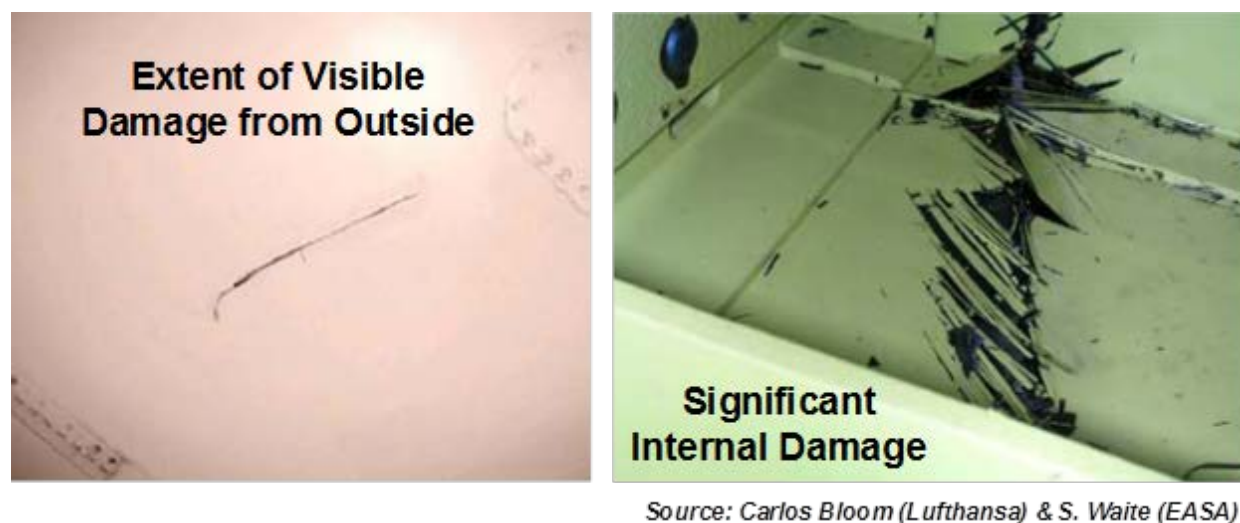


Figure 21. Example of external impact creating minor surface demarcation but significant internal damage

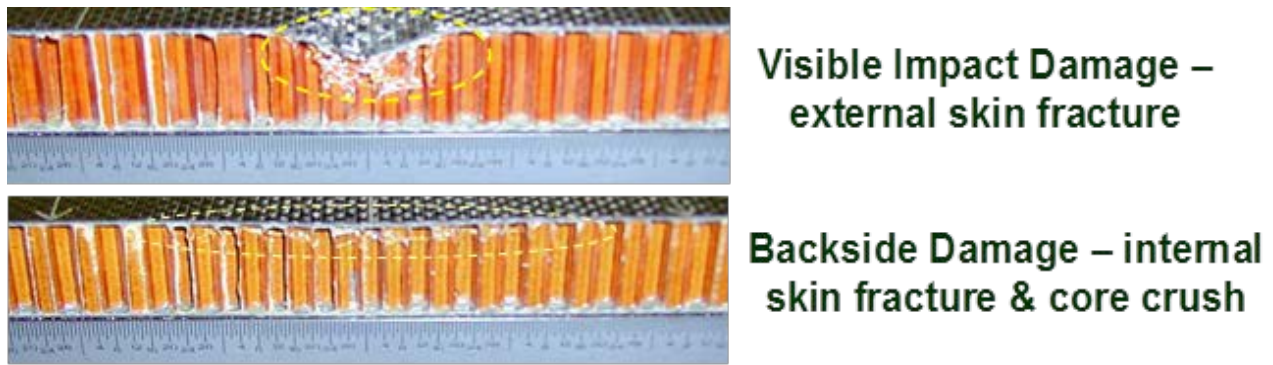


Figure 22. Comparison between visible and backside damage (crushed core and backside fiber fracture) in honeycomb structures

Figure 23 shows a tap test inspection of a composite engine shroud. Tap testing has been used for many years and is still one of the primary methods used to assess the health of composite honeycomb structure. During tap test inspections, low-energy impacts are applied to the surface of the honeycomb sandwich structure. Subtle variations in the audible response from the structure are detected by the inspector and used to infer the presence of flaws. The subjective nature of this approach, coupled with the high probability of human factors issues adversely affecting its performance, were the main reasons that prompted this study. The desire to validate advanced NDI techniques for more demanding composite inspections was another major reason for undertaking this research effort.

This study used a series of composite honeycomb specimens with statistically relevant flaw profiles to evaluate flaw detection via widely used tap test methods. Tap tests were conducted using both human impact techniques and NDI equipment that has recently been introduced to automate and improve acoustic tap testing. The effort focused on understanding the factors influencing composite honeycomb inspections and used NDI experimentation to assess flaw detection performance. Some portions of the testing took the form of blind PoD studies whereas other portions determined signal-to-noise ratios from which flaw detection could be inferred. The primary factors affecting NDI that were included in this study were: composite materials, laminate type and thickness, flaw types and profiles, mechanical interactions (impact and audible response), and environmental conditions. One phase of this effort used airline personnel to study tap test PoD in the field and to formulate improvements in this critical inspection procedure. The tap test results were compared with quantitative data from other NDI devices. Whereas tap testing was the initial focus of this effort, other composite inspection techniques, such as LFBT, resonance, through-transmission and pulse-echo UT, and MIA were applied to complete a comprehensive assessment of flaw detection in composite honeycomb structures using conventional NDI. In addition, improvements obtained through the use of advanced NDI methods were quantified through the application of instrumented tap testing, pulsed thermography, induction thermography, vibro thermography, resonance scanning, MIA scanning, pulse-echo UT imaging, through-transmission UT, UT spectroscopy, phased array UT, linear array UT, terahertz UT, laser UT, laser velocimetry, shearography, digital X-ray, and microwave. Sections 3 and 4 describe each of the techniques listed in more detail.



Figure 23. Tap test inspections of composite aircraft structure

3. CONVENTIONAL INSPECTION METHODS FOR COMPOSITE HONEYCOMB STRUCTURE

NDI tests enable direct and individual inspections of parts and assemblies in as-manufactured and in-service condition. They identify any possible defects without affecting the integrity of the structure. This section presents the array of conventional NDI techniques that are applicable to flaw detection in composite honeycomb structures. The method of inspection selected for a particular area depends on several factors, including accessibility, type of defect, material, geometry, structural configuration, area to be inspected, NDI device deployment, and degree of sensitivity required. Optimum inspection methods provide maximum detection sensitivity while requiring a minimum of airplane disassembly or component removal.

Recent developments in more advanced NDI techniques have produced a number of new inspection options. Many of these methods can be categorized as wide-area techniques that produce two-dimensional flaw maps of the structure. New inspection techniques available today or in the immediate future hold promise for reducing the direct maintenance costs while improving the capacity of detecting damage. Improved NDI techniques could also help detect damage in its early stages, thus reducing the costs associated with the restoration of a larger affected area. The set of advanced NDI methods that are applicable to composite honeycomb inspections are presented in section 4.

The conventional and advanced NDI methods that were applied to the CHE are summarized in table 1. This table contains a list of applicable in-service NDI methods for composite honeycomb

structures and a summary concerning their application for: 1) investigating the quality and integrity of these structures, and 2) determining their viability for continued service.

3.1 BOND TESTING

The inspection, maintenance, and repair of bonded structures are critical tasks for the aviation industry [13]. Bonded structures can take a variety of forms—from adhesively bonded metallic or composite plates to sandwich structures with various face sheets and core material. Honeycomb sandwich structures are widely used on aerospace structures, especially as light control surfaces such as ailerons, spoilers, rudders, and trailing edge flaps. The main objective for the NDI of bonded structures is to detect the presence of delaminations in composite laminates and disbonds between adhesively bonded layers and between the face sheet and sandwich core. Delaminations and disbonds in adhesively bonded structures almost invariably lead to a reduction in the stiffness of the structure, especially the contact stiffness on the surface. This change in stiffness is exploited by a number of NDI techniques. Two main causes for the delamination and disbond damage are low-velocity impacts occurring during maintenance, such as that due to dropped tools, and impact damage caused by hail, runway debris, and bird strikes. Depending on the face sheet thickness and stiffness, impact damage of honeycomb sandwich structures may not leave clear visual indications on the surface (referred to as barely visual impact damage or BVID). One of the NDI goals is, therefore, to characterize the severity of the defects or damage in terms of their size, shape, location, and severity. In applying the NDI methods, accessibility of the inspection area plays an important role. Certain techniques, such as through-transmission air-coupled UT testing, can only be applied when two-sided access is available. For thick honeycomb sandwiches with only one-sided access, the detection of far-side disbonds becomes more challenging.

Table 1. Inspection methods applied to the composite honeycomb flaw-detection experiment

Item No.	Conventional NDI Techniques	Company/Devices Used
1	Manual tapping	Airbus and Boeing tap hammers
2	Low frequency bond test (LFBT)	S-9R, S-5 Sondicator, BondMaster
3	Mechanical impedance analysis (MIA)	V-95, BondMaster
4	Instrumented tap hammer	WichiTech Digital Tap Hammer (DTH)
5	Instrumented and automated tap hammer	Mitsui Woodpecker

Item No.	Advanced NDI Techniques	Company/Devices Used
1	*Acoustography - digital acoustic video (DAV)	Imperium AcoustoCam™
2	Air-coupled UT	QMI SONDA 0070CX AIRSCAN Pulser and Receiver System
3	Instrumented and automated tap hammer	Computer-Aided Tap Tester (CATT)
4	Advanced scanning X-ray system	Digiray® Motionless Laminography X-ray (MLX)™
5	Laser UT	Lockheed Martin Laser Ultrasonic Technology
6	Mechanical impedance analysis (MIA)	Boeing Mobile Automated Scanner (MAUS)
7	Microwave	Evisive Scan Microwave
8	Phased array UT	NDT Solutions FlawInspecta® UT Array
9	Resonance	Boeing Mobile Automated Scanner (MAUS)
10	Shearography	Laser Technology Inc. Vacuum Stress Shearography
11	Structural Anomaly Mapping (SAM) System	Honeywell Structural Anomaly Mapping (SAM) System
12	*Terahertz Imaging	GMA Industries Benchtop System
13	Thermography	Thermal Wave Imaging Inc. Flash Thermography System

*Did not participate in the blind Composite Honeycomb Detection Experiment

The NDI techniques for testing bonded structures may be divided into three categories: 1) mechanical methods of testing; 2) low-frequency methods of testing; and 3) emerging NDI methods with bond testing capability [14, 15]. The mechanical methods include the manual (qualitative) tap test, instrumented (quantitative) tap test, and portable load-displacement devices such as the elasticity laminate checker. The low-frequency methods refer to several established test methods that do not require a coupling fluid or gel between the transducer and the part surface; these include the MIA, membrane resonance method, and pitch-catch method. In addition to the low-frequency “sonic” methods, UT testing using the low end of the frequency spectrum (typically less than 0.5 MHz) is sometimes used on bonded structures as well. In the past 10–20 years, many newer NDI methods have emerged that have proved to be effective in

the inspection of bonded structures; these methods include shearography [16], thermography and thermal wave imaging [17], air-coupled ultrasound, and laser peening tests [18].

3.2 MANUAL MECHANICAL TAP TESTING

In NDI of adhesively bonded structures, such as honeycomb panels, the oldest and still widely used method is the simple tap test. The tap test is a local method in which the surface contact stiffness is determined by tapping. Tapping a location without damage will produce a crisp and solid sound whereas a damaged region will produce a dull sound. These subtle variations in audible response from the structure are detected by the inspector and used to infer the presence or absence of flaws. The hearing-based and manually operated tap test, although inexpensive and quick to perform, is hampered by operator-dependent subjectivity and background noise within the work environment. Research over the years on the mechanical response of a tap test has led to the evolution of instrumented methods, with imaging capability, that are less dependent on an operator's subjective interpretations. Figure 24 describes this transition to more sophisticated and sensitive tap test devices. The physical response to a tap involves the force data and sound data. Although the acoustic spectrum has been used in some instrumented tap test systems, most of the instrumentation of the tap test focuses on the force response [19–24].

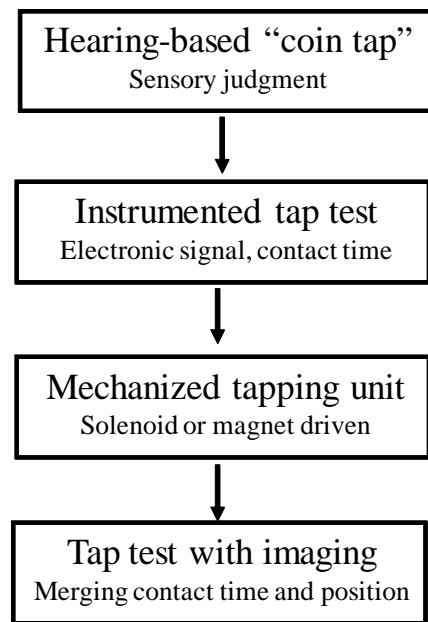


Figure 24. Evolution of the tap test method in nondestructive testing

The mechanical tap test is a manual method wherein a small diameter rod or hammer with a spherical tip is used to tap the surface of a structure while the human ear is used to monitor the audible results (see figure 23). Tap testing has been used for many years and is still one of the primary methods used to assess the health of composite structures. During tap test inspections, low-energy impacts are applied to the surface of the structure being inspected. Subtle variations in the audible response from the structure are detected by the inspector and used to infer the presence of flaws. The audible sound resonating from the part will be characteristic of the mass, cohesive stiffness, and the cross-sectional thickness of the part or assembly being inspected. The

characteristics of the impact are dependent on the local impedance of the structure and on the mass of the tap test device used. When a defective area is tapped, the higher structural vibration modes are not excited as strongly as when a structurally sound area is tapped. The sound produced from a defective area has less high-frequency content, and the structure sounds duller.

The tap test inspection is a simple and fast inspection method that is based on the difference in sound produced by an impacted clean structure and the same structure when it contains damage. In using the tap test tool—that is, tapping the entire surface of the inspection area—it is possible to have the following situations:

- Distinct clear sound indicates that the area tested is sound.
- Dull, damped sound indicates the presence of a flaw.

Manual tap testing using a coin or other metal pieces is the most widely practiced inspection for bonded structures and composites. The equipment usually used in the tap test inspection is a special hammer. For hearing-based manual tap test of bonded structures on aircraft, manufacturers recommend various convenient tapper size and mass in their service manuals. Figures 25 and 26 show the official Airbus and Boeing tap test devices that are deployed manually. Inspectors sometimes use devices that deviate from the tap hammers specified in the OEM NDT manuals. Figure 27 shows some of the alternate tappers that were discovered during the course of this investigation. These alternative tap devices were not assessed in this study. Figures 28–30 show the deployment of a tap test inspection along with the typical types of damage detected with this method [25]. Tap testing has been used for many years and is still one of the primary methods used to assess the health of composite structures. The tap test inspection is useful to detect subsurface disbonding and delamination in honeycomb sandwich construction. Despite its qualitative nature, it remains the most convenient and cost-effective method for inspecting bonds. Tap testing is most effective on honeycomb structure with thin face sheets. The subjective nature of this approach and the possibility of human factors issues adversely affecting its performance were among the main factors prompting this study.

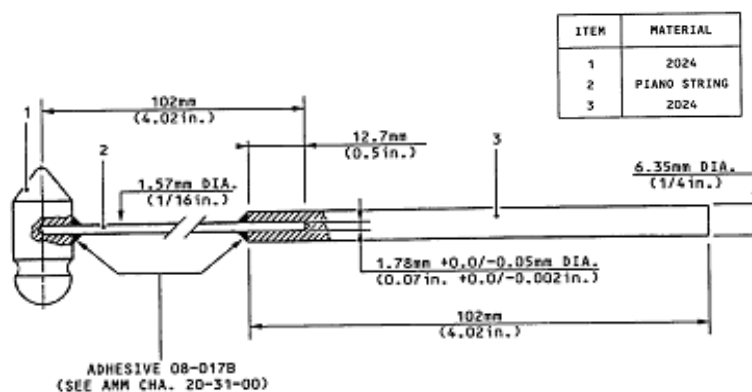


Figure 25. Mechanical tap hammer specified by Airbus

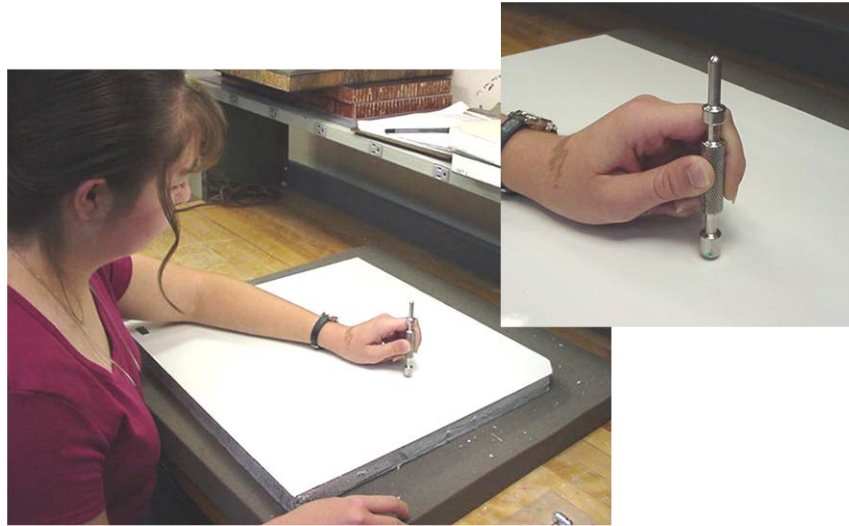


Figure 26. Mechanical tap hammer specified by Boeing

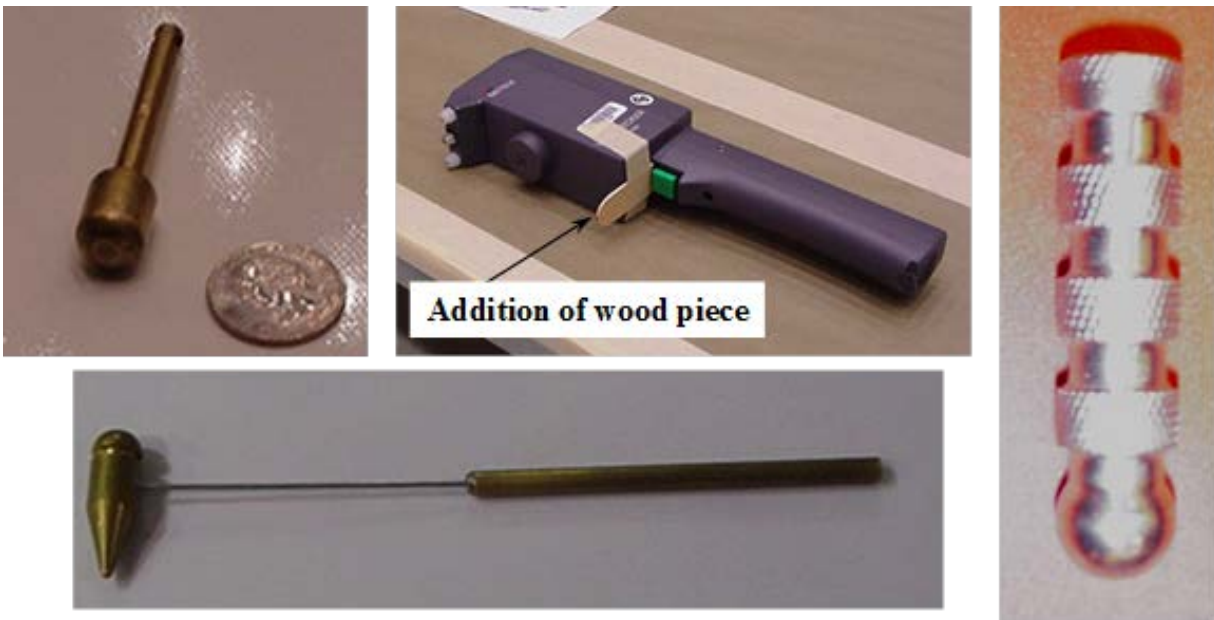


Figure 27. Samples of homemade tappers used in the field, including modification to Woodpecker device (addition of wood piece) to ensure that automated tap is perpendicular to the surface being inspected

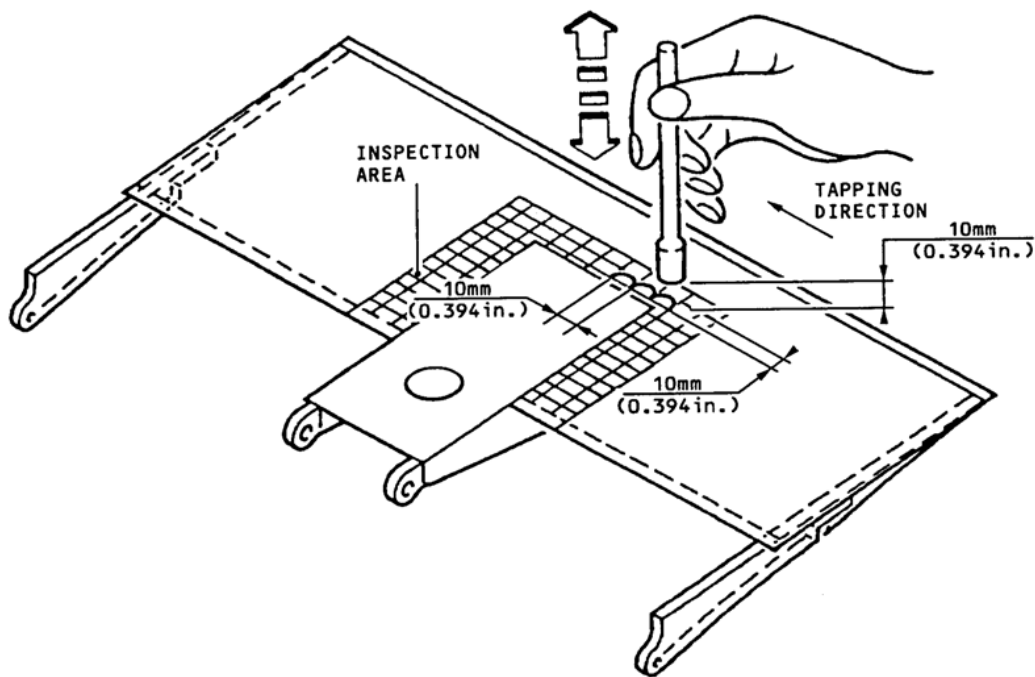


Figure 28. General test pattern used for mechanical impact inspections

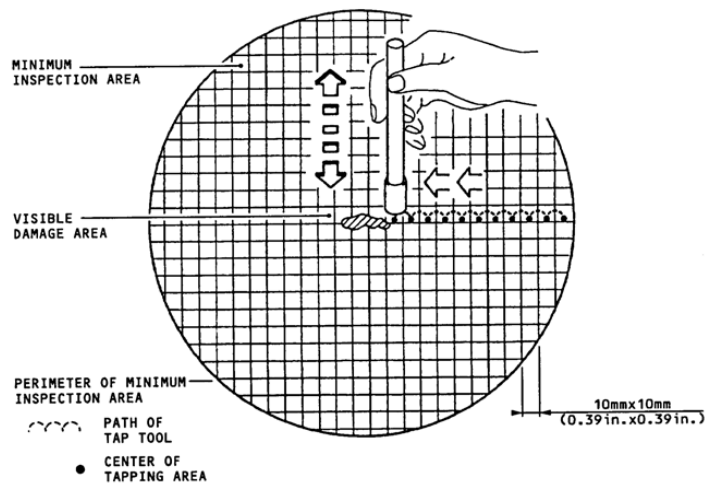


Figure 29. Detailed view of test pattern used for mechanical impact inspections

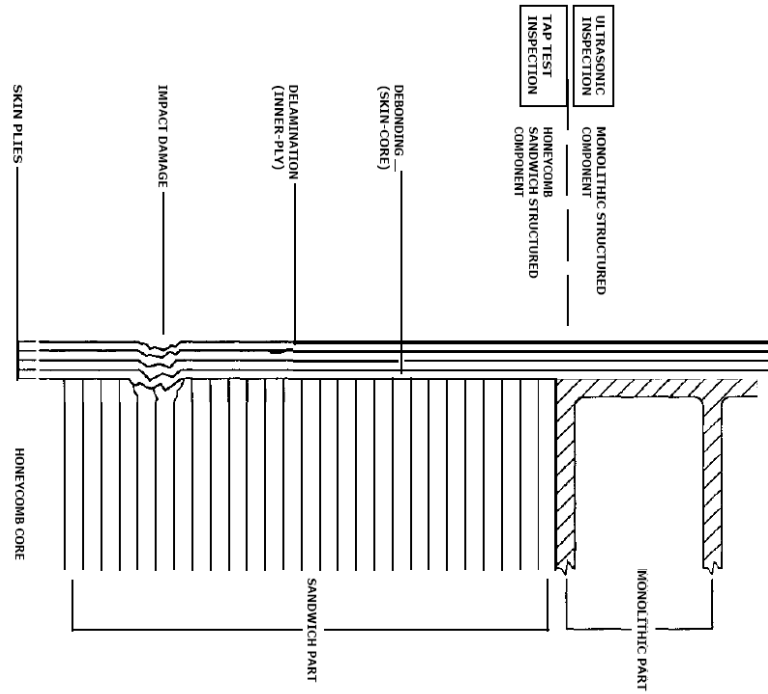


Figure 30. Sample composite honeycomb damage to be detected with mechanical tap test

3.3 AUTOMATED/INSTRUMENTED MECHANICAL TAP TESTING

A commonly cited model for the tap test is the simple spring model, for which a tapper mass, (m) is bounced off the surface represented by a spring constant (k). In this model, the force-time curve is taken to be one half cycle of the mass-spring oscillation. The contact time is therefore:

$$\tau = \pi (m/k)^{1/2} \quad (1)$$

Thus, the physical basis of the tap test is that the time of contact (τ) between the tapper and surface (i.e., the width of the force-versus-time curve) is a function of the stiffness constant (k) of the surface and the mass (m) of the tapper [24]. For a given m , a good structure with a higher stiffness (k) will produce a shorter contact time (τ) and a higher-pitched “crispy” sound. Conversely, a damaged region with a lower stiffness will lead to a longer contact time and, therefore, a lower-pitched dull sound. As a result, the local contact stiffness (k) can be deduced from the contact time (τ) measured by an instrumented tap test device. The significance of this relationship is that a meaningful engineering quantity of the structure, the local stiffness, can be obtained from a tap test using any impactor of a known mass without the need for reference standards.

The stiffness deduced from the tap test has been compared with the stiffness at the same location measured in static load tests [26]. The measurements were made of a number of honeycomb sandwich panels with carbon and graphite face sheets of various thicknesses. The comparison of the stiffness deduced from the tap test and measured by static loading is shown in figure 31. It was demonstrated using aircraft composite parts that the stiffness (k) deduced from the tap test

was in good agreement with the contact stiffness determined in mechanical load-displacement tests. Thus, an instrumented tap test can produce a quantity that is indicative of the integrity, or damage condition, of the structure.

The physical quantity most central to the tap test of structures is the contact time or impact duration between the tapping mass and the part surface. When a surface is tapped with a different force, the amplitude of the vibration changes, but the time of contact (τ), which is related to the period of frequency of the vibration, remains approximately the same. The contact time at a location with internal damage is often much longer than that at an undamaged region. The contact time can be measured by incorporating an accelerometer or force sensor into the tapping mass. The contact time of a tap depends on the local contact stiffness of the surface and the mass of the tapper, but it is relatively insensitive to the velocity or the force of the tap.

Figure 32(a) shows the time of contact response on an undamaged part of a composite honeycomb panel tapped by an accelerometer. The larger amplitudes correspond to taps of greater force. The Y-axis shows the force or acceleration while the width of the curve on the X-axis represents the contact time for the impactor. Figure 32(b) shows the time of contact response of an impact-damaged portion of the panel, as tapped by the same accelerometer. The damage in the honeycomb core caused a reduction of the contact stiffness (k) and, therefore, led to a longer time of contact (τ).

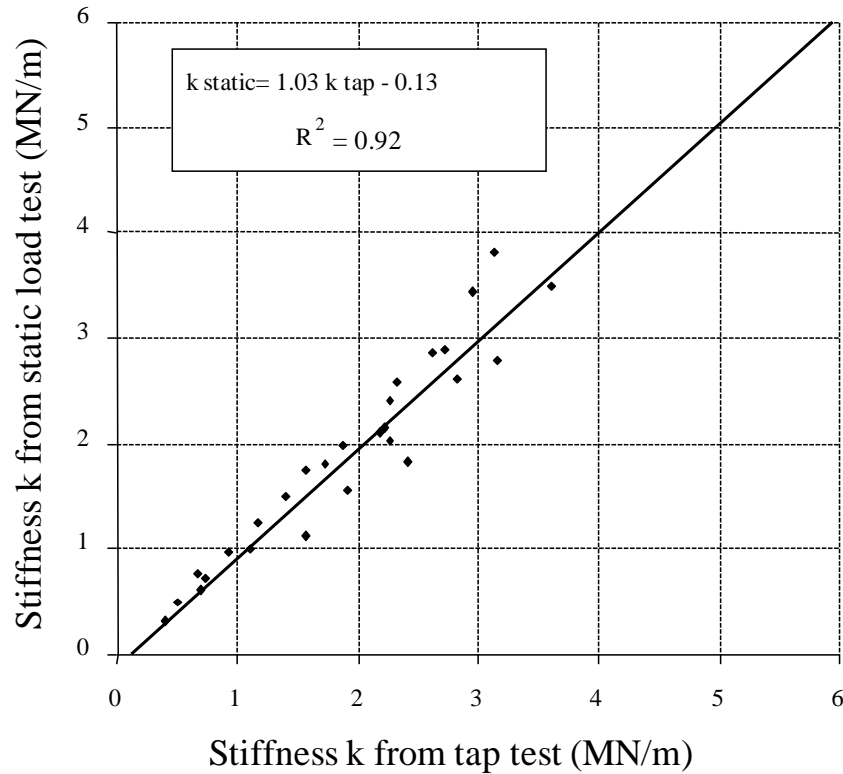


Figure 31. Comparison of the surface stiffness deduced from the tap test with the stiffness measured in a static load test

The range of contact time obtained with a small mass, of the order of 15 grams, on composite honeycomb sandwiches with glass or carbon face sheets up to 7 or 8 plies is several hundred microseconds. The sensitivity of the tap test on structures with thicker face sheets (greater than ~9–12 plies) is too low to be useful even with instrumented units. As the thickness of the skin laminates increases, it becomes more difficult to hear subtle differences between pristine and damaged structure. Thus, the performance of the tap test method diminishes as the skin becomes thicker. This experiment includes a variety of honeycomb skin thicknesses to quantify the change in performance corresponding to three-, six-, and nine-ply carbon and fiberglass skins. The results in figure 32 show that the contact time—the parameter used to detect hidden damage—is approximately constant for different tapping forces in either a good region or in a damaged region. The contact time of a handheld tapping mass has proven to be surprisingly consistent among different operators despite the differences in tapping force, velocity, strike angle, and grasping force [24, 26].

Electronic tap test instruments, such as those shown in figure 33, have been developed to automate the inspection process. These devices use the physics discussed above and a force/acceleration transducer to quantify the stiffness of the local impact region. Changes in stiffness can be observed by the user to infer the presence of damage. Some of these instruments measure the duration of the impact while others measure the frequency content of the tap signal. These will be discussed further in section 4.

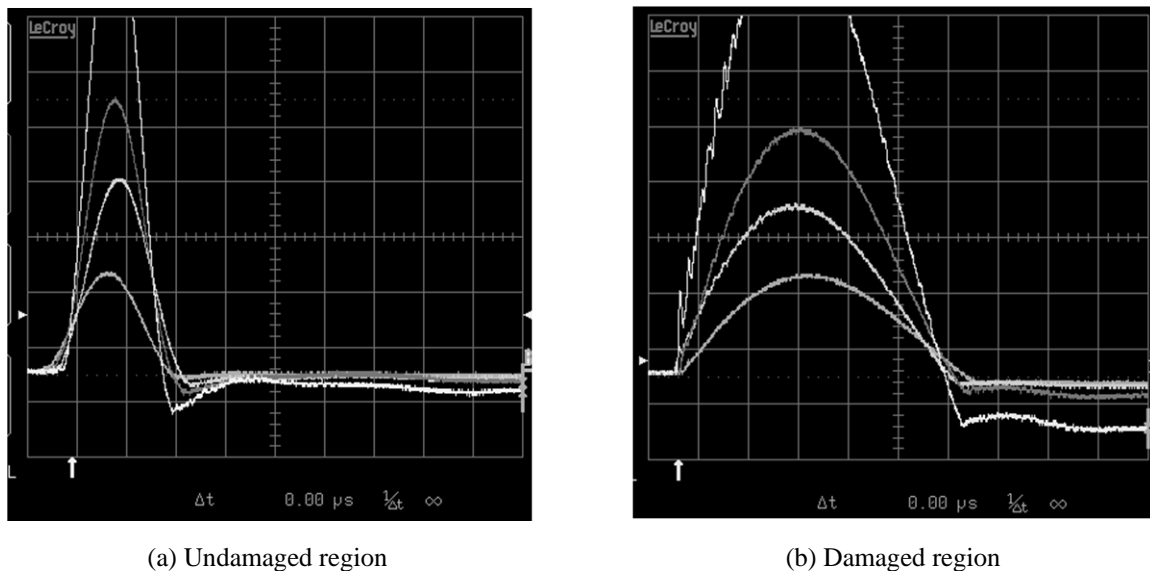


Figure 32. Force vs. time history for various tapping forces in a good region and a damaged region on a composite honeycomb panel



Figure 33. Instrumented tap test devices: DTH (left) and Woodpecker (right)

3.4 LOW FREQUENCY BOND TESTING

Low Frequency Bond Testing (LFBT) refers to ultrasonic bond testers that operate below 100 kHz and are generally called sonic bond testers. Figure 34 shows an inspection of a composite panel using an S-9 LFBT device. Sonic bond testers generally do not require the use of liquid couplant (dry-coupled), and operate in the audio or near-audio frequency range. Different techniques for transmitting and receiving energy have been developed for LFBT applications. Each technique introduces a pressure wave into the specimen and then detects the transmitted or reflected wave. The pitch-catch impulse test method uses a dual-element, point contact, non-couplant, low-frequency sonic probe. One element transmits acoustic waves into the test part, and a separate element receives the sound. The sound propagates in a complex wave mode across the test piece between the probe tips. The return signals are processed, and the difference between the effects of good and bad areas of the part along the sound path are analyzed and compared. A complex wave front is generated internally in the material as a result of velocity characteristics, acoustical impedance, and thickness. The time and amount of received energy is affected by the changes in material properties, such as thickness, disbonds, and discontinuities. The instrument processes the received impulse and displays the received information on a phase and amplitude meter. Figure 34 shows the LFBT transducer deployed on the MAUS V scanning device. LFBT signals, which contain both amplitude and phase information from each location on the test article, can also be translated into a two-dimensional, color-coded C-scan image.

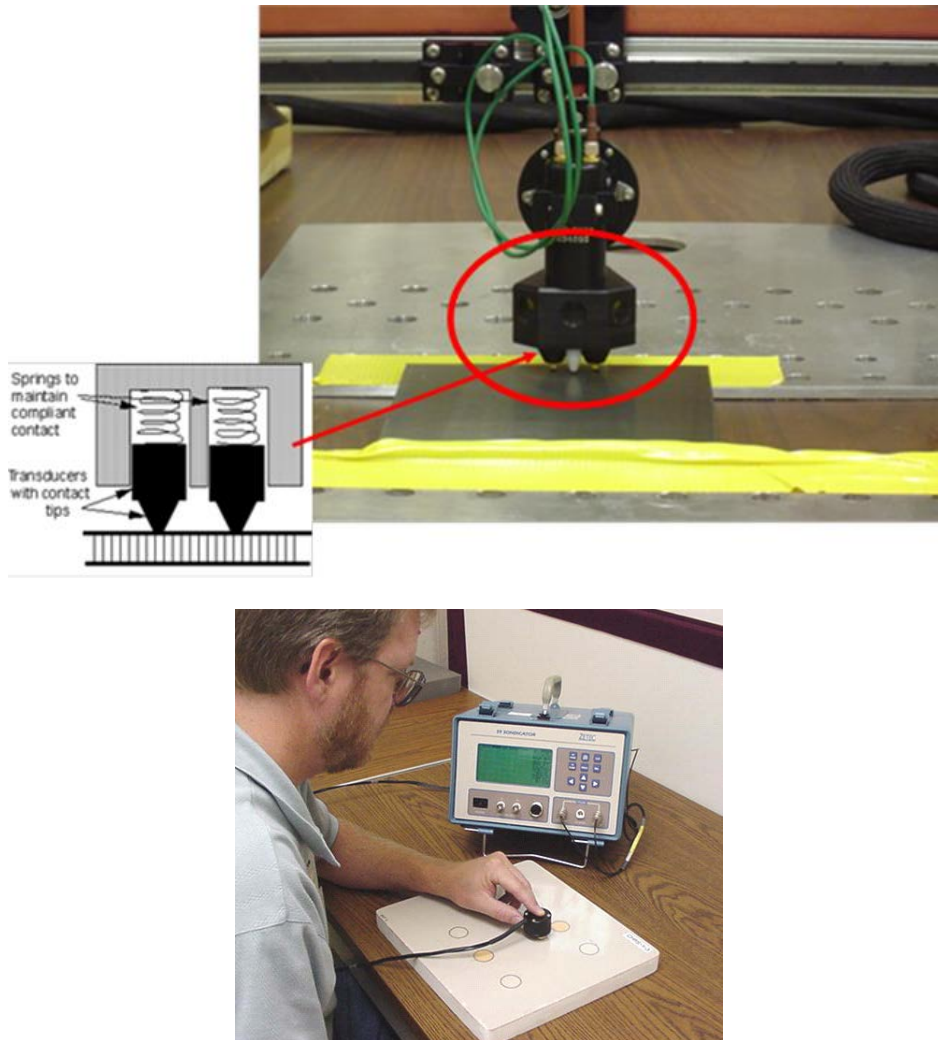


Figure 34. S-9 Sondicator low-frequency bond test device

3.5 HIGH FREQUENCY BOND TESTING – RESONANCE MODE

HFBT is often referred to as resonance testing and uses interrogating frequencies of 25–500 kHz. It is similar in application to contact ultrasonics in that a transducer with a hardware face is acoustically coupled to the item under inspection using a liquid couplant. HFBT uses special narrow bandwidth transducers, which, when coupled to the item under test, produce a continuous sound field in the material. The test material, in turn, provides a mass loading on the transducer, increasing the transducer bandwidth as well as changing the transducer's resonant frequency. Anomalies (such as disbonds) or changes in material thickness result in changes to the transducer loading that cause changes in transducer resonance. These changes are subsequently detected as differences in phase and amplitude of the electronic detection circuits. Acoustic impedance changes can be thought of as variation in the ability to transmit sound between the probe and the material under test. Changes in the materials acoustic impedance cause a corresponding change in the electrical impedance of the transducer; it is these electrical impedance changes that are monitored by the instrument. HFBT has been proven to be effective for inspection of multilayer metal and non-metal laminates for the detection of disbonds as well as multi-ply, non-metallic

composite structure for the detection of inter-ply delaminations. Figure 35 shows the use of a BondMaster device in resonance test mode to inspect a composite panel. The data on the right show the typical display, known as the “flying dot” response, used to determine the presence of damage. The constantly changing path of the flying dot can make the signal interpretation difficult. This is especially true in the areas where signal changes corresponding to changes in part geometry can be misinterpreted. The challenge associated with flaw detection from this type of signal is, in some part, the cause for a reduction in the performance of this NDI method for handheld resonance testing. When these data are transformed into a resonance C-scan image, the test results, as shown in this report, are quite good.

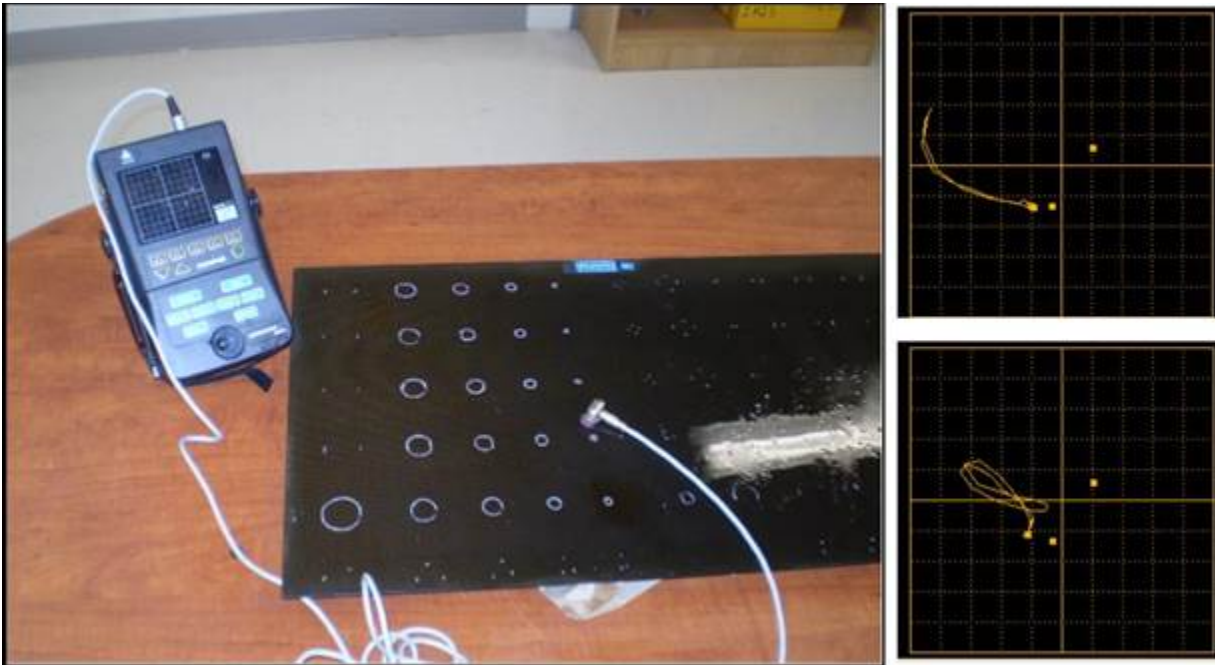


Figure 35. Olympus BondMaster device operating in HFBT/resonance test mode

3.6 MECHANICAL IMPEDANCE ANALYSIS

MIA is the method of bond testing that compares the stiffness of a structure in contact with the probe tip. The probe, in direct contact with the test surface, sends sonic vibrations into the structure and then measures how these vibrations resonate within the structure. A flaw in the structure causes a reduction in its mechanical impedance (stiffness), which changes the displayed signal. The stiffness of the bonded structure is a function of thickness, geometry, elastic variables, and densities of the bonded components. The bonded structure under test is vibrated. Disbonds or other anomalies normally cause a reduction in mechanical impedance (stiffness) and can result in a phase or amplitude change to the displayed signal depending on the frequency of the probe.

The mechanical impedance of a structure, defined as the ratio of the applied force (F) and the resultant velocity (v) is a measure of the resistance to motion of the part. Like the tap test, the MIA method also exploits the reduced stiffness, and, hence, a reduction in the resistance to motion, of a structure containing damage. For example, when the same force is applied to the

face sheet of a composite honeycomb panel over a region of fractured core, the resultant velocity will be higher, and the mechanical impedance will be lower than a region of no damage. Like electrical impedance, the mechanical impedance is also frequency dependent. In commercial MIA instruments, the probe typically contains a driving piezoelectric element and a receiving piezoelectric element. An oscillatory voltage of a certain frequency is applied to the driving element; the receiving element—sandwiched between the driving element and the structural surface with a spring loaded force—then produces a response voltage with an amplitude and phase dependent on the mechanical impedance of the structure. In practice, the spring-loaded probe is moved slowly over the part surface to detect disbonds or delaminations. The V-95 MIA device, which uses a simple meter deflection and alarm system based on probe calibration of a known, undamaged area, is shown in figure 36.

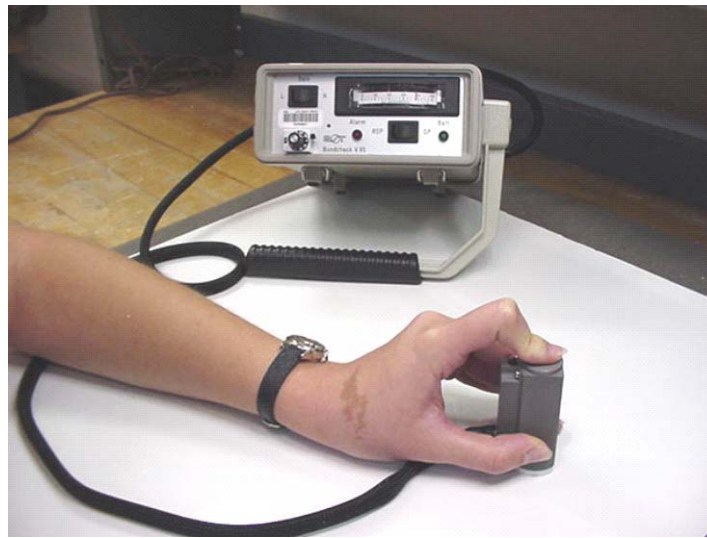


Figure 36. Mechanical impedance analysis inspection with V-95 device

In commercial MIA instruments, the probe typically contains a driving piezoelectric element and a receiving piezoelectric element. The probe consists of two piezoelectric crystals with a driver positioned behind the receiver within the same holder. An oscillatory voltage of a certain frequency is applied to the driving element; the receiving element, sandwiched between the driving element and the structural surface with a spring-loaded force, produces a response voltage with an amplitude and phase dependent on the mechanical impedance of the structure. The driver converts electrical energy into sonic vibrations, and the receiver, in direct contact with the test surface, converts the modified vibrations into electrical signals for processing by the instrument. If the probe is placed on an infinitely stiff structure, and the driver crystal is set to vibrate at a given frequency, the receiver crystal will compress and expand in opposition to the driver crystal (180° phase shift) at maximum signal amplitude. If the probe is now placed on an infinitely flexible structure (free air), and the driver set to vibrate at a given frequency, the receiver crystal will simply move back and forth in space but will not be compressed or expanded and, thus, produce no output. Somewhere between these two extremes lies reality—and, in general, a defect will produce a signal containing amplitude proportional to its stiffness with a possible phase change. The displayed information can be impedance plane (flying dot), meter deflection, or horizontal bar graph. Alarm thresholds can be used to provide audible or

visual warnings. With the aid of some simple position tracking devices and software, certain inspection devices are able to generate two-dimensional images of the inspected area [27].

3.7 ULTRASONIC INSPECTION METHODS

UT inspections can be used for bond evaluation. With respect to composite honeycomb inspections, only certain forms of UT are normally applied. TTU and PE-UT inspection techniques are suitable to detect disbonds in many cases, with the latter's utilization on honeycomb structure being limited to thick laminates. TTU is commonly used for sandwich structures when access to both sides can be accommodated. Nonlinear ultrasound and spectroscopy methods have been investigated for bond testing, with the specific intention of extracting greater information about the bond condition. Parameters such as modulus, density, thickness, and resonant frequency can be useful in the characterization of the consistency of the bonding process. At this time, these methods are not routinely used for honeycomb inspections. Air-coupled inspection is an accepted method for in-service inspection of control surfaces for skin-to-core disbonds. The low frequency (50–400 kHz) is effective despite the significant reflection loss at an air-solid interface due to the acoustic impedance difference between air and material. There are two types of air-coupled transducers—piezoceramic-based (disk or composite) and capacitive type—while most of the field applications use the piezoceramic type. The air-coupled ultrasonic NDI was implemented in the through-transmission mode with the transducers mounted on a yoke for aircraft components to afford two-sided access. A general discussion on UT inspection follows.

In general, UT inspection uses high-frequency sound waves as a means of detecting anomalies in parts. UT test equipment usually operates in the range of 200 kHz–25 MHz. The speed with which the sound waves travel through a material is dependent on the composition and density of the material. The speed of sound in carbon graphite composite material is approximately 0.117 in/ μ s. Thus, the time it takes for an UT pulse to travel from the front surface to the back surface and back to the front surface of a 0.1" thick composite laminate (0.2" total travel) is approximately 1.7 μ s. In PE UT inspections, short bursts of high-frequency sound waves are introduced into materials for the detection of surface and subsurface flaws in the material. The sound waves travel through the material with some attendant loss of energy (attenuation) and are reflected at interfaces. The reflected beam is displayed and then analyzed to define the presence and location of flaws. Sound is transmitted into the test item by means of a transducer. The reflected waves are then received by a transducer, often the same transducer for PE-UT, and converted back into electrical signals for display.

3.7.1 A-scan Mode:

UT testing involves one or more of the following measurements—time of wave transit (or delay), path length, frequency, phase angle, amplitude, impedance, and angle of wave deflection (reflection and refraction). In conventional PE UT, pulses of high-frequency sound waves are introduced into a structure being inspected. A-scan signals represent the response of the stress waves, in amplitude and time, as they travel through the material. As the waves interact with defects within the solid, portions of the pulse's energy are reflected back to the transducer and the flaws are detected, amplified, and displayed on a computer screen. The interaction of the UT waves with defects and the resulting time versus amplitude signal produced on the computer

screen depends on the wave mode, its frequency, and the material properties of the structure. Flaw size can be estimated by comparing the amplitude of a discontinuity signal with that of a signal from a discontinuity of known size and shape. Flaw location (depth) is determined from the position of the flaw echo along a calibrated time base. In the pitch-catch UT method, one transducer introduces a pressure wave into the specimen, and a second transducer detects the transmitted wave. A complex wave front is generated internally in the material as a result of velocity characteristics, acoustical impedance, and thickness. The time and amount of energy is affected by the changes in material properties, such as thickness, disbonds, and discontinuities. The mechanical vibration (ultrasound) is introduced into the specimen through a couplant and travels by wave motion through the specimen at the velocity of sound. If the pulses encounter a reflecting surface, some or all of the energy is reflected and monitored by the transducer. The reflected beam, or echo, can be created by any normal or abnormal (flaw) interface. Complete reflection, partial reflection, scattering, or other detectable effects on the UT waves can be used as the basis of flaw detection. Most instruments with an A-scan display allow the signal to be displayed in its natural radio frequency (RF) form, as a fully rectified RF signal, or as either the positive or negative half of the RF signal.

In most pulse-echo systems, a single transducer acts alternately as the sending and receiving transducer. If the pulses encounter a reflecting surface, some or all of the energy is reflected and monitored by the transducer. The reflected beam, or echo, can be created by any normal (e.g., layer in a multilayered structure) or abnormal (flaw) interface. Figure 37 is a schematic of the pulse-echo technique. It shows the interaction of UT waves with various interfaces within a structure and the corresponding A-scan waveforms that are displayed on a UT inspection instrument. Complete reflection, partial reflection, scattering, or other detectable effect on the UT waves can be used as the basis of flaw detection. In addition to wave reflection, other variations in the wave that can be monitored include time of transit through the test piece, attenuation, and features of the spectral response [28, 29]. Sometimes it is advantageous to use separate sending and receiving transducers for pulse-echo inspection. The term pitch-catch is often used in connection with separate sending and receiving transducers. The degree of reflection depends largely on the physical state of the materials forming the interface. Cracks, delaminations, shrinkage cavities, pores, disbonds, and other discontinuities that produce reflective interfaces can be detected.

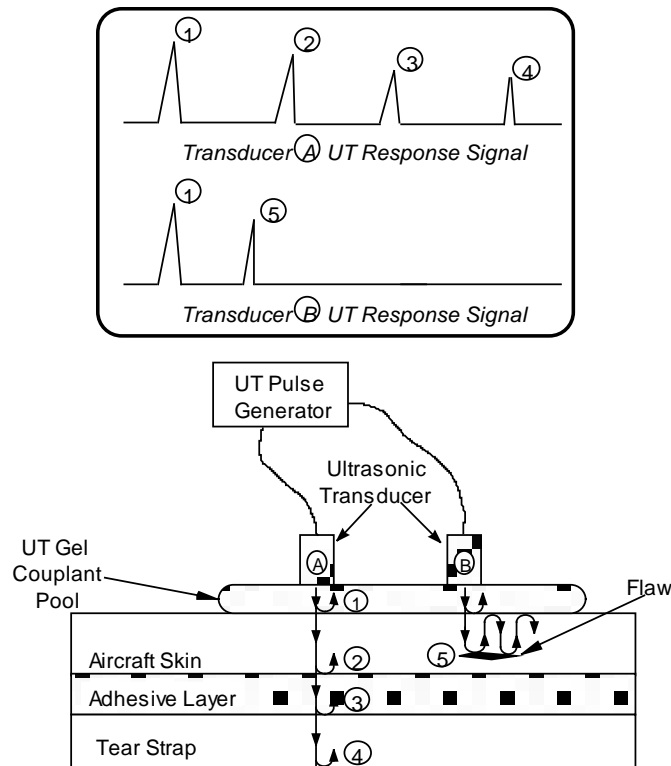


Figure 37. Schematic of pulse-echo ultrasonic inspection and A-scan signal showing reflection of UT waves at assorted interfaces

Figure 38 contains two A-scan signals produced by the handheld UT inspection of a composite specimen that contained intentional, engineered flaws at discrete locations. Changes in the A-Scan signal (i.e., lack of reflected signal from the back wall), caused by the presence of the disbond, are clearly visible. Key portions of the signal in figure 38 are identified to highlight how the A-Scan can be used to detect disbonds and delaminations. The primary items of note are: 1) the unique signature of the amplitude vs. time waveform which allows the user to ascertain the transmission of the UT pulse through various layers of the test article and which indicates a good bond and 2) the absence of signature waveforms indicating a disbond.

3.7.2 B-scan Mode

The B-scan presentations provide a profile (cross-sectional) view of the test specimen. In the B-scan, the time-of-flight (travel time) of the sound energy is displayed along the vertical axis, and the linear position of the transducer is displayed along the horizontal axis. From the B-scan, the depth of the reflector and its approximate linear dimensions in the scan direction can be determined. Thus, it can be considered a cross-sectional view of the part showing the depth and in-plan dimension of the various interfaces within the part—both natural and those produced by internal damage. The B-scan is typically produced by establishing a trigger gate on the A-scan.

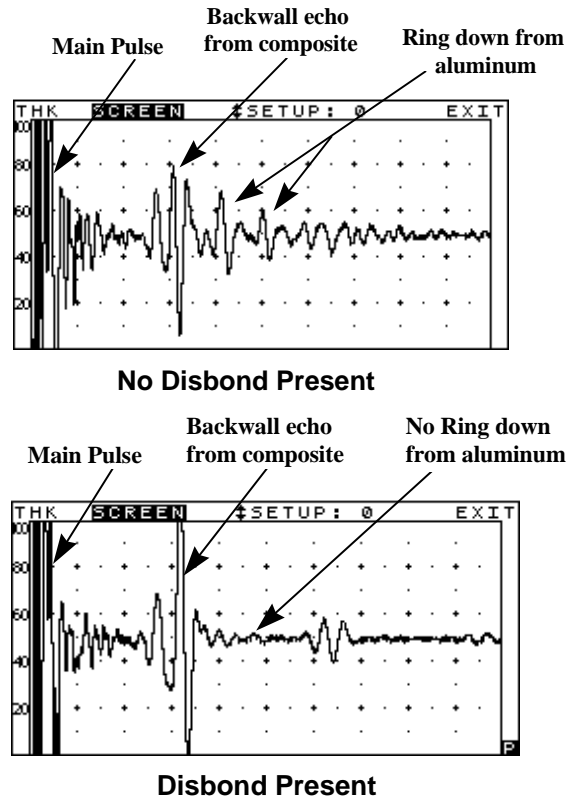


Figure 38. A-scan waveform from bonded and disbonded portions of a composite structure

3.7.3 C-scan Mode—Use of UT Scanning Technology

It is sometimes difficult to clearly identify flaws using UT A-scan signals alone. Small porosity pockets commonly found in composites, coupled with signal fluctuations caused by material nonuniformities, can create signal interpretation difficulties. Significant improvements in disbond and delamination detection can be achieved by taking the A-scan signals and transforming them into a single C-scan image of the part being inspected. C-scans are two-dimensional images (area maps) produced by digitizing the point-by-point signal variations of an interrogating sensor while it is scanned over a surface. A computer converts the point-by-point data into a color representation and displays it at the appropriate point in an image. Specific “gates” can be set within the data acquisition software to focus on response signals from particular regions within the structure. C-scan area views provide the inspector with easier-to-use and more reliable data with which to recognize flaw patterns. This format provides a quantitative display of signal amplitudes or time-of-flight data obtained over an area. The X-Y position of flaws can be mapped and time-of-flight data can be converted and displayed by image processing equipment to provide an indication of flaw depth. A variety of PC-based manual and automated scanning devices can provide position information with digitized UT signals [30].

The basic C-scan system is shown schematically in figure 39. The scanning unit containing the transducer is moved over the surface of the test piece using a search pattern of closely spaced parallel lines. A mechanical linkage connects the scanning unit to X-axis and Y-axis position indicators, which feed position data to the computer. The echo signal is recorded, versus its X-Y

position on the test piece, and a color-coded image is produced from the relative characteristics of the sum total of signals received. Typically, a data collection gate is established on the A-scan signal, and the amplitude, or time-of-flight of the signal, is recorded at regular intervals as the transducer is scanned over the test piece. The relative signal amplitude, or the time-of-flight, is displayed as a shade of gray or a color for each of the positions where data were recorded. The C-scan presentation provides an image that indicates the reflection and scatter of the sound within and on the surfaces of the test piece and their features relative to the gate settings.

A photograph of an automated (motorized) scanner, the Boeing MAUS system, inspecting an aircraft fuselage section is shown in figure 40. The entire UT C-scan device is attached to the structure using suction cups connected to a vacuum pump. The unit is tethered to a remotely located computer for control and data acquisition. Figure 41 shows a comparison of A-scan signals from damaged and undamaged portions of a composite structure that were produced by the PE-UT method. Note the clear reflection peak produced by uninterrupted signal travel to the back wall in the “undamaged” A-scan signal. Compare this to the A-scan signal from the “damaged” region where the amplitude of the back wall signal is decreased, and a new intermediate peak (reflection) is observed. Both of these A-scan changes indicate the presence of damage or other anomaly. Figure 42 shows a sample C-scan image (based on amplitude) from a PE-UT inspection of a composite fuselage structure containing stringers and frame shear ties (see figure 40). Dark spots and irregularly shaped regions of non-uniform color indicate the presence of impact damage in this panel. The value of using two-dimensional color coding, stemming from the sum total of the A-scan signals, to identify and size composite flaws is evident in this C-scan image.

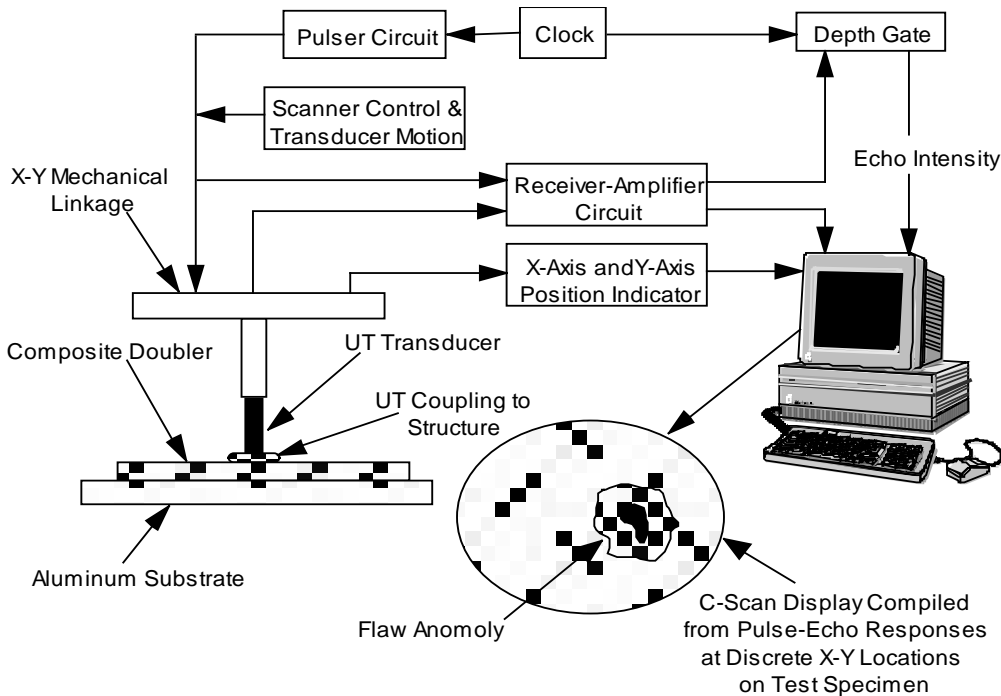
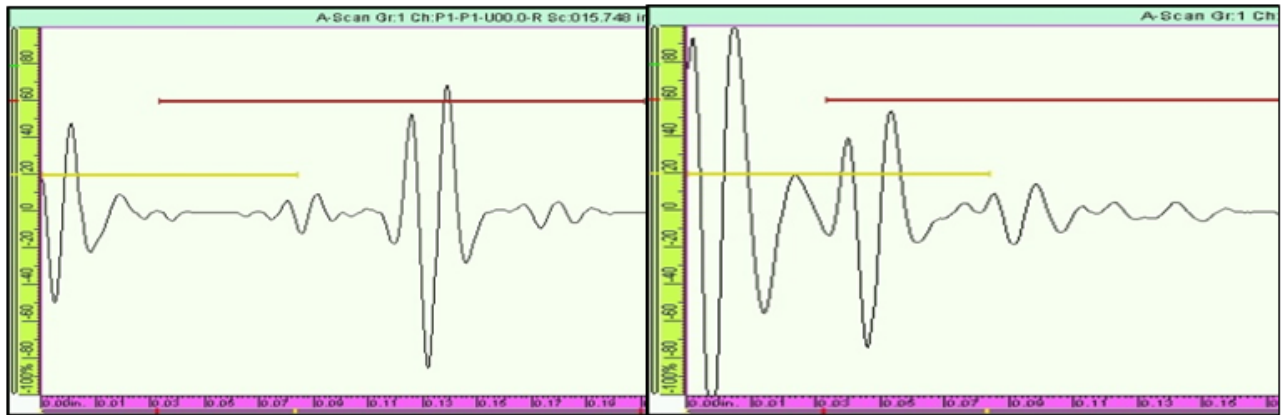


Figure 39. Schematic of C-scan setup for pulse-echo ultrasonic inspection



Figure 40. MAUS automated ultrasonic scanning system



a)

b)

Figure 41. Sample ultrasonic signals generated from: a) structure without damage and b) structure with damage

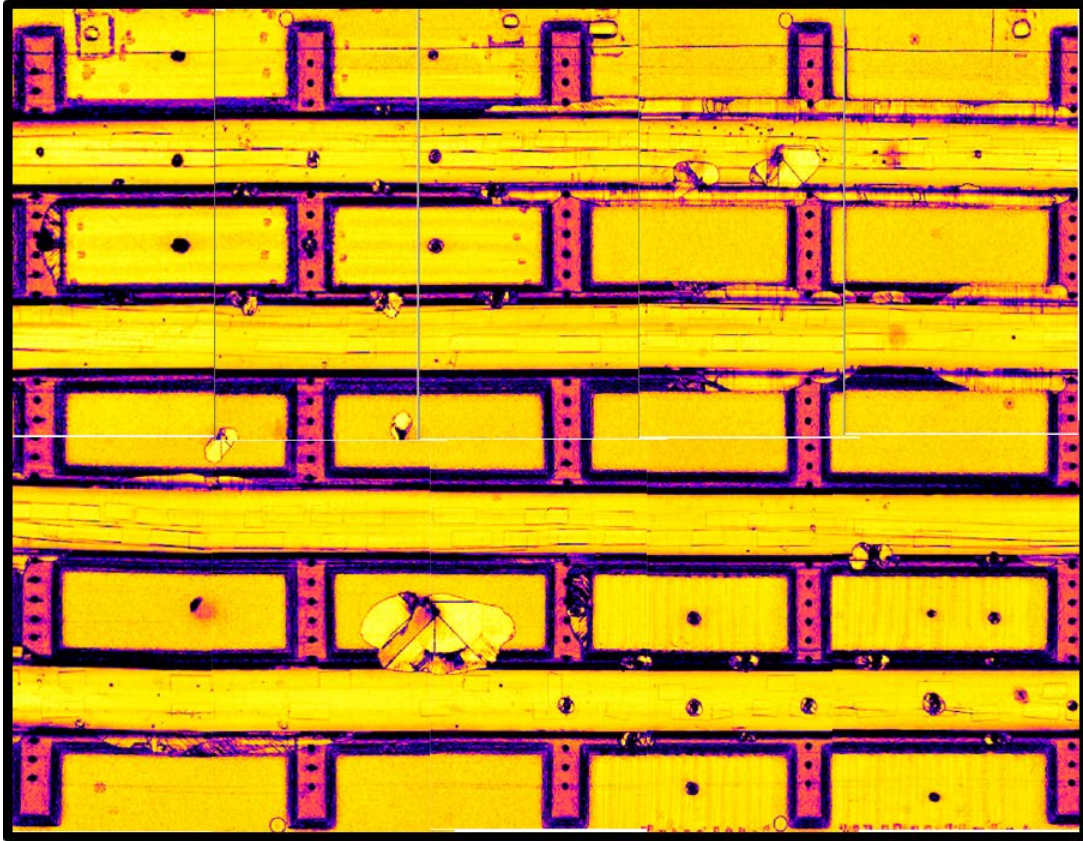


Figure 42. Sample C-scan produced by an automated ultrasonic scanning device

4. ADVANCED COMPOSITE HONEYCOMB INSPECTION TECHNIQUES

This section presents the array of advanced, state-of-the-art inspection methods that are applicable to flaw detection in composite honeycomb structures. Advanced NDI methods that have shown great promise for inspecting composite honeycomb structures—and in some instances gained acceptance for specific applications—include thermography, shearography, scanning UT, acoustic laser Doppler velocimetry (SAM system), phased array UT, laser UT, and acoustography. The advanced NDI techniques that were evaluated ranged from an automated, sensor-based form of tap testing (CATT) to C-scan technology for improved flaw identification (MAUS).

Advanced NDI methods that were evaluated were: Laser Technology Inc. (shearography), Honeywell (laser velocimetry – SAM), Imperium, Inc. (UT imaging AcoustoCam), Iowa State University (CATT and air-coupled UT), Boeing (MAUS in MIA and Resonance mode), Thermal Wave Imaging (thermography), Sonatest (linear array UT), Southern Research Institute (UT spectroscopy), Lockheed Martin (laser UT), Sonatest (Rapidscan linear array UT), Evisive (microwave), GMA Industries, Inc. (terahertz UT imaging), NDT Solutions Inc. (FlawInspecta phased array UT), QUEST Integrated (induction thermography), and Digiray (digital x-ray laminography).

4.1 INSTRUMENTED AND AUTOMATED TAP TEST DEVICES

The manual, mechanical tap test method described in section 3 is an NDI practice that is very simple and inexpensive to apply for inspecting composites. However, it has several drawbacks in that it is dependent on the inspector's proper deployment, their subjective hearing of the audible response, and their interpretation of that audible tone. This approach is unable to provide quantitative data. The results are also subject to interference from workplace noise. Another difficulty with the qualitative, manual tap test is that hidden substructures such as ply overlap, core splice, ribs, and spars of a part can often lead to confusing acoustic responses that can hamper actual flaw detection. To address these concerns and enhance the performance of tap testing technology, a number of new devices have been developed with varying degrees of tap testing automation. These devices use digital readouts, solenoid-driven impacts, and computer data analysis to aid the tap test process. These devices are presented in the following section.

As the tap test is a local inspection technique, full coverage of the inspection area requires tapping in a grid pattern with a "pixel" size appropriate for the flaw size of interest. As figures 28 and 29 indicate, aircraft maintenance manuals often call for this mode of inspection coverage. However, a raster scan using a handheld impactor can be tedious and impractical for larger areas. A mechanized tapper is therefore desirable. Over the years, a number of instrumented tap test devices have been developed to acquire quantitative tap response data and to use that data to automate the interpretation process.

These mechanized tappers have substantially alleviated the operator fatigue problem often associated with the tap test. A mechanized device not only ensures uniformity of the tapping force and angle of strike but is indispensable in a system that generates tap test images. The basic premise behind the instrumented tap test devices is the same. The force data and sound data of the tap test are acquired with electronic circuits so as to eliminate the dependence on the operator's sensory response. Certain features of the digital data are extracted and used in the detection of flaws, damage, and property degradation. Further processing of the data, using Fourier spectral analysis, for example, has also been used. However, the most beneficial instrumentation of the tap test is still the acquisition of the contact time electronically. By incorporating an accelerometer into the tapping device, the contact time may be measured with a simple circuit without the need for acquiring a digitized force-time curve. For example, a counter may be started when the output voltage exceeds a certain threshold and stopped when the voltage falls below the threshold. The value of the contact time can be used directly in the differentiation of damaged and undamaged regions based on the established contact time of a good region for the tapper mass used. Alternatively, the stiffness deduced from the contact time, a tapper mass-independent quantity, may be used as the differentiating parameter.

Figure 43 shows a sample cross-section of a solenoid-driven tapping device and the inclusion of a force transducer or accelerometer on the tip to record the impact response of the structure being inspected. Figure 44 shows a voltage waveform of an impact that allows the impact duration—related to the stiffness of the structure—to be measured. Changes in the stiffness of an area, which produce changes in the duration of impact, can be observed in the plots contained in figure 45. As the structure becomes less stiff, the duration of impact gets longer, and this can be related to the presence of damage. Some devices have used changes in the frequency response spectrum to infer the presence of damage. In this case, the Fourier transform of the acceleration/force

versus time plot is used to produce the plots shown in figure 46. In both cases, the differences between the “good” and “bad” areas can be automatically detected in the instrumented tap test device and various feedbacks can be used (e.g., alarms, lights) to signal the presence of damage or, at least, the need for additional scrutiny of the area.

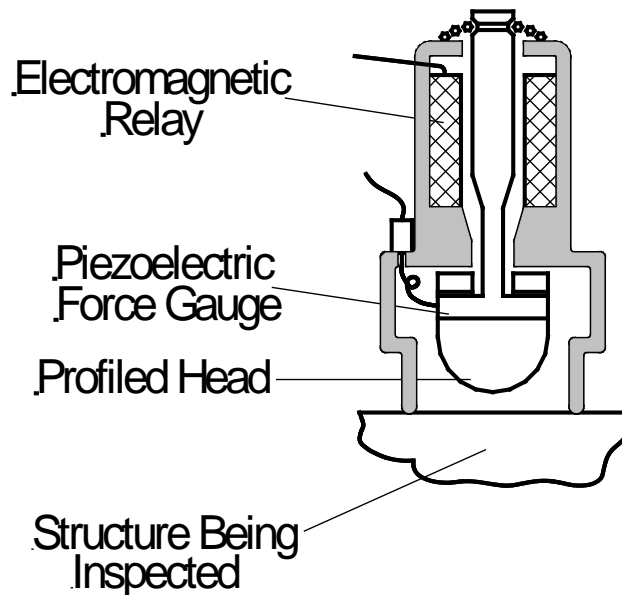


Figure 43. Tapping head

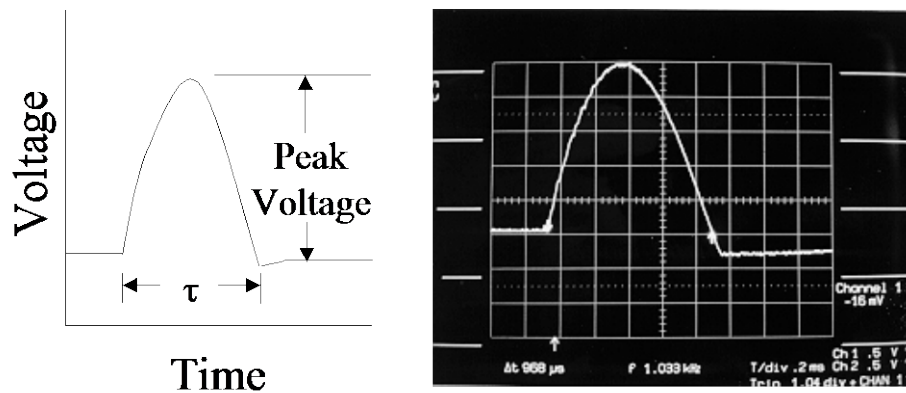


Figure 44. Determination of the impact duration, τ , from an accelerometer output and a photograph of an oscilloscope trace with a $\tau = 968 \mu\text{s}$

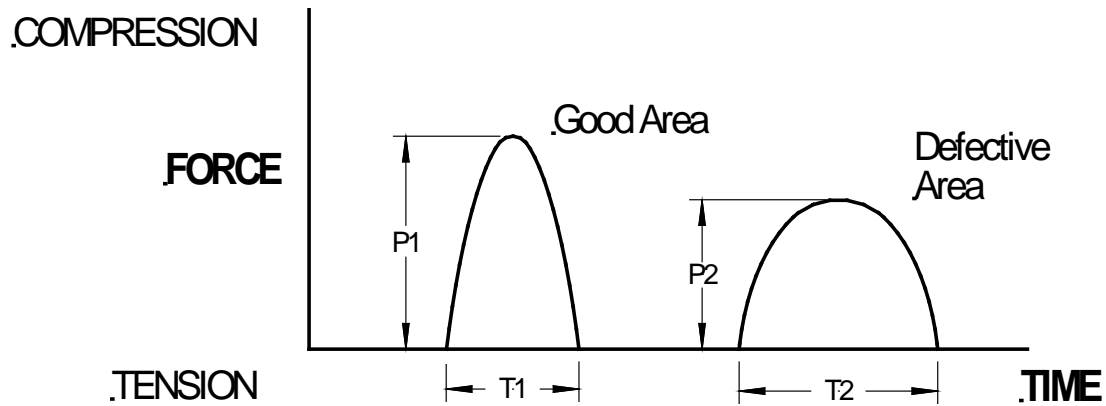


Figure 45. Sample force pulses

Over the years, a number of instrumented tap test devices have been developed. Instrumented tap test devices, like the Woodpecker, DTH, and CATT have been developed to improve the performance of the tap test method. These devices use embedded sensors in the hammer heads to quantify the stiffness of the contact area and display this stiffness as a relative numeric value. Structural anomalies appear as distinct variations in the stiffness measured by the sensor as determined by the impact force-time characteristics. This approach greatly reduces the human factors concerns and results in more repetitive inspections.

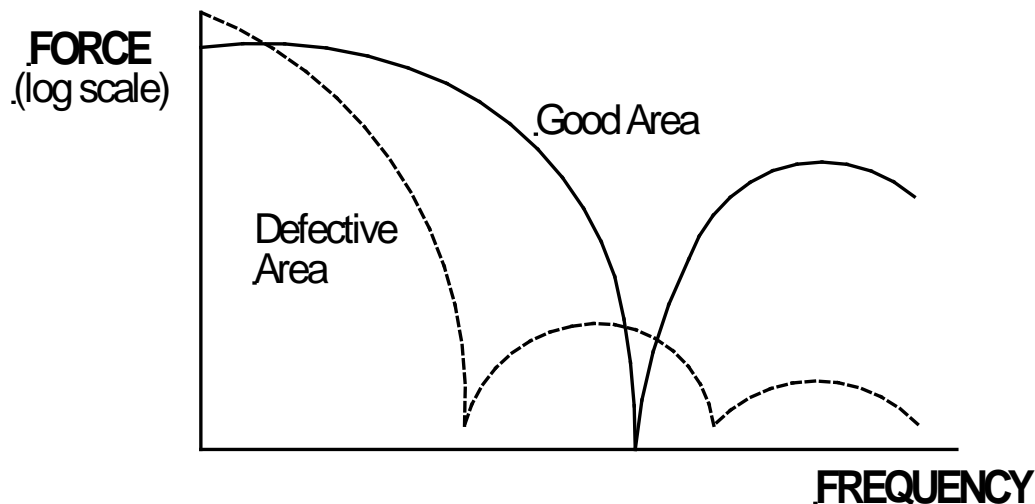


Figure 46. Fourier transform of the impulse

A mechanized, and at one time commercialized, tap test device, called the Tapometer, uses a force transducer in a solenoid-driven impactor [31]. The system makes use of the Fourier transform of the force-time history for differentiating defective and good regions on a structure. When combined with a motorized scanner, the device was shown to produce good tap test images of honeycomb sandwich structures. A handheld, battery-powered tap tester, called the Mitsui Woodpecker [32], employs a solenoid-driven hammer that contains an accelerometer for measuring the contact time during which the hammer is in contact with the surface. A hand-

operated digital hammer, called the WichiTech DTH or Rapid Damage Detection Device (RD³), is also commercially available [33, 34]. The DTH uses a digital LCD readout to display the value of the contact time. For this device, the impactor is a hand-deployed plastic hammer that contains an acceleration sensor. Finally, the CATT, developed at Iowa State University, uses a piezoelectric accelerometer fitted with a hemispherical tip as a handheld impactor and also in a semi-automated, cart-deployed magnetic tapper. The CATT uses the contact time data and converts it into the local stiffness based on the mass of the impactor [35]. Figure 47 shows three of the four systems described above.



Figure 47. Three examples of instrumented tap test devices: a) Woodpecker, b) RD³, and c) CATT

4.1.1 Woodpecker

The Woodpecker device, developed by Mitsui, is shown in figure 48. It uses automatic tapping, produced by an electric solenoid, to drive the hammer tip. The device uses a calibration feature to store a response corresponding to an undamaged region, which it then compares with the response from subsequent inspection regions. The device then displays green (good), yellow (possible damage), and red (probable damage) lights, along with audible alarms, to relay the results from this relative comparison in real time. Thus, it does not depend on the audible responses, which may be difficult to distinguish from each other, especially in noisy environments. The quantitative values associated with the impacts are transmitted to the Woodpecker's monitoring unit. A user-selected number of taps can be averaged into a single impact duration number to better normalize the results and minimize the detrimental effects of noise sources (e.g., a non-perpendicular deployment angle). An attachment to the Woodpecker displays the numerical value of the contact time in microseconds. This separate monitoring unit can be used for displaying and storing measured values. This unit can also be connected to a computer so that a grid of measurements can be logged corresponding to various locations on a structure. In this manner, the duration of impact values can be color-coded according to specific bins, and two-dimensional images (C-scans) can be produced of the structure's surface. The Woodpecker is small and lightweight to permit operation with one hand.

4.1.2 Rapid Damage Detection Device

The RD³ developed by Boeing, and distributed by WichiTech, consists of a lightweight hammer containing an accelerometer connected by cable through the handle to a handheld module that contains digital logic components and a liquid crystal digital display (see figure 49). The accelerometer in the head of the hammer translates the force time pulse at the hammer head due to each tap into a voltage pulse. A programmable array logic integrated circuit receives the signal and measures the pulse amplitude. The display resets and shows a new value after each hammer tap. If the minimum set point is not reached (i.e., the tap is too light), a zero (0) is displayed. With this technique, the hand-held hammer is retained as the basic means of obtaining tap data. By instrumenting a traditional tap hammer with a force transducer and associated electronics, quantitative, objective data can be obtained simply and inexpensively. RD³ is a low-cost instrumented tap hammer that provides a quantitative measure of the hammer/composite impulse time that can be correlated to delaminations or other stiffness-reducing damage in the structure. The instrumented tap hammer supplements the tonal discrimination of the operator with a numeric readout that can readily be related to local part quality. The user is able to compare the contact time at a region of unknown condition with that of a known good region. The effect of background noise and operator differences on the inspection results can be minimized.



Figure 48. Woodpecker automated tap test device

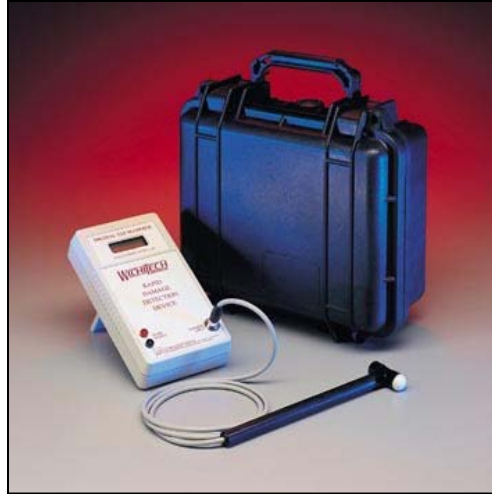


Figure 49. RD³ automated tap test device

4.1.3 Computer-Aided Tap Test Device

The CATT collects quantitative data relating to the surface stiffness of the component and completely eliminates the reliance on the audio signal [35, 36]. It measures the duration of a tap impact and relates this quantity to an effective spring stiffness of the structure. It can be deployed manually over a prescribed grid or in a semi-automated fashion using a rolling wheel that controls both the magnitude and spacing of the impacts. Figures 50–53 show both modes of deployment for the CATT system. The instrumented tapper consists of an accelerometer connected to a battery-operated signal conditioning circuit. The voltage waveform of an impact is digitized, and the impact duration is measured, as shown in figure 44. The output voltage waveform of an impact (i.e., the force-time history of a tap) resembles one half cycle of a sine wave. The impact duration, τ , is measured near the zero baseline using a high gain and low threshold.

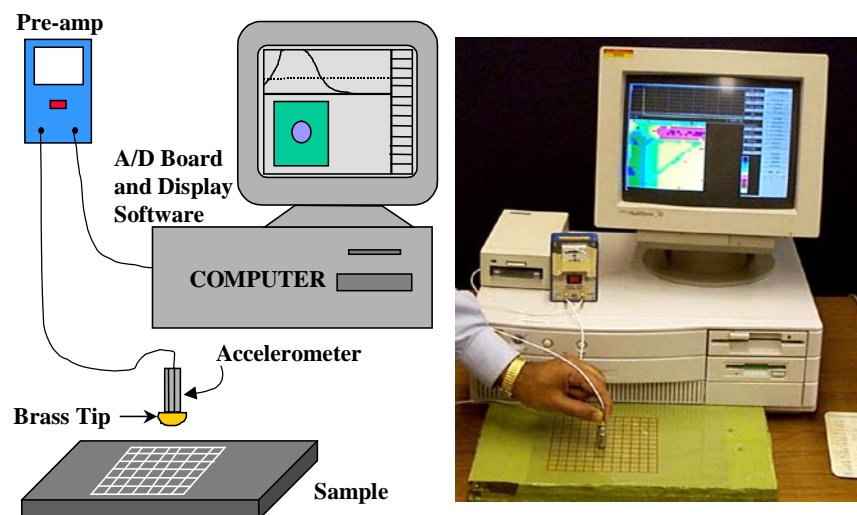


Figure 50. Manual deployment of CATT device

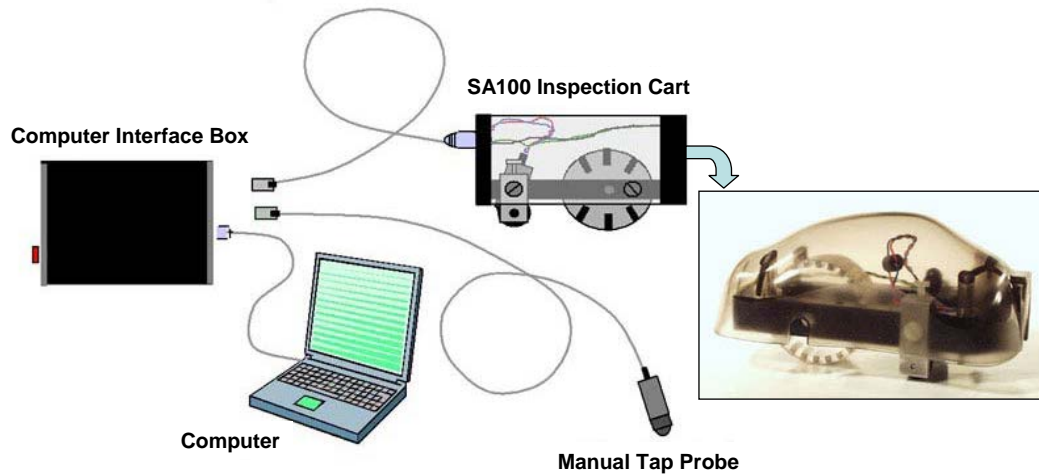


Figure 51. Manual tap probe and hand-deployed cart for semi-automated scanning using CATT system



Figure 52. CATT system being deployed by Iowa State University developers on honeycomb flaw detection experiment test panels



Figure 53. Close-up of CATT tapper and transfer of data from computer to grading sheets

To take advantage of the visual interpretive power of the inspector, the impact duration of an instrumented tapper is measured and fed into a Microsoft Excel spreadsheet to produce C-scan images. A graphical user interface is used to produce a C-scan image by displaying the relative stiffness values acquired across the scan as color-coded values of impact durations. The system significantly improves the quality of the inspection by producing a visual image of the condition of the structure. To initiate a scan, a transparent plastic sheet with a printed grid is taped over the region to be tapped. The number of taps in the length and width directions is entered into the computer. The operator then taps each square of the grid with the handheld accelerometer tapper in a systematic manner (for example, from left to right and top to bottom) until all the squares are tapped. The manual tap probe is used to inspect small or confined areas and surfaces with a significant curvature. The semi-automated version of the CATT system uses a magnet-operated cart that impacts the surface with the accelerometer at a pre-set spacing interval as the cart is pushed over the surface (see figures 51 and 52). Using the cart, a large area can be inspected very rapidly. Each tap triggers the A/D board and prompts the program to record one impact duration value for the corresponding location. A C-scan type image is generated as the tap scan progresses. The measured values of the impact duration are displayed in 16 different colors. The resulting image shows a damaged area as a region of higher impact duration values. Such an image also reveals internal substructures of the composite part, including core splices, ply drop-off or build-up, reinforcing doublers, and septum changes. Based on a mechanical model of the impact response, the impact duration image can be converted into an image of an effective spring constant that indicates the local stiffness of the structure. Tap scan images of different parts of a component or of different components may be stored in the computer for future reference and assessment of damage progression.

Images can also be produced to display the local stiffness (an effective spring constant) of the structure and the percentage loss of stiffness caused by damage. Figure 54 shows a tap test image of a carbon-fiber-reinforced polymer honeycomb sandwich panel containing six engineered flaws that simulate disbonds and delaminations. The figure is an image of the local stiffness (k) converted from the measured contact time using the impactor mass. Figure 54 shows that the background stiffness of the panel is approximately 1.4 MN/m while at the two worst flaws, the stiffness has decreased to approximately 0.5 MN/m. The main advantage of an image display of the tap test results is that the visual and analytical power of the operator is immediately put to use. The size, shape, and severity of the defects can be easily assessed. In addition, the distinction between defects and normal substructures is much easier to ascertain using an image that displays both the defects and the normal substructures such as ply overlaps, core splices, and repair patches. Figure 55 shows a similar C-scan based on the color-coded results from the duration of impact parameters. The C-scan is plotted with the X and Y locations of the part displayed to allow for flaw location and sizing. For the purposes of this CHE, all CATT results were transferred to grading sheets using the data transfer process shown in figure 53. Test specimen flaw layout drawings were also overlaid on the CATT C-scans, as shown in figure 55, to allow for accurate grading of the CATT performance.

The C-scan images can be displayed as two-dimensional or three-dimensional surface plots. For example, figure 56 reveals structural features (stiffeners), damage, and flaws within a component. An example of an intensive application of tap test imaging in the field is shown in figure 57. The image shows the inner and outer surfaces of a composite rudder that was

recovered from an aircraft accident that involved both the vertical stabilizer and rudder components. Parts of the rudder were broken apart so the tap test scans, made with the semiautomatic magnetic cart of the CATT system over intact regions, were assembled afterward. The assembled image in figure 4-15 represents more than 60 scans of 2 x 3 ft (60 x 90 cm) each and covered a total scanned area of approximately 400 ft² (37 m²). The overall image revealed considerable information about the damage distribution and fracture orientation on the rudder.

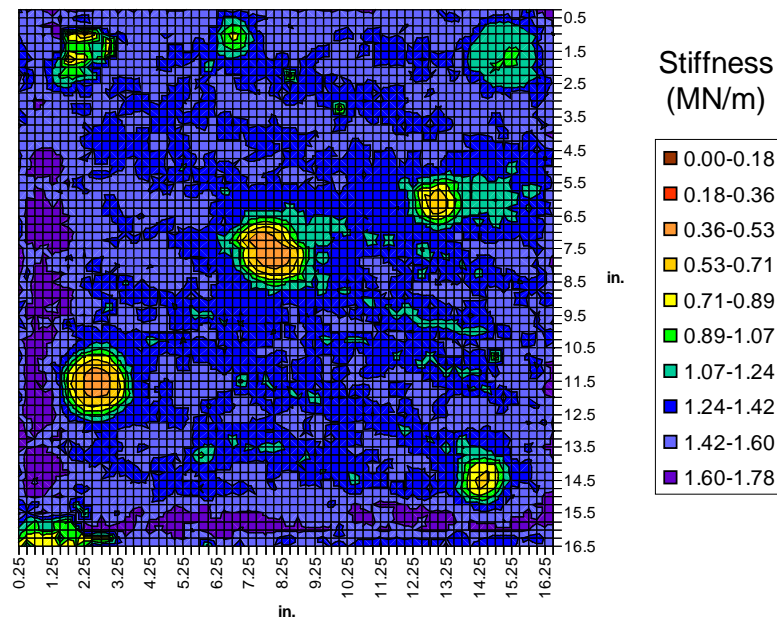


Figure 54. CATT C-scan tap test image of surface contact stiffness of a composite honeycomb sandwich panel containing engineered defects

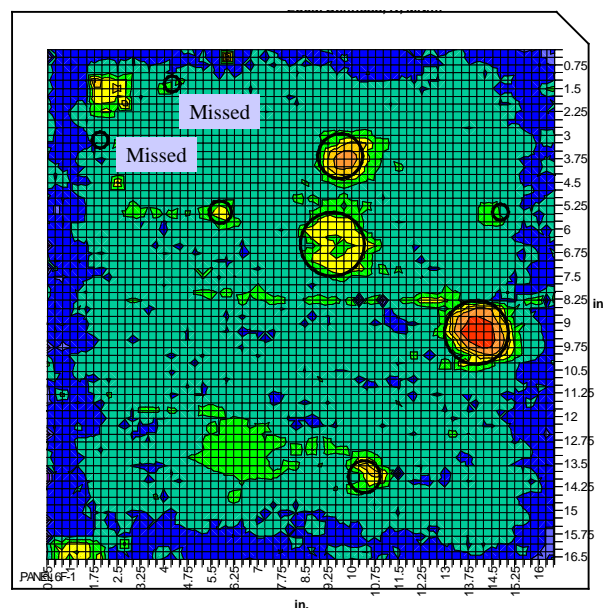


Figure 55. Sample CATT C-scan of a 6-ply fiberglass test panel with flaw template overlay showing hits and misses

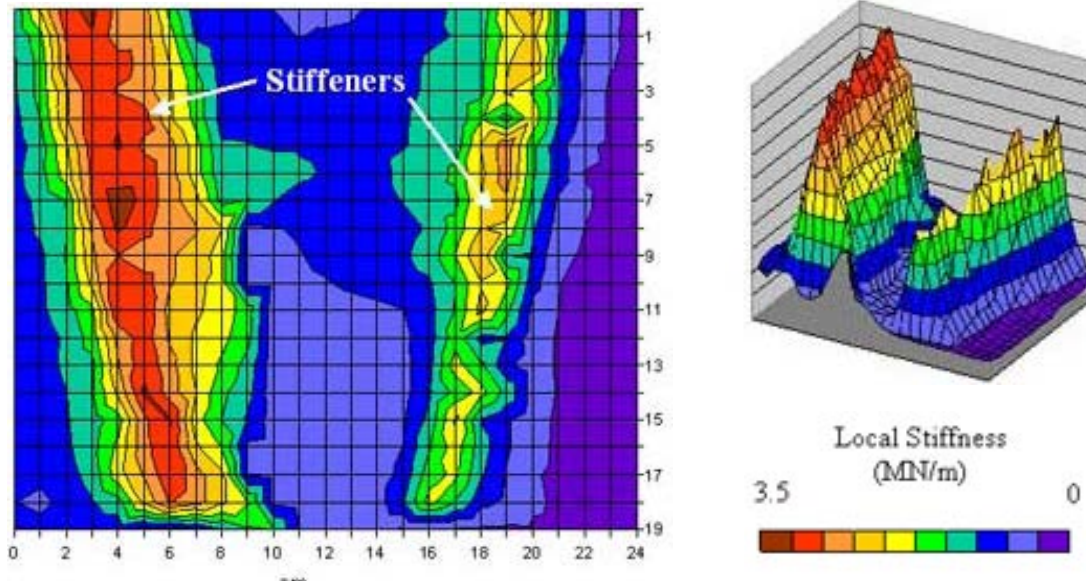


Figure 56. Two-dimensional and three-dimensional C-scan images produced from a CATT inspection of a B767 elevator

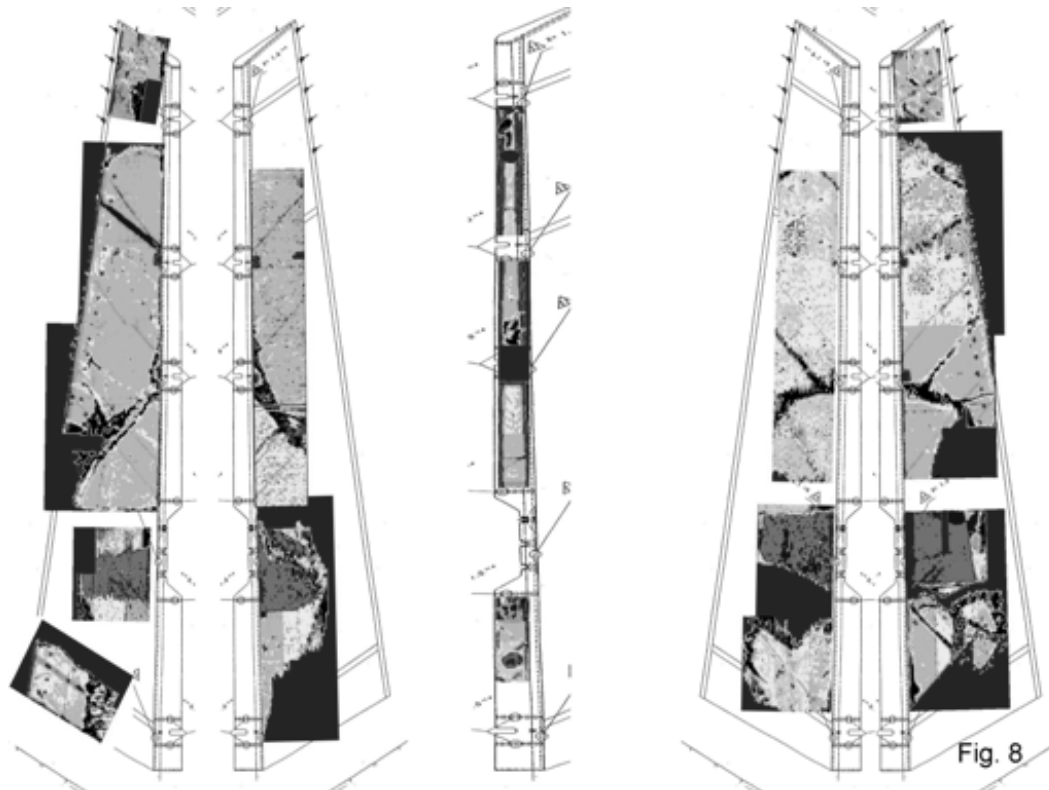


Figure 57. Assembled CATT tap test image of the inner and outer surfaces of a composite rudder recovered from an aircraft accident

4.2 PULSED THERMOGRAPHY

Thermography is an NDI method that uses thermal gradients to analyze the physical characteristics of a structure such as internal defects. This is done by converting a thermal gradient into a visible image by using a thermally sensitive detector such as an infrared (IR) camera [37, 38]. Flash thermography relies on the heat absorption characteristics of the structure to indicate the presence of defects. In thermographic NDI, part of the IR band of the electromagnetic spectrum is used to map the surface temperature of an inspected item. The temperature distribution on a structure can be measured optically by the radiation that it produces at IR wavelengths. Many defects affect the thermal properties of materials. Examples are corrosion, disbonds, cracks, impact damage, panel thinning, and fluid ingress into composite or honeycomb materials. In general, a source of energy is used to create a temperature difference between the specimen and the surrounding environment. Variations in the structure or material properties result in variations in heat flow and surface temperature, which are recorded by the IR camera. Figure 58 shows a schematic of a thermographic inspection system and highlights the physics of flaw detection.

Thermographic inspection is accomplished using high-power flash lamps or other heat source, an IR video camera, and image processing hardware and software—all of which are controlled by a personal computer. By the judicious application of external heat sources, common aircraft defects can be detected by an appropriate IR survey. The heat source, such as flash lamps, is used to raise the surface temperature of the structure. The subsequent heat transfer into the material is affected by any defects that may be present. The resulting temperature distribution is then recorded by the IR camera and displayed on the computer monitor. As the heat diffuses through the structure, the surface temperature is monitored for a period of time by an IR camera. In practice, the computer actually obtains several images at progressively later times after each flash. Areas that appear hotter than normal may indicate the presence of a delamination or disbond beneath the surface that is preventing heat diffusion into deeper layers. By using a computer to analyze and manipulate the IR data captured over time, subtle variations can be enhanced in the image. Typical computer enhancements include analysis of the first and second derivatives of the heat-versus-time signatures at each point in the time sequence to produce images showing rates of change. Through the use of temperature-versus-time images produced by the thermography system, it is possible to determine the depths of disbonds, delaminations, and other flaws in a structure. Typical gantry-based and handheld thermographic inspection systems are shown in figure 59.

Thermographic inspection procedures on aircraft parts can be used to detect certain local changes in materials that occur in homogenous parts. These may typically be considered (but not exclusively) as voids, inclusions, disbonds, fluid ingress or contamination, foreign objects, and damaged or broken structural assemblies. Thermographic inspection can be carried out on almost every type of material used in the construction of aircraft. The means of excitation, the detection method, and the inspection parameters can be varied depending on the material to be inspected and the flaws to be detected.

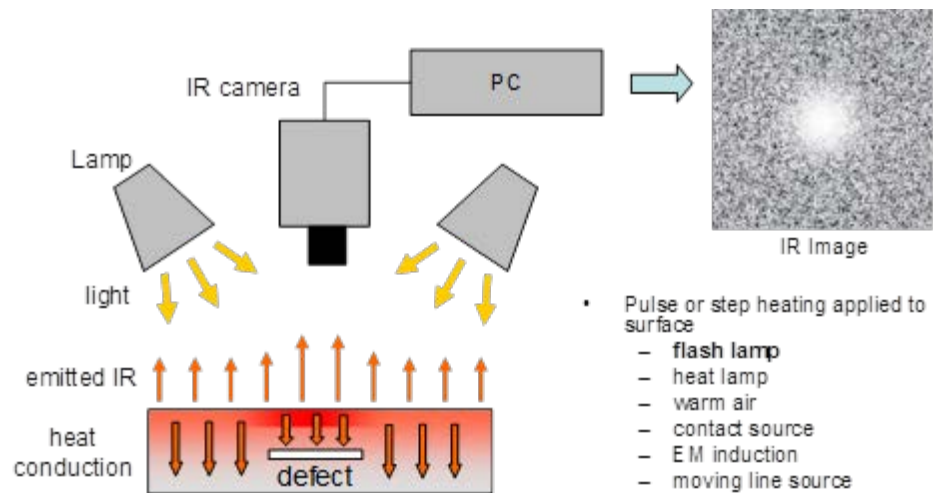


Figure 58. Principle of active pulsed thermography

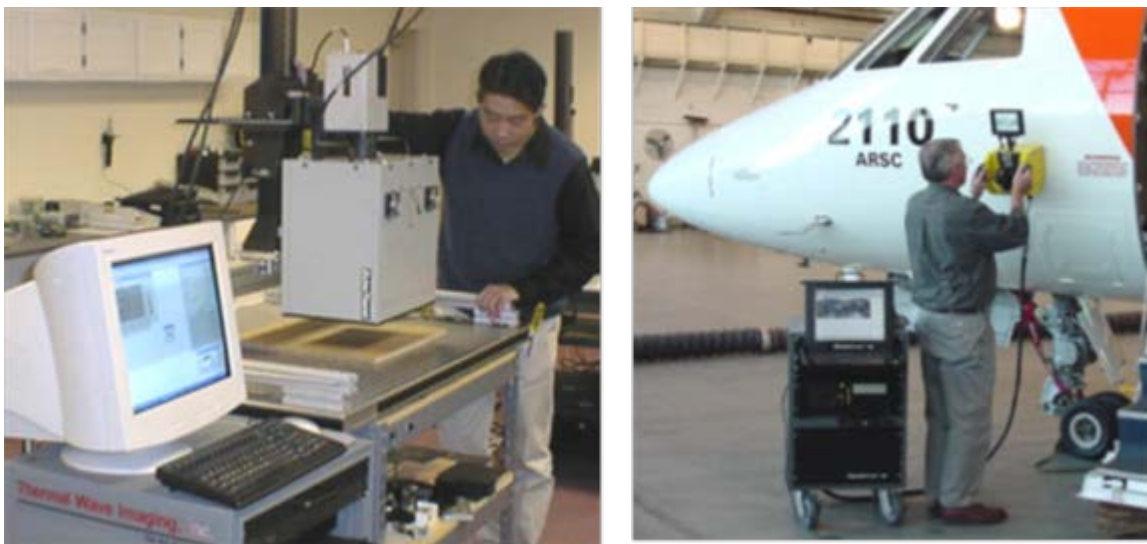


Figure 59. Laboratory thermal wave imaging system inspecting composite flow detection panels and a portable field system inspecting an aircraft fuselage

Some of the advantages of the thermography inspection method are enumerated below:

1. Thermography can be performed without physical contact with the surface.
2. Single images can include relatively large areas (1–2 ft²), allowing for rapid inspections of large surface areas.
3. Two-dimensional images of the inspected surface help the operator visualize the location and extent of any defect.

The primary disadvantages of thermography are:

1. It is often necessary to apply a high-emissivity coating during inspections to obtain an acceptable image (steps have been taken to minimize the labor time associated with this task).
2. Damage to layers deep within a structure is more difficult to detect than damage in surface layers because the larger mass of material tends to dissipate the applied heat energy.

After presenting the thermography principles and equipment, it is worthwhile to discuss some specifics on the critical component: the IR camera. An IR camera is a non-contact device that detects IR energy (heat) and converts it into an electronic signal, which is then processed to produce a thermal image on a video monitor and perform temperature calculations. Heat sensed by an IR camera can be very precisely quantified, or measured, to monitor thermal performance as well as identify and evaluate the relative severity of heat-related problems. Recent innovations (in particular, detector technology) pertaining to the incorporation of built-in visual imaging, automatic functionality, and IR software development deliver more cost-effective thermal analysis solutions. A brief comparison of some IR cameras used for thermographic inspection systems is provided in figure 60.

		
<u>A40</u>	<u>Merlin Mid</u>	<u>Phoenix</u>
Detector Material:	Vanadium Oxide (VOx)	Indium Antimonide (InSb)
Detector Cooling:	Uncooled Microbolometer	Integral Stirling or LN2
Spectral Range:	7.5-13 micron	3-5 micron
Thermal Sensitivity:	0.08° C	0.025 °C
Focal Plane Array:	320 x 240	640 x 512
Frame Rate:	60 Hz	30 Hz
Weight:	3.1 lbs	Camera: 7 lbs & RTIE: 6 lbs
Size:	8.2" x 4.3" x 3.6"	Camera: 7.5" x 4.4" x 5.2"

Figure 60. Comparison of IR cameras for thermography inspection

4.2.1 Thermal Wave Imaging EchoTherm Thermography Inspection System

In the solid laminate flaw detection experiment, a turnkey thermography inspection system—the Thermal Wave Imaging (TWI)—was used to assess the merits of thermography to detect flaws in composite honeycomb construction. Figure 61 shows a photo of this inspection device and example applications on aircraft. The TWI ThermoScope[®] and EchoTherm[®] NDI systems are designed for in-service applications and are integrated hardware and software systems for analyzing and measuring physical properties of materials using pulsed thermography. The system includes TWI's Thermographic Signal Reconstruction[®] (TSR) processing technique, which increases spatial and temporal resolution of a thermogram sequence.

Figures 62 and 63 show sample results from thermographic inspections on bonded tear straps and composite honeycomb structure, respectively. Figure 62 shows how a disbond between an aircraft skin and the substructure tear strap affects the thermographic image by changing the heat transfer in that local region. Similarly, the IR image in figure 63 indicates the various flaws that were engineered into the honeycomb panel. Figures 64 and 65 contain additional IR images of various flaws in composite honeycomb and composite laminate structures. One of the limitations of thermography is the depth of penetration of the inspection. For composite laminates, the inspection depth limit is approximately 0.2". Only flaws that manifest themselves as variations in the surface temperature of the structure can be readily imaged by the IR camera. Novel heating methods are currently being used to infuse higher levels of heat energy into the structure and improve the detection of deeper flaws.



Figure 61. TWI system equipment and inspection of aircraft

Tear Strap
Disbond

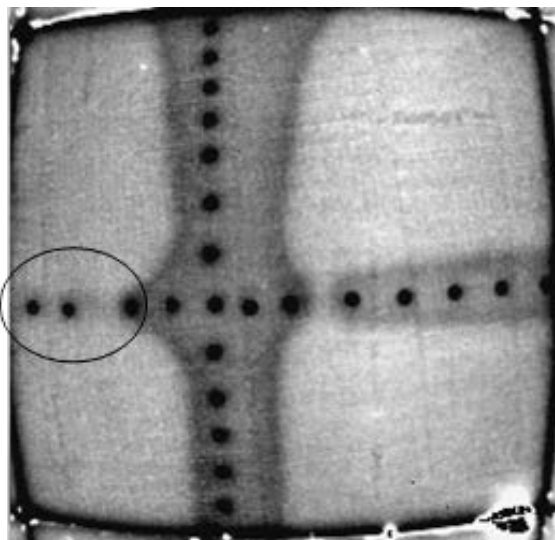


Figure 62. Sample thermography image showing a disbond in an aluminum fuselage tear strap structure

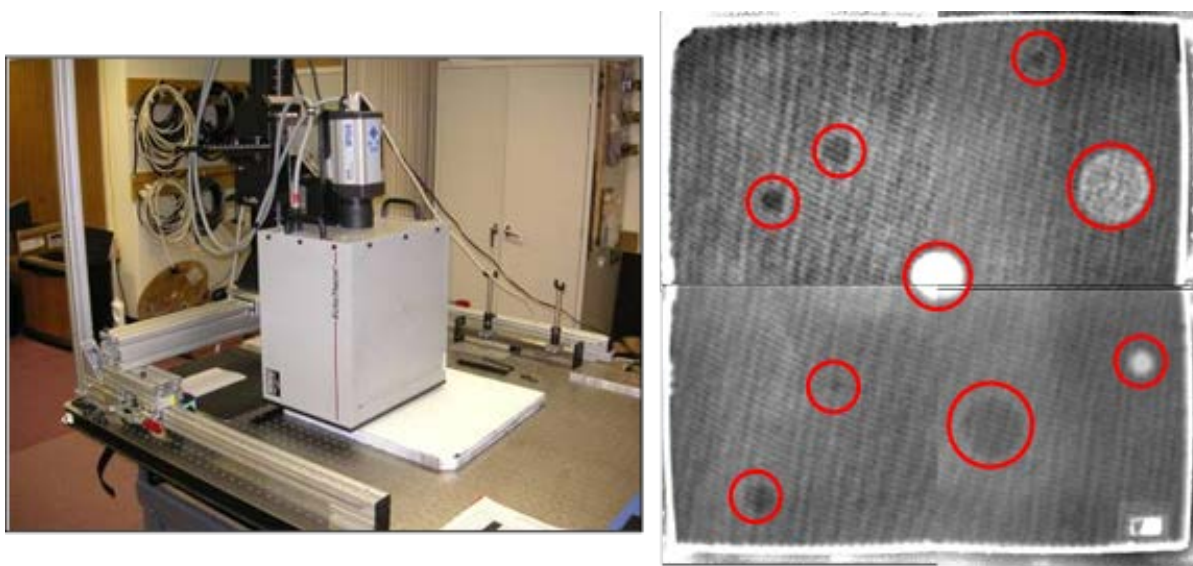


Figure 63. FLIR A40 uncooled camera inspecting the honeycomb test panels and a sample IR image from a fiberglass panel

The TWI IR system was applied to a bonded, composite doubler repair that was installed on a DC-9 fuselage section in the FAA-AANC hangar. Figure 66 shows a schematic of the 10-ply doubler highlighting the size, shape, and location of the embedded flaws. The resultant sequence of images produced by a TWI inspection is also contained in figure 66. The features seen in the images associated with the earlier times are defects closest to the outside surface of the patch (note appearance of flaws #1 and #2 in the first few frames). The disbonds, located at the base of the doubler, and deeper delaminations appear in the later frames, corresponding to their delayed effect on the thermal field. All six embedded flaws were identified in the TWI images, and flaws smaller than 0.5” in diameter could be detected.

Pulsed Thermography

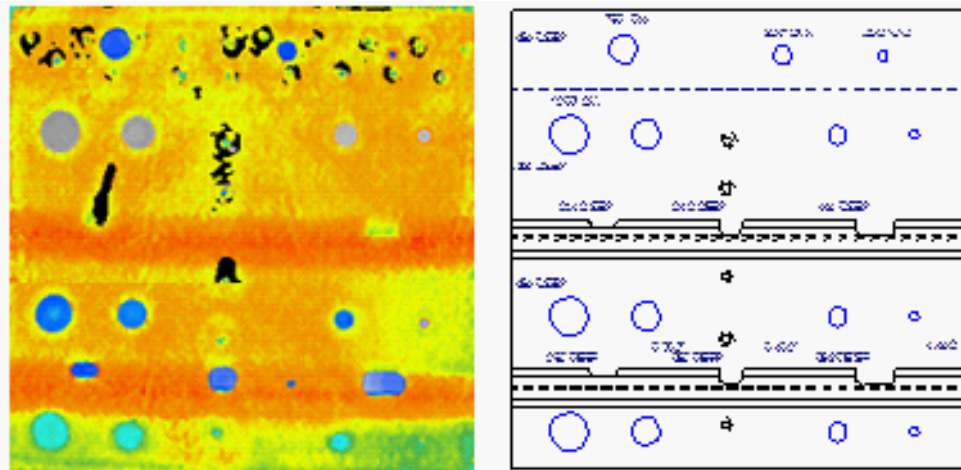
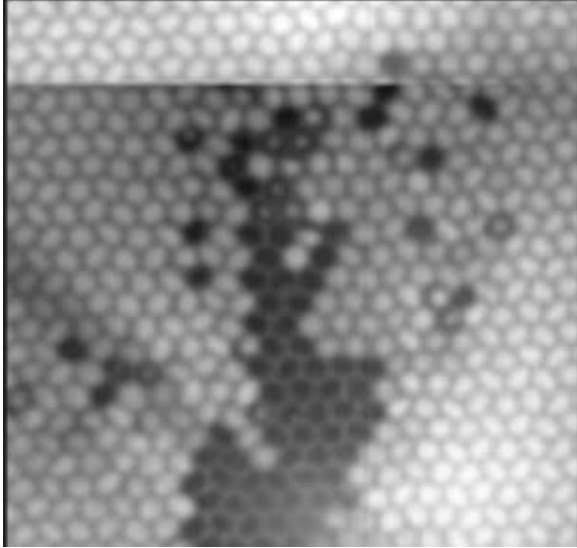
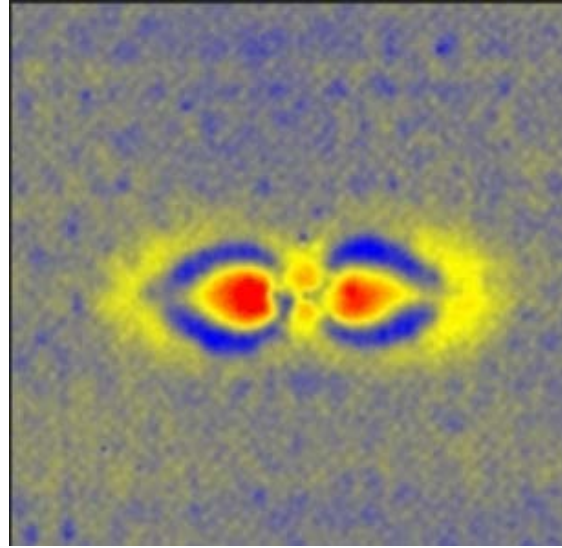


Figure 64. Thermography image produced from inspection of composite laminate panel with flaw profile as shown in drawing on the right

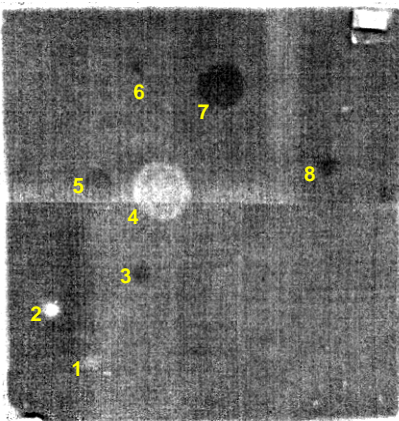


Water Ingress in a Composite Honeycomb Structure

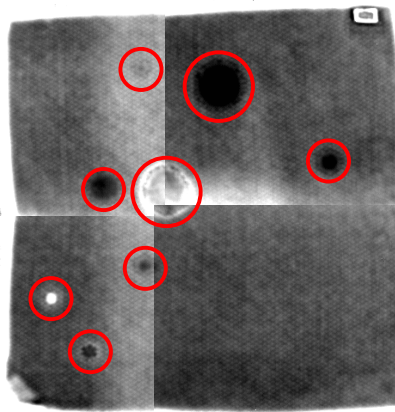


Impact Damage in a Solid Laminate Composite Structure

FLIR A40 Uncooled IR Camera



FLIR Phoenix IR Camera



Radiance HS IR Camera

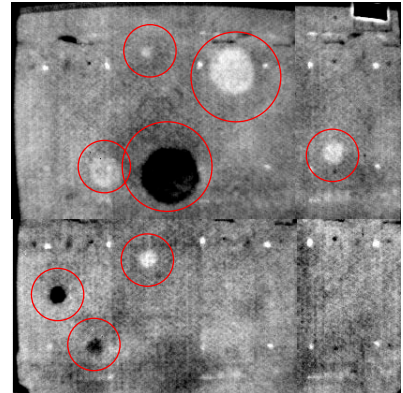


Figure 65. Sample thermography images showing damage in composite structures with comparisons from three different IR cameras on 3-ply carbon honeycomb panel (all flaws identified by all cameras)

Boron/Epoxy Doubler on the DC-8 Test Bed (AFT section)
 10 Ply Lay-Up with Engineered Flaws
 8" H X 6" W with Ply Orientations of [0,+45,-45,90,0]

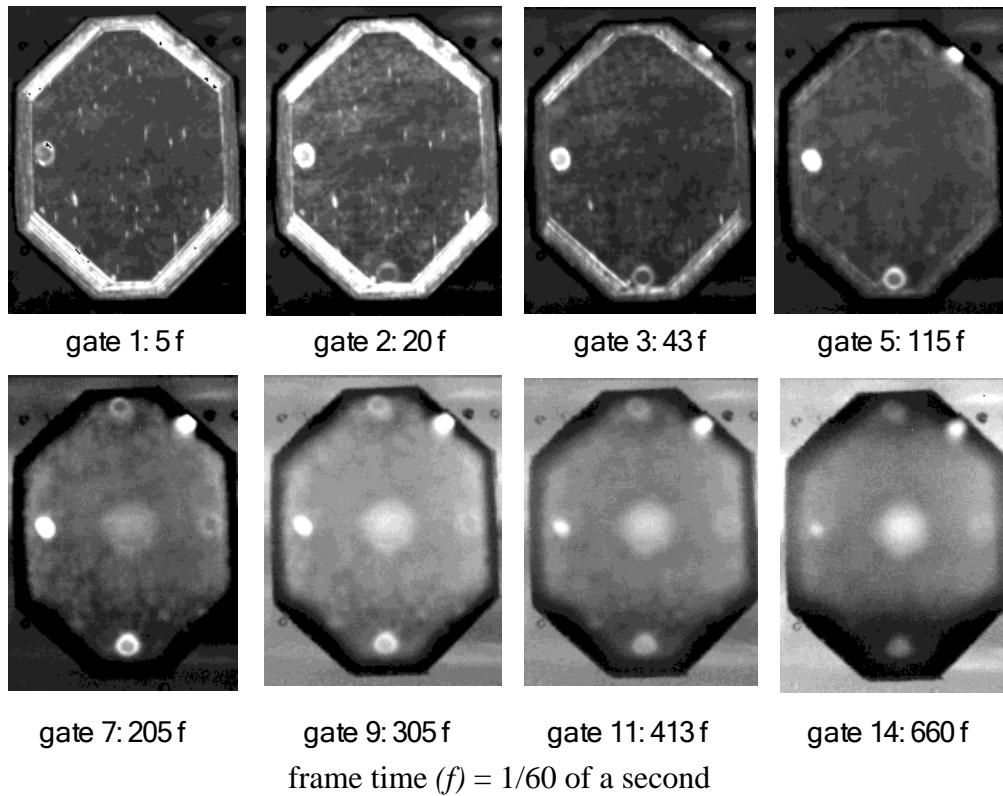
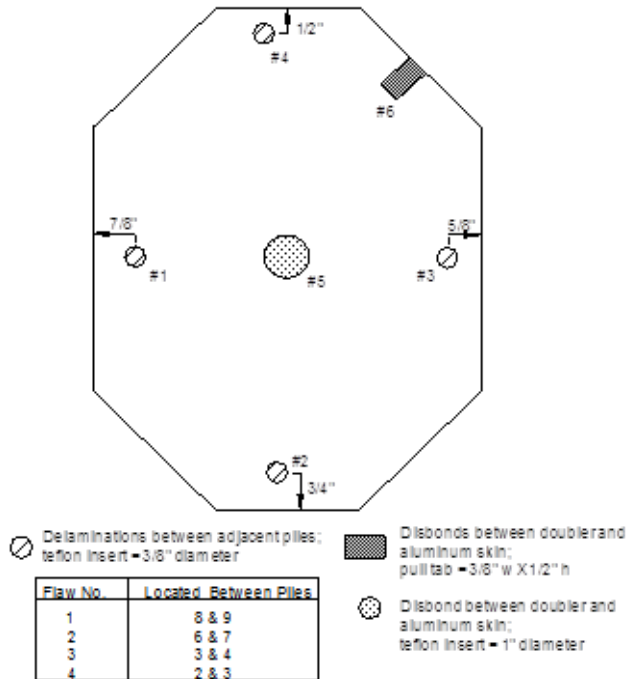


Figure 66. Sequence of thermal wave images from DC-9 composite doubler inspection

4.3 LINE SCANNING THERMOGRAPHY

LST is a non-contact inspection method based on dynamic thermography. The LST technique provides a quick and efficient methodology to scan wide areas rapidly. The technique has been used for the inspection of composite propellers, sandwich panels, motor case tubes, and wind turbine blades, among other applications. Figure 67 shows some examples of composite structures scanned using the LST technique.

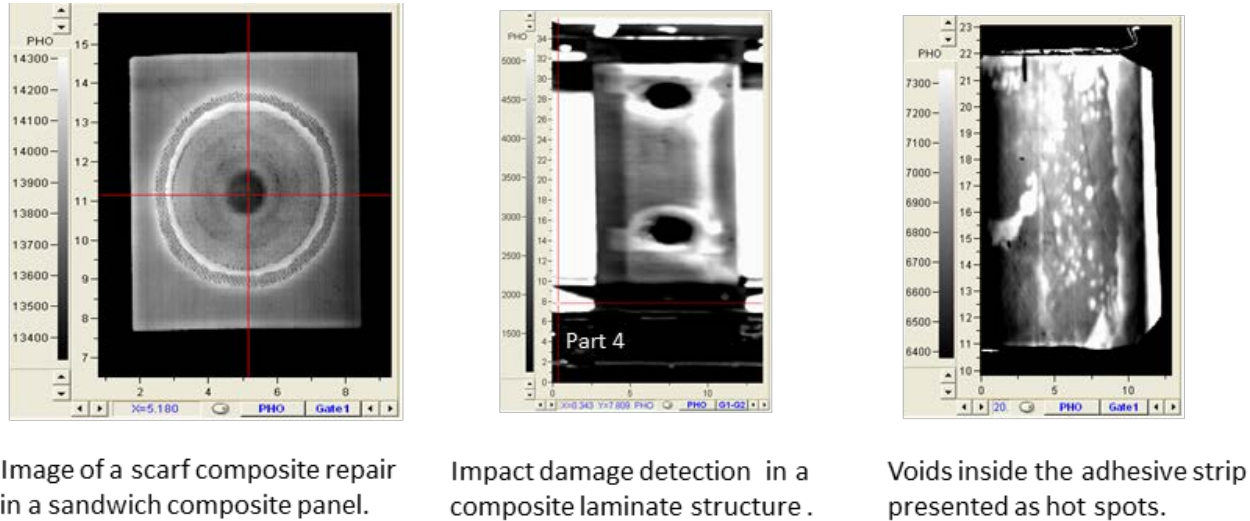


Figure 67. Examples of thermal images generated after scanning a composite structure using the LST technique

After heat deposition in a dynamic thermography technique, internal flaws in the material show up by variations in both the surface temperature distribution and transient surface temperature decay rate. LST is a dynamic thermography technique patented by NASA [39, 40]. This technique deposits heat along a thin line that is swept from edge to edge of the surface under inspection. An IR camera moves in tandem with the heat source at a set speed, and it is able to capture the thermal profile of the sample after the heat deposition takes place. A diagram of the basic setup is shown in figure 68, where one can observe that the field of view of the camera is restricted to an area of the sample surrounding the heat application region. The image on the left shows a side view of the heat source, IR camera, and surface being studied. The image on the right shows the LST thermal image generated by stacking a selected pixel line captured in every frame. During the scan, the temperature of the region swept by the heat source increases, whereas the surface temperature of the region in front of the heat application remains constant. In LST, the scanning speed and heat intensity should be optimized to match the heat diffusion in the inspected material. A thin material with good thermal conductivity will require fast scanning speed and significant heat deposition. Conversely, a thick material or a material with lower thermal conductivity will require a slower scan with a reduced heat deposition intensity.

The LST technique produces a series of images of the whole area scanned. Each image in the series shows the surface temperature distribution at a given time after heat deposition. The images are generated by defining an observation window or a given pixel line from all frames

acquired from the camera during the scan. The final image or image of the whole area scanned is formed by stacking the selected pixel line from all the frames captured during the scan. When using images with a sensor resolution of 240×320 pixels, a maximum of 240 images of the whole area can be constructed. The time elapsed between consecutive pixel lines depends on the scanning speed and the camera frame rate. Figure 69 shows an example of the images that can be generated using the LST technique following heat deposition. The images show the same scale and were generated using different observation windows. Each image in the series shows the surface temperature distribution of the whole area scanned at a given time after heat deposition; the time is defined by the distance between the heat application, observation gate, and speed at which the scan is set. The LST thermal image is generated by stacking the selected observation line from all frames recorded during the scan. The panel on the right in figure 69 shows a collection of LST thermal images generated from different observation gates. The images show the same scale and represent how the surface temperature drops after heat deposition.

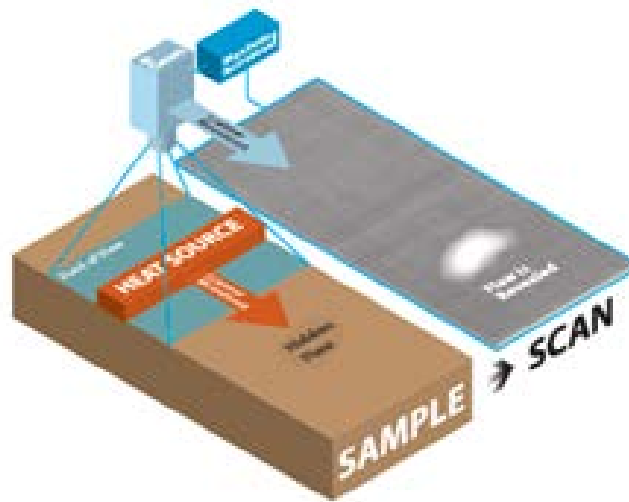


Figure 68. Setup of LST where IR camera and heat source move in tandem through the surface to be inspected

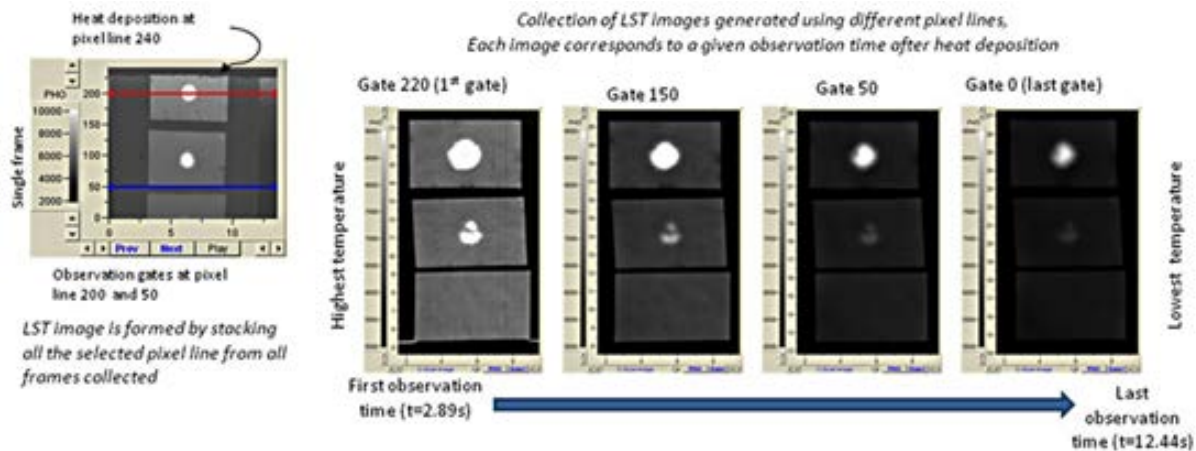


Figure 69. Panel showing the observation gate selection with respect to the heat deposition location

Observation of a defect using LST requires proper optimization of the scanning parameters (i.e., scan velocity, and heat deposition intensity), as these determine the section of the cooling curve that will be observed. The amount of heat deposited over the surface should be sufficient to produce a thermal gradient between the defect and the sound area. In particular, when scanning thin materials displaying good thermal conductivities, the scanning speed should be set higher than the speed used on materials that have lower thermal diffusivities. Scanning at high speeds provides observation of earlier times after heat deposition; scanning at lower speeds provides images corresponding to latter observation times.

4.3.1 MISTRAS Line Scan Thermography Inspection System

Figures 70 and 71 show the MISTRAS Line Scan Thermography™ (LST) scanner used for scanning composites. The LST technique requires that the camera moves in sync with the lamp used for depositing the heat over the surface of interest. The movement is controlled using a motor. These components have been organized in different ways depending on the structure to be scanned and the size of the area of interest. MISTRAS has fabricated mainly three different systems for inspecting different structures. The first one is a gantry-type system capable of performing vertical scans of up to 1.5 m long and 40.64 cm in width. The system employs a cooled IR camera working in the mid-wave IR range (3–5 micrometers). The lamp employed in the system corresponds with a quartz lamp 40.6 cm long. The second LST system is a small area scanner that offers a 30.5 cm x 81.2 cm area scan and uses suction cups for attaching to the surface of interest. This scanner uses a microbolometer working in the 8–12 micrometers range. Finally, the third MISTRAS LST system is a motorized crawler designed to scan flat areas. This scanner offers a 4–6 cm wide field of view and can cover scan lengths of up to 12 m in a single scan. This scanner can hold a cooled camera or a microbolometer. This crawler can be easily modified to scan composite structures of different thicknesses, like fiber glass wind turbine blades, for which it is necessary to wait significant time for observation after the heat deposition. This is achieved by adding a train that increases the separation between the observation area and the heat deposition location.



Figure 70. MISTRAS LST system—crawler used on composites



Figure 71. MISTRAS LST system—small area scanner

Figure 72 shows some sample inspection results from the MISTRAS LST system applied to a 32-ply (0.23" thick skin) solid laminate composite panel with a 58-ply (0.192" thick) upper stringer and 50-ply (0.125" thick) lower stringer. Most of the flaws are detected in the LST image, with the deeper flaws providing the biggest challenge to LST detection.

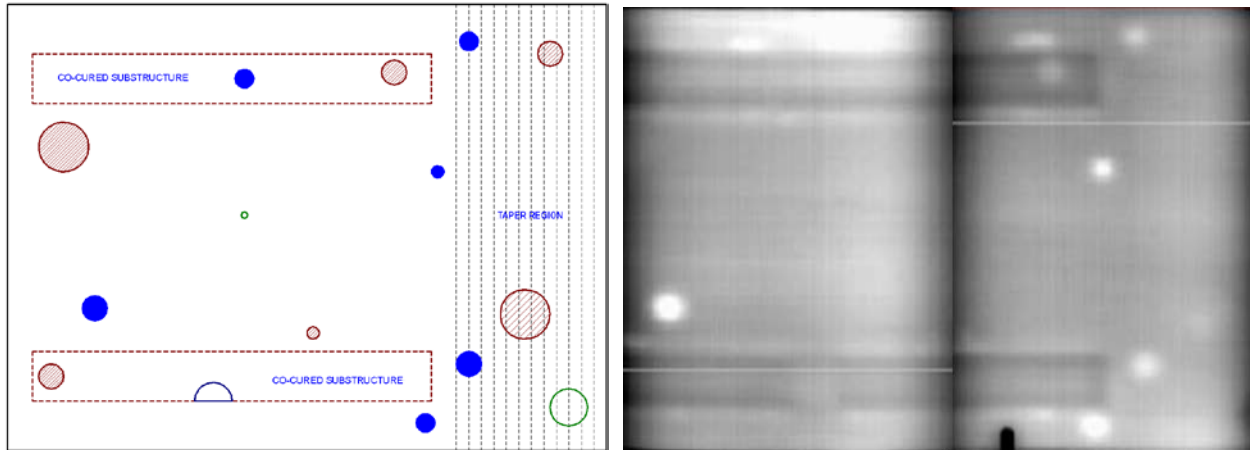


Figure 72. Results produced by MISTRAS LST system on a 32-ply panel with substructure elements

4.4 LOCK-IN THERMOGRAPHY

The principle of lock-in thermography is based on the application of a periodic input energy wave (i.e., thermal emitter, ultrasound, microwave, eddy current, flash lamp) to the surface of the object being inspected and an examination of the resulting local temperatures on the surface of the object [41]. When the wave generated by the input energy penetrates the object's surface, it is absorbed, and the phase angle of the wave is shifted. When the input wave reaches internal areas

of the object where a delamination or inclusion is present, the thermophysical properties are not homogeneous in relation to the surrounding material—hence, the input wave is partially reflected. The reflected portion of the wave interferes with the incoming input wave at the surface of the object and causes an interference pattern in the local surface temperature. In turn, this oscillates at the same frequency as the thermal wave. The internal structure of the object being examined can then be derived by evaluating the phase shift of the local surface temperatures in relation to the input energy wave. However, the ability to derive internal thermophysical inconsistencies within the object requires the input energy source be used at an optimal frequency. This depends on both the thermophysical characteristics of the object, as well as its thickness. A schematic of a typical equipment setup for lock-in thermography is shown in figure 73. The dynamic stimulus can be applied from a wide variety of sources when using lock-in thermography. For composite inspection, this includes halogen lamps, ultrasound, and mechanical stimulation.

For lock-in thermography, the recorded temperature information gathered by the IR camera is transformed into the frequency domain. The measured temporal evolution in each pixel of the temperature is Fourier-transformed for all images of the recorded sequence. Phase and amplitude information are derived and presented as an image [41].

Below are some of the advantages of the lock-in thermography method:

- Summation results in noise-filtering, which enhances the contrast in inspection results.
- Depth range for phase information is twice that of pulse thermography mode.
- Lock-in allows detection of thermal waves with a sensitivity that is 100–1,000 times greater than the best thermal camera—down to μ -Kelvin range.
- The phase image is insensitive to external effects, such as sunlight, reflections depending on surface finish, dirt, and emissivity differences—problems common to conventional thermography.
- The phase information is insensitive to uneven distribution of the applied heat.
- Large areas can be examined within a few minutes from a distance via non-contact measurement.
- A less-costly, uncooled IR camera is normally sufficient.
- Affordable heat sources are widely available (e.g., halogen lamps).
- Visualization of deep defects is possible.

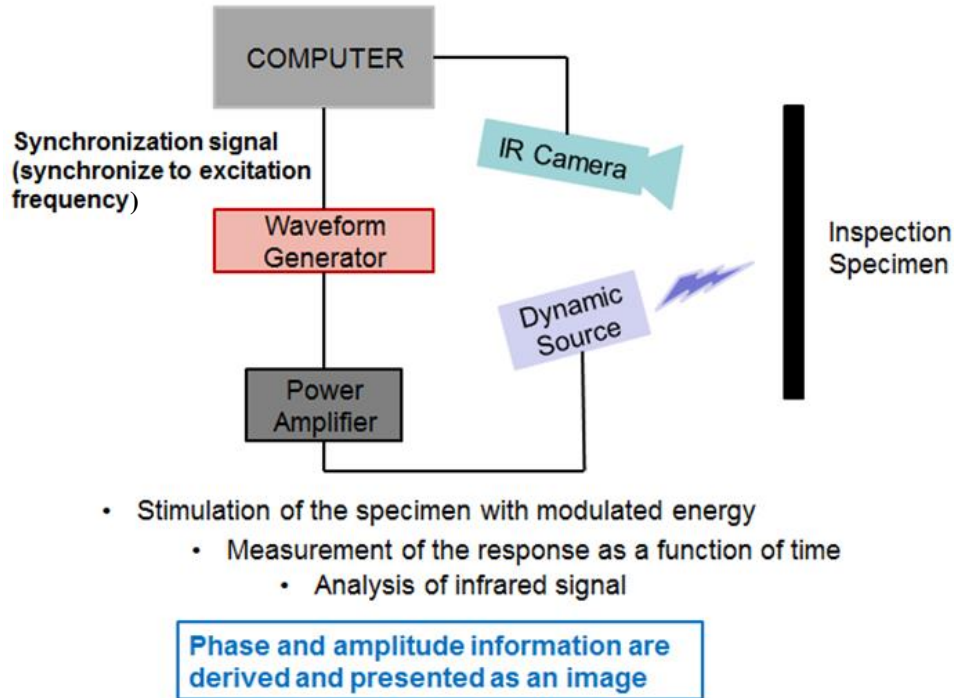


Figure 73. Equipment setup used for typical lock-in thermography inspection

4.4.1 MoviTHERM Lock-In Thermography System

The most common excitation source for lock-in thermography is the halogen lamp. Figure 74 shows the MoviTHERM lock-in thermography equipment featuring a FLIR camera SR2 SC7650 with a Hedler 2500 watt lamp. Lock-in thermography can be used to detect damages such as delamination, inclusions, and impact in composite structures. Figure 75 shows inspection results from a 32-ply (0.23" thick skin) solid laminate composite panel with a 58-ply (0.192" thick) upper stringer and 50 ply (0.125" thick) lower stringer. The engineered flaw profile is also shown on the left for comparison purposes.

An important excitation source used in lock-in thermography is ultrasound. Typical settings for this method are 100 watts at 20 kHz with a 200 ms burst frequency for synchronization. A disadvantage of the UT technique is that it can be destructive, and care is required during excitation of the part. A powerful tool for laboratory and factory measurements is the use of mechanical excitation for heat generation through the thermoelastic effect. Applications of this technique include measurement of fatigue limits, imaging of stress patterns, crack propagation studies, and imaging of vibration patterns.



Figure 74. MoviTHERM lock-in thermography with halogen heat lamp being used as the excitation source

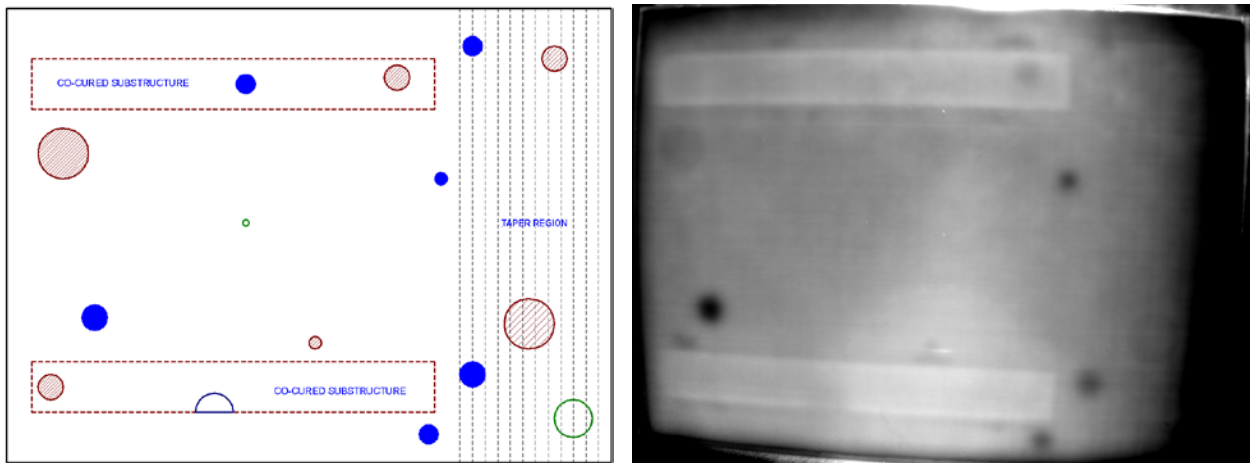


Figure 75. Results produced by lock-in thermography on a 32-ply panel with substructure elements

4.5 SHEAROGRAPHY

Shearography is a wide-area interferometric imaging technique that is capable of detecting micron-sized displacements in the surface of a structure. Shearography equipment, shown in figure 76, monitors the surface of a structure for any changes in the surface strain field. Stressing the material in the appropriate way ensures that the subsurface anomalies are manifested on the

surface of the structure. Shearography is implemented by comparing two interference patterns on a detector plane, typically “before” and “after” an object motion. If the motion, and subsequent out-of-plane deformations, cause changes in the optical path, then the speckle patterns differ. These images can be compared by subtraction or other algorithms to obtain an image of the object with fringe patterns superimposed. These fringe patterns can then be used to identify the presence, size, and depth of flaws in a structure.

A typical shearography system uses a charge-coupled device (CCD) camera with a shearing lens, which is completely integrated into a compact measurement head, to view laser light reflected from the surface under inspection. The object under test is illuminated with laser light, and images from the object at different states of loading are taken. The loading of the surface is created by different excitation methods such as vacuum, thermal, vibration, or mechanical load, which induce some deformation of the outer surface. Such deformations are locally altered by the presence of subsurface defects (e.g., disbonding or delaminations in composites). A comparison of the different images captured before and after loading allows a deformation gradient to be calculated. This deformation gradient can be a sensitive measure for identifying local defects. Overlapping sheared images are produced in the interferometric process. Two overlapped portions of the sheared images combine and interfere to produce a speckle pattern. When an applied stress deforms the specimen, the speckle pattern is slightly modified. A comparison of the two speckle patterns (stressed and unstressed) produces a fringe pattern that depicts the relative displacement of the area being inspected. Figure 77 shows the basic principles of shearography.



Figure 76. LTI-5200 portable shearography system with camera on test specimen

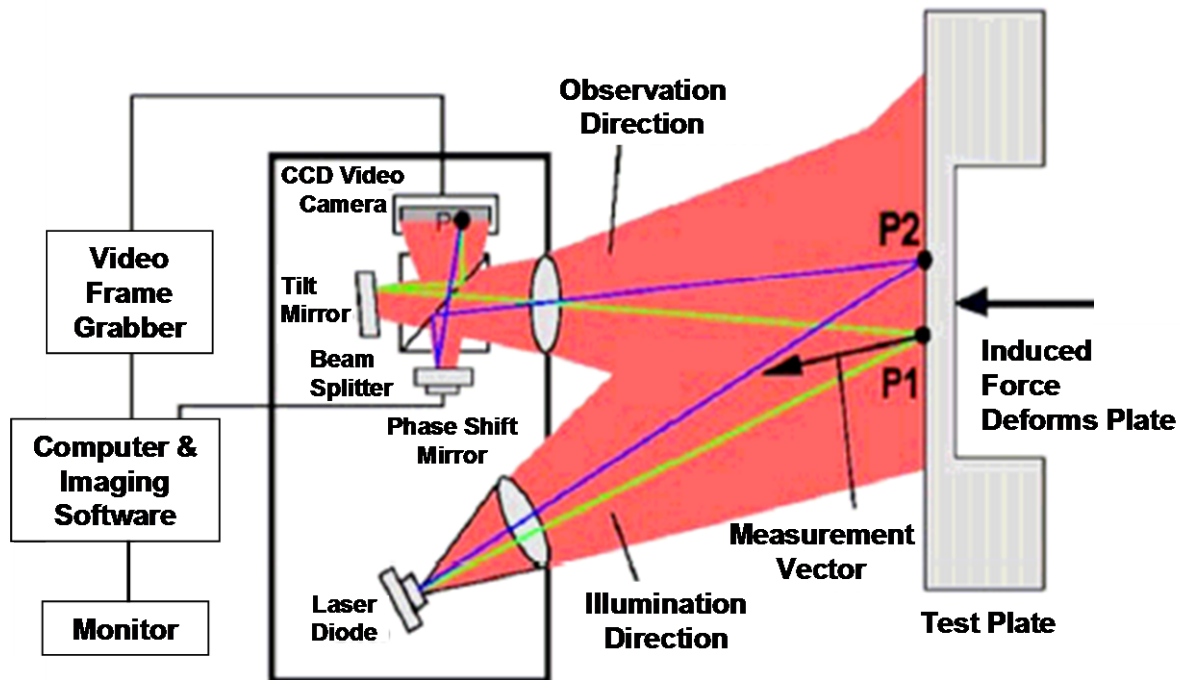


Figure 77. Basic principles of shearography

Shearography inspections can detect anomalies like disbonds, delaminations, voids, separation of structural components, wrinkles, kissing disbonds, impact damage, internal corrosion, crushed core, changes in sections, and core splices [42]. With the use of the CCD-camera technique, no photo laboratory is required. This makes it possible to use shearography for real-time, NDI of structures. Laser shearography views only the surface and does not penetrate into the material. As a result, subsurface defects must affect the surface strain field to be detectable.

4.5.1 Laser Technology Inc. LTI-5200 System

The LTI-5200 is designed for large-area inspections of bonded metallic or composite structures. Inspection rates of 14 m² per hour and the capability to inspect face sheet, core bond lines (near and far side), core splice joints, and bonded repairs make this system well-suited for composite applications. The LTI-5200 is a compact, portable vacuum shearography system designed for large-area inspections of aerospace, marine, and rail composite and cored sandwich structures and components. The LTI-5200 vacuum attaches in any orientation. Increasing vacuum level allows imaging and measurement of subsurface defects. Figure 78 shows the LTI-5200 inspecting a composite honeycomb aircraft rudder assembly. Figure 79 shows a schematic of this setup where detection of both near-side and far-side honeycomb disbonds are possible. Figures 80–82 show samples of shearography images that identify flaws in composite honeycomb panels, while figure 83 shows shearography images of a damaged solid laminate composite structure.

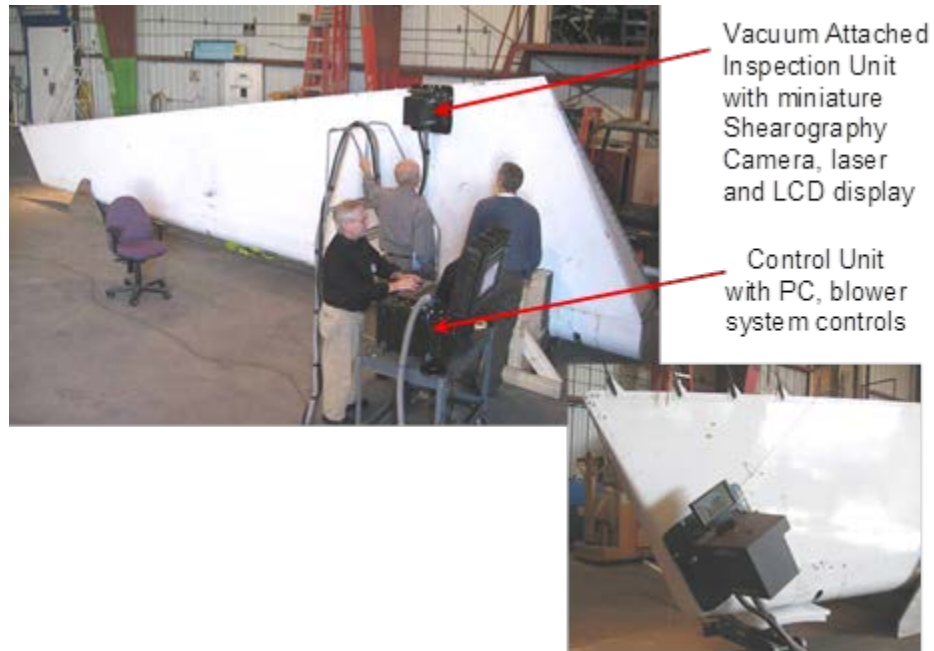


Figure 78. Composite rudder inspection using LTI-5200 portable vacuum shearography system

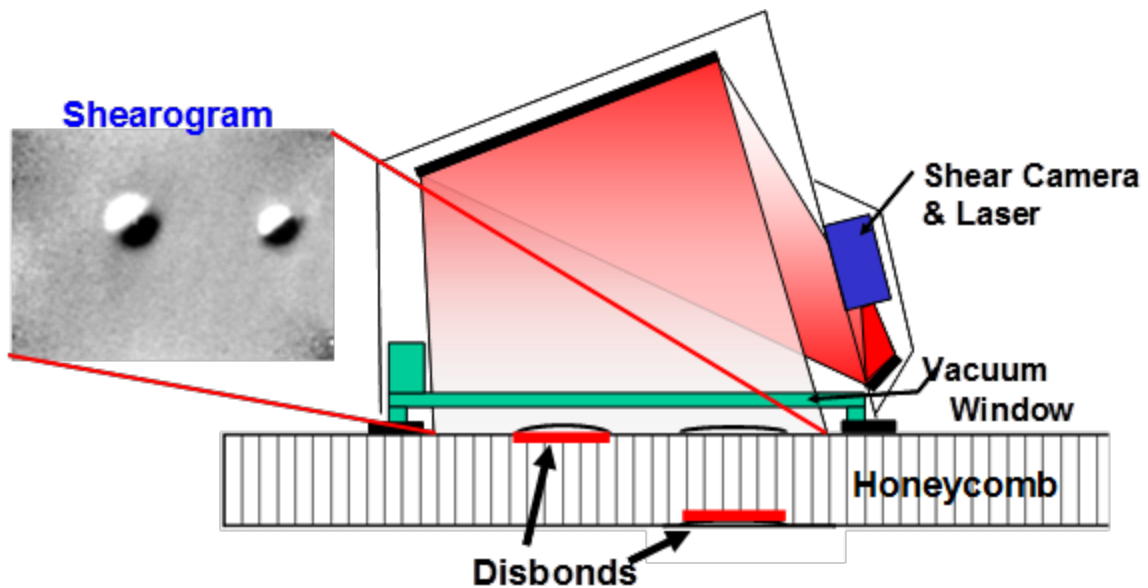


Figure 79. Schematic of shearography inspection for near-side and far-side disbond detection

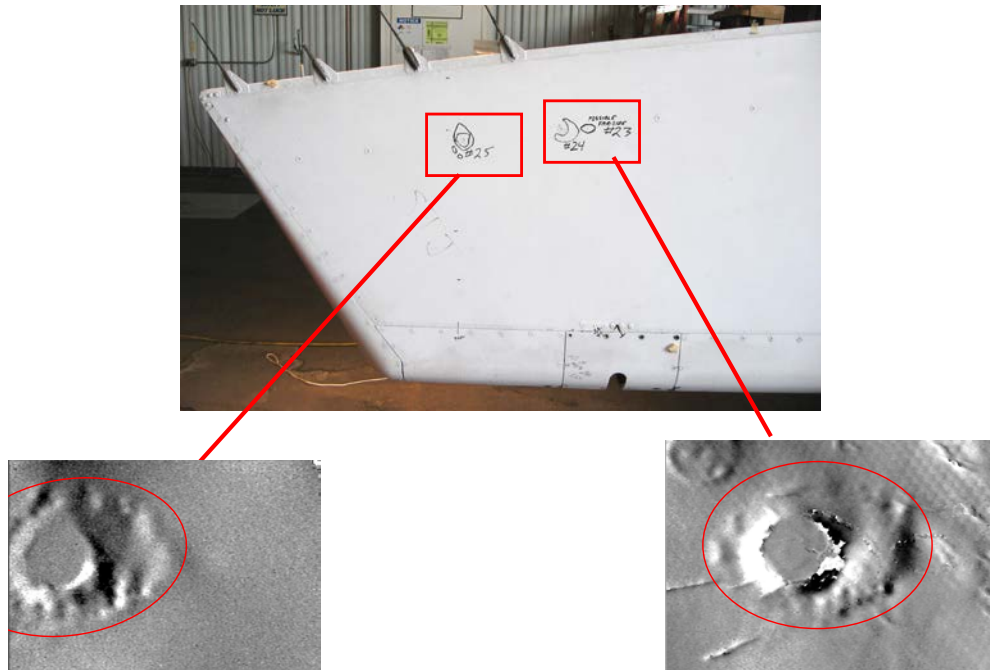
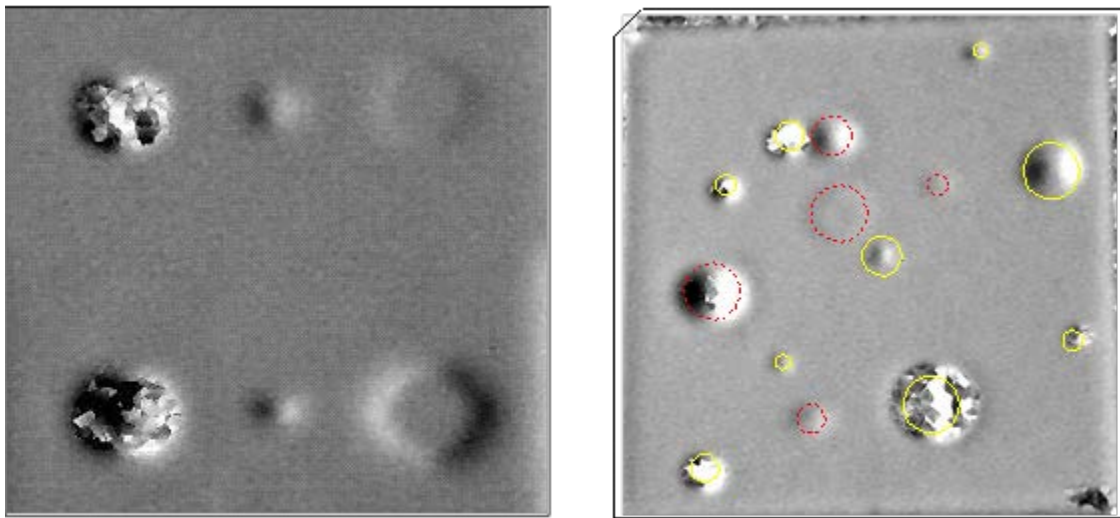


Figure 80. Near-side and far-side disbonds detected by LTI-5200 shearography system in A310 composite rudder



Yellow = Hits (all)
Red Dashed = Backside Detections

Figure 81. Close-up view of LTI-5200 shearography image showing flaws in a composite honeycomb structure and a sample shearography result for 6-ply fiberglass panel showing near-side and far-side flaw imaging

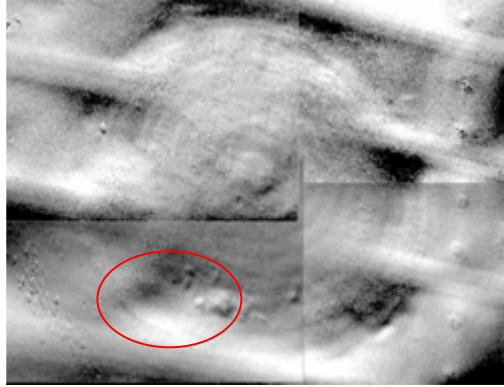


Figure 82. LTI-5200 shearographic inspection image of a scarfed repair to a honeycomb structure with anomaly indications in the repair plies

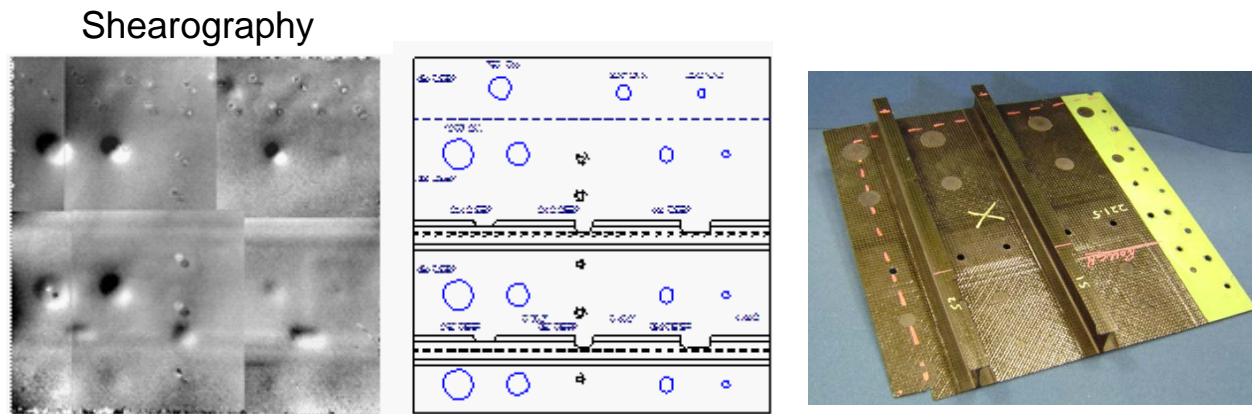


Figure 83. Shearography image produced from inspection of composite laminate panel (0.11" thick skin) with flaw profile as shown in drawing

4.5.2 Dantec Dynamics Q-810 Laser Shearography System

The Q-810 laser shearography system, shown in figure 84, is oriented toward use on composite materials over large surface areas. It can detect defects such as delaminations, disbonds, kissing bonds, wrinkling, impact damage, and crushed core with no surface preparation. The turnkey optical systems are non-contact and full-field, and will work on such materials as carbon-fiber, glass-fiber, laminates, honeycomb, foam, metal, and GLARE (glass laminate aluminum reinforced epoxy). The integrated systems are optimized for large surface area inspections—for example on aircraft fuselages, wings, control surfaces, ship hulls, wind turbine blades, and rocket components.



Figure 84. Q-810 laser shearography system

The full-field inspection rate of the Q-810 laser shearography system is approximately 300 mm x 200 mm every 10 seconds. With adaptive seals, the Q-810 can be used on flat as well as highly curved surfaces. The system operates independently of the local environmental conditions and can be used for production or in-field inspections. The interferometric technique measures microscopic surface deformations caused by internal flaws when a small loading is applied to the object. This can be done using thermal, pressure, vibration, or mechanical excitation. The results are displayed live as the material responds to the excitation. Further image processing is also available for export and reporting. Figure 85 shows a sample shearography image produced by the Q-810 system while inspecting a composite laminate that contains wrinkles.

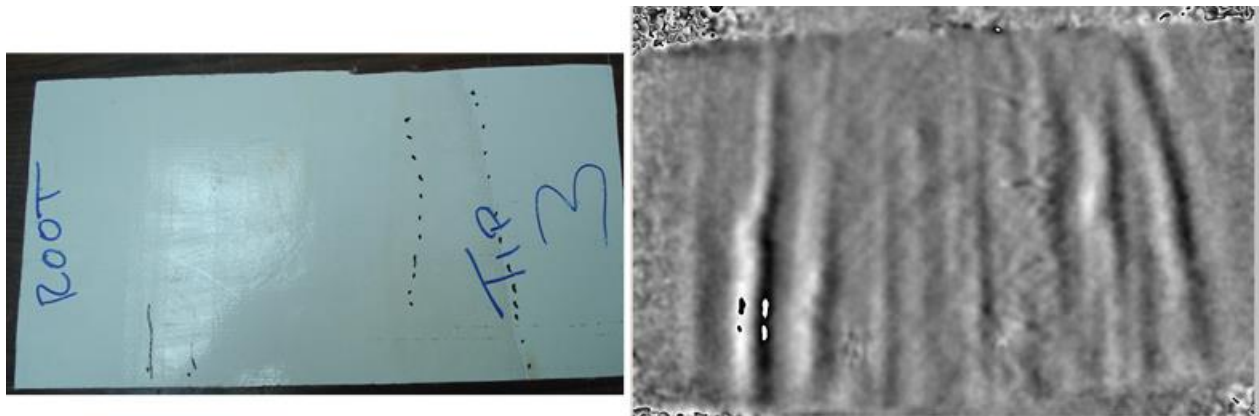


Figure 85. Test specimen (left) and Q-810 shearography image of wrinkles in a composite laminate (right)

4.6 MOBILE AUTOMATED SCANNER IN RESONANCE AND MIA MODES

Section 3.7 discusses the value of using two-dimensional NDI images to more clearly and reliably identify and characterize damage in structures. It is sometimes difficult to clearly identify flaws using screen signal displays alone. These include A-scan signals, meter deflections, flying dot displays, and impedance plan plots. Small porosity pockets commonly found in composites, coupled with signal fluctuations caused by material non-uniformities, can create signal interpretation difficulties. Significant improvements in damage detection can be achieved by taking the analog display signals and transforming them into a single C-scan image of the part being inspected. C-scans are two-dimensional images (area maps) produced by digitizing the point-by-point signal variations of an interrogating sensor while it is scanned over a surface. A computer converts the point-by-point data into a color representation and displays it at the appropriate point in an image. A mechanical linkage connects the scanning unit to X-axis and Y-axis position indicators, which feed position data to the computer. The transducer signal is recorded, versus its X-Y position on the test piece, and a color-coded image is produced from the relative characteristics of the sum total of signals received.

This C-scan capability was included in the MAUS scanner to produce two-dimensional color-coded images of both MIA and resonance inspection modes (see sections 3.5 and 3.6). A photograph of an automated (motorized) scanner, the Boeing MAUS system, inspecting an aircraft fuselage is shown in figure 86. The entire UT C-scan device is attached to the structure using suction cups connected to a vacuum pump. The unit is tethered to a remotely located computer for control and data acquisition. The scanning unit containing the transducer is moved over the surface of the test piece using a search pattern of closely spaced parallel lines.

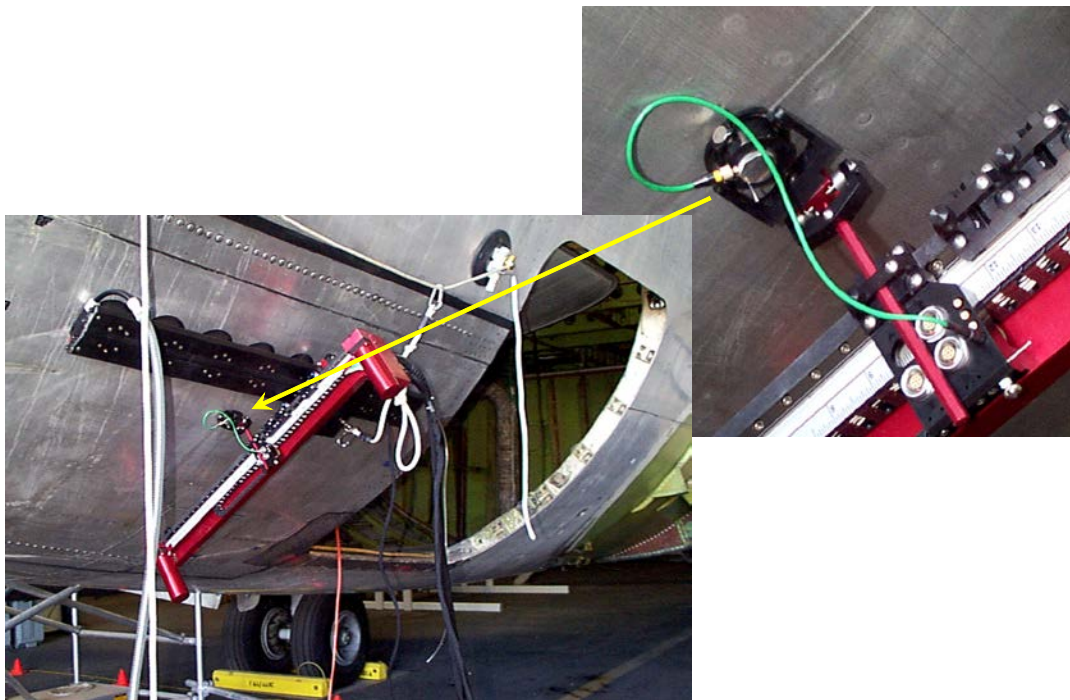


Figure 86. MAUS inspections on aircraft fuselage section

The MAUS, shown in figures 87 and 88, is a portable, multimodal, large-area scanning system that integrates several inspection techniques into a single package. This system can be used in a variety of production manufacturing and aircraft maintenance environments for process quality inspections, damage assessment, aging structure evaluation, and repair validation programs. Unique features of the MAUS V system include equipment portability, ease of setup, inspection versatility, and rapid inspection rates. It incorporates an X-Y scanner to match the transducer position with its corresponding signal so that C-scans can be constructed for the surface being inspected. The probe is held in place using a gimble arrangement on a spring-loaded mount that allows the probe to accurately follow, and maintain proper orientation, over curved surfaces. The scanner motor moves the sensors across an inspection surface. As the scanner is moved forward or backward, a strip of data is collected by each sensor. The total width of the data strip is defined by the scanner stroke and the number of sensors attached to the scanner. The MAUS flexible track provides fully automated hands-free scanning capability. It attaches to the part surface using vacuum pressure created from a shop air source. The system incorporates PE-UT, eddy current, resonance, LFBT, and MIA inspection modalities. The MAUS was applied to the CHE using both MIA and resonance modalities. Sample C-scans produced by the MAUS, deployed in both resonance and MIA inspection modes, are shown in figures 87–89.

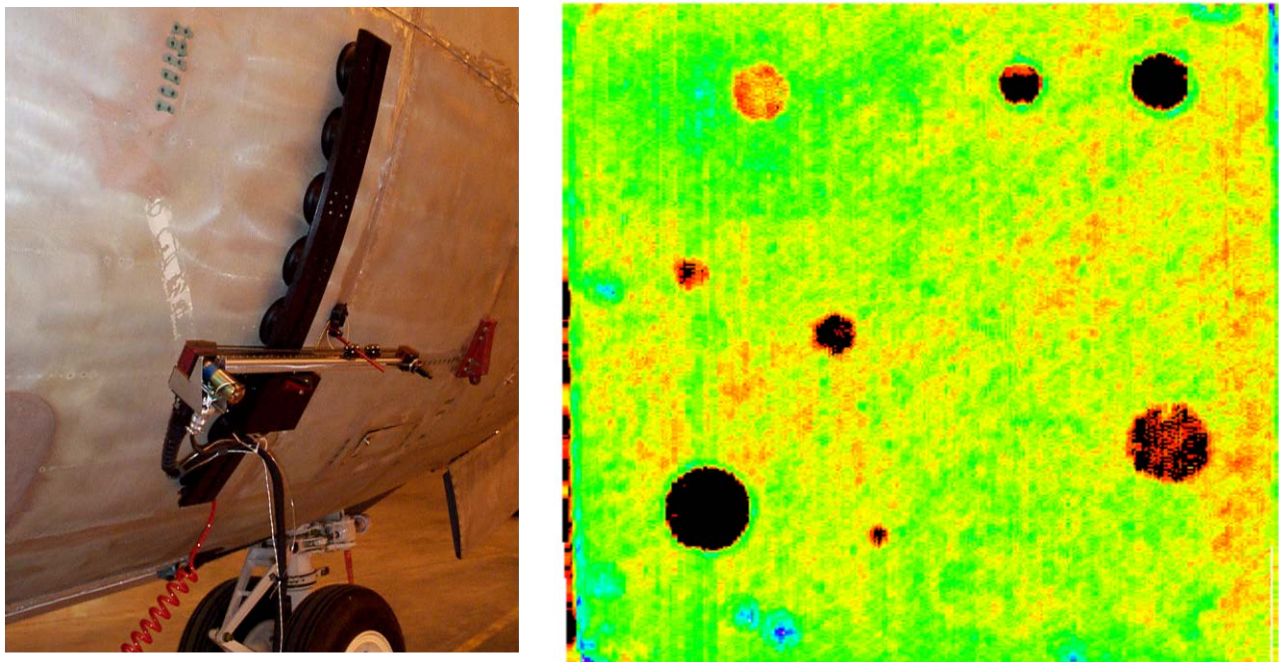


Figure 87. MAUS system operating on an aircraft fuselage with sample C-scan image produced from resonance inspection on a 6-ply carbon skin honeycomb panel

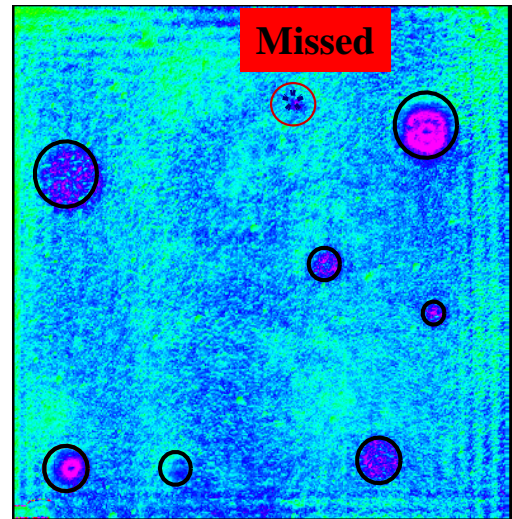
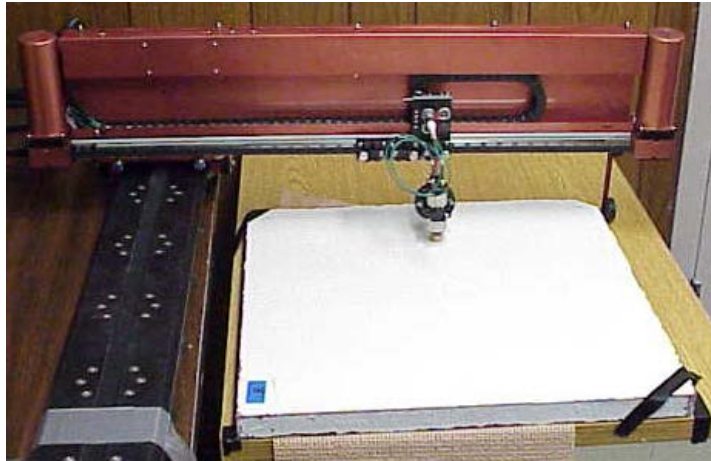


Figure 88. MAUS MIA inspections on honeycomb panel with sample C-scan image produced

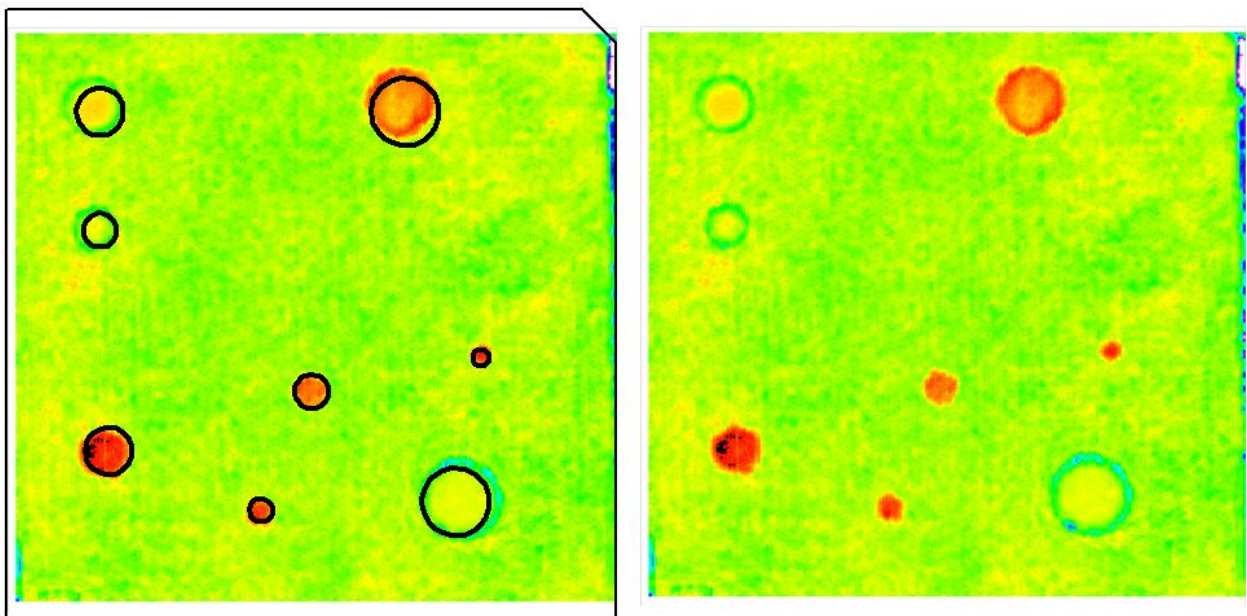


Figure 89. X and Y scans of a composite honeycomb panel produced by the MAUS inspection system deployed in resonance mode

4.7 MICROWAVE

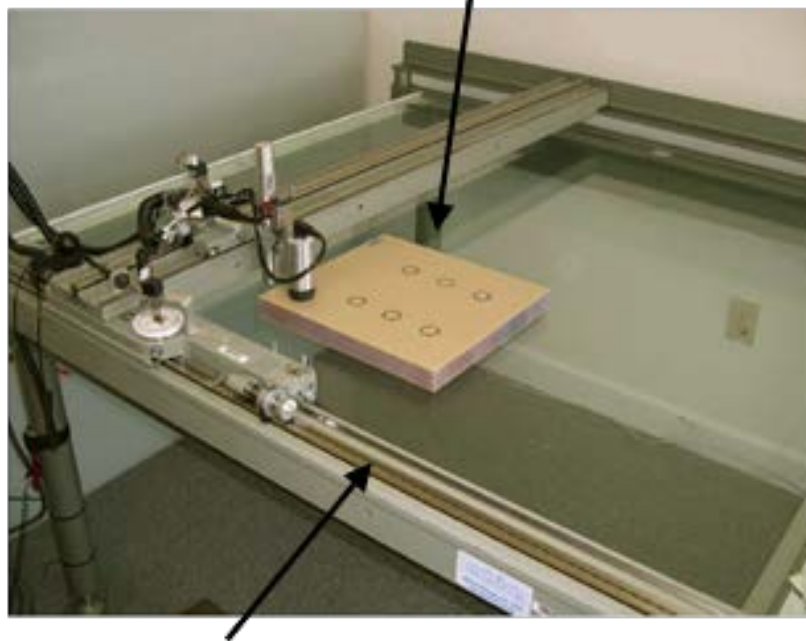
Microwave inspection works by using a specialized transducer to bathe the material of interest in microwave energy of an essentially constant frequency [43]. Several different system setups for microwave inspection are shown in figures 90 and 91. The energy is reflected from each interface between materials possessing differing dielectric constants within the specimen. The reflected energy is superimposed, creating a signal that is acquired as an analog voltage that is

then digitized. This signal is sampled at numerous discrete locations across the sample to create a two-dimensional image of the surface that highlights damage or other anomalies.

The ability of microwaves to penetrate inside dielectric materials makes microwave inspections an NDT technique very suitable for interrogating structures made of composites. Additionally, the sensitivity of microwaves to the presence of dissimilar layers in such materials allows for accurate thickness measurement and variation detection. The quality of the experimental images captured with these systems has demonstrated the potential of the technique for material NDT purposes. Basically, these systems use an antenna (a horn antenna used in the first experiments or open-ended rectangular waveguide used in recent years) to illuminate the composite with electromagnetic waves—for this particular application, the electromagnetic wavelength goes from 1–100 mm—and monitor the reflected waves. The electromagnetic waves penetrate deep into the dielectric material where they interact with its interior and reflect back to the antenna. The properties of the reflected wave will convey the needed information about the composite at hand. The imaging mechanism is based on the idea that microwaves are very sensitive to discontinuities in the material space and the presence of water (the water reflects specularly with the wavelength of microwaves).

Microwave NDT techniques may be conducted on a contact or non-contact basis. In addition, these techniques are conducted from only one side of the sample (reflection techniques). Furthermore, when compared with UT techniques, microwave NDT approaches require no coupling material (glass or water) and do not suffer from signal attenuation. Indeed, microwaves have good propagation in the air.

Fiberglass Honeycomb Test Specimen



Automated scan table

Figure 90. Configuration of microwave inspection system on a laboratory scan table



Figure 91. Basic equipment setup for microwave inspection

Microwave techniques are able to detect voids, delaminations, porosity variation in a variety of materials, impact damage, and water infiltration—all problems that affect composite materials. It can also provide the possibility of process control during the manufacturing of composites so that the final product may not need any scrutiny and may only require occasional testing once under some loading. Finally, microwave NDT techniques do not require a high level of expertise from an operator and can be conducted in real time with simple, portable hardware. The main limitation of the microwave method is that it is limited to non-conductive materials. Thus, it has been successfully applied to fiberglass composite structures but cannot be used to inspect carbon-graphite composites. Figure 92 shows microwave results highlighting delamination in a fiberglass laminate boom structure. Figure 93 and 94 show results from the microwave tests on Sandia National Laboratories' composite honeycomb panels ranging in thickness from 3–12 plies. Note that the microwave method performs better on fiberglass skin panels than on the carbon skin panels; this is because the carbon material does not possess dielectric properties appropriate for the propagation of the microwave scan waves.

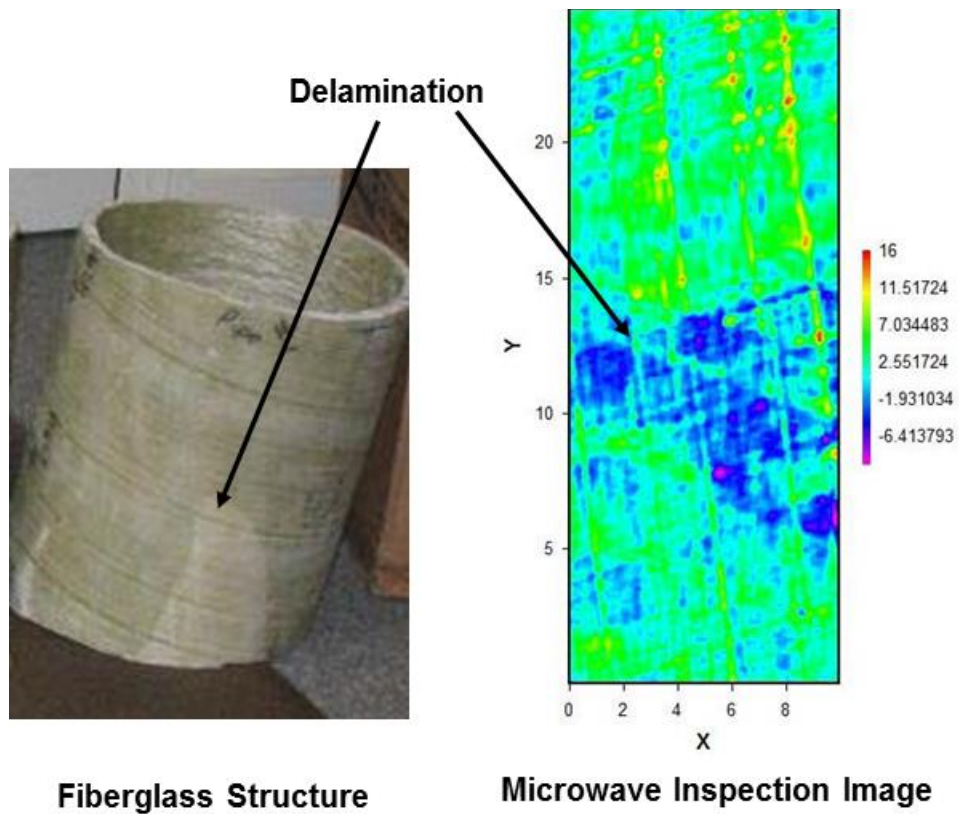


Figure 92. Microwave C-scan of a fiberglass boom structure showing the presence of interply delaminations

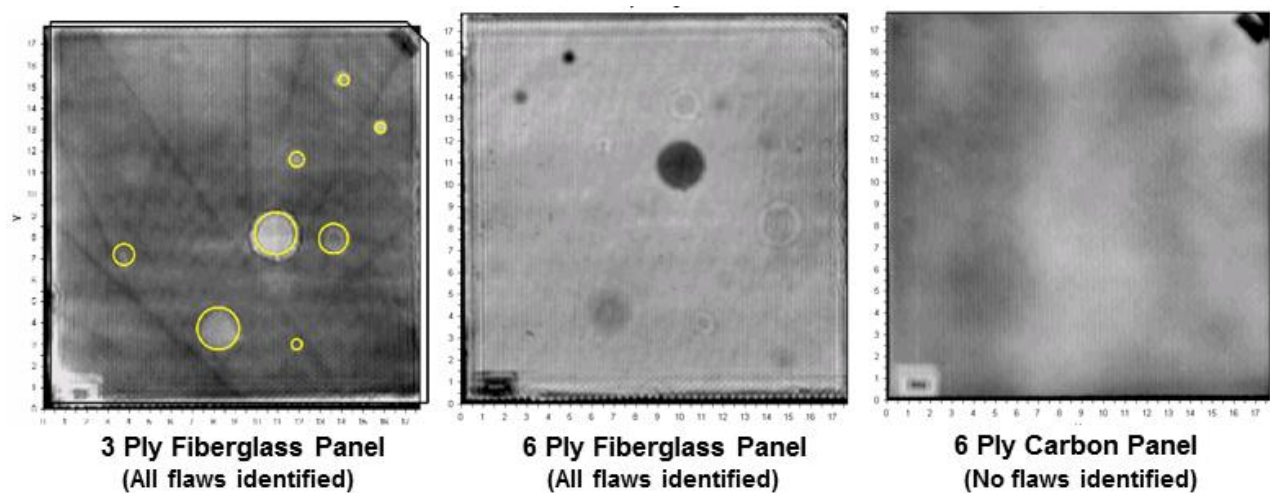


Figure 93. Microwave inspection results for fiberglass and carbon skin honeycomb panels with engineered flaws (skins bonded to Nomex honeycomb)

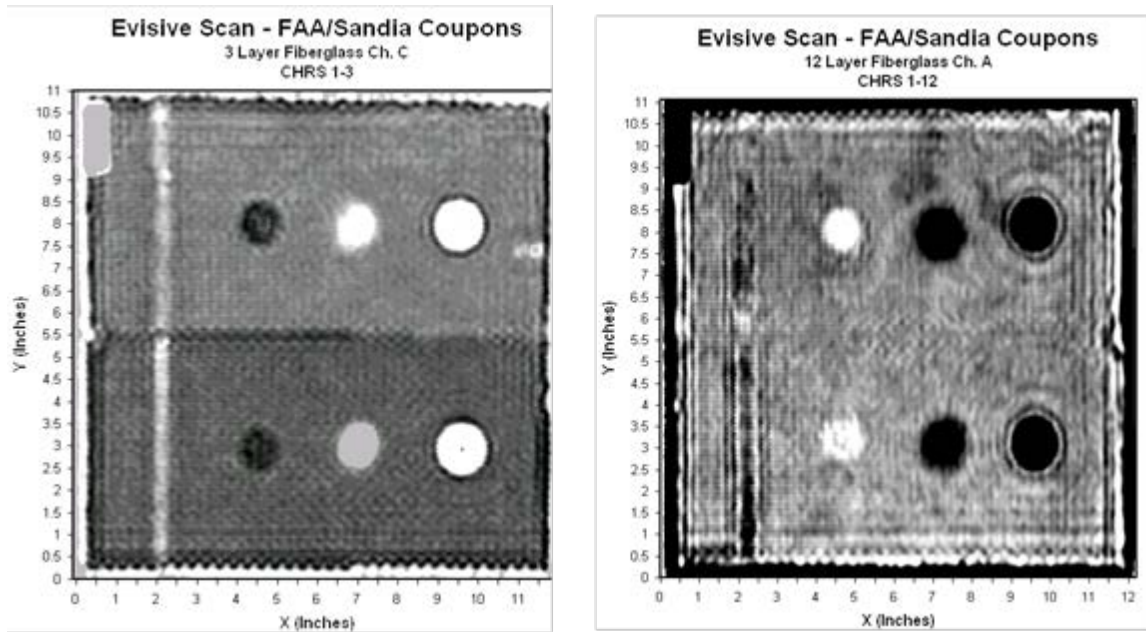


Figure 94. Sample microwave inspection results for 3-ply and 12-ply fiberglass panels with delamination, disbonds, potted core, and core splice

4.8 STRUCTURAL ANOMALY MAPPING SYSTEM

The SAM system uses laser velocimetry to measure out-of-plane motion in a dynamically loaded structure [44–45]. By studying localized or unusual velocities/displacements, it is possible to image and identify anomalies or flaws in a structure. The excitation (loading) is applied in a non-contact, acoustic manner to provide uniform, wide-area loading and inspections. The SAM system was developed to provide an automated, wide-area inspection method that does not require contact with the airframe structure. The system consists of a database coordination system, a laser-guided robotically controlled sensor delivery system, an acoustic source for structural excitation, and a scanning laser vibrometer sensor suite. The database coordination system includes software for command/control, signal processing, and data base management. The results, consisting of anomaly size, classification, and location, are visualized on a three-dimensional airframe model or in a two-dimensional C-scan image that represents the surface area covered in the inspection scan. The database also holds information pertaining to previous similar inspections of the airframe and any other similar airframes in the same fleet. This allows for quick comparisons to previous measurements so that change detection can be used to monitor changes in the airframe that may occur from operation.

Figure 95 depicts the principle behind the SAM device. This system uses acoustic excitation, along with laser Doppler velocimetry instrumentation, to selectively excite and identify flaws that manifest themselves in unique, out-of-plane deformations in the structure. This non-contact technique relies on the vibration response of a structure to a remotely administered acoustic shock. A device called a spark-gap generator delivers a rapid series of acoustic pulses that are focused in a cone toward the part several feet away. A scanning laser vibrometer monitors the part's surface in response to these acoustic shocks, mapping the vibration data as different color shades. Areas of reduced stiffness produce changed patterns, indicating the presence of a defect

or other anomaly. Figures 96 and 97 show the SAM device inspecting one of the composite honeycomb panels for the flaw detection experiment, including how the results scans from the inspections were traced onto the data logging sheets

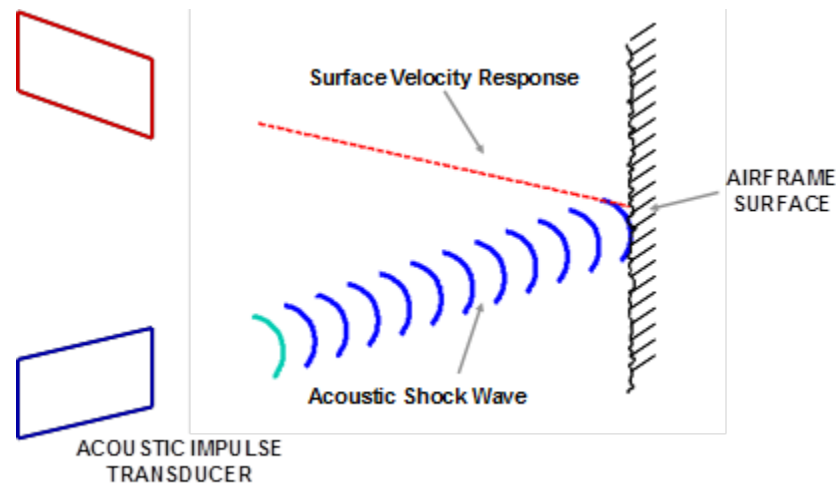


Figure 95. Schematic showing the principle of the SAM inspection method

When using the scanning laser vibrometer, the forced frequency response data at two distinct excitation amplitudes are processed to identify areas of the panel that exhibit significant nonlinear response characteristics. These local nonlinearities are shown to coincide with subsurface damage in the panel. Because the nonlinearities distort the frequency response, it is possible to locate the damage without comparing the response to an undamaged, or baseline, measurement. In addition, rudimentary modeling has shown results confirming this reference-free method of detecting damage by direct comparison of frequency response functions excited by multiple amplitude signals, particularly at higher modal frequencies [44]. Figure 98 shows raw frequency response data comparing undamaged and damaged portions of a honeycomb engine cowling. These data are used to produce color-coded response maps from all points on the structure. Figure 99 shows the C-scans produced from the frequency domain signatures. The C-scan is able to display the areas with engineered defects, as indicated on the photo of the engine cowling. A sample SAM scan from the CHE is shown in figure 100, where the subsurface disbond and delamination damage is shown as hot spots in the color palette.

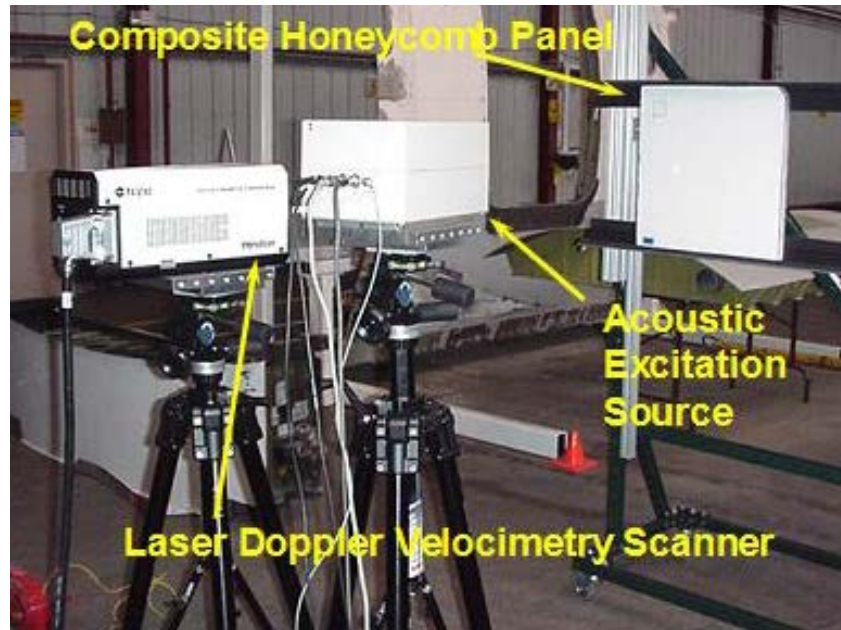


Figure 96. SAM laser Doppler velocimetry camera and acoustic excitation device; composite test specimen in the background

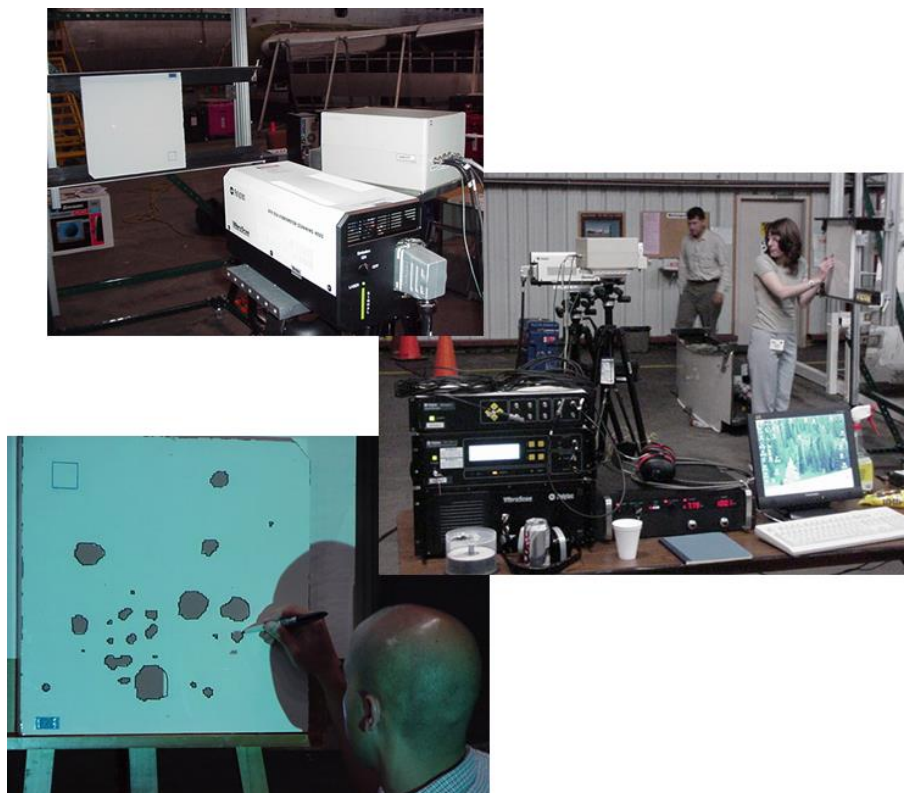


Figure 97. SAM system inspecting composite honeycomb panels and transfer of scan data onto experiment grading sheets

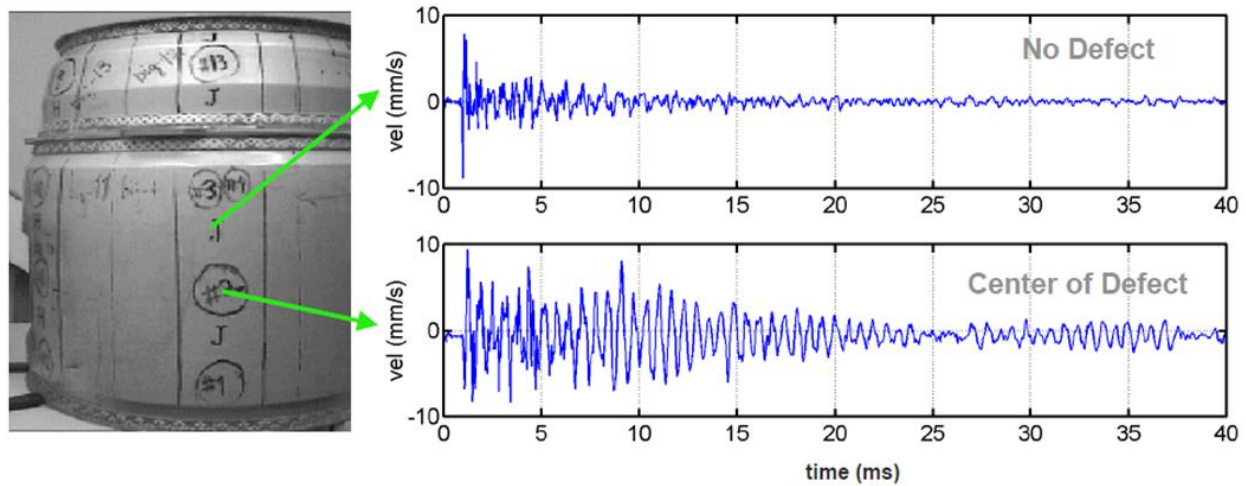


Figure 98. Frequency response plots produced during the application of the SAM inspection system on an engine cowling

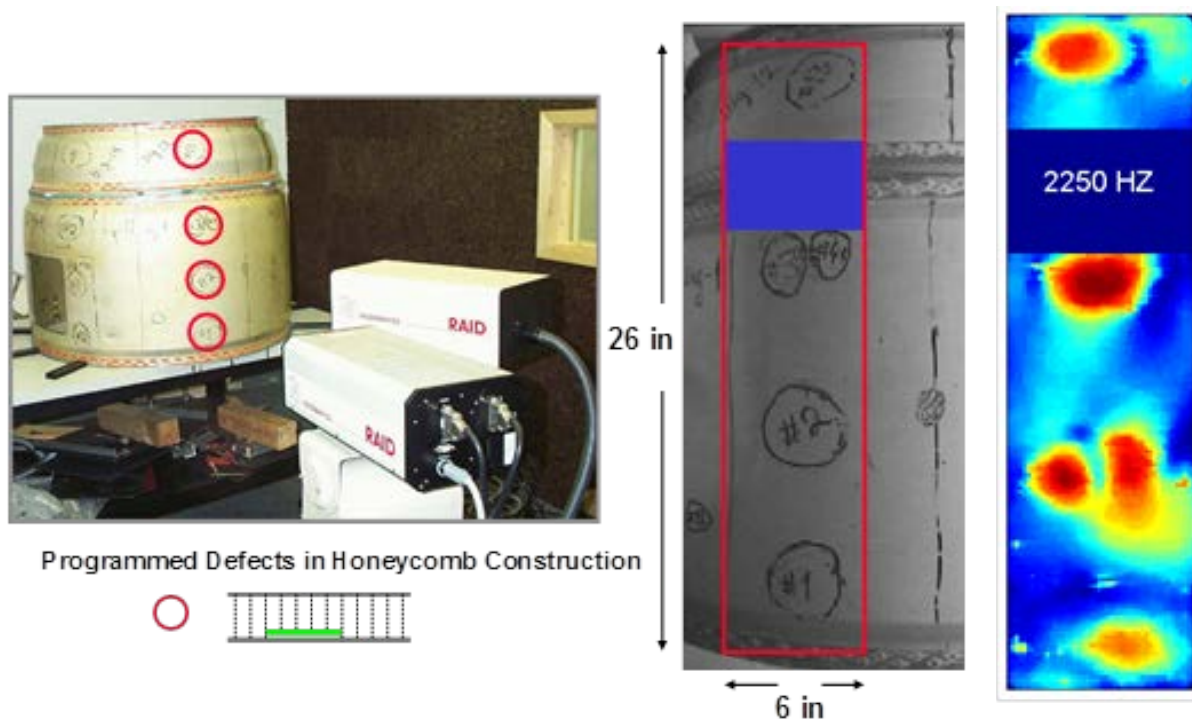


Figure 99. SAM system inspecting an engine cowling and sample image showing flaws

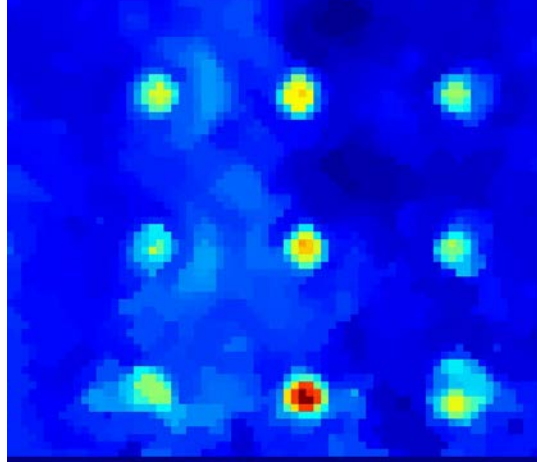


Figure 100. Sample image produced by SAM system showing flaws in a fiberglass composite honeycomb structure

4.9 PHASED ARRAY AND LINEAR ARRAY ULTRASONICS

Conventional UT transducers for NDI commonly consists of either a single active element that both generates and receives high-frequency sound waves or two paired elements: one for transmitting and one for receiving. Phased array probes, on the other hand, typically consist of a transducer assembly with 16 to as many as 256 small individual elements that can each be pulsed separately. A phased array system will also include a sophisticated computer-based instrument that is capable of driving the multi-element probe, receiving and digitizing the returning echoes, and plotting that echo information in various standard formats. Unlike conventional flaw detectors, phased array systems can sweep a sound beam through a range of refracted angles or along a linear path, or dynamically focus at a number of different depths, thus increasing both flexibility and capability in inspection setups. The main difference between a phased array and a linear array is that linear arrays aren't capable of steering the sound beam at different angles or focusing the beam. Thus, the sound waves stay parallel to each other regardless of the depth.

Phased array ultrasonics (PA-UT) involves the use of multiple signals from a contained series of transducers (phased arrays) to produce diagnostic images in the form of UT C-scans. The operation is similar to handheld UT; however, the simultaneous use of multiple sensors allows for rapid coverage and two-dimensional images from which to assess structural integrity. A linear array of UT sensors is placed within a single, scanning probe. The width of the linear probe array determines the swath of the inspection "scan" as the probe is moved along the surface. A compression wave beam is electronically scanned along the array at pulse repetition frequencies in excess of 10 kHz. The response of each individual sensor is monitored and assessed using the UT wave analysis approaches described above. High-speed pulsing combined with rapid data capture permits the linear array to be quickly moved over the structure. The individual responses from each UT sensor are integrated to produce a real-time C-scan image of the covered area. An example of a PA-UT inspection device deployed by Sonoscan in a rolling wheel arrangement is shown in figure 101. The physics of how the UT array works is depicted in figure 102. By carefully controlling the generation of UT signals and data acquisition from select elements in the array, it is possible to produce customized focusing of the array to improve the

sensitivity of the inspection. Electronic focusing permits optimizing the beam shape and size at the expected defect location, thus further optimizing probability of flaw detection. The ability to focus at multiple depths also improves flaw sizing of critical defects in volumetric inspections. Focusing can significantly improve the signal-to-noise ratio in challenging applications and electronic scanning across many groups of elements allows for C-scan images to be produced very rapidly.

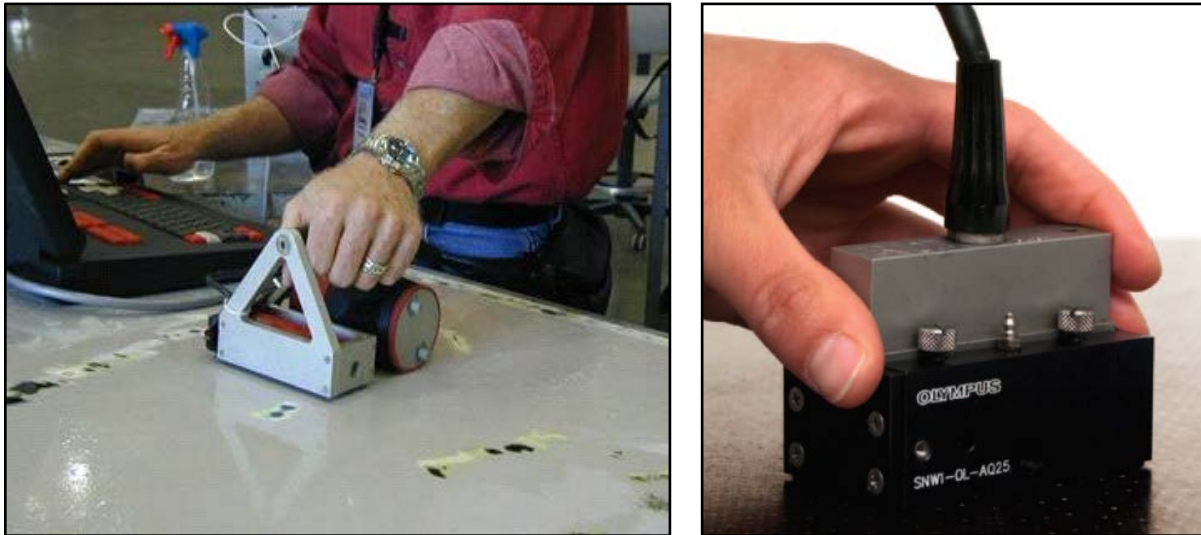


Figure 101. PA-UT deployed in rolling wheel mechanism (left) and contained in a single-probe housing (right)

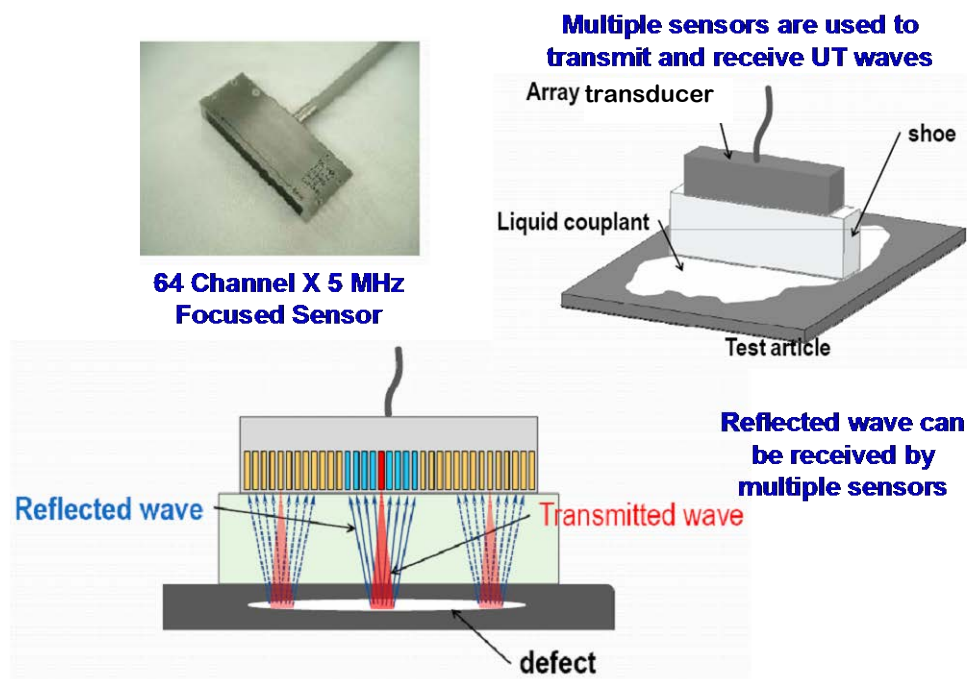


Figure 102. Schematic showing the operation of an ultrasonic array that allows for the generation and acquisition of multiple UT signals

The Olympus OmniScan PA-UT system, shown in figure 103, is one example of a PA-UT device. Figures 104 and 105 show sample results produced by the OmniScan PA-UT system from the inspection of carbon laminate test specimens that contain engineered flaws. Damage in the parts is shown in the photos and schematics, while the accompanying C-scan images show the ability of the inspection method and equipment to detect the flaws.

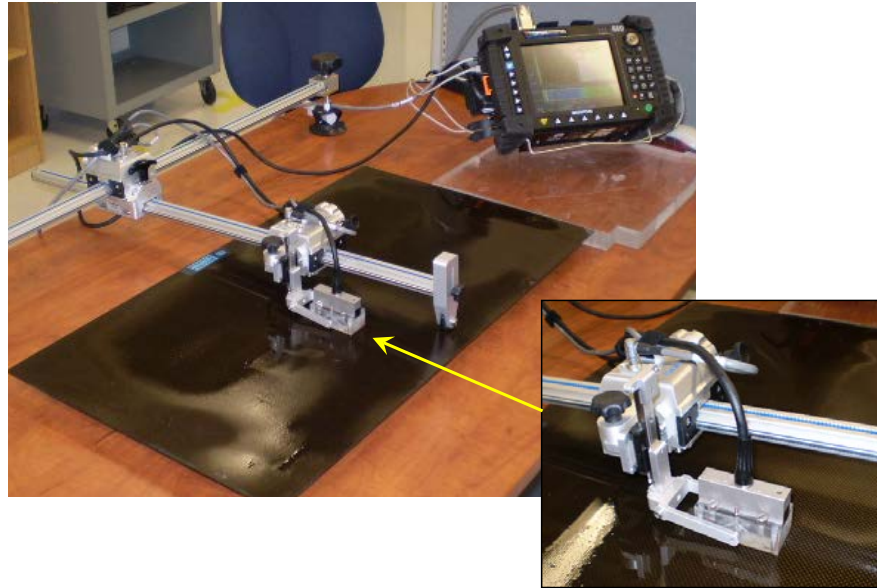


Figure 103. Olympus OmniScan device with a 16:128 phased array transducer

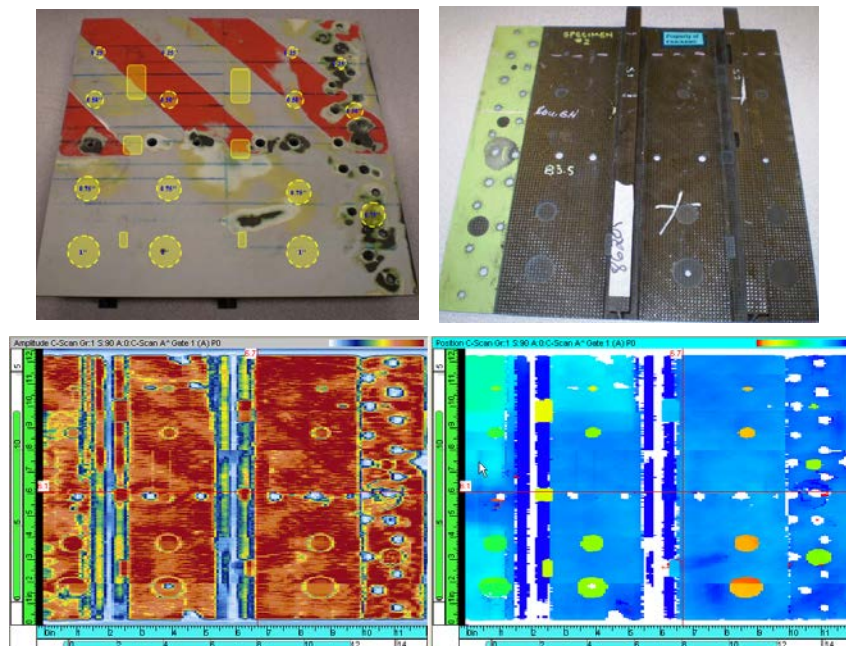


Figure 104. Amplitude (right) and time of flight (left) data produced by OmniScan inspection of composite laminate aircraft panel with flaw profile as shown

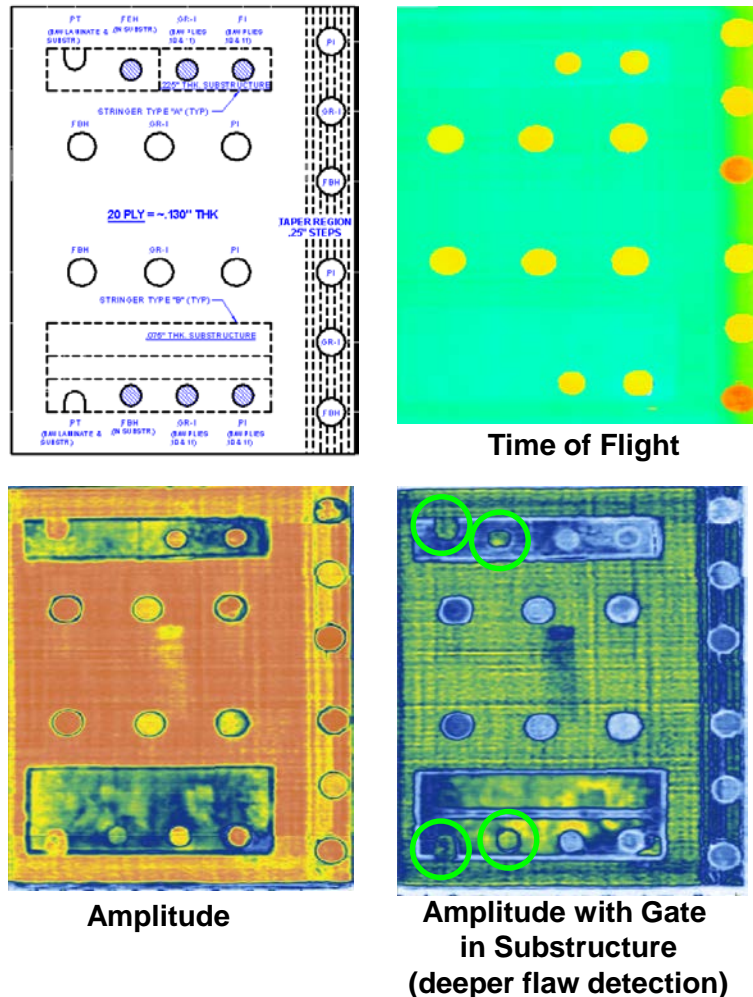


Figure 105. C-Scan images produced by OmniScan PA-UT inspection of 20-ply composite laminate feedback panel with the flaw profile as shown

4.9.1 Boeing MAUS FlawInspecta Linear Array UT System and the Diagnostic Sonar FlawInspecta PA-UT System

The FlawInspecta system, shown in figures 106 and 107, was designed to address the requirement for a rapid, low-cost UT phased/linear array inspection system. The imager is a laptop-based device that allows for easy transfer of images to other applications or via the Internet to remote locations. It works with a wide range of integrated arrays and is suited for applications ranging from rapid large-area flaw detection to high-speed, low-cost corrosion mapping with 100% coverage. The data acquisition is fast enough to allow for interactive B-scan imaging or rapid C-scanning—typically 40,000 mm²/s (64 in.²/s) for 1 mm pixels—for manual coverage of large areas. The system is also able to perform full waveform capture (FWC), in which the full A-scan (RF or rectified) is acquired and stored for every point on the inspection surface. This volumetric representation offers the ultimate in data acquisition for archiving and offline review yet is achieved at similar data rates. The FlawInspecta system is capable of a pulse rate of 30 kHz, corresponding to a scan rate of 10 in./second or 19.3 ft²/minute, with a 128-element array. Smart arrays can be used with a wide range of conventional equipment such as

flaw detectors, but their full capability is not realized unless used with a real-time imaging system such as the FlawInspecta. At the heart of the system is Diagnostic Sonar's FIRE-technology (Flaw Imaging and Reconstruction Engine) for real-time full-waveform acquisition and B-scan imaging. A position sensor attachment to the array extends this capability to C-scans for mapping of inspection areas. The latest FlawInspecta uses proprietary FIRE-technology to provide fast, manual imaging and mapping with FWC—typically more than 1 m²/minute for 1 mm pixels. This FIRE-technology has now been integrated into other proprietary ultrasound mapping systems and provides an easy upgrade path to high-performance acquisition for users of these systems.

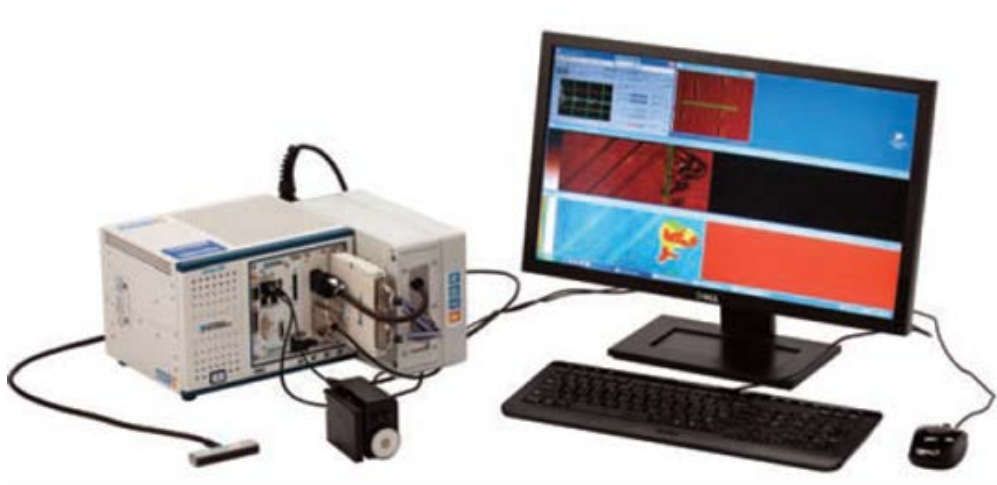


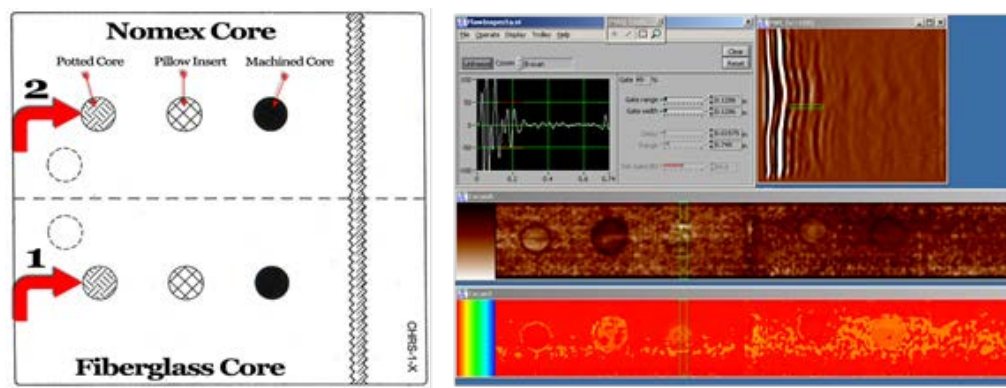
Figure 106. Diagnostic sonar FlawInspecta PA-UT inspection system



Figure 107. FlawInspecta linear array UT system deployed on MAUS V scanner platform—linear array UT probe includes a delay line shoe

In trial tests on composite honeycomb test specimens, such as the one shown in figures 108 and 109, the FlawInspecta system was able to detect nearly all of the engineered defects. Some of the indications are best detected while observing the B-scan display. The majority of the defects in the composite solid laminate test specimen can be seen on the C-scan images shown in figure 110. The FlawInspecta is a high-speed UT array system with dynamic real-time B-scan capability as well as FWC and C-scan capability.

The MAUS V C-scan system uses an OEM version of the FlawInspecta UT array system that is controlled by the MAUS software via a dynamic link library. The combination of the MAUS V system with the FlawInspecta system allows for the rapid inspection of large areas of composite structures in a seamless easy-to-use package. One of the differences between the Diagnostic Sonar FlawInspecta and the add-on FlawInspecta to the MAUS V is the phased array capability. The MAUS V FlawInspecta does not have phased array capability and is deployed in a linear array. The addition of the NDT Solutions-designed vacuum-assisted couplant delivery and recovery system provides for excellent coupling of large arrays to the parts with the ability to recover and recycle the couplant to nearly eliminate the watery mess of flowing copious amounts of water required to couple large transducers to the inspection area.



**Figure 108. Composite honeycomb reference standard and sample FlawInspecta results—
3-ply carbon skin with 1" thick core**

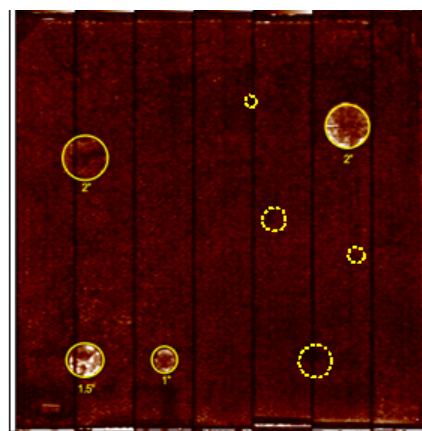


**Figure 109. Sample result from FlawInspecta PA-UT system on 6-ply carbon specimen
(dashed lines represent missed flaws)**

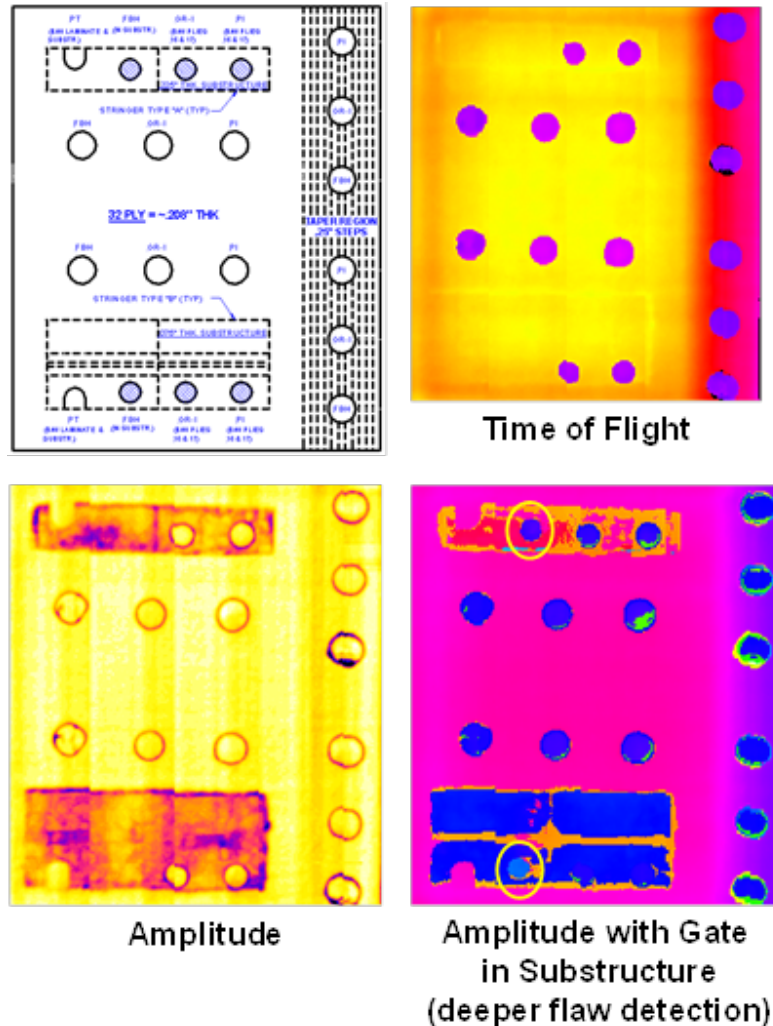


Figure 110. C-scan images produced by FlawInspecta MAUS V linear array UT system on a 32-ply composite laminate feedback panel with the flaw profile as shown

4.10 AIR-COUPLED ULTRASONICS

UT inspection is a nondestructive method in which beams of high-frequency sound waves are introduced into materials for the detection of surface and subsurface flaws in the material. The sound waves, normally at frequencies between 0.1 and 25 MHz, travel through the material with some attendant loss of energy (attenuation) and are reflected at interfaces. The reflected or transmitted beam is displayed and then analyzed to define the presence and location of flaws. UT testing involves one or more of the following measurements: time of wave transit (or delay), path length, frequency, phase angle, amplitude, impedance, and angle of wave deflection (reflection and refraction).

When sound passes across an interface between two materials, only a portion of the sound is transmitted while the rest of the sound is reflected. The proportion of the sound that is transmitted depends on how close the acoustic impedance of the two materials matches. UT inspections traditionally involve the use of a couplant material often deployed in a continuous

manner using a water pump, immersion tank, or a water squirter system to properly transmit the UT wave from the transducer into the part being inspected. Water is a fairly good match for most commonly used materials—for example, typically around half the sound energy is transmitted at the interface between water and a carbon laminate. After four solid-liquid interfaces (from the probe, to the couplant, to the test piece, and then back again), there is still a small, sufficient amount of the original energy left to allow for accurate measurements. UT inspection by immersion or squirter systems cannot always be conveniently applied in the field. For these practical and operational reasons, non-contact, air-coupled ultrasonic testing (AC-UT) has the distinct advantage of being a couplant-free UT inspection technique [46–49]. For this reason, it is an attractive alternative for certain applications, even though AC-UT also suffers from several significant disadvantages, the most significant of which is the attenuation and loss of signal that accompanies air transmission of the UT signals. However, if the sound has to move between the test piece and air (which has very low acoustic impedance), only a small percentage of the sound energy is transmitted. Typically, the overall path loss may be 100 dB higher using air as a couplant than when water is used.

Thus, the main limitations of AC-UT are the large reflection loss at the air-solid interface and the large attenuation of high-frequency ultrasound in air. The latter has limited the application of AC-UT to frequencies mainly below 1 MHz or so. It is therefore necessary to minimize losses at every stage to achieve acceptable signal-to-noise levels for AC-UT for the inspection. Despite the enormous reflection loss at an air-solid interface due to their acoustic impedance difference, the advances in transducer technology and electronics are gradually making AC-UT a viable NDI technique for bonded structures in the field. There are two types of air-coupled transducers: piezoceramic-based (disk or composite) and capacitive transducers. Most of the field applications use the piezoceramic type.

AC-UT has the potential for being developed into a practical NDI tool for aircraft inspection for which portable equipment is needed to inspect water-incompatible materials [48]. However, because of the tremendous difference in transmitted and received signal amplitudes, and the inherent difficulties in achieving adequate transducer/amplifier isolation and recovery, no current air-coupled NDT systems work in single-probe mode; separate transmit and receive transducers are always used. In the NDE of aerospace structures, where internal flaws and defects are to be detected and imaged, the current state of AC-UT technology uses mainly transmission mode that requires two-sided access, as shown in figure 111.

AC-UT, which transmits the interrogating UT wave into the test article without the use of a liquid couplant, was applied to the composite honeycomb specimens in this study. A commercially available UT system from Quality Material Inspection, Inc. (QMI) was used in conjunction with a scanning frame and software produced by Sonix, Inc. The inspections were made in through-transmission mode, as depicted in figure 111, using the hardware setup shown in figure 112. In this case, there are separate sending and receiving transducers. As a result, it should be noted that the AC-UT results presented here correspond to the capabilities of this inspection method when: a) both sides of the structure are accessible, and b) it is possible to fixture the probes such that they are in proper alignment. Cracks, delaminations, shrinkage cavities, pores, disbonds, and other discontinuities that produce reflective interfaces can be detected.

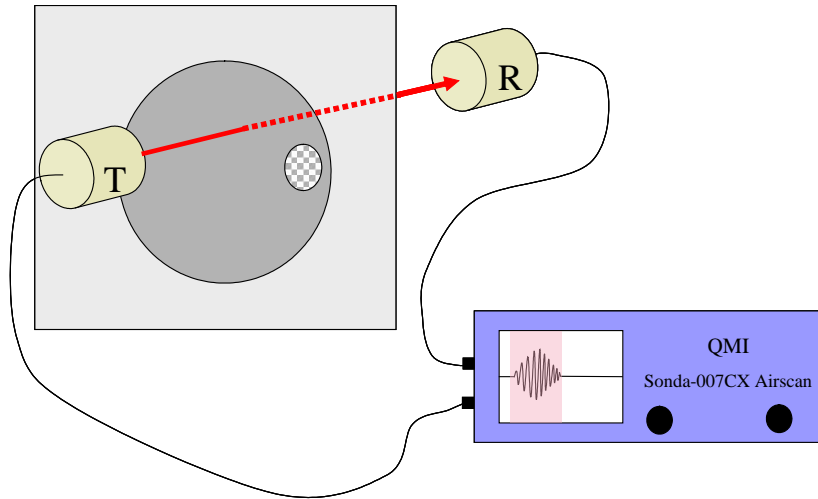


Figure 111. Schematic of air-coupled ultrasonic inspection of panel in through-transmission mode

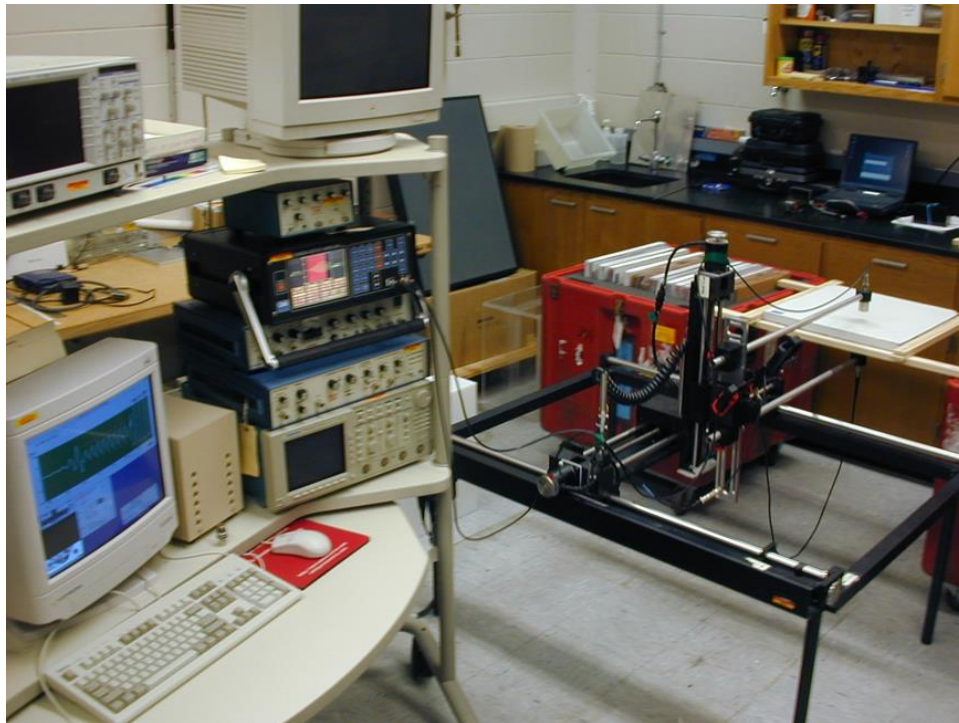


Figure 112. Equipment setup for air-coupled ultrasonic inspections of composite honeycomb panels shown in background

In the through-transmission mode of deployment for AC-UT, the transducers are mounted on a yoke for aircraft components that allow for two-sided access. With the aid of portable position encoding devices and software in a laptop computer, C-scan images of AC-UT inspections can be obtained in the field [35]. A summary of the AC-UT hardware and setup used in these inspections is as follows:

- Scanner with UTEX Winspect software
- QMI SONDA 007CX pulser/receiver
- QMI focused UT probes
- Both 120 kHz and 225 kHz frequencies

The photos in figure 113 show the AC-UT test setup for both TTU and one-sided pitch/catch mode. The AC-UT TTU method was applied to a fiberglass skin foam core specimen with the flaw profile shown in figure 114. This specimen contains a wide array of flaw types found in composite sandwich construction. The resulting C-scan image from the AC-UT TTU is shown in figure 115. This image shows that the AC-UT TTU inspection revealed only the pull tab (skin-to-core disbonds) and pillow insert (interplay delamination) flaws, along with the through holes in the core (red dots), which acted as resonance cavities to produce high amplitudes in the TTU signals. The grease contamination and micro-balloon (porosity) flaws were not detected.

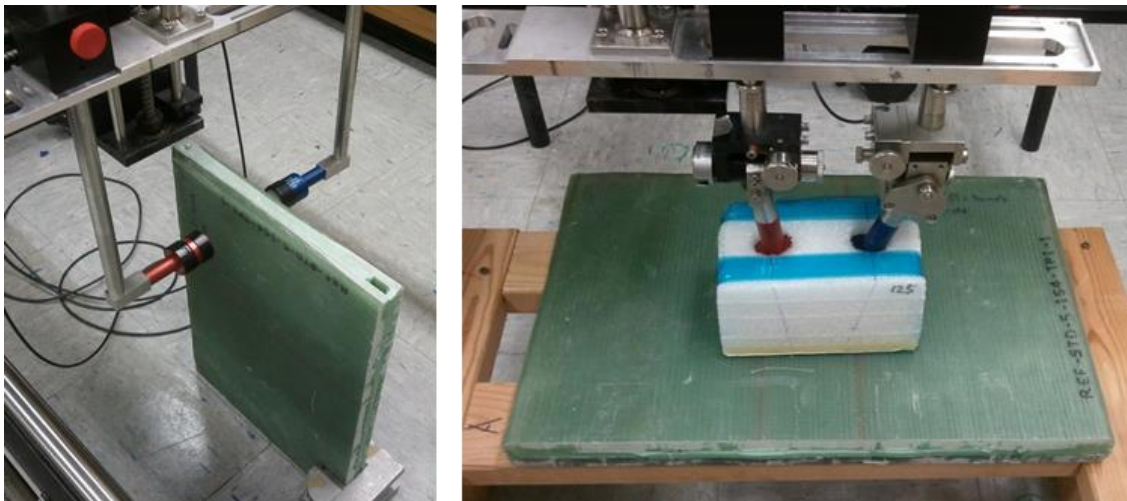


Figure 113. AC-UT applied to a composite panel test specimen in both through-transmission mode (left photo) and one-sided pitch/catch mode (right photo)

AC-UT scanning has been used in nondestructive imaging of composite honeycomb sandwiches and repairs on such structures. A considerable fraction of composite components and control surfaces on aircraft are honeycomb sandwiches. AC-UT can readily transmit through such honeycomb structures. Very little sound energy can be transmitted through two face sheets separated by air. Practically all the energy transmitted through a honeycomb sandwich has propagated along the cell walls of the honeycomb core. This does not seem to hamper the ability of AC-UT to image disbonds between the face sheet and the core or defects within the face sheets. Figure 116 shows six disbond defects in an aluminum honeycomb sandwich with 0.032" face sheets and 3/8" cells. The image is obtained with focused 120 kHz air-coupled, 3/4" diameter transducers.

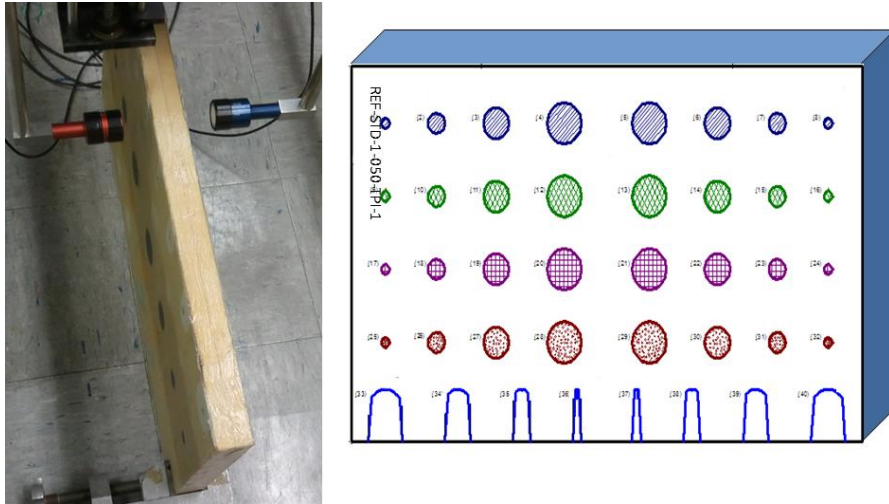


Figure 114. AC-UT TTU test setup on fiberglass skin and foam core test specimen

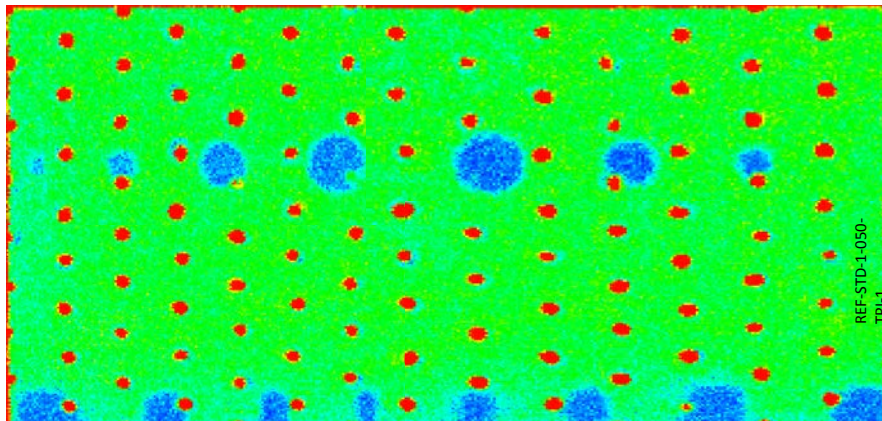


Figure 115. AC-UT TTU C-scan image produced by 120 kHz inspection of composite foam core test specimen

The set of composite panels from the CHE was examined using AC-UT. A commercially available UT system from QMI was used in conjunction with a scanning frame and software produced by Sonix, Inc. The inspections were all made in through-transmission mode using the equipment setup shown in figures 111–113. This means that both face sheets of the honeycomb sandwich are inspected simultaneously. Thus, flaws from both sides of the panel are superimposed in the resultant AC-UT image, and there is no way to determine which face sheet contains a particular indication. The C-scan images have a pixel size of 0.1" and took approximately 18 minutes to complete the 2.25 ft² area. Each panel was scanned using a pair of 120 kHz planar probes. Some panels were also scanned using 120 kHz focused probes. The transducers were placed at a distance of 1" from the panels. Figure 117 shows a sample C-scan produced by AC-UT TTU on a panel from the CHE. All flaws in the panel were detected. Note that this includes the flaws located on the backside of the panel. This is due to the deployment of the AC-UT method in TTU mode such that both sides of the panel were inspected simultaneously.

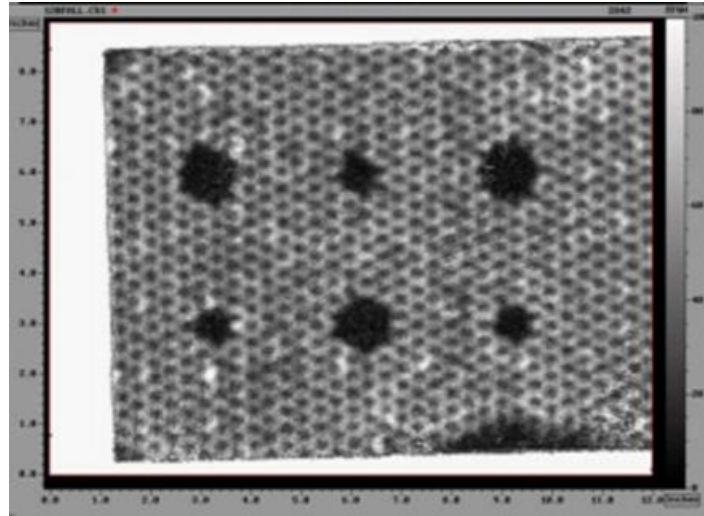


Figure 116. AC-UT TTU C-scan showing disbands in skin-to-core bondline of a composite honeycomb panel

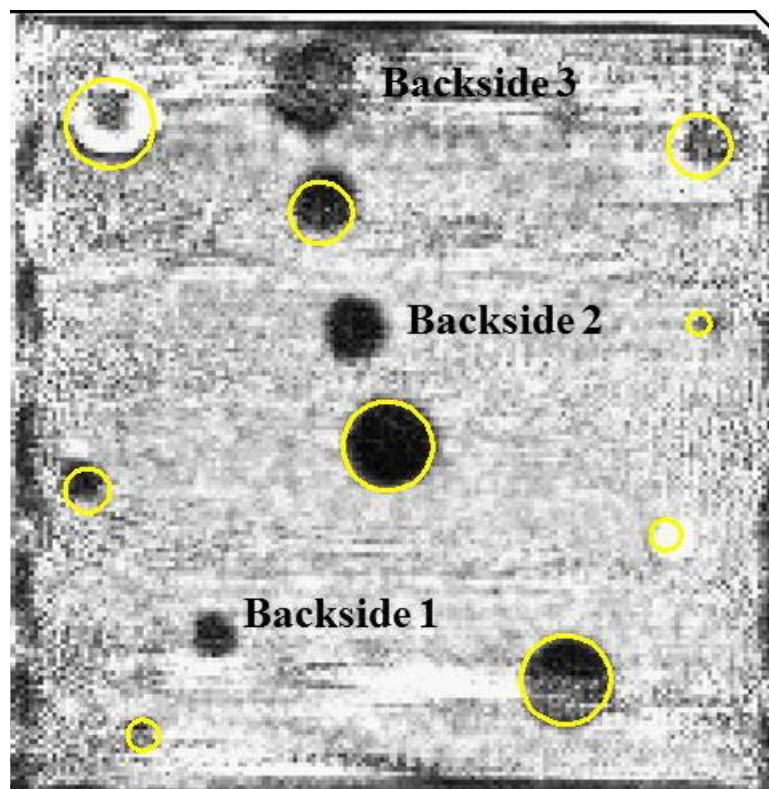


Figure 117. Sample C-scan data produced by AC-UT method on composite honeycomb test specimen

4.11 LASER ULTRASONICS

LUS is generally defined as a technology in which one laser generates UT waves and another laser coupled to a detection system detects the associated UT displacements [50–52]. There are four main issues that have limited the adoption of LUS for the inspection of composites:

1. The lack of reliability of various prototypes used to validate the technology for production
2. The acquisition cost of the LUS equipment
3. The small but significant differences between conventional and LUS signals
4. The unavailability of fieldable (portable) system for use in hangar environments, even as gantry-based LUS systems for production environments have demonstrated excellent results

4.11.1 LUS deployment

LUS is a non-contact technique that uses a scanning laser beam to quickly move across the part in a uniform coverage pattern (see figure 118). Ultrasound is generated by pulsing the laser beam, causing the surface layer to rapidly expand and contract through thermal expansion. The absorbed laser energy is converted into heat in the top 10–100 μm of the surface. The resultant temperature rise creates a local expansion of the material in the frequency of ultrasound (1–10 MHz). Thus, a longitudinal UT wave is introduced into the part. Echoes from this wave, when they again reach the surface, are sensed by a coaxial detection laser and converted to images proportional to the echo strength. Laser light scattered off the surface is analyzed by an interferometer to extract the UT signals that are “imprinted” on the laser as phase and frequency modulations caused by the moving surface. The UT signals that are extracted are basically the same as those obtained with conventional UT systems. The two laser beams can be indexed over the material with a scanner to produce standard C-scan images [51].

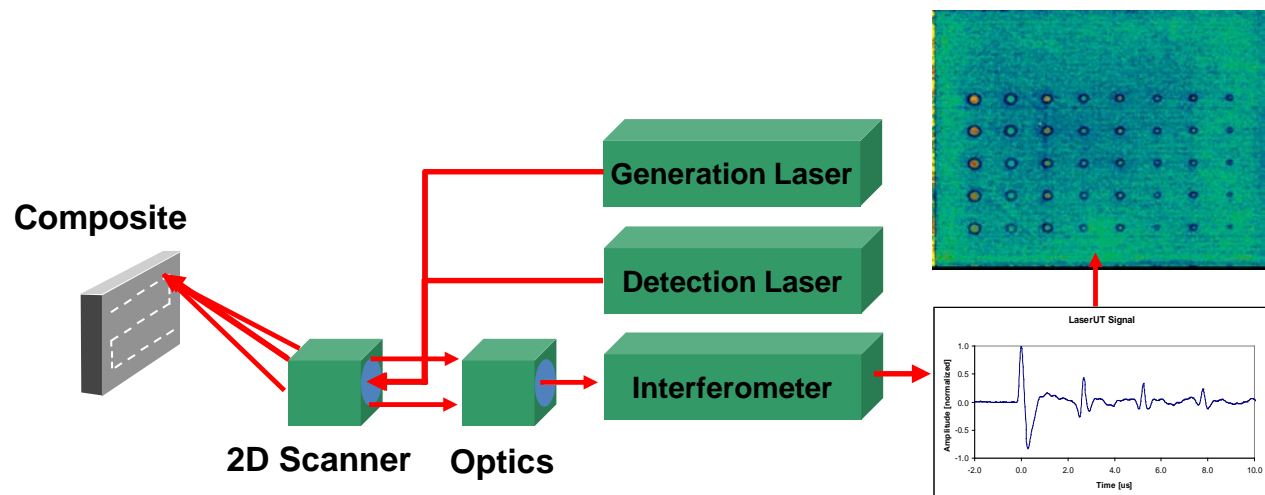


Figure 118. Schematic of laser UT system operation

This data transmission and acquisition do not require the laser beam to be deployed perpendicular to the structure as in other UT methods. Thus, it is possible to scan complex parts

without detailed contour following. Ultrasound propagates perpendicular to the surface regardless of the laser incident angle (up to $\pm 45^\circ$). Currently, the laser UT systems are deployed using a gantry system that provides a high-speed two-dimensional optical scanner to index the beams over the part. This allows for rapid inspections and generation of the C-scan images. Hand-scanning using UT can be slow and tedious, leading to human factors concerns with respect to coverage and human vigilance. In addition, water-coupled UT can be difficult and time-consuming to implement on complex-shaped parts. Figure 119 compares traditional UT inspections to a laser UT interrogation. The first LUS systems mounted on robots [15] used gantry-type robots. Optical alignment of the CO₂ laser beam in the optical scanner must be precisely maintained to obtain valid UT results. The CO₂ laser cannot be efficiently transmitted by optical fibers. Therefore, the most obvious solution is to move the CO₂ laser along with the optical scanner. This approach requires gantry robots because only this type of robot can move equipment as large and heavy as an industrial CO₂ laser. Gantry robots present several disadvantages, the most important being the cost. The gantry robot is typically the single most expensive element of an LUS system that includes such a robot. Several different deployments of the laser UT inspection technique and a schematic showing the ability to inspect parts without maintaining a perpendicular inspection orientation are shown in figure 120.

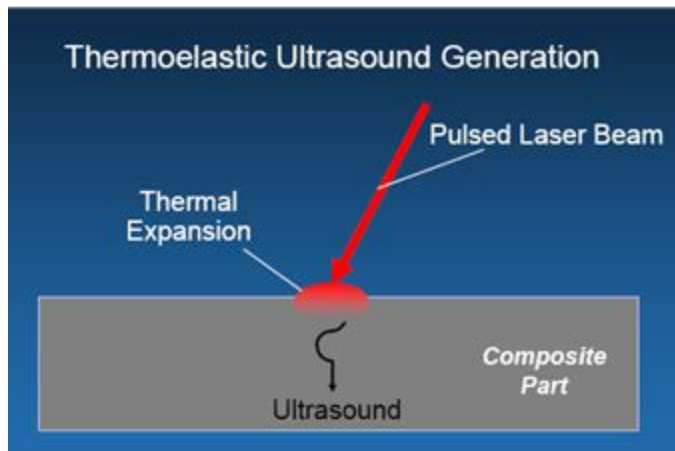
The LUS technology offers flexibility and faster inspection cycle time. However, even though LUS signals are UT signals, there are some differences with UT signals obtained with conventional UT transducers. Those differences must be understood when trying to adapt processing and analysis techniques coming from decades of experience using piezoelectric transducers. Key advantages of laser UT are:

1. The ability to scan quickly in a non-contact mode, all the way to the edge of a part
2. The ability to launch a through-thickness longitudinal wave even when the laser beam impinges on the surface at an angle.

This means that the laser beam can be directed at the surface of complex shapes and scan them efficiently without the need for contour following, complicated scan shoes, or angled water jet arrangements. A laser beam can also be directed through apertures to scan the interior of a structure. Disadvantages of laser UT include:

1. Sensitivity to surface coatings (variations in coatings can affect the strength of the UT signal)
2. Maximum sensitivity, requiring tuning for each structure type
3. Need for system expertise/training to ensure alignment to produce uniform signal
4. Safety concerns necessitating personnel exclusion zones
5. Potential damage to the part surface from laser if not used with caution

Thermoelastic mechanism can efficiently generate ultrasound in composite materials (less efficient on bare metal)



Conventional coupled UT must maintain the transducer normal to the surface

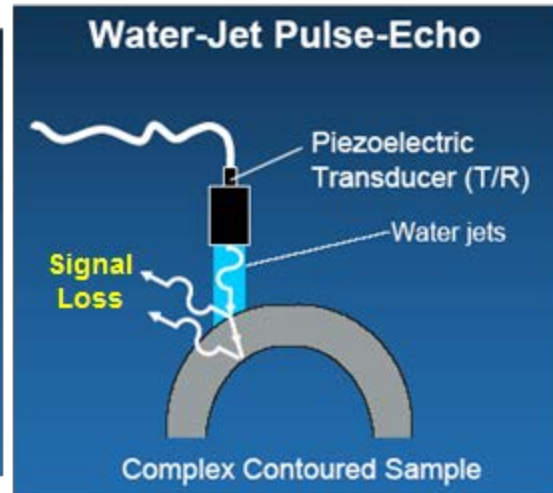
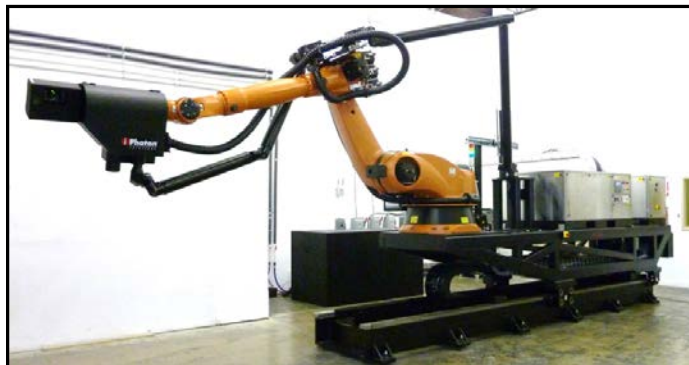
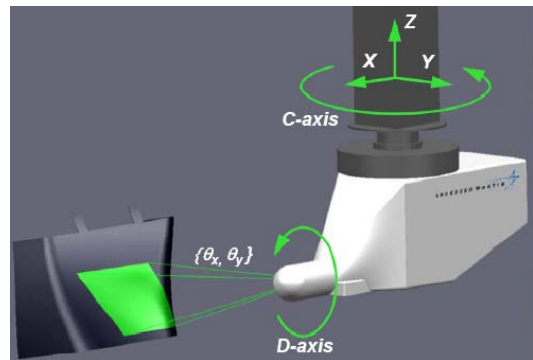


Figure 119. Comparison of conventional and laser UT interrogation of components

Ultrasound propagates perpendicular to surface regardless of the laser incident angle (up to $\pm 45^\circ$)



Articulated robot system on a linear rail
Freq. Range = 0.5 MHz – 20 MHz



Figure 120. Schematic of laser UT method and deployment in gantry system and rail system

4.11.2 iPhoton LUS (iPLUS)

The iPhoton LUS concept, called iPLUS™, was used to conduct the LUS inspections listed in this report. An iPLUS III system is shown in figures 120 and 121. It uses a beam delivery system mounted on an articulated robot. To increase the working envelope, the robot, beam delivery system, and CO₂ laser are mounted on a linear rail. The linear rail provides an almost unlimited working envelope to the iPLUS system in one direction. Articulated robots provide flexibility not possible with gantry-based approaches. Some applications require the inspection of composite substructures inside larger structures, such as stringers inside a fuselage. Therefore, the iPLUS configuration was developed as a response to these applications. In the iPLUS III systems, the beam delivery system is composed of two standard beam delivery systems joined together on axis 3 of the robot. This approach, combined with a cantilevered linear rail, provides more than 6 m of penetration inside a structure (e.g., a fuselage). For the inspection of parts, the iPLUS scan head is positioned using the articulating robot. Once the scan head is in position, the scanning is carried out by moving the laser beams along the surface of the sample using only the two mirrors of the scanner. The scan area is defined by the angular movement, θ_x and θ_y , of the scanner's two mirrors. This process is illustrated in figures 121. When the scanning of one area is completed, the robot moves the scan head to the next pose to scan the next area.

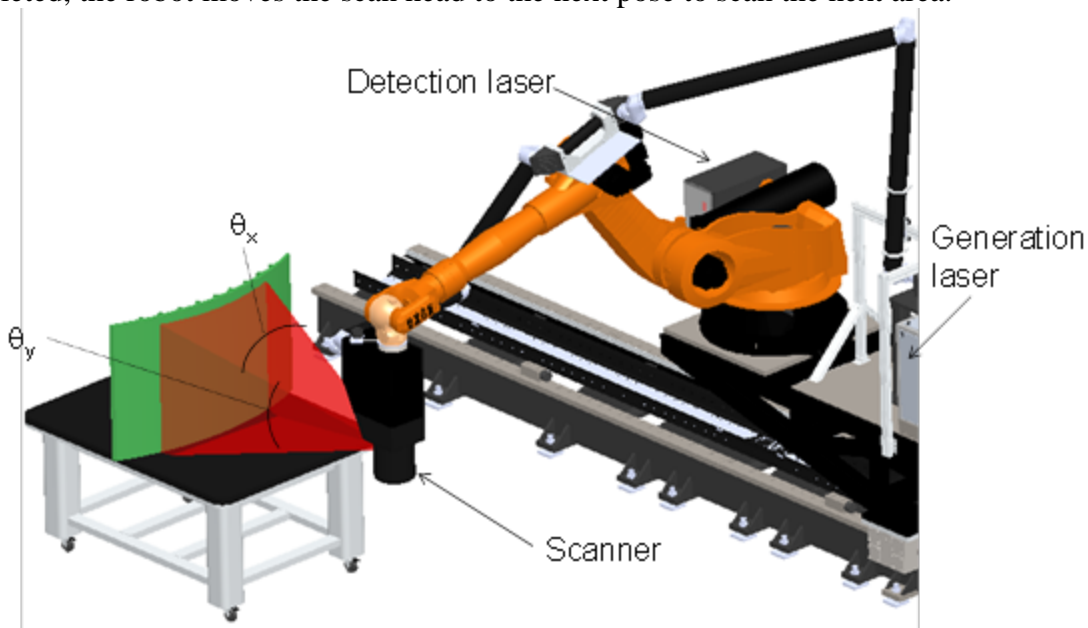


Figure 121. Inspection of a part using the iPLUS scan head and articulating robot

Figures 122–125 provide sample images produced by laser UT inspections on various composite parts, some of which contain substructure elements. Note that surface and subsurface structural details are imaged in the scan. The clarity of the flaws and sensitivity for flaw detection down to 0.25" diameter are depicted in the C-scan images. Figure 122 shows the iPLUS LUS results from a 16-ply, 12" x 12" composite laminate panel that was damaged by simulated hail impact. The top left and right are the amplitude and time-of-flight C-scan images, respectively. The bottom graphics show an A-scan and B-scan corresponding to the line in the top C-scans. Figure 125 is just a flaw map produced by the LUS inspection as applied to a honeycomb panel in the CHE. It can be seen that all but one of the smallest 0.25" diameter flaws was detected.

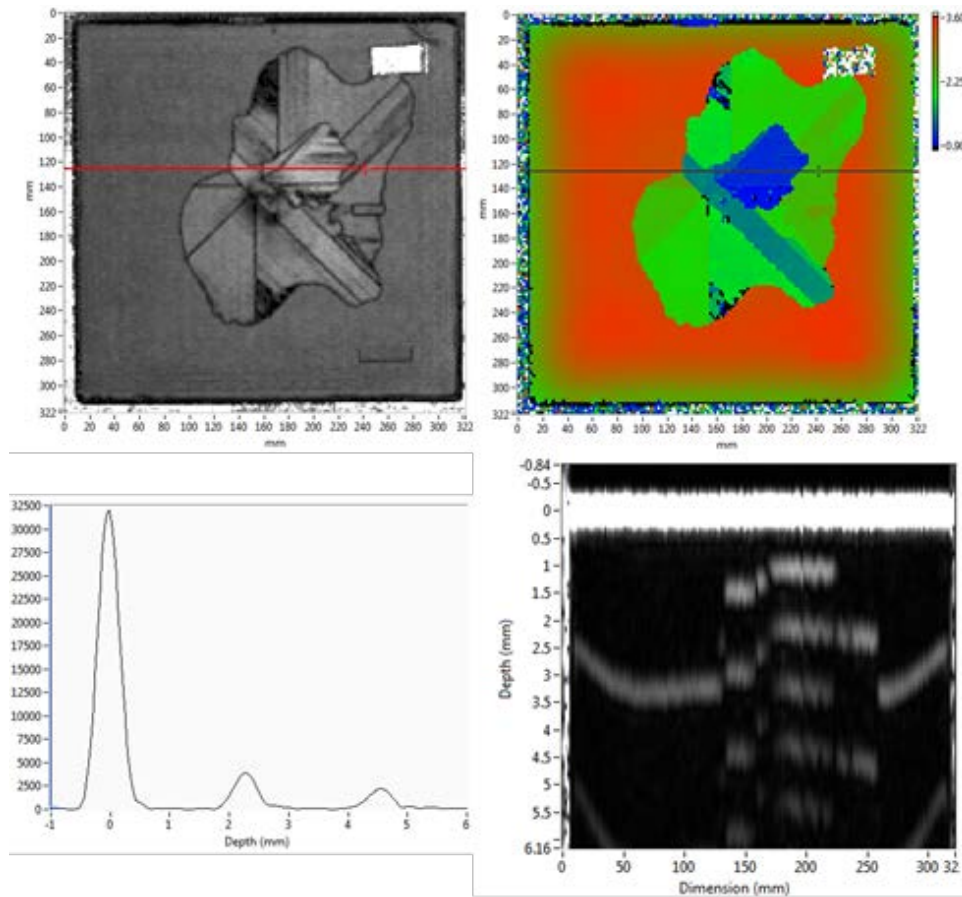


Figure 122. iPLUS laser-ultrasonic scan of a 16-ply composite laminate with impact damage

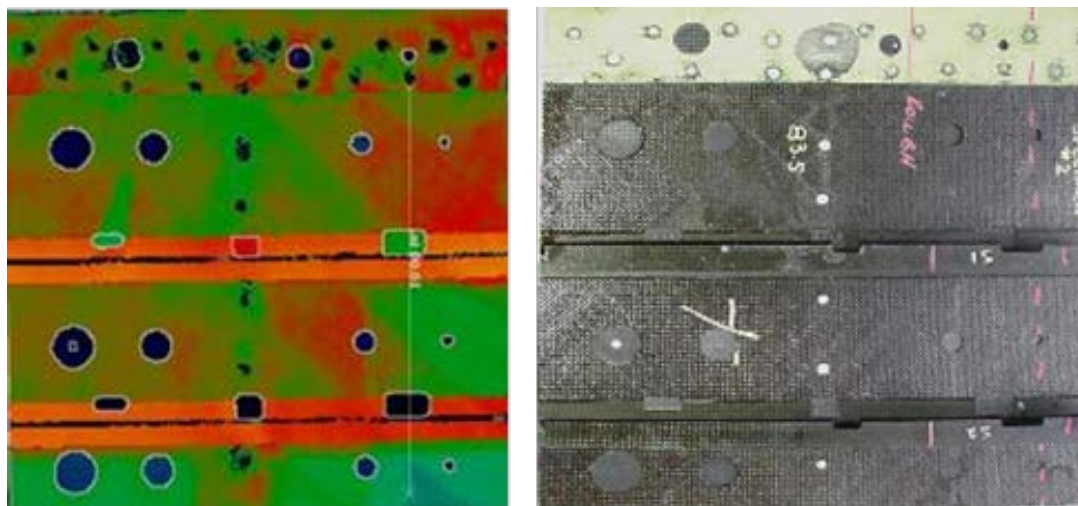


Figure 123. iPLUS laser-ultrasonic inspection of 0.111" thick composite laminate test specimen; photo on right shows the layout of the engineered flaws

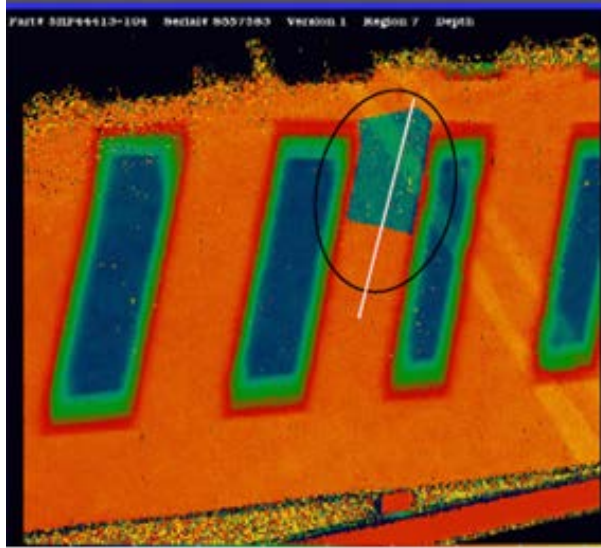


Figure 124. iPLUS laser-ultrasonic image of a composite part containing an inclusion as highlighted

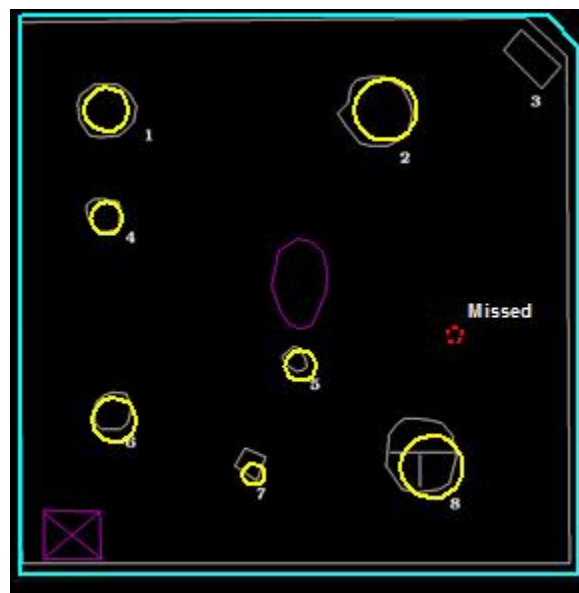


Figure 125. Sample results from laser UT inspection of 3-ply fiberglass panel

4.12 LAMINOGRAPHY

A motionless laminography system, developed by Digiray[®], uses a reverse geometry scanning X-ray source and an array of 64 small detectors to generate a sequence of laminographic slices that may be reconstructed to produce three-dimensional X-ray images. The technology facilitates an inspection through an object, layer-by-layer, to detect and pinpoint the location of a feature or defect without moving either the object or the X-ray source. Laminography has been shown to image defects in composites, porosity voids in adhesive bonds, and cracks and voids in metals. NASA Ames has used laminography to inspect the thermal protection tiles for the X-37

development project. In trial tests with Boeing, the equipment was used to detect cracks caused by foam impact on a reinforced carbon panel representative of the leading-edge heat shield on the Space Shuttle wings.

Figure 126 illustrates the Digiray Reverse Geometry X-ray[®] (RGX) concept. The reverse geometry shows the object close to the source instead of close to the detector as in conventional systems. The result is that most of the scattered X-rays are not detected by the system. The single detector may be replaced by an array of detectors that are simultaneously exposed to X-rays of the object shown in figure 127. The diagram in figure 127 shows the X-ray source on the left. A scanning beam generated in a raster pattern using a magnetically deflected electron beam inside the X-ray tube produces X-rays. The fan beam is then transmitted through a thin anode window and the adjacent object. When these X-rays impinge on the detectors, they produce an output signal that enters an amplifier. An analog-to-digital converter digitizes the amplifier's output. The resulting digitized signals are then synchronized with the raster pattern generated in the X-ray tube and stored in the computer's memory. The result is a two-dimensional pattern of picture elements associated with each detector in the array. The patterns are shifted and added together to create a layer-by-layer view of the object. The photos in figure 128 show the difference between a transmission X-ray on the left and laminography on the right. Using laminography, the two sides of a U.S. quarter are shown with the image of the head separated from the image of the tail.

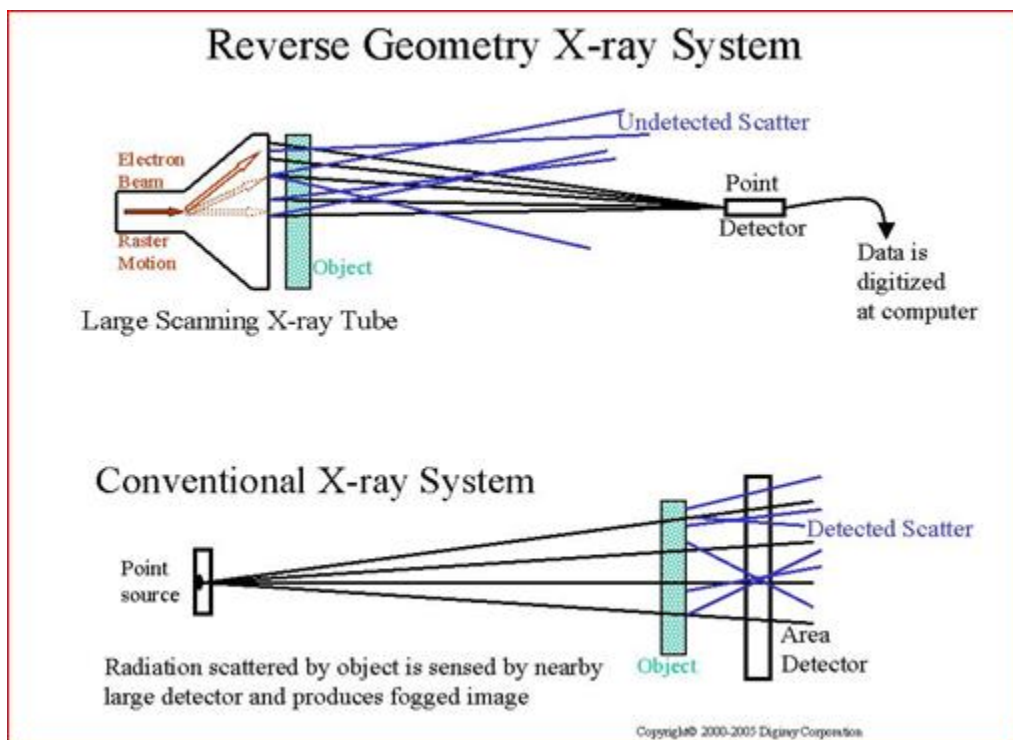


Figure 126. Schematic of the reverse geometry laminography concept

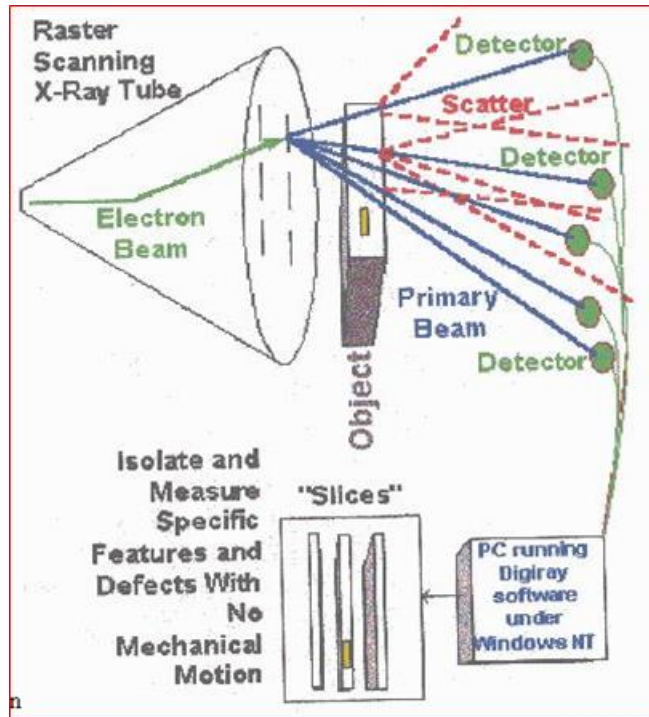


Figure 127. Use of array of detectors and scanning beam to produce images of layers within the part being inspected

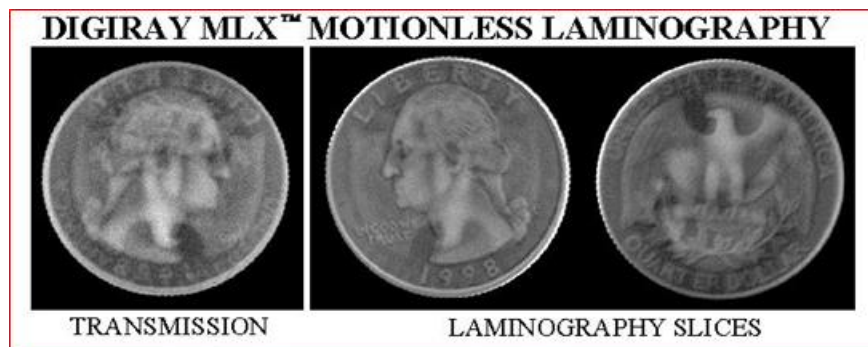


Figure 128. Images highlighting the sensitivity of laminography and ability to produce slices for improved detail recognition

The basic features of laminography are that it:

- Looks through an object layer-by-layer during inspection.
- Detects the location of defects rapidly.
- Eliminates most X-ray scattering (see figure 126).
- Produces high-resolution digital images.
- Captures 1,000 X-ray slices, each 1 mil thick, with a single exposure.
- Enables quick setup—alignment of tube and detectors is fixed.
- Requires structure to be removed from aircraft.
- Has contrast sensitivity $< 0.3\%$ —contrast ratio is 1500:1.

Digiray developed this equipment by combining:

1. An electronically scanned beam X-ray source placed close to the object and 64 small detectors placed at a distance; this geometry is the reverse of conventional X-ray and greatly reduces X-ray scattering effects, thus attaining sharper X-ray images
2. Multiple detectors (an array of 64 photomultipliers), each “viewing” the object from a different angle
3. Special software that generates laminography without the need to move the object or the detectors

The result of these features is a specialized X-ray inspection method that provides two-dimensional spatial resolution of 12 microns; resolution in the third dimension of 8 mils; and contrast sensitivity of 0.3%. In operation, the Digiray Motionless Laminography X-ray™ (MLX) system displays one image after another of multiple layers of the object. In a single short X-ray exposure, it captures 1,000 X-ray slices that are 8 mils thick. These slices may be displayed individually or in a consecutive layer-by-layer motion picture. It also provides zoom magnification capability without loss of resolution by electronically compressing the raster into a smaller area. The reduced-size raster can then be moved about the face of the screen so that it can pan within the field of view without using any mechanical means. The operator sets instantaneous electronic controls to zoom and pan.

Figure 129 shows laminography slices of a Lucite wedge made up of seven steps ranging 1-4". A four-hole penetrameter is mounted on each step, with holes ranging 0.5-2T or 1-4% change in density compared with the total density of each step. Each hole is visible on all seven steps.

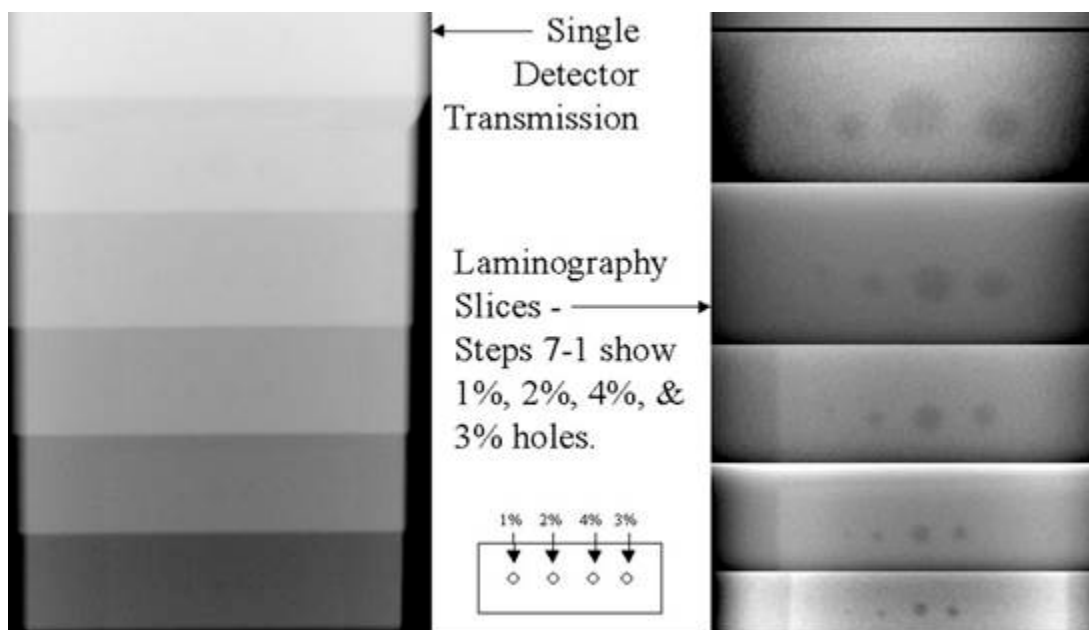


Figure 129. Comparison of normal X-ray with laminography images showing ability of laminography to detect damage in a 4" thick Lucite part

Damage detection in composite honeycomb parts is shown in figures 130 and 131, which highlight two of the flaw types found in the CHE. Machined core regions were used as one method to produce gross disbond flaws between the skin and the core structure, while pillow inserts were used to create interply delaminations in the skins. The test setup for the experiment panels is shown in the photo contained in figure 132. Nine shots were used to construct a complete image of the 2' x 2' panel where various flaws within the sample panel can be seen in the laminography image.

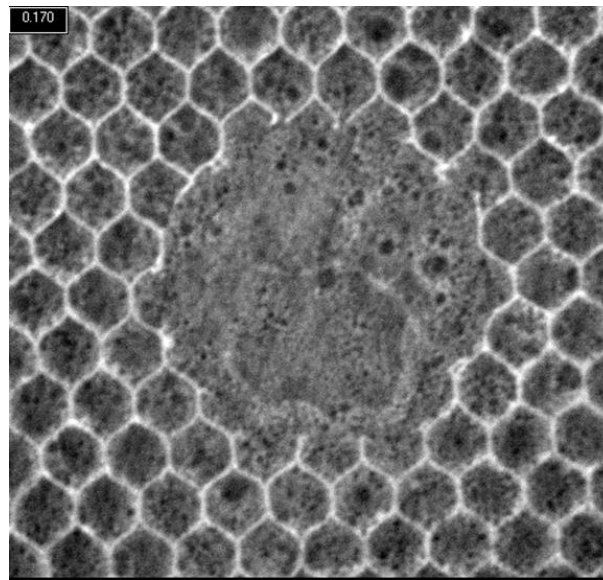


Figure 130. Laminography slices of machined honeycomb core that simulate a disbond in the fiberglass skin-to-core bond line

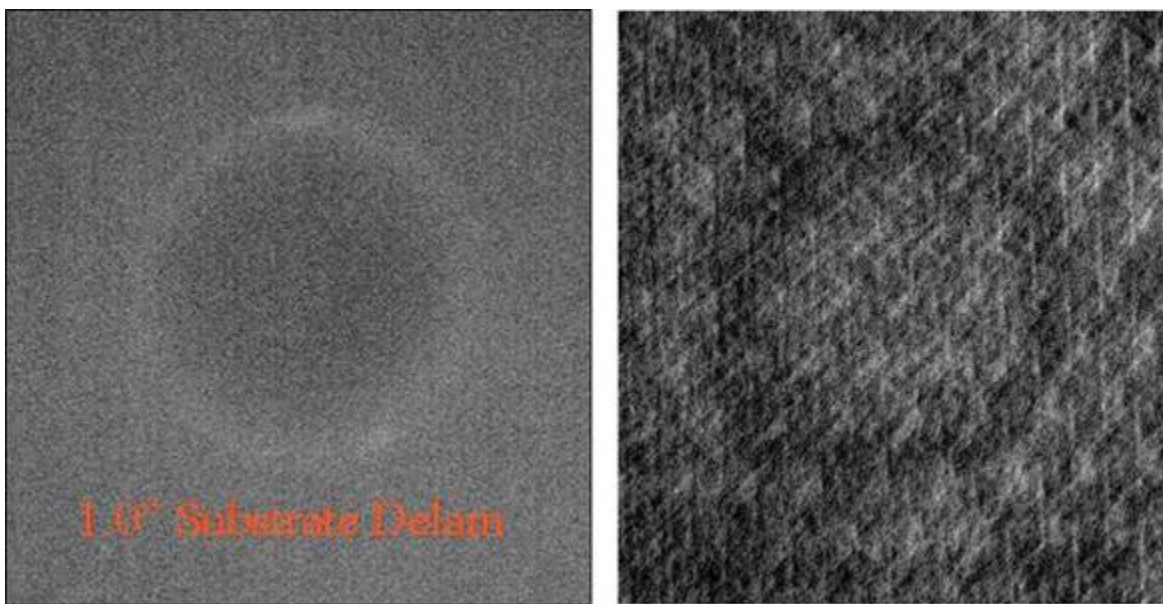


Figure 131. Laminography slices of interply delaminations in a 3-ply fiberglass honeycomb panel

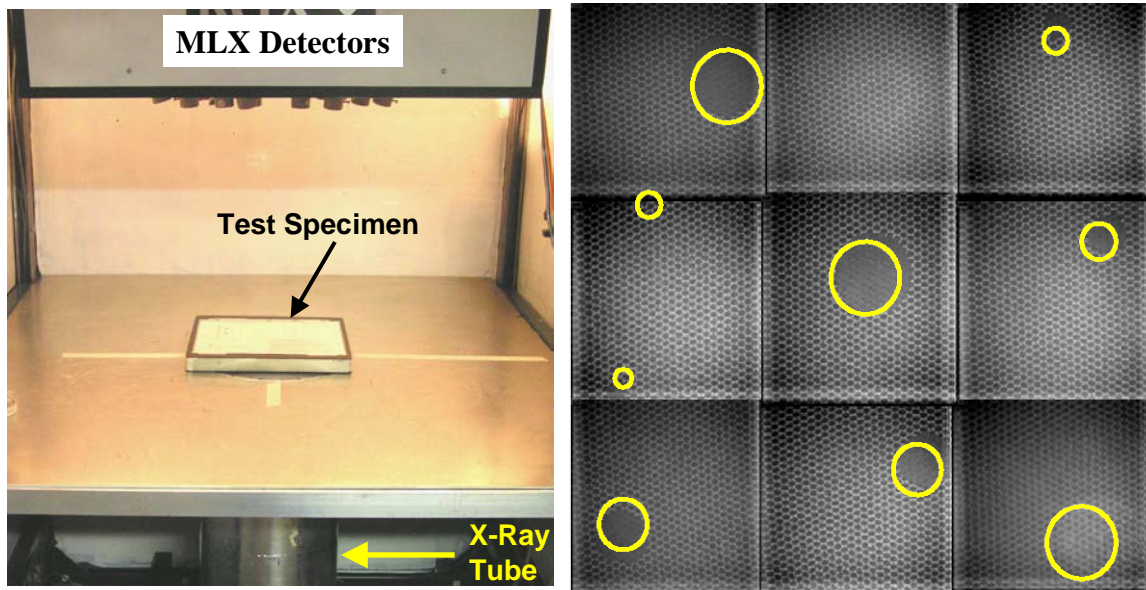


Figure 132. Laminography test setup and sample image showing all flaws detected in 3-ply fiberglass panel

5. COMPOSITE HONEYCOMB FLAW DETECTION EXPERIMENT DESIGN

The CHE was developed to assess the performance of both conventional and advanced NDI techniques in detecting voids, disbonds, delaminations, and impact damage in adhesively bonded composite aircraft parts. A series of composite honeycomb specimens with statistically relevant flaw profiles were inspected using both human tap test techniques and NDI equipment introduced to automate and improve acoustic tap testing. The majority of the testing was in the form of blind PoD studies while other portions of the testing determined signal-to-noise (S/N) ratios from which flaw detection could be inferred. The primary factors affecting inspections were incorporated into this study, including composite materials and construction type, flaw profiles, mechanical interactions (impact and audible response), and subsurface damage and environmental conditions. The critical phase of this effort used airline personnel to study PoD performance in the field and formulate improvements to conventional inspection practices.

The test articles for this experiment were modeled after the general range of construction scenarios found on commercial aircraft. A set of 44 composite honeycomb test specimens containing engineered and natural flaws were manufactured. Flaws of various size, shape, and type were randomly located across the specimen footprints. Details of the specimen construction are as follows:

- Skin type: carbon graphite and fiberglass
- Skin thickness: panels have three-, six-, and nine-ply skins
- Core: 1" thick Nomex core
- Paint: all panels are painted as per current aircraft specifications

The flaw types included in the test specimens are:

- Interply delaminations (pillow inserts).
- Machined core disbonds simulating an air gap skin-to-core disband.
- Pillow insert disbonds simulating tight contact but no adhesive strength (kissing disbond).
- Naturally formed impact damage (e.g., crushed core, disbonds, delaminations, broken fibers).

One critical technical challenge required a parallel research effort to determine how to produce representative flaws in composite honeycomb structure. For example, an extensive test series was completed to produce impact damage that was subsurface only (core crush and/or backside fiber fracture) and not accompanied by any surface demarcations.

The CHE traveled to airlines and third-party maintenance depots to acquire flaw detection data as provided by qualified aviation inspectors. The experiment required approximately 2–3 days of each inspector's time. In general, inspectors were asked to locate and size hidden flaws in the test specimens. The test program was intended to evaluate the technical capability of the inspector, inspection procedures, and equipment (i.e., NDI method). The inspections emphasized flaw detection methods applicable to composite honeycomb structures. During the experiment, each blind inspection was preceded by inspections on appropriate reference standards supplied by the experiment monitors. These feedback specimens contain all of the same construction and flaw types as those found in the blind PoD tests specimens. The inspectors were given information on the manufactured flaws present in the reference standards and were allowed to use these specimens to ensure the proper operation of their equipment and allow them to become comfortable with the inspection demands before moving on to the blind PoD specimens. Figure 133 shows some of the composite honeycomb test specimens while figures 134 and 135 show the honeycomb reference standards. The same reference standard design was used for both carbon and fiberglass skins, and repeated for three, six, nine, and 12 plies [53–55].

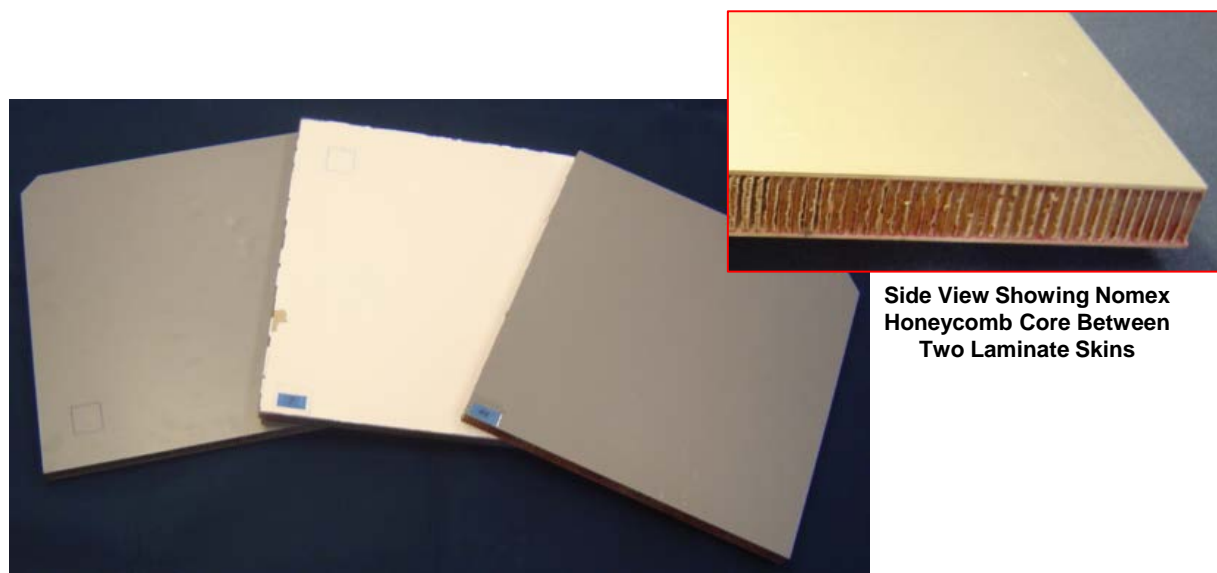


Figure 133. Test specimens used in composite honeycomb flaw detection experiment

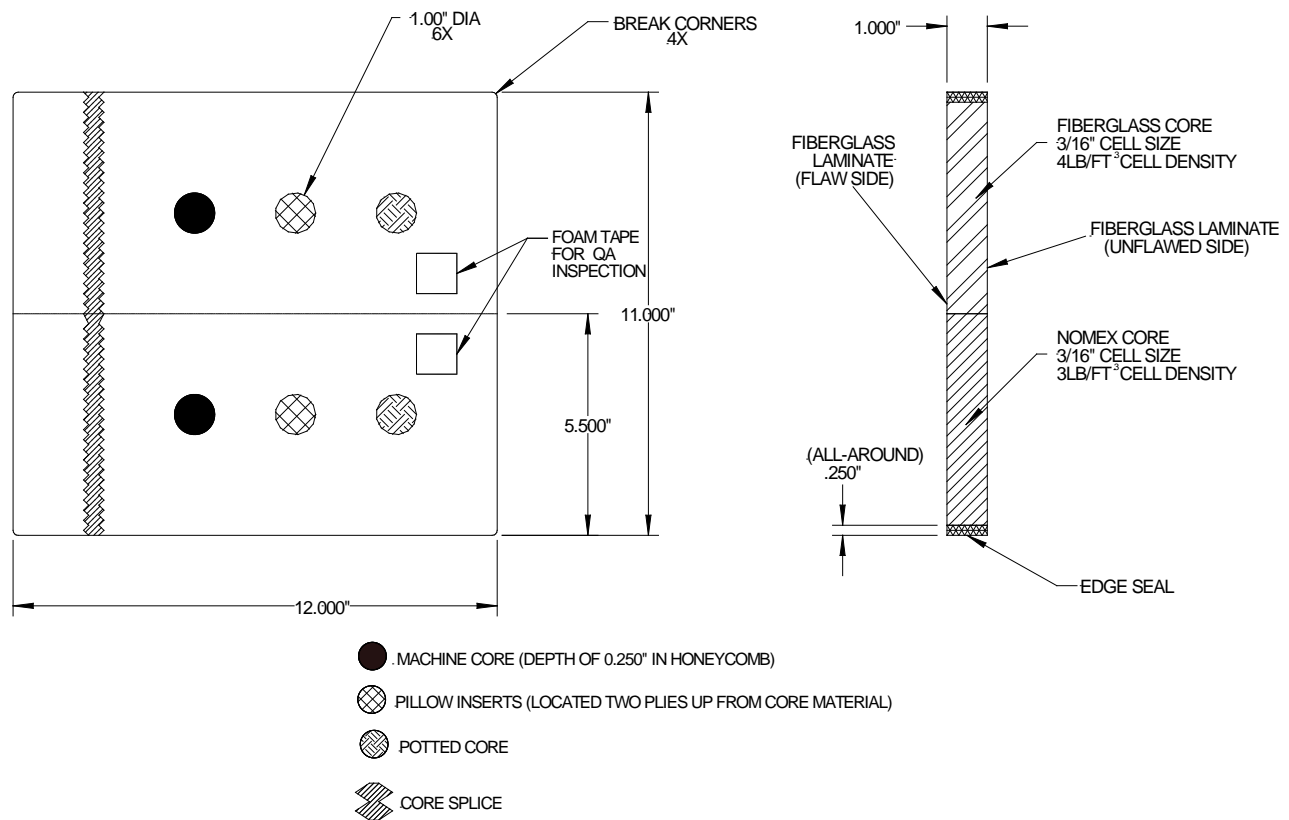


Figure 134. Schematic of composite honeycomb NDI reference standards showing construction and flaw profiles

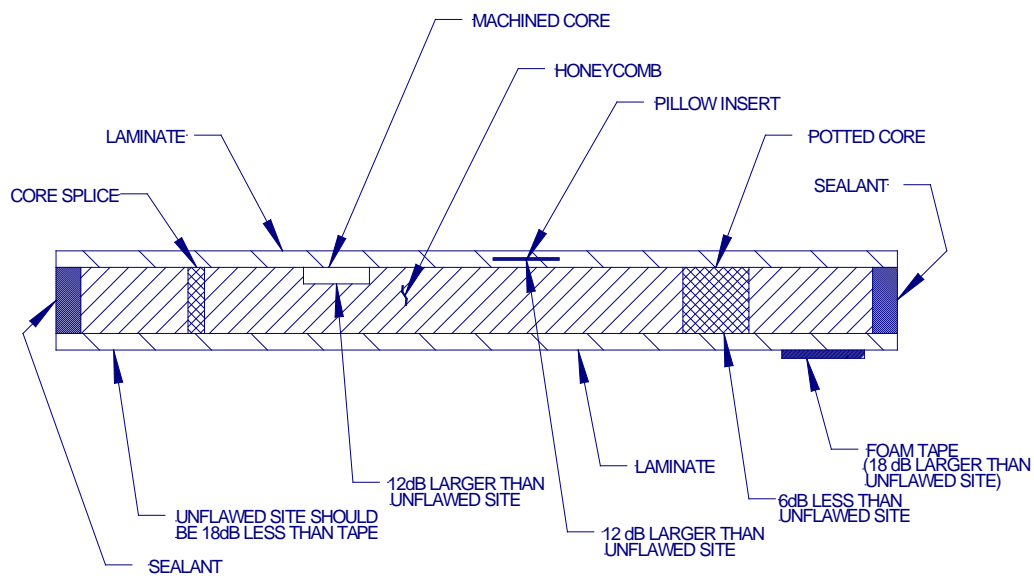


Figure 135. Cross-section of honeycomb reference standard design

These tests were conducted using NDI equipment that the inspectors are experienced in using for this type of inspection. The effort focuses on understanding the factors influencing the performance of NDI methods (device and inspector) when applied to the inspection of composite honeycomb structures. The experiment results evaluated inspection performance attributes, including accuracy and sensitivity (e.g., flaw hits, misses, false calls, and flaw sizing) and usability features such as versatility, portability, complexity, and inspection time (human factors). This report includes the results from the application of conventional honeycomb inspection methods as well as the results from the application of advanced NDI methods.

5.1 EXPERIMENT DESIGN CRITERIA

The list of criteria that were used to design this experiment are as follows:

- Conventional and advanced inspection techniques are being assessed.
- Use information from completed composite reference standard study [53–56] to produce the critical set of composite honeycomb panels (i.e., use only design variables that affect NDI).
- Use knowledge of general composite inspections and tap tester responses to eliminate or minimize additional variables to arrive at a workable number of test specimens.
- Sufficient number, type, and sizes of flaws are included to produce a statistically relevant PoD analysis. Specimens contain sufficient unflawed regions to allow for assessment of the probability of flaw detection as well as the likelihood of false calls.
- Flaw types to be studied: 1) interply delaminations, 2) gross skin-to-core disbonds, 3) tight/subtle skin-to-core disbonds simulating tight contact but no adhesive strength (kissing disbond), and 4) impact damage (crushed core, disbonds, delaminations, broken fibers).
- Engineered flaws were placed on both sides of the honeycomb panels. This reduced specimen costs (reduced material and fabrication time) and minimized the number of panels to transport.
- Application of NDI:
 - Blind application of techniques to study hits, misses, false calls, and flaw sizing; blind tests will employ some procedural guidance to ensure uniformity of results. The procedures will also study:
 - Use of no grids on the specimens (inspecting “freehand”).
 - Use of 1” grid spacing on the specimens to control NDT coverage.
 - Use of a 0.5” grid spacing on the specimens to assess improvements stemming from decreasing tap test spacing.
 - Apply NDI devices with knowledge of flaw locations to determine quantitative S/N ratios; flaw detection can be inferred by studying S/N levels.
- Conventional composite inspection techniques studied were: Boeing and Airbus manual tap hammers, LFBT, HFBT (resonance), and MIA. In addition, 15 different advanced NDI methods were evaluated in these experiments, including: Mitsui Woodpecker

automated tap hammer, WichiTech DTH, CATT, thermography, shearography, PE-UT, AC-UT, MAUS C-scanning in MIA and resonance mode, laser UT, shearography, microwave, laser Doppler velocimetry, UT linear array, and laminography.

5.2 EXPERIMENT TEST SPECIMEN DESIGN

To implement a realistic experiment, it was necessary to design representative specimens that include a full spectrum of variables found on composite aircraft structures. Another important factor in the specimen design was to determine the most prevalent flaw types found on this type of structure and develop ways to engineer representative flaws. This included determining the various flaw sizes required for the statistical analysis.

While the size of flaw, or damage, that must be detected is affected by many parameters, the general goal for composite inspections is to detect flaws that are 1" diameter or larger. Many of the NDI reference standards in OEM NDT manuals use 1" diameter flaws to guide equipment setup. In addition, the CACRC ITG members generally conclude that 1" flaw detection provides a good center point for this CHE SLE. Thus, the flaw sizes in the experiment design were established with 1" diameter at the center. Larger and smaller flaws were included such that PoD values smaller than 1" (as small as 0.25") and PoD values larger than 1" (as large as 2") could be ascertained.

The list of criteria for the change of the test specimens is as follows:

1. Specimen types – modeled after range of construction found on aircraft; carbon graphite and fiberglass skin over Nomex core.
2. Skin thickness – panels have three-, six-, and nine-ply skins.
3. Paint – all panels were painted as per current aircraft specifications.
4. Flaw types – statistically relevant flaw distribution, with sizes ranging from 0.2 in.² to 3 in.²
 - a. Interply delaminations
 - b. Skin-to-core air gap disbonds (machined core disbonds simulating presence of air gap)
 - c. Skin-to-core “kissing” disbonds (pillow insert disbonds simulating tight contact but no adhesive strength)
 - d. Impact damage – crushed core, disbonds, delaminations, broken fibers
5. A minimum of 2" separation between flaws is maintained to eliminate signal cross-talk; include a few flaw pairs that are closely clustered to study ability to define boundaries of flaws.
6. A minimum of 1.5" distance from flaws to edge of panels is maintained; includes a few instances of flaws close to edge to study flaw detection near a natural edge.
7. Desired flaw size to detect is 1" diameter; minimum flaw size is half this value (0.5" dia.), maximum flaw size is twice this value (2" dia.). The 0.5"–2.0" dia. flaws were divided into five discrete sizes—0.5", 0.75", 1.0", 1.5", and 2.0"—and distributed throughout the specimen set. One large 3" dia. flaw was added to provide a flaw that should be found by all techniques.

8. Proper flaw spacing, including the need to produce sufficient unflawed regions to determine false call rates, required 44 specimens that are 18" W x 18" H.
9. Flaw engineering – The methods used to engineer controlled flaws include “loose” disbonds (machined core), “tight” or kissing disbonds (pillow inserts placed between honeycomb core and adhesive), impact damage (fracture, delamination/disbond, crushed core), and delaminations (pillow inserts placed between adjacent composite plies). In various circumstances, the engineered flaws may be more or less difficult to detect than actual aircraft flaws. A three-year study was completed to develop methods for producing repeatable, realistic flaws.
10. To provide the proper challenge to the tap test and artificially showing NDI in a poor light, it was decided to add impact flaws to the specimen matrix. The impact panels provide “natural” disbonds and crushed core damage scenarios to the experiment. A focused impact study on representative honeycomb sandwich structures was used to guide the impact levels such that subsurface damage could be achieved without creating surface demarcations. Post-impact TTU was used to characterize the flaw profiles in the test specimens.
11. Impact specimens – Two impact panels were added for each of the six- and nine-ply families. Nominal impactor sizes of 0.75", 1", 1.5", and 2" diameter were used to create representative flaws of different sizes. As the impact panels represent normal manufactured structure, the laminate and honeycomb core were co-cured in an autoclave at elevated pressures (45 psi versus the 11 psi panels with engineered flaws that represent worst-case repair cures). Figure 136 shows the different impactors along with the drop-table apparatus that was used to produce repeatable, controlled impact energy for the impact panels. Figure 137 shows one of the impact calibration tables that was produced using trial impacts on duplicate composite honeycomb panels. Similar curves were made for fiberglass and carbon skin panels of three-, six-, and nine-ply thickness. Then, these predetermined energy levels were used to produce the actual impact damage on the experiment honeycomb panels. Sample damage produced by the impacts are shown in figures 138 (fiber and matrix cracking) and 139 (crushed core and disbonds).

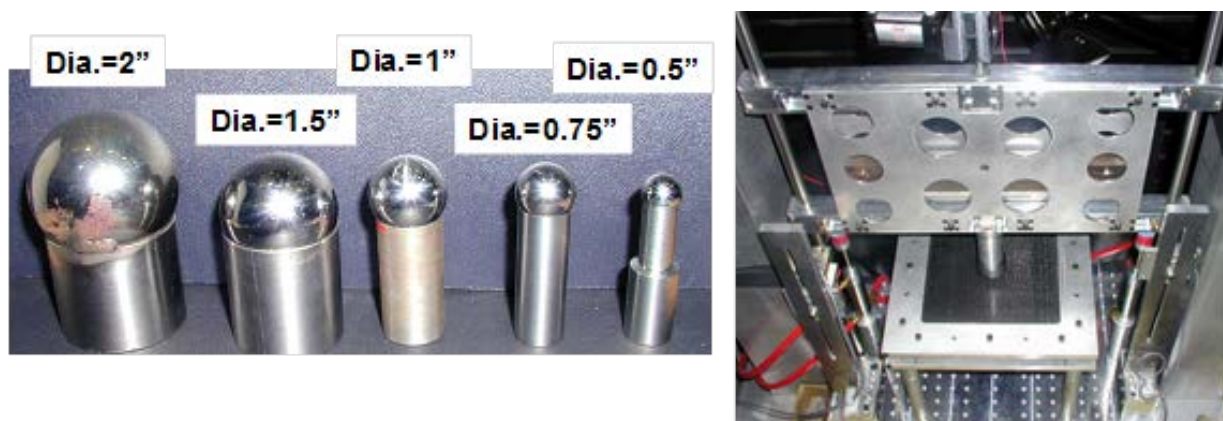


Figure 136. Impactors and impactor drop-table apparatus used to produce damaged area on test panels

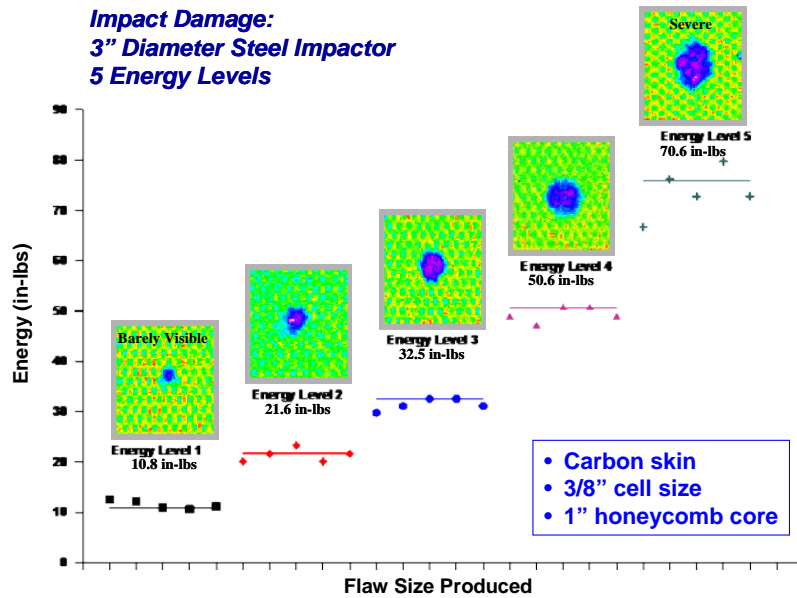


Figure 137. Sample results from calibration shots used to determine energy levels needed to produce damage in composite honeycomb panels without producing surface demarcations

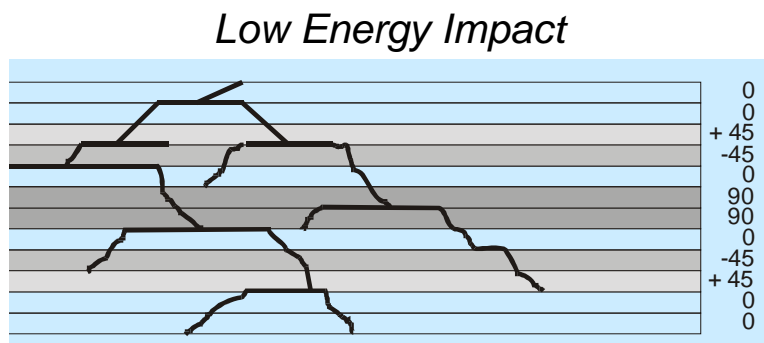


Figure 138. Pyramid pattern matrix crack produced by impact of composite skin



Figure 139. Cross-section of sample impact damage in composite honeycomb experiment panels showing crushed core but no skin deformation

12. Specimen reduction – The specimen matrix was reduced by determining the core type that provides the most difficult flaw detection for the tap test: Nomex. Nomex is softer than fiberglass, thus its loss via a disbond will produce a relatively smaller change in

stiffness. A series of tap tests were conducted using the Woodpecker device on an array of honeycomb specimens. The results are shown in tables 2 and 3. With the exception of a single anomaly, disbonds in the Nomex cores displayed a lower signal and were more difficult to detect. Note that in the thicker plies, the loss of core has less effect on the stiffness so the signal change is less. Thus, it was determined that the specimen set would only include Nomex core. It is expected that the PoD results for fiberglass core will be slightly better than that calculated for Nomex core.

Table 2. Digital tap test results from Mitsui Woodpecker comparing flaw detection in Nomex and fiberglass cores

Core Type	3-Ply Carbon Skin*		3-Ply Fiberglass Skin*	
	Pillow Insert Flaw	Machined Core Flaw	Pillow Insert Flaw	Machined Core Flaw
Nomex	41/56 (15)	41/73 (32)	41/63 (22)	41/81 (40)
Fiberglass	35/51 (16)	35/70 (35)	36/52 (16)	36/80 (44)

Core Type	6-Ply Carbon Skin*		6-Ply Fiberglass Skin*	
	Pillow Insert Flaw	Machined Core Flaw	Pillow Insert Flaw	Machined Core Flaw
Nomex	35/38 (3)	35/42 (7)	34/41 (7)	34/45 (11)
Fiberglass	34/37 (3)	34/41 (7)	31/38 (7)	31/43 (12)

* Information presented as “Baseline Signal/Flaw Signal” with differential shown in parentheses

Table 3. Digital tap test results from Mitsui Woodpecker showing relative stiffness values for different cores

6-Ply Fiberglass Skin	
Core Type	Signal from Unflawed Region*
No Core	65
Nomex Core	35
Fiberglass Core	32.5

* Lower number (shorter pulse duration) = stiffer core

Softer core = harder to detect loss of core (harder to find disbonds)

13. Final specimen matrix – The final test specimen matrix is shown in table 4. The two specimen types produce a total of 44 specimens. Table 4 shows the engineered and “natural” impact specimen combinations for the following variables: skin type (carbon, fiberglass), skin thickness (three, six, and nine plies), honeycomb type (Nomex), and damage type (engineered disbonds and delaminations, and impact flaws). Notice that the number of specimen configurations was reduced by applying several NDI assumptions that are described in the following section. This allowed us to have a manageable number of specimens in the study. A summary of the test specimen configurations follows:
 - a. Engineered honeycomb test specimens:
 - i. 6 specimens x 3 configurations (3, 6, and 9 plies) = 18 specimens for carbon skin with Nomex core
 - ii. 6 specimens x 3 configuration (3, 6, and 9 plies) = 18 specimens for fiberglass skin with Nomex core
 - b. Natural impact test specimens:
 - i. 2 specimens x 2 configurations (6 and 9 plies) = 4 specimens for carbon skin with Nomex core
 - ii. 2 specimens x 2 configurations (6 and 9 plies) = 4 specimens for fiberglass skin with Nomex core

Table 4. Test specimen matrix for composite honeycomb flaw-detection study

Engineered Specimens			
Skin	Number of Plies	Honeycomb Core	Resulting Number of Configurations
Carbon	3, 6, 9	Nomex	3
Fiberglass	3, 6, 9	Nomex	3
			6 configurations x 6 each = 36 specimens total

Flaws = MC disbonds, PI disbonds, PI delaminations.

Flaw Sizes = ½", ¾", 1", 1.5", 2.0" diameter.

Flaw Numbers = 51 per configuration; spread over 6 specimens to allow for assessment of false calls.

“Natural” Impact Specimens			
Skin	Number of Plies	Honeycomb Core	Resulting Number of Configurations
Carbon	6, 9	Nomex	2
Fiberglass	6, 9	Nomex	2
			4 configurations x 2 each = 8 specimens total

Flaws = ID impact disbonds, IC impact crushed core.

Flaw Sizes = as generated by impactors with 0.75", 1", 1.5", and 2.0" diameter.

Flaw Numbers = 8 per configuration, concentration on 1" diameter requirement.

14. Methods for engineering flaws – Inspection results from a custom, preliminary suite of specimens were used to determine the best way of producing realistic and reliable skin-to-core disbond and interply delamination flaws. A series of inspections were carried out on trial standards that were manufactured with various candidate methods for engineering delamination flaws. Figure 140 shows the engineering drawing for one of these honeycomb specimens for evaluating flaw insertion methods. One carbon specimen and one fiberglass skin specimen were produced with this flaw layout. The three methods employed to engineer the delamination flaws were: 1) pillow insert consisting of Kapton tape around four layers of tissue paper; 2) brass shims coated with a silicon mold release to prevent bonding to the plies; and 3) Teflon disk inserts. Each flaw method was used to generate three like delamination flaws to test for repeatability as well as to statistically determine the amount of NDI signal disruption generated by the flaw method. Note also that the trial specimen includes potted core and core splice areas. To expand the utilization of these standards, potted core and core splice areas were included as a tool to aid in the interpretation of NDI signals. This will help minimize false calls caused by the presence of potted cores or core splices that can alter NDI equipment readings.

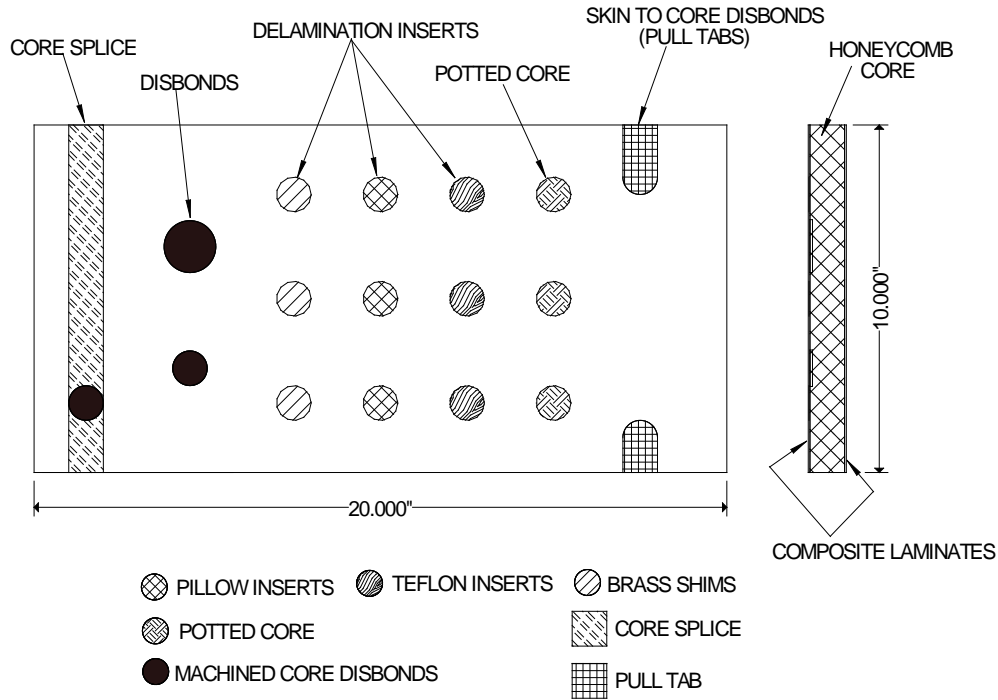


Figure 140. Engineering drawing to evaluate honeycomb reference standard design and fabrication

- a. Disbonds – Machining the honeycomb core (recessing) away from the laminate provides the best way of producing reliable skin-to-core disbond flaws. This method also produces flaw sites that can support tap testing. Pull tabs were also included as an alternate disbond engineering method; however, the required proximity of the pull tab flaws to the edge of the specimen produces boundary condition effects in some NDI methods and limits the value of these types of flaws.
- b. Delaminations – The goal was to realistically and repeatably produce interply delamination flaws. The methods were repeated multiple times to assess consistency. The methods employed to engineer the delamination flaws were as follows: 1) pillow insert; 2) brass shims coated with a silicon mold release agent; and 3) Teflon inserts (individual inserts with 0.003", 0.005", and 0.008" thicknesses, and two plies of stacked 0.003" inserts). Figure 141 shows how the pillow inserts were fabricated. Experiments determined that the four layers of tissue paper are needed to produce a uniform and repeatable interruption (i.e., flaw indication) of an interrogating NDI signal.

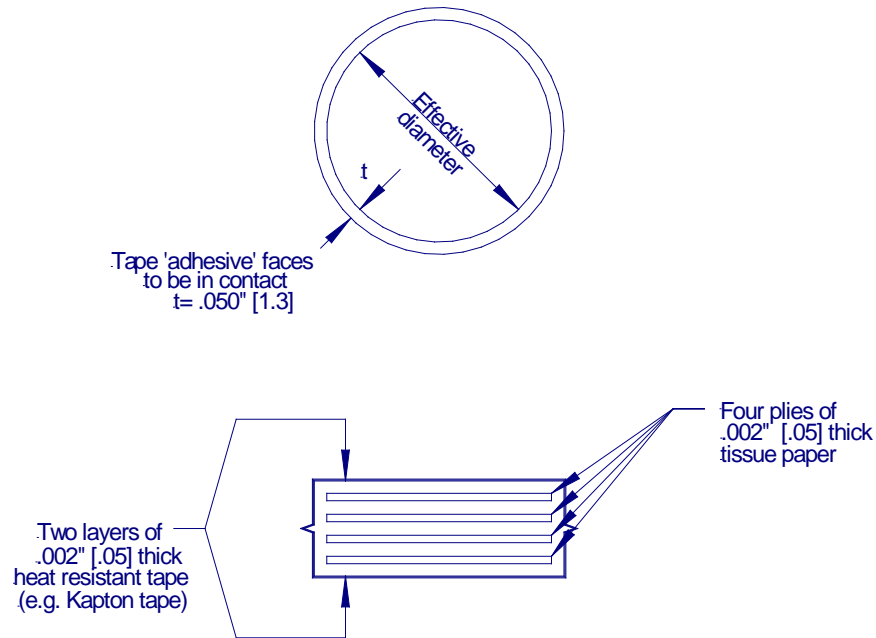


Figure 141. Construction of pillow insert for delamination flaws

- c. Potted core and core splice (used as reference not calibration) – The trial specimen included potted core (BMS 5-28 Type 7 material) and core splice (AF-3028 material) areas. To expand the utilization of these standards, potted core and core splice areas were included as a tool to aid the interpretation of NDI signals. A process was developed wherein the potting material was placed in a vacuum chamber just prior to insertion in the core cells with a syringe. This produced a uniform potting, and no porosity was visible in subsequent TTU inspections. Figure 142 shows the process for creating a potted core area in the honeycomb. A profile of a machined core region to create disbonds is also shown in this schematic.

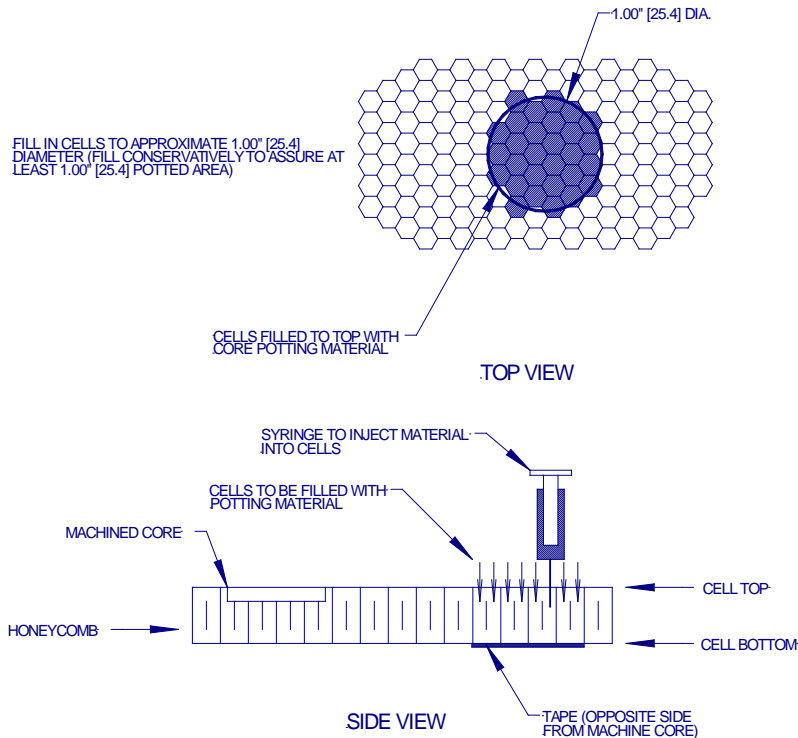


Figure 142. Process for creating potted honeycomb core areas

TTU was used to evaluate the flaw engineering methods as it has the best resolution and the ability to provide quantitative signal attenuation values. TTU results for the trial honeycomb panels (see figure 140 for design drawing) are shown in figure 143. All of the flaws can be clearly seen; however, the Teflon inserts and brass shim inserts, second and fourth row down, respectively, are smaller than their original 1" diameter area. This is probably due to ingress of the adhesive around the perimeter of these inserts and an associated coupling of the UT signal. As a result, attenuation levels in the Teflon and brass shim areas are less than those measured in the pillow inserts regions. Furthermore the pillow insert regions were able to retain their 1" diameter size. The machined core disbond areas were also very consistent with uniform signal attenuation levels. Finally, the potted core regions shown in the top row provided enhanced signal coupling and an associated decrease in UT attenuation through the panel. This is expected, and the results show a very uniform and repeatable signal level to support NDT calibration.

Two other laminate skin specimens were produced to complete the evaluation of various delamination inserts. TTU results from scanning these two skins are shown in figures 144 and 145. This exercise determined that the use of multiple layers (i.e., four plies of tissue in pillow inserts and two plies of Teflon stacked together) produce better signal attenuation and more repeatable flaws than single-ply inserts, even if the single plies are thicker. These results indicate that the best method(s) to engineer delaminations are: 1) pillow inserts with four plies of tissue, and 2) Teflon inserts with two to three plies of 0.003" material. Measured signal attenuation through these disbond flaws ranged from 26–46 dB. BondMaster and S-9 inspections also support the use of these flaw insertion methods. A minimum of 18 dB attenuation is required at the flaw sites.

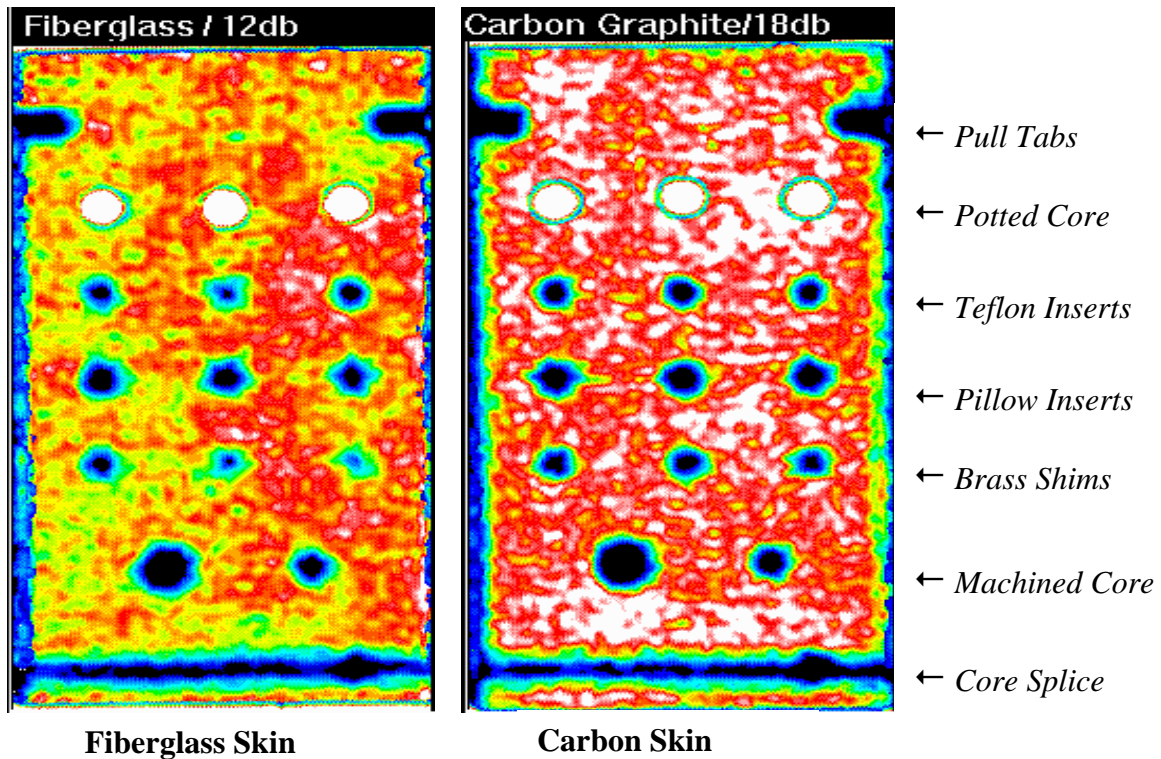


Figure 143. TTU inspection of honeycomb panel—assessment of methods to engineer repeatable flaws

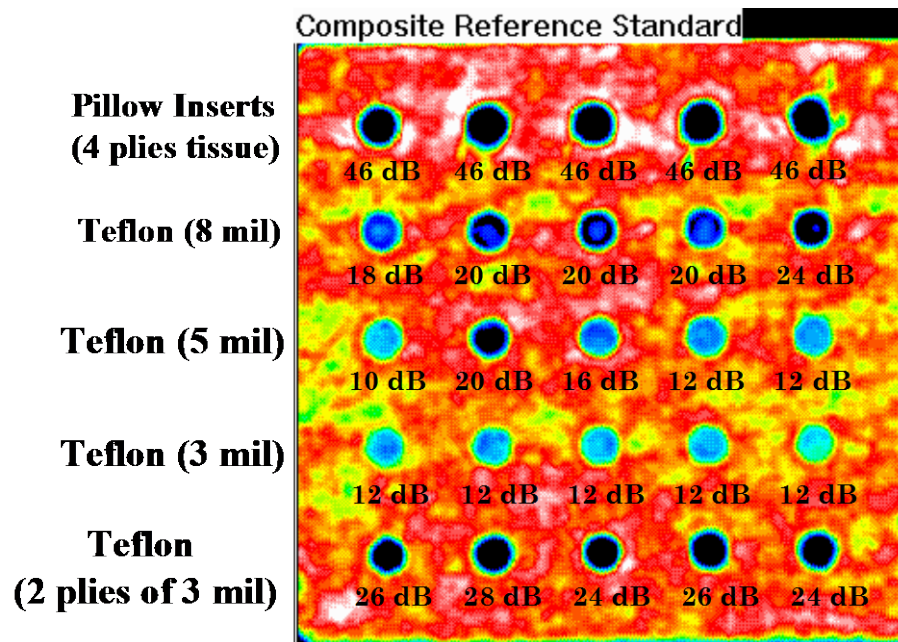


Figure 144. TTU C-scan showing signal attenuation produced by inserts; tests on 6-ply fiberglass laminate

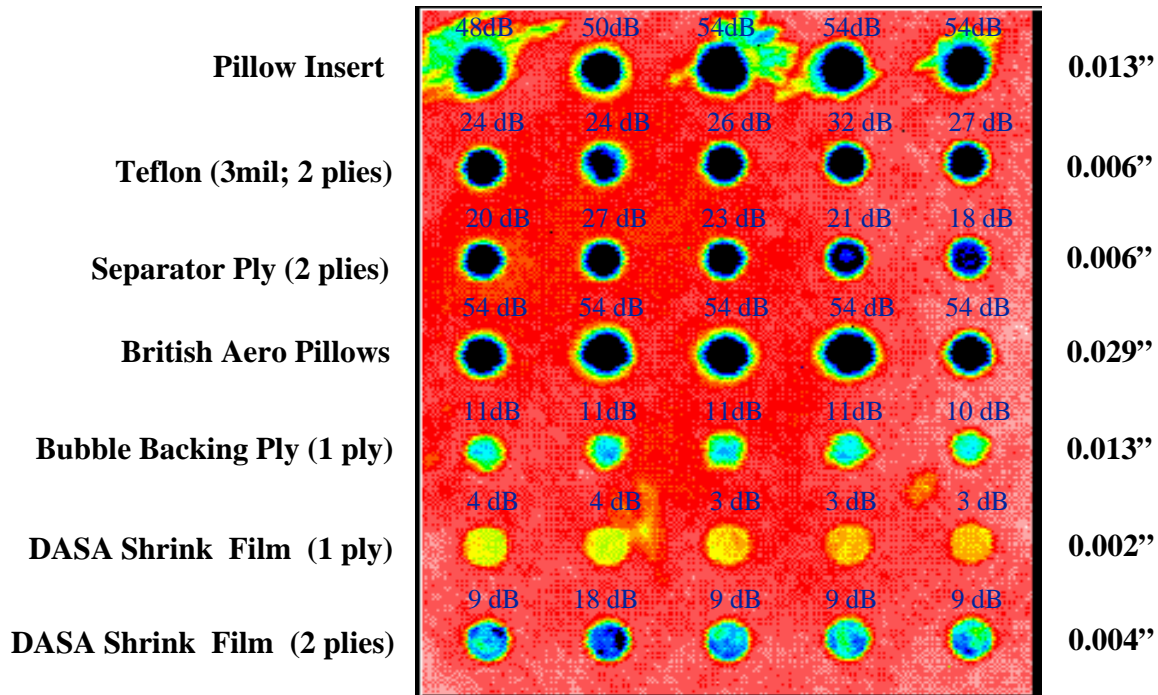


Figure 145. TTU C-scan showing signal attenuation produced by inserts; tests on 6-ply fiberglass laminate (numbers in right hand column represent thicknesses of inserts)

15. Test specimen characterization—to determine if the engineered flaws are adequate and able to be detected, a comprehensive flaw characterization effort was conducted. In one set of tests, TTU inspections were completed on a set of composite honeycomb test specimens. Figure 146 shows one sample TTU image in which signal attenuation values were ascertained to make sure that each flaw produced at least 12 dB of signal loss. A second flaw characterization step involved the use of S/N ratios to infer whether or not a particular flaw should and could be detected by normal NDI means.

To intercompare the results from different NDI methods that use different indicators to infer the presence of defects, each inspection measured the S/N of each defect versus the surrounding good structure. The noise level was determined by examining the output variation corresponding to inspections along adjacent sections of good structure. This was compared to the signal obtained during inspections of the flawed areas.

BS = base signal; peak signal at unflawed area
 NS = noise signal; (max-min)/2 over range of unflawed area in each quadrant
 FS = flaw signal; peak signal at each flaw site
 S/N = signal-to-noise ratio

$$S / N = \frac{FS - BS}{NS} \quad (2)$$

Data from equipment providing digital signal values (e.g., Woodpecker, S-9 Sondicator) were logged directly into a data acquisition computer. Several different inspection methods were applied to each flaw that was used in the CHE so that numerous S/N values for each flaw could be calculated. Normally, an inspector will look for S/N values in the vicinity of 3 to make a flaw call. Thus, the S/N assessment conducted here used an $S/N = 3$ as the threshold for determining the suitability of including an engineered flaw in this study. All flaws were determined to produce S/N values in excess of 3, so it was not necessary to exclude any flaws from the experiment. Testing using this scheme did not require calibration on a “median” or “neutral” reference standard. The key measurement for each case was the difference between unflawed areas of the test panel and the defect area. Sample data from S/N testing from different flaw types using the MIA mode of inspection are presented in table 5.

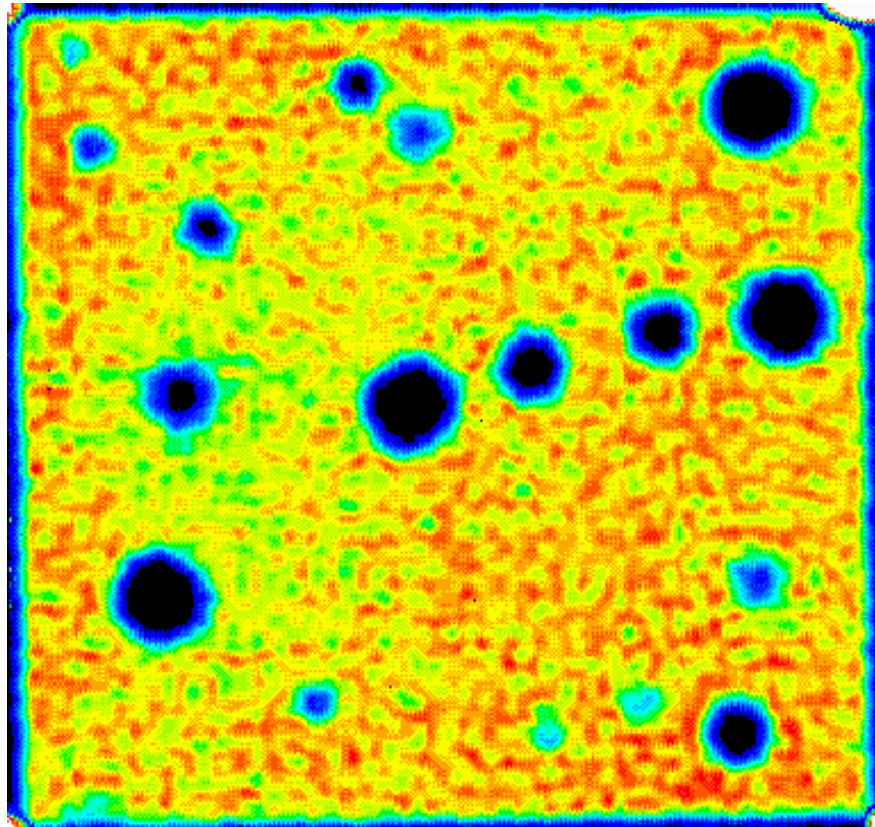


Figure 146. Specimen characterization—TTU C-scan of honeycomb test panel used to verify fabrication and location of engineered flaws

Table 5. Sample S/N data from various flaws demonstrating the viability of each flaw for use in the composite honeycomb flaw detection experiment

Specimen No.	Flaw No.	Flaw Type	Equipment Setup	Mean at Null Area	Std. Dev. at Null Area	Peak Value at Defect	Signal-to-Noise
6CI-1	307	1.046" IM	Fine Gain = .96	80.00	5.00	20.00	12.00
6CI-1	308	1.118" IM	Fine Gain = .96	80.00	5.00	16.00	12.80
6CI-1	309	0.658" IM	Fine Gain = .96	80.00	5.00	55.00	5.00
6CI-2	313	1.490" IM	Fine Gain = .96	80.00	4.00	9.00	17.75
6CI-2	314	1.078" IM	Fine Gain = .96	80.00	4.00	14.00	16.50
6FI-1	315	0.802" IM	Fine Gain = .90	80.00	4.00	40.00	10.00
6FI-1	316	1.810" IM	Fine Gain = .90	80.00	4.00	11.00	17.25
6FI-1	317	1.002" IM	Fine Gain = .90	80.00	4.00	46.00	8.50
6FI-1	318	1.730" IM	Fine Gain = .90	80.00	4.00	20.00	15.00
6FI-1	319	0.814" IM	Fine Gain = .90	80.00	4.00	39.00	10.25
6FI-2	322	1.060" IM	Fine Gain = .92	80.00	5.00	45.00	7.00
9CI-1	323	1.040" IM	Fine Gain = .58	80.00	6.00	39.00	6.83
9CI-1	324	1.980" IM	Fine Gain = .58	80.00	6.00	10.00	11.67
9CI-1	325	0.790" IM	Fine Gain = .58	80.00	6.00	37.00	7.17
9CI-1	326	1.042" IM	Fine Gain = .58	80.00	6.00	26.00	9.00
9CI-2	330	1.038" IM	Fine Gain = .58	80.00	5.00	20.00	12.00
9FI-1	331	1.610" IM	Fine Gain = .54	80.00	4.00	50.00	7.50
9FI-1	332	0.536" IM	Fine Gain = .54	80.00	4.00	63.00	4.25
9FI-1	333	1.760" IM	Fine Gain = .54	80.00	4.00	49.00	7.75
9FI-2	336	0.786" IM	Fine Gain = .54	80.00	5.00	55.00	5.00
9FI-2	337	1.020" IM	Fine Gain = .54	80.00	5.00	58.00	4.40
9FI-2	338	1.710" IM	Fine Gain = .54	80.00	5.00	37.00	8.60

Specimen No.	Flaw No.	Flaw Type	Equipment Setup	Mean at Null Area	Std. Dev. at Null Area	Peak Value at Defect	Signal-to-Noise
6F-5	188	2.00" MC	Fine Gain = 1.06	80.00	6.00	19.00	10.17
6F-5	189	1.40" PI-DE	Fine Gain = 1.06	80.00	6.00	13.00	11.17
6F-5	190	1.00" PI-DE	Fine Gain = 1.06	80.00	6.00	42.00	6.33
6F-5	191	0.50" MC	Fine Gain = 1.06	80.00	6.00	55.00	4.17
6F-5	192	1.00" MC	Fine Gain = 1.06	80.00	6.00	20.00	10.00
6F-5	193	1.40" MC	Fine Gain = 1.06	80.00	6.00	19.00	10.17
6F-5	194	2.00" PI-DE	Fine Gain = 1.06	80.00	6.00	7.00	12.17
6F-5	195	0.75" MC	Fine Gain = 1.06	80.00	6.00	32.00	8.00
6F-6	196	0.75" MC	Fine Gain = 1.02	80.00	5.00	36.00	8.80
6F-6	197	0.75" MC	Fine Gain = 1.02	80.00	5.00	34.00	9.20
6F-6	198	1.00" PI-DE	Fine Gain = 1.02	80.00	5.00	9.00	14.20
6F-6	199	0.50" PI-DE	Fine Gain = 1.02	80.00	5.00	35.00	9.00
6F-6	200	1.40" PI-DI	Fine Gain = 1.02	80.00	5.00	27.00	10.60
6F-6	201	3.00" MC	Fine Gain = 1.02	80.00	5.00	18.00	12.40
6F-6	202	0.50" PI-DI	Fine Gain = 1.02	80.00	5.00	55.00	5.00
6F-6	203	1.40" MC	Fine Gain = 1.02	80.00	5.00	20.00	12.00
6F-6	204	0.75" PI-DI	Fine Gain = 1.02	80.00	5.00	56.00	4.80

6. COMPOSITE HONEYCOMB FLAW DETECTION EXPERIMENT IMPLEMENTATION

The CHE traveled to airlines, third-party maintenance depots, and NDI developer labs to acquire flaw detection data. A sufficient number of inspectors performed the blind tests to produce statistically valid PoD curves representative of the industry as a whole. Testing on all conventional and advanced NDI methods was completed, and the data were analyzed to produce a final, comprehensive evaluation of composite honeycomb inspections. A total of eight to ten inspectors deployed each conventional NDI technique to arrive at the final overall performance assessments. The experiment was deployed in maintenance hangars to provide representative inspection environments and inspection impediments such as poor lighting, noise, or distractions. Although the experiment made no attempt to uncouple the effects of these variables, it did include inspectors of different age and experience levels. The experience level of the experimenters was varied as a result of the volume of participants, but this variable was not controlled.

The test program was intended to evaluate the technical capability of the inspection procedures and the equipment (i.e., NDI technique). Evaluation of inspector-specific or environment-specific factors associated with performing this inspection was not the primary objective of this experiment. However, notes were taken by the experiment monitor when such factors seemed to influence results or when unplanned events occurred that could impact the results of the inspection. Specific notice was taken if issues such as deployment or maneuverability adversely affected the outcome of the inspection.

All inspectors were provided with the appropriate inspection procedures from the Boeing and Airbus maintenance manuals. While these procedures contain specific deployment information, such as the recommended tap spacing, the inspectors were allowed to interpret and apply the procedures as they saw fit. Specific deployment of the inspection devices was not enforced by the experiment monitors. Use of and adherence to OEM recommended procedures were noted by the experiment monitors. Each blind inspection process was preceded by inspections on appropriate reference standards supplied by the experiment monitors. The inspectors were given information on the manufactured flaws present in the reference standards and were allowed to use these specimens to ensure the proper operation of their inspection equipment. The reference standards have the same construction as the blind test specimens and include similar flaws. Thus, they also can be used to allow inspectors to become familiar with an inspection device and learn about specific equipment's response to various composite structures and flaws within those structures.

A set of experiment protocols were written to guide the implementation of the CHE. The experiment protocols ensured that the information provided to all experiment participants was consistent and comprehensive, such that all participants received similar guidance and inspection aids. The experiment protocols also provided step-by-step guidance to the experiment monitors so that all data and observations associated with the tests were acquired in a consistent manner. Appendix A contains the "Experiment Briefing and Information Packet" for the CHE. This information was sent to each inspector in advance of the experiment and also reviewed with the inspectors during airline briefing sessions, which were completed at each site prior to beginning the NDI tests. The set of Honeycomb NDI Reference Standards, with flaw locations clearly

marked, were also sent out in advance so that experiment participants could conduct inspections to familiarize themselves with the composite structure and flaw detection requirements.

Prior to conducting the tests, all experimenters were given a briefing on the CHE.

Figure 147 shows one of the briefings being provided to inspectors. This briefing explained the purpose of the experiment and the process the inspectors would be using to indicate their flaw findings. The briefing was used at each facility to ensure a consistent presentation on the experiment goals and a thorough explanation of how the experiment would proceed. It also allowed the inspectors to ask questions. At this time, the inspectors were introduced to the inspection devices that they could optionally use. Inspectors could also decide to deploy their own composite honeycomb inspection equipment and transducers.



Figure 147. Experiment instructions being provided to supplement the written experimenter briefing and information packet

Guidance and instructions provided to inspectors were:

- Inspection coverage should be 100% of the panel with the exception of a small 1" band around the perimeter of the panels where edge effects may create problems.
- The Composite Honeycomb Reference Standards, or equivalent, should be used to set up the equipment. Minor equipment adjustments stemming from in-situ calibration on the parts being inspected are allowed.
- Inspectors should draw the entire size/shape of the flaw (i.e., delineate the edges).
- Reference standards should be used as an aid to determine where to make flaw call edges. This is based on the diameter of the probe and how much of the probe needs to be over the flaw to react/detect.
- Inspectors do not need to determine the type of flaw—just the location, size, and shape of the suspected anomaly.
- Inspectors should ignore any visual clues (surface anomalies in the paint or small surface marks) and avoid using these as flaw detection aids. It was indicated that such anomalies may be intentionally planted to add complexity to the inspection. Guidance to the inspectors instructed them to indicate only those flaws detected by their inspection device.

The inspections were conducted on the series of 18" x 18" panels described in section 5. The panels were placed on a foam pad, as shown in figure 148, to produce uniform boundary conditions across all experimenters. Experimenters were asked to work at a pace that is comfortable for them. Although experiment monitors did note start and stop times for each panel inspection, time-to-inspect was a secondary variable of the experiment. Inspectors were instructed to take whatever time was necessary to ensure that any and all flaws in the test specimens were found. Experiment monitors logged observations using the data sheets shown in appendix B. For example, monitors noted: 1) the tap spacing used by the inspector; 2) whether visual clues were used by the experimenters to aid in flaw detection; and 3) whether use of and adherence to OEM recommended procedures were used. An array of acceptable tap test devices (see official Boeing and Airbus tap hammers in section 3) were provided, and the inspectors chose one. This eliminated the use of flashlights, washers, and other devices that do not meet the size and weight criteria (see figures 149 and 150).

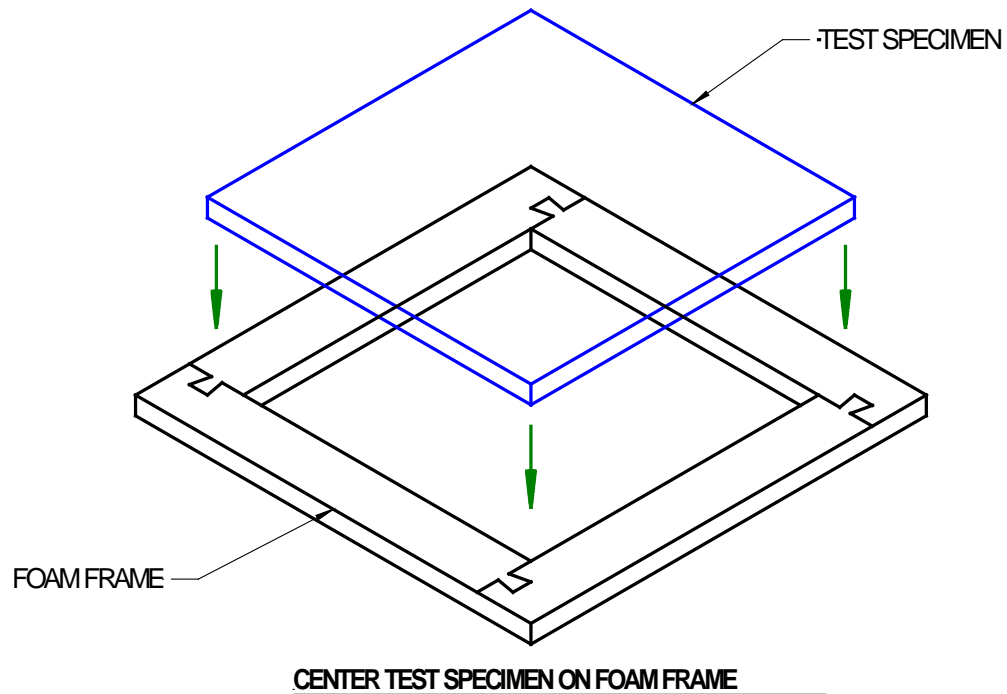


Figure 148. During inspections, each panel was supported around its perimeter by a foam frame to provide uniform boundary conditions

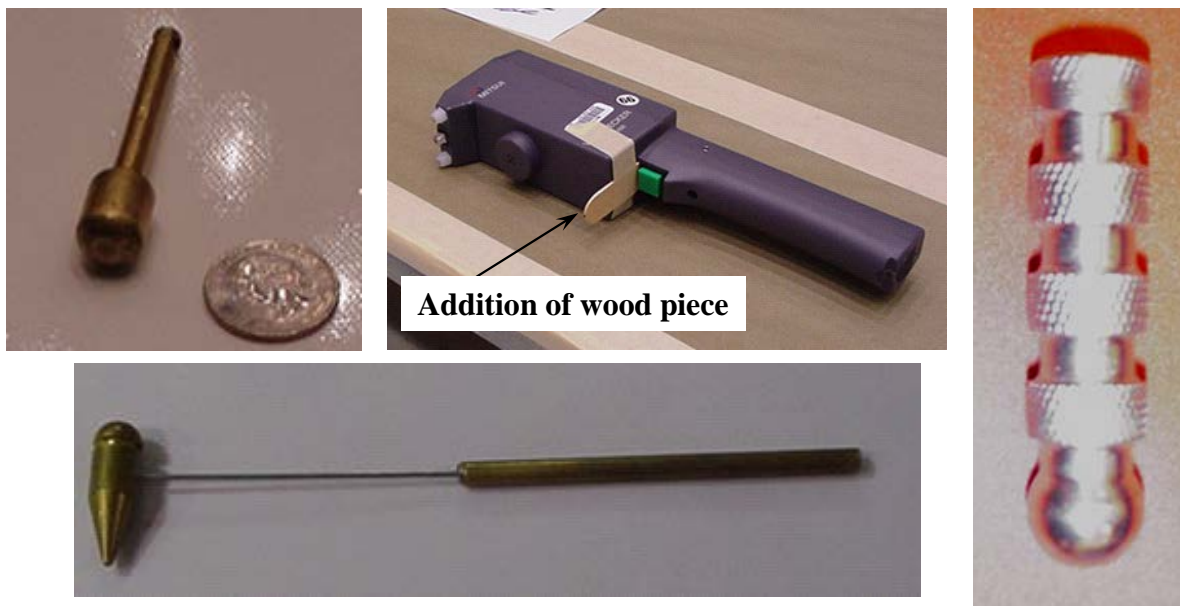


Figure 149. Samples of homemade tappers used in the field and modification to Woodpecker device to ensure that automated tap is perpendicular to the surface



Figure 150. Sample tap testing at maintenance depots and alternative tappers identified in study

A total of 75 inspectors from 22 airlines and maintenance and repair organizations located around the world participated in the experiment. The maintenance facilities included Delta Air Lines (four facilities), United Airlines (three facilities), American Airlines (two facilities), Aloha Airlines, Alaska Airlines, US Airways, British Airways, KLM Airlines, Air France, FedEx (two facilities), SR Technics, GKN Westland Aerospace, and FLS Aerospace Manchester. The participating companies, including those that deployed advanced NDI methods, are shown in figures 151 and 152. The typical setups for the experiment deployment are shown in figures 153–156, where each inspector has a workstation on which to set up their equipment and test specimens. Inspectors were asked to inspect each test specimen and provide any information they could about the presence of applicable flaws. If they determined that flaws were present, they then provided size and shape information about each detected flaw. The results were marked directly on the test specimen using markers provided by the experiment monitors. Figure 157 shows sample sets of flaw marks on one of the honeycomb test specimens along with grid marks that some inspectors used to guide the surface coverage of their inspection transducers.

Inspector feedback on performance provided excellent training for the experimenter, while their results produced a valuable baseline for how well the industry is able to inspect composite honeycomb structures using conventional NDI methods (flaw hits/misses, false calls, flaw sizing, effects of construction scenarios, and effects of environment). Furthermore, results from the 18 advanced NDI methods allowed the team to quantify the degree of inspection improvements possible via the application of more sophisticated inspection methods and procedures. The experiment results also allowed the experimenters to determine which NDI methods possessed unique capabilities to address specific inspection requirements.



Figure 151. Airline and aircraft maintenance depot participants in composite honeycomb flaw detection experiment



Figure 152. Advanced NDI companies that participated in composite honeycomb flaw detection experiment



Figure 153. Sample implementation of experiment in Alaska Airlines' hangar environment



Figure 154. CHE being implemented at American Airlines' maintenance facility



**Figure 155. Typical experiment setup with separate inspector—
Airbus facility hosting multiple airlines**



Figure 156. Inspectors completing inspections and marking flaw detections on the test specimens—clockwise from upper right: Airbus tap hammer, Boeing tap hammer, DTH, LFBT, Woodpecker, and MIA

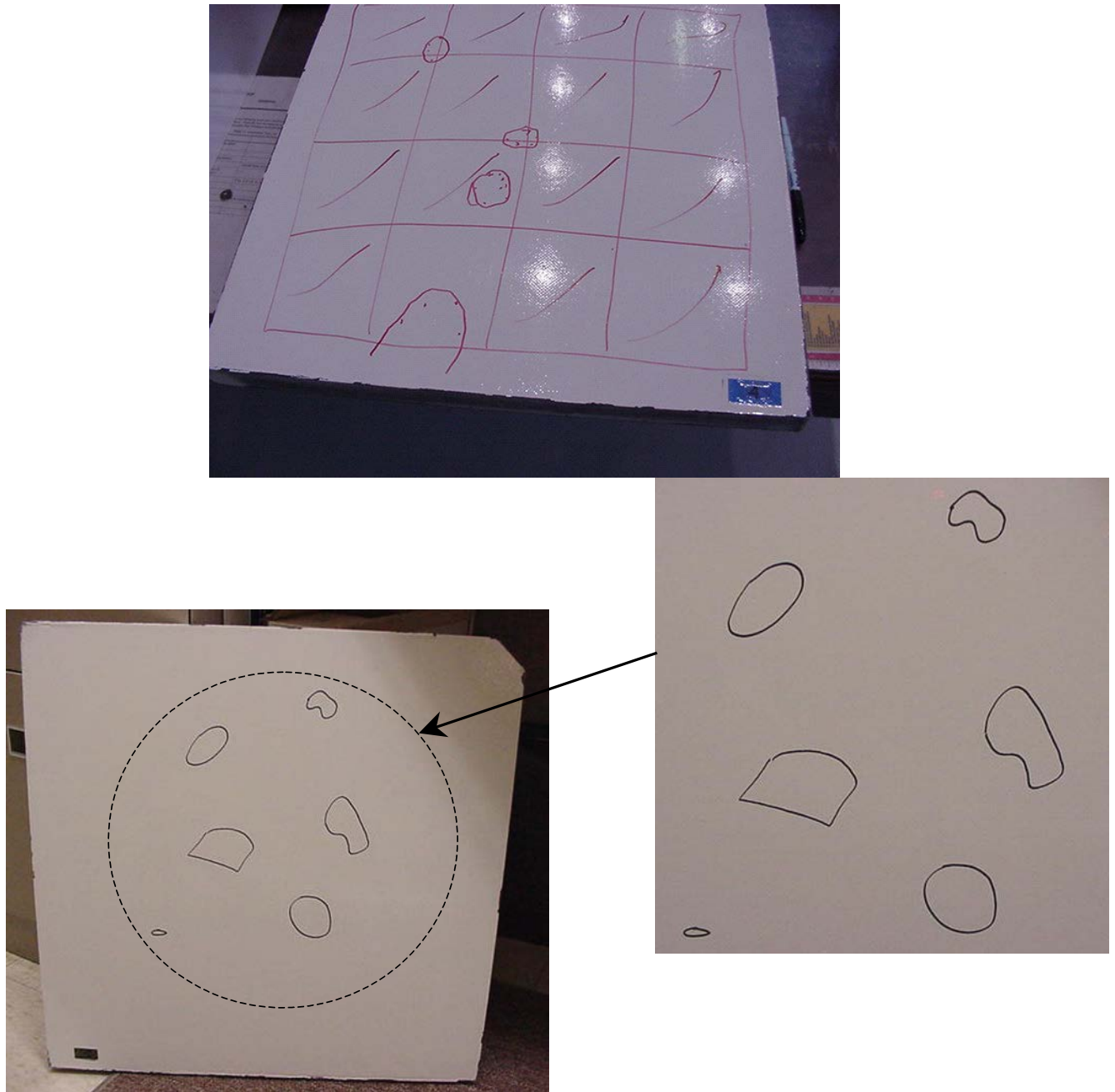


Figure 157. Honeycomb panel with sample grid markings used by inspector during inspection of panel along with flaw markings within the grid

The CHE was deployed with conventional NDI methods for composite honeycomb structures and also completed using a wide array of advanced NDI methods. The conventional and advanced NDI methods evaluated with these tests included: conventional tap test (Boeing- and Airbus-designated tap hammers), automated/instrumented tap test (Mitsui Woodpecker, WichiTech DTH, and CATT), HFBT/resonance (S-5, S-9, Sondicator, BondMaster), LFBT (BondMaster), MIA (MIA-3000, V-95 Bondcheck, BondMaster), scanning in resonance and MIA mode (Boeing MAUS), Thermography (TWI EcoTherm), shearography (Laser Technology

Inc. LTI-5200), microwave (Evisive microwave scanner), laser Doppler velocimetry (SAM system), linear array UT (Boeing FlawInspecta Linear Array), AC-UT (QMI SONDA 007CX), LUS (iPLUS), and laminography (Digiray RGX). This report describes the PoD results from both the conventional and advanced NDI methods.

The overall performance attributes that were evaluated include: 1) accuracy and sensitivity (e.g., hits, misses, false calls, and sizing), 2) versatility and complexity (e.g., human factors), 3) data analysis capabilities, 4) portability, and 5) inspection time. Test results were graded to evaluate the accuracy of quantitative measurements and assess qualitative measurement parameters. Each inspector's flaw calls were used to identify hits (calls with any amount of overlap between the call and the solution), misses (no call for an area of a known flaw), false calls (call with no overlap of a flaw), and the degree of overlap between experimenter calls and actual flaw areas. Typical results include PoD curves, tabulated flaw detection and false call data, and scatter charts relating accuracy in delineating flaw size and shape. All of the data were sorted by the attributes of the structure being inspected. Figure 158 is a grading parameter drawing that shows how the hits/misses/false calls results were to be graded. The percentage of flaw covered was another variable of primary interest. Errors in lateral extent of flaw and maximum linear extent of overcall were variables of secondary concern and not considered part of the current grading plan.

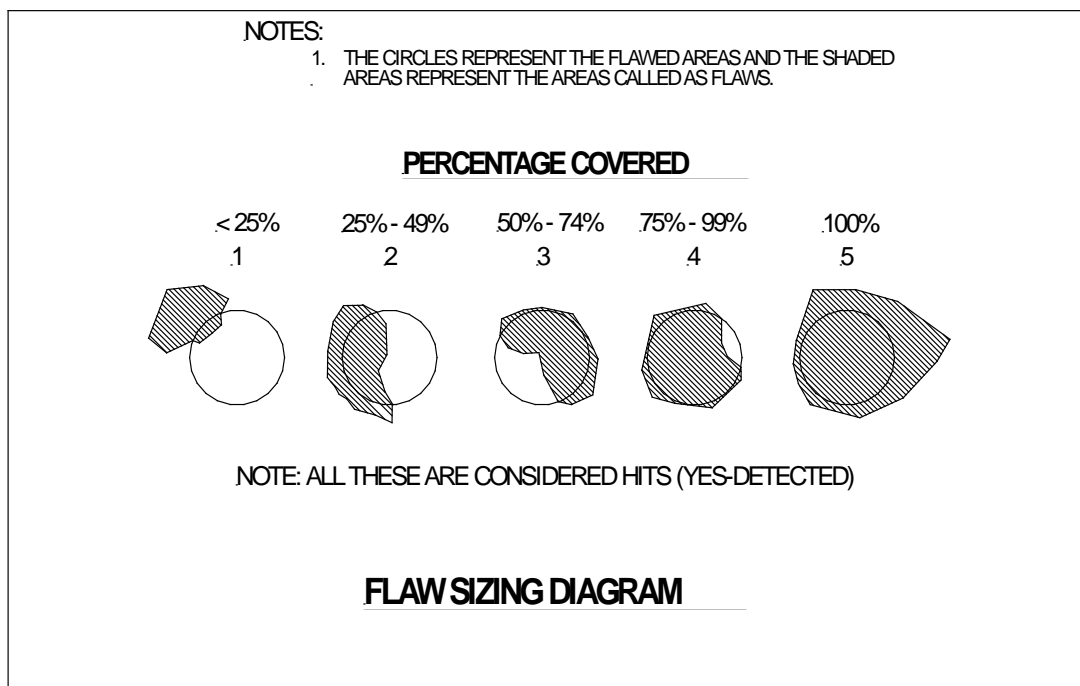


Figure 158. Schematic showing the grading categories comparing experimenter flaw calls with actual flaw information

7. RESULTS FROM COMPOSITE HONEYCOMB FLAW DETECTION EXPERIMENT

Each inspection technique that was applied in this blind flaw detection experiment was evaluated using the following performance attributes: 1) accuracy and sensitivity, 2) data analysis capabilities, 3) versatility, 4) portability, 5) complexity, 6) human factors, and 7) inspection time. The most important of these parameters are the quantitative metrics, as they are objective standards that can be numerically counted or quantified. Accuracy is the ability to detect flaws reliably and correctly in composite structures and repairs without overcalling (false calls). Sensitivity is the extent to which the inspection system responds to flaws as a function of size, type, and location in the structure (e.g., proximity to repair edges, underlying or adjacent structural elements). During the tests, the inspectors attempt to optimize their accuracy and sensitivity without producing a significant number of false calls. More than 70 inspectors from airline maintenance facilities and NDI developers around the world participated in the blind tests. The results were used to establish an industry inspection baseline indicating the current performance of aviation maintenance practices.

To acquire flaw detection data, the test panels were shipped to airlines, third-party maintenance depots, and NDI developer labs around the world. The inspectors performed the blind tests to produce statistically valid PoD curves that were representative of the industry as a whole. At aircraft maintenance depots, inspectors of different ages and experience levels (see table 6) participated in the experiment. In addition, 14 inspectors applied 11 different advanced NDI methods (see table 7) to determine PoD performance. The NDI techniques that were evaluated ranged from manually applied tap testing (e.g., Airbus tap hammer and Boeing tap hammer) to an automated, sensor-based form of tap testing (e.g., Woodpecker, DTH, and CATT) and C-scan technology for improved flaw identification (MAUS). The conventional devices that were used in this experiment were randomly assigned to each inspector with the exception of LFBT devices, for which previous experience and knowledge of the device used was required. It should be noted that all results shown for thermography in this report are for pulsed thermography, and there were three different cameras used. The three cameras were a FLIR A40 uncooled IR (results shown as thermography uncooled), FLIR Indigo Phoenix large format array (results shown as thermography FLIR), and a Radiance HS (results shown as thermography).

Table 6. Inspectors' NDI experience level for conventional methods

Inspector Experience Level	
Years of NDI Experience	No. of Inspectors
1–4	15
5–8	13
9–12	11
13–16	11
17–20	2
21–24	2
25 or greater	2

Table 7. Advanced NDI methods deployed on composite honeycomb flaw-detection experiment

Advanced NDI Methods
Air-coupled UT
Computer-aided tap tester (CATT)
FlawInspecta UT array
Laminography
Laser UT
Microwave
Mobile Automated Scanner (MAUS)
Mechanical impedance analysis (MIA)
Shearography
Structural anomaly mapping (SAM) system
Thermography

Each inspector's flaw calls were used to identify hits (calls with any amount of overlap between the call and the solution), misses (no call for an area of a known flaw), false calls (call with no overlap with a flaw), and the ability to properly size flaws (degree of overlap between experimenter calls and actual flaw areas). Typical results include PoD curves, tabulated flaw detection and false call data, and scatter charts relating the effects of inspection time on false calls and PoD values along with the effect of false calls on PoD values. All of the data were sorted by the attributes of the structure being inspected: 1) three-ply fiberglass skin; 2) three-ply carbon skin; 3) six-ply fiberglass skin; 4) six-ply carbon skin; 5) nine-ply fiberglass skin; and 6) nine-ply carbon skin. The set of graphs in this section presents all of the detailed results for all aspects of the solid laminate flaw detection experiment. These include the PoD curves for each

inspector as well as the resulting cumulative PoD curve. Tabulated results are also provided to summarize various aspects of the experiments. The tables present the percentage of flaws detected for each flaw size in the different inspection and composite honeycomb construction categories. The tables also show the inspector's ability to properly size each flaw they detected. For example, of all the flaws they found in the Constant Thickness category, 21% were correctly sized (100% coverage). Additional tables show the False Calls for each inspector completing the Thin and Thick Laminate experiments as well as an average false call rate broken down into the different geometry categories and sizes.

Overall, the PoD results were consistent with only a few outliers. This is fairly common for human performance assessment experiments. A large number of variables were studied and isolated to determine their impact on PoD values. Figure 159 shows a sample PoD curve from the completed experiments. The PoD curve relates the probability of finding a flaw to the size of the flaw for a particular specimen construction (in this case, six-ply carbon skin). The curves show that to achieve a 90% chance of finding a flaw, the flaw size must be between 1.7" and 3.0" in diameter depending on the inspection device used. The graph in figure 160 shows another way of presenting the data. The series of PoD curves indicate the performance of a single inspection device—the Woodpecker automated tap instrument—over the entire range of specimens. The greatest sensitivity is found in the thinnest three-ply fiberglass skin panels while the worst flaw detection occurred in the thickest nine-ply carbon skin panels. This phenomenon was typical for most inspection methods deployed. This is probably because a defect creates the greatest loss of stiffness in the weakest fiberglass structure, and the effect of similar-sized defects is lessened as the skin thickness increases and the stiffer carbon material is used. The entire set of PoD curves, such as the samples shown in figures 159 and 160, established a baseline of how well current inspection methods are able to detect flaws in composite honeycomb structures. This is essentially a measure of current flaw detection at aircraft maintenance depots with these devices. Overall, for the conventional methods, the MIA mode of inspection produced the best results for the range of specimen types tested, with the exception being on the nine-ply carbon where the WichiTech DTH performed the best. Except for instances in which only large flaws need to be detected, the limit of manual tap testing was established at around six plies (PoD values for six-ply panels ranged from 2.3 to greater than 3). In addition to quantifying the capabilities of conventional inspection methods, this study highlighted many potential procedural and equipment deployment improvements.

The results shown in this section are broken down into the following composite honeycomb structure categories:

- 3C = three-ply carbon
- 3F = three-ply fiberglass
- 6C = six-ply carbon
- 6F = six-ply fiberglass
- 9C = nine-ply carbon
- 9F = nine-ply fiberglass

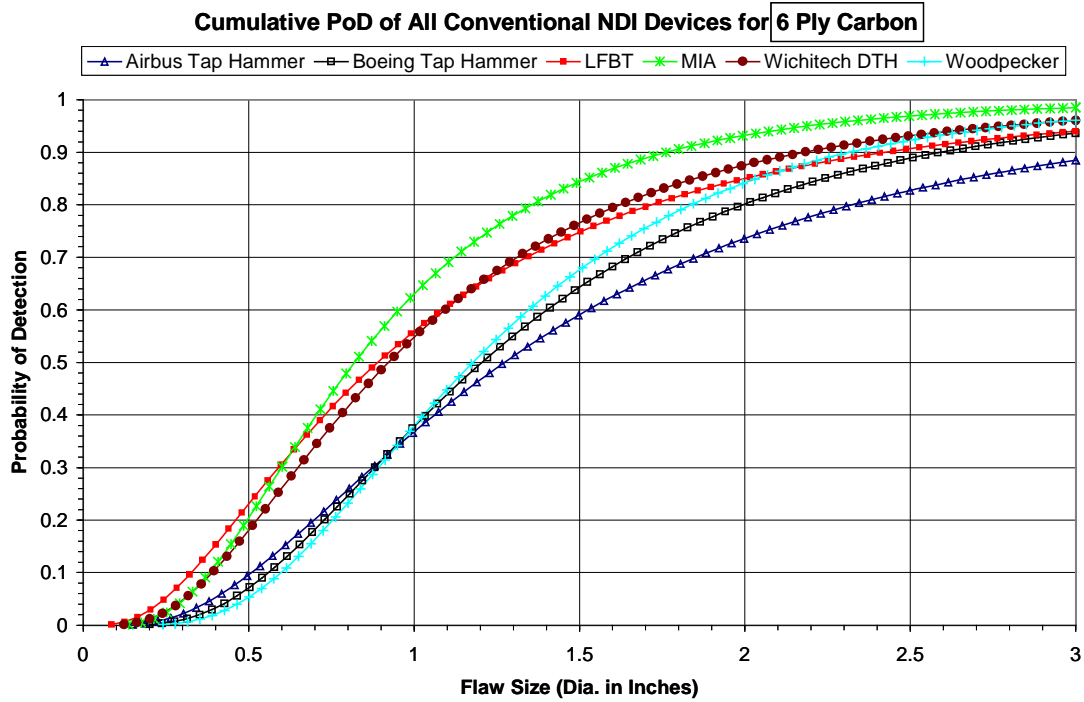


Figure 159. Probability of detection curves showing the performance of multiple NDI devices for a single type of test specimen: 6-ply carbon

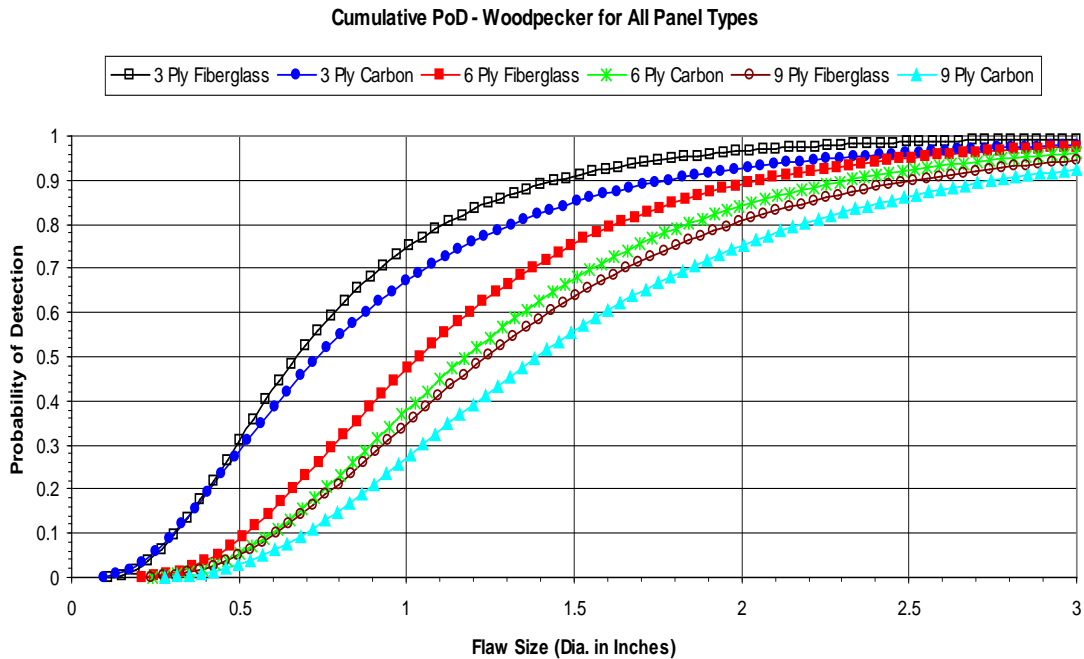


Figure 160. Probability of detection curves for flaw detection performance of a single device (Woodpecker) over the range of test specimen types

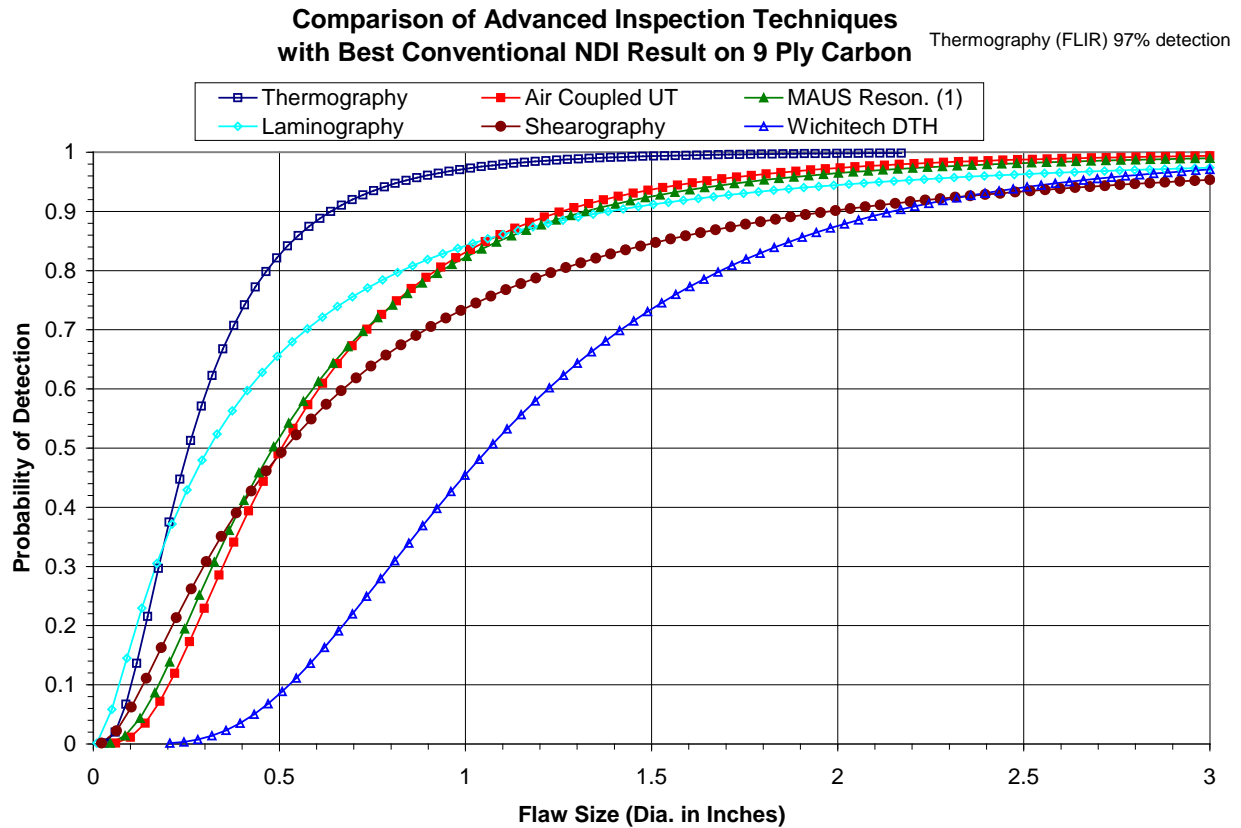
With this data set as a foundation, it was then possible to quantify the improvements via the application of advanced NDI techniques. Figure 161 compares the performance of the best conventional NDI technique, the DTH for the nine-ply carbon set shown, with those obtained from the array of advanced NDI techniques evaluated. The 90% PoD level was achieved at a 2.2" flaw diameter for the best, conventional NDI technique (WichiTech DTH). However, that PoD number was reduced to less than 0.7" diameter when the best performing inspection device, in this case thermography, was deployed. This level of inspection improvement was very consistent, and the POD numbers were reduced 66–72% in each of the composite construction scenarios studied. Furthermore, the advanced NDI techniques were all wide-area inspection techniques as opposed to the conventional methods that are more localized. This minimizes some of the human factors issues by producing more uniform and rapid coverage of the entire surface area.

Table 8 provides a summary of the overall accuracy of the evaluated NDI techniques for one of the honeycomb construction scenarios: six-ply fiberglass. The PoD results are shown alongside the false call data. Normally, there are adjustments that can be made in equipment's signal thresholds such that smaller flaws might be identified. However, this may be accompanied by a corresponding increase in the number of false indications produced by the instrument. Thus, the inspections become a delicate balance between optimizing flaw detection and maintaining the number of false calls within acceptable levels.

Another indicator of equipment accuracy pertains to the ability of the NDI technique to correctly size the flaws that it finds. Flaw sizing is important when considering damage tolerance and critical flaw growth in the structure. Table 8 summarizes the flaw sizing capability of each inspection device by placing each instrument's flaw coverage into five different sizing bins. Each bin describes the degree of overlap between an instrument's predicted flaw size and the actual engineered flaw in the specimen. The 100% column, for example, lists the percentage of called flaws that were correctly sized by the inspection method while the 50–74% column lists the percentage of called flaws that were only 50–74% of the actual flaw size. The table shows that thermography, laminography, microwave, and the MAUS automated scanner (MIA mode) produced the best flaw sizing results for the six-ply fiberglass set.

**Table 8. Summary of overall flaw detection for 6-ply fiberglass construction—
PoD levels along with false calls and ability to correctly size flaws**

Flaw Sizing and False Call Summary Table for 6-Ply Fiberglass							
Flaw Coverage							
Inspection Device	100%	99– 75%	74– 50%	49– 25%	<25%	90% PoD Level	False Calls
Airbus Tap Hammer	28%	30%	27%	13%	0%	2.44	2.9
Boeing Tap Hammer	21%	34%	25%	16%	4%	2.33	4.7
LFBT	28%	29%	20%	18%	5%	2.55	3.3
MIA	26%	26%	26%	18%	4%	1.49	1.9
WichiTech DTH	32%	39%	19%	8%	2%	1.71	1.6
Woodpecker	31%	28%	20%	14%	7%	2.05	0.1
CATT	28%	38%	19%	13%	2%	1.10	1.0
MAUS Resonance 1	47%	31%	4%	4%	14%	0.55	9.0
SAM	11%	40%	32%	9%	8%	0.84	8.0
Shearography	49%	27%	15%	9%	0%	≤0.50	0.0
Thermography	75%	15%	5%	5%	0%	0.70	3.0
MAUS Resonance 2	39%	33%	18%	9%	0%	2.07	2.0
MAUS MIA	84%	8%	8%	0%	0%	1.48	6.0
Laminography	86%	6%	0%	2%	6%	1.43	2.0
Microwave	75%	17%	2%	0%	6%	0.93	12.0
Thermography (uncooled)	55%	24%	2%	2%	17%	2.19	2.0
Thermography (FLIR)	N/A	N/A	N/A	N/A	N/A	≤0.50	4.0
FlawInspecta UT Array	31%	13%	25%	6%	25%	≥3.00	0.0
Air-coupled UT	21%	43%	34%	2%	0%	0.90	0.0
Laser UT	N/A	N/A	N/A	N/A	N/A	N/A	N/A



9-Ply Carbon		
Device	False Calls	90% POD Value
Thermography (FLIR)	0	$\leq .50$
Thermography	0	0.64
Air-coupled UT	2	1.26
MAUS Resonance 1	0	1.32
Laminography	0	1.39
Shearography	0	2.00
WichiTech DTH	4.4	2.15

(Highlighted = best conventional method for comparison purposes)

Figure 161. Probability of detection curves quantifying inspection improvements possible through the application of advanced NDI techniques

During the testing, inspectors were asked to work at their normal pace so that no time restrictions were placed on the experiment. However, time-of-inspection was recorded as a secondary variable. Figure 162 shows one of the plots relating inspection time to the resulting 90% PoD level. This graphic shows that flaw detection improved (i.e., PoD levels decreased) as the inspector took more time to inspect each panel. Most of the improvements are in the shorter inspection times in which increasing the inspection time from 5 to 15 minutes for each 2.25 ft.² panel could reduce the inspection PoD by as much as 60%. The improvement levels off to the point where increased inspection time does not yield better results, so optimum inspection rates can be determined by this type of data.

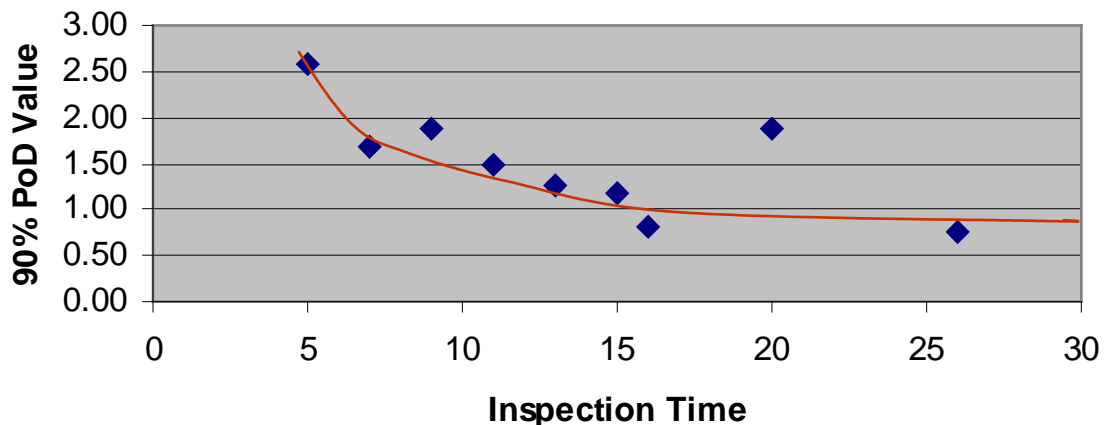


**Figure 162. Sample effect of inspection time on flaw detection performance
(example for Boeing tap hammer on 3-ply fiberglass)**

The comprehensive set of analyzed data produced during this study includes the following performance data for the conventional and advanced inspection methods (see table 9). A comparison of performance results for all conventional and advanced NDI methods will be provided at the end of this section detailing the following:

- PoD curves comparing the performance of individual inspectors and a cumulative result for a particular inspection method in each of the specific composite honeycomb structure categories
- PoD curves comparing the overall cumulative performance of several conventional inspection methods when performance outliers are removed from the calculation in a couple of the specific composite honeycomb structure categories
- PoD curves comparing the overall cumulative performance of conventional inspection methods with the 95% confidence bound
- PoD curves comparing the performance of advanced NDI techniques in each of the specific composite honeycomb structure categories
- PoD curves comparing the overall cumulative performance of conventional inspection techniques in each of the specific composite honeycomb structure categories
- PoD curves comparing the overall cumulative performance of all mechanical tap test devices in each of the specific composite honeycomb structure categories

- PoD curves comparing the overall cumulative performance of a specific conventional inspection technique over all of the composite honeycomb structure categories
- PoD curves comparing the overall performance of a specific advanced inspection technique over all of the composite honeycomb structure categories
- PoD curves comparing the performance of laminography with all hit/miss data versus hit/miss data with impact flaws removed from data set, and when edge flaw misses were changed from misses to hits (most likely due to lack of inspection image overlap and not inspection method sensitivity). Edge flaws for this purpose are defined as flaws that were located at the edges of their system images (C-scans) where the resolution was less than optimum
- PoD curves comparing the performance of laser UT on three-ply carbon and fiberglass along with the exceptions on the three-ply fiberglass that included the removal of some flaws from the data set in the center region of the panels, where their system could not attenuate the laser light level sufficiently because of the specular nature of the glossy paint
- PoD curves comparing the performance of the best conventional inspection method to the best performing advanced NDI methods in each of the specific composite honeycomb structure categories
- Tabulated values comparing inspection times for each of the conventional and advanced NDI techniques in each of the specific composite honeycomb structure categories
- Tabulated values summarizing individual and average false calls for each composite honeycomb structure category; false call averages arranged by inspection method and panel type
- Tabulated values summarizing detection of far-side flaws for each composite honeycomb structure category. Far-side flaws are flaws on the side of the panel opposite the inspection surface. This is a secondary variable, and detection of these flaws was not required in the experiment. However, positive indications in these regions were tabulated
- Scatter diagrams showing effect of inspection time on PoD and false call values for each composite honeycomb structure category
- Scatter diagrams showing effect of the number of false calls on PoD values for each composite honeycomb structure category
- Tabulated performance results summary—flaw sizing capability alongside PoD values and false calls for each composite honeycomb structure category
- Tabulated performance results summary—flaw detection capability alongside PoD values and false calls for each composite honeycomb structure category

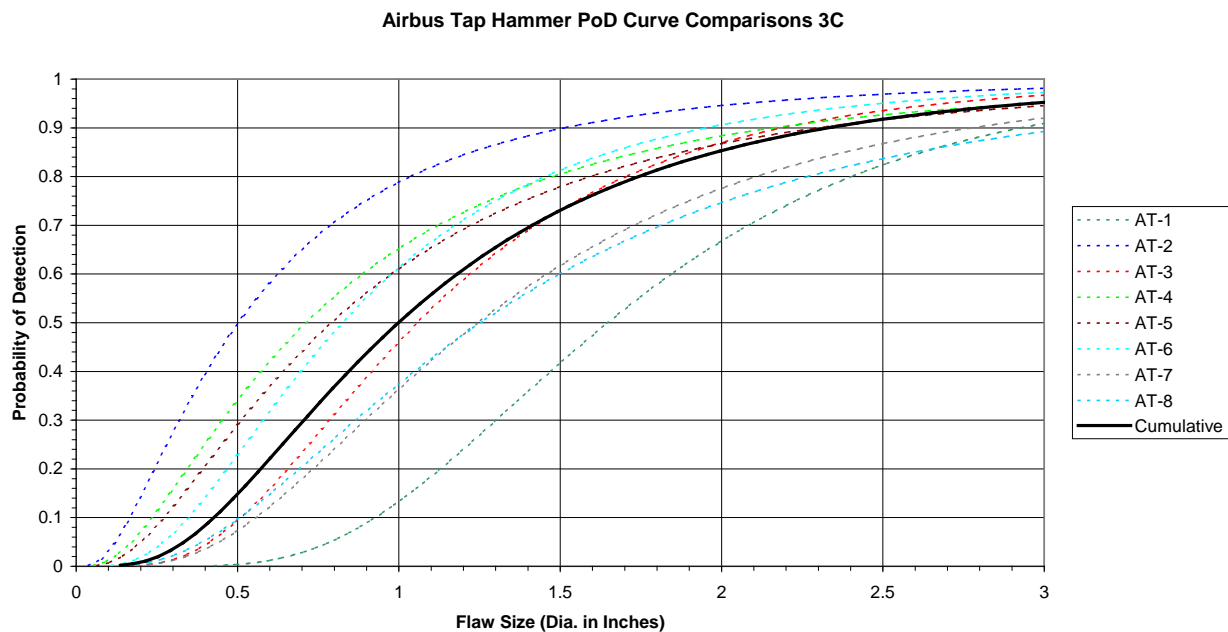
Table 9. Inspection summary—description of all figures and tables showing the variables captured in the results

Inspection Summary – Figure/Table Performance Data			
Figure/Table No.	Inspection Method(s)	Composite Honeycomb Structure Category	Variation /Description
Figures 163–168	Airbus tap hammer	Full suite (3-, 6-, and 9-ply carbon and fiberglass)	Individual and cumulative POD curve comparisons along with tabulated values of POD and false calls
Figures 169–174	Boeing tap hammer	Full suite (3-, 6-, and 9-ply carbon and fiberglass)	Individual and cumulative POD curve comparisons along with tabulated values of POD and false calls
Figures 175–180	Low frequency bond test (LFBT)	Full suite (3-, 6-, and 9-ply carbon and fiberglass)	Individual and cumulative POD curve comparisons along with tabulated values of POD and false calls
Figures 181–186	Mechanical impedance analysis (MIA)	Full suite (3-, 6-, and 9-ply carbon and fiberglass)	Individual and cumulative POD curve comparisons along with tabulated values of POD and false calls
Figures 187–192	WichiTech Digital Tap Hammer (DTH)	Full suite (3-, 6-, and 9-ply carbon and fiberglass)	Individual and cumulative POD curve comparisons along with tabulated values of POD and false calls
Figures 193–198	Woodpecker	Full suite (3-, 6-, and 9-ply carbon and fiberglass)	Individual and cumulative POD curve comparisons along with tabulated values of POD and false calls
Figures 199–202	Airbus tap hammer and LFBT	6- and 9-ply carbon and fiberglass	Cumulative POD curves with and without performance outliers
Figures 203–238	All conventional methods	Full suite (3-, 6-, and 9-ply carbon and fiberglass)	Cumulative POD curves with 95% confidence bound
Figures 239–250	All advanced NDI methods	Full suite (3-, 6-, and 9-ply carbon and fiberglass)	POD curve comparisons within a specific composite honeycomb structure along with tabulated values of POD and false calls
Figures 251–256	All conventional methods	Full suite (3-, 6-, and 9-ply carbon and fiberglass)	Cumulative POD curve comparisons within a specific composite honeycomb structure category along with tabulated values of POD and average number of false calls
Figures 257–262	All mechanical impact tap test methods	Full suite (3-, 6-, and 9-ply carbon and fiberglass)	Cumulative POD curve comparisons (conventional) versus advanced (CATT)
Figures 263–268	All conventional methods	Full suite (3-, 6-, and 9-ply carbon and fiberglass)	Cumulative POD curve comparison of a single device on all composite honeycomb structure categories along with tabulated values of POD and number of false calls
Figures 269–278	All advanced NDI methods	Full suite (3-, 6-, and 9-ply carbon and fiberglass)	POD curve comparison of advanced NDI method (individually) on all composite honeycomb structure categories along with tabulated values of POD and number of false calls

Table 9. Inspection summary—description of all figures and tables showing the variables captured in the results (continued)

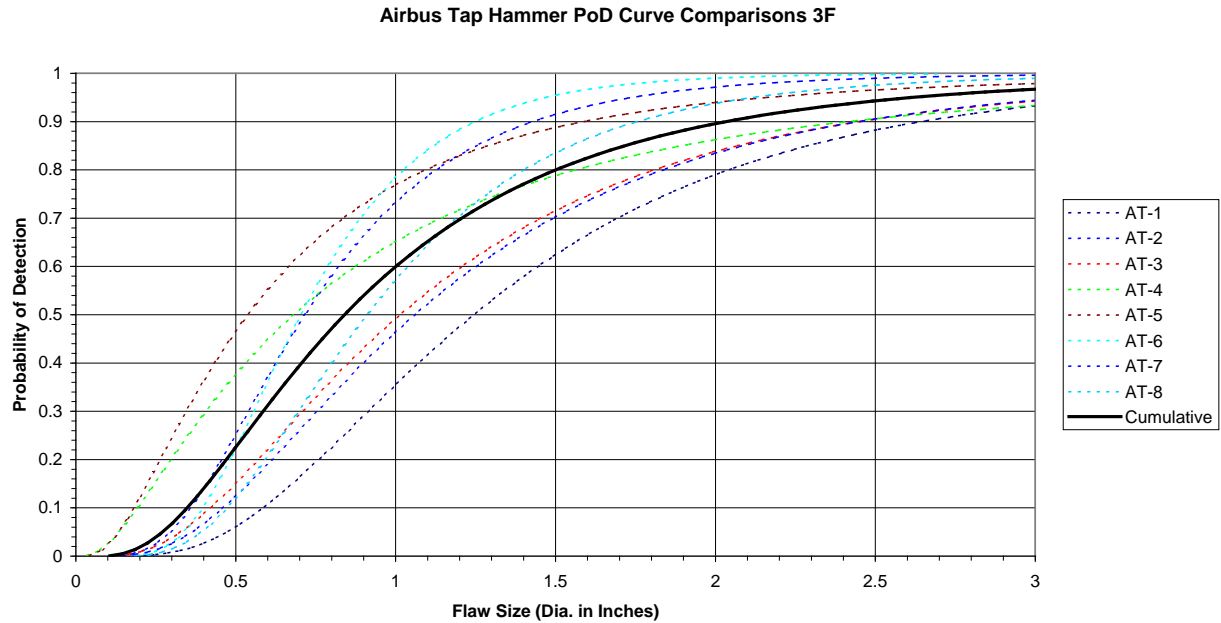
Inspection Summary – Figure/Table Performance Data			
Figure/Table No.	Inspection Method(s)	Composite Honeycomb Structure Category	Variation /Description
Figures 279–282	Laminography	6- and 9-ply carbon and fiberglass	Overall POD curve comparison with certain exceptions including impact flaw removal and flaws located in areas where there was lack of image overlap
Figure 283	Laser UT	3-ply carbon and fiberglass	Overall POD curve comparison with exception for center area misses due to system inability to attenuate the laser light sufficiently
Figures 284–289	Best conventional method and advanced NDI methods	Full suite (3-, 6-, and 9-ply carbon and fiberglass)	POD curve comparisons along with tabulated values of advanced NDI and best conventional method in each composite honeycomb structure category
Table 10–13	All conventional and advanced NDI methods	Full suite (3-, 6-, and 9-ply carbon and fiberglass)	Tabulated values comparing inspection times in each of the specific composite honeycomb structure categories
Table 14–16	All conventional and advanced NDI methods	Full suite (3-, 6-, and 9-ply carbon and fiberglass)	Tabulated values summarizing individual and average false calls for each composite honeycomb structure category
Table 17–19	All conventional and advanced NDI methods	Full suite (3-, 6-, and 9-ply carbon and fiberglass)	Tabulated values summarizing detection of farside (backside) flaws for each composite honeycomb structure category
Figures 290–295	All conventional NDI methods	Full suite (3-, 6-, and 9-ply carbon and fiberglass)	Scatter diagrams showing the effect of inspection time on POD and false call values for each composite honeycomb structure category
Figures 296–298	All conventional NDI methods	Full suite (3-, 6-, and 9-ply carbon and fiberglass)	Scatter diagrams showing the effect of the number of false calls on POD values for each composite honeycomb structure category
Table 20–22	All conventional and advanced NDI methods	Full suite (3-, 6-, and 9-ply carbon and fiberglass)	Tabulated performance results summary with flaw sizing capability alongside POD values and false calls for each composite honeycomb structure category
Table 23–25	All conventional and advanced NDI methods	Full suite (3-, 6-, and 9-ply carbon and fiberglass)	Tabulated performance results summary with flaw detection capability alongside POD values and false calls for each composite honeycomb structure category

The PoD curves and summary tabulations in figures 163–198 compare the performance of individual inspectors for a particular inspection device/method in each of the specific composite honeycomb structure categories. In each figure, the cumulative PoD result is displayed as a bold solid line. The individual inspector results for the desired 90% PoD level are listed above the overall cumulative industry baseline.



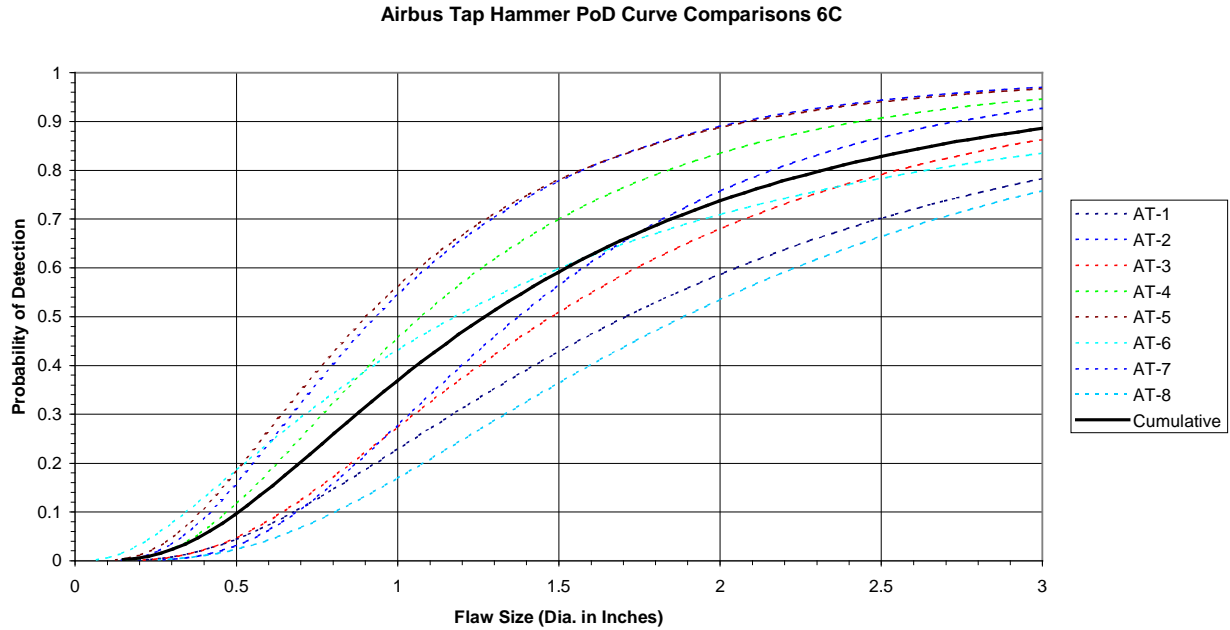
Airbus Tap Hammer 3-Ply Carbon		
Inspector	False Calls	90% POD Value
AT-1	0	2.93
AT-2	1	1.52
AT-3	1	2.20
AT-4	0	2.16
AT-5	0	2.33
AT-6	1	1.98
AT-7	3	2.81
AT-8	0	>3.00
Cumulative All Inspectors		2.34

Figure 163. Individual and cumulative PoD curve comparisons along with tabulated values for the Airbus tap hammer deployed on 3-ply carbon test specimen set



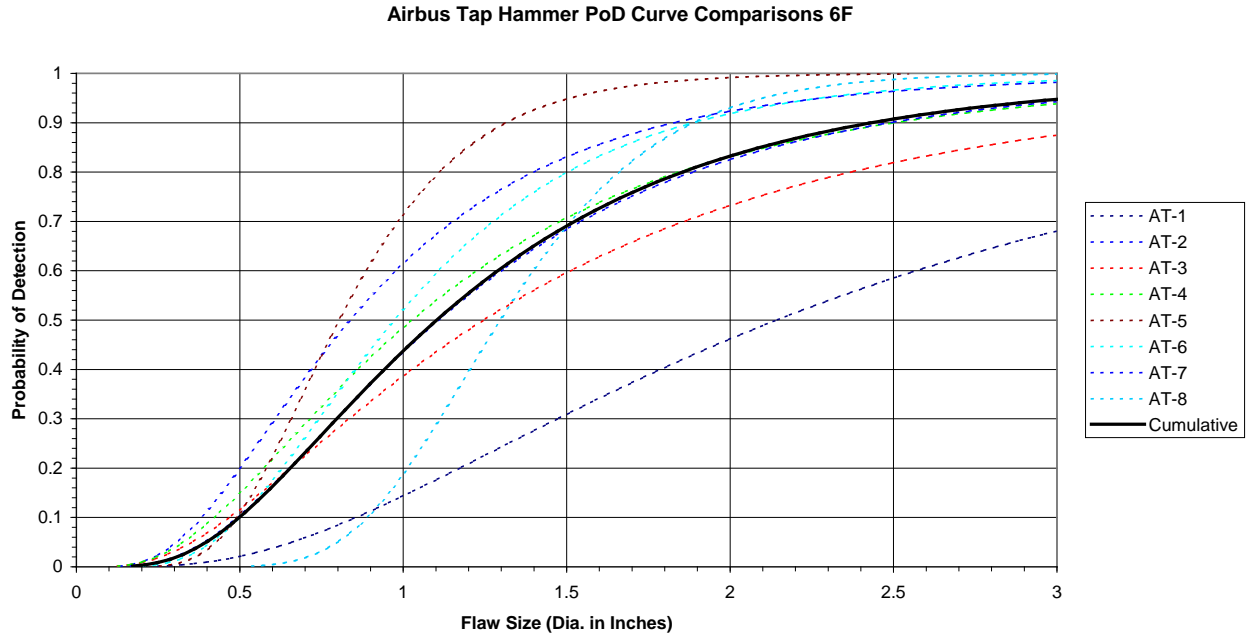
Airbus Tap Hammer 3-Ply Fiberglass		
Inspector	False Calls	90% POD Value
AT-1	1	2.66
AT-2	0	1.42
AT-3	1	2.45
AT-4	0	2.44
AT-5	0	1.60
AT-6	0	1.27
AT-7	0	2.46
AT-8	0	1.75
Cumulative All Inspectors		2.03

Figure 164. Individual and cumulative PoD curve comparisons along with tabulated values for the Airbus tap hammer deployed on 3-ply fiberglass test specimen set



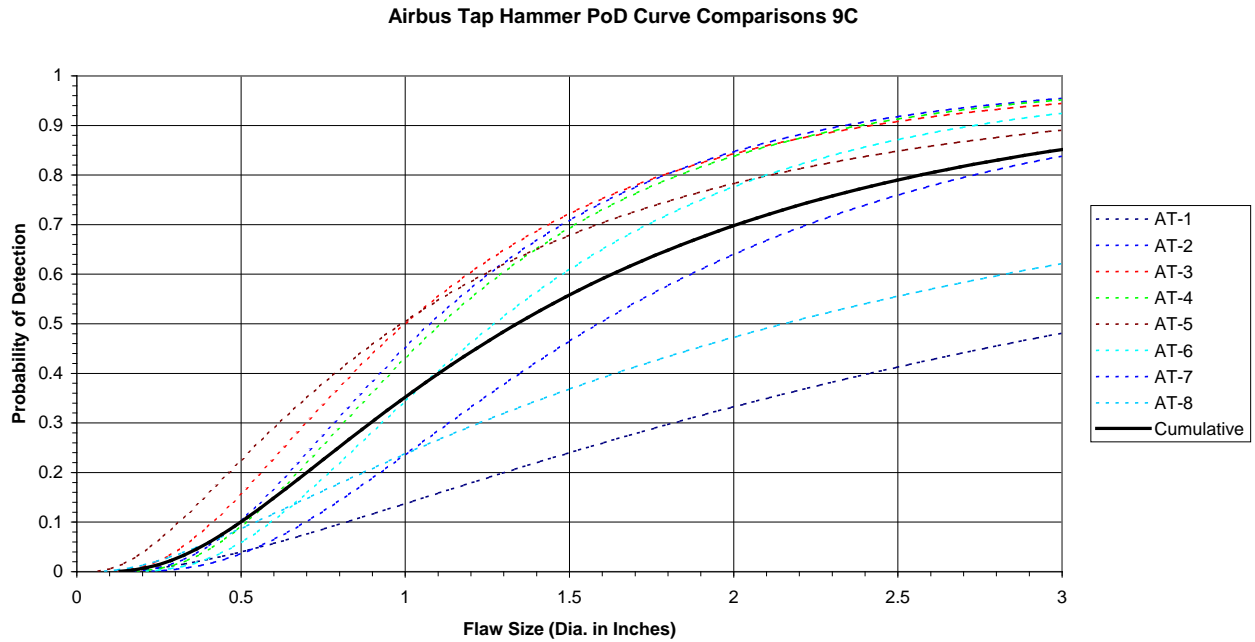
Airbus Tap Hammer 6-Ply Carbon		
Inspector	False Calls	90% POD Value
AT-1	2	>3.00
AT-2	3	2.07
AT-3	1	>3.00
AT-4	4	2.46
AT-5	4	2.11
AT-6	9	>3.00
AT-7	2	2.74
AT-8	3	>3.00
Cumulative All Inspectors		>3.00

Figure 165. Individual and cumulative PoD curve comparisons along with tabulated values for the Airbus tap hammer deployed on 6-ply carbon test specimen set



Airbus Tap Hammer 6-Ply Fiberglass		
Inspector	False Calls	90% POD Value
AT-1	1	>3.00
AT-2	2	1.84
AT-3	13	>3.00
AT-4	0	2.50
AT-5	1	1.31
AT-6	0	1.90
AT-7	6	2.50
AT-8	0	1.90
Cumulative All Inspectors		2.44

Figure 166. Individual and cumulative PoD curve comparisons along with tabulated values for the Airbus tap hammer deployed on 6-ply fiberglass test specimen set



Airbus Tap Hammer 9-Ply Carbon		
Inspector	False Calls	90% POD Value
AT-1	13	>3.00
AT-2	2	2.31
AT-3	26	2.42
AT-4	1	2.39
AT-5	1	>3.00
AT-6	3	2.74
AT-7	6	>3.00
AT-8	2	>3.00
Cumulative All Inspectors		>3.00

Figure 167. Individual and cumulative PoD curve comparisons along with tabulated values for the Airbus tap hammer deployed on 9-ply carbon test specimen set

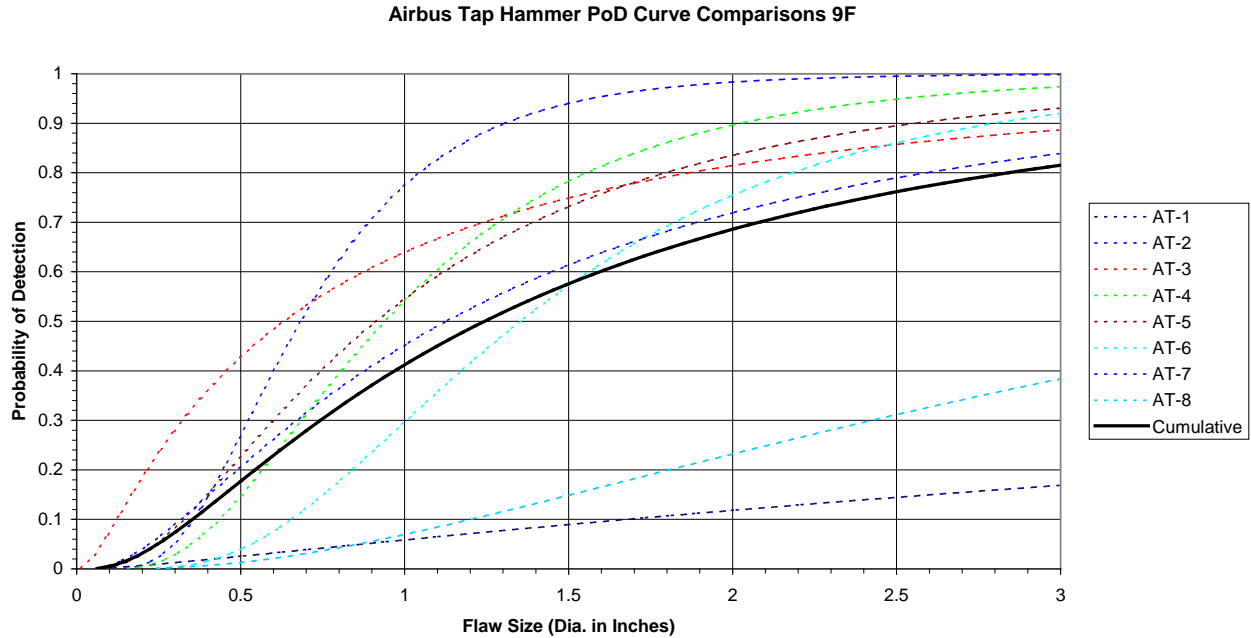
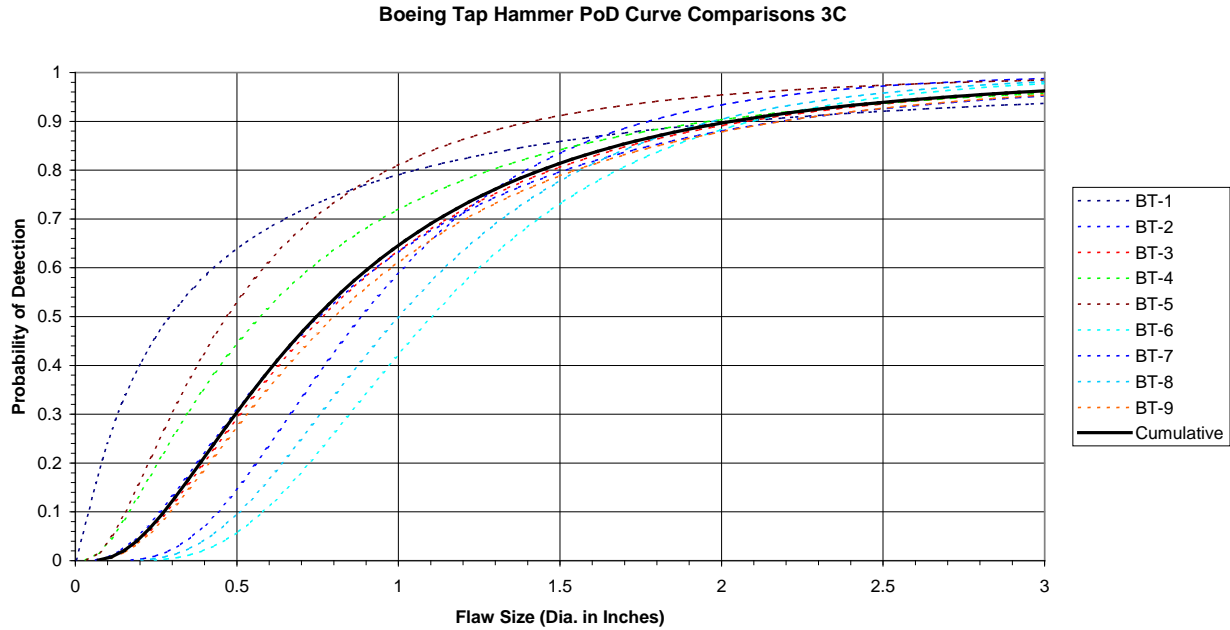
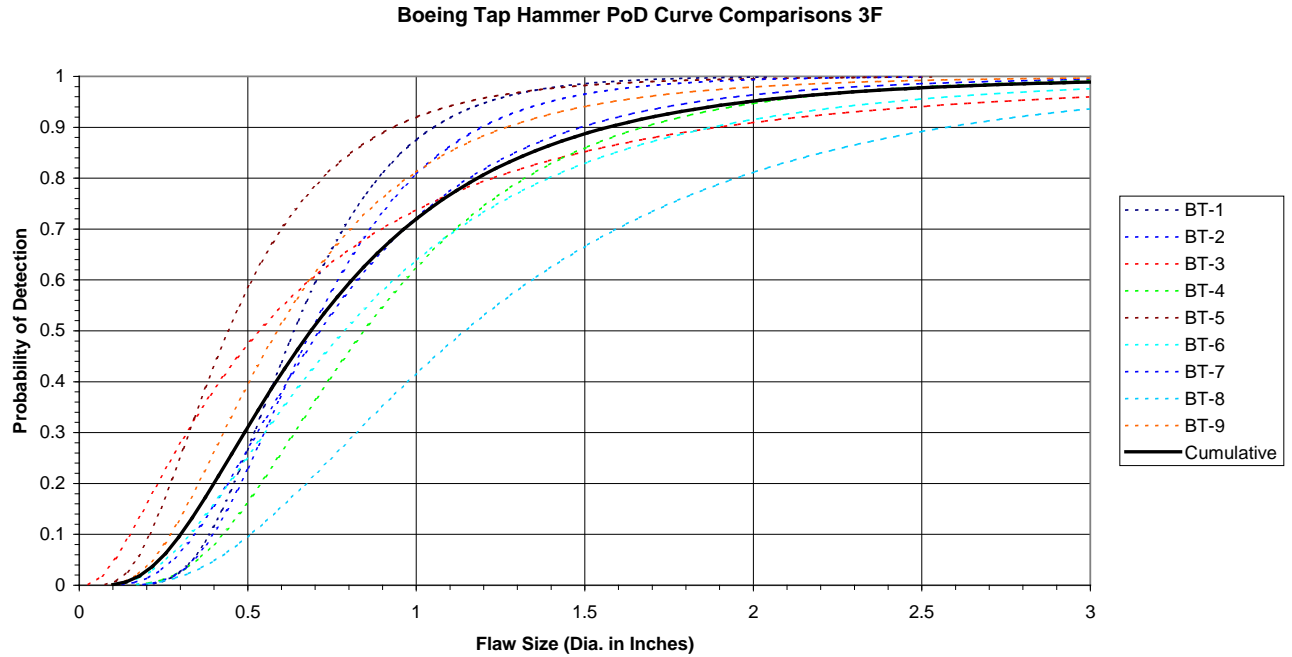


Figure 168. Individual and cumulative PoD curve comparisons along with tabulated values for the Airbus tap hammer deployed on 9-ply fiberglass test specimen set



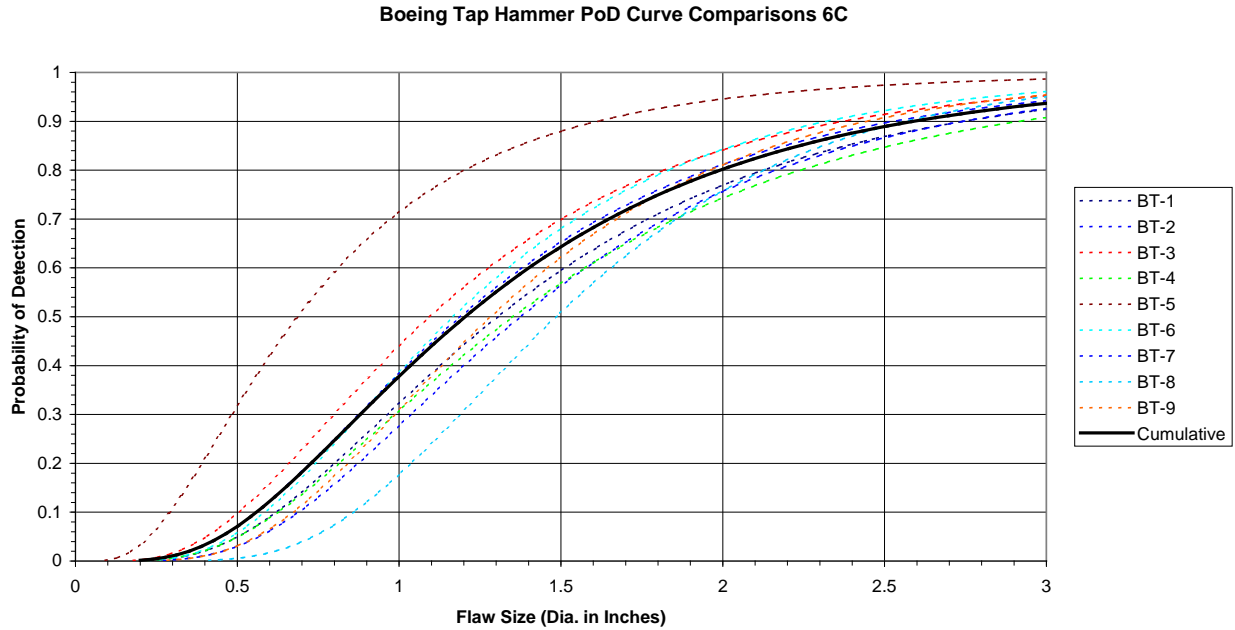
Boeing Tap Hammer 3-Ply Carbon		
Inspector	False Calls	90% POD Value
BT-1	0	2.03
BT-2	1	1.78
BT-3	3	2.09
BT-4	1	1.96
BT-5	1	1.44
BT-6	2	2.07
BT-7	0	2.17
BT-8	1	1.98
BT-9	0	2.17
Cumulative All Inspectors		2.03

Figure 169. Individual and cumulative PoD curve comparisons along with tabulated values for the Boeing tap hammer deployed on 3-ply carbon test specimen set



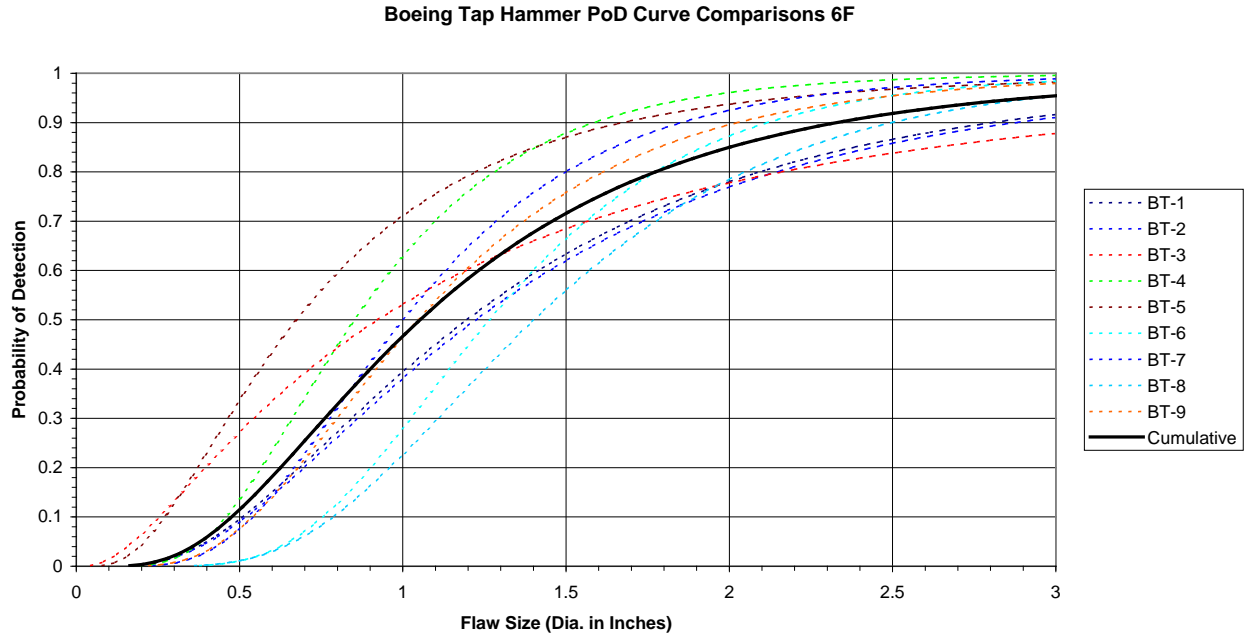
Boeing Tap Hammer 3-Ply Fiberglass		
Inspector	False Calls	90% POD Value
BT-1	4	1.05
BT-2	3	1.49
BT-3	3	1.88
BT-4	0	1.67
BT-5	0	0.94
BT-6	6	1.90
BT-7	0	1.19
BT-8	0	2.58
BT-9	0	1.27
Cumulative All Inspectors		1.57

Figure 170. Individual and cumulative PoD curve comparisons along with tabulated values for the Boeing tap hammer deployed on 3-ply fiberglass test specimen set



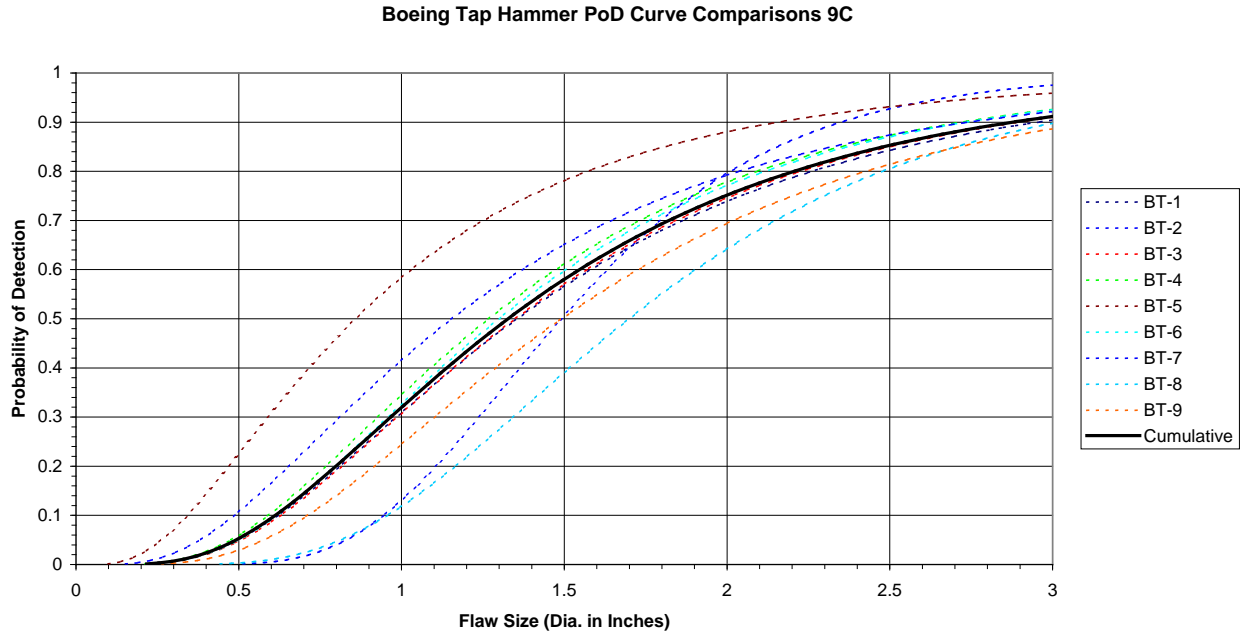
Boeing Tap Hammer 6-Ply Carbon		
Inspector	False Calls	90% POD Value
BT-1	0	2.74
BT-2	4	2.74
BT-3	6	2.39
BT-4	4	2.92
BT-5	8	1.62
BT-6	13	2.33
BT-7	2	2.51
BT-8	2	2.58
BT-9	3	2.45
Cumulative All Inspectors		2.59

Figure 171. Individual and cumulative PoD curve comparisons along with tabulated values for the Boeing tap hammer deployed on 6-ply carbon test specimen set



Boeing Tap Hammer 6-Ply Fiberglass		
Inspector	False Calls	90% POD Value
BT-1	0	2.81
BT-2	6	2.89
BT-3	6	>3.00
BT-4	1	1.60
BT-5	7	1.70
BT-6	17	2.12
BT-7	2	1.88
BT-8	2	2.50
BT-9	1	2.03
Cumulative All Inspectors		2.33

Figure 172. Individual and cumulative PoD curve comparisons along with tabulated values for the Boeing tap hammer deployed on 6-ply fiberglass test specimen set



Boeing Tap Hammer 9-Ply Carbon		
Inspector	False Calls	90% POD Value
BT-1	3	2.96
BT-2	2	2.36
BT-3	7	2.89
BT-4	2	2.70
BT-5	14	2.18
BT-6	14	2.72
BT-7	5	2.73
BT-8	1	>3.00
BT-9	1	>3.00
Cumulative All Inspectors		2.88

Figure 173. Individual and cumulative PoD curve comparisons along with tabulated values for the Boeing tap hammer deployed on 9-ply carbon test specimen set

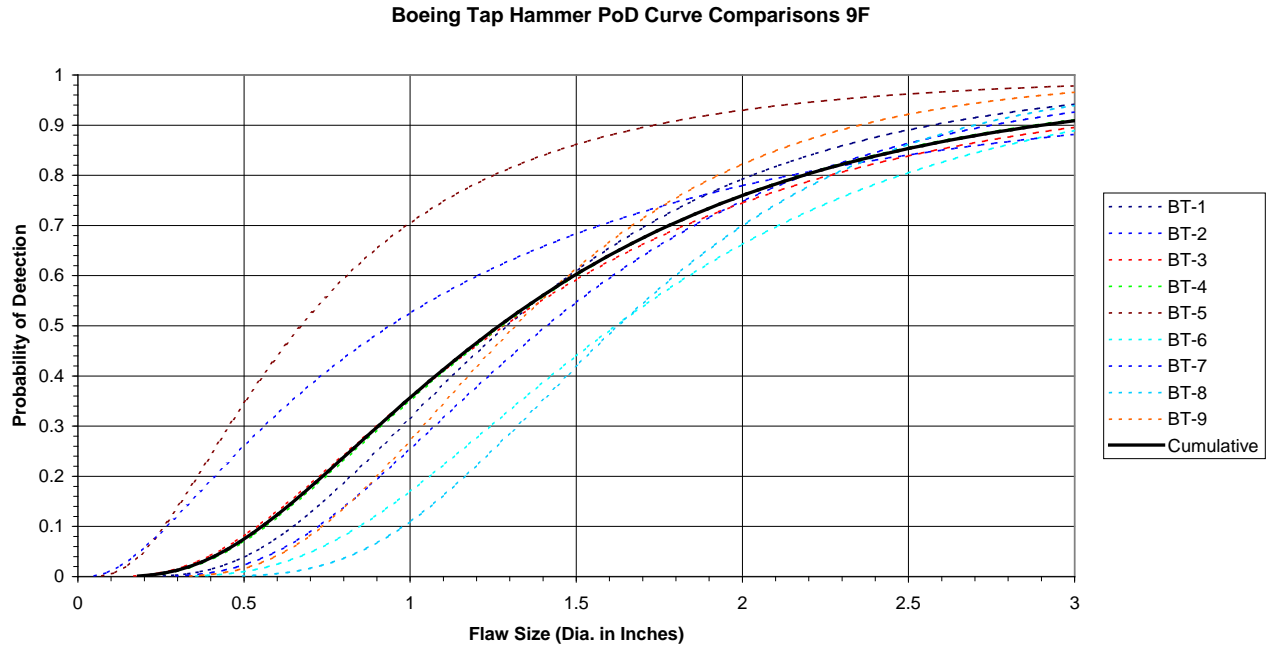
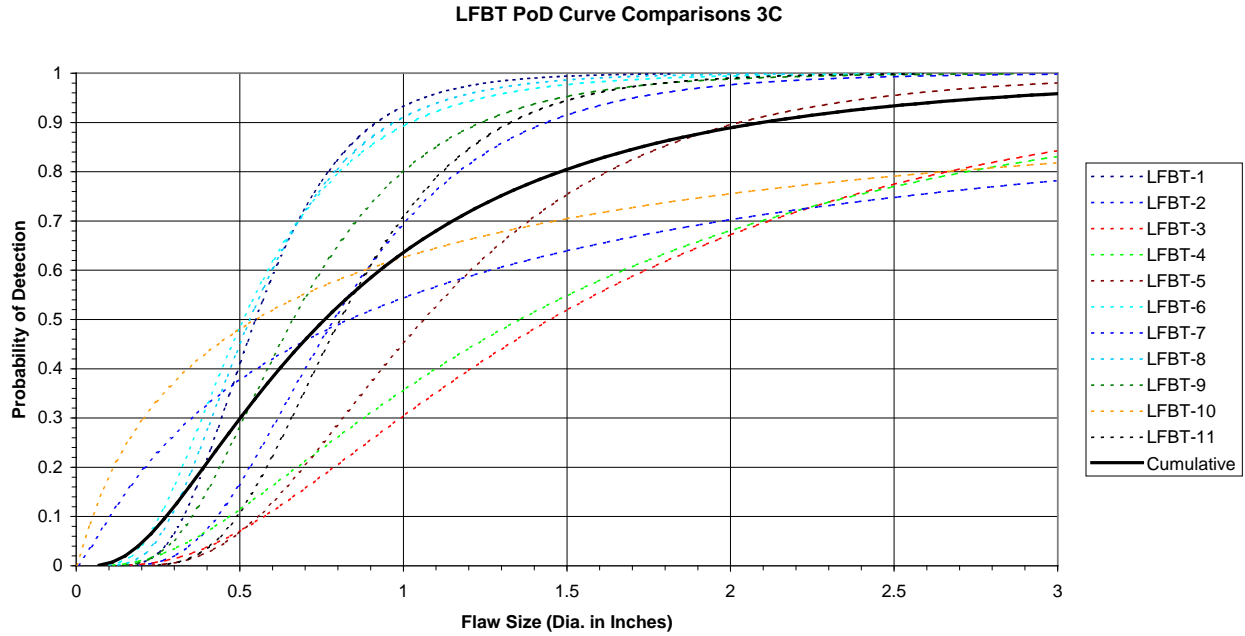
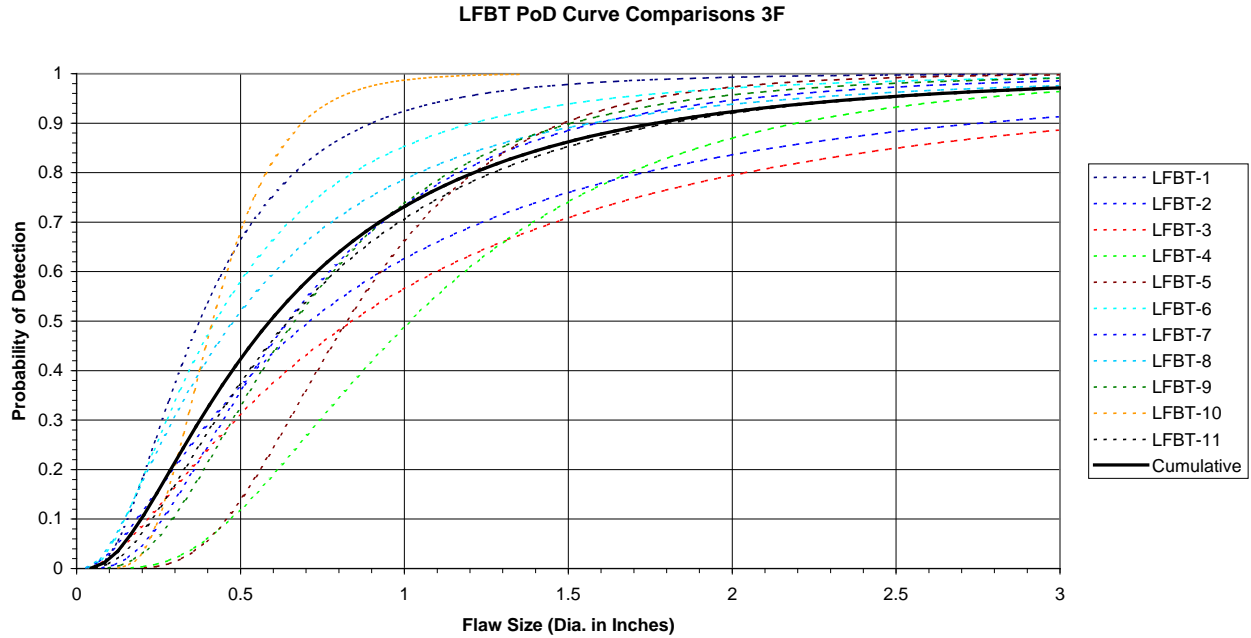


Figure 174. Individual and cumulative PoD curve comparisons along with tabulated values for the Boeing tap hammer deployed on 9-ply fiberglass test specimen set



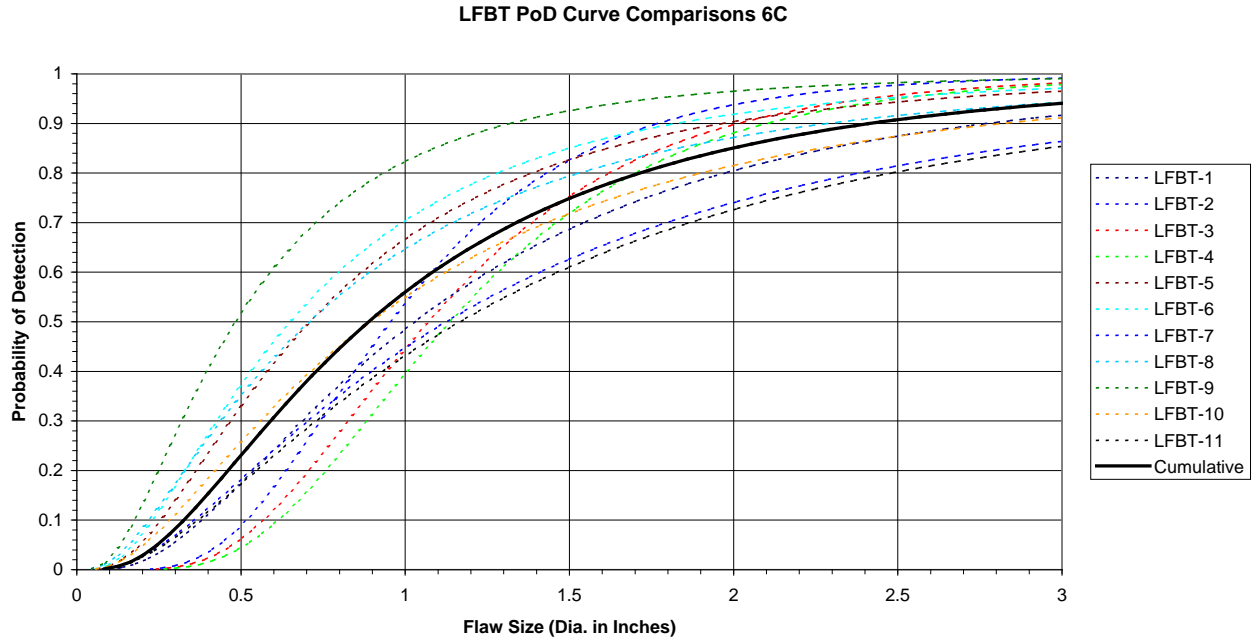
LFBT 3-Ply Carbon		
Inspector	False Calls	90% POD Value
LFBT-1	0	0.93
LFBT-2	0	1.44
LFBT-3	14	>3.00
LFBT-4	0	>3.00
LFBT-5	0	2.03
LFBT-6	0	1.01
LFBT-7	2	>3.00
LFBT-8	2	0.96
LFBT-9	0	1.25
LFBT-10	0	>3.00
LFBT-11	7	1.33
Cumulative All Inspectors		2.10

Figure 175. Individual and cumulative PoD curve comparisons along with tabulated values for LFBT deployed on 3-ply carbon test specimen set



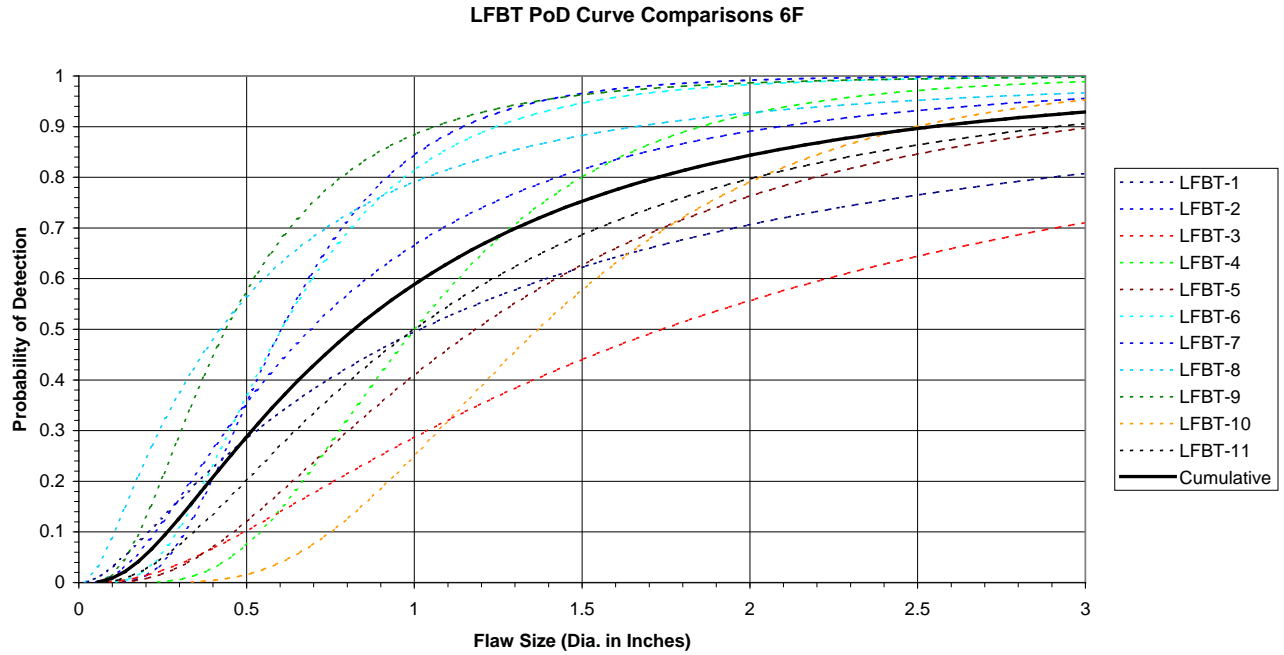
LFBT 3-Ply Fiberglass		
Inspector	False Calls	90% POD Value
LFBT-1	0	0.90
LFBT-2	0	1.58
LFBT-3	8	>3.00
LFBT-4	0	2.20
LFBT-5	1	1.49
LFBT-6	0	1.20
LFBT-7	0	2.76
LFBT-8	1	1.59
LFBT-9	0	1.51
LFBT-10	0	0.69
LFBT-11	0	1.81
Cumulative All Inspectors		1.77

Figure 176. Individual and cumulative PoD curve comparisons along with tabulated values for LFBT deployed on 3-ply fiberglass test specimen set



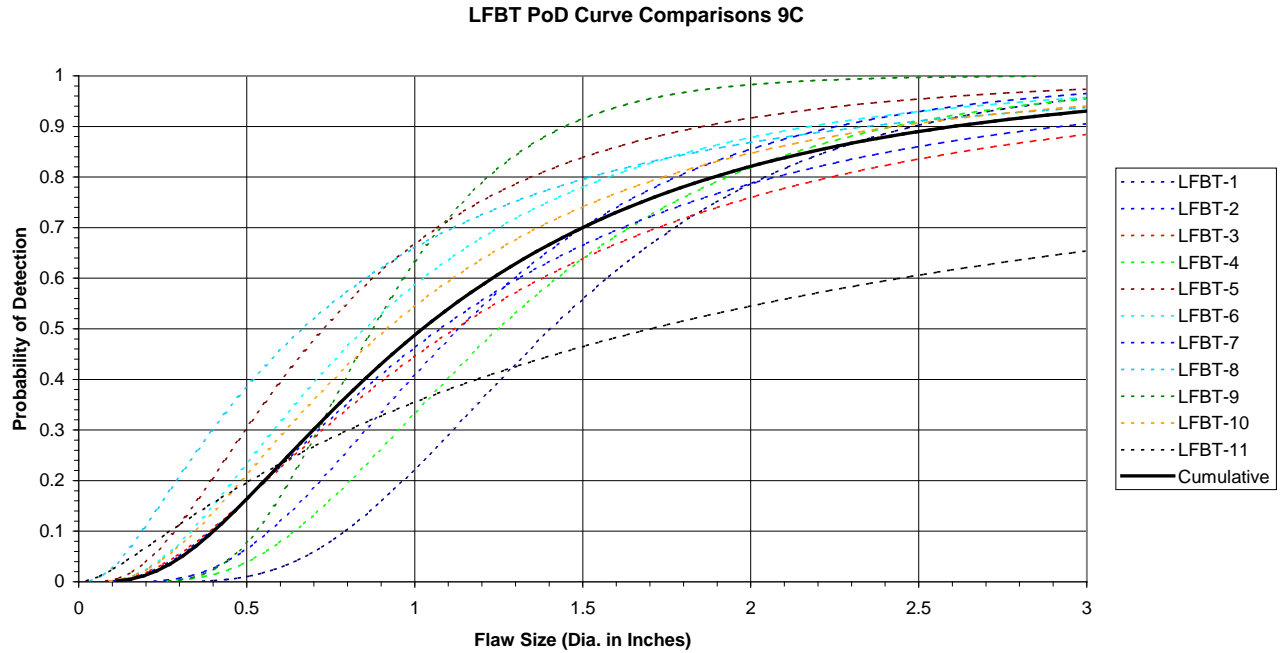
LFBT 6-Ply Carbon		
Inspector	False Calls	90% POD Value
LFBT-1	0	2.77
LFBT-2	0	1.76
LFBT-3	33	2.03
LFBT-4	1	2.11
LFBT-5	1	1.97
LFBT-6	0	1.85
LFBT-7	1	>3.00
LFBT-8	0	2.28
LFBT-9	2	1.32
LFBT-10	0	2.84
LFBT-11	34	>3.00
Cumulative All Inspectors		2.24

Figure 177. Individual and cumulative PoD curve comparisons along with tabulated values for LFBT deployed on 6-ply carbon test specimen set



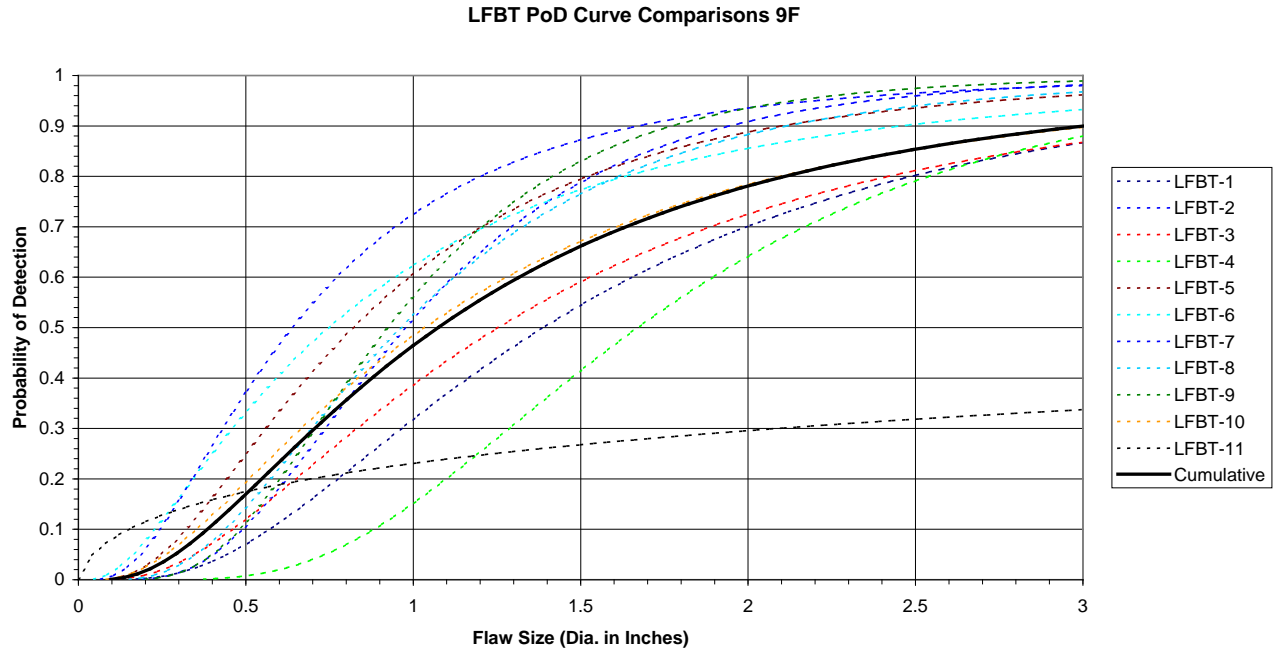
LFBT 6-Ply Fiberglass		
Inspector	False Calls	90% POD Value
LFBT-1	0	>3.00
LFBT-2	0	1.14
LFBT-3	24	>3.00
LFBT-4	0	1.87
LFBT-5	6	>3.00
LFBT-6	0	1.24
LFBT-7	1	2.08
LFBT-8	2	1.67
LFBT-9	1	1.05
LFBT-10	0	2.50
LFBT-11	2	2.92
Cumulative All Inspectors		2.55

Figure 178. Individual and cumulative PoD curve comparisons along with tabulated values for LFBT deployed on 6-ply fiberglass test specimen set



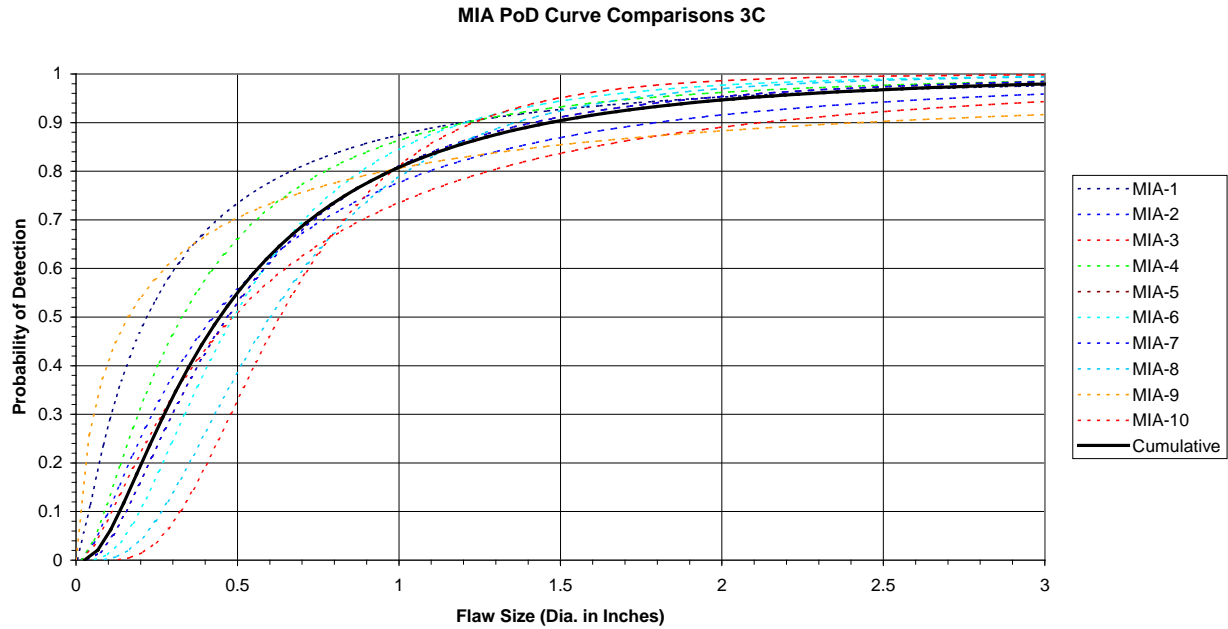
LFBT 9-Ply Carbon		
Inspector	False Calls	90% POD Value
LFBT-1	0	2.49
LFBT-2	0	2.25
LFBT-3	1	>3.00
LFBT-4	3	2.46
LFBT-5	1	1.86
LFBT-6	0	2.18
LFBT-7	4	2.92
LFBT-8	0	2.36
LFBT-9	0	1.45
LFBT-10	0	2.45
LFBT-11	33	>3.00
Cumulative All Inspectors		2.61

Figure 179. Individual and cumulative PoD curve comparisons along with tabulated values for LFBT deployed on 9-ply carbon test specimen set



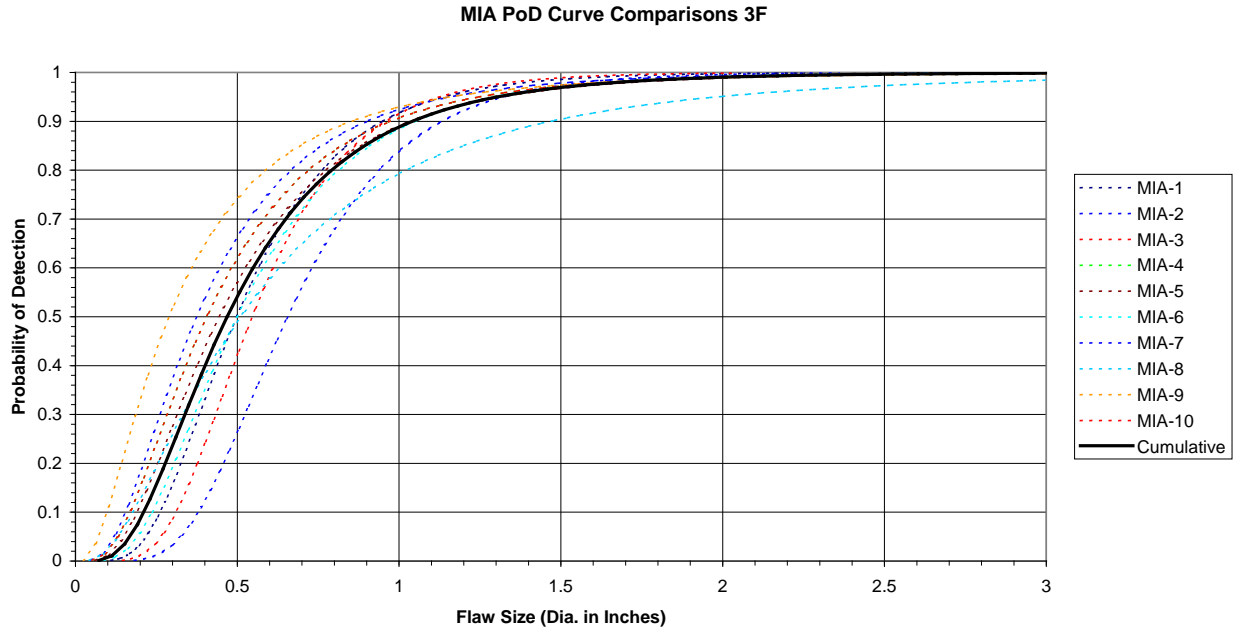
LFBT 9-Ply Fiberglass		
Inspector	False Calls	90% POD Value
LFBT-1	0	>3.00
LFBT-2	0	1.94
LFBT-3	0	>3.00
LFBT-4	3	>3.00
LFBT-5	0	2.10
LFBT-6	0	2.44
LFBT-7	0	1.68
LFBT-8	0	2.11
LFBT-9	3	1.79
LFBT-10	0	>3.00
LFBT-11	25	>3.00
Cumulative All Inspectors		3.00

Figure 180. Individual and cumulative PoD curve comparisons along with tabulated values for LFBT deployed on 9-ply fiberglass test specimen set



MIA 3-Ply Carbon		
Inspector	False Calls	90% POD Value
MIA-1	1	1.23
MIA-2	1	1.79
MIA-3	0	2.11
MIA-4	4	1.23
MIA-5	0	1.44
MIA-6	0	1.23
MIA-7	0	1.40
MIA-8	0	1.35
MIA-9	0	2.40
MIA-10	0	1.26
Cumulative All Inspectors		1.46

Figure 181. Individual and cumulative PoD curve comparisons along with tabulated values for MIA deployed on 3-ply carbon test specimen set



MIA 3-Ply Fiberglass		
Inspector	False Calls	90% POD Value
MIA-1	2	0.95
MIA-2	1	1.15
MIA-3	0	0.96
MIA-4	1	0.97
MIA-5	0	1.05
MIA-6	0	1.05
MIA-7	1	0.91
MIA-8	0	1.48
MIA-9	0	0.87
MIA-10	0	0.97
Cumulative All Inspectors		1.04

Figure 182. Individual and cumulative PoD curve comparisons along with tabulated values for MIA deployed on 3-ply fiberglass test specimen set

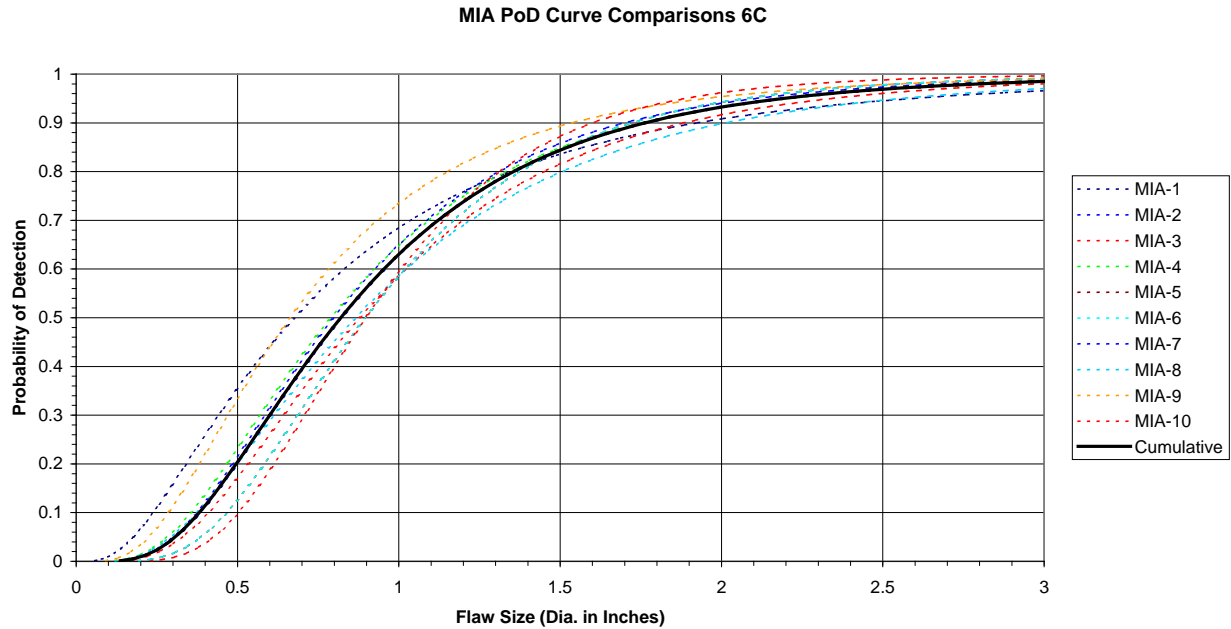
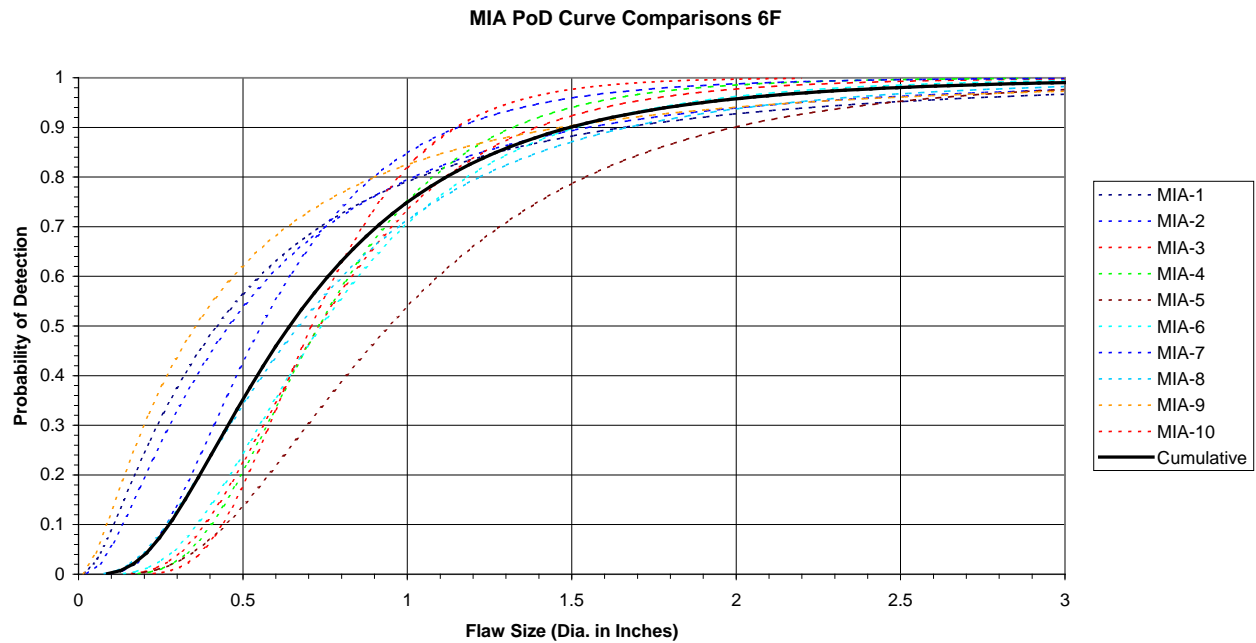
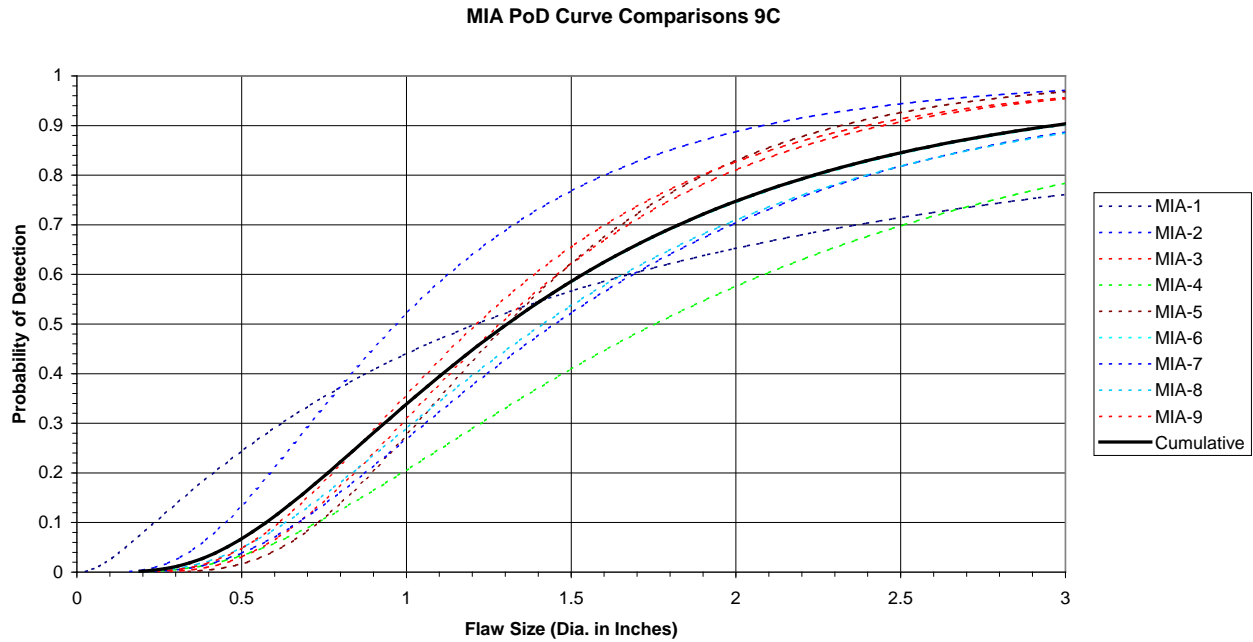


Figure 183. Individual and cumulative PoD curve comparisons along with tabulated values for MIA deployed on 6-ply carbon test specimen set



MIA 6-Ply Fiberglass		
Inspector	False Calls	90% POD Value
MIA-1	1	1.65
MIA-2	0	1.55
MIA-3	0	1.39
MIA-4	0	1.33
MIA-5	0	2.00
MIA-6	0	1.51
MIA-7	1	1.18
MIA-8	0	1.66
MIA-9	15	1.47
MIA-10	2	1.16
Cumulative All Inspectors		1.49

Figure 184. Individual and cumulative PoD curve comparisons along with tabulated values for MIA deployed on 6-ply fiberglass test specimen set



MIA 9-Ply Carbon		
Inspector	False Calls	90% POD Value
MIA-1	0	>3.00
MIA-2	1	2.08
MIA-3	3	2.45
MIA-4	6	>3.00
MIA-5	1	2.32
MIA-6	4	3.00
MIA-7	4	>3.00
MIA-8	5	>3.00
MIA-9	N/A	N/A
MIA-10	4	2.40
Cumulative All Inspectors		1.49

Figure 185. Individual and cumulative PoD curve comparisons along with tabulated values for MIA deployed on 9-ply carbon test specimen set

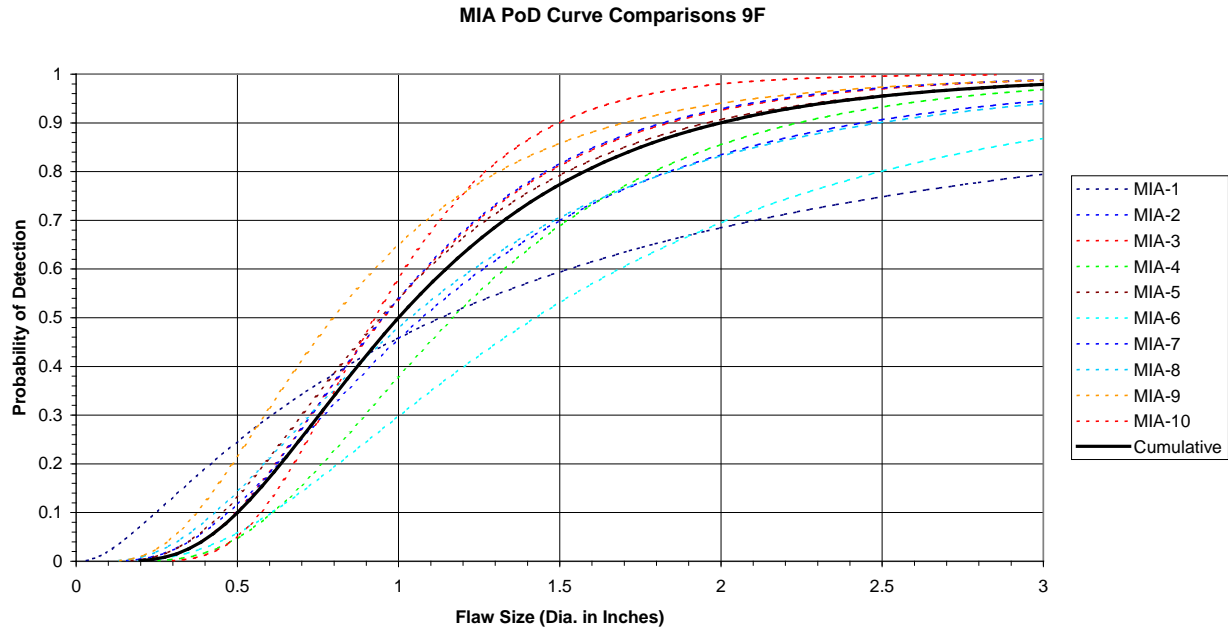
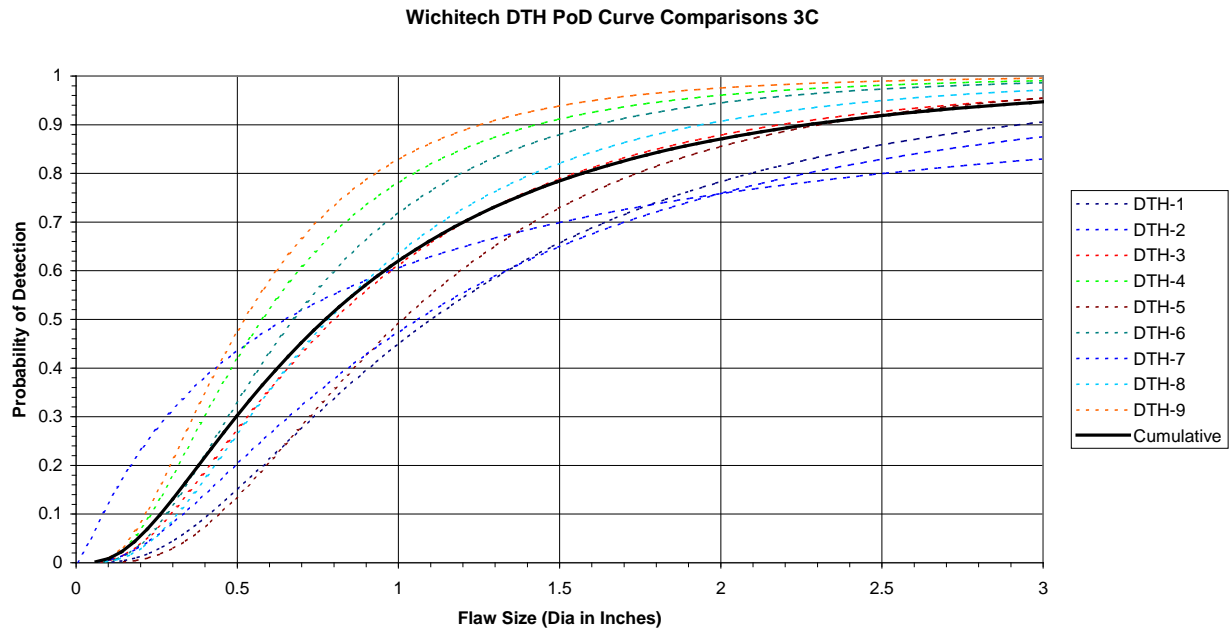
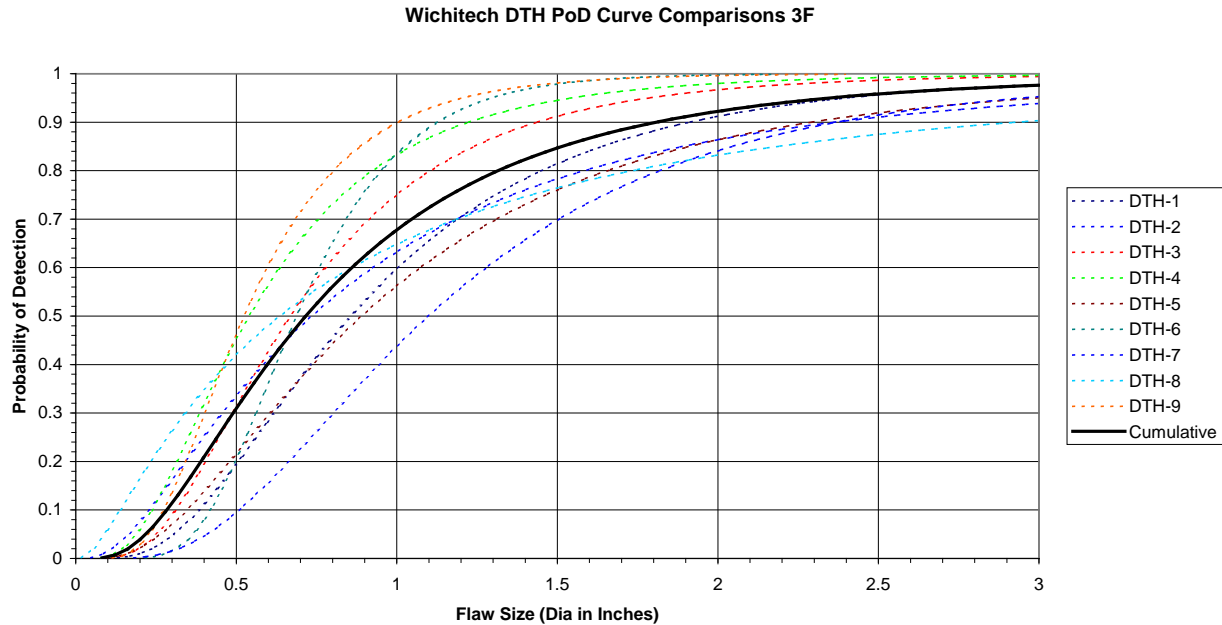


Figure 186. Individual and cumulative PoD curve comparisons along with tabulated values for MIA deployed on 9-ply fiberglass test specimen set



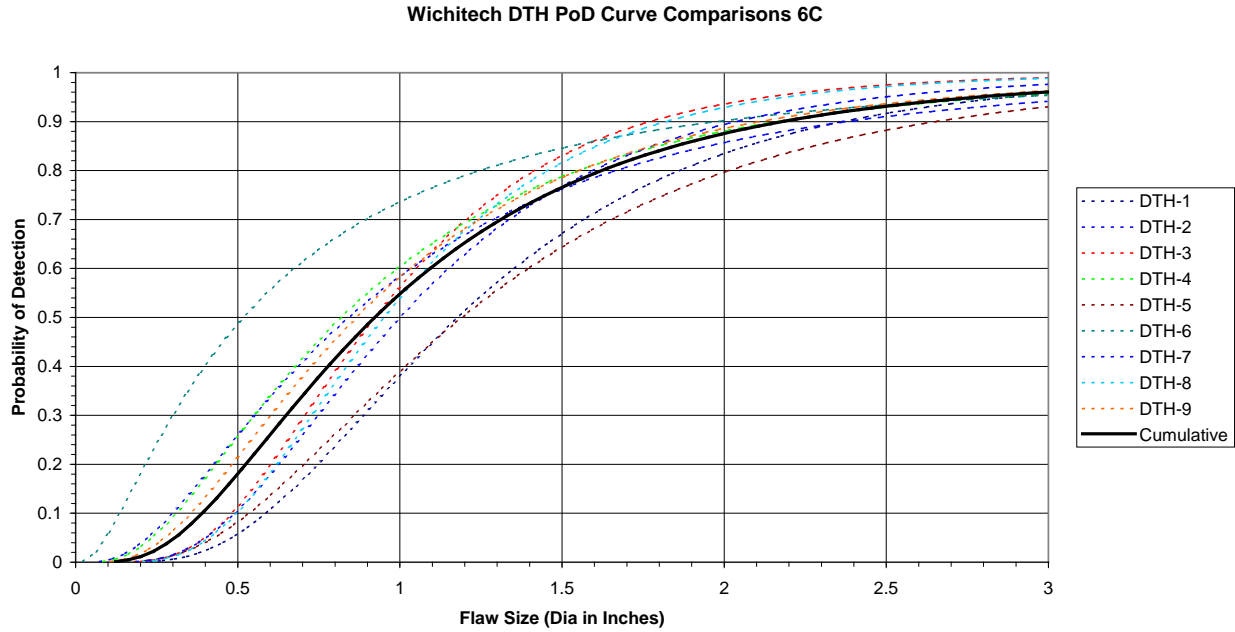
DTH 3-Ply Carbon		
Inspector	False Calls	90% POD Value
DTH-1	0	2.92
DTH-2	5	>3.00
DTH-3	0	2.20
DTH-4	0	1.46
DTH-5	0	2.31
DTH-6	0	1.62
DTH-7	0	>3.00
DTH-8	0	1.94
DTH-9	0	1.26
Cumulative All Inspectors		2.28

Figure 187. Individual and cumulative PoD curve comparisons along with tabulated values for WichiTech DTH deployed on 3-ply carbon test specimen set



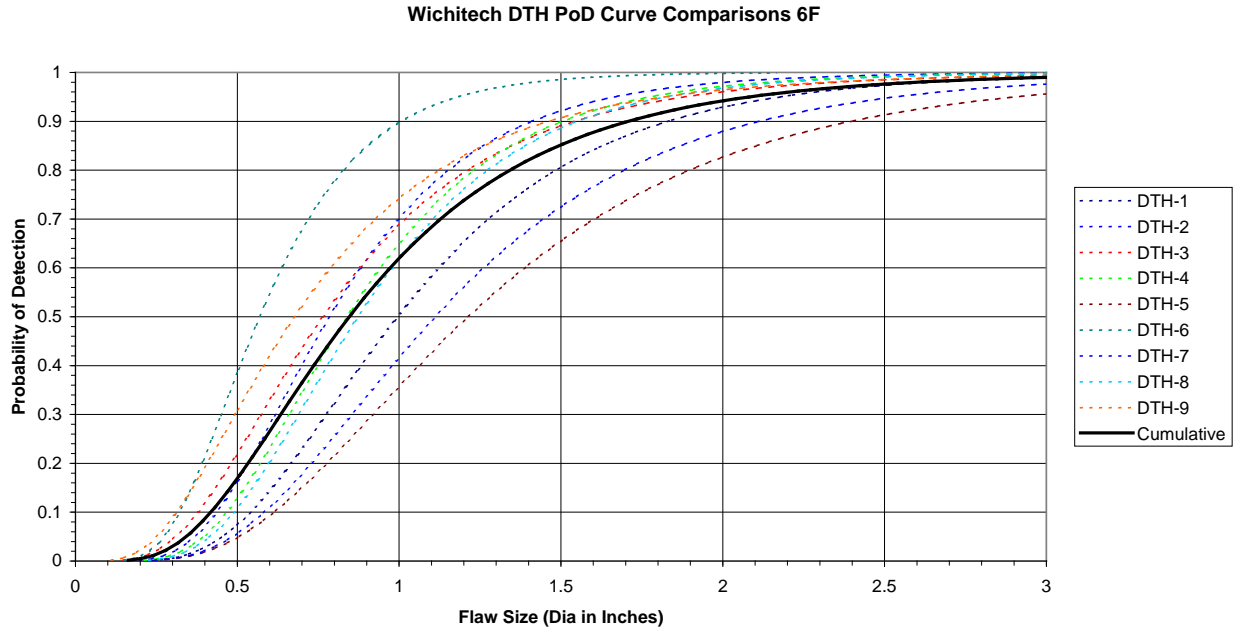
DTH 3-Ply Fiberglass		
Inspector	False Calls	90% POD Value
DTH-1	0	1.91
DTH-2	8	2.36
DTH-3	0	1.44
DTH-4	0	1.22
DTH-5	0	2.29
DTH-6	0	1.12
DTH-7	0	2.39
DTH-8	0	2.92
DTH-9	0	1.00
Cumulative All Inspectors		1.81

Figure 188. Individual and cumulative PoD curve comparisons along with tabulated values for WichiTech DTH deployed on 3-ply fiberglass test specimen set



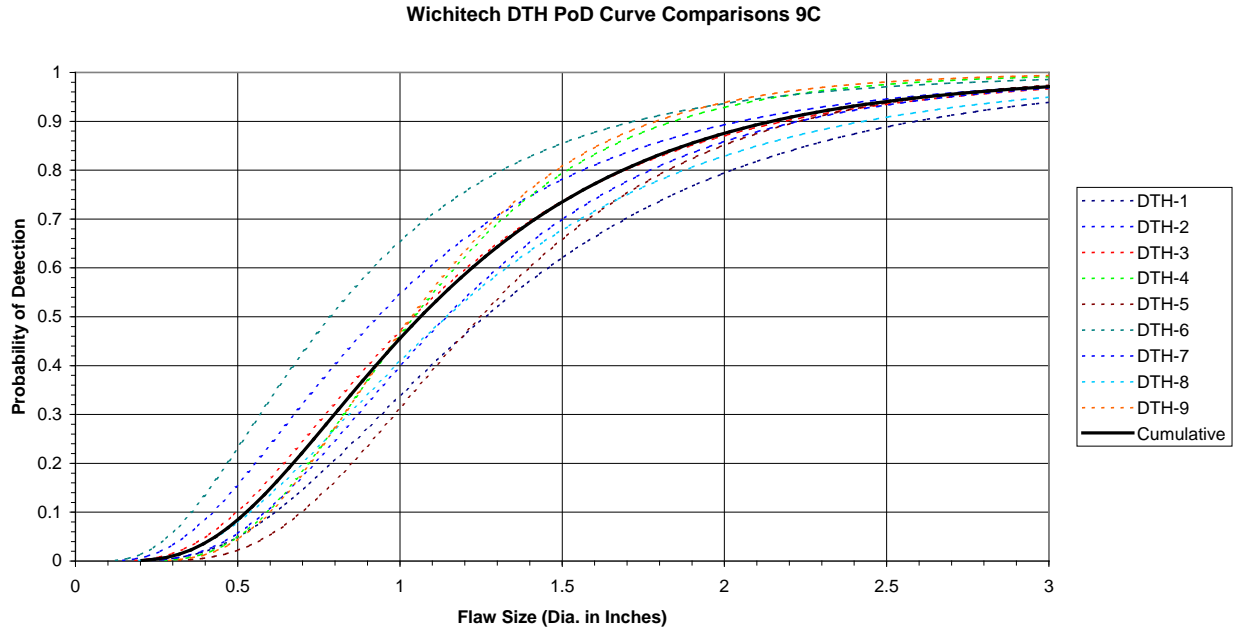
DTH 6-Ply Carbon		
Inspector	False Calls	90% POD Value
DTH-1	0	2.36
DTH-2	6	2.37
DTH-3	0	1.79
DTH-4	1	2.17
DTH-5	0	2.66
DTH-6	0	1.99
DTH-7	0	2.05
DTH-8	1	1.83
DTH-9	0	2.10
Cumulative All Inspectors		2.18

Figure 189. Individual and cumulative PoD curve comparisons along with tabulated values for WichiTech DTH deployed on 6-ply carbon test specimen set



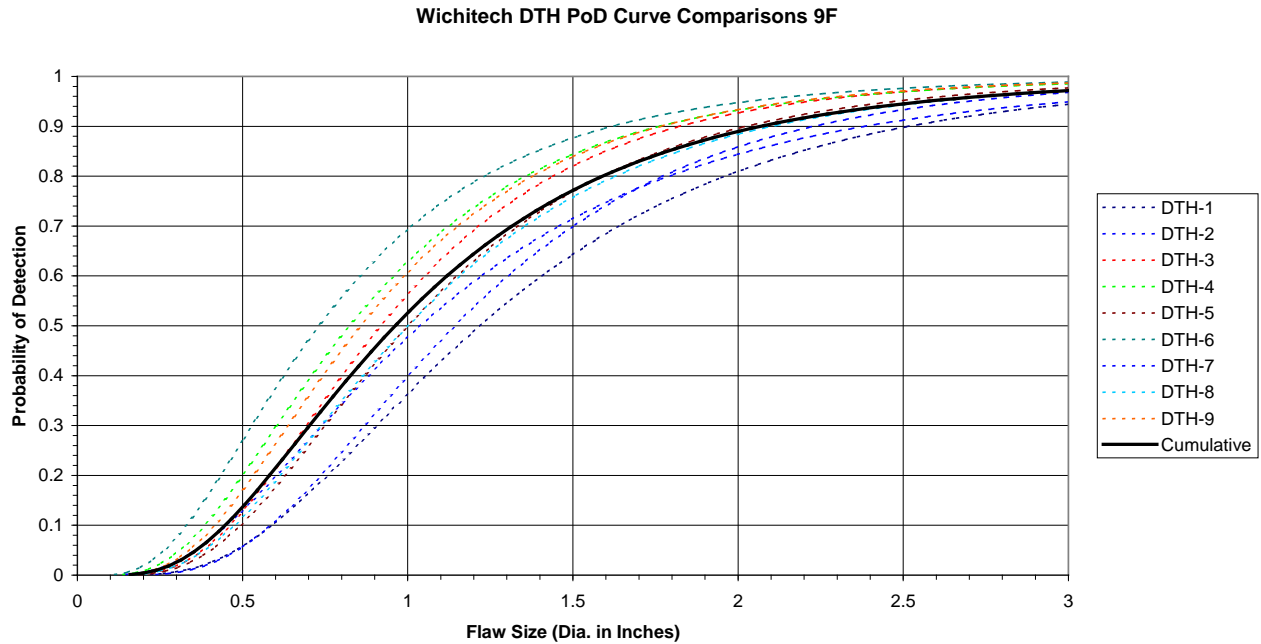
DTH 6-Ply Fiberglass		
Inspector	False Calls	90% POD Value
DTH-1	0	1.84
DTH-2	8	1.41
DTH-3	0	1.54
DTH-4	0	1.50
DTH-5	0	2.40
DTH-6	6	1.01
DTH-7	0	2.11
DTH-8	0	1.55
DTH-9	0	1.48
Cumulative All Inspectors		1.71

Figure 190. Individual and cumulative PoD curve comparisons along with tabulated values for WichiTech DTH deployed on 6-ply fiberglass test specimen set



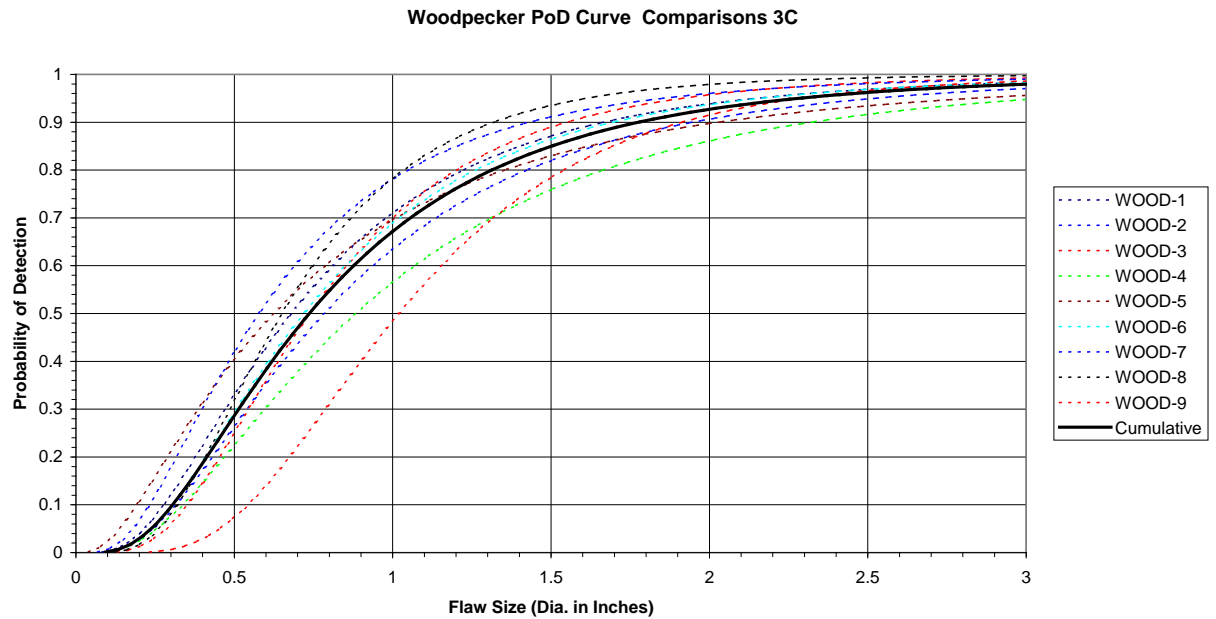
DTH 9-Ply Carbon		
Inspector	False Calls	90% POD Value
DTH-1	0	2.59
DTH-2	5	2.04
DTH-3	0	2.20
DTH-4	0	1.86
DTH-5	0	2.24
DTH-6	31	1.72
DTH-7	0	2.25
DTH-8	0	2.43
DTH-9	4	1.79
Cumulative All Inspectors		2.15

Figure 191. Individual and cumulative PoD curve comparisons along with tabulated values for WichiTech DTH deployed on 9-ply carbon test specimen set



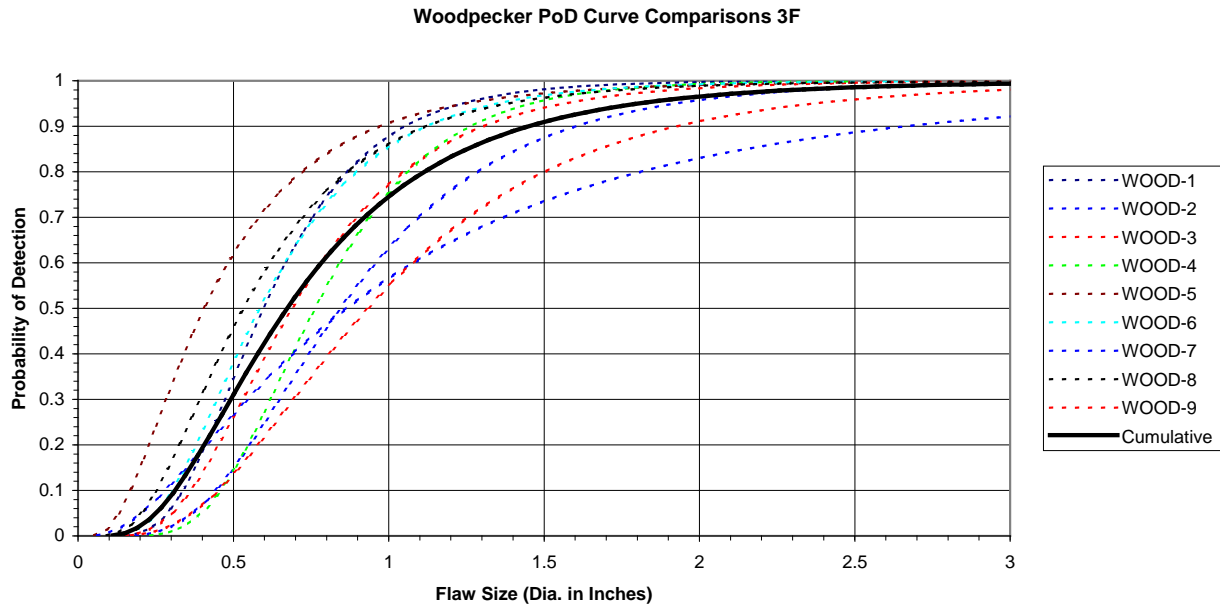
DTH 9-Ply Fiberglass		
Inspector	False Calls	90% POD Value
DTH-1	0	2.51
DTH-2	12	2.21
DTH-3	0	1.82
DTH-4	0	1.76
DTH-5	0	2.01
DTH-6	32	1.63
DTH-7	0	2.38
DTH-8	0	2.10
DTH-9	0	1.77
Cumulative All Inspectors		2.07

Figure 192. Individual and cumulative PoD curve comparisons along with tabulated values for WichiTech DTH deployed on 9-ply fiberglass test specimen set



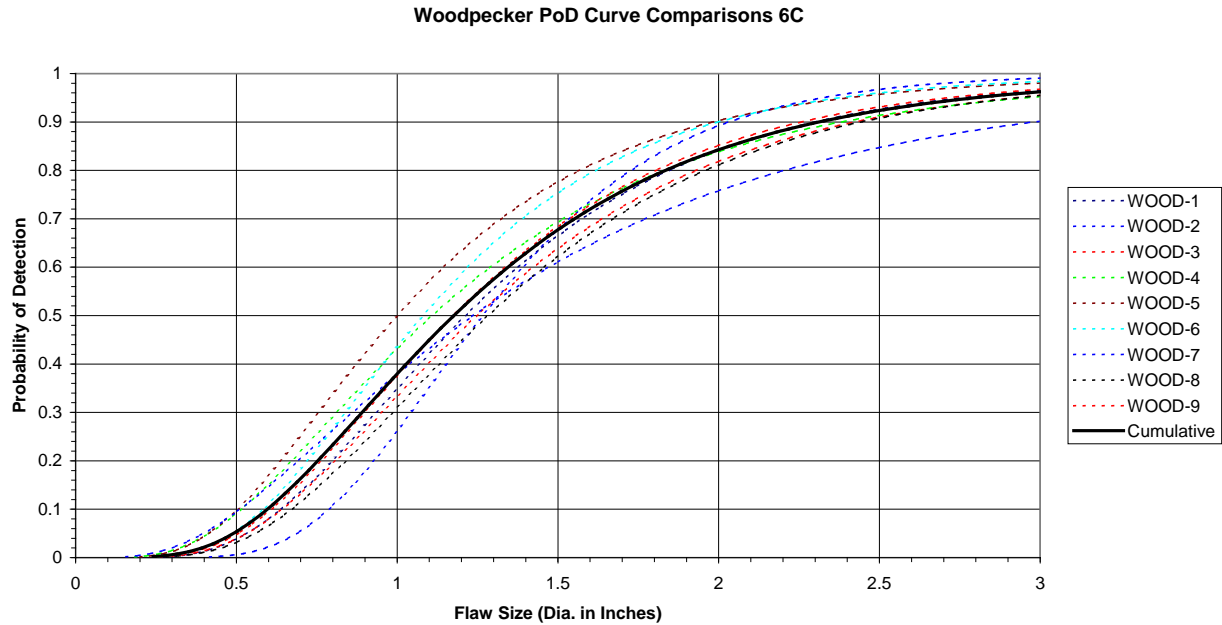
Woodpecker 3-Ply Carbon		
Inspector	False Calls	90% POD Value
WOOD-1	0	1.70
WOOD-2	0	1.94
WOOD-3	0	1.56
WOOD-4	0	2.33
WOOD-5	0	2.04
WOOD-6	0	1.70
WOOD-7	0	1.42
WOOD-8	0	1.32
WOOD-9	0	1.92
Cumulative All Inspectors		1.78

Figure 193. Individual and cumulative PoD curve comparisons along with tabulated values for Woodpecker deployed on 3-ply carbon test specimen set



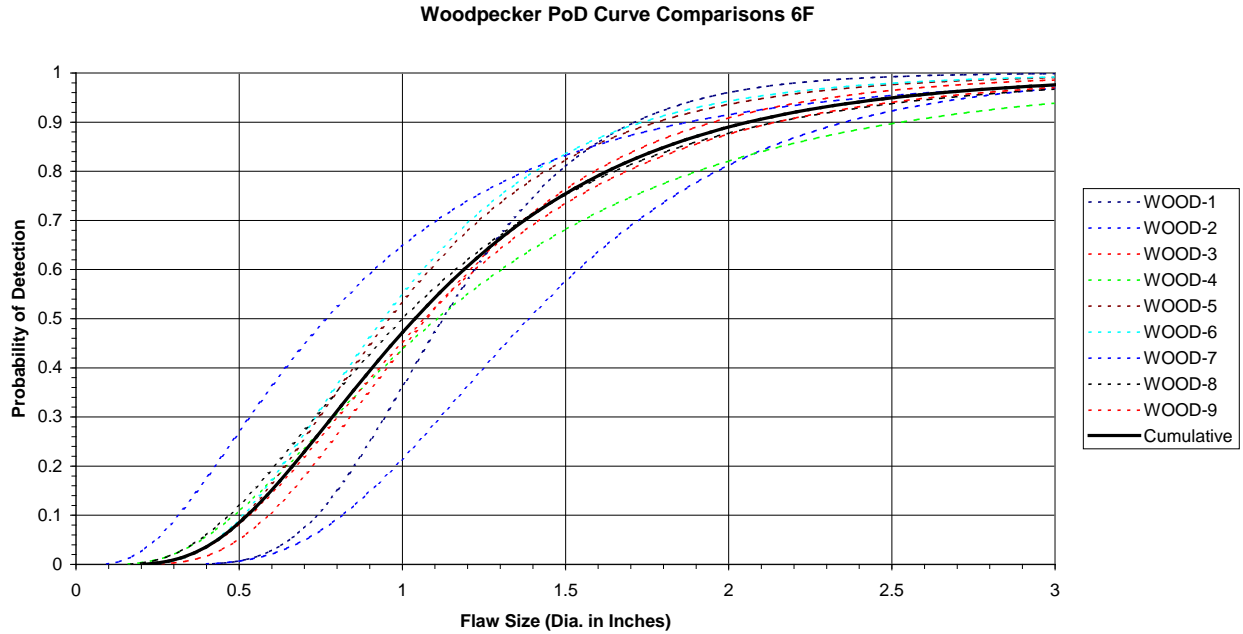
Woodpecker 3-Ply Fiberglass		
Inspector	False Calls	90% POD Value
WOOD-1	0	1.06
WOOD-2	0	1.60
WOOD-3	0	1.30
WOOD-4	3	1.27
WOOD-5	0	0.97
WOOD-6	0	1.13
WOOD-7	0	2.68
WOOD-8	0	1.12
WOOD-9	0	1.93
Cumulative All Inspectors		1.45

Figure 194. Individual and cumulative PoD curve comparisons along with tabulated values for Woodpecker deployed on 3-ply fiberglass test specimen set



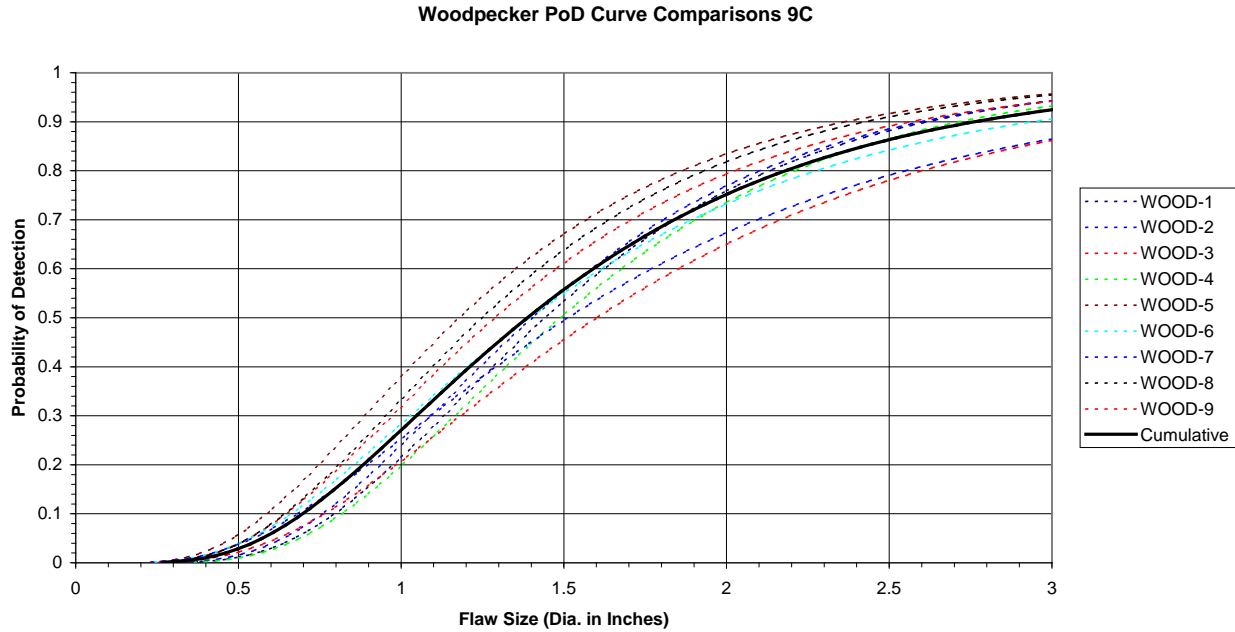
Woodpecker 6-Ply Carbon		
Inspector	False Calls	90% POD Value
WOOD-1	0	2.30
WOOD-2	0	2.03
WOOD-3	0	2.44
WOOD-4	0	2.39
WOOD-5	1	1.98
WOOD-6	1	2.00
WOOD-7	4	3.00
WOOD-8	0	2.45
WOOD-9	0	2.26
Cumulative All Inspectors		2.32

Figure 195. Individual and cumulative PoD curve comparisons along with tabulated values for Woodpecker deployed on 6-ply carbon test specimen set



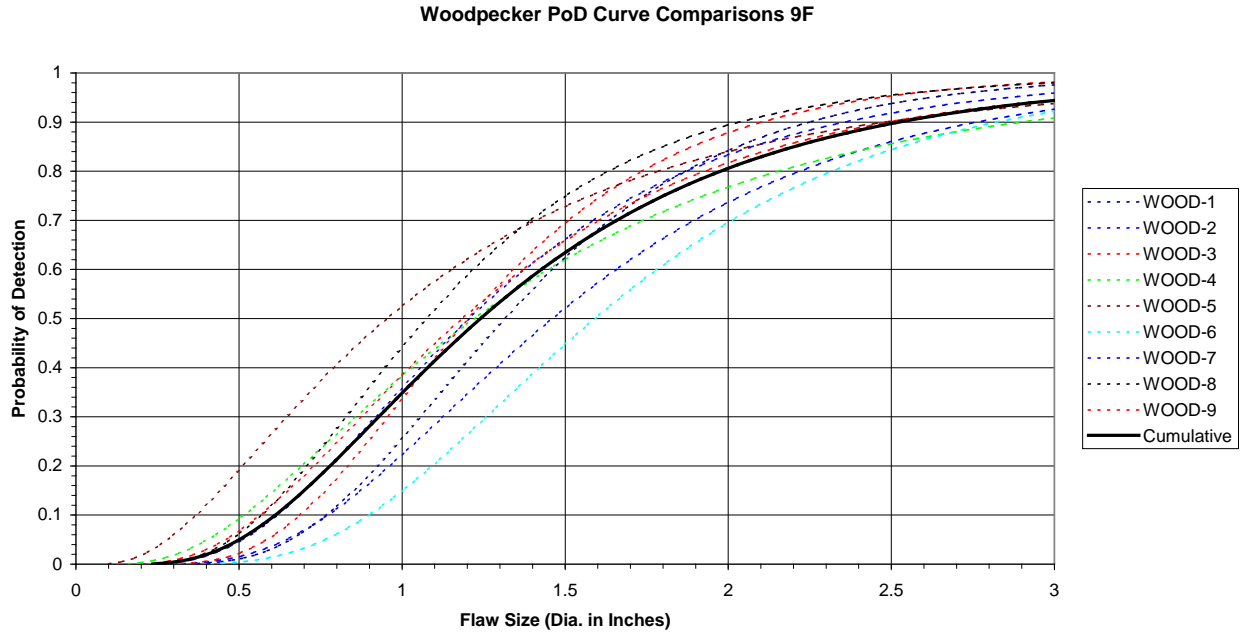
Woodpecker 6-Ply Fiberglass		
Inspector	False Calls	90% POD Value
WOOD-1	0	1.71
WOOD-2	0	2.37
WOOD-3	0	1.96
WOOD-4	0	2.54
WOOD-5	0	1.77
WOOD-6	0	1.75
WOOD-7	0	1.87
WOOD-8	0	2.15
WOOD-9	1	2.14
Cumulative All Inspectors		2.05

Figure 196. Individual and cumulative PoD curve comparisons along with tabulated values for Woodpecker deployed on 6-ply fiberglass test specimen set



Woodpecker 9-Ply Carbon		
Inspector	False Calls	90% POD Value
WOOD-1	0	2.61
WOOD-2	1	2.60
WOOD-3	2	2.59
WOOD-4	2	2.72
WOOD-5	1	2.36
WOOD-6	9	2.93
WOOD-7	0	>3.00
WOOD-8	8	2.44
WOOD-9	2	>3.00
Cumulative All Inspectors		2.76

Figure 197. Individual and cumulative PoD curve comparisons along with tabulated values for Woodpecker deployed on 9-ply carbon test specimen set



Woodpecker 9-Ply Fiberglass		
Inspector	False Calls	90% POD Value
WOOD-1	5	2.25
WOOD-2	0	2.75
WOOD-3	5	2.10
WOOD-4	16	2.88
WOOD-5	3	2.49
WOOD-6	13	2.82
WOOD-7	5	2.36
WOOD-8	6	2.08
WOOD-9	7	2.48
Cumulative All Inspectors		2.52

Figure 198. Individual and cumulative PoD curve comparisons along with tabulated values for Woodpecker deployed on 9-ply fiberglass test specimen set

Several NDI devices, such as the Airbus tap hammer and the LFBT equipment, included some outlier data where an inspector's performance was quite higher than the other inspectors. The PoD curves in figures 199–202 compare the cumulative PoD performance of all inspectors for a particular inspection method with performance curves produced when performance outliers are removed from the calculation. The results are broken down into the various composite

honeycomb structure categories. The improvements observed when these outliers are removed indicate that additional training and experience with these devices could increase PoD levels.

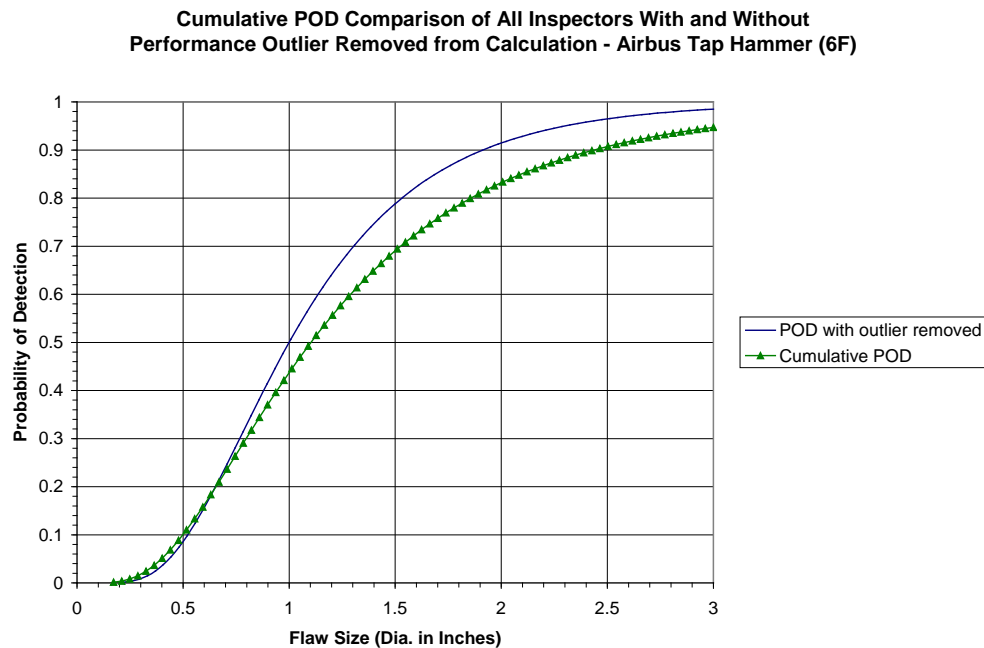


Figure 199. Comparison showing level of PoD improvement when single performance outlier is removed from the calculation—Airbus tap hammer, 6-ply fiberglass

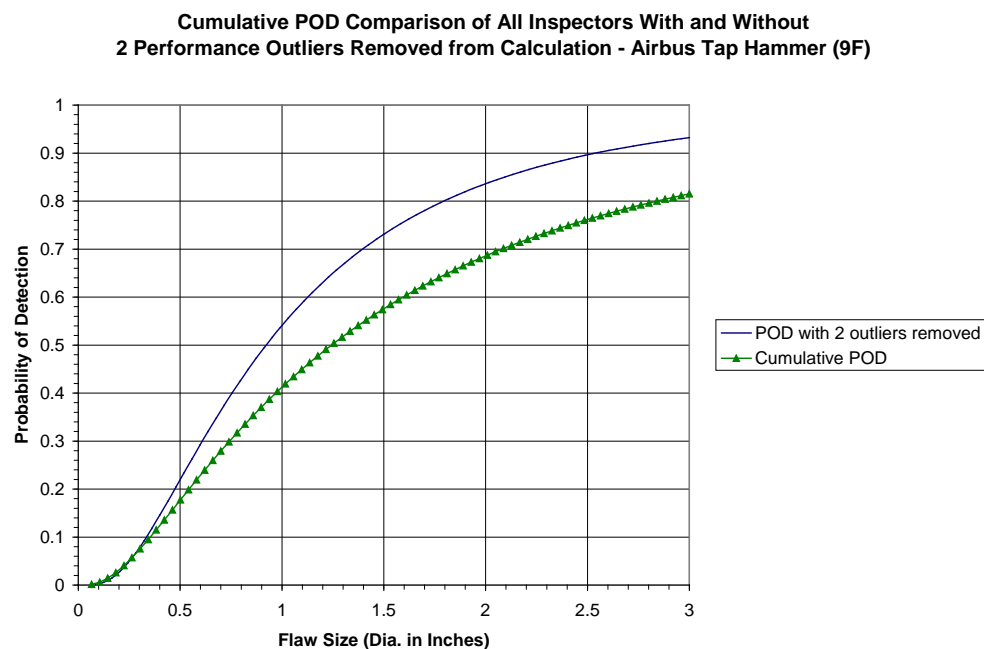


Figure 200. Comparison showing level of PoD improvement when performance outliers are removed from the calculation—Airbus tap hammer, 9-ply fiberglass

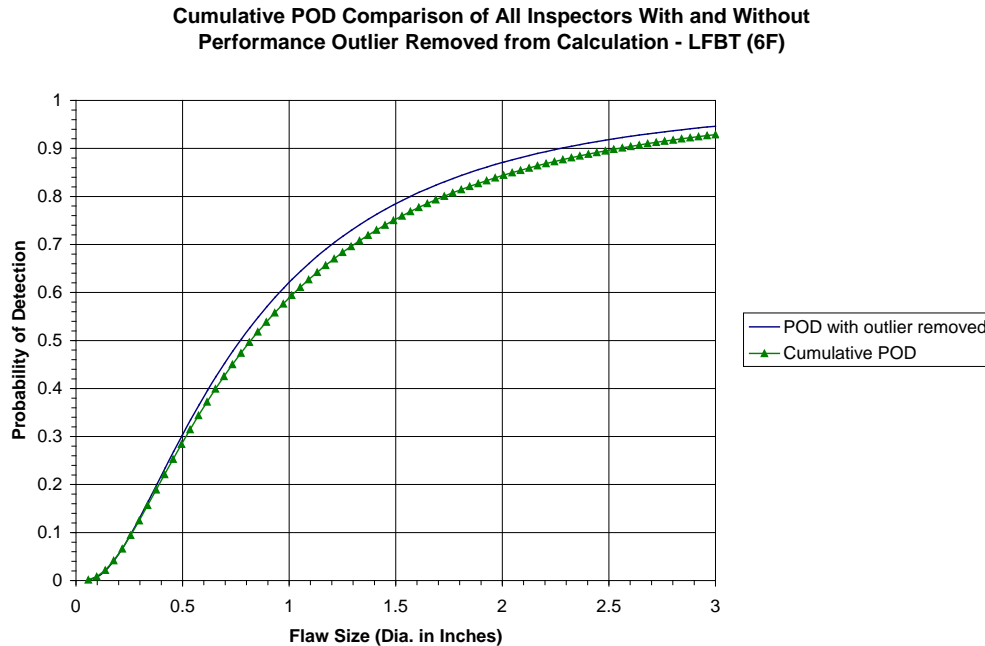


Figure 201. Comparison showing level of PoD improvement when single performance outlier is removed from the calculation—LFBT, 6-ply fiberglass

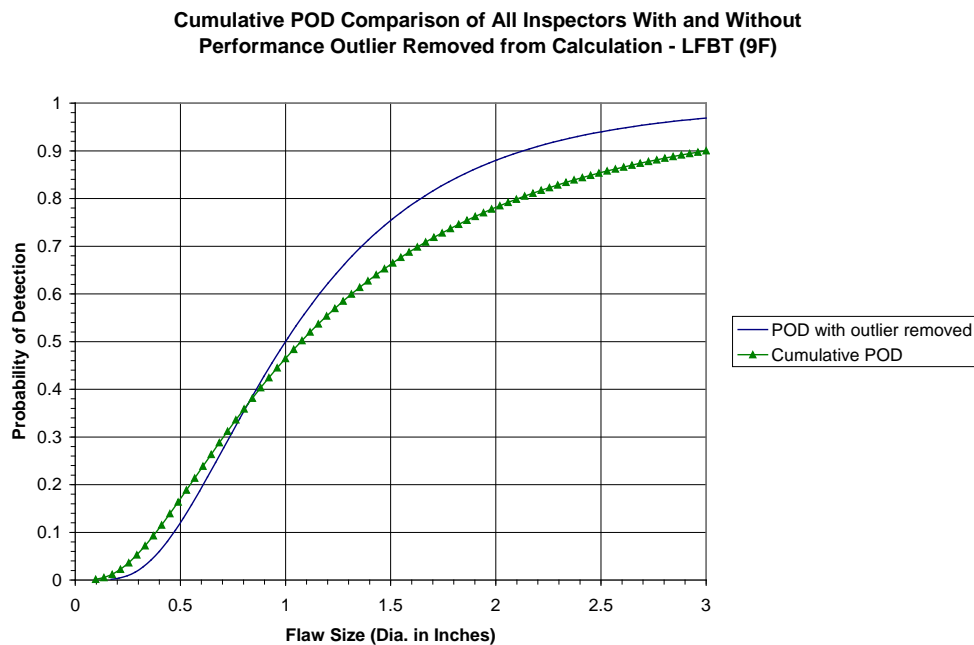


Figure 202. Comparison showing level of PoD improvement when single performance outlier is removed from the calculation—LFBT, 9-ply fiberglass

Normally, when using PoD curves to establish the performance of an NDI method, it is common to use the 90% PoD level with a 95% confidence. The additional confidence bound consideration

shifts the PoD slightly to the left. The PoD curves in figures 203–238 compare the cumulative PoD performance when the 95% Confidence Bound is imposed with the maximum likelihood estimate PoD when there is no required confidence level. The results are broken down into the various composite honeycomb structure categories.

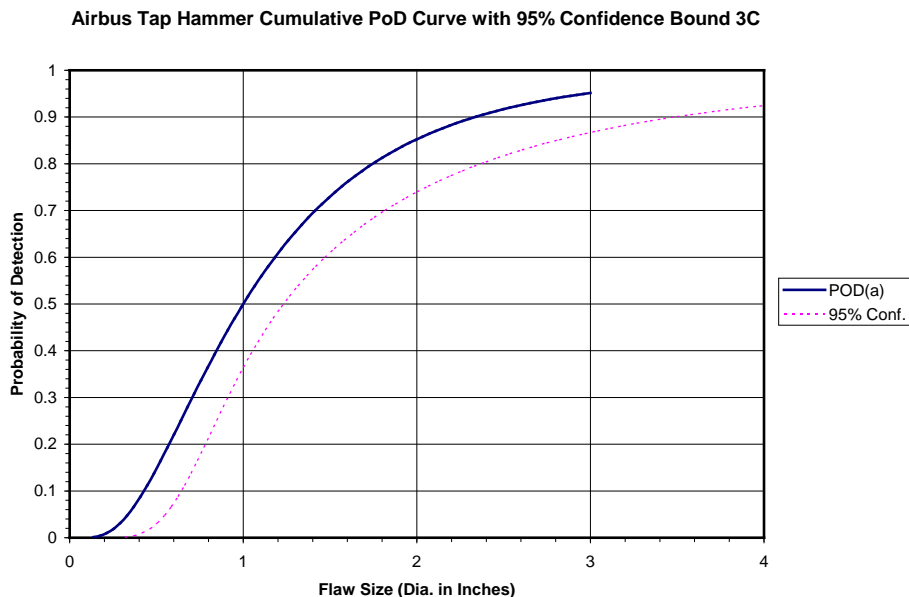


Figure 203. Cumulative PoD curve with 95% confidence bound—Airbus tap hammer, 3-ply carbon

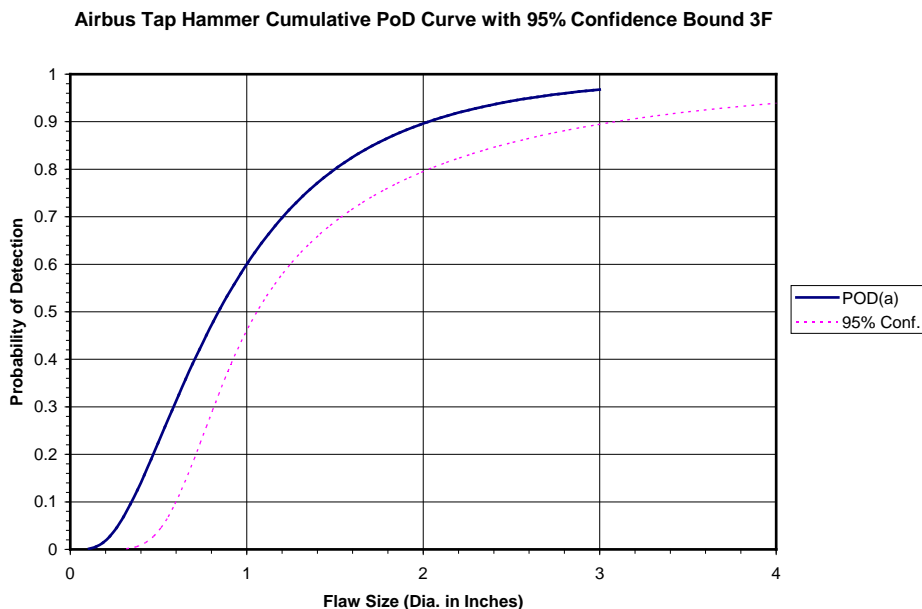


Figure 204. Cumulative PoD curve with 95% confidence bound—Airbus tap hammer, 3-ply fiberglass

Airbus Tap Hammer Cumulative PoD Curve with 95% Confidence Bound 6C

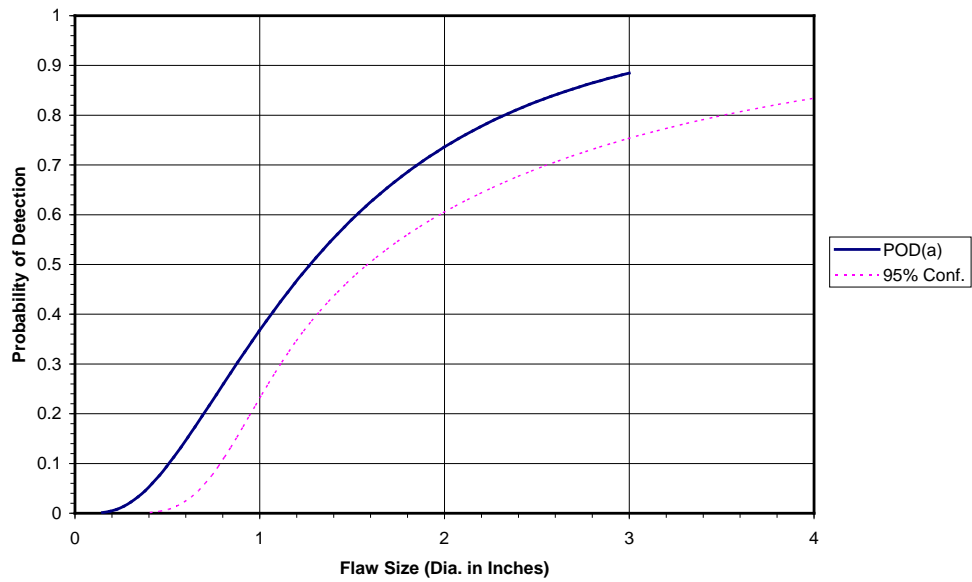


Figure 205. Cumulative PoD curve with 95% confidence bound—Airbus tap hammer, 6-ply carbon

Airbus Tap Hammer Cumulative PoD Curve with 95% Confidence Bound 6F

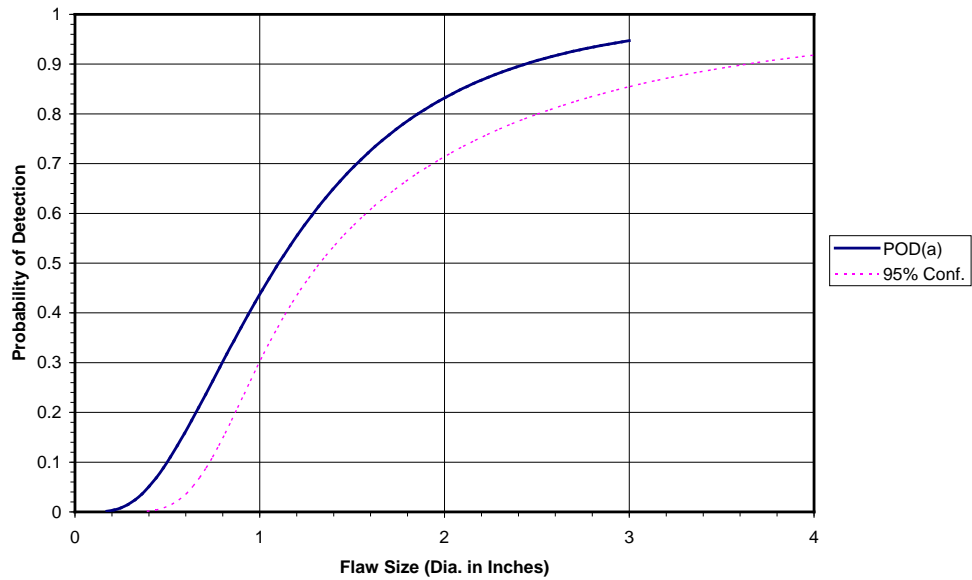


Figure 206. Cumulative PoD curve with 95% confidence bound—Airbus tap hammer, 6-ply fiberglass

Airbus Tap Hammer Cumulative PoD Curve with 95% Confidence Bound 9C

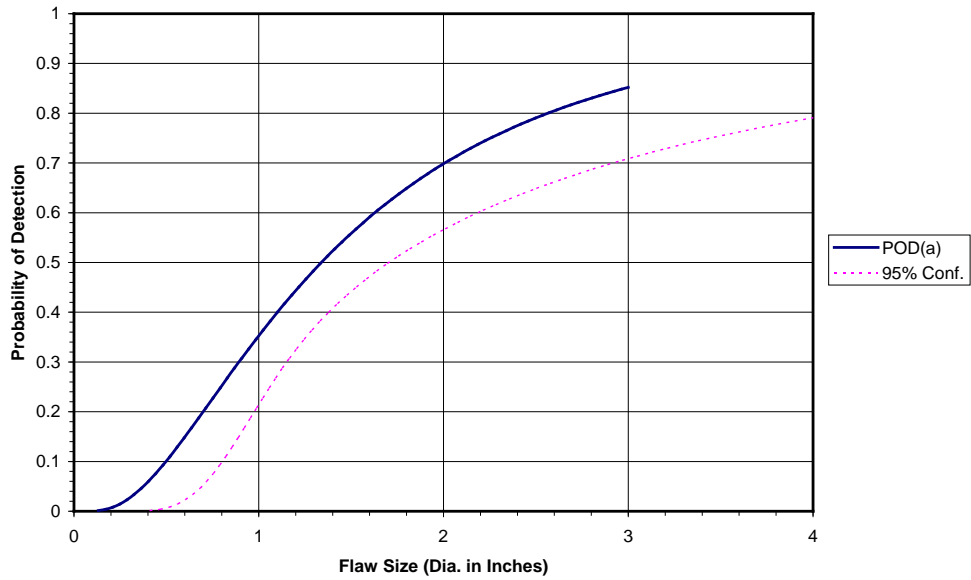


Figure 207. Cumulative PoD curve with 95% confidence bound—Airbus tap hammer, 9-ply carbon

Airbus Tap Hammer Cumulative PoD Curve with 95% Confidence Bound 9F

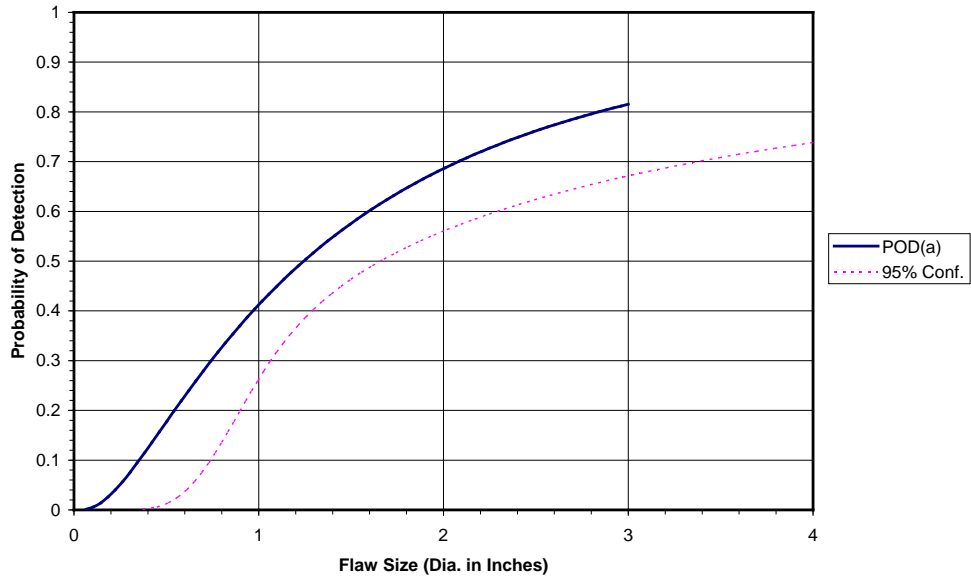


Figure 208. Cumulative PoD curve with 95% confidence bound—Airbus tap hammer, 9-ply fiberglass

Boeing Tap Hammer Cumulative PoD Curve with 95% Confidence Bound 3C

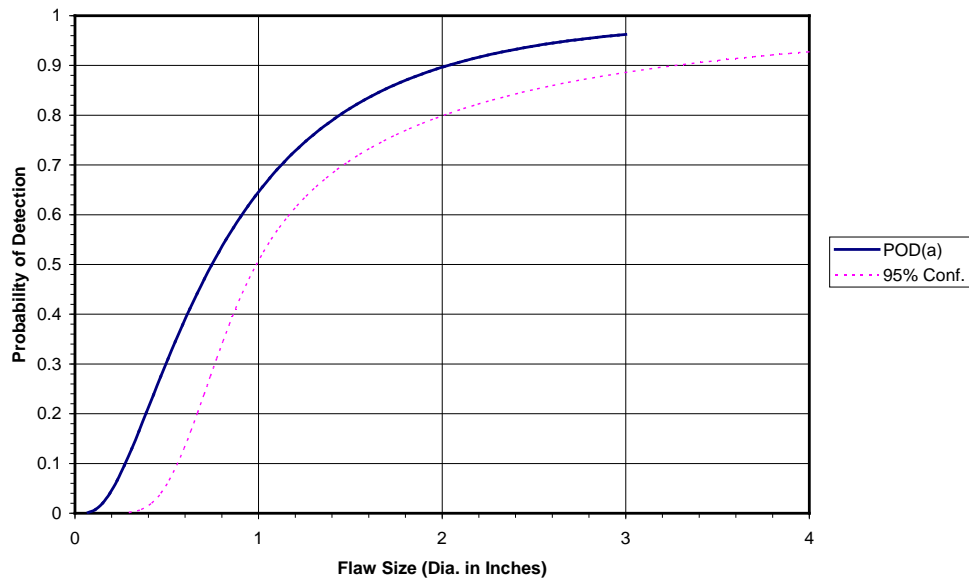


Figure 209. Cumulative PoD curve with 95% confidence bound—Boeing tap hammer, 3-ply carbon

Boeing Tap Hammer Cumulative PoD Curve with 95% Confidence Bound 3F

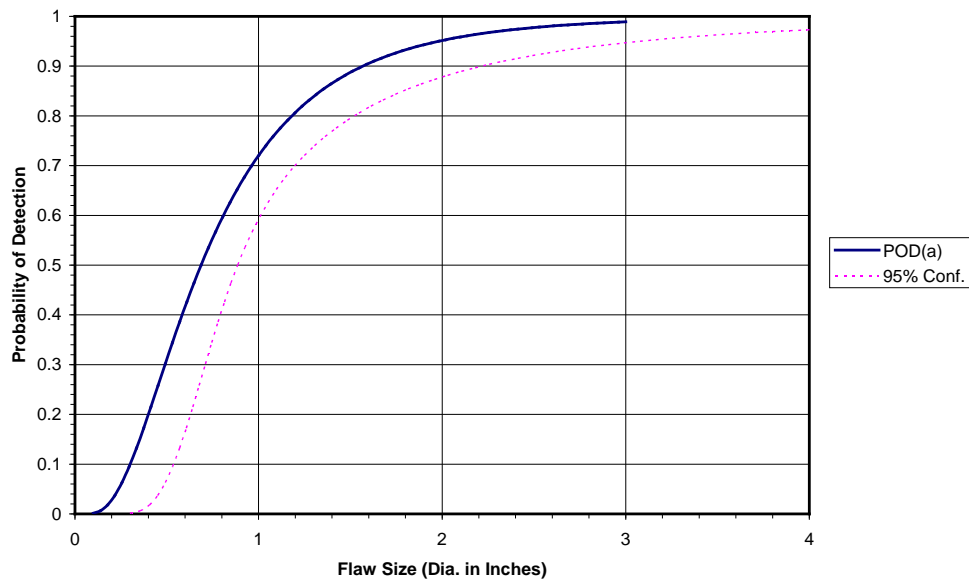


Figure 210. Cumulative PoD curve with 95% confidence bound—Boeing tap hammer, 3-ply Fiberglass

Boeing Tap Hammer Cumulative PoD Curve and 95% Confidence Bound 6C

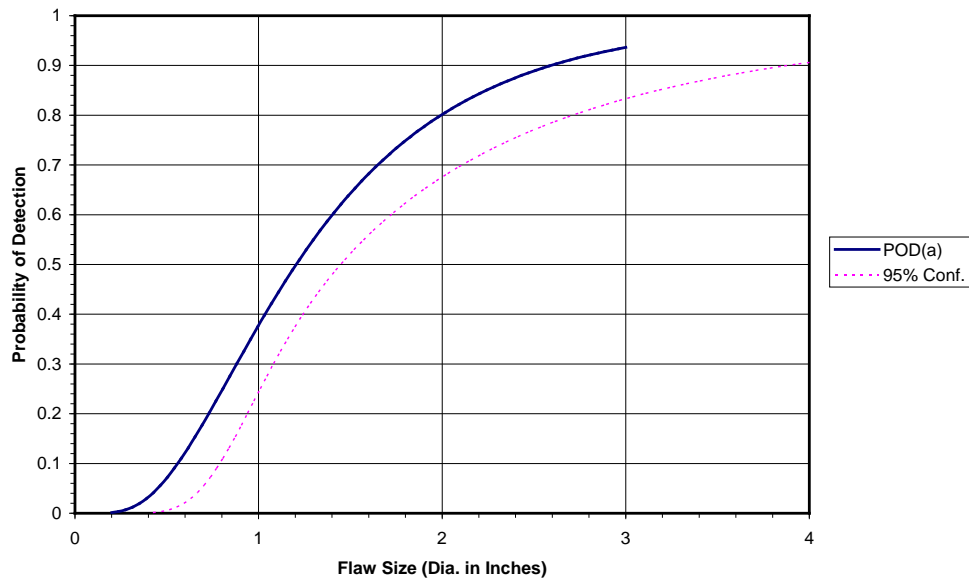


Figure 211. Cumulative PoD curve with 95% confidence bound—Boeing tap hammer,6-ply carbon

Boeing Tap Hammer Cumulative PoD Curve with 95% Confidence Bound 6F

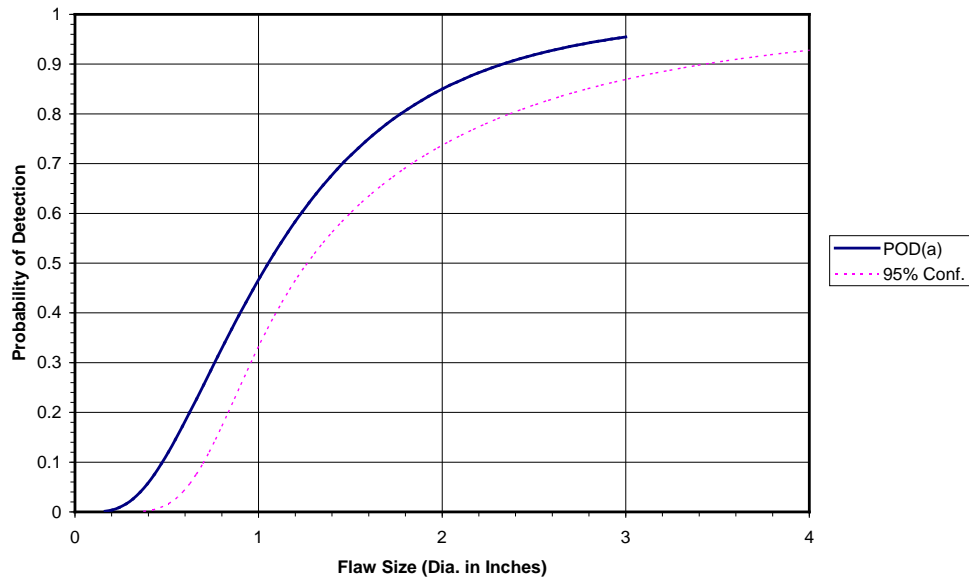


Figure 212. Cumulative PoD curve with 95% confidence bound—Boeing tap hammer, 6-ply fiberglass

Boeing Tap Hammer Cumulative PoD Curve with 95% Confidence Bound 9C

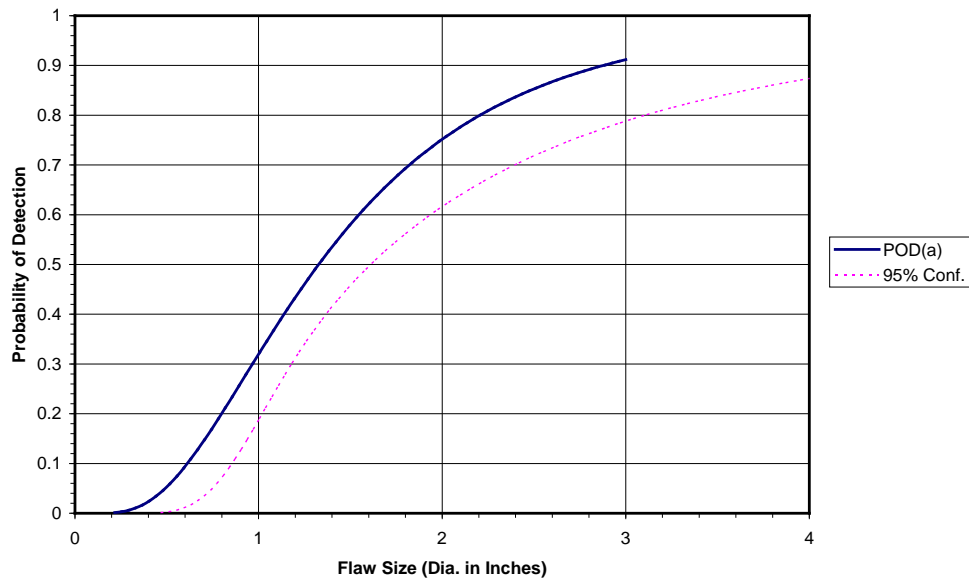


Figure 213. Cumulative PoD curve with 95% confidence bound—Boeing tap hammer,9-ply carbon

Boeing Tap Hammer Cumulative PoD Curve with 95% Confidence Bound 9F

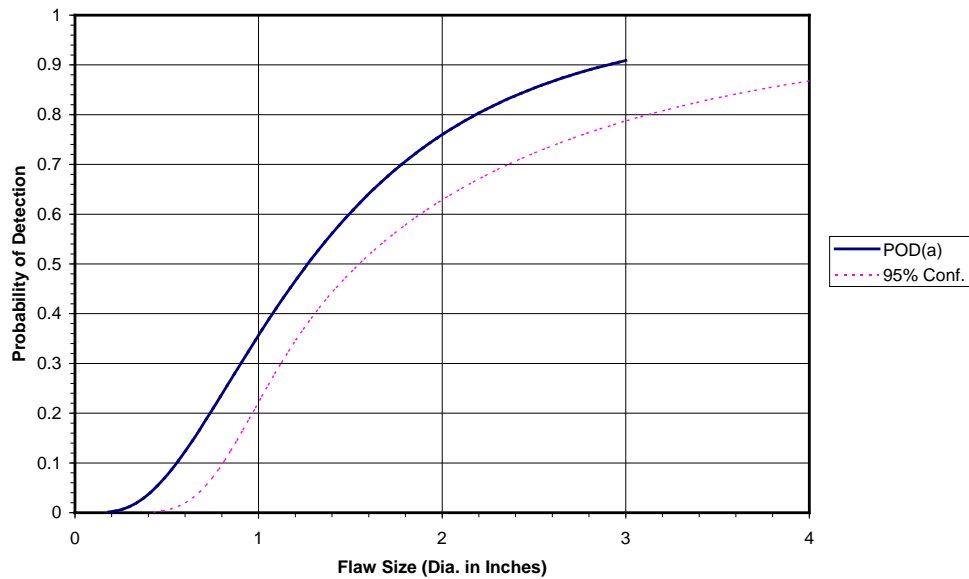


Figure 214. Cumulative PoD curve with 95% confidence bound—Boeing tap hammer, 9-ply fiberglass

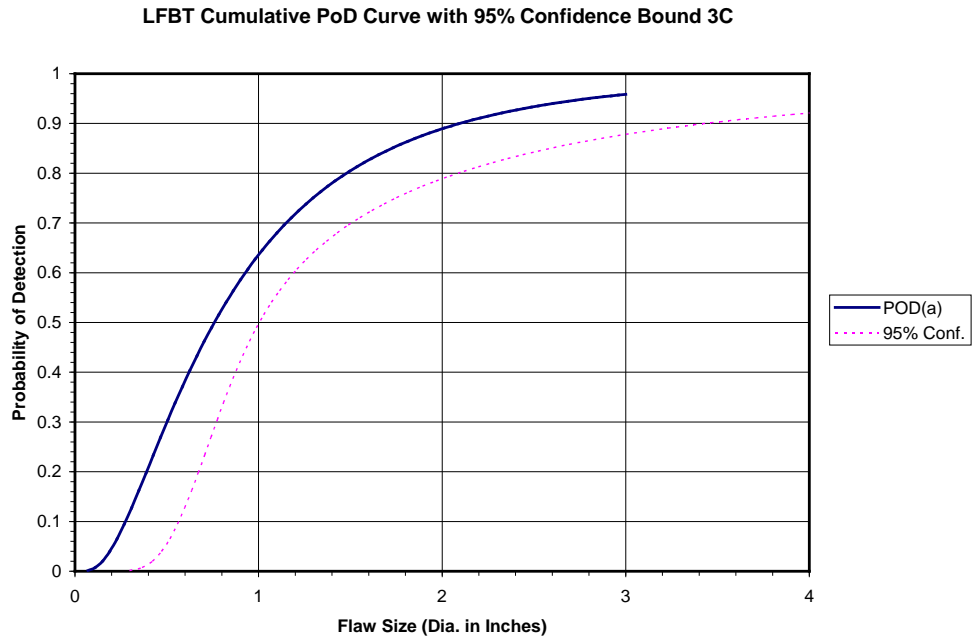


Figure 215. Cumulative PoD curve with 95% confidence bound—LFBT, 3-ply carbon

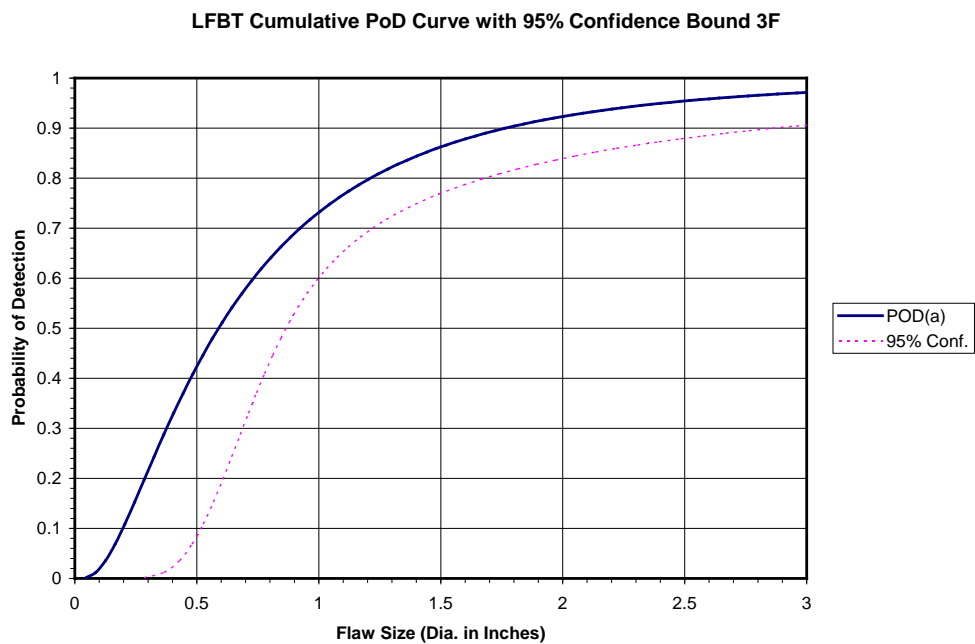


Figure 216. Cumulative PoD curve with 95% confidence bound—LFBT, 3-ply fiberglass

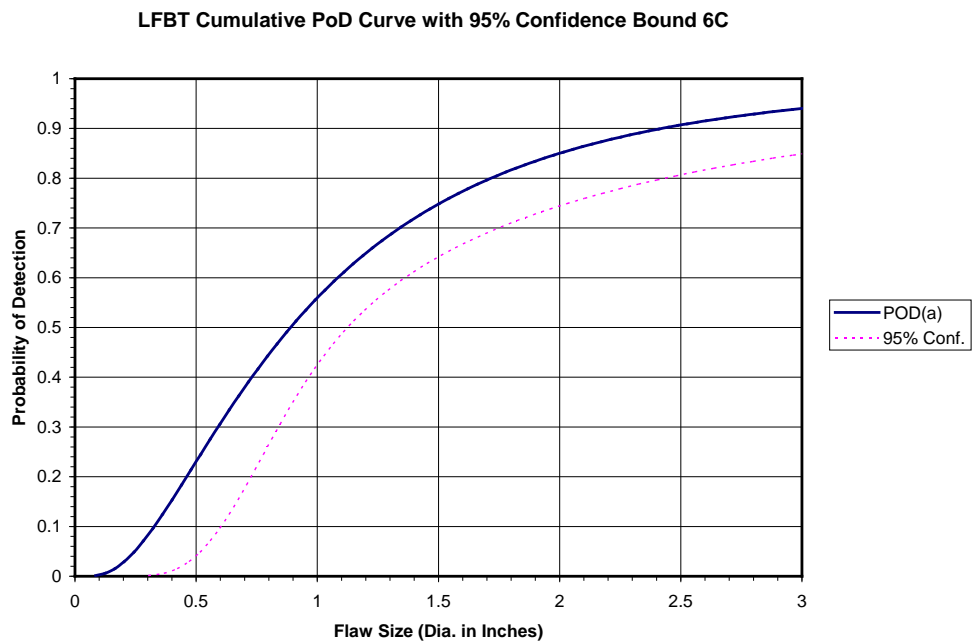


Figure 217. Cumulative PoD curve with 95% confidence bound—LFBT, 6-ply carbon

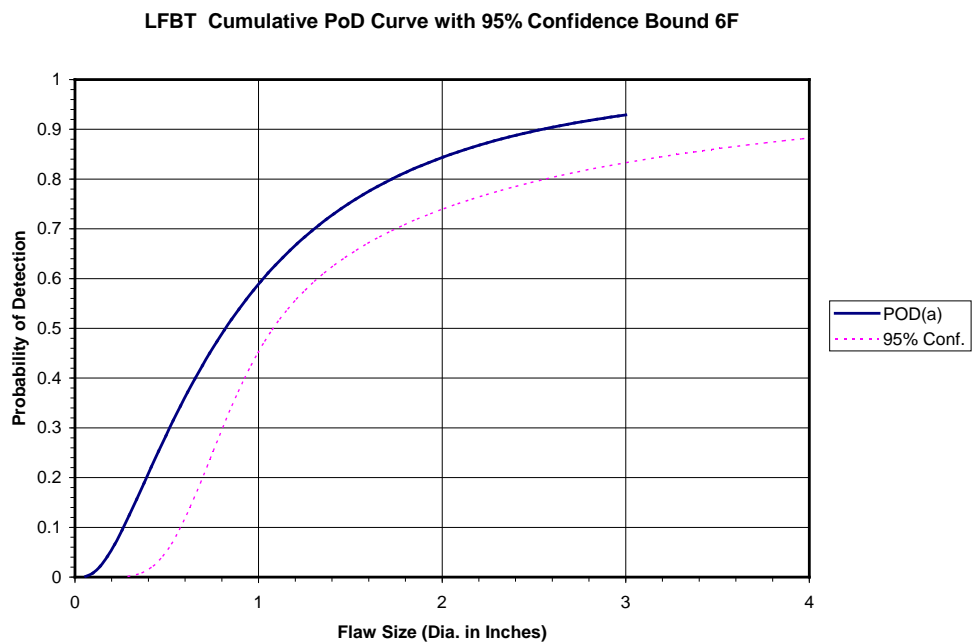


Figure 218. Cumulative PoD curve with 95% confidence bound—LFBT, 6-ply fiberglass

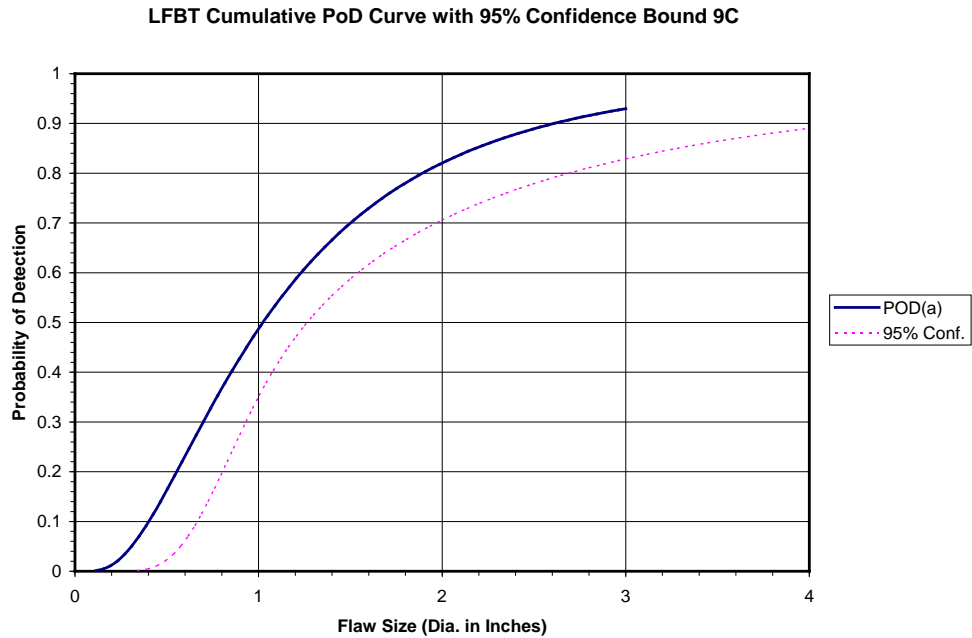


Figure 219. Cumulative PoD curve with 95% confidence bound—LFBT, 9-ply carbon

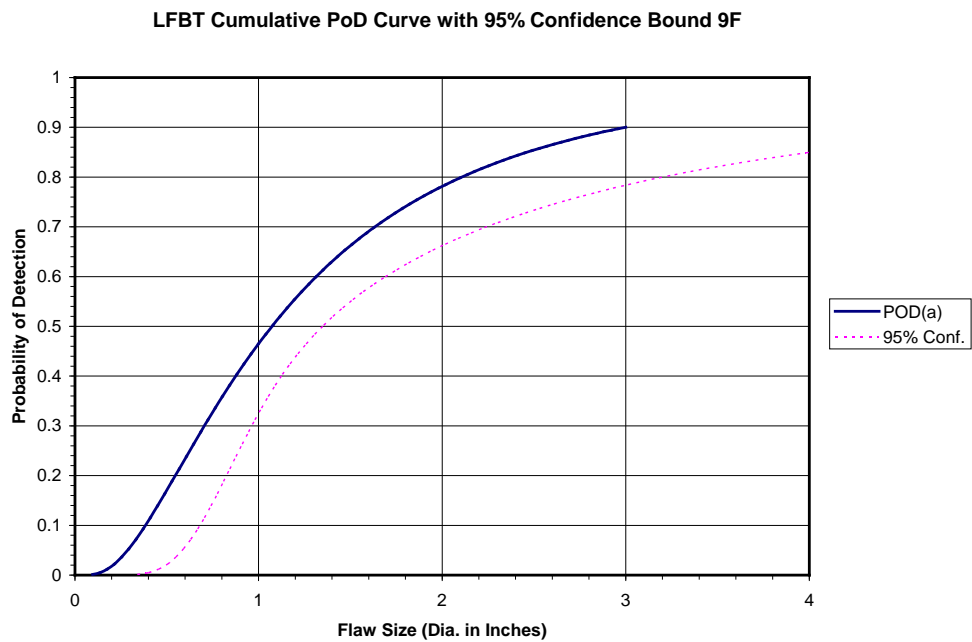


Figure 220. Cumulative PoD curve with 95% confidence bound—LFBT, 9-ply fiberglass

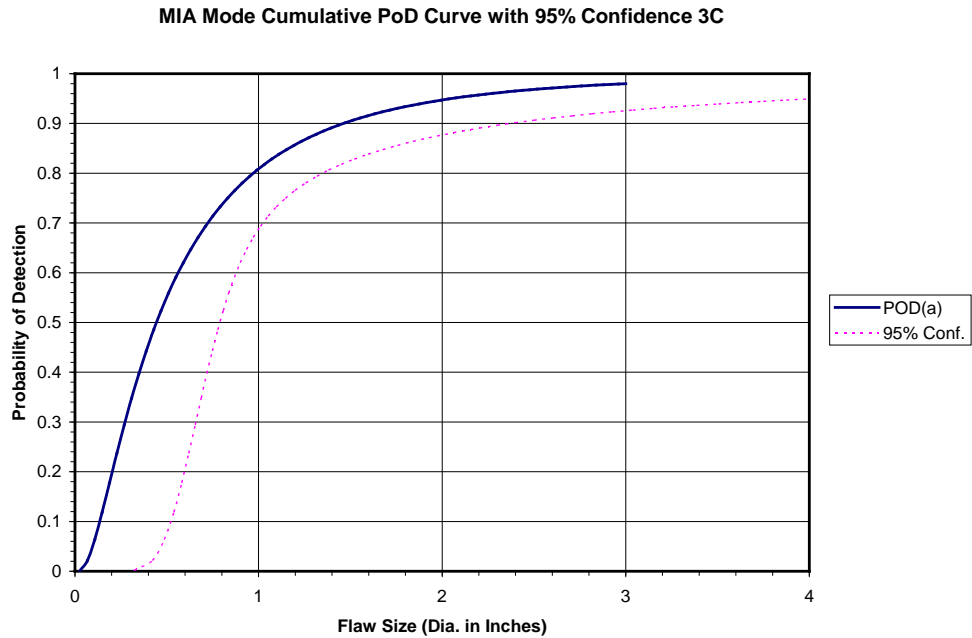


Figure 221. Cumulative PoD curve with 95% confidence bound—MIA, 3-ply carbon

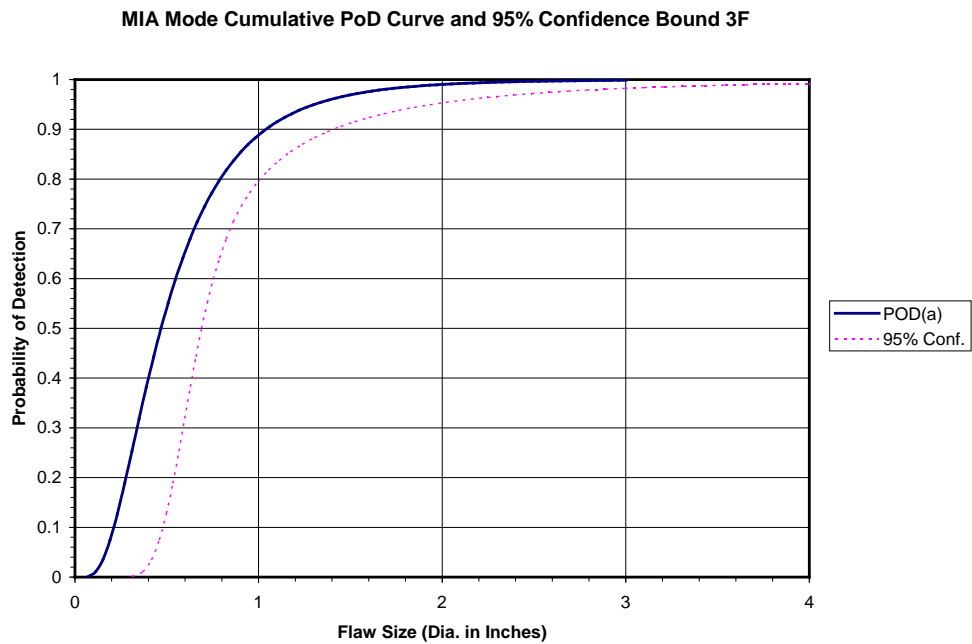


Figure 222. Cumulative PoD curve with 95% confidence bound—MIA, 3-ply fiberglass

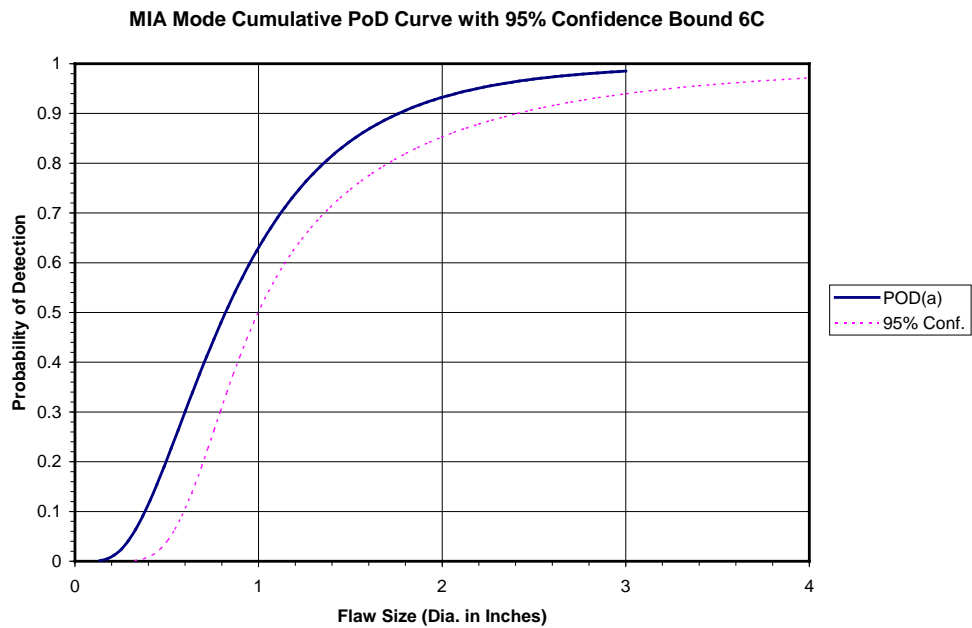


Figure 223. Cumulative PoD curve with 95% confidence bound—MIA, 6-ply carbon

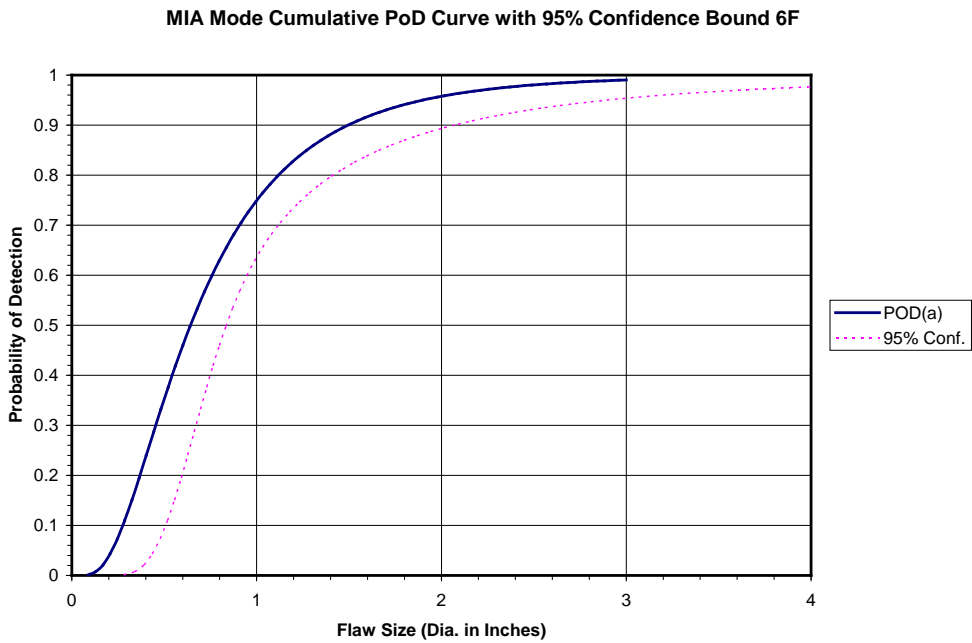


Figure 224. Cumulative PoD curve with 95% confidence bound—MIA, 6-ply fiberglass

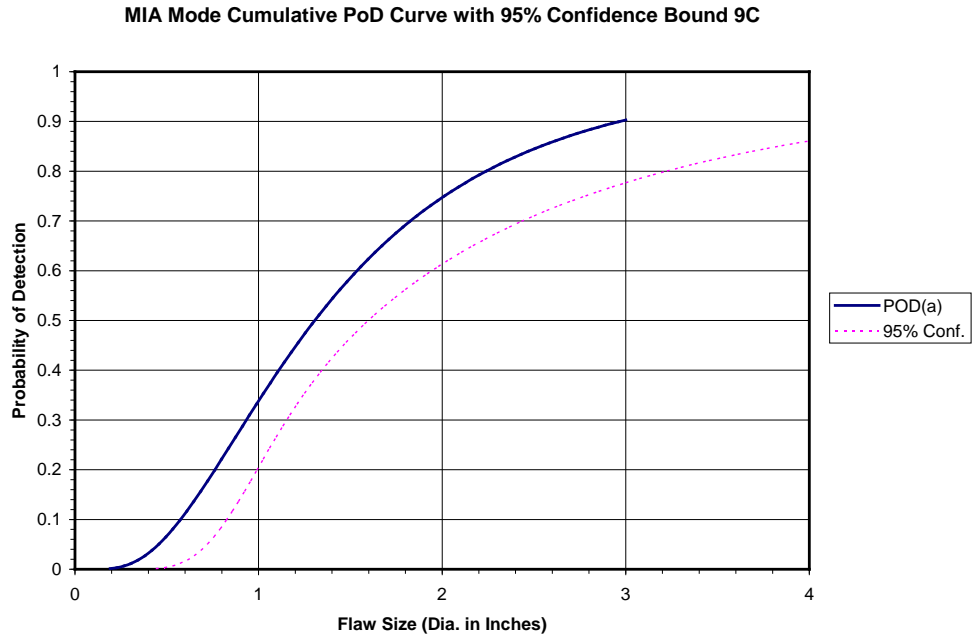


Figure 225. Cumulative PoD curve with 95% confidence bound—MIA, 9-ply carbon

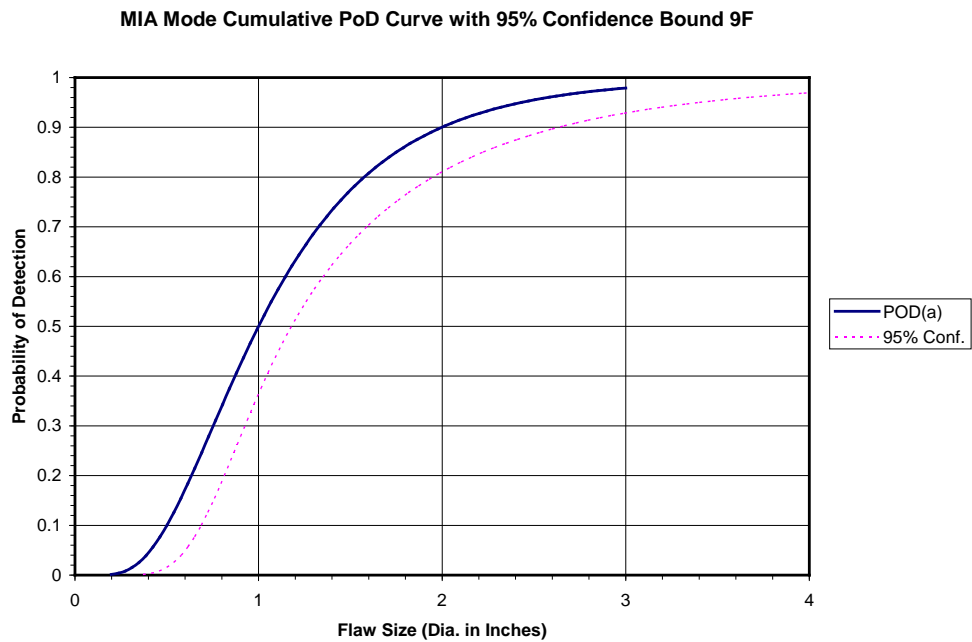


Figure 226. Cumulative PoD curve with 95% confidence bound—MIA, 9-ply fiberglass

Wichitech DTH Cumulative PoD Curve with 95% Confidence Bound 3C

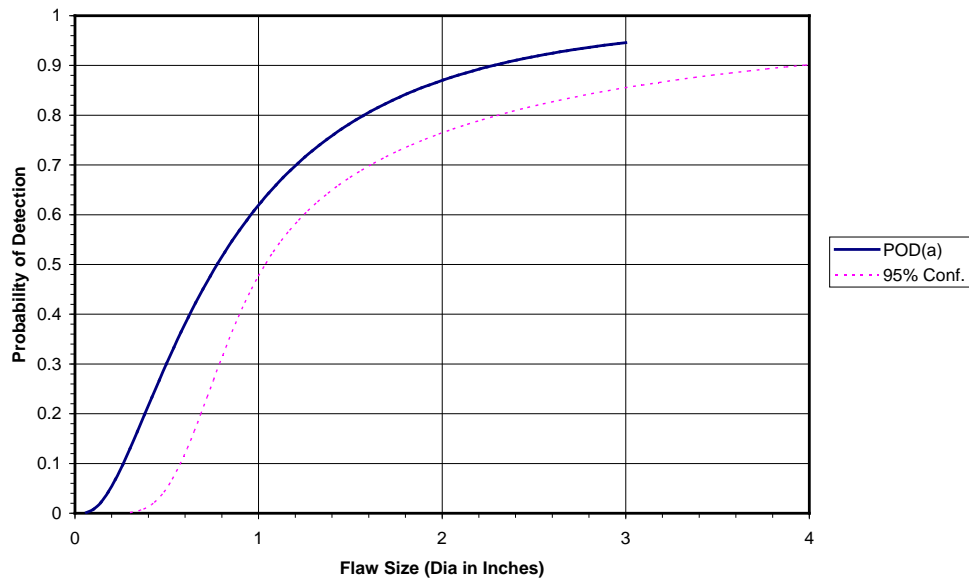


Figure 227. Cumulative PoD curve with 95% confidence bound—WichiTech DTH, 3-ply carbon

Wichitech DTH Cumulative PoD Curve with 95% Confidence Bound 3F

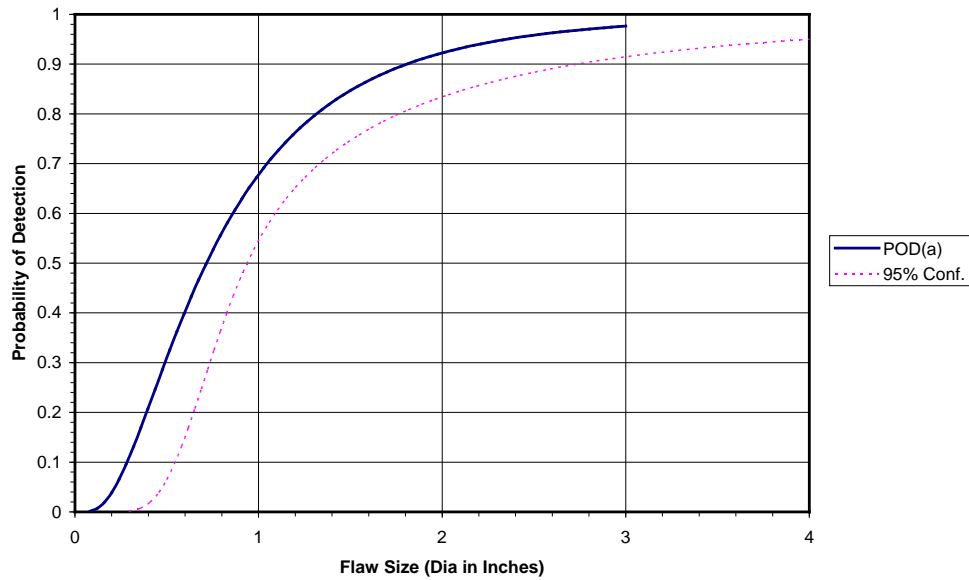


Figure 228. Cumulative PoD curve with 95% confidence bound—WichiTech DTH, 3-ply fiberglass

Wichitech DTH Cumulative PoD Curve with 95% Confidence Bound 6C

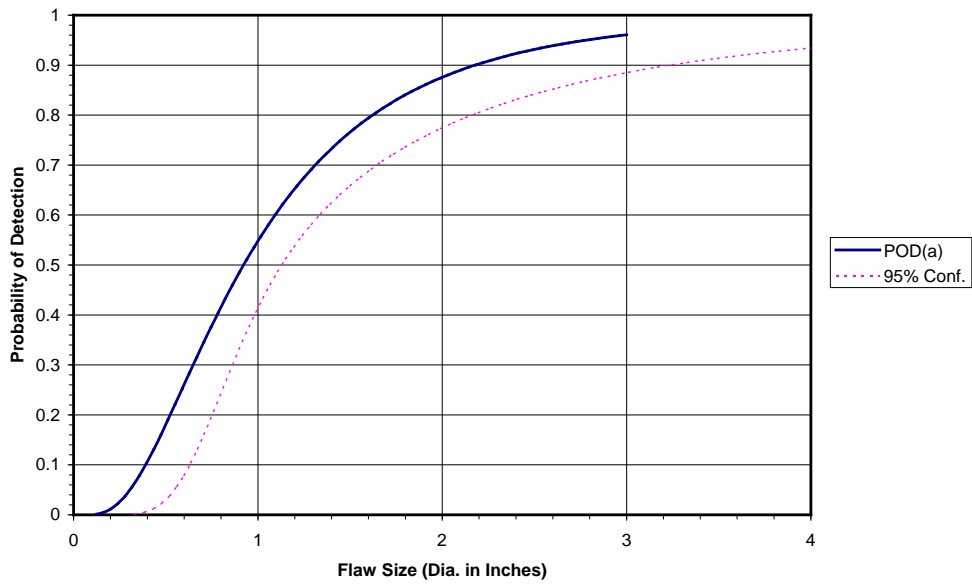


Figure 229. Cumulative PoD curve with 95% confidence bound—WichiTech DTH, 6-ply carbon

Wichitech DTH Cumulative PoD Curve with 95% Confidence Bound 6F

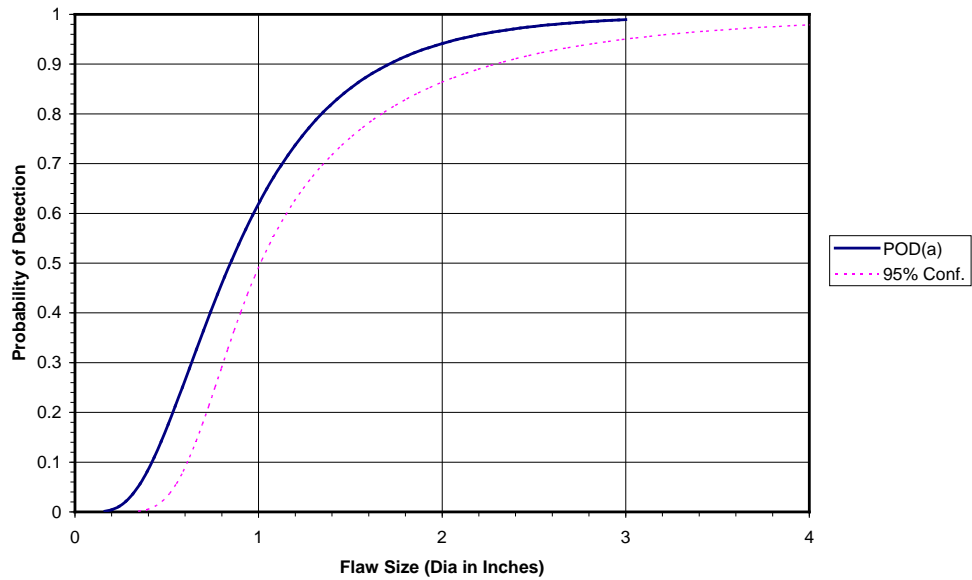


Figure 230. Cumulative PoD curve with 95% confidence bound—WichiTech DTH, 6-ply fiberglass

Wichitech DTH Cumulative PoD Curve with 95% Confidence Bound 9C

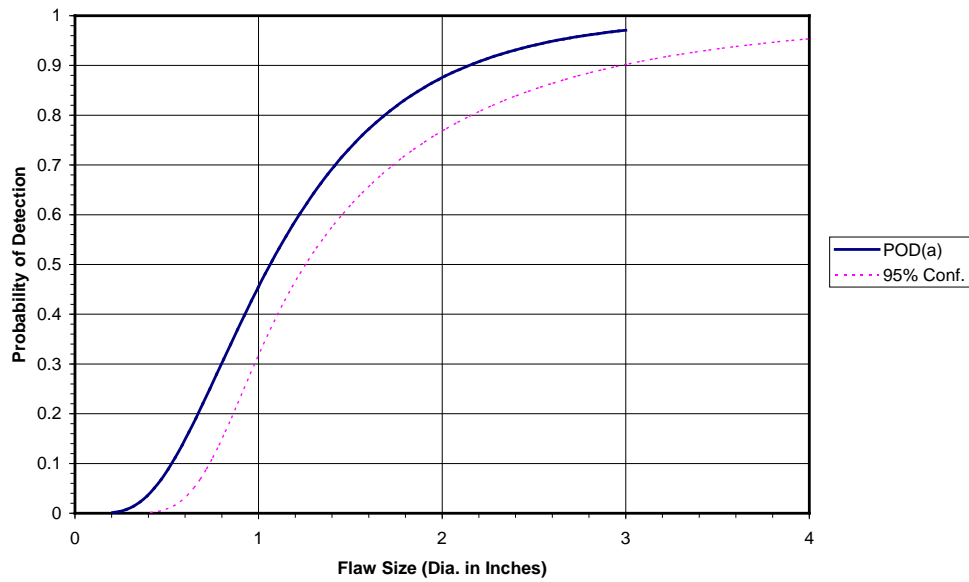


Figure 231. Cumulative PoD curve with 95% confidence bound—WichiTech DTH, 9-ply carbon

Wichitech DTH Cumulative PoD Curve with 95% Confidence Bound 9F

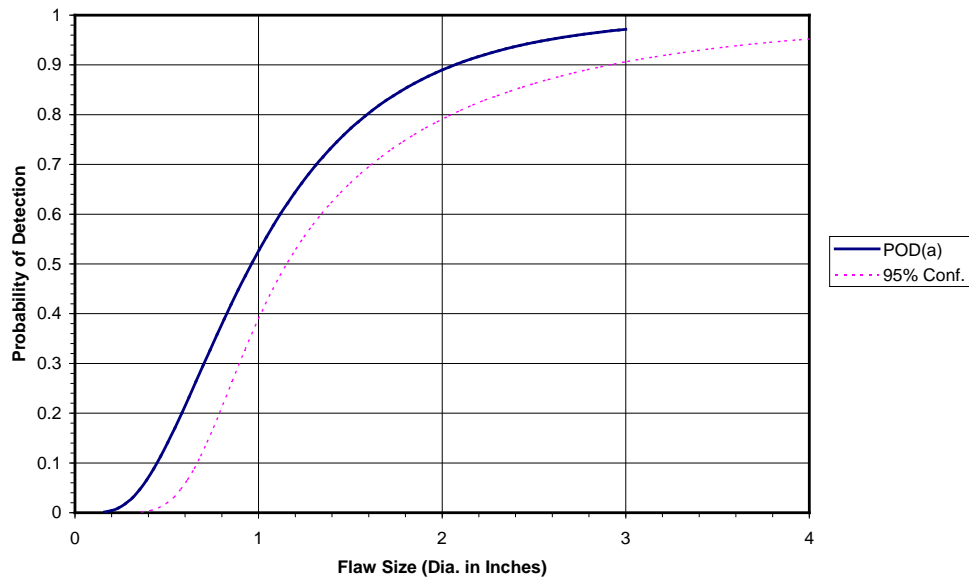


Figure 232. Cumulative PoD curve with 95% confidence bound—WichiTech DTH, 9-ply fiberglass

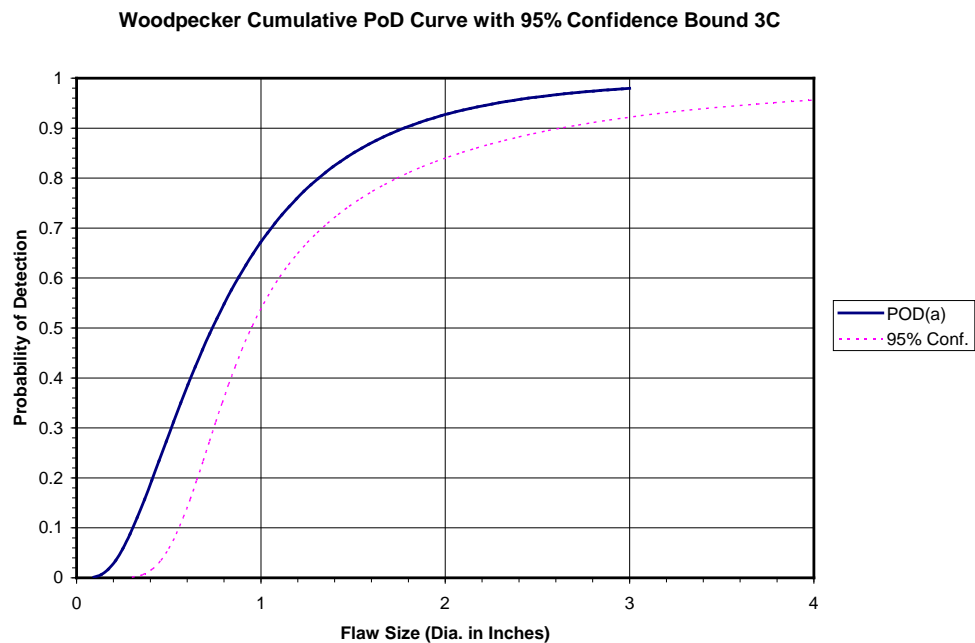


Figure 233. Cumulative PoD curve with 95% confidence bound—Woodpecker, 3-ply carbon

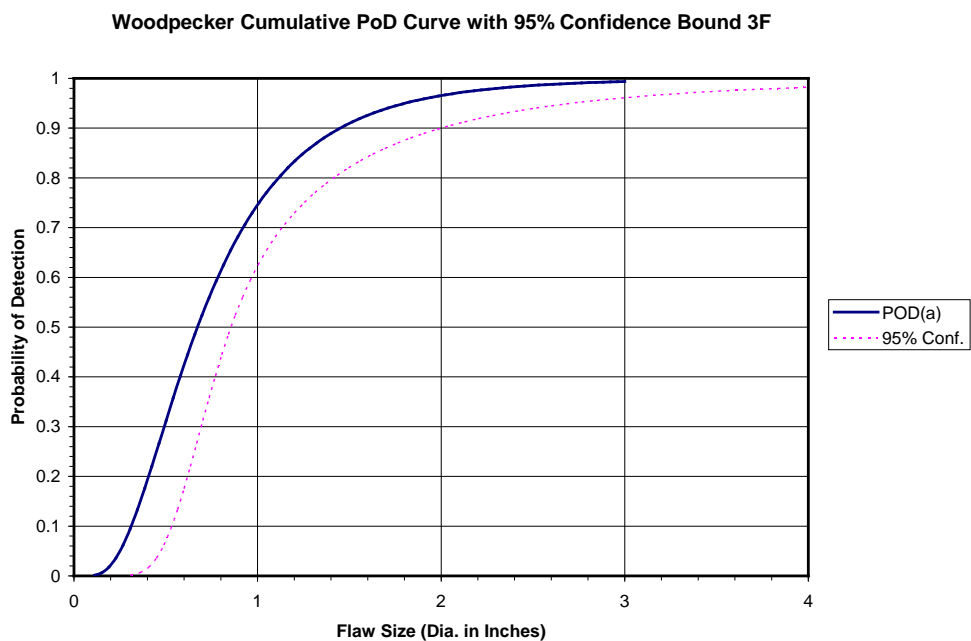


Figure 234. Cumulative PoD curve with 95% confidence bound—Woodpecker, 3-ply fiberglass

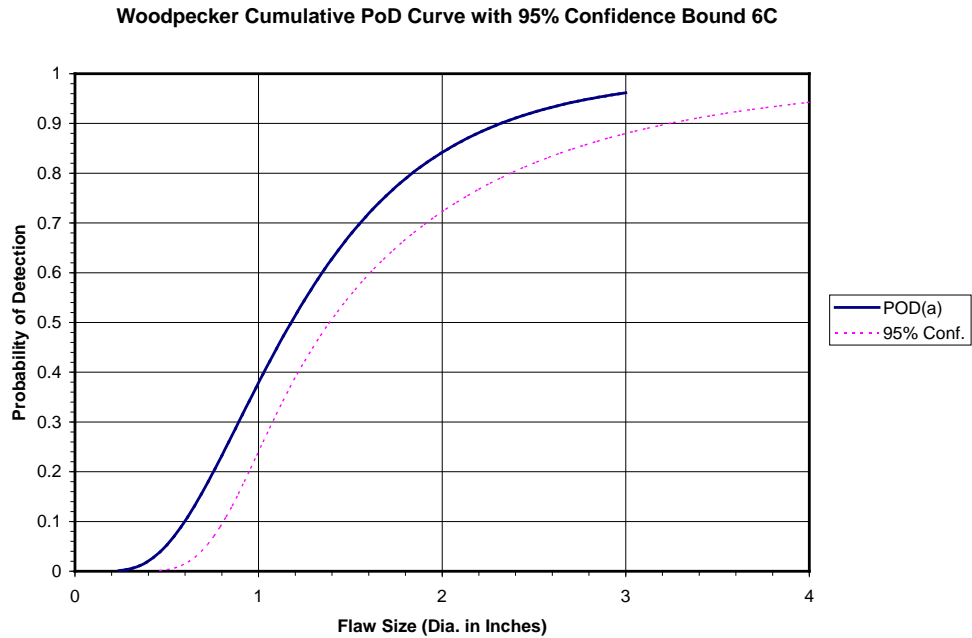


Figure 235. Cumulative PoD curve with 95% confidence bound—Woodpecker, 6-ply carbon

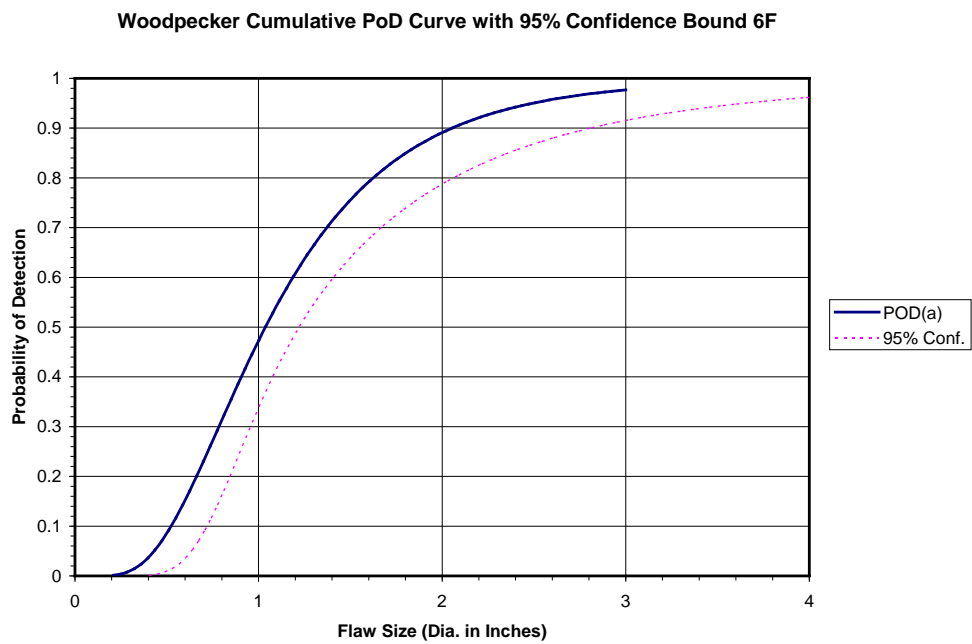


Figure 236. Cumulative PoD curve with 95% confidence bound—Woodpecker, 6-ply fiberglass

Woodpecker Cumulative PoD Curve with 95% Confidence Bound 9C

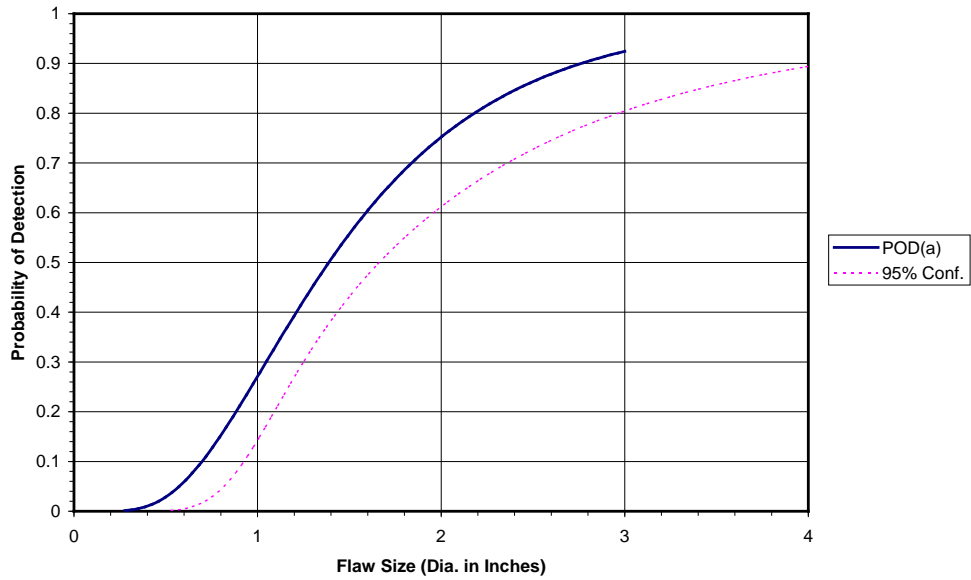


Figure 237. Cumulative PoD curve with 95% confidence bound—Woodpecker, 9-ply carbon

Woodpecker Cumulative PoD Curve with 95% Confidence Bound 9F

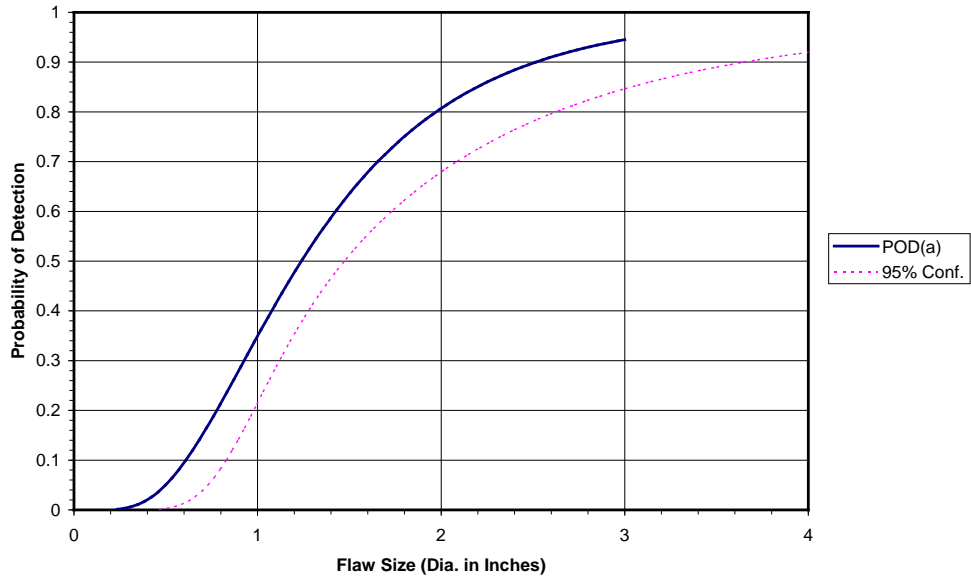
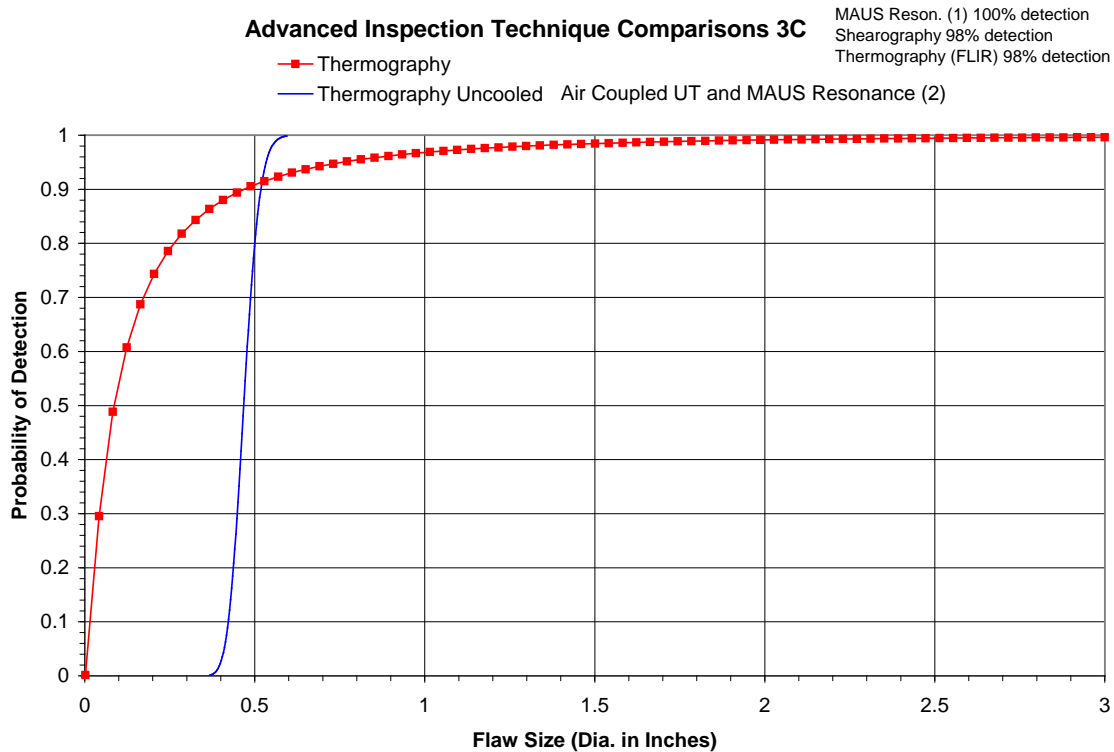


Figure 238. Cumulative PoD curve with 95% confidence bound—Woodpecker, 9-ply fiberglass

The PoD curves, along with tabulated values in figures 239–250, display and compare the performance of the advanced NDI techniques in each of the specific composite honeycomb structure categories. Note that PoD curves are not plotted for specific methods when the detection percentage is exceptionally high. In these cases, it is not possible to generate a curve fit for this data because of the extremely high flaw detection rate. For these methods, the flaw detection rate is listed at the top of the PoD plots. However, the 90% PoD values for all methods are listed in each figure. For each category of 3F, 3C, 6F, 6C, 9F, and 9C, the results are divided into Tier 1 (top set of performers) and Tier 2 (second set of performers) groups. This allows for greater clarity in the PoD plots. It can be seen that the best performing advanced NDI methods produce 90% PoD levels at flaws that are less than 0.5" diameter.



3-Ply Carbon		
Device	False Calls	90% POD Value
MAUS Resonance 1	3	$\leq .50$
Shearography	0	$\leq .50$
Thermography (FLIR)	0	$\leq .50$
Thermography	2	$\leq .50$
Thermography (uncooled)	0	0.52
Air-coupled UT	0	0.52
MAUS Resonance 2	2	0.53

Figure 239. Individual PoD curve comparisons along with tabulated values for advanced inspection methods on 3-ply carbon (Tier 1 results)

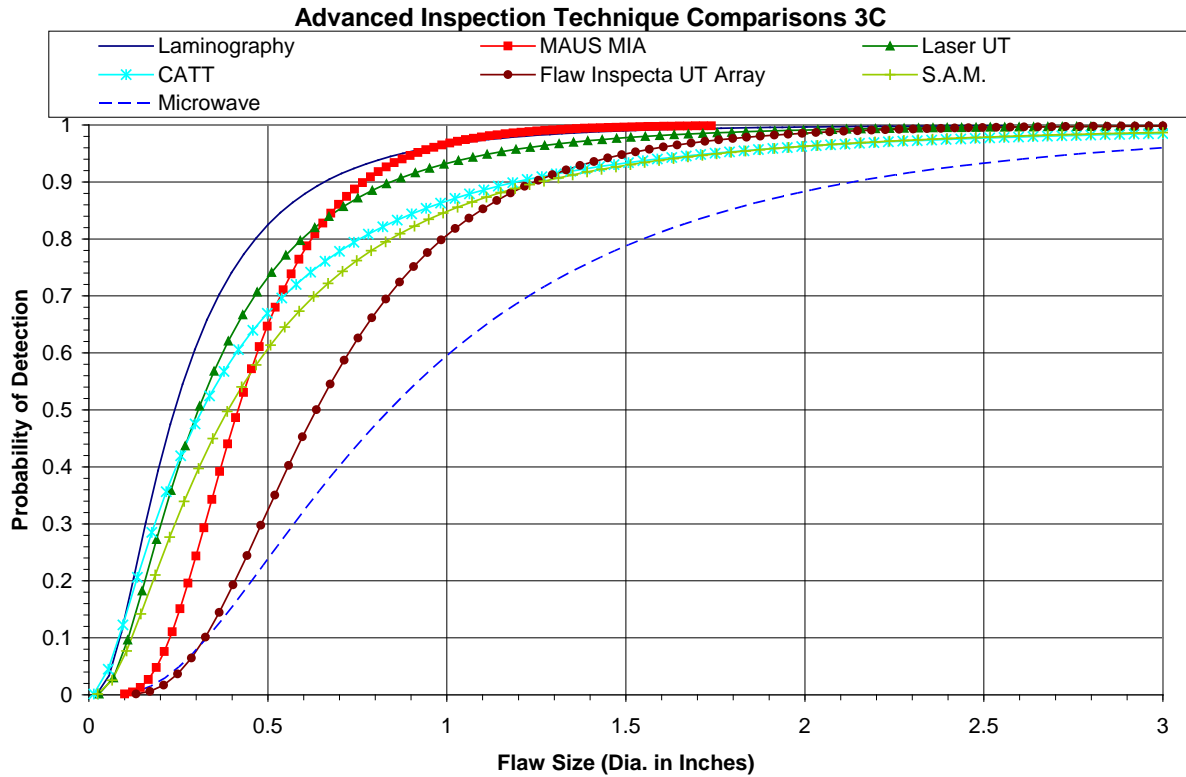
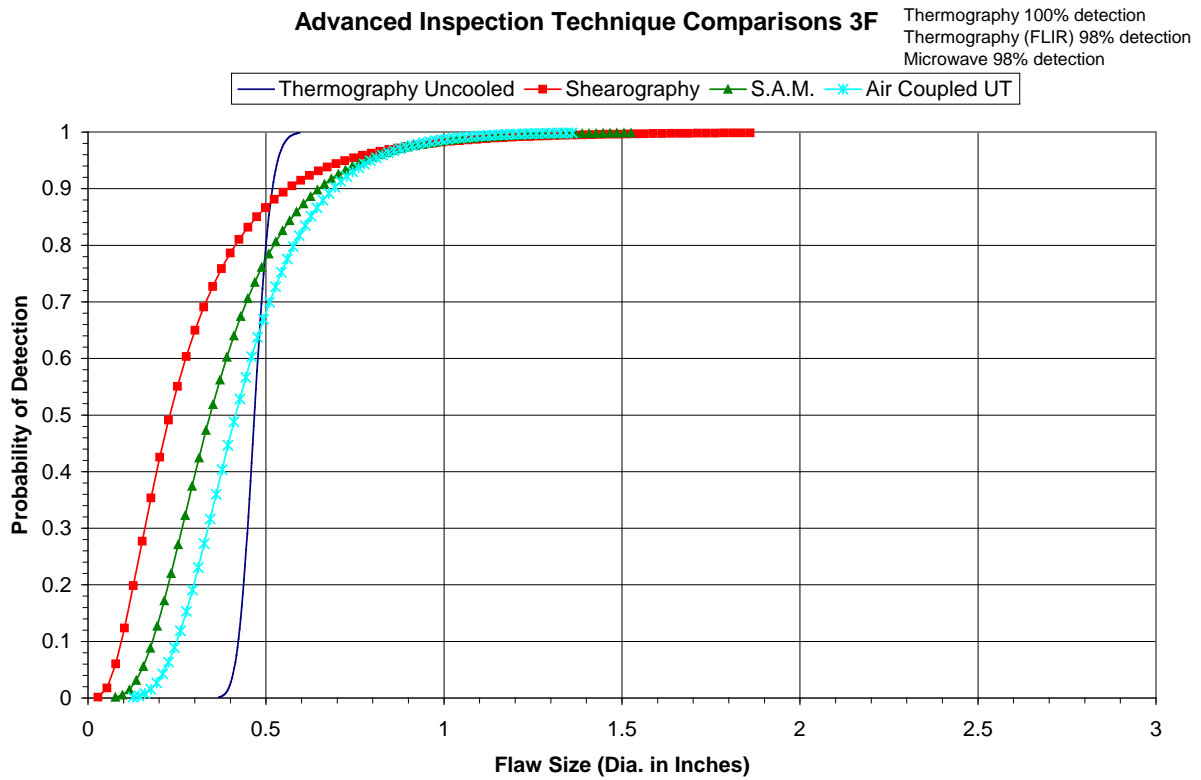


Figure 240. Individual PoD curve comparisons along with tabulated values for advanced inspection methods on 3-ply carbon (Tier 2 results)



3-Ply Fiberglass		
Device	False Calls	90% POD Value
Thermography	0	$\leq .50$
Thermography (FLIR)	0	$\leq .50$
Microwave	2	$\leq .50$
Thermography (uncooled)	0	0.52
Shearography	1	0.56
SAM	0	0.65
Air-coupled UT	0	0.69

Figure 241. Individual PoD curve comparisons along with tabulated values for advanced inspection methods on 3-ply fiberglass (Tier 1 results)

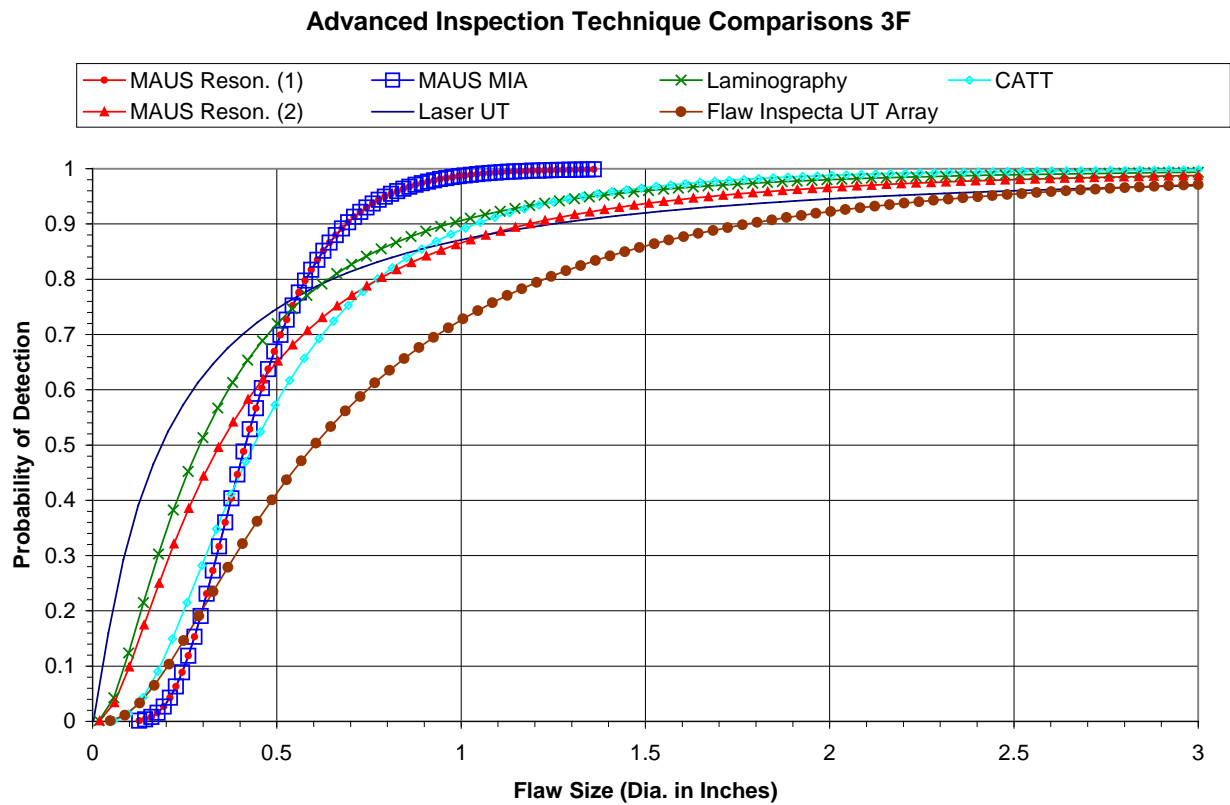
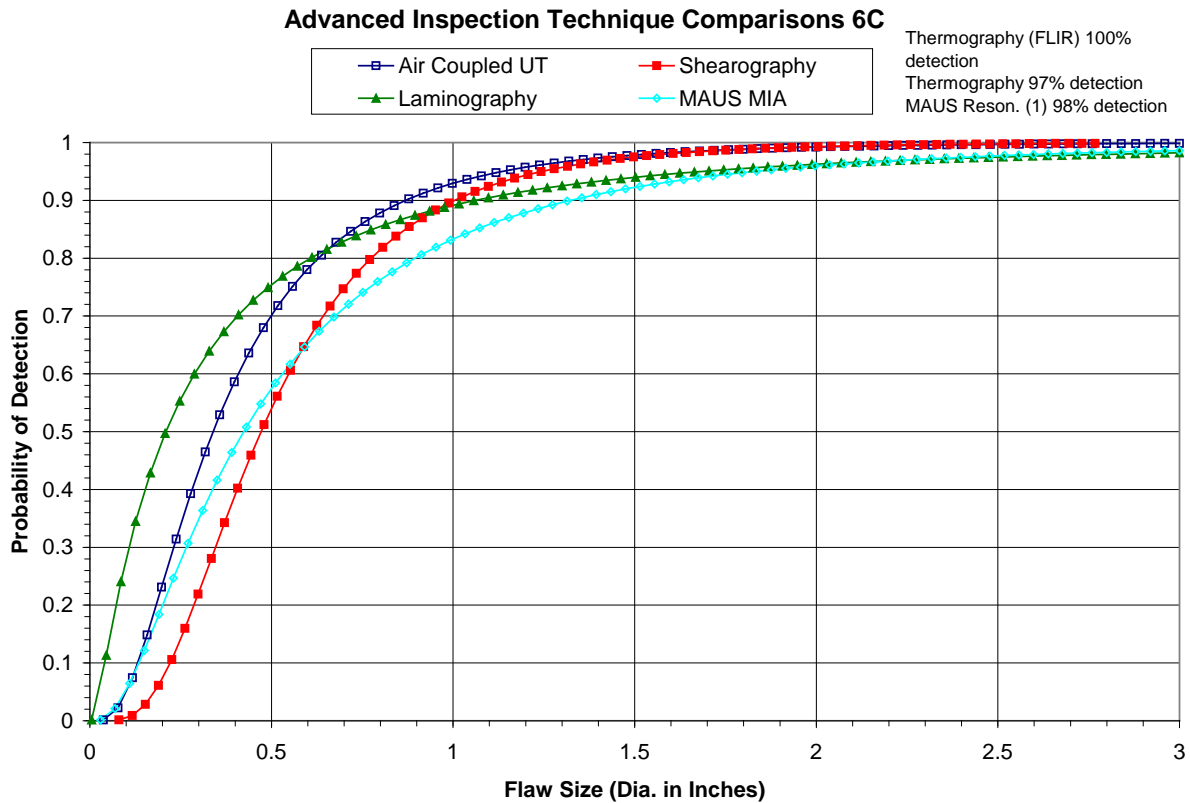
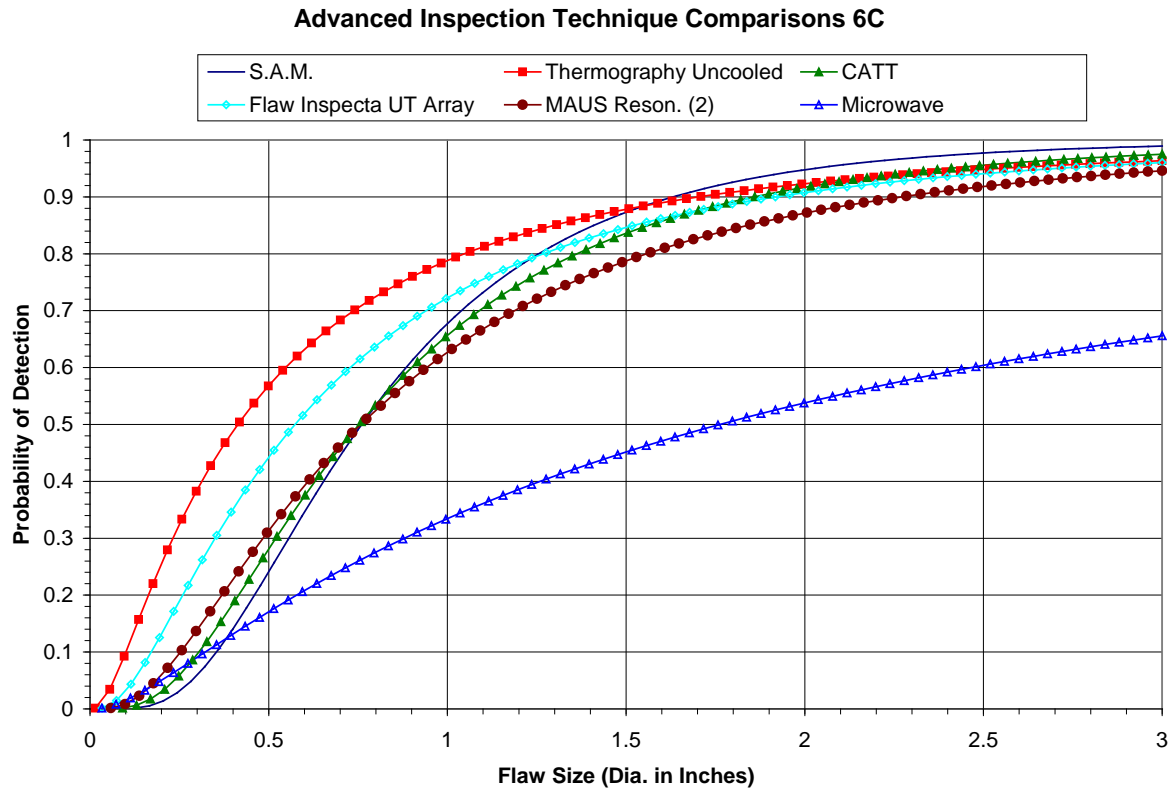


Figure 242. Individual PoD curve comparisons along with tabulated values for advanced inspection methods on 3-ply fiberglass (Tier 2 results)



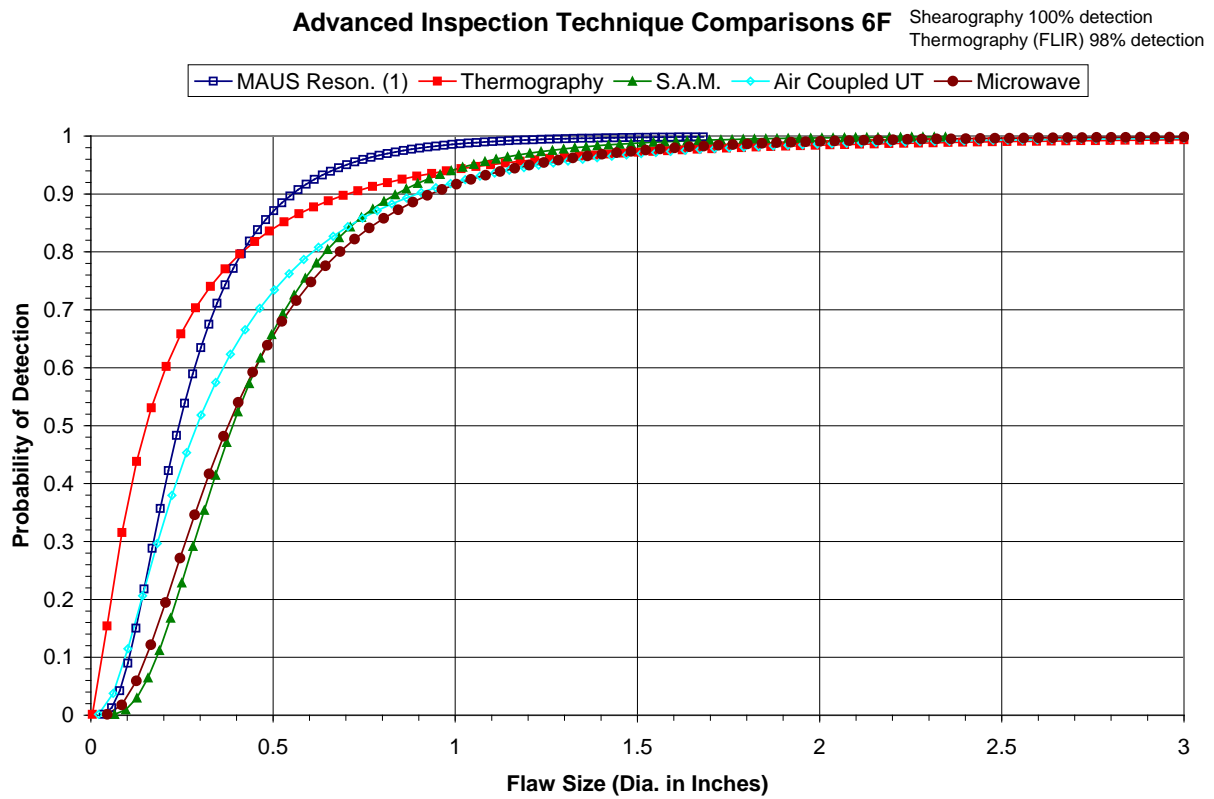
6-Ply Carbon		
Device	False Calls	90% POD Value
Thermography (FLIR)	1	$\leq .50$
Thermography	2	$\leq .50$
MAUS Resonance 1	12	$\leq .50$
Air-coupled UT	0	0.87
Shearography	0	1.00
Laminography	0	1.10
MAUS MIA	6	1.32

Figure 243. Individual PoD curve comparisons along with tabulated values for advanced inspection methods on 6-ply carbon (Tier 1 results)



6-Ply Carbon		
Device	False Calls	90% POD Value
SAM	37	1.63
Thermography (uncooled)	2	1.70
CATT	1	1.85
FlawInspecta UT Array	0	1.92
MAUS Resonance 2	4	2.27
Microwave	10	>3.00
Laser UT	N/A	N/A

Figure 244. Individual PoD curve comparisons along with tabulated values for advanced inspection methods on 6-ply carbon (Tier 2 results)



6-Ply Fiberglass		
Device	False Calls	90% POD Value
Shearography	0	$\leq .50$
Thermography (FLIR)	4	$\leq .50$
MAUS Resonance 1	9	0.55
Thermography	3	0.70
SAM	8	0.84
Air-coupled UT	0	0.90
Microwave	12	0.93

Figure 245. Individual PoD curve comparisons along with tabulated values for advanced inspection methods on 6-ply fiberglass (Tier 1 results)

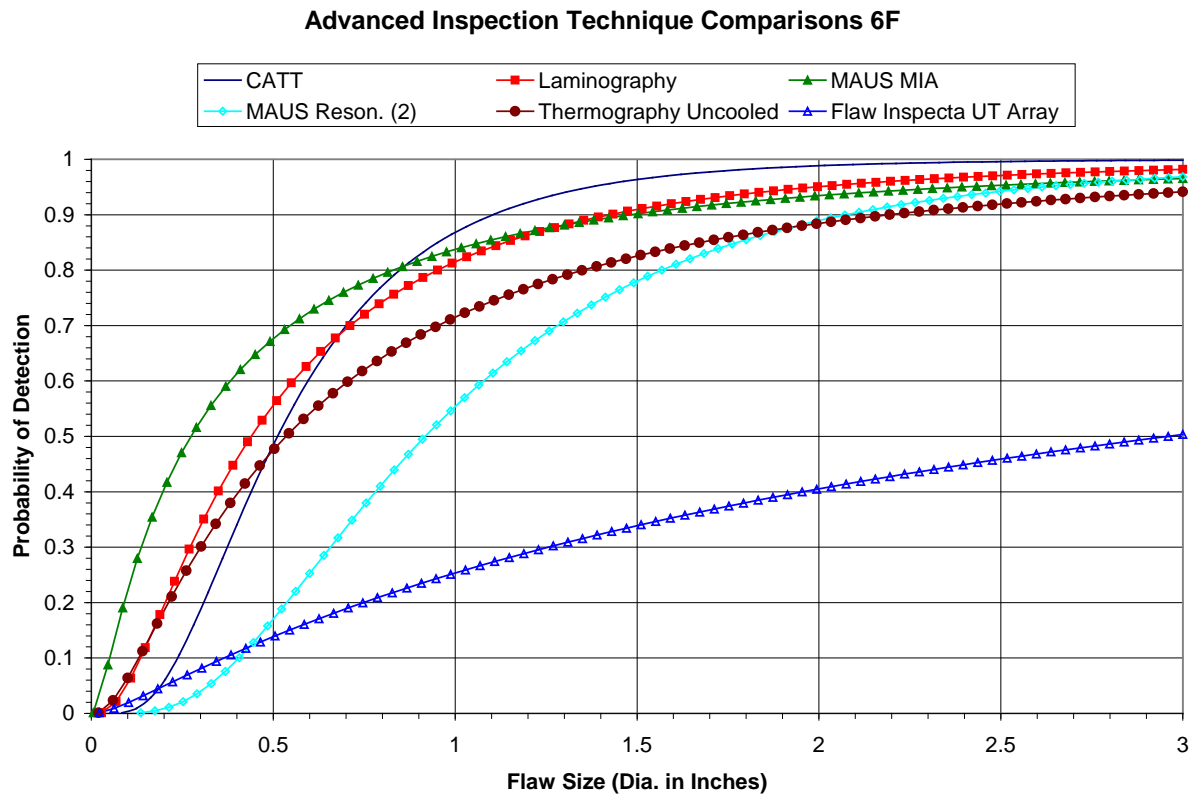
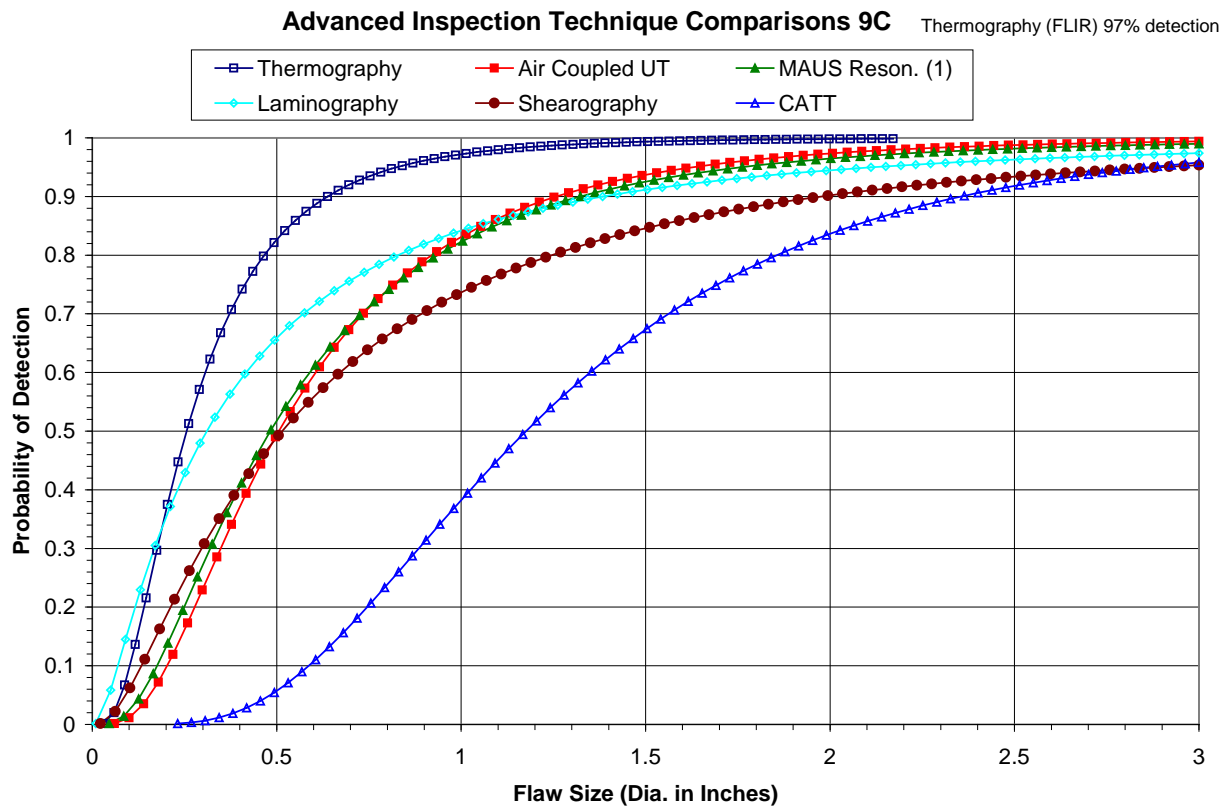


Figure 246. Individual PoD curve comparisons along with tabulated values for advanced inspection methods on 6-ply fiberglass (Tier 2 results)



9-Ply Carbon		
Device	False Calls	90% POD Value
Thermography (FLIR)	0	$\leq .50$
Thermography	0	0.64
Air-coupled UT	2	1.26
MAUS Resonance 1	0	1.32
Laminography	0	1.39
Shearography	0	2.00
CATT	4	2.36

Figure 247. Individual PoD curve comparisons along with tabulated values for advanced inspection methods on 9-ply carbon (Tier 1 results)

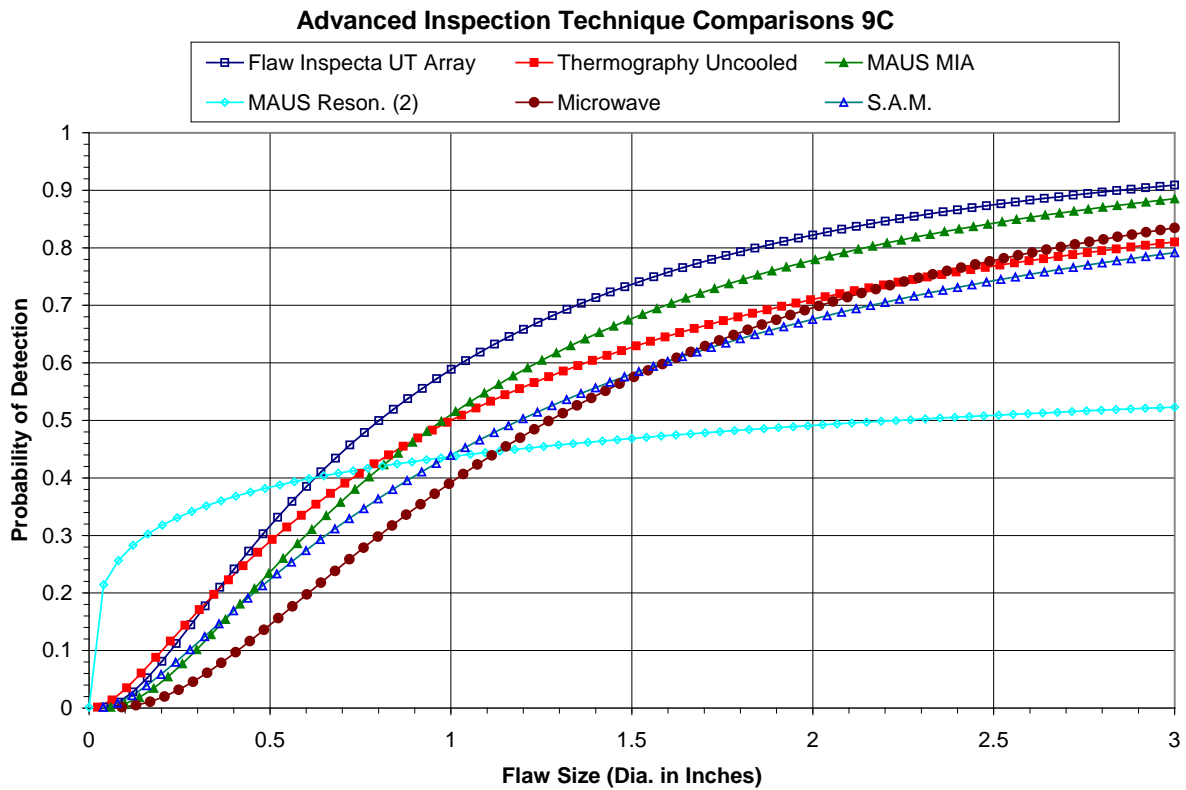
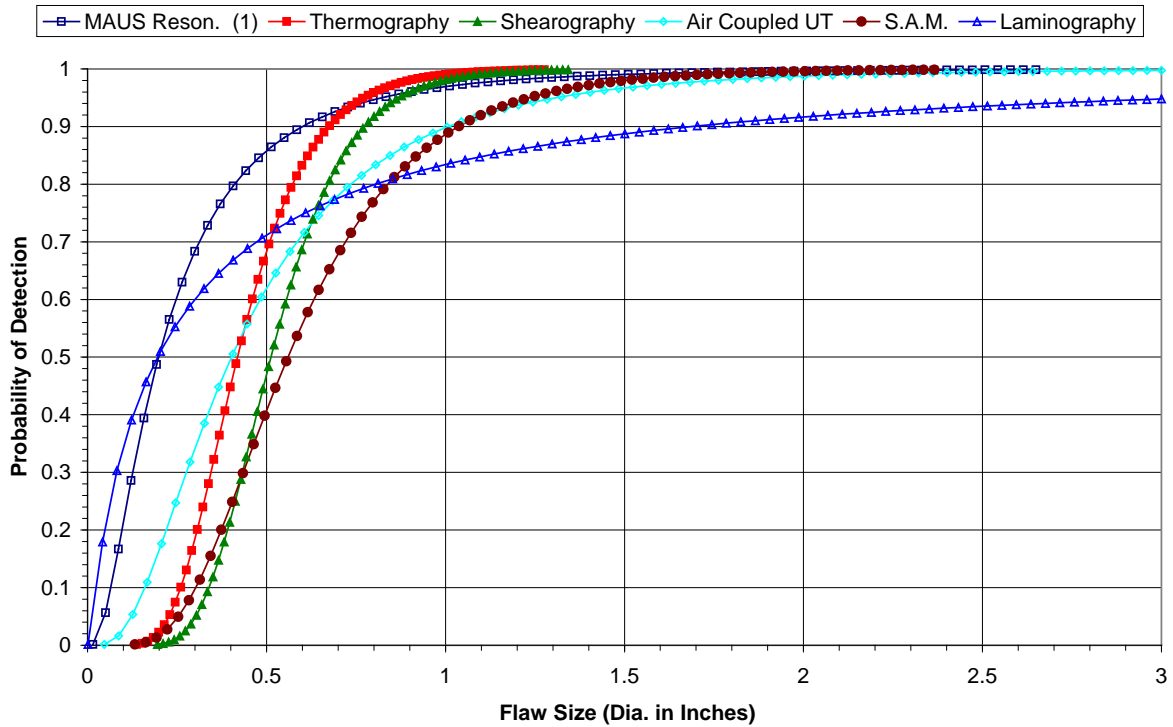


Figure 248. Individual PoD curve comparisons along with tabulated values for advanced inspection methods on 9-ply carbon (Tier 2 results)

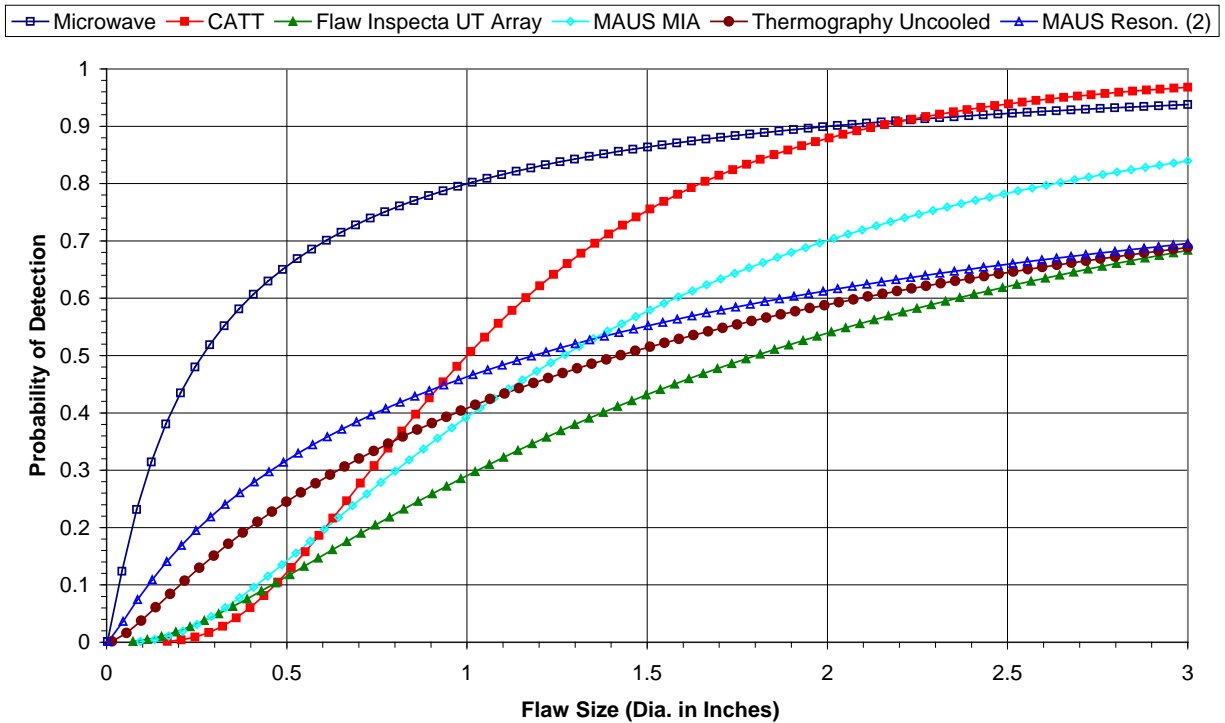
Advanced Inspection Technique Comparisons 9F Thermography (FLIR) 97% detection



9-Ply Fiberglass		
Device	False Calls	90% POD Value
Thermography (FLIR)	1	$\leq .50$
MAUS Resonance 1	2	0.60
Thermography	2	67.00
Shearography	0	0.77
Air-coupled UT	1	1.01
SAM	17	1.04
Laminography	1	1.69

Figure 249. Individual PoD curve comparisons along with tabulated values for advanced inspection methods on 9-ply fiberglass (Tier 1 results)

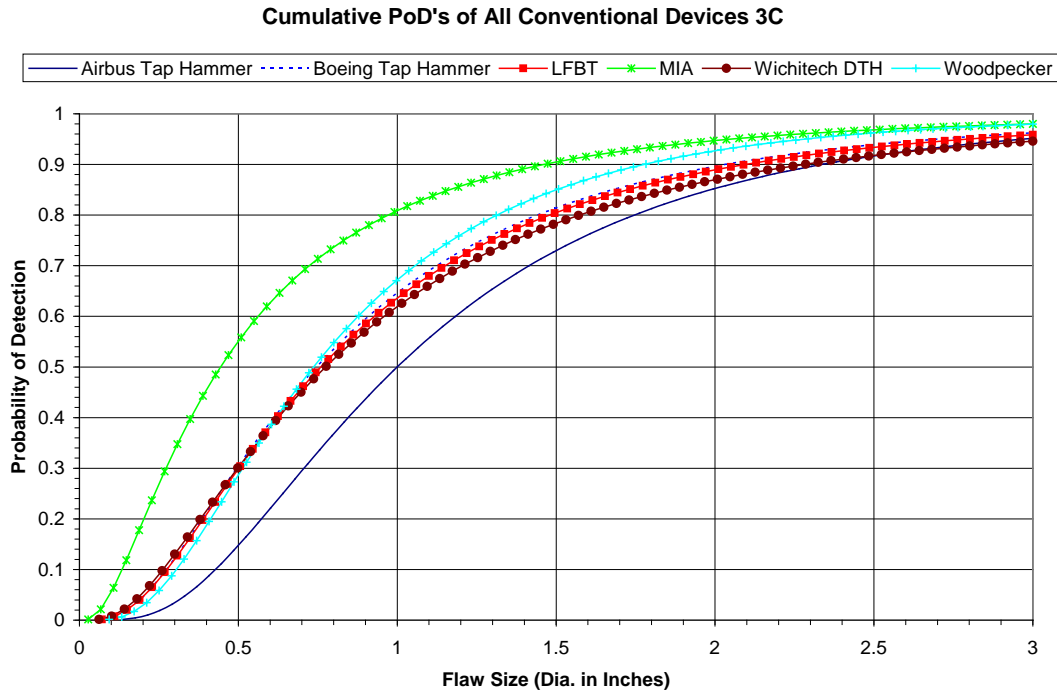
Advanced Inspection Technique Comparisons 9F



9-Ply Fiberglass		
Device	False Calls	90% POD Value
Microwave	8	2.00
CATT	0	2.27
FlawInspecta UT Array	1	>3.00
MAUS MIA	8	>3.00
Thermography (uncooled)	4	>3.00
MAUS Resonance 2	11	>3.00
Laser UT	N/A	N/A

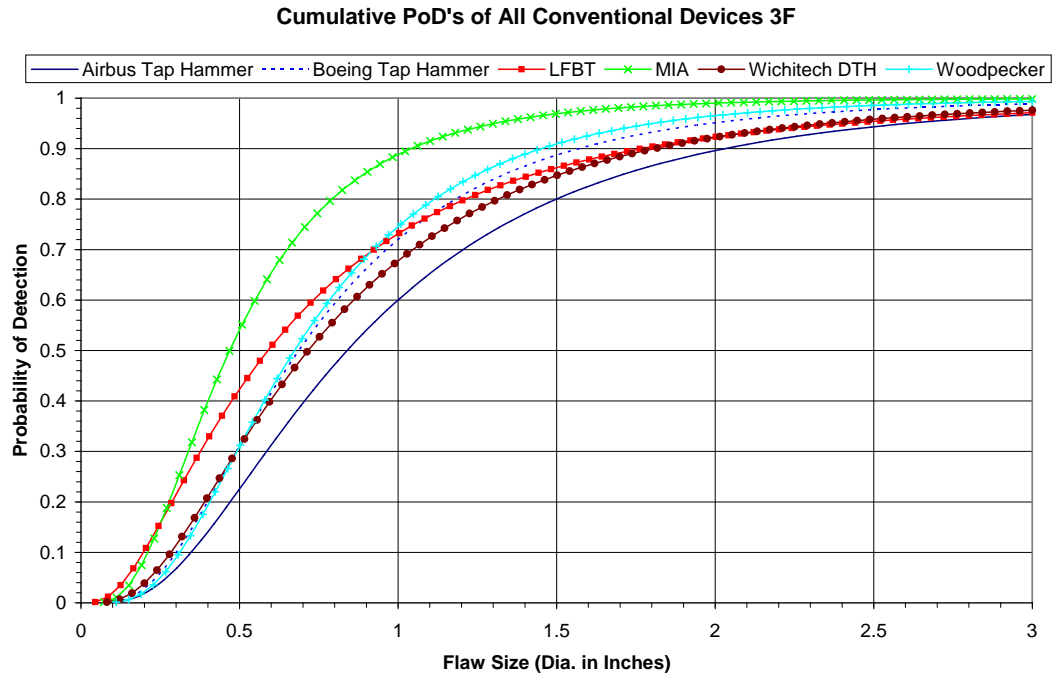
Figure 250. Individual PoD curve comparisons along with tabulated values for advanced inspection methods on 9-ply fiberglass (Tier 2 results)

Figures 163–198 show the individual inspector results and the resulting cumulative 90% PoD values for each of the conventional inspection methods studied in the CHE. Figures 251–256 provide comparison PoD performance plots for the five conventional NDI methods: Boeing tap hammer, Airbus tap hammer, LFBT, MIA, WichiTech DTH, and Woodpecker. The data are divided into the specific composite honeycomb structure categories. It can be seen that the false calls are quite low, and the best 90% POD levels range from 1–2" diameter, depending on the construction scenario.



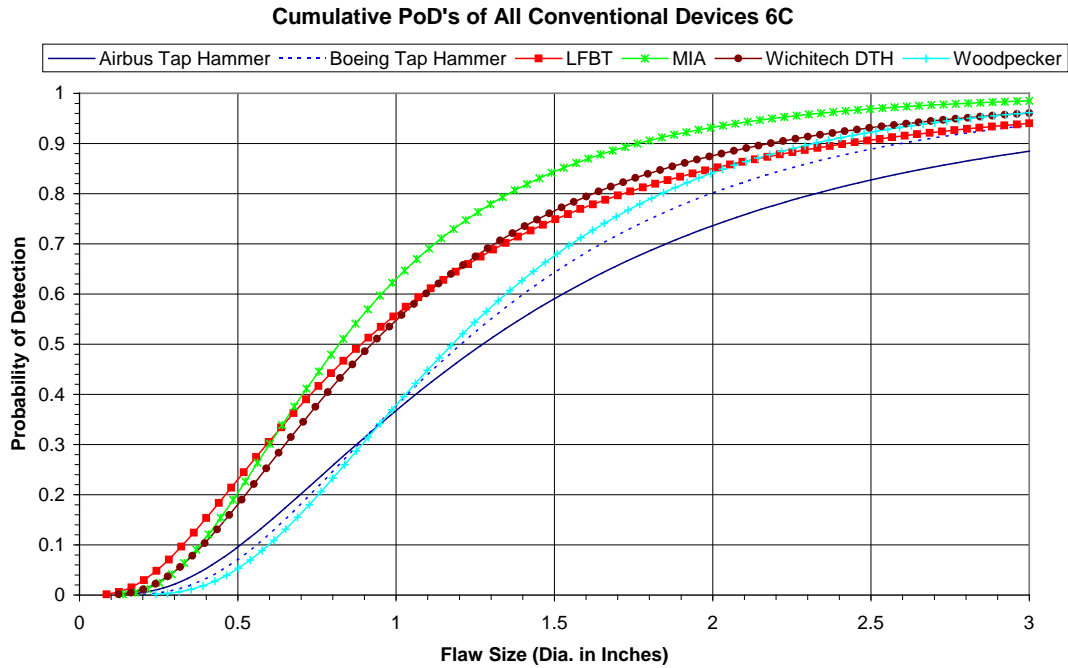
3-Ply Carbon		
Device	False Calls	90% POD Value
Airbus tap hammer	0.8	2.34
Boeing tap hammer	1.0	2.03
LFBT	2.3	2.10
MIA	0.6	1.46
WichiTech DTH	0.6	2.28
Woodpecker	0.0	1.78

Figure 251. Cumulative PoD curve comparisons along with tabulated values of all conventional NDI devices on 3-ply carbon (average results for all inspectors)



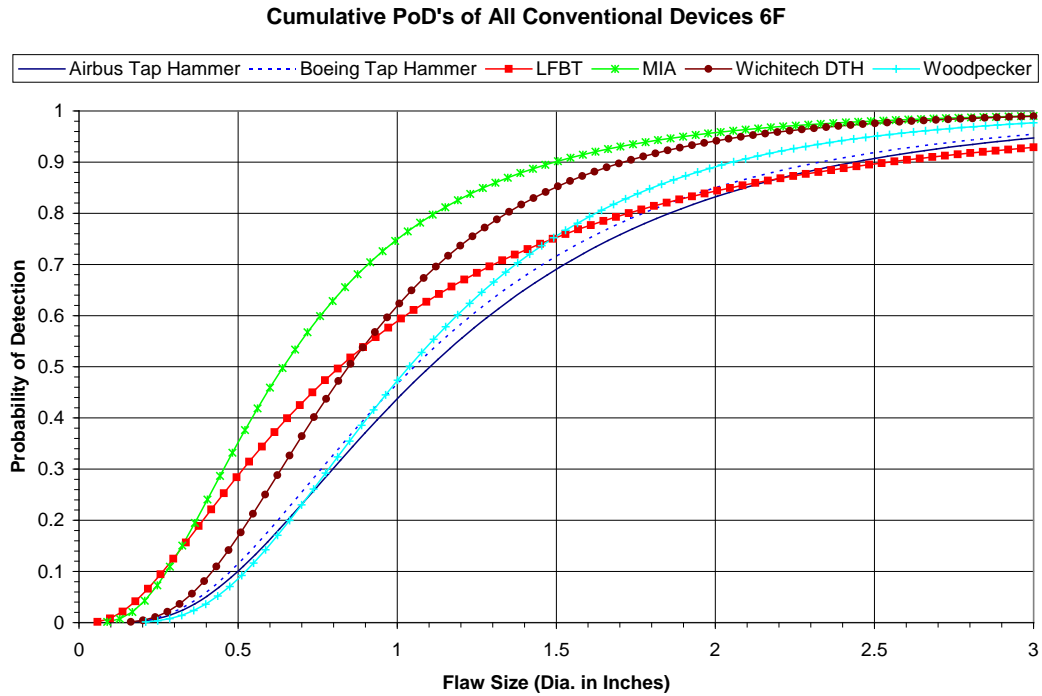
3-Ply Fiberglass		
Device	False Calls	90% POD Value
Airbus tap hammer	0.3	2.03
Boeing tap hammer	1.8	1.57
LFBT	0.9	1.77
MIA	0.5	1.04
WichiTech DTH	0.9	1.81
Woodpecker	0.3	1.45

Figure 252. Cumulative PoD curve comparisons along with tabulated values of all conventional NDI devices on 3-ply fiberglass (average results for all inspectors)



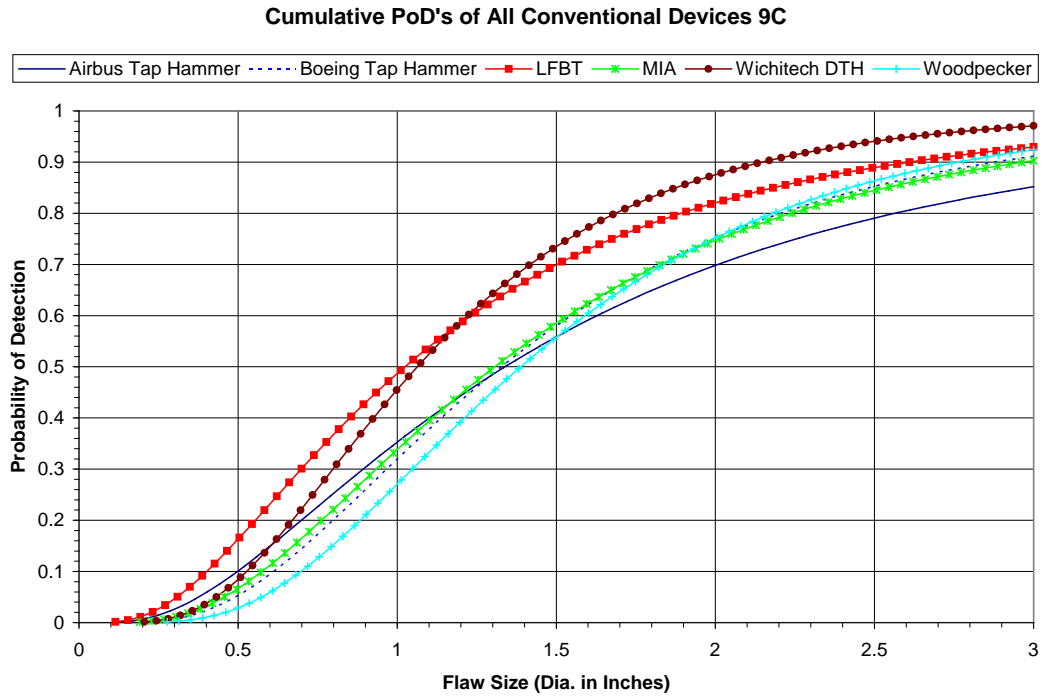
6-Ply Carbon		
Device	False Calls	90% POD Value
Airbus tap hammer	3.5	>3.00
Boeing tap hammer	4.7	2.59
LFBT	6.5	2.42
MIA	1.3	1.76
WichiTech DTH	0.9	2.18
Woodpecker	0.7	2.23

Figure 253. Cumulative PoD curve comparisons along with tabulated values of all conventional NDI devices on 6-ply carbon (average results for all inspectors)



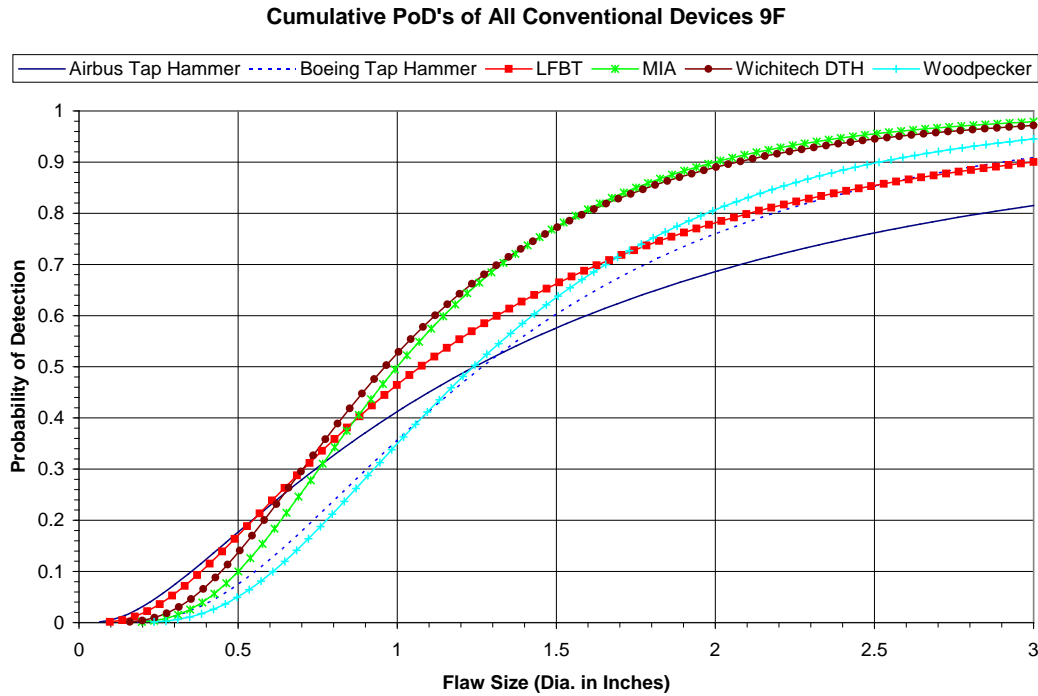
6-Ply Fiberglass		
Device	False Calls	90% POD Value
Airbus tap hammer	2.9	2.44
Boeing tap hammer	4.7	2.33
LFBT	3.3	2.55
MIA	1.9	1.49
WichiTech DTH	1.6	1.71
Woodpecker	0.1	2.05

Figure 254. Cumulative PoD curve comparisons along with tabulated values of all conventional NDI devices on 6-ply fiberglass (average results for all inspectors)



9-Ply Carbon		
Device	False Calls	90% POD Value
Airbus tap hammer	6.8	>3.00
Boeing tap hammer	5.4	2.88
LFBT	3.8	2.61
MIA	3.1	2.97
WichiTech DTH	4.4	2.15
Woodpecker	2.8	2.76

Figure 255. Cumulative PoD curve comparisons along with tabulated values of all conventional NDI devices on 9-ply carbon (average results for all inspectors)



9-Ply Fiberglass		
Device	False Calls	90% POD Value
Airbus tap hammer	7.1	>3.00
Boeing tap hammer	6.9	2.90
LFBT	2.8	3.00
MIA	6.8	2.00
WichiTech DTH	4.9	2.07
Woodpecker	6.7	2.52

Figure 256. Cumulative PoD curve comparisons along with tabulated values of all conventional NDI devices on 9-ply fiberglass (average results for all inspectors)

Figures 257–262 provide comparison PoD performance plots for the mechanical tap test techniques only: Boeing tap hammer, Airbus tap hammer, WichiTech DTH, Woodpecker, and the CATT system. The data are divided into the specific composite honeycomb structure categories. It can be seen that the automated CATT system, with its C-scan display of data, produced the best results and that the best 90% POD values range from 1.0–2.3" diameter, depending on the construction scenario.

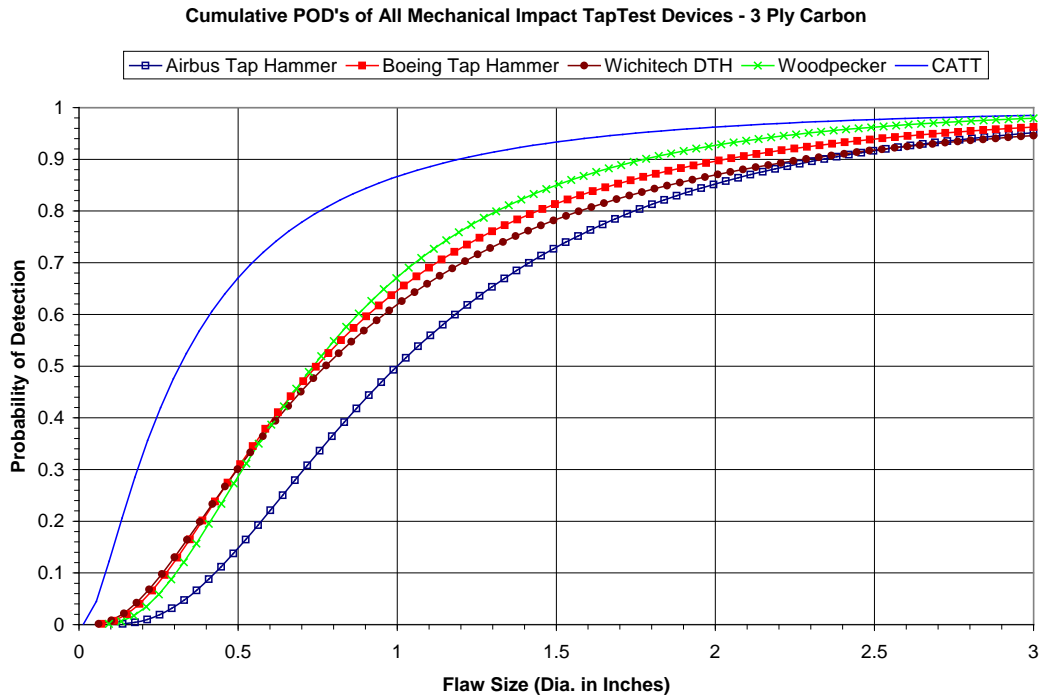


Figure 257. Comparison of all mechanical tap test devices on 3-ply carbon

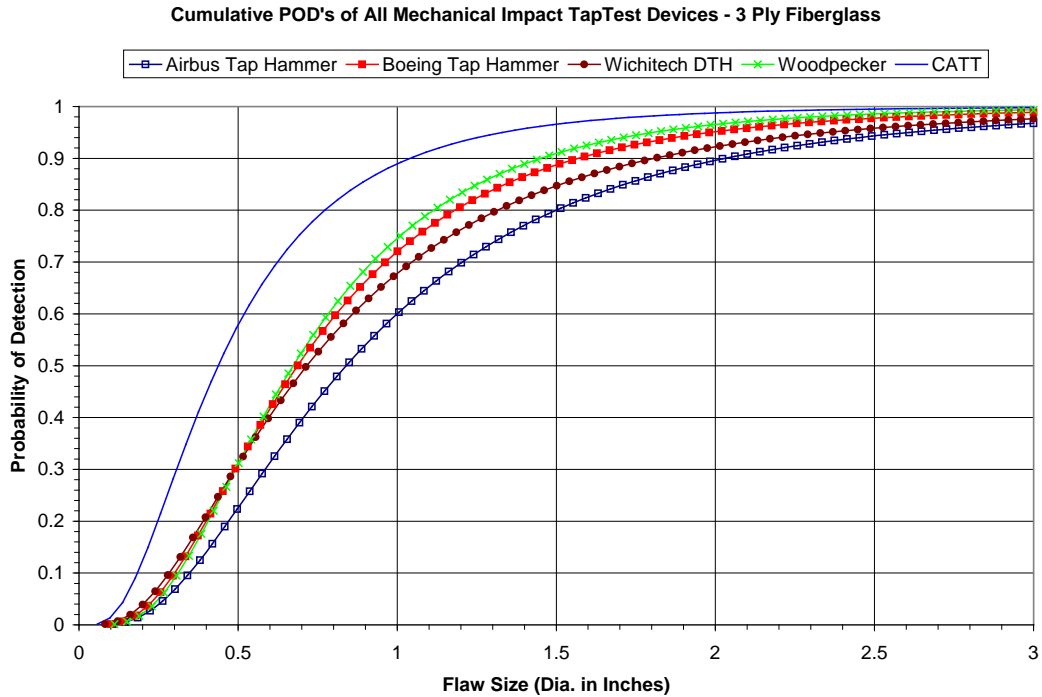


Figure 258. Comparison of all mechanical tap test devices on 3-ply fiberglass

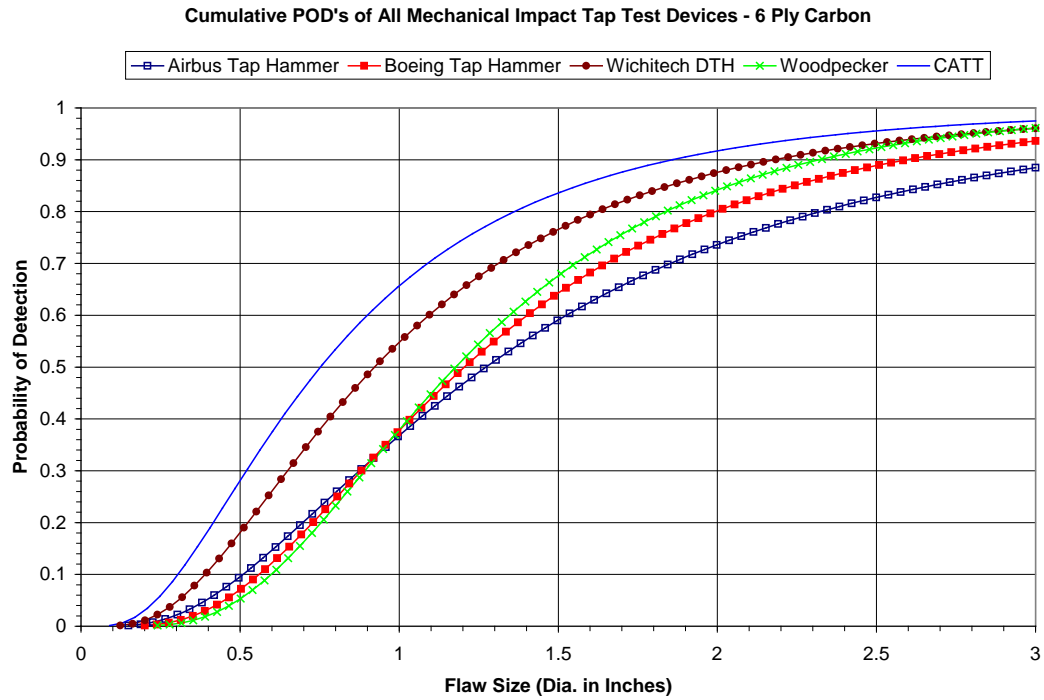


Figure 259. Comparison of all mechanical tap test devices on 6-ply carbon

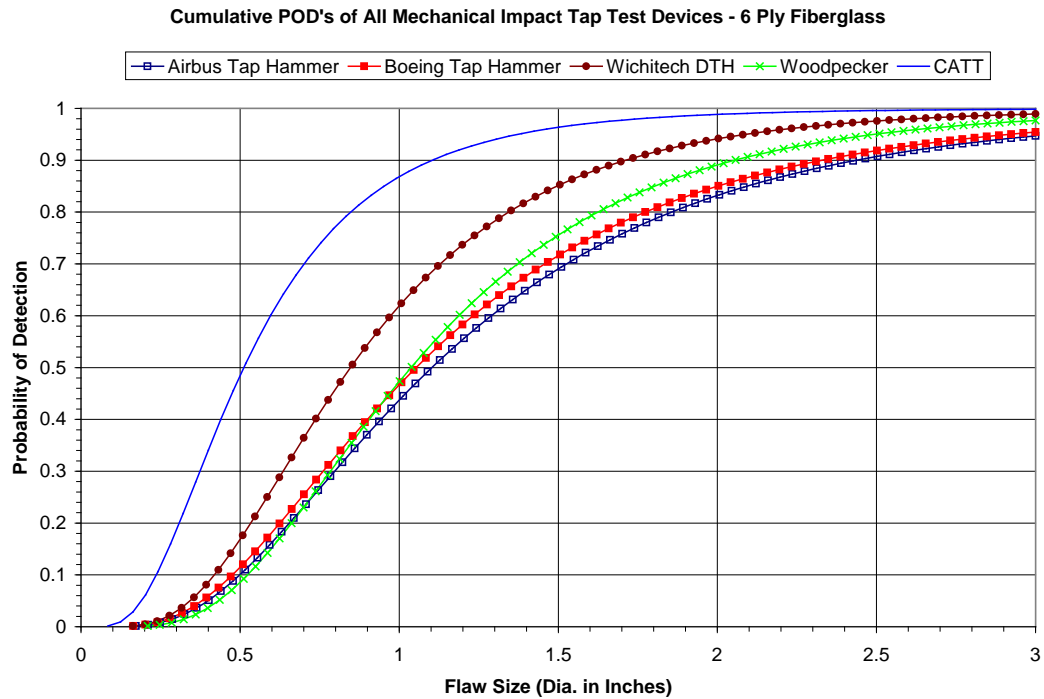


Figure 260. Comparison of all mechanical tap test devices on 6-ply fiberglass

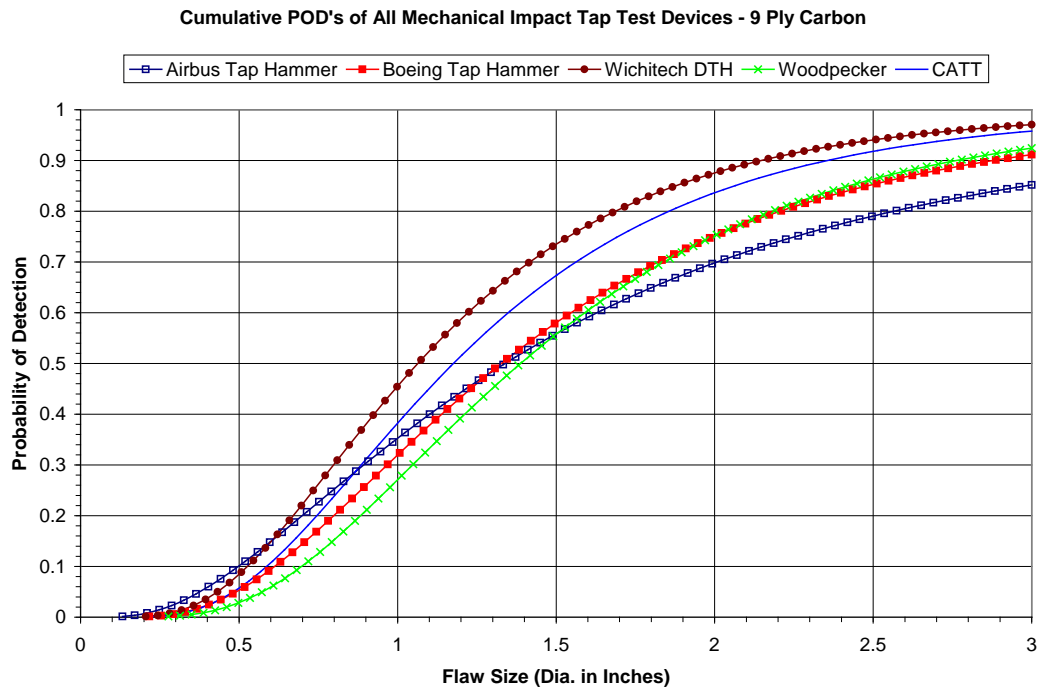


Figure 261. Comparison of all mechanical tap test devices on 9-ply carbon

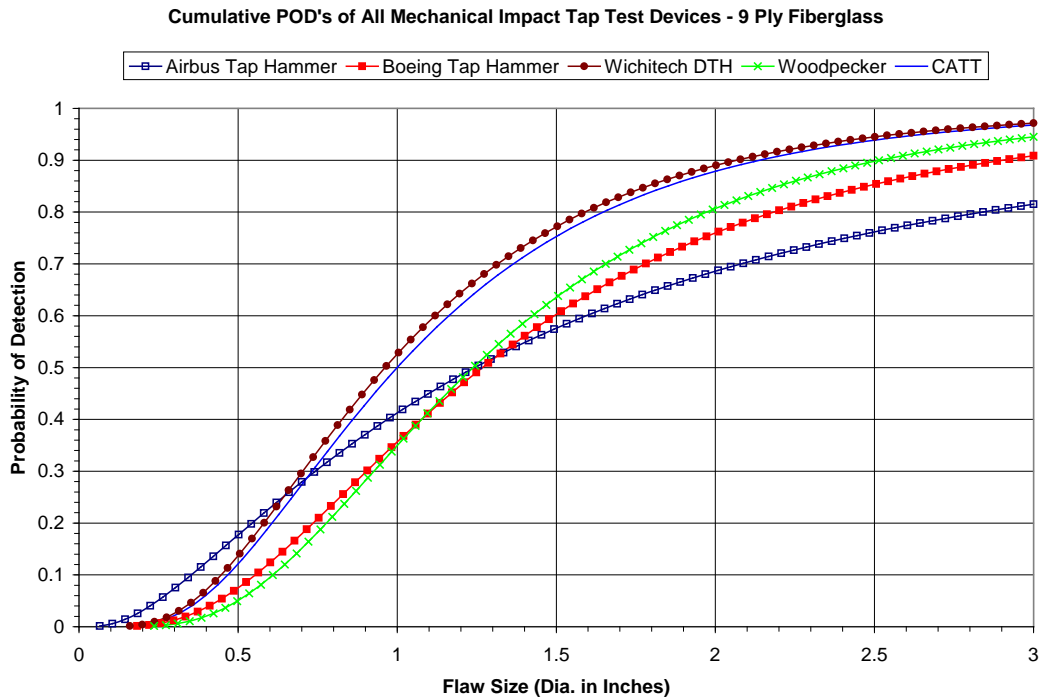
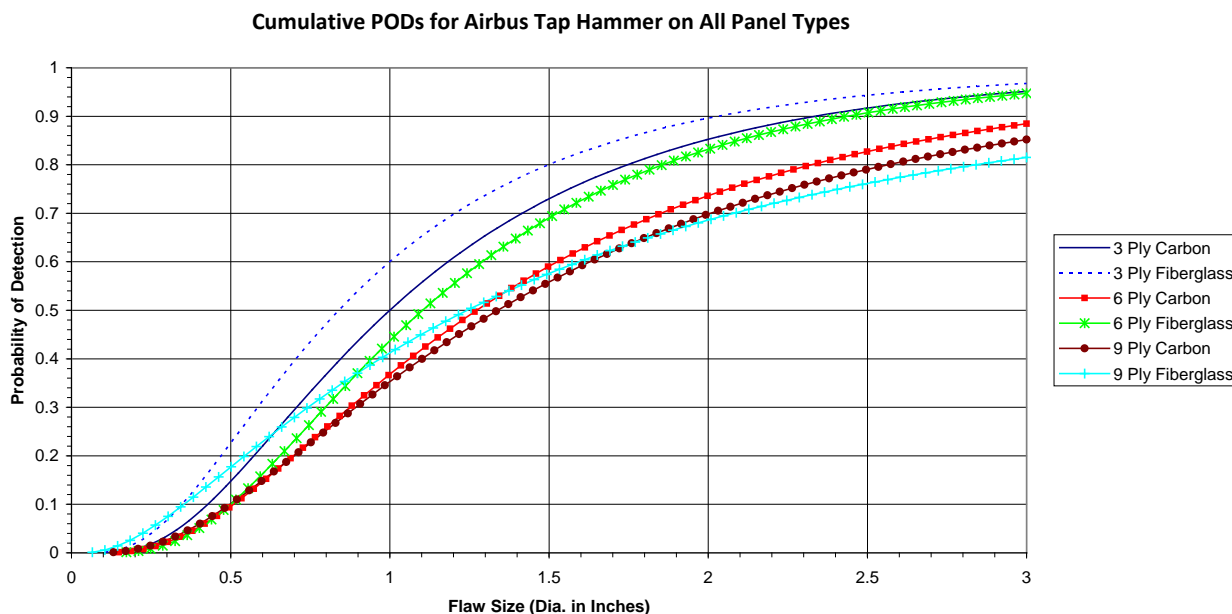


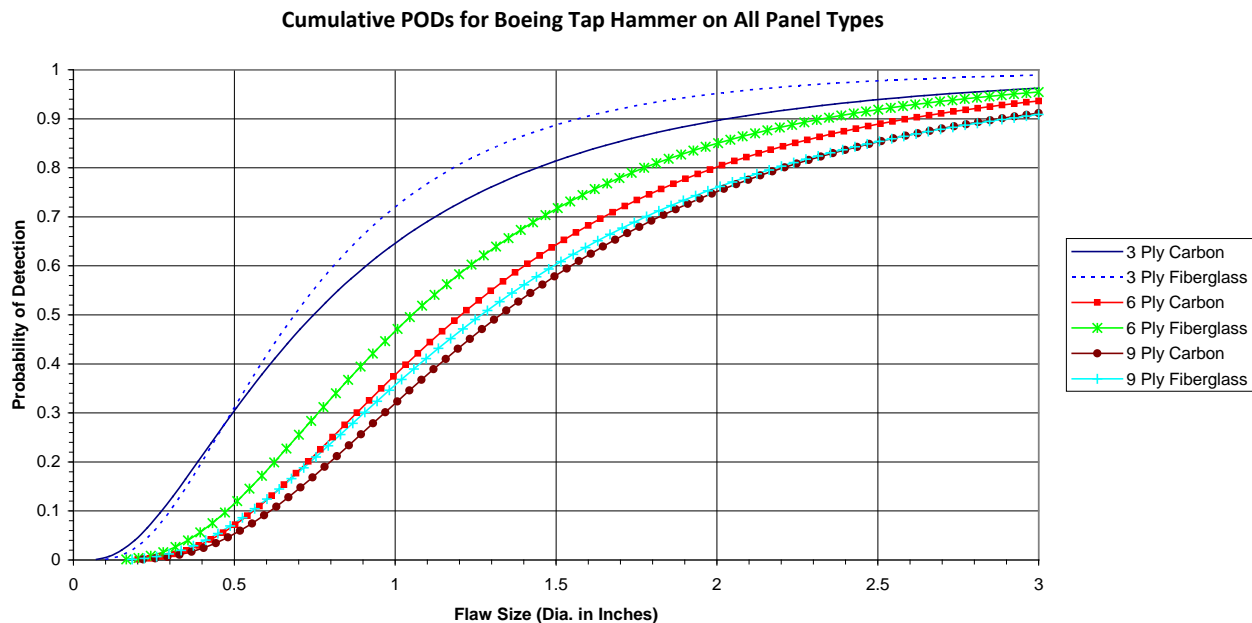
Figure 262. Comparison of all mechanical tap test devices on 9-ply fiberglass

The results from this experiment can also be divided to show the performance of each individual conventional inspection method for each of the composite honeycomb structure categories. Figures 263–268 compare the overall cumulative performance of a specific conventional inspection technique and show the results from all six construction types (i.e., 3F, 3C, 6F, 6C, 9F, and 9C) on a single plot. Tabulated 90% PoD levels are also compared along with the false calls associated with composite honeycomb type. These data show the rise in 90% PoD levels as the inspection becomes more challenging (i.e., skin gets thicker).



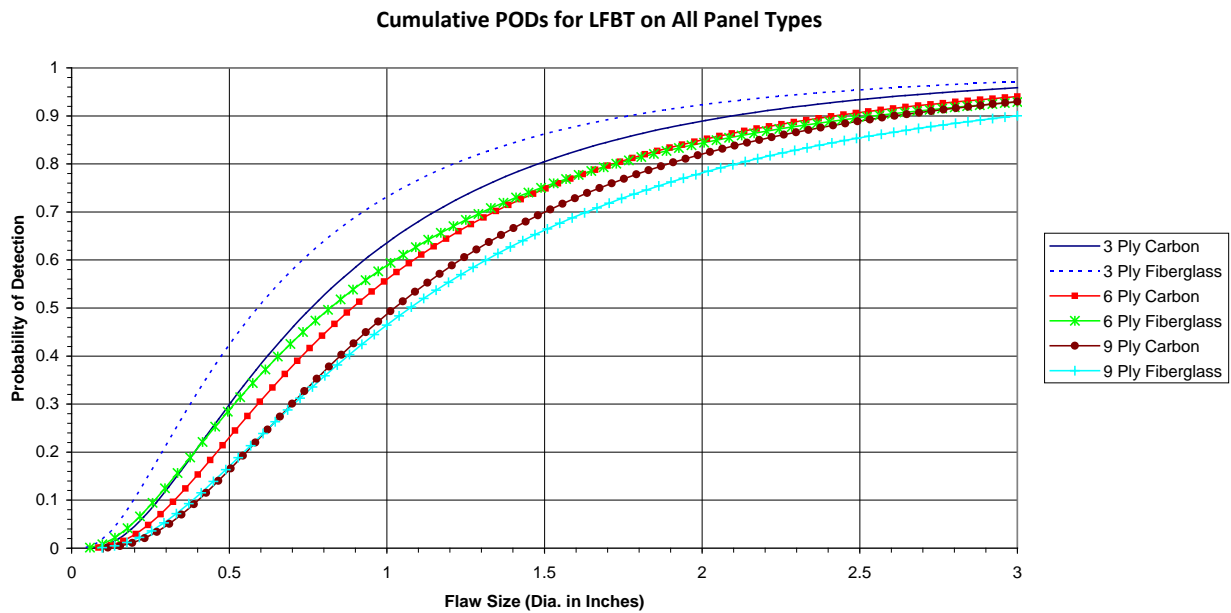
Airbus Tap Hammer		
Panel Type	False Calls	90% POD Value
3-ply carbon	0.8	2.34
3-ply fiberglass	0.3	2.03
6-ply carbon	3.5	>3.00
6-ply fiberglass	2.9	2.44
9-ply carbon	6.8	>3.00
9-ply fiberglass	7.1	>3.00

Figure 263. Cumulative PoD curves for Airbus tap hammer along with tabulated values on all panel types (average results for all inspectors)



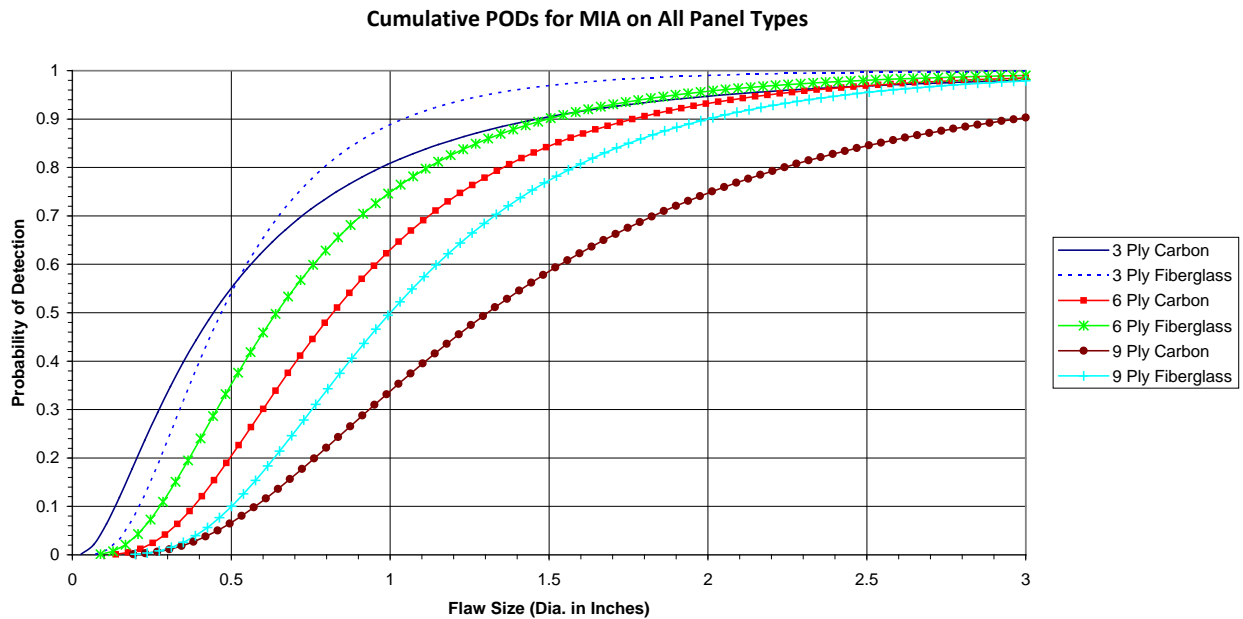
Boeing Tap Hammer		
Panel Type	False Calls	90% POD Value
3-ply carbon	1.0	2.03
3-ply fiberglass	1.8	1.57
6-ply carbon	4.7	2.59
6-ply fiberglass	4.7	2.33
9-ply carbon	5.4	2.88
9-ply fiberglass	6.9	2.90

Figure 264. Cumulative PoD curves for Boeing tap hammer along with tabulated values on all panel types (average results for all inspectors)



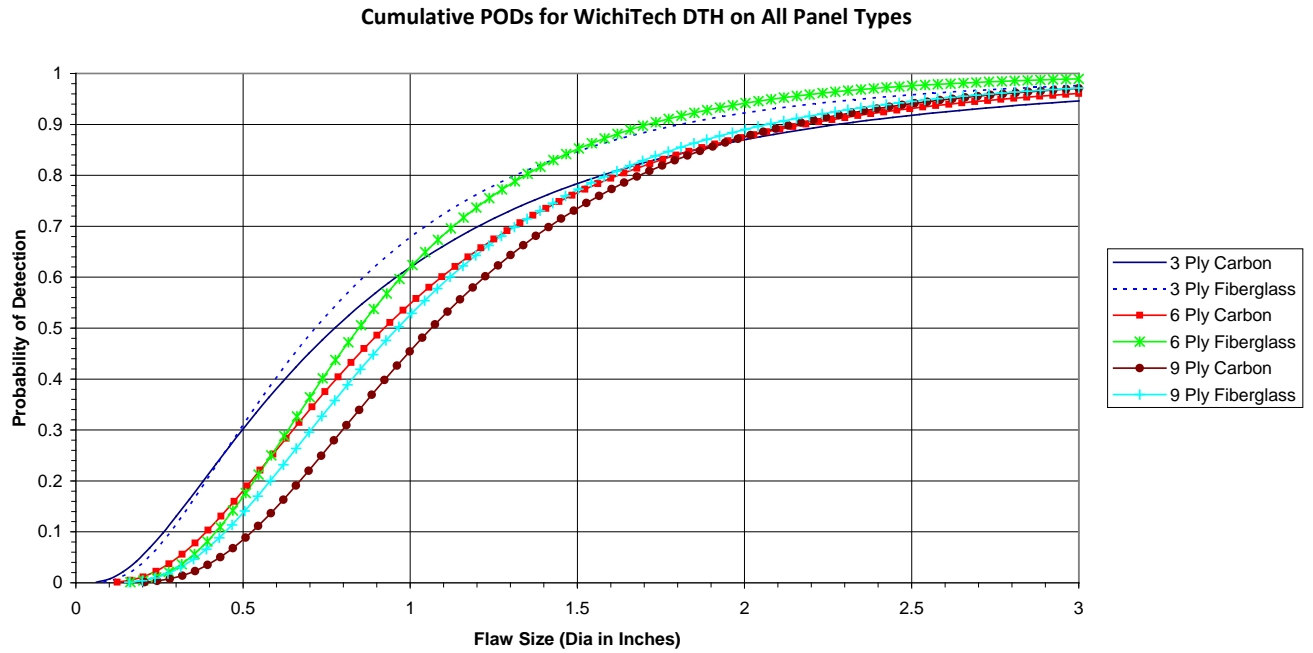
LFBT		
Panel Type	False Calls	90% POD Value
3-ply carbon	2.3	2.10
3-ply fiberglass	0.9	1.77
6-ply carbon	6.5	2.42
6-ply fiberglass	3.3	2.55
9-ply carbon	3.8	2.61
9-ply fiberglass	2.8	3.00

Figure 265. Cumulative PoD curves for LFBT along with tabulated values on all panel types (average results for all inspectors)



MIA		
Panel Type	False Calls	90% POD Value
3-ply carbon	0.6	1.46
3-ply fiberglass	0.5	1.04
6-ply carbon	1.3	1.76
6-ply fiberglass	1.9	1.49
9-ply carbon	3.1	2.97
9-ply fiberglass	6.8	2.00

Figure 266. Cumulative PoD curves for MIA along with tabulated values on all panel types (average results for all inspectors)



WichiTech DTH		
Panel Type	False Calls	90% POD Value
3-ply carbon	0.6	2.28
3-ply fiberglass	0.9	1.81
6-ply carbon	0.9	2.18
6-ply fiberglass	1.6	1.71
9-ply carbon	4.4	2.15
9-ply fiberglass	4.9	2.07

Figure 267. Cumulative PoD curves for WichiTech DTH along with tabulated values on all panel types (average results for all inspectors)

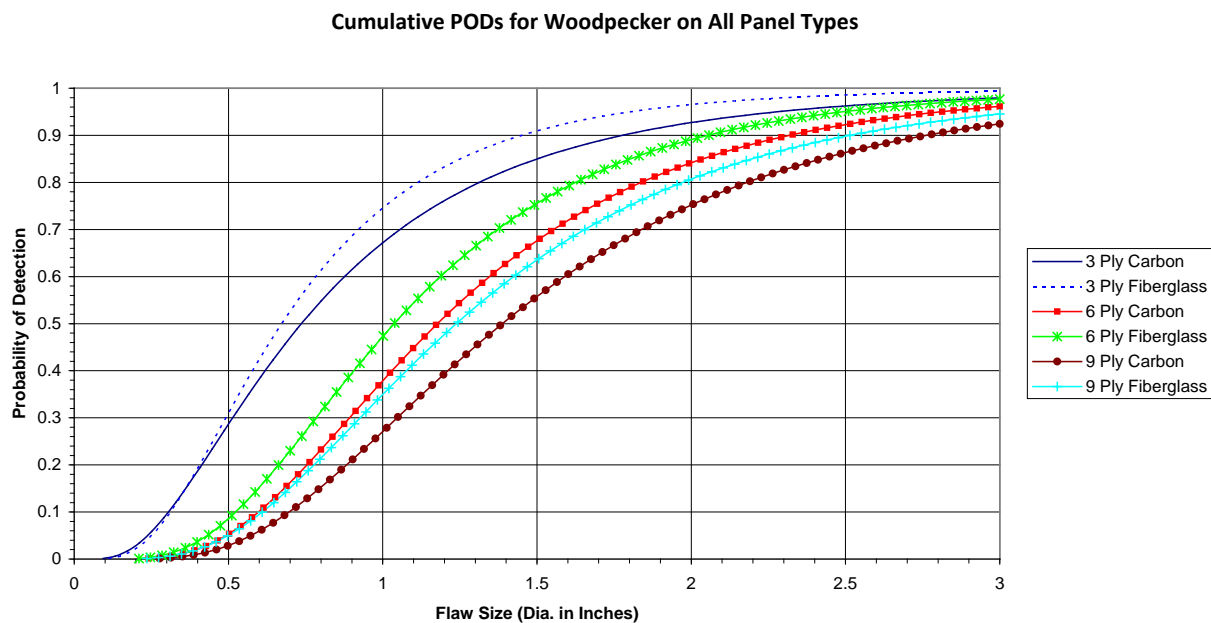
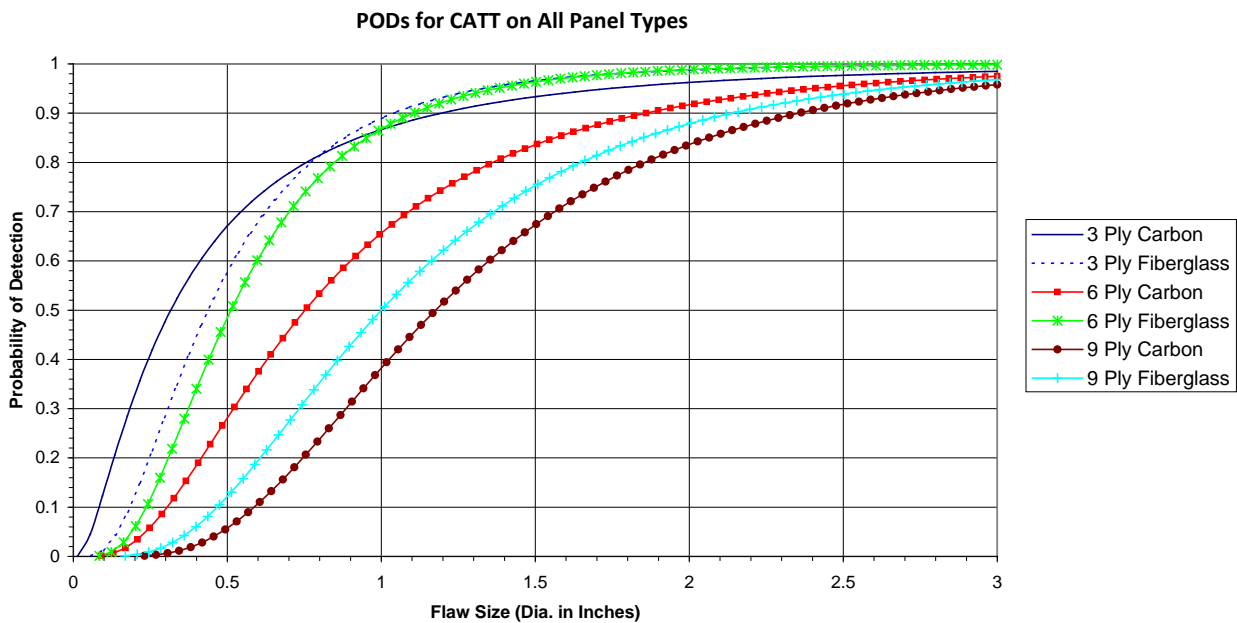


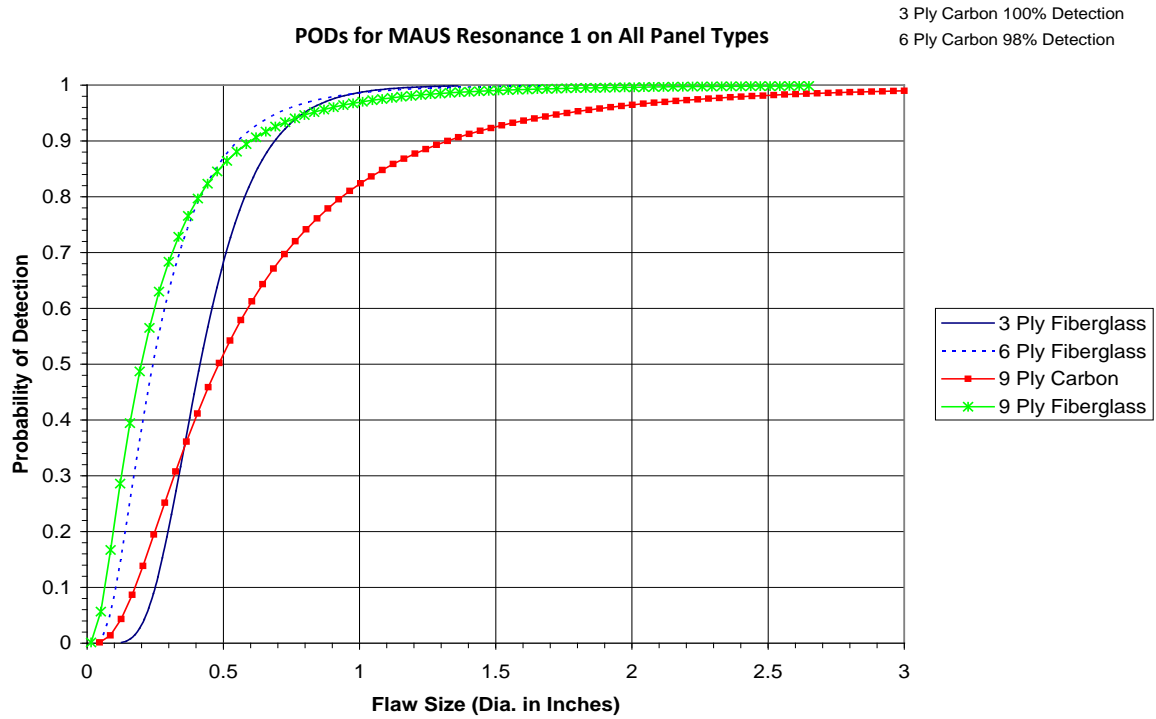
Figure 268. Cumulative PoD curves for Woodpecker along with tabulated values on all panel types (average results for all inspectors)

The results from this experiment can also be divided to show the performance of each individual advanced inspection method for each of the composite honeycomb structure categories. Figures 269–278 compare the overall cumulative performance of a specific advanced inspection technique and show the results from all six construction types (i.e., 3F, 3C, 6F, 6C, 9F, and 9C) on a single plot. Tabulated 90% PoD levels are also compared along with the false calls associated with composite honeycomb type. These data show the rise in 90% PoD levels as the inspection becomes more challenging (i.e., skin gets thicker). Overall, when both 90% PoD levels and false calls are considered, thermography provided the best overall performance. Note that PoD curves are not plotted for specific methods when the detection percentage is exceptionally high. In these cases, it is not possible to generate a curve fit for these data because of the extremely high flaw detection rate. For these methods, the flaw detection rate is listed at the top of the PoD plots.



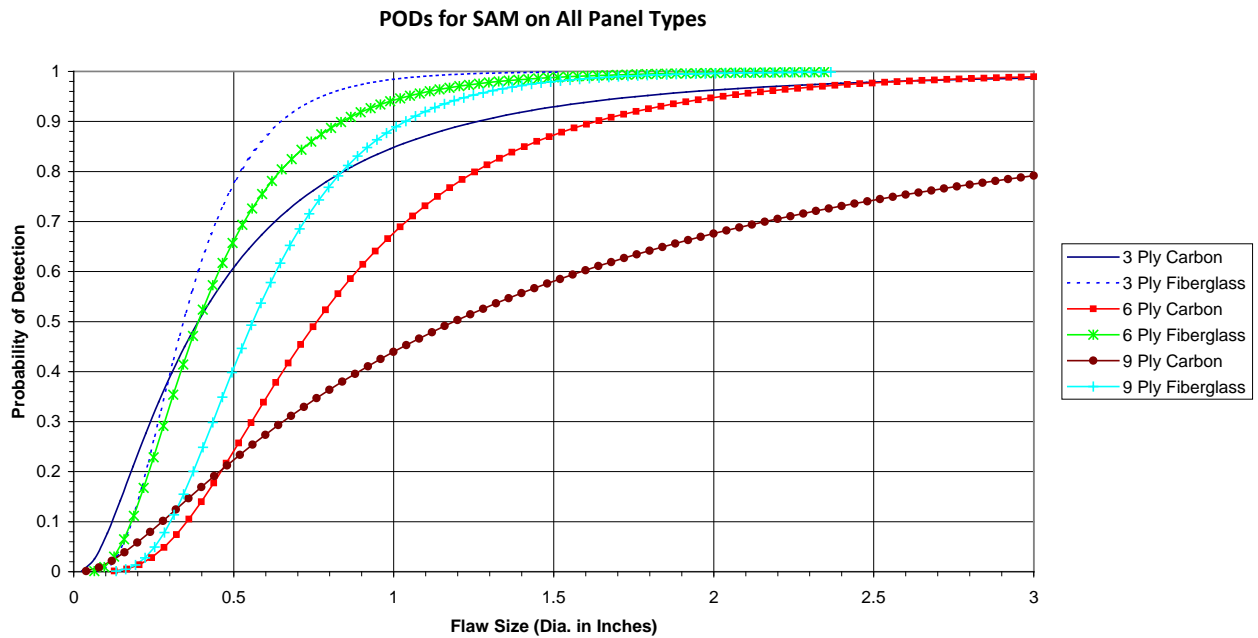
CATT		
Panel Type	False Calls	90% POD Value
3-ply carbon	0.0	1.19
3-ply fiberglass	4.0	1.04
6-ply carbon	1.0	1.85
6-ply fiberglass	1.0	1.10
9-ply carbon	4.0	2.36
9-ply fiberglass	0.0	2.27

Figure 269. PoD curve comparisons for CATT along with tabulated values on all panel types



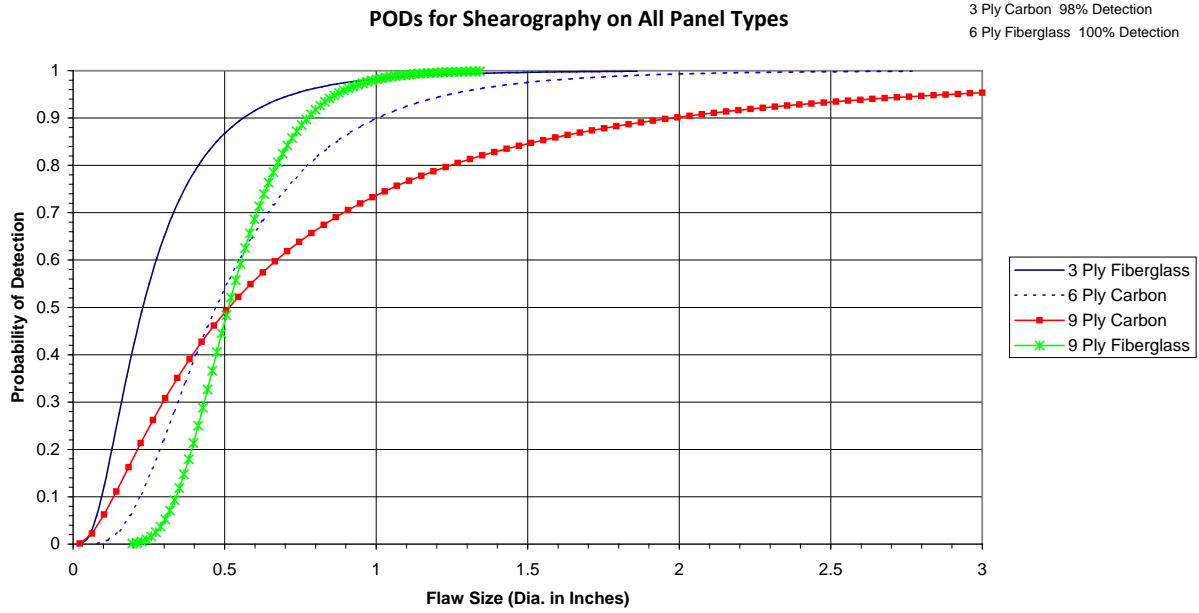
MAUS Resonance 1		
Panel Type	False Calls	90% POD Value
3-ply carbon	3.0	$\leq .50$
3-ply fiberglass	5.0	0.69
6-ply carbon	12.0	$\leq .50$
6-ply fiberglass	9.0	0.55
9-ply carbon	0.0	1.32
9-ply fiberglass	2.0	0.60

Figure 270. PoD curve comparisons for MAUS Resonance 1 inspections along with tabulated values on all panel types (results shown for resonance experimenter #1 only)



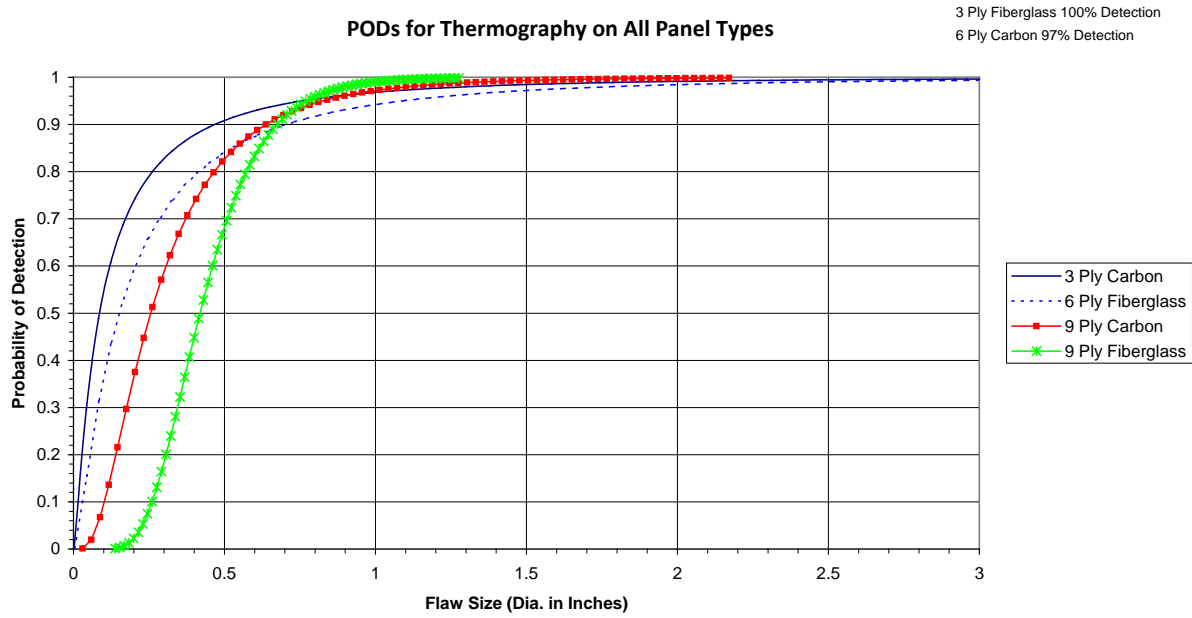
SAM		
Panel Type	False Calls	90% POD Value
3-ply carbon	2.0	1.26
3-ply fiberglass	0.0	0.65
6-ply carbon	37.0	1.63
6-ply fiberglass	8.0	0.84
9-ply carbon	74.0	>3.00
9-ply fiberglass	17.0	1.04

Figure 271. PoD curve comparisons for SAM inspections along with tabulated values on all panel types



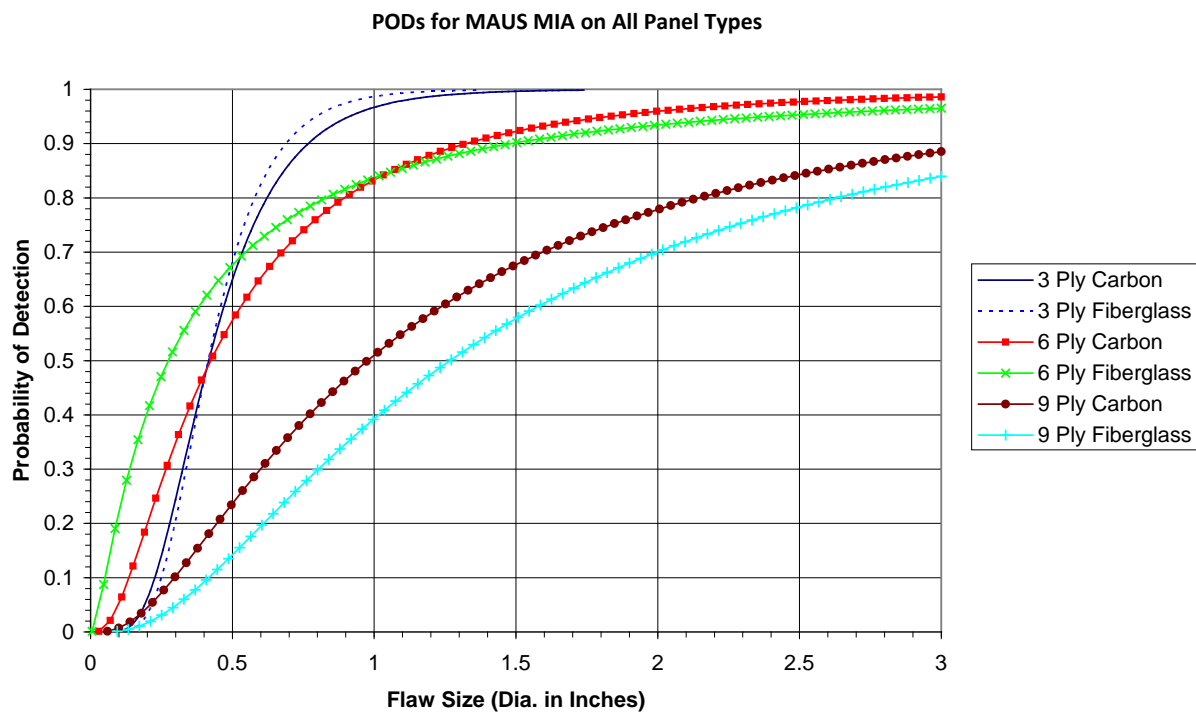
Shearography		
Panel Type	False Calls	90% POD Value
3-ply carbon	0.0	$\leq .50$
3-ply fiberglass	1.0	0.56
6-ply carbon	0.0	1.00
6-ply fiberglass	0.0	$\leq .50$
9-ply carbon	0.0	2.00
9-ply fiberglass	0.0	0.77

Figure 272. PoD curve comparisons for shearography inspections along with tabulated values on all panel types



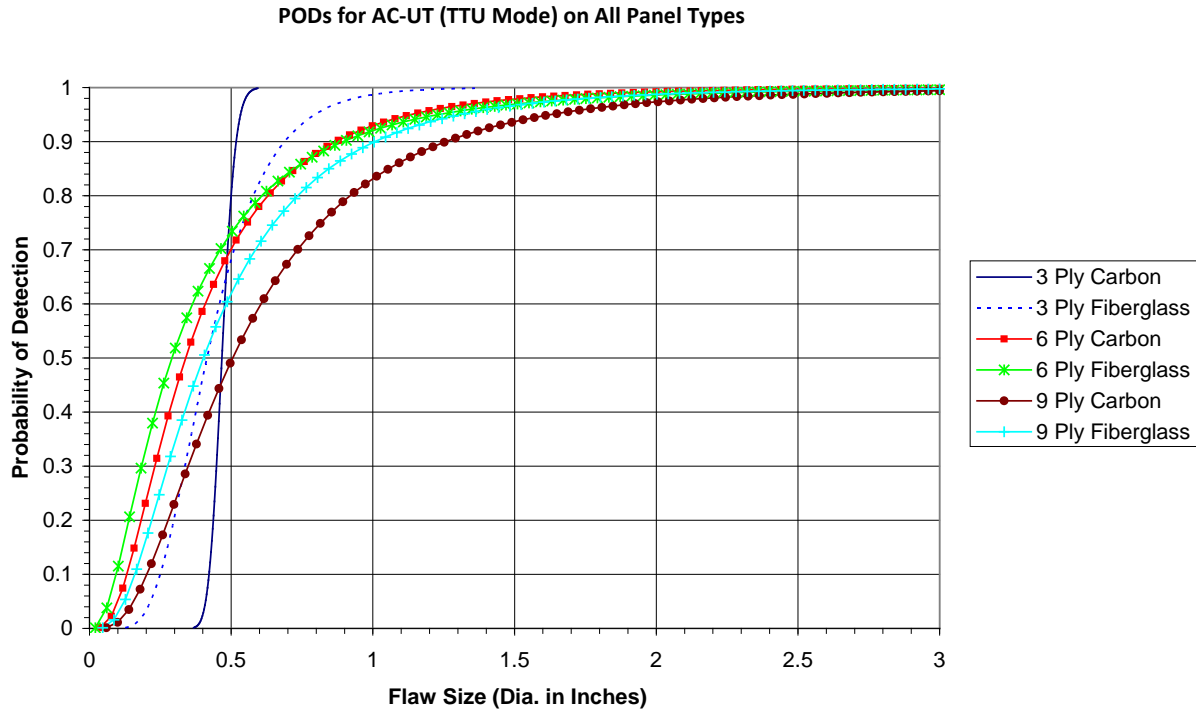
Thermography		
Panel Type	False Calls	90% POD Value
3-ply carbon	2.0	$\leq .50$
3-ply fiberglass	0.0	$\leq .50$
6-ply carbon	2.0	$\leq .50$
6-ply fiberglass	3.0	0.70
9-ply carbon	0.0	0.64
9-ply fiberglass	2.0	0.67

Figure 273. PoD curve comparisons for thermography inspections along with tabulated values on all panel types



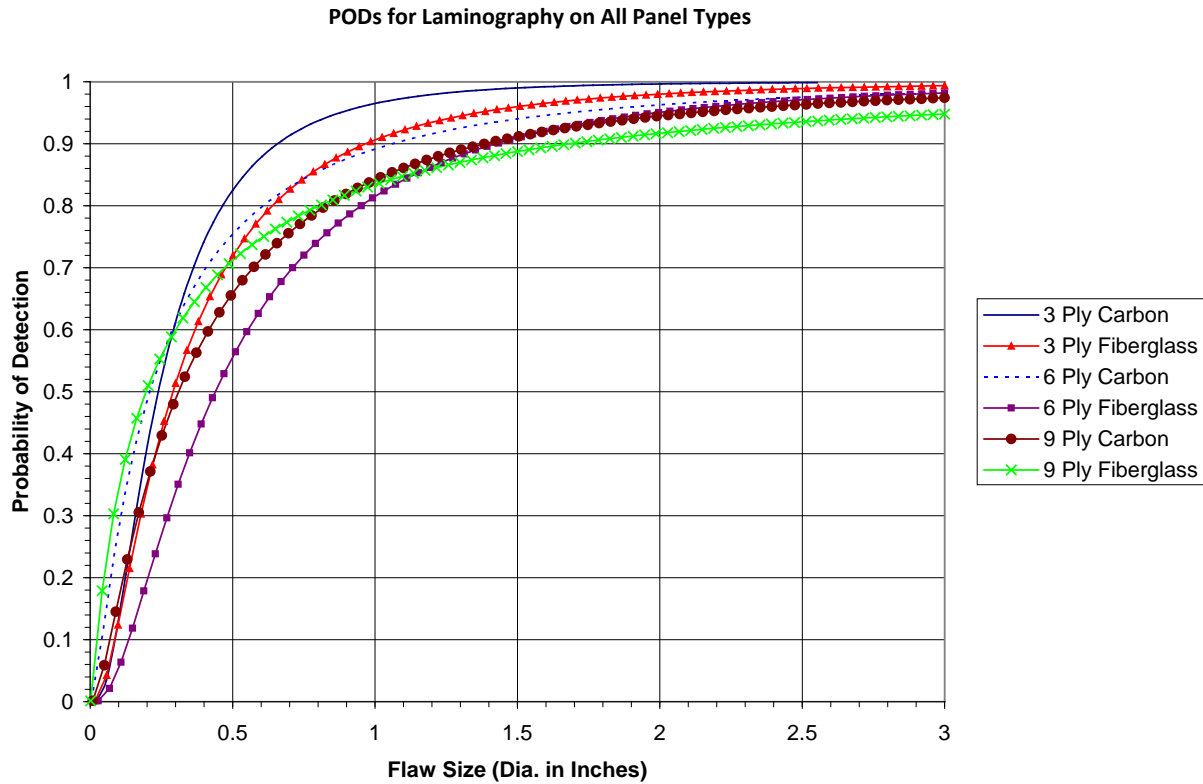
MAUS MIA		
Panel Type	False Calls	90% POD Value
3-ply carbon	0.0	0.77
3-ply fiberglass	0.0	0.69
6-ply carbon	6.0	1.32
6-ply fiberglass	6.0	1.48
9-ply carbon	8.0	>3.00
9-ply fiberglass	8.0	>3.00

Figure 274. PoD curve comparisons for MAUS IV MIA inspections along with tabulated values on all panel types



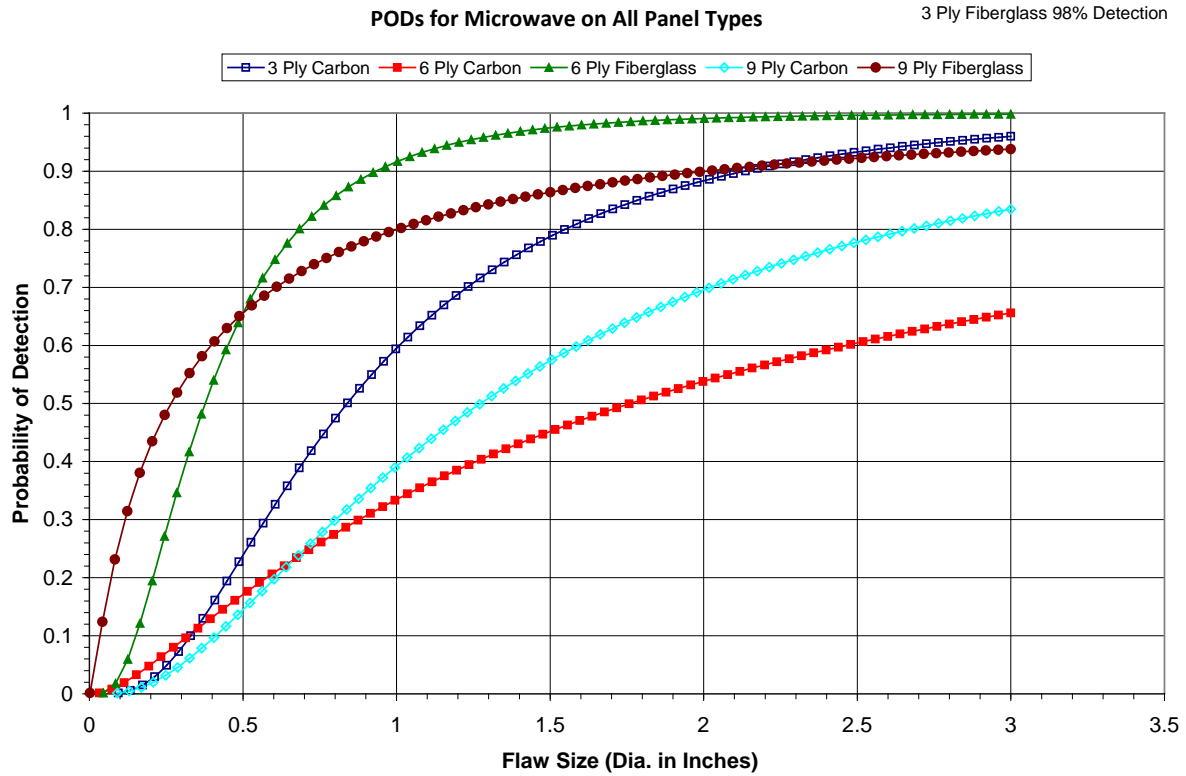
AC-UT		
Panel Type	False Calls	90% POD Value
3-ply carbon	0.0	0.52
3-ply fiberglass	0.0	0.69
6-ply carbon	0.0	0.87
6-ply fiberglass	0.0	0.90
9-ply carbon	2.0	1.26
9-ply fiberglass	1.0	1.01

Figure 275. PoD curve comparisons for AC-UT inspections (TTU mode) along with tabulated values on all panel types



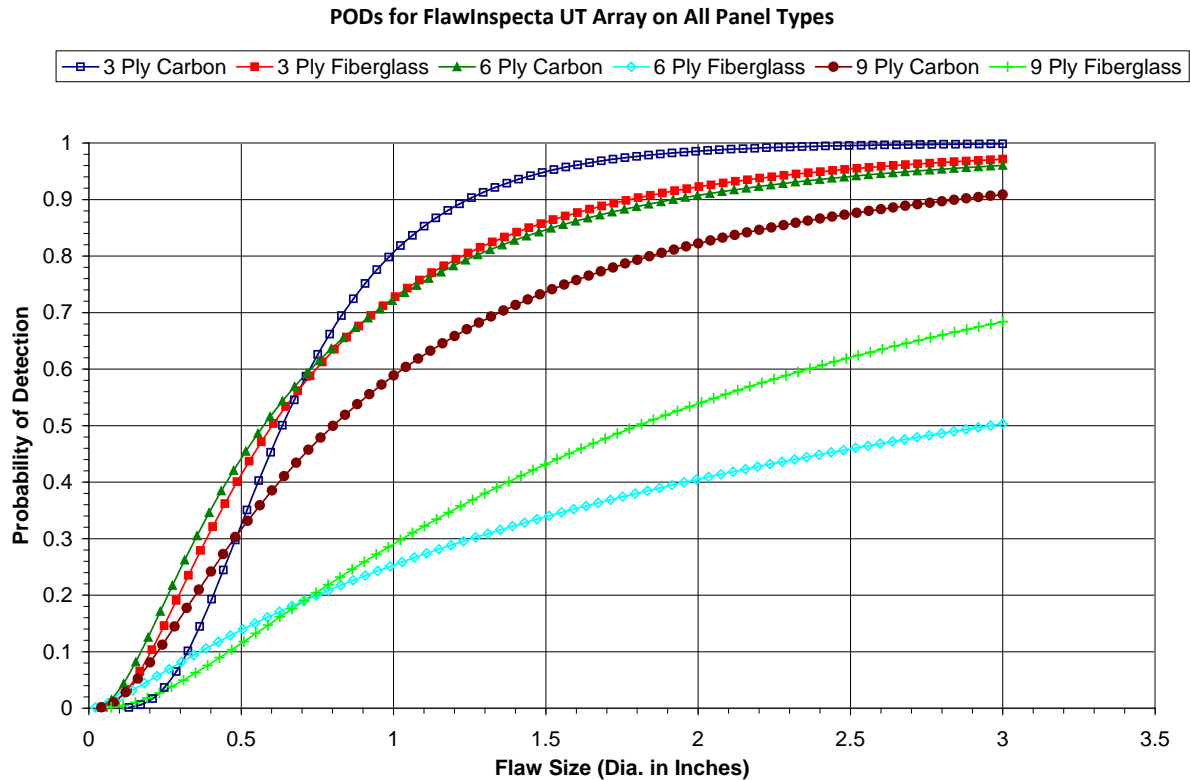
Laminography		
Panel Type	False Calls	90% POD Value
3-ply carbon	0.0	0.66
3-ply fiberglass	0.0	0.97
6-ply carbon	0.0	1.10
6-ply fiberglass	2.0	1.43
9-ply carbon	0.0	1.39
9-ply fiberglass	1.0	1.69

Figure 276. PoD curve comparisons for laminography inspections along with tabulated values on all panel types



Microwave		
Panel Type	False Calls	90% POD Value
3-ply carbon	9.0	2.13
3-ply fiberglass	2.0	0.50
6-ply carbon	10.0	>3.00
6-ply fiberglass	12.0	0.93
9-ply carbon	23.0	>3.00
9-ply fiberglass	8.0	2.00

Figure 277. PoD curve comparisons for microwave inspections along with tabulated values on all panel types



FlawInspecta UT Array		
Panel Type	False Calls	90% POD Value
3-ply carbon	3.0	1.24
3-ply fiberglass	0.0	1.78
6-ply carbon	0.0	1.92
6-ply fiberglass	0.0	>3.00
9-ply carbon	1.0	2.85
9-ply fiberglass	1.0	>3.00

Figure 278. PoD curve comparisons for FlawInspecta UT array along with tabulated values on all panel types

The laminography inspections were completed edge to edge with no overlap between adjacent shots. This made detection of flaws at these edge junctions difficult and was probably the cause for the flaw misses in these areas. In addition, impact flaws were very difficult for laminography to detect, more so than any other flaw type. It is believed that if more time were spent looking at various time slices, there possibly could have been a higher detection rate. The PoD curves in figures 279–282 compare the overall cumulative performance of laminography while considering the different inspection challenges noted above. The plots show the results produced when all flaws are considered and compares them with the curves produced when certain exceptions are removed from the flaw data. These include removing impact flaw data (difficult to detect) and

flaws located in areas where there was a lack of image overlap that resulted in misses. It can be seen that these adjustments result in a significant improvement in the 90% PoD levels. This indicates that laminography improvements in impact detection and changes in inspection deployment procedures could make laminography one of the top performing inspection options.

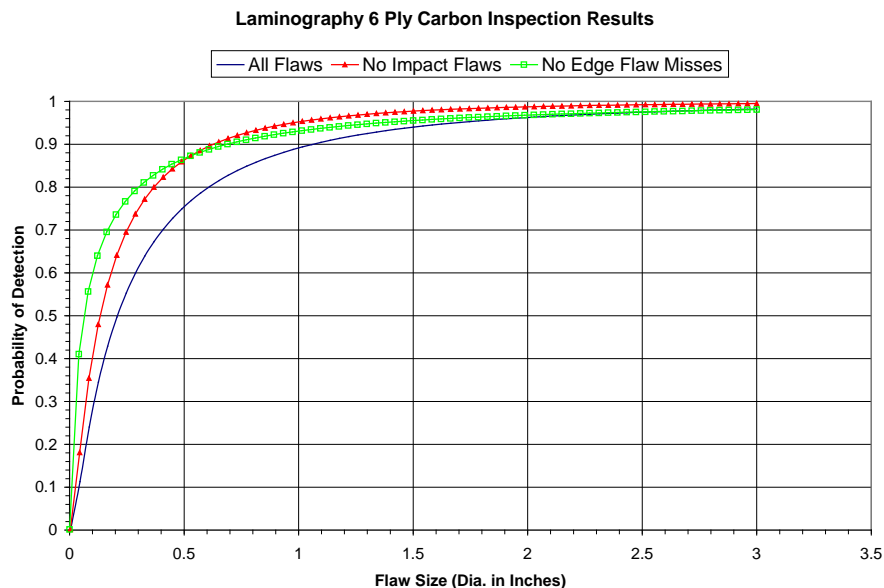


Figure 279. PoD curve comparisons for laminography showing the improvement when impact and edge (inspection image overlap) flaws are removed from PoD calculation on 6-ply carbon

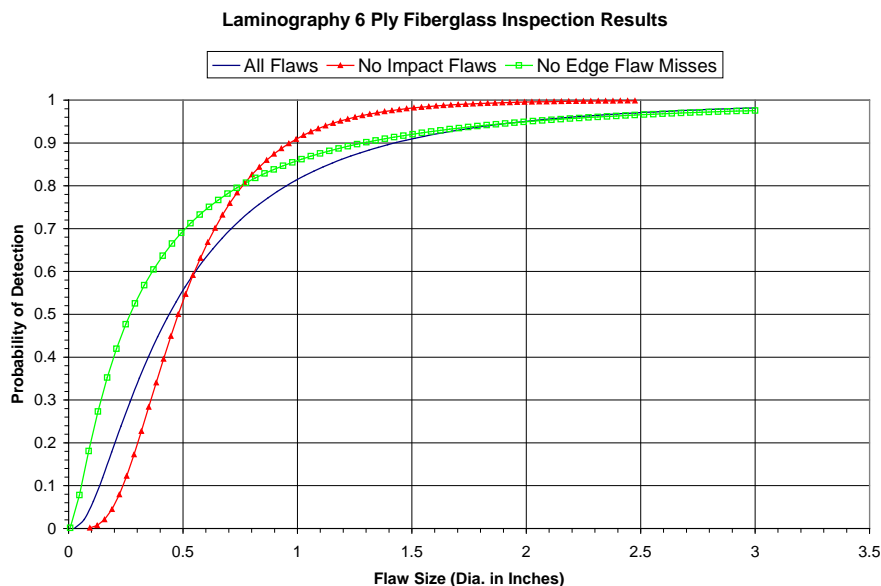


Figure 280. PoD curve comparisons for laminography showing the improvement when impact and edge (inspection image overlap) flaws are removed from PoD calculation on 6-ply fiberglass

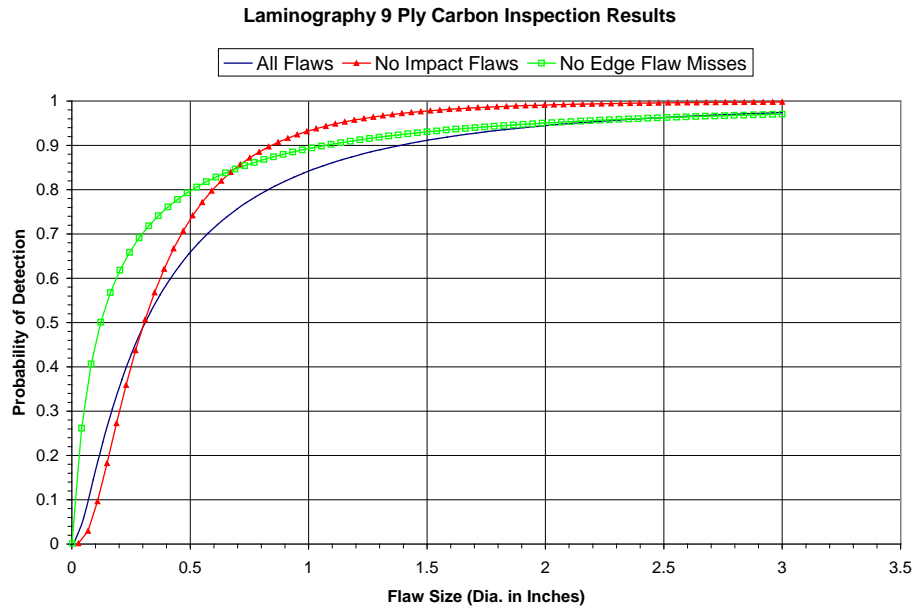


Figure 281. PoD curve comparisons for laminography showing the improvement when impact and edge (inspection image overlap) flaws are removed from PoD calculation on 9-ply carbon

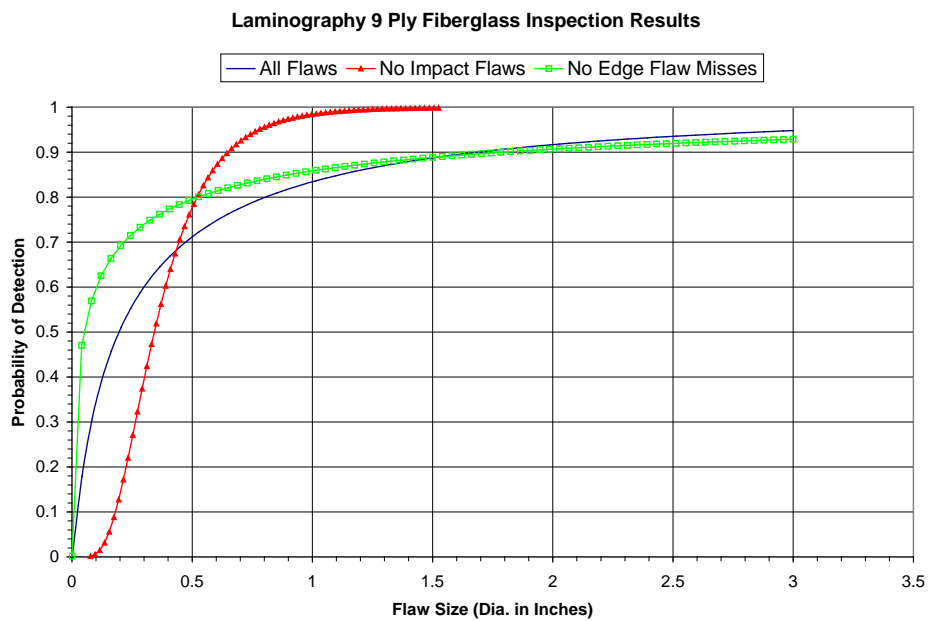
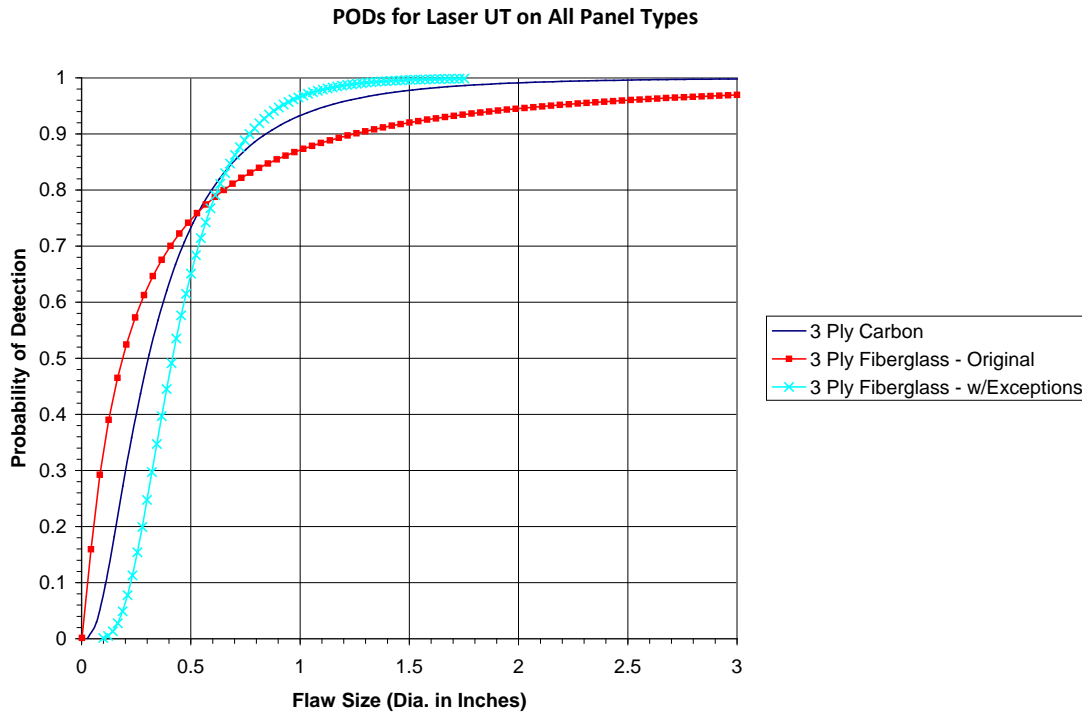


Figure 282. PoD curve comparisons for laminography showing the improvement when impact and edge (inspection image overlap) flaws are removed from POD calculation on 9-ply fiberglass

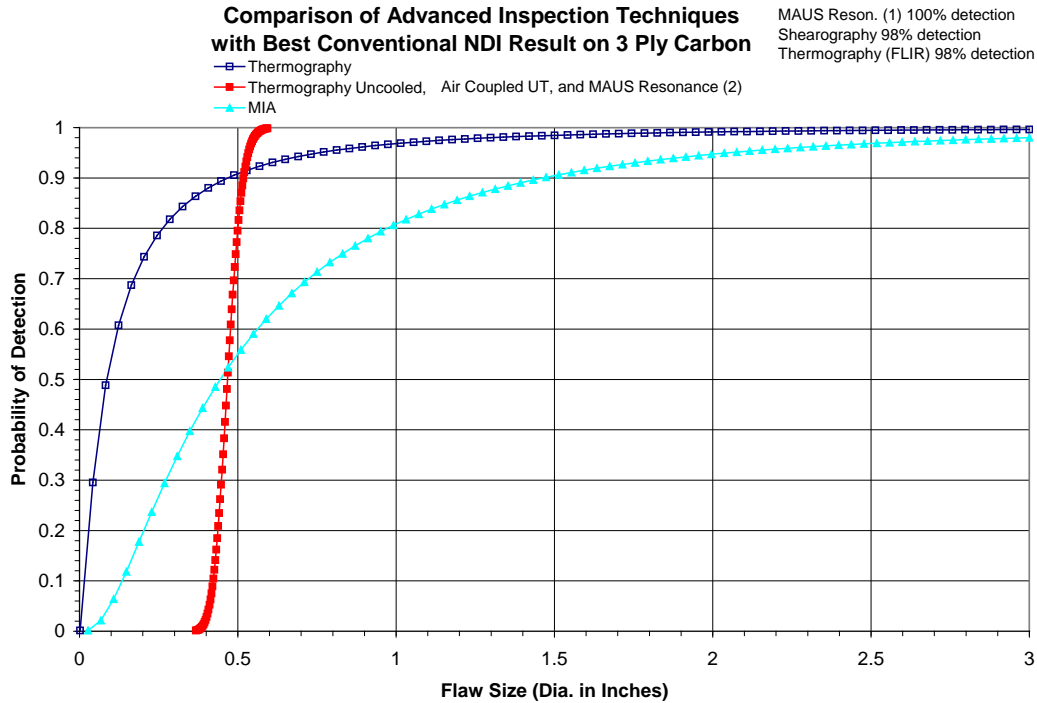
Similarly, when the laser UT method was applied to the three-ply fiberglass test specimens, multiple flaws in the center region of specimens were missed. This is probably because of the difficulties faced by experimenters engaged in data acquisition in this region. The PoD curve and tabulated values shown in figure 283 compare the overall cumulative performance of laser UT. The plots show the results produced when all flaws are considered and compares them with the curves produced when certain exceptions are removed from the flaw data. These include removing flaws located near the center area of the test specimens (difficulty in detecting due to system's inability to attenuate the laser light from the shiny painted surface). If these flaws are omitted from the PoD calculations, the detection percentage improves, and the 90% PoD level reduces to 0.77" diameter. Once again, this example shows that the laser UT performance could be improved with some changes in the system tuning and inspection procedures.



Laser UT		
Panel Type	False Calls	90% POD Value
3-ply carbon	4.0	0.84
3-ply fiberglass	0.0	1.25
6-ply carbon	N/A	N/A
6-ply fiberglass	N/A	N/A
9-ply carbon	N/A	N/A
9-ply fiberglass	N/A	N/A

Figure 283. PoD curve comparisons along with tabulated values for laser-ultrasonic inspections with exception that includes removing flaws located in center area of specimen from PoD calculations on 3-ply fiberglass

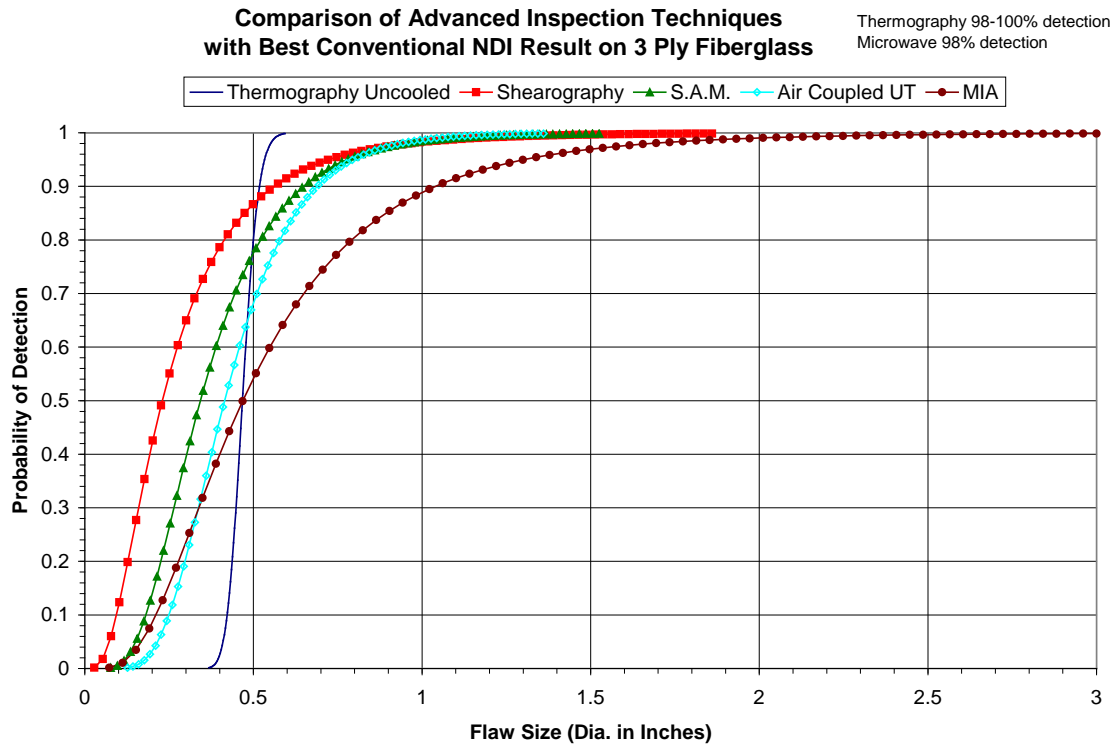
The final comparison matches the top performing advanced NDI methods in each honeycomb construction category with the best performing conventional NDI method. The PoD curves and tabulated values in figures 284–289 show the improvements that can be achieved through the application of advanced NDI methods to inspection composite honeycomb structures. In general, the level of improvement becomes higher as the inspection challenge increases (i.e., skin becomes thicker and moves from fiberglass to carbon). The 90% POD improvements range from 50–75%.



3-Ply Carbon		
Device	False Calls	90% POD Value
MAUS Resonance 1	3.0	$\leq .50$
Shearography	0.0	$\leq .50$
Thermography (FLIR)	0.0	$\leq .50$
Thermography	2.0	$\leq .50$
Thermography (uncooled)	0.0	0.52
Air-coupled UT	0.0	0.52
MAUS Resonance 2	2.0	0.53
MIA	0.6	1.46

(Highlighted = best conventional method for comparison purposes)

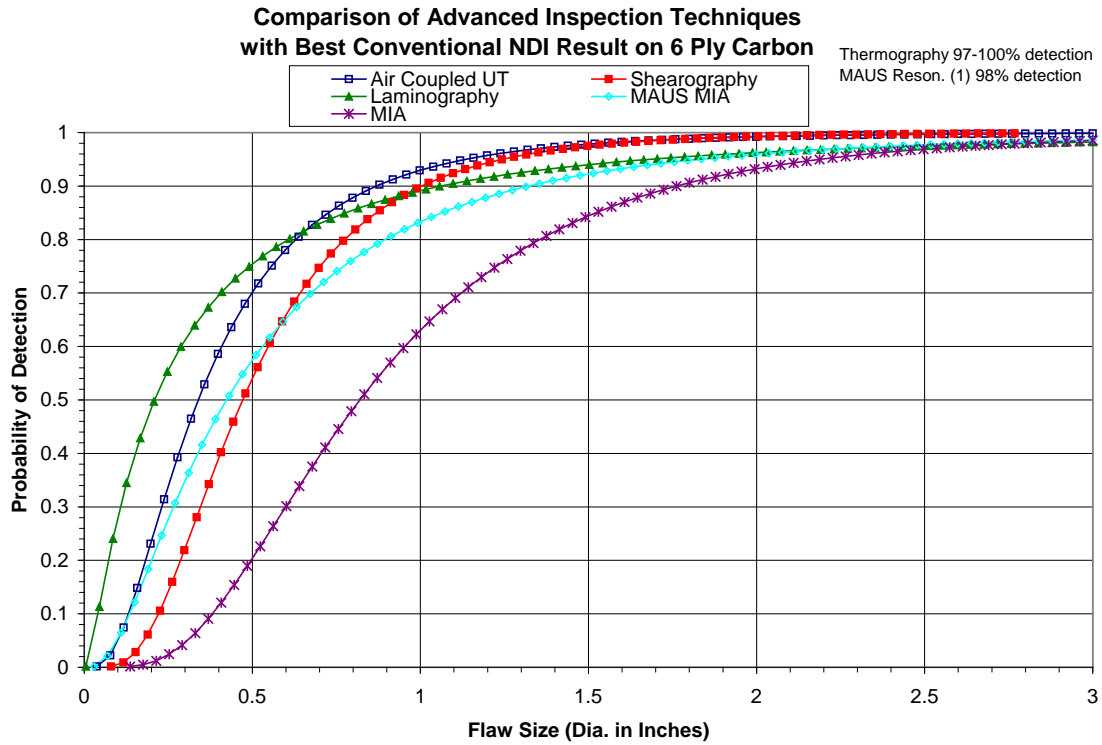
Figure 284. PoD curve comparisons along with tabulated values for advanced inspection methods and best performing conventional method on 3-ply carbon



3-Ply Fiberglass		
Device	False Calls	90% POD Value
Thermography	0.0	$\leq .50$
Thermography (FLIR)	0.0	$\leq .50$
Microwave	2.0	$\leq .50$
Thermography (uncooled)	0.0	0.52
Shearography	1.0	0.56
SAM	0.0	0.65
Air-coupled UT	0.0	0.69
MIA	0.5	1.04

(Highlighted = best conventional method for comparison purposes)

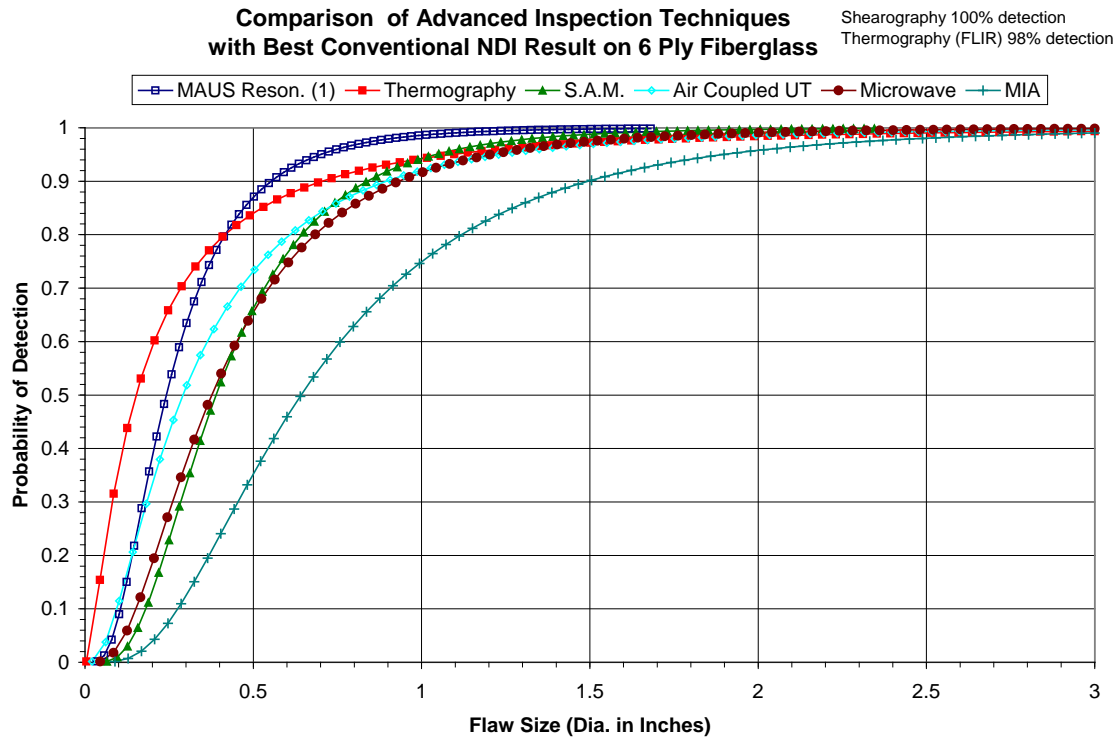
Figure 285. PoD curve comparisons along with tabulated values for advanced inspection methods and best performing conventional method on 3-ply fiberglass



6-Ply Carbon		
Device	False Calls	90% POD Value
Thermography (FLIR)	1.0	$\leq .50$
Thermography	2.0	$\leq .50$
MAUS Resonance 1	12.0	$\leq .50$
Air-coupled UT	0.0	0.87
Shearography	0.0	1.00
Laminography	0.0	1.10
MAUS MIA	6.0	1.32
MIA	1.3	1.76

(Highlighted = best conventional method for comparison purposes)

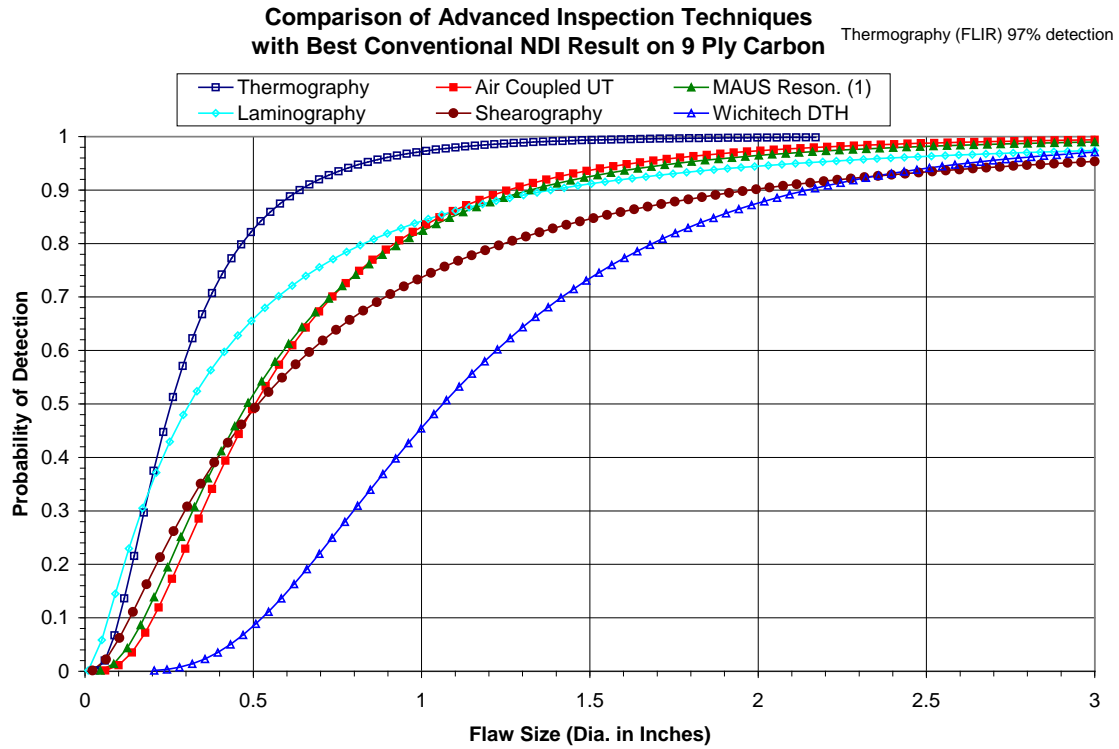
Figure 286. PoD curve comparisons along with tabulated values for advanced inspection methods and best performing conventional method on 6-ply carbon



6-Ply Fiberglass		
Device	False Calls	90% POD Value
Shearography	0.0	$\leq .50$
Thermography (FLIR)	4.0	$\leq .50$
MAUS Resonance 1	9.0	0.55
Thermography	3.0	0.70
SAM	8.0	0.84
Air-coupled UT	0.0	0.90
Microwave	12.0	0.93
MIA	1.9	1.49

(Highlighted = best conventional method for comparison purposes)

Figure 287. PoD curve comparisons along with tabulated values for advanced inspection methods and best performing conventional method on 6-ply fiberglass

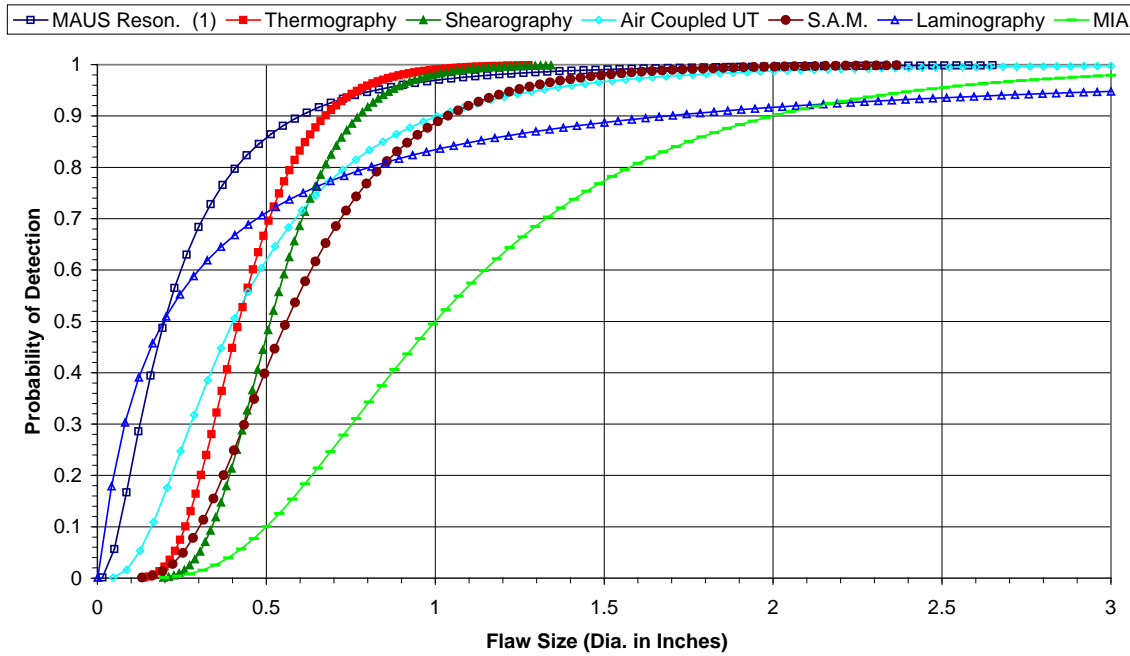


9-Ply Carbon		
Device	False Calls	90% POD Value
Thermography (FLIR)	0.0	$\leq .50$
Thermography	0.0	0.64
Air-coupled UT	2.0	1.26
MAUS Resonance 1	0.0	1.32
Laminography	0.0	1.39
Shearography	0.0	2.00
CATT	4.0	2.36
WitchiTech DTH	4.4	2.15

(Highlighted = best conventional method for comparison purposes)

Figure 288. PoD curve comparisons along with tabulated values for advanced inspection methods and best performing conventional method on 9-ply carbon

Comparison of Advanced Inspection Techniques Thermography (FLIR) 97% detection
with Best Conventional NDI Result on 9 Ply Fiberglass



9-Ply Fiberglass		
Device	False Calls	90% POD Value
Thermography (FLIR)	1.0	≤.50
MAUS Resonance 1	2.0	0.60
Thermography	2.0	0.67
Shearography	0.0	0.77
Air-coupled UT	1.0	1.01
SAM	17.0	1.04
Laminography	1.0	1.69
MIA	6.8	2.00

(Highlighted = best conventional method for comparison purposes)

Figure 289. PoD curve comparisons along with tabulated values for advanced inspection methods and best performing conventional method on 9-ply fiberglass

While the time to complete the inspections was considered a secondary variable, timing data were recorded so that some trends analysis could be completed. Tables 10–13 compare inspection times for each of the conventional and advanced NDI techniques in each of the specific composite honeycomb structure categories. Results for the conventional NDI methods indicate fairly consistent results for the average time to inspect each 18" x 18" panel, as well as the extreme values of minimum and maximum inspection times. Some of the advanced NDI methods that used automated scanning deployment completed the inspections in less time; however, when data analysis time was included in the timing calculations, many advanced NDI methods took slightly longer than the conventional NDI methods.

**Table 10. Average inspection times per 18" x 18" panel and max/min times for 3-ply panels
—conventional NDI methods**

3-Ply Carbon Inspection Time Comparisons			
Inspection Device	Low Insp. Time	High Insp. Time	Ave. Insp. Time
Airbus tap hammer	5.2	16.8	11.7
Boeing tap hammer	5.2	25.2	12.8
LFBT	6.8	23.5	13.8
MIA	7.8	20.3	13.7
WichiTech DTH	9.7	23.3	14.7
Woodpecker	6.8	22.7	15.7

3-Ply Fiberglass Inspection Time Comparisons			
Inspection Device	Low Insp. Time	High Insp. Time	Ave. Insp. Time
Airbus tap hammer	6.0	16.7	10.9
Boeing tap hammer	5.0	25.8	13.6
LFBT	6.7	28.7	16.6
MIA	9.7	32.5	18.0
WichiTech DTH	8.7	30.5	16.7
Woodpecker	7.8	21.3	15.7

(Times shown in minutes)

**Table 11. Average inspection times per 18" x 18" panel and max/min times for 6-ply panels
—conventional NDI methods**

6-Ply Carbon Inspection Time Comparisons			
Inspection Device	Low Insp. Time	High Insp. Time	Ave. Insp. Time
Airbus tap hammer	6.5	21.6	12.3
Boeing tap hammer	5.1	26.6	11.8
LFBT	6.8	30.1	14.2
MIA	9.4	24.8	13.9
WichiTech DTH	5.8	20.8	13.1
Woodpecker	5.8	22.0	13.0

6-Ply Fiberglass Inspection Time Comparisons			
Inspection Device	Low Insp. Time	High Insp. Time	Ave. Insp. Time
Airbus tap hammer	6.4	23.9	12.8
Boeing tap hammer	6.4	28.3	12.9
LFBT	6.5	20.9	12.2
MIA	9.0	34.3	16.6
WichiTech DTH	8.0	21.4	14.5
Woodpecker	4.4	23.6	15.1

(Times shown in minutes)

**Table 12. Average inspection times per 18" x 18" panel and max/min times for 9-ply panels
—conventional NDI methods**

9-Ply Carbon Inspection Time Comparisons			
Inspection Device	Low Insp. Time	High Insp. Time	Ave. Insp. Time
Airbus tap hammer	4.3	16.3	9.6
Boeing tap hammer	6.8	28.4	12.0
LFBT	9.5	19.3	12.4
MIA	8.4	16.8	12.2
WichiTech DTH	6.8	27.4	13.6
Woodpecker	5.0	22.5	12.5

(Times shown in minutes)

**Table 12. Average inspection times per 18" x 18" panel and max/min times for 9-ply panels
—conventional NDI methods (continued)**

9-Ply Fiberglass Inspection Time Comparisons			
Inspection Device	Low Insp. Time	High Insp. Time	Ave. Insp. Time
Airbus tap hammer	4.4	16.1	10.1
Boeing tap hammer	5.6	28.4	11.6
LFBT	8.0	20.4	12.2
MIA	8.9	41.5	16.5
WichiTech DTH	7.1	23.5	15.0
Woodpecker	5.1	21.0	13.3

(Times shown in minutes)

**Table 13. Average inspection times per 18" x 18" panel and max/min times for all panels—
advanced NDI methods (times shown in minutes)**

Advanced Inspection Methods' Time Comparisons (all panel types)						
Inspection Device	3-Ply Carbon Ave. Insp. Time Per Panel	3-Ply Fiberglass Ave. Insp. Time Per Panel	6-Ply Carbon Ave. Insp. Time Per Panel	6-Ply Fiberglass Ave. Insp. Time Per Panel	9-Ply Carbon Ave. Insp. Time Per Panel	9-Ply Fiberglass Ave. Insp. Time Per Panel
CATT	21.0	23.8	23.8	24.6	25.4	25.9
MAUS Resonance 1	N/A	N/A	N/A	N/A	N/A	N/A
SAM	34.3	29.0	27.5	30.3	31.8	26.5
Shearography	15.5	19.8	14.8	14.1	10.8	10.5
Thermography	12.0	12.0	13.0	12.0	13.8	13.9
MAUS Resonance 2	15.0	15.0	15.0	15.0	15.0	15.0
MAUS MIA	40.3	41.0	40.8	42.9	49.1	49.9
Laminography	36.0	36.0	36.0	36.0	36.0	36.0
Microwave	44.0	44.0	44.0	44.0	44.0	43.0
Thermography (uncooled)	N/A	N/A	N/A	N/A	N/A	N/A
Thermography (FLIR)	N/A	N/A	N/A	N/A	N/A	N/A
FlawInspecta UT Array	8.0	9.0	8.0	8.0	9.0	6.0
Air-coupled UT	18.0	18.0	18.0	18.0	18.0	18.0
Laser UT	N/A	N/A	N/A	N/A	N/A	N/A

Table 14 summarizes the false calls generated by the individual inspector for a particular inspection device/method in each of the specific composite honeycomb structure categories. It also tabulates the average number of false calls for each inspection method. Table 15 compares the average false call rates for each of the inspection methods and highlights the lowest (yellow highlight) and highest (red highlights) false call rates in each of the honeycomb construction categories. The Woodpecker device produced the lowest overall false call rate while the Boeing tap hammer produced the highest overall false call rate. Table 16 compares the false calls produced by each of the advanced NDI methods. The lowest number of false calls occurred with the laminography and CATT system, while, in general, the number of false calls did not seem to increase as the inspections became more challenging (i.e., thicker skin laminates).

Table 14. Summary of individual and average false calls for all inspectors and false call averages per inspection method and panel type—conventional NDI

Airbus Tap Hammer False Calls									
Panel Type /Insp. ID	AT-1	AT-2	AT-3	AT-4	AT-5	AT-6	AT-7	AT-8	Ave.
3-ply carbon	0	1	1	0	0	1	3	0	0.8
3-ply fiberglass	1	0	1	0	0	0	0	0	0.3
6-ply carbon	2	3	1	4	4	9	2	3	3.5
6-ply fiberglass	1	2	13	0	1	0	6	0	2.9
9-ply carbon	13	2	26	1	1	3	6	2	6.8
9-ply fiberglass	13	11	23	2	3	2	2	1	7.1
Total	30	19	65	7	9	15	19	6	21.3

Boeing Tap Hammer False Calls										
Panel Type /Insp. ID	BT-1	BT-2	BT-3	BT-4	BT-5	BT-6	BT-7	BT-8	BT-9	Ave.
3-ply carbon	0	1	3	1	1	2	0	1	0	1.0
3-ply fiberglass	4	3	3	0	0	6	0	0	0	1.8
6-ply carbon	0	4	6	4	8	13	2	2	3	4.7
6-ply fiberglass	0	6	6	1	7	17	2	2	1	4.7
9-ply carbon	3	2	7	2	14	14	5	1	1	5.4
9-ply fiberglass	1	7	6	1	25	18	3	1	0	6.9
Total	8	23	31	9	55	70	12	7	5	24.4

LFBT False Calls												
Panel Type /Insp. ID	LFBT-1	LFBT-2	LFBT-3	LFBT-4	LFBT-5	LFBT-6	LFBT-7	LFBT-8	LFBT-9	LFBT-10	LFBT-11	Ave.
3-ply carbon	0	0	14	0	0	0	2	2	0	0	7	2.3
3-ply fiberglass	0	0	8	0	1	0	0	1	0	0	0	0.9
6-ply carbon	0	0	33	1	0	0	1	0	2	0	34	6.5
6-ply fiberglass	0	0	24	0	6	0	1	2	1	0	2	3.3
9-ply carbon	0	0	1	3	1	0	4	0	0	0	33	3.8
9-ply fiberglass	0	0	0	3	0	0	0	0	3	0	25	2.8
Total	0	0	80	7	8	0	8	5	6	0	101	19.5

Table 14. Summary of individual and average false calls for all inspectors and false call averages per inspection method and panel type—conventional NDI (continued)

MIA False Calls											
Panel Type /Insp. ID	MIA-1	MIA-2	MIA-3	MIA-4	MIA-5	MIA-6	MIA-7	MIA-8	MIA-9	MIA-10	Ave.
3-ply carbon	1	1	0	4	0	0	0	0	0	0	0.6
3-ply fiberglass	2	1	0	1	0	0	1	0	0	0	0.5
6-ply carbon	0	0	0	4	0	0	1	1	6	1	1.3
6-ply fiberglass	1	0	0	0	0	0	1	0	15	2	1.9
9-ply carbon	0	1	3	6	1	4	4	5	N/A	4	3.1
9-ply fiberglass	0	2	2	5	0	2	15	0	36	6	6.8
Total	4	5	5	20	1	6	22	6	57	13	13.9

WitchiTech DTH False Calls										
Panel Type /Insp. ID	DTH-1	DTH-2	DTH-3	DTH-4	DTH-5	DTH-6	DTH-7	DTH-8	DTH-9	Ave.
3-ply carbon	0	5	0	0	0	0	0	0	0	0.6
3-ply fiberglass	0	8	0	0	0	0	0	0	0	0.9
6-ply carbon	0	6	0	1	0	0	0	1	0	0.9
6-ply fiberglass	0	8	0	0	0	6	0	0	0	1.6
9-ply carbon	0	5	0	0	0	31	0	0	4	4.4
9-ply fiberglass	0	12	0	0	0	32	0	0	0	4.9
Total	0	44	0	1	0	69	0	1	4	13.2

Woodpecker False Calls										
Panel Type /Insp. ID	WOOD-1	WOOD-2	WOOD-3	WOOD-4	WOOD-5	WOOD-6	WOOD-7	WOOD-8	WOOD-9	Ave.
3-ply carbon	0	0	0	0	0	0	0	0	0	0.0
3-ply fiberglass	0	0	0	3	0	0	0	0	0	0.3
6-ply carbon	0	0	0	0	1	1	4	0	0	0.7
6-ply fiberglass	0	0	0	0	0	0	0	0	1	0.1
9-ply carbon	0	1	2	2	1	9	0	8	2	2.8
9-ply fiberglass	5	0	5	16	3	13	5	6	7	6.7
Total	5	1	7	21	5	23	9	14	10	10.6

Table 15. Average number of false calls produced by conventional NDI devices on carbon and fiberglass specimens

Conventional Inspection Technique False Call Averages						
Panel Type / Insp. Method	Airbus Tap Hammer	Boeing Tap Hammer	LFBT	MIA	WichiTech DTH	Woodpecker
3-ply carbon	0.8	1.0	2.3	0.6	0.6	0.0
3-ply fiberglass	0.3	1.8	0.9	0.5	0.9	0.3
6-ply carbon	3.5	4.7	6.5	1.3	0.9	0.7
6-ply fiberglass	2.9	4.7	3.3	1.9	1.6	0.1
9-ply carbon	6.8	5.4	3.8	3.1	4.4	2.8
9-ply fiberglass	7.1	6.9	2.8	6.8	4.9	6.7
Total	21.3	24.4	19.5	13.9	13.2	10.6

Yellow highlights = lowest average number of false calls

Red highlights = highest average number of false calls

Table 16. False calls generated by advanced inspection techniques (arranged by panel type)

Advanced Inspection Technique False Calls							
Panel Type / Insp. Method	Shearography	Lamino graphy	Air-coupled UT	Laser UT	FlawInspecta UT Array	Thermography (FLIR)	Thermography (uncooled)
3-ply carbon	0	0	0	4	3	0	0
3-ply fiberglass	1	0	0	0	0	0	0
6-ply carbon	0	0	0	N/A	0	1	2
6-ply fiberglass	0	2	0	N/A	0	4	2
9-ply carbon	0	0	2	N/A	1	0	0
9-ply fiberglass	0	1	1	N/A	1	1	4
Total	0	3	3	4	5	6	8

**Table 16. False calls generated by advanced inspection techniques
(arranged by panel type) (continued)**

Advanced Inspection Technique False Calls							
Panel Type / Insp. Method	Thermo graphy	CATT	MAUS MIA	MAUS Resonance 1	MAUS Resonance 2	Microwave	SAM
3-ply carbon	2	0	0	3	2	9	2
3-ply fiberglass	0	4	0	5	6	2	0
6-ply carbon	2	1	6	12	4	10	37
6-ply fiberglass	3	1	6	9	2	12	8
9-ply carbon	0	4	8	0	10	23	74
9-ply fiberglass	2	0	8	2	11	8	17
Total	9	10	28	31	35	64	138

The test panels used in this experiment contained flaws on both sides of the honeycomb core. Each side was treated as a separate specimen number, as front-side flaw detection was the primary assessment being conducted. However, some NDI methods were able to detect flaws on the backside of the specimens (i.e., signal penetration provided some resolution of damage on the far side of the test specimen). Such detections of far-side flaws—flaws on the side of the panel opposite the inspection surface—were recorded. Tables 17–19 summarize detection of far side flaws for each composite honeycomb structure category. This is a secondary variable, and detection of these flaws was not required in the experiment.

**Table 17. Backside flaw detection for all inspectors and average backside flaws detected
per inspection method and panel type—conventional NDI**

Airbus Tap Hammer Backside Calls									
Panel Type	AT-1	AT-2	AT-3	AT-4	AT-5	AT-6	AT-7	AT-8	Ave.
3-ply carbon	0	7	0	4	3	0	1	0	1.9
3-ply fiberglass	0	0	0	3	0	0	3	0	0.8
6-ply carbon	0	13	1	9	5	4	10	0	5.3
6-ply fiberglass	1	11	2	4	9	3	11	0	5.1
9-ply carbon	1	12	12	13	15	9	10	0	9.0
9-ply fiberglass	3	15	11	10	21	9	15	1	10.6
Total	5	58	26	43	53	25	50	1	32.6

Table 17. Backside flaw detection for all inspectors and average backside flaws detected per inspection method and panel type—conventional NDI (continued)

Boeing Tap Hammer Backside Calls										
Panel Type	BT-1	BT-2	BT-3	BT-4	BT-5	BT-6	BT-7	BT-8	BT-9	Ave.
3-ply carbon	1	1	1	2	9	1	2	3	2	2.4
3-ply fiberglass	3	1	1	0	4	0	0	2	1	1.3
6-ply carbon	0	1	3	1	16	2	2	6	3	3.8
6-ply fiberglass	2	3	2	1	8	1	7	2	9	3.9
9-ply carbon	1	0	3	1	22	3	10	2	2	4.9
9-ply fiberglass	2	2	2	2	22	6	16	8	6	7.3
Total	9	8	12	7	81	13	37	23	23	23.7

LFBT Backside Calls												
Panel Type	LFBT-1	LFBT-2	LFBT-3	LFBT-4	LFBT-5	LFBT-6	LFBT-7	LFBT-8	LFBT-9	LFBT-10	LFBT-11	Ave.
3-ply carbon	6	0	0	0	0	0	0	5	10	15	1	3.4
3-ply fiberglass	0	0	1	0	0	0	0	8	3	21	1	3.1
6-ply carbon	5	0	8	3	3	1	14	18	23	18	9	9.3
6-ply fiberglass	0	0	1	0	0	8	3	16	8	13	1	4.5
9-ply carbon	14	0	19	1	4	10	5	19	11	22	1	10.1
9-ply fiberglass	14	0	21	0	0	0	0	17	2	19	6	6.7
Total	39	0	50	4	7	19	22	83	57	108	19	37.1

MIA Backside Calls												
Panel Type	MIA-1	MIA-2	MIA-3	MIA-4	MIA-5	MIA-6	MIA-7	MIA-8	MIA-9	MIA-10	MIA-11	Ave.
3-ply carbon	11	3	1	7	3	1	4	4	3	7		4.4
3-ply fiberglass	1	2	2	3	0	0	2	1	0	5		1.6
6-ply carbon	18	2	2	3	3	0	5	3	7	4		4.7
6-ply fiberglass	12	3	4	2	0	0	5	2	7	4		3.9
9-ply carbon	7	4	2	1	2	1	2	1	N/A	7		3.0
9-ply fiberglass	14	4	6	2	6	1	6	3	10	8		6.0
Total	63	18	17	18	14	3	24	14	27	35		23.3

WichiTech DTH Backside Calls										
Panel Type	DTH-1	DTH-2	DTH-3	DTH-4	DTH-5	DTH-6	DTH-7	DTH-8	DTH-9	Ave.
3-ply carbon	3	0	1	4	0	6	1	7	4	2.9
3-ply fiberglass	3	2	1	0	1	0	1	1	2	1.2
6-ply carbon	3	1	7	3	1	11	3	8	4	4.6
6-ply fiberglass	3	3	5	5	1	10	2	4	6	4.3
9-ply carbon	6	7	7	8	4	11	6	13	10	8.0
9-ply fiberglass	5	6	7	7	6	11	6	13	8	7.7
Total	23	19	28	27	13	49	19	46	34	28.7

Table 17. Backside flaw detection for all inspectors and average backside flaws detected per inspection method and panel type—conventional NDI (continued)

Woodpecker Backside Calls										
Panel Type	WOOD-1	WOOD-2	WOOD-3	WOOD-4	WOOD-5	WOOD-6	WOOD-7	WOOD-8	WOOD-9	Ave.
3-ply carbon	0	0	1	0	3	1	1	1	1	0.9
3-ply fiberglass	0	0	0	1	0	0	1	1	0	0.3
6-ply carbon	1	0	1	4	2	4	1	2	2	1.9
6-ply fiberglass	3	0	2	2	3	6	1	1	0	2.0
9-ply carbon	1	1	2	1	5	1	1	3	2	1.9
9-ply fiberglass	3	1	4	7	9	2	4	9	6	5.0
Total	8	2	10	15	22	14	9	17	11	12.0

Positive indications (i.e., backside flaws correctly detected) in these regions reflect an NDI penetration through the 1" honeycomb core that can be useful in regions where far-side access is not possible. The Airbus tap hammer, with its lower frequency excitation, and LFBT method produced the highest number of backside flaw detections for the conventional NDI methods. AC-UT, as it is a through-transmission method, and shearography produced the best backside flaw detection among the advanced NDI methods.

Table 18. Summary of average backside flaw detection for conventional inspection techniques listed by panel type

Average Number of Backside Calls Per Device						
Device/Panel Type	Airbus Tap Hammer	Boeing Tap Hammer	LFBT	MIA	WichiTech DTH	Woodpecker
3-ply carbon	1.9	2.4	3.4	4.4	2.9	0.9
3-ply fiberglass	0.8	1.3	3.1	1.6	1.2	0.3
6-ply carbon	5.3	3.8	9.3	4.7	4.6	1.9
6-ply fiberglass	5.1	3.9	4.5	3.9	4.3	2.0
9-ply carbon	9.0	4.9	10.1	3.0	8.0	1.9
9-ply fiberglass	10.6	7.3	6.7	6.0	7.7	5.0
Total	32.6	23.7	37.1	23.3	28.7	12.0

Yellow highlights = lowest number of backside calls

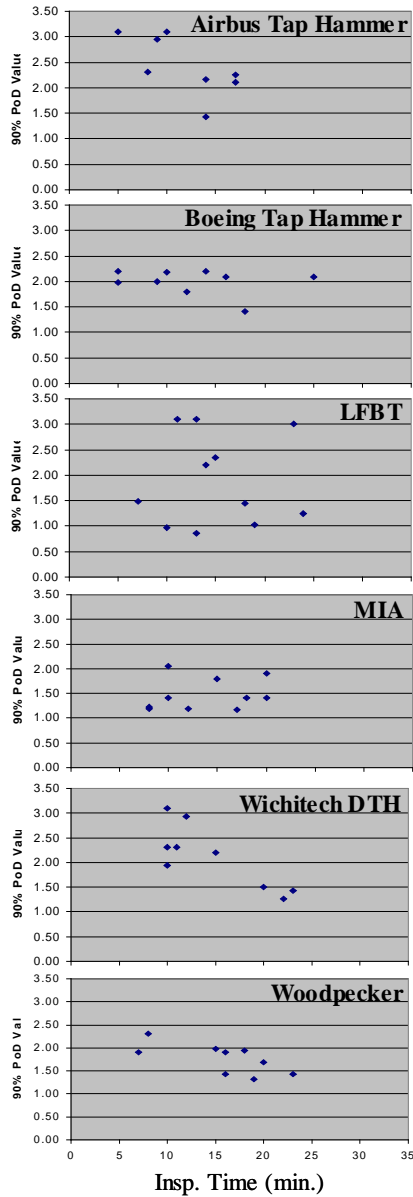
Red highlights = highest number of backside calls

**Table 19. Backside flaw detection for advanced inspection techniques by panel type
(note: AC-UT was executed in through-transmission mode)**

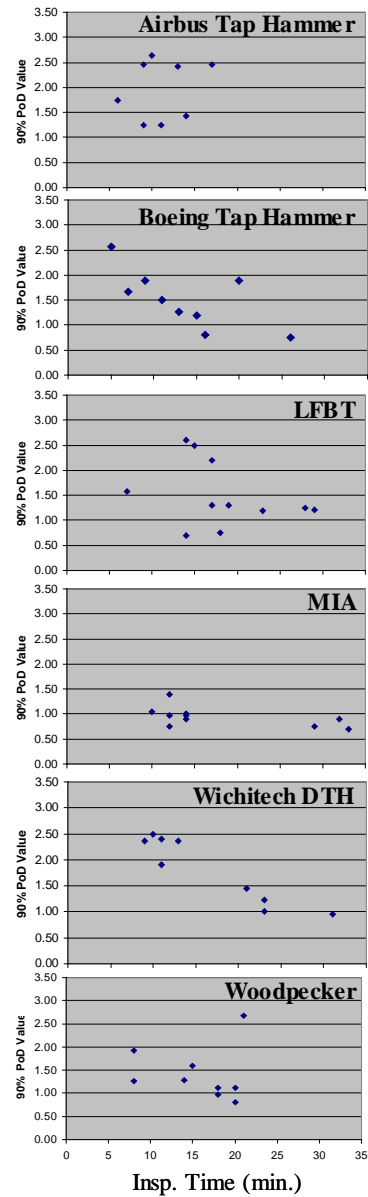
Advanced Inspection Techniques Backside Calls							
Panel Type / Insp. Method	Air-Coupled UT	Shearography	SAM	Microwave	MAUS MIA	CATT	MAUS Resonance 1
3-ply carbon	49	26	20	5	12	9	0
3-ply fiberglass	47	27	21	27	10	4	1
6-ply carbon	46	26	23	0	11	7	3
6-ply fiberglass	45	26	22	25	10	7	8
9-ply carbon	41	24	18	2	7	4	0
9-ply fiberglass	44	26	34	25	3	3	3
Total	272	155	138	84	53	34	15

Advanced Inspection Techniques Backside Calls							
Panel Type / Insp. Method	MAUS Resonance 2	FlawInspecta UT Array	Thermography (uncooled)	Thermography (FLIR)	Lamino graphy	Thermo graphy	Laser UT
3-ply carbon	0	0	0	0	0	0	0
3-ply fiberglass	0	0	0	0	0	0	0
6-ply carbon	1	0	0	0	0	0	N/A
6-ply fiberglass	3	0	0	0	0	0	N/A
9-ply carbon	2	2	1	0	0	0	N/A
9-ply fiberglass	0	0	0	0	0	0	N/A
Total	6	2	1	0	0	0	0

Figures 290–295 are scatter diagrams showing the effect of inspection time on PoD and false call performance for each composite honeycomb structure category. These are plots of each inspector’s average time of inspection versus their resulting performance. For the PoD category, the trends analyses showed that there was some improvement in PoD levels as the inspection time per panel increased from 5 minutes to 15 minutes. However, increased inspection times beyond 15 minutes did not provide much improvement in the PoD. Thus, the optimum inspection rate for a 2.25 ft.² area is approximately 15 minutes. For the false call category, the trends analyses did not show any reduction in false call rates as the inspection times were increased. This indicates that the false call rate was much more dependent on individual interpretations than on the rate of making the interpretations.



3-Ply Carbon



3-Ply Fiberglass

Figure 290. Scatter diagram showing effect of inspection time on PoD values for 3-ply panels

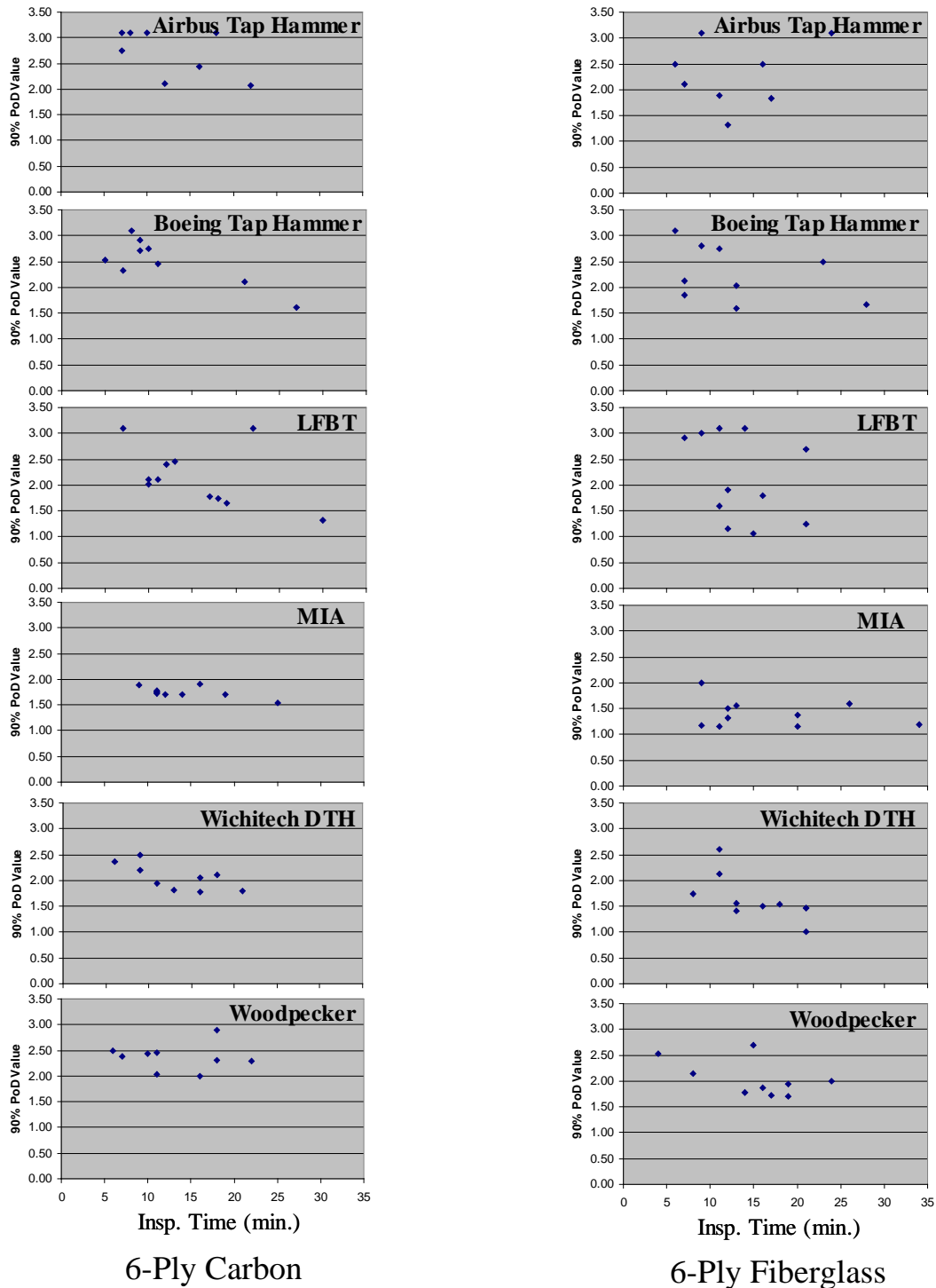


Figure 291. Scatter diagram showing effect of inspection time on PoD values for 6-ply panels

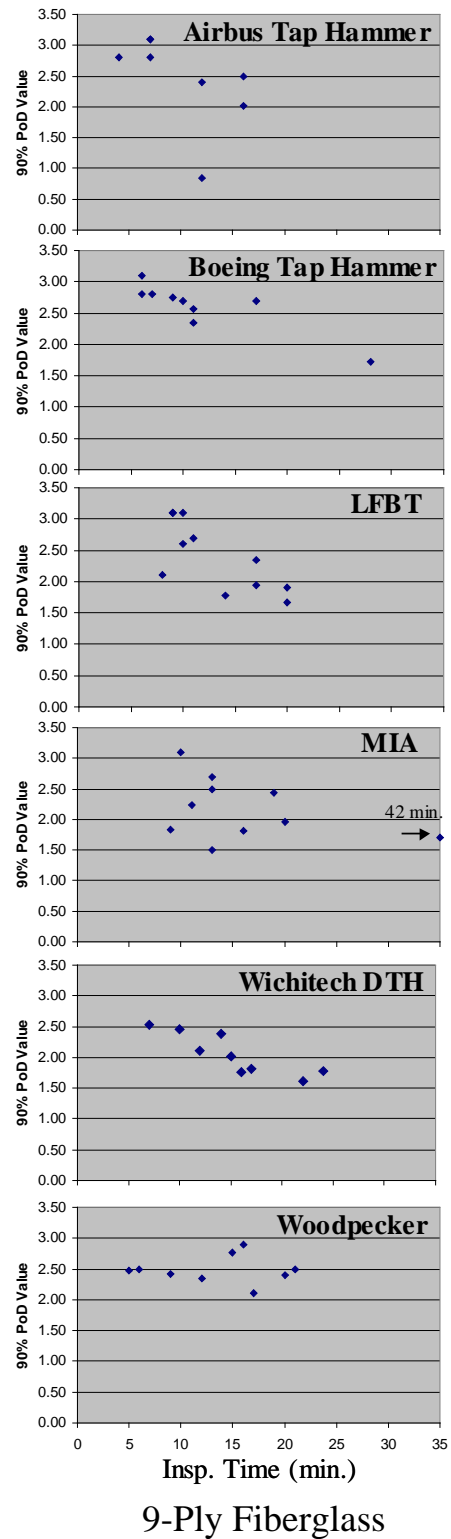
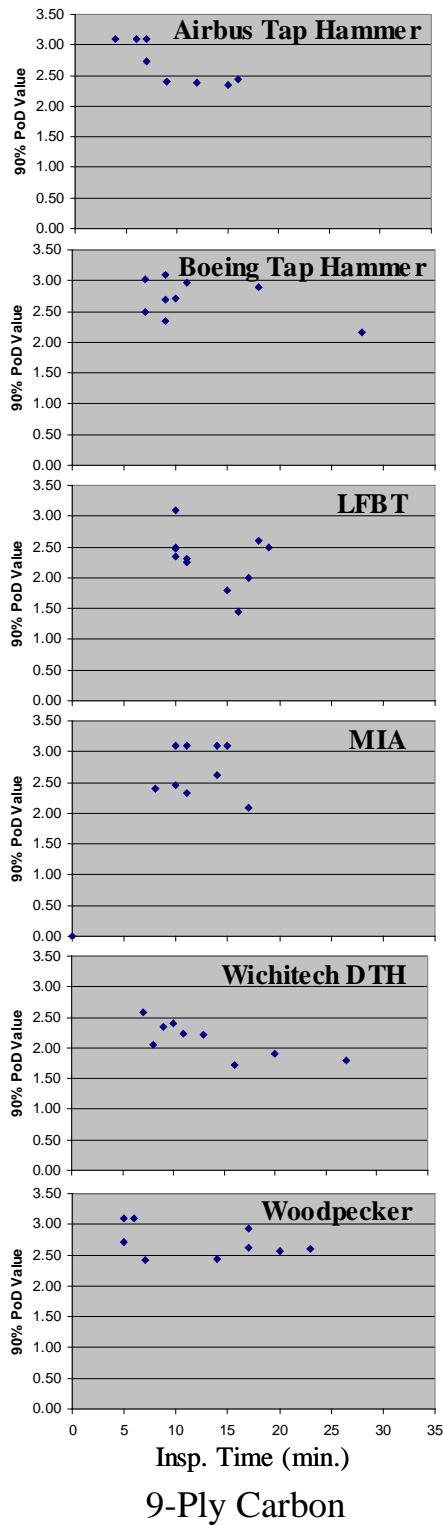


Figure 292. Scatter diagram showing effect of inspection time on PoD values for 9-ply panels

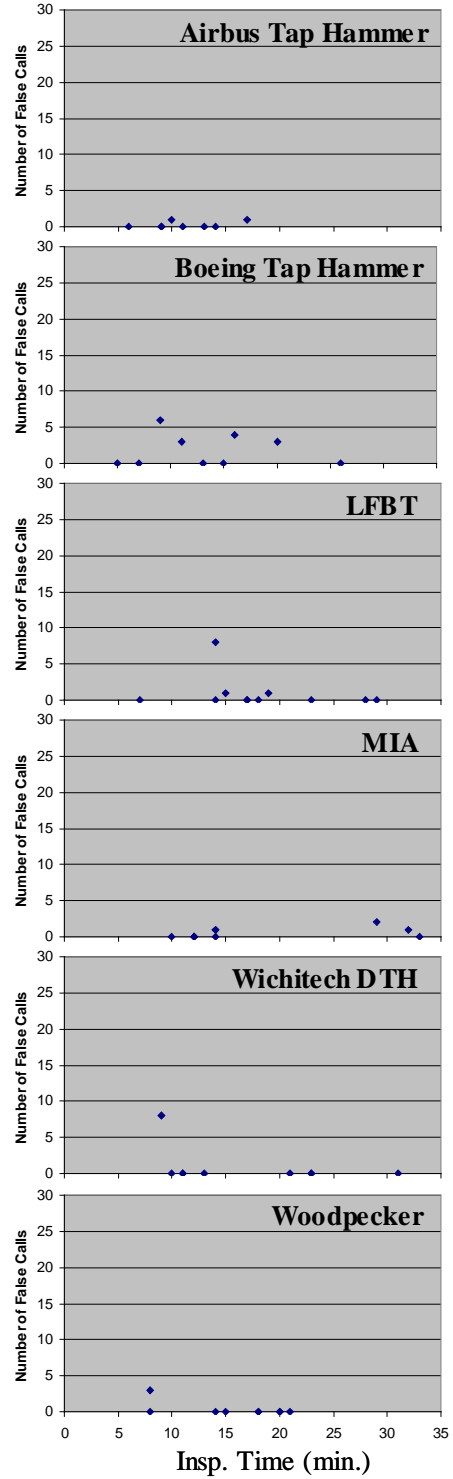
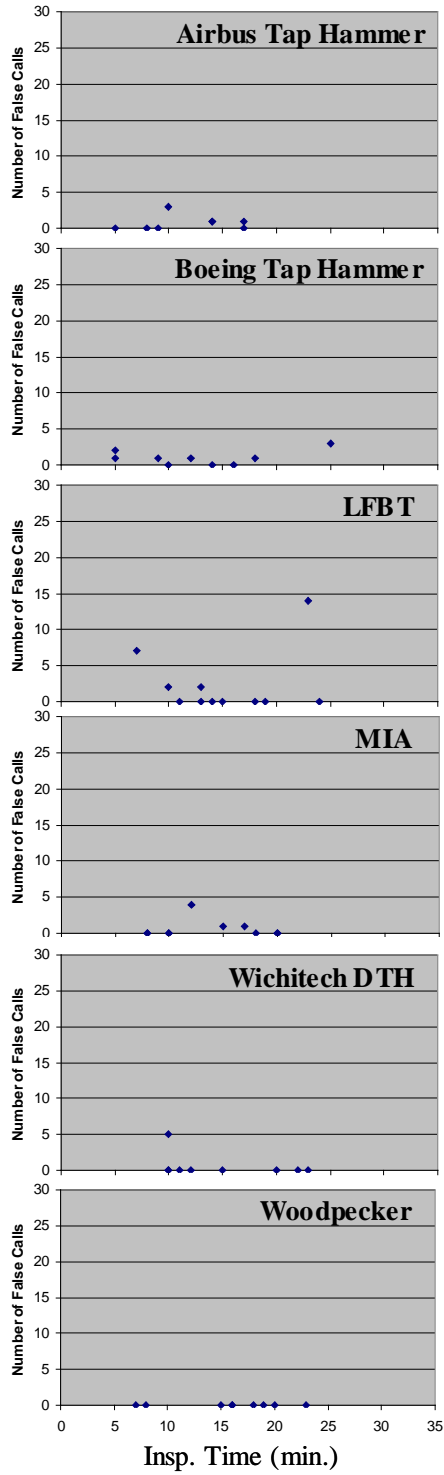


Figure 293. Scatter diagram showing effect of inspection time on false calls for 3-ply panels

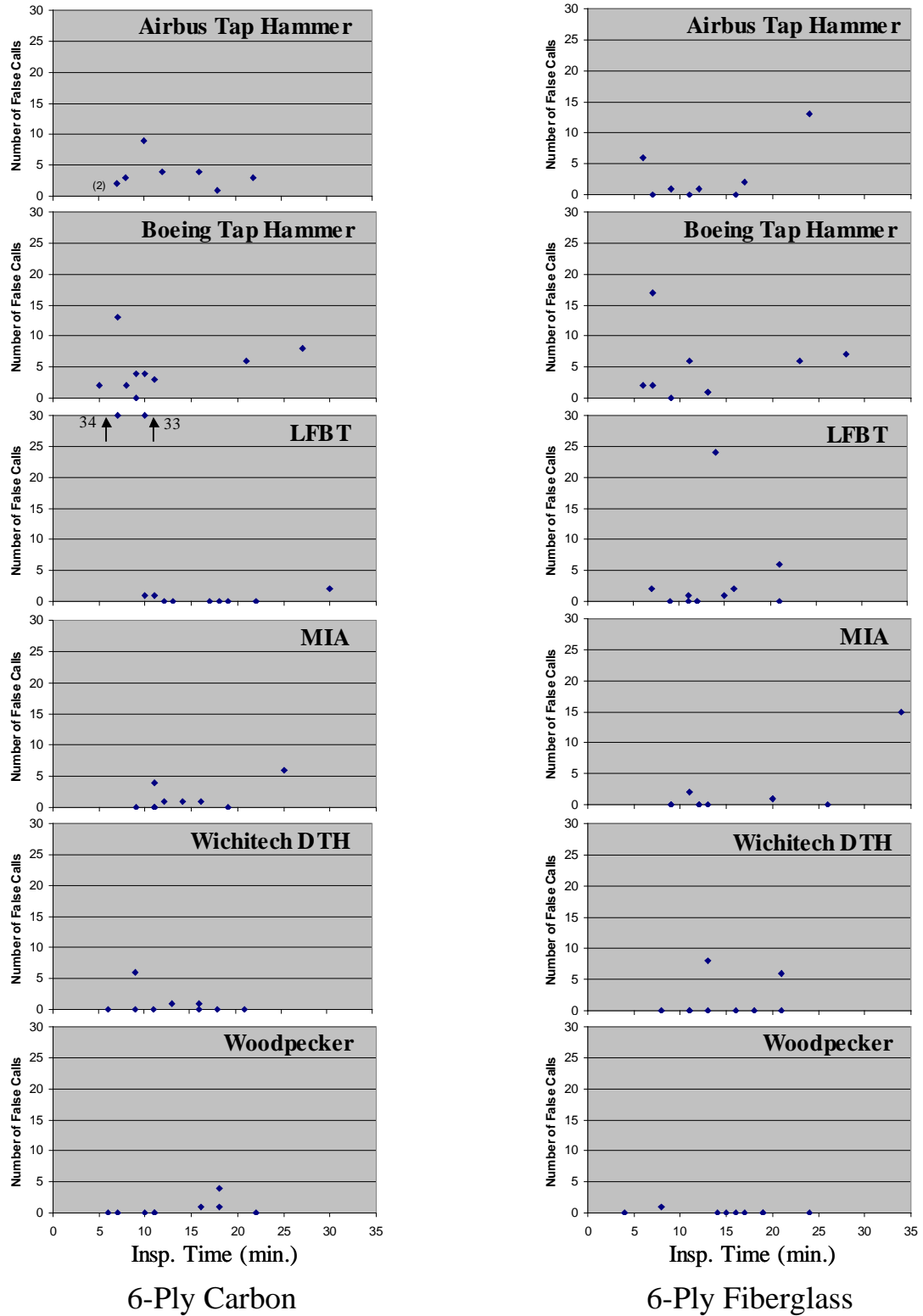


Figure 294. Scatter diagram showing effect of inspection time on false calls for 6-ply panels

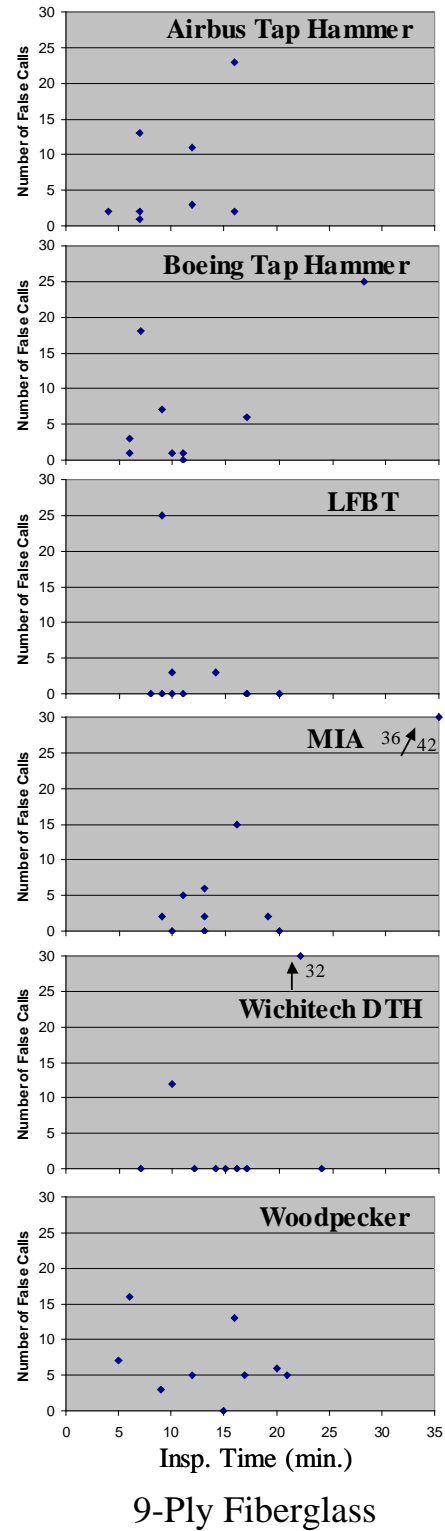
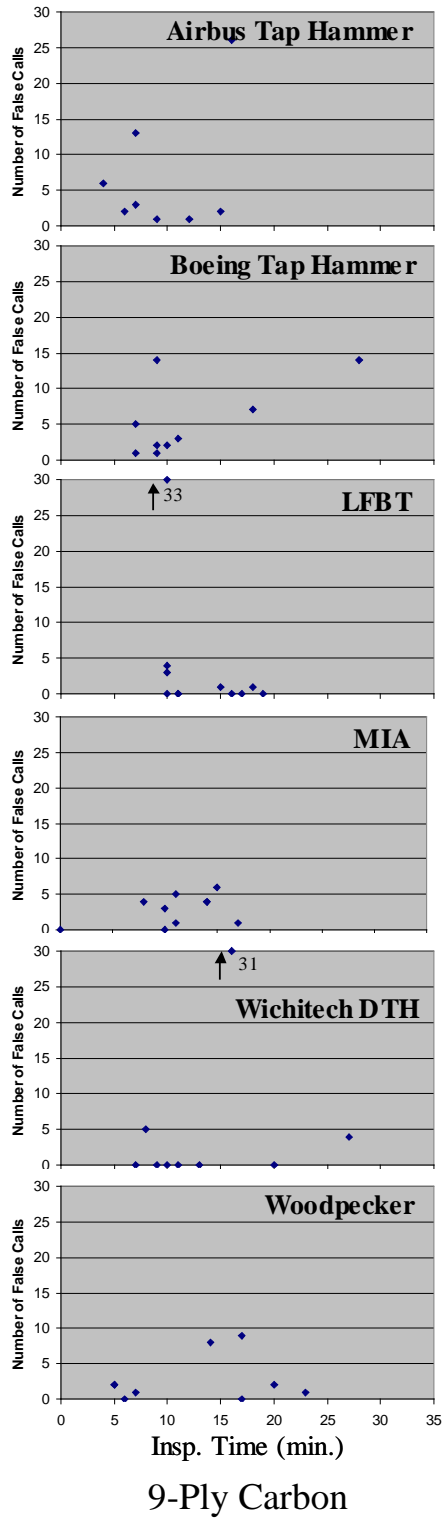


Figure 295. Scatter diagram showing effect of inspection time on false calls for 9-ply panels

The scatter diagrams in figures 296–298 show that there is no relation between the number of false calls and the resulting PoD values for each composite honeycomb structure category. This is primarily because the inspectors were not trying to improve PoD performance by marking a large number of areas; rather, they were trying to earnestly discern flaw regions from pristine regions.

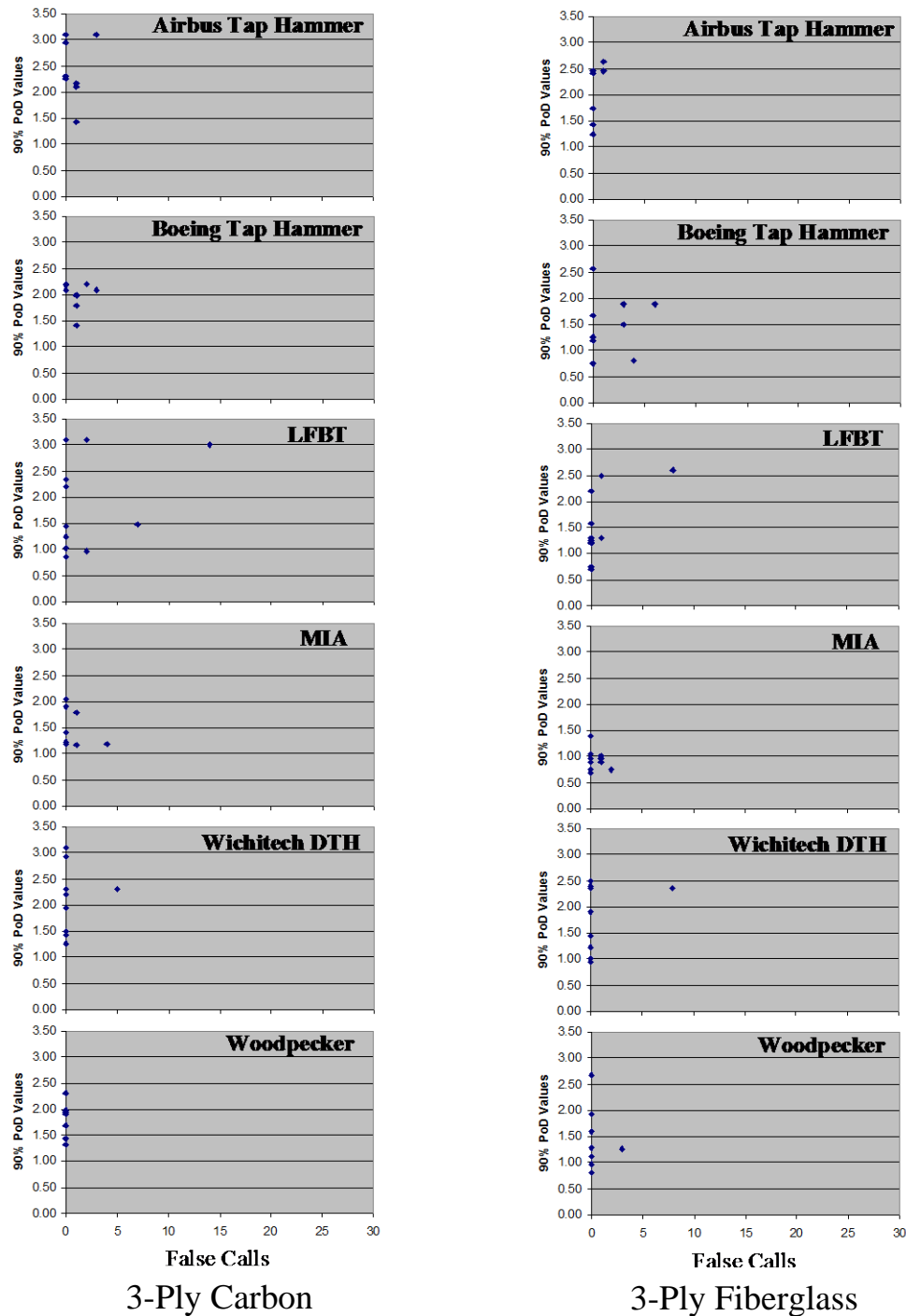


Figure 296. Scatter diagram showing the effect of the number of false calls on PoD values for 3-ply panels

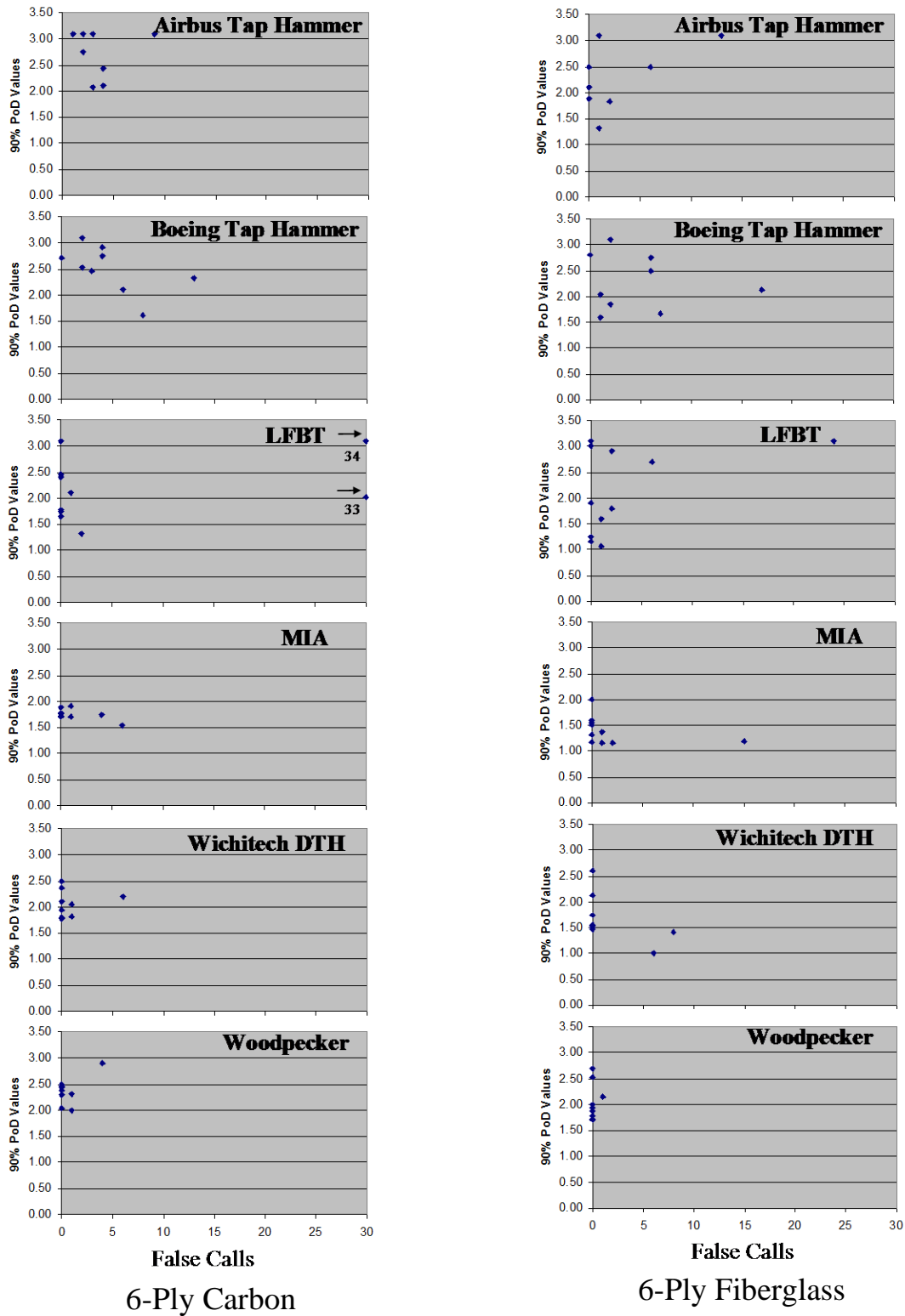


Figure 297. Scatter diagram showing the effect of the number of false calls on PoD values for 6-ply panels

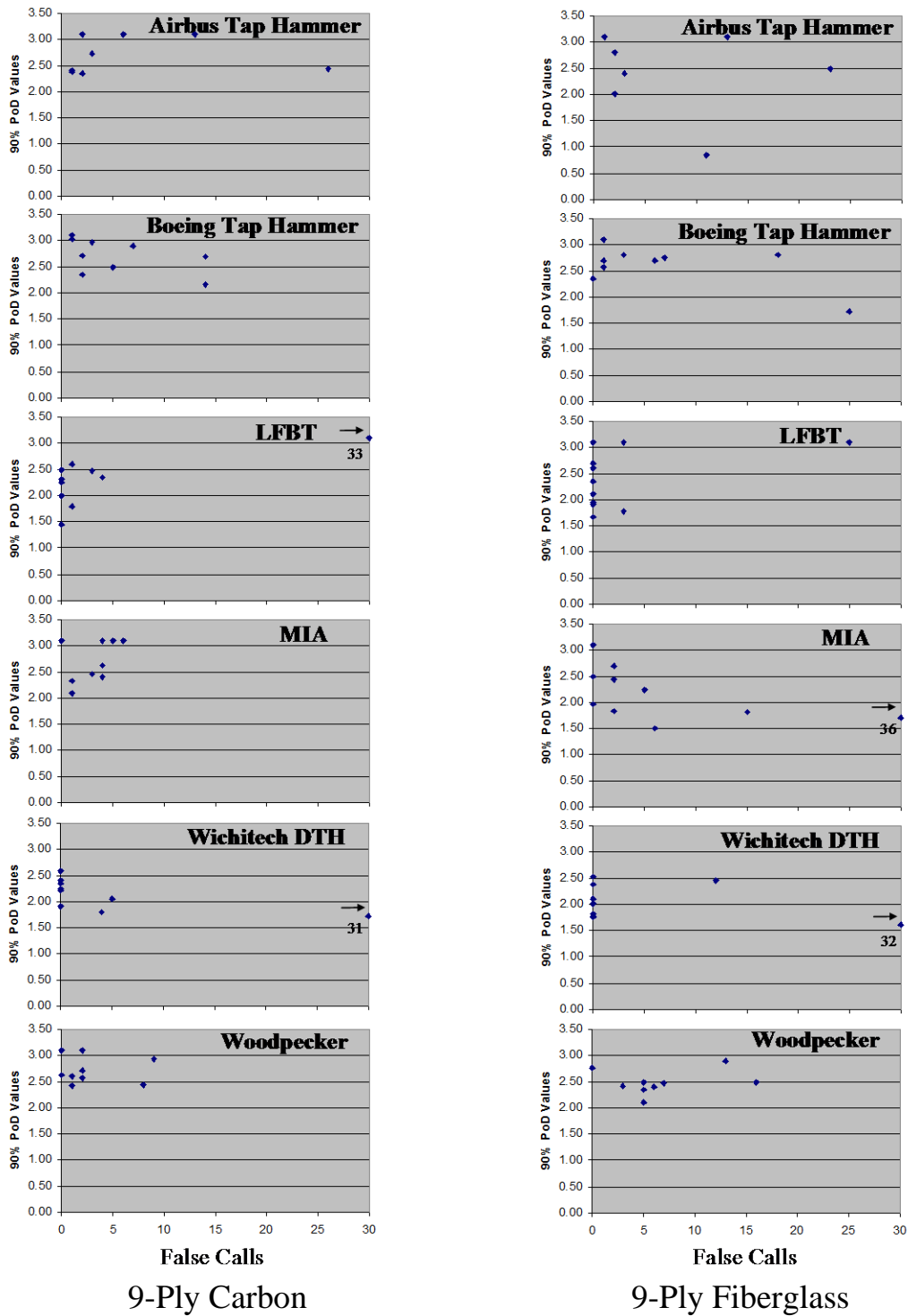


Figure 298. Scatter diagram showing the effect of the number of false calls on PoD values for 9-ply panels

Tables 20–25 summarize the overall performance results including flaw sizing capability, 90% PoD values, and false call rates for each NDI method in this study and broken down by the various composite honeycomb structure categories. These tables provide the best single view of the capability of conventional and advanced NDI methods to detect flaws/damage in composite honeycomb structures.

Table 20. Summary of all NDI performance for 3-ply carbon and fiberglass test specimens—flaw sizing, overall 90% PoD levels, and false calls

Flaw Sizing and False Call Summary Table for 3-Ply Carbon							
Flaw Coverage							
Inspection Device	100%	99%–75%	74%–50%	49%–25%	<25%	90% POD Level	False Calls
Airbus tap hammer	42%	40%	15%	3%	1%	2.34	0.8
Boeing tap hammer	38%	42%	15%	5%	1%	2.03	1.0
LFBT	34%	26%	21%	13%	6%	2.10	2.3
MIA	34%	37%	15%	11%	3%	1.46	0.6
WichiTech DTH	46%	38%	12%	4%	1%	2.28	0.6
Woodpecker	38%	41%	12%	7%	1%	1.78	0.0
CATT	12%	53%	14%	16%	5%	1.19	0.0
MAUS Resonance 1	68%	19%	13%	0%	0%	≤.50	3.0
SAM	26%	38%	21%	10%	5%	1.26	2.0
Shearography	74%	18%	8%	0%	0%	≤.50	0.0
Thermography	84%	12%	4%	0%	0%	≤.50	2.0
MAUS Resonance 2	56%	38%	6%	0%	0%	0.53	2.0
MAUS MIA	91%	4%	4%	0%	0%	0.77	0.0
Laminography	92%	8%	0%	0%	0%	0.66	0.0
Microwave	90%	0%	0%	3%	7%	2.13	9.0
Thermography (uncooled)	92%	6%	0%	2%	0%	0.52	0.0
Thermography (FLIR)	N/A	N/A	N/A	N/A	N/A	≤.50	0.0
FlawInspecta UT Array	79%	16%	5%	0%	0%	1.24	3.0
Air-coupled UT	4%	59%	20%	16%	0%	0.52	0.0
Laser UT	93%	7%	0%	0%	0%	0.84	4.0

(Highlighted = best performers)

Table 20. Summary of all NDI performance for 3-ply fiberglass test specimens—flaw sizing, overall 90% PoD levels, and false calls (continued)

Flaw Sizing and False Call Summary Table for 3-Ply Fiberglass							
Flaw Coverage							
Inspection Device	100%	99%– 75%	74%– 50%	49%– 25%	<25%	90% POD Level	False Calls
Airbus tap hammer	32%	40%	21%	5%	2%	2.03	0.3
Boeing tap hammer	40%	35%	17%	7%	2%	1.57	1.8
LFBT	32%	29%	21%	15%	3%	1.77	0.9
MIA	34%	37%	19%	8%	1%	1.04	0.5
WichiTech DTH	35%	44%	16%	4%	1%	1.81	0.9
Woodpecker	42%	39%	12%	5%	2%	1.45	0.3
CATT	28%	58%	12%	2%	0%	1.04	4.0
MAUS Resonance 1	61%	22%	17%	0%	0%	0.69	5.0
SAM	21%	38%	25%	15%	2%	0.65	0.0
Shearography	59%	31%	8%	2%	0%	0.56	1.0
Thermography	75%	20%	6%	0%	0%	≤.50	0.0
MAUS Resonance 2	58%	37%	5%	0%	0%	1.18	6.0
MAUS MIA	89%	6%	4%	0%	0%	0.69	0.0
Laminography	93%	5%	2%	0%	0%	0.97	0.0
Microwave	92%	6%	0%	2%	0%	≤.50	2.0
Thermography (uncooled)	86%	10%	2%	2%	0%	0.52	0.0
Thermography (FLIR)	N/A	N/A	N/A	N/A	N/A	≤.50	0.0
FlawInspecta UT Array	67%	25%	6%	3%	0%	1.78	0.0
Air-coupled UT	4%	36%	45%	15%	0%	0.69	0.0
Laser UT	82%	18%	0%	0%	0%	1.25	0.0

(Highlighted = best performers)

Table 21. Summary of all NDI performance for 6-ply carbon and fiberglass test specimens—flaw sizing, overall 90% PoD levels, and false calls

Flaw Sizing and False Call Summary Table for 6-Ply Carbon							
Flaw Coverage							
Inspection Device	100%	99%– 75%	74%– 50%	49%– 25%	<25%	90% POD Level	False Calls
Airbus tap hammer	18%	26%	23%	24%	8%	>3.00	3.5
Boeing tap hammer	20%	33%	27%	16%	4%	2.59	4.7
LFBT	28%	24%	23%	19%	6%	2.42	6.5
MIA	18%	33%	26%	21%	2%	1.76	1.3
WichiTech DTH	34%	36%	19%	9%	2%	2.18	0.9
Woodpecker	31%	31%	20%	15%	4%	2.32	0.7
CATT	29%	47%	18%	5%	0%	1.85	1.0
MAUS Resonance 1	48%	34%	10%	8%	0%	≤.50	12.0
SAM	3%	49%	31%	10%	8%	1.63	37.0
Shearography	62%	18%	8%	10%	2%	1.00	0.0
Thermography	82%	7%	4%	7%	0%	≤.50	2.0
MAUS Resonance 2	49%	27%	22%	3%	0%	2.27	4.0
MAUS MIA	90%	6%	4%	0%	0%	1.32	6.0
Laminography	90%	2%	0%	0%	8%	1.10	0.0
Microwave	43%	19%	0%	24%	14%	>3.00	10.0
Thermography (uncooled)	74%	11%	2%	7%	7%	1.70	2.0
Thermography (FLIR)	N/A	N/A	N/A	N/A	N/A	≤.50	1.0
FlawInspecta UT Array	64%	12%	2%	19%	19%	1.92	0.0
Air-coupled UT	23%	49%	17%	11%	11%	0.87	0.0
Laser UT	N/A	N/A	N/A	N/A	N/A	N/A	N/A

(Highlighted = best performers)

Table 21. Summary of all NDI performance for 6-ply carbon and fiberglass test specimens—flaw sizing, overall 90% PoD levels, and false calls (continued)

Flaw Sizing and False Call Summary Table for 6-Ply Fiberglass							
Flaw Coverage							
Inspection Device	100%	99%– 75%	74%– 50%	49%– 25%	<25%	90% POD Level	False Calls
Airbus tap hammer	28%	30%	27%	13%	2%	2.44	2.9
Boeing tap hammer	21%	34%	25%	16%	4%	2.33	4.7
LFBT	28%	29%	20%	18%	5%	2.55	3.3
MIA	26%	26%	26%	18%	4%	1.49	1.9
WichiTech DTH	32%	39%	19%	8%	2%	1.71	1.6
Woodpecker	31%	28%	20%	14%	7%	2.05	0.1
CATT	28%	38%	19%	13%	24%	1.10	1.0
MAUS Resonance 1	47%	31%	4%	4%	14%	0.55	9.0
SAM	11%	40%	32%	9%	8%	0.84	8.0
Shearography	49%	27%	15%	9%	0%	≤.50	0.0
Thermography	75%	15%	5%	5%	0%	0.70	3.0
MAUS Resonance 2	39%	33%	18%	9%	0%	2.07	2.0
MAUS MIA	84%	8%	8%	0%	0%	1.48	6.0
Laminography	86%	6%	0%	2%	6%	1.43	2.0
Microwave	75%	17%	2%	0%	6%	0.93	12.0
Thermography (uncooled)	55%	24%	2%	2%	17%	2.19	2.0
Thermography (FLIR)	N/A	N/A	N/A	N/A	N/A	≤.50	4.0
FlawInspecta UT Array	31%	13%	25%	6%	25%	>3.00	0.0
Air-coupled UT	21%	43%	34%	2%	0%	0.90	0.0
Laser UT	N/A	N/A	N/A	N/A	N/A	N/A	N/A

(Highlighted = best performers)

Table 22. Summary of all NDI performance for 9-ply carbon and fiberglass test specimens—flaw sizing, overall 90% PoD levels, and false calls

Flaw Sizing and False Call Summary Table for 9-Ply Carbon							
Flaw Coverage							
Inspection Device	100%	99%– 75%	74%– 50%	49%– 25%	<25%	90% POD Level	False Calls
Airbus tap hammer	35%	25%	17%	18%	5%	>3.00	6.8
Boeing tap hammer	19%	20%	27%	28%	6%	2.88	5.4
LFBT	32%	23%	17%	20%	8%	2.61	3.8
MIA	14%	22%	25%	30%	9%	2.97	3.1
WichiTech DTH	41%	30%	19%	6%	3%	2.15	4.4
Woodpecker	22%	27%	26%	19%	6%	2.76	2.8
CATT	12%	31%	38%	19%	0%	2.36	4.0
MAUS Resonance 1	44%	28%	5%	19%	5%	1.32	0.0
SAM	0%	41%	22%	11%	26%	>3.00	74.0
Shearography	53%	21%	16%	7%	2%	2.00	0.0
Thermography	86%	9%	0%	5%	0%	0.64	0.0
MAUS Resonance 2	50%	31%	15%	4%	0%	>3.00	10.0
MAUS MIA	74%	19%	6%	0%	0%	>3.00	8.0
Laminography	90%	2%	2%	0%	6%	1.39	0.0
Microwave	24%	20%	8%	16%	32%	>3.00	23.0
Thermography (uncooled)	71%	0%	6%	6%	16%	>3.00	0.0
Thermography (FLIR)	N/A	N/A	N/A	N/A	N/A	≤.50	0.0
FlawInspecta UT Array	71%	9%	6%	9%	6%	2.85	1.0
Air-coupled UT	17%	55%	19%	4%	4%	1.26	2.0
Laser UT	N/A	N/A	N/A	N/A	N/A	N/A	N/A

(Highlighted = best performer)

Table 22. Summary of all NDI performance for 9-ply carbon and fiberglass test specimens—flaw sizing, overall 90% PoD levels, and false calls (continued)

Flaw Sizing and False Call Summary Table for 9-Ply Fiberglass							
Flaw Coverage							
Inspection Device	100%	99%– 75%	74%– 50%	49%– 25%	<25%	90% POD Level	False Calls
Airbus tap hammer	33%	27%	23%	13%	5%	>3.00	7.1
Boeing tap hammer	18%	30%	24%	21%	6%	2.90	6.9
LFBT	25%	26%	24%	20%	5%	3.00	2.8
MIA	14%	22%	30%	23%	10%	2.00	6.8
WichiTech DTH	43%	32%	18%	6%	1%	2.07	4.9
Woodpecker	35%	28%	16%	11%	11%	2.52	6.7
CATT	13%	23%	30%	33%	0%	2.27	0.0
MAUS Resonance 1	45%	33%	10%	2%	10%	0.60	2.0
SAM	0%	75%	23%	2%	0%	1.04	17.0
Shearography	65%	21%	12%	2%	0%	0.77	0.0
Thermography	80%	5%	7%	7%	0%	0.67	2.0
MAUS Resonance 2	39%	29%	11%	21%	0%	>3.00	11.0
MAUS MIA	72%	8%	12%	8%	0%	>3.00	8.0
Laminography	92%	6%	0%	0%	2%	1.69	1.0
Microwave	87%	13%	0%	0%	0%	2.00	8.0
Thermography (uncooled)	60%	4%	4%	4%	28%	>3.00	4.0
Thermography (FLIR)	N/A	N/A	N/A	N/A	N/A	≤.50	1.0
FlawInspecta UT Array	58%	0%	3%	16%	26%	>3.00	1.0
Air-coupled UT	12%	47%	31%	10%	0%	1.01	1.0
Laser UT	N/A	N/A	N/A	N/A	N/A	N/A	N/A

(Highlighted = best performer)

Table 23. Summary of all NDI flaw-detection capability for 3-ply carbon and fiberglass test specimens—overall flaw detection, highest detection (by individual inspector), lowest detection (by individual inspector), overall 90% PoD levels, and false calls

Flaw Detection Percentage Summary Table for 3-Ply Carbon					
Inspection Device	Overall Detection Percentage	Highest Detection Percentage	Lowest Detection Percentage	90% POD Level	False Calls
Airbus tap hammer	52%	76%	25%	2.34	0.8
Boeing tap hammer	64%	78%	47%	2.03	1.0
LFBT	63%	82%	35%	2.10	2.3
MIA	79%	86%	73%	1.46	0.6
WichiTech DTH	61%	78%	47%	2.28	0.6
Woodpecker	65%	75%	51%	1.78	0.0
CATT	84%	N/A	N/A	1.19	0.0
MAUS Resonance 1	100%	N/A	N/A	≤ 0.50	3.0
SAM	82%	N/A	N/A	1.26	2.0
Shearography	98%	N/A	N/A	≤ 0.50	0.0
Thermography	96%	N/A	N/A	≤ 0.50	2.0
MAUS Resonance 2	94%	N/A	N/A	0.53	2.0
MAUS MIA	90%	N/A	N/A	0.77	0.0
Laminography	94%	N/A	N/A	0.66	0.0
Microwave	59%	N/A	N/A	2.13	9.0
Thermography (uncooled)	96%	N/A	N/A	0.52	0.0
Thermography (FLIR)	98%	N/A	N/A	≤ 0.50	0.0
FlawInspecta UT Array	75%	N/A	N/A	1.24	3.0
Air-coupled UT	96%	N/A	N/A	0.52	0.0
Laser UT	90%	N/A	N/A	0.84	0.0

Table 23. Summary of all NDI flaw-detection capability for 3-ply carbon and fiberglass test specimens—overall flaw detection, highest detection (by individual inspector), lowest detection (by individual inspector), overall 90% PoD levels, and false calls (continued)

Flaw Detection Percentage Summary Table for 3-Ply Fiberglass					
Inspection Device	Overall Detection Percentage	Highest Detection Percentage	Lowest Detection Percentage	90% POD Level	False Calls
Airbus tap hammer	60%	75%	41%	2.03	0.3
Boeing tap hammer	69%	86%	45%	1.57	1.8
LFBT	71%	92%	51%	1.77	0.9
MIA	84%	90%	79%	1.04	0.5
WichiTech DTH	66%	82%	47%	1.81	0.9
Woodpecker	70%	86%	55%	1.45	0.3
CATT	84%	N/A	N/A	1.04	4.0
MAUS Resonance 1	92%	N/A	N/A	0.69	5.0
SAM	94%	N/A	N/A	0.65	0.0
Shearography	96%	N/A	N/A	0.56	1.0
Thermography	100%	N/A	N/A	≤.50	0.0
MAUS Resonance 2	84%	N/A	N/A	1.18	6.0
MAUS MIA	92%	N/A	N/A	0.69	0.0
Laminography	88%	N/A	N/A	0.97	0.0
Microwave	98%	N/A	N/A	≤.50	2.0
Thermography (uncooled)	96%	N/A	N/A	0.52	0.0
Thermography (FLIR)	98%	N/A	N/A	≤.50	0.0
FlawInspecta UT Array	71%	N/A	N/A	1.78	0.0
Air-coupled UT	92%	N/A	N/A	0.69	0.0
Laser UT	86%	N/A	N/A	1.25	0.0

Table 24. Summary of all NDI flaw-detection capability for 6-ply carbon and fiberglass test specimens—overall flaw detection, highest detection (by individual inspector), lowest detection (by individual inspector), overall 90% PoD levels, and false calls

Flaw Detection Percentage Summary Table for 6-Ply Carbon					
Inspection Device	Overall Detection Percentage	Highest Detection Percentage	Lowest Detection Percentage	90% POD Level	False Calls
Airbus tap hammer	41%	58%	24%	>3.00	3.5
Boeing tap hammer	43%	69%	31%	2.59	4.7
LFBT	57%	80%	46%	2.42	6.5
MIA	63%	71%	59%	1.76	1.3
WichiTech DTH	56%	73%	44%	2.18	0.9
Woodpecker	44%	53%	39%	2.32	0.7
CATT	64%	N/A	N/A	1.85	1.0
MAUS Resonance 1	98%	N/A	N/A	≤.50	12.0
SAM	66%	N/A	N/A	1.63	37.0
Shearography	85%	N/A	N/A	1.00	0.0
Thermography	97%	N/A	N/A	≤.50	2.0
MAUS Resonance 2	63%	N/A	N/A	2.27	4.0
MAUS MIA	81%	N/A	N/A	1.32	6.0
Laminography	88%	N/A	N/A	1.10	0.0
Microwave	36%	N/A	N/A	>3.00	10.0
Thermography (uncooled)	78%	N/A	N/A	1.70	2.0
Thermography (FLIR)	100%	N/A	N/A	≤.50	1.0
FlawInspecta UT Array	71%	N/A	N/A	1.92	0.0
Air-coupled UT	90%	N/A	N/A	0.87	0.0
Laser UT	N/A	N/A	N/A	N/A	N/A

Table 24. Summary of all NDI flaw-detection capability for 6-ply carbon and fiberglass test specimens—overall flaw detection, highest detection (by individual inspector), lowest detection (by individual inspector), overall 90% PoD levels, and false calls (continued)

Flaw Detection Percentage Summary Table for 6-Ply Fiberglass					
Inspection Device	Overall Detection Percentage	Highest Detection Percentage	Lowest Detection Percentage	90% POD Level	False Calls
Airbus tap hammer	47%	66%	20%	2.44	2.9
Boeing tap hammer	50%	69%	34%	2.33	4.7
LFBT	59%	85%	32%	2.55	3.3
MIA	72%	81%	56%	1.49	1.9
WichiTech DTH	61%	81%	42%	1.71	1.6
Woodpecker	50%	64%	34%	2.05	0.1
CATT	81%	N/A	N/A	1.10	1.0
MAUS Resonance 1	97%	N/A	N/A	0.55	9.0
SAM	90%	N/A	N/A	0.84	8.0
Shearography	100%	N/A	N/A	≤.50	0.0
Thermography	93%	N/A	N/A	0.70	3.0
MAUS Resonance 2	56%	N/A	N/A	2.07	2.0
MAUS MIA	83%	N/A	N/A	1.48	6.0
Laminography	80%	N/A	N/A	1.43	2.0
Microwave	88%	N/A	N/A	0.93	12.0
Thermography (uncooled)	71%	N/A	N/A	2.19	2.0
Thermography (FLIR)	98%	N/A	N/A	≤.50	4.0
FlawInspecta UT Array	27%	N/A	N/A	>3.00	0.0
Air-coupled UT	90%	N/A	N/A	0.90	0.0
Laser UT	N/A	N/A	N/A	N/A	N/A

Table 25. Summary of all NDI flaw-detection capability for 9-ply carbon and fiberglass test specimens—overall flaw detection, highest detection (by individual inspector), lowest detection (by individual inspector), overall 90%PoD levels, and false calls

Flaw Detection Percentage Summary Table for 9-Ply Carbon					
Inspection Device	Overall Detection Percentage	Highest Detection Percentage	Lowest Detection Percentage	90% POD Level	False Calls
Airbus tap hammer	40%	53%	17%	>3.00	6.8
Boeing tap hammer	38%	59%	24%	2.88	5.4
LFBT	51%	66%	34%	2.61	3.8
MIA	39%	54%	27%	2.97	3.1
WichiTech DTH	50%	64%	41%	2.15	4.4
Woodpecker	35%	44%	29%	2.76	2.8
CATT	44%	N/A	N/A	2.36	4.0
MAUS Resonance 1	80%	N/A	N/A	1.32	0.0
SAM	46%	N/A	N/A	>3.00	74.0
Shearography	73%	N/A	N/A	2.00	0.0
Thermography	95%	N/A	N/A	0.64	0.0
MAUS Resonance 2	44%	N/A	N/A	>3.00	10.0
MAUS MIA	53%	N/A	N/A	>3.00	8.0
Laminography	83%	N/A	N/A	1.39	0.0
Microwave	42%	N/A	N/A	>3.00	23.0
Thermography (uncooled)	53%	N/A	N/A	>3.00	0.0
Thermography (FLIR)	97%	N/A	N/A	≤.50	0.0
FlawInspecta UT Array	59%	N/A	N/A	2.85	1.0
Air-coupled UT	80%	N/A	N/A	1.26	2.0
Laser UT	N/A	N/A	N/A	N/A	N/A

Table 25. Summary of all NDI flaw-detection capability for 9-ply carbon and fiberglass test specimens—overall flaw detection, highest detection (by individual inspector), lowest detection (by individual inspector), overall 90%PoD levels, and false calls (continued)

Flaw Detection Percentage Summary Table for 9-Ply Fiberglass					
Inspection Device	Overall Detection Percentage	Highest Detection Percentage	Lowest Detection Percentage	90% POD Level	False Calls
Airbus tap hammer	44%	73%	7%	>3.00	7.1
Boeing tap hammer	41%	69%	25%	2.90	6.9
LFBT	49%	71%	24%	3.00	2.8
MIA	52%	64%	36%	2.00	6.8
WichiTech DTH	55%	68%	42%	2.07	4.9
Woodpecker	41%	54%	27%	2.52	6.7
CATT	51%	N/A	N/A	2.27	0.0
MAUS Resonance 1	86%	N/A	N/A	0.60	2.0
SAM	81%	N/A	N/A	1.04	17.0
Shearography	88%	N/A	N/A	0.77	0.0
Thermography	93%	N/A	N/A	0.67	2.0
MAUS Resonance 2	47%	N/A	N/A	>3.00	11.0
MAUS MIA	42%	N/A	N/A	>3.00	8.0
Laminography	83%	N/A	N/A	1.69	1.0
Microwave	80%	N/A	N/A	2.00	8.0
Thermography (uncooled)	42%	N/A	N/A	>3.00	4.0
Thermography (FLIR)	97%	N/A	N/A	≤.50	1.0
FlawInspecta UT Array	32%	N/A	N/A	>3.00	1.0
Air-coupled UT	86%	N/A	N/A	1.01	1.0
Laser UT	N/A	N/A	N/A	N/A	N/A

8. CONCLUSIONS AND RECOMMENDATIONS

The rapidly increasing use of composites on commercial airplanes, coupled with the potential for economic savings associated with their use, means that the demand for composite materials technology will continue to increase. Inspecting these composite structures is a critical element in assuring their continued airworthiness. Extensive damage tolerance analysis associated with the use of composites in primary structures will likely identify areas requiring more sensitive health monitoring. Many composite honeycomb structure inspections are performed by tap test methods that use a human-detected change in acoustic response to locate flaws. More sophisticated nondestructive inspection (NDI) methods could be applied to improve the damage detection in adhesively bonded composite aircraft parts. The Composite Honeycomb Flaw Detection Experiment (CHE) was developed to assess the performance of both conventional and advanced NDI techniques in detecting voids, heat damage, disbonds, delaminations, and impact damage in adhesively bonded composite aircraft parts.

The conventional composite inspection techniques studied were: Boeing and Airbus manual tap hammers, low frequency bond testing, high frequency bond testing (resonance), Mitsui Woodpecker automated tap hammer, WichiTech digital tap hammer (DTH), and mechanical impedance analysis (MIA). In addition, 14 different advanced NDI methods were evaluated in these experiments including: computer assisted tap hammer (CATT), thermography (pulsed and induction), pulse-echo ultrasonics (PE-UT), air-coupled UT (AC-UT), Mobile Automated Scanner (MAUS) C-scanning in MIA and resonance mode, laser UT, shearography, microwave, structural anomaly mapping (SAM), UT linear array, digital acoustic video, laminography, and terahertz imaging.

The CHE traveled to airlines, third-party maintenance depots, and aircraft manufacturers to acquire flaw detection data. The experiment was deployed in a hangar to provide a representative inspection environment including impediments such as poor lighting and noise distractions. A total of 75 inspectors from 22 airlines and maintenance and repair organizations (MRO) located around the world participated in the experiment. Inspector feedback on performance provided excellent training for the experimenter while their results produced a valuable baseline of how well the industry is able to inspect composite structures (e.g., flaw hits/misses, false calls, flaw sizing, effects of construction scenarios, and effects of environment). These blind tests produced statistically valid probability of detection (PoD) curves representative of the industry as a whole. Furthermore, results from the 18 advanced NDI methods allowed the team to quantify the degree of inspection improvements possible via the application of more sophisticated inspection methods and procedures. The experiment results also allowed the team to determine which NDI methods possess unique capabilities to address specific inspection requirements.

Inspectors conducted tests in accordance with Boeing and/or Airbus maintenance guidelines but were otherwise free to apply nondestructive test (NDT) techniques and interpret the data according to their own standards. Using 90% PoD as a benchmark, the study generally found that the more sophisticated the technique, the smaller the flaw that could be detected. Yet all the techniques achieved 90% PoD for flaws 3" in size. This level of reliability may be sufficient for many secondary structures. With automated tap testers, the 90% PoD flaw size decreased to approximately 1.5". The largest factors affecting PoD levels were determined to be the thickness of the skin and the material type (e.g., fiberglass or carbon skins).

A summary of the overall experiment results, observations, and recommendations associated with these results follows.

- This program assessed current industry capabilities by quantifying flaw detection performance in composite laminate structures. Overall, the results from the CHE produced a capability baseline for current NDI techniques and quantified improvements stemming from advanced NDI.
- This experiment provides overall PoD values for inspecting composite honeycomb structures so that the aviation industry can: 1) better understand what type of damage detection is possible for specific inspection scenarios; 2) adjust inspection procedures to optimize performance; and 3) smartly enhance inspector preparation and training to generate the performance improvements possible via optimized NDI deployment, sufficient knowledge of the inspection idiosyncrasies, and increased exposure to realistic, composite inspection demands.
- The viability of certain NDI methods, selected to meet specific application demands, and the quantification of performance, must be continually pursued. Toward that end, this CHE is available for continued testing. All future testing will have the results from this assessment to serve as the basis of comparison and help quantify NDI improvements.
 - While the size of flaw, or damage, that must be detected is affected by many parameters (e.g., structure type, location on aircraft, and stress and fatigue levels), the general goal for composite honeycomb inspections is to detect flaws that are 1" diameter or larger. Many of the NDI reference standards in original equipment manufacturer (OEM) NDT manuals use 1" diameter flaws to guide equipment setup. In addition, the Commercial Aircraft Composite Repair Committee Inspection Task Group members generally concur that a 1" flaw detection provides a good center point for the CHE. Thus, the flaw sizes in the design were established with a 1" diameter at the center. Larger and smaller flaws were included such that PoD values smaller than 1" (as small as 0.25") and PoD values larger than 1" (as large as 2") could be ascertained.
- Of the conventional NDI methods for composite honeycomb, the top performers and 90% PoD levels for each category are listed below:
 - 3-ply fiberglass – MIA (PoD₉₀ = 1.0" dia.)
 - 3-ply carbon – MIA (PoD₉₀ = 1.5" dia.)
 - 6-ply fiberglass – MIA (PoD₉₀ = 1.5" dia.)
 - 6-ply carbon – MIA (PoD₉₀ = 1.8" dia.)
 - 9-ply fiberglass – MIA (PoD₉₀ = 2.0" dia.)
 - 9-ply carbon – WichiTech DTH (PoD₉₀ = 2.2" dia.)
- For the manually deployed tap hammers only, the top performance level that can be expected for each category are listed below. It should be noted that the transition from manually deployed tapping to automated, with C-scan imaging via the CATT system, produced improvements by 20–50% over the values listed below:

- 3-ply fiberglass – Boeing tap hammer (PoD₉₀ = 1.6" dia.)
 - 3-ply carbon – Boeing tap hammer (PoD₉₀ = 2.0" dia.)
 - 6-ply fiberglass – Boeing tap hammer (PoD₉₀ = 2.3" dia.)
 - 6-ply carbon – Boeing tap hammer (PoD₉₀ = 2.6" dia.)
 - 9-ply fiberglass – Boeing tap hammer (PoD₉₀ = 2.9" dia.)
 - 9-ply carbon – Boeing tap hammer (PoD₉₀ < 2.9" dia.)
- Of the advanced NDI methods, the top performers and 90% PoD levels for each category are listed below. In general, the level of improvement over conventional NDI methods becomes higher as the inspection challenge increases (i.e., skin becomes thicker and moves from fiberglass to carbon). The 90% PoD improvements range from 50–75% over conventional NDI methods.
 - 3-ply fiberglass – Thermography and microwave (PoD₉₀ < 0.5" dia.)
 - 3-ply carbon – Thermography, MAUS Resonance, Shearography, and AC-UT (PoD₉₀ < 0.5" dia.)
 - 6-ply fiberglass – Thermography, MAUS Resonance, and Shearography UT (PoD₉₀ < 0.5" dia.)
 - 6-ply carbon – Thermography and MAUS Resonance (PoD₉₀ < 0.5" dia.)
 - 9-ply fiberglass – Thermography (PoD₉₀ < 0.5" dia.)
 - 9-ply carbon – Thermography (PoD₉₀ < 0.5" dia.)
 - It should be noted that the advanced NDI techniques that were evaluated are in different states of maturity. Overall, the improvement in flaw detection ranged from 66–72% over the conventional methods. Automated deployment and data presentation/analysis reduces many human factors concerns such as ensuring surface area coverage and interpretation of inspection results (i.e., 100% coverage and flaw recognition on C-scan images).
 - Advanced NDI generally produced slower inspections for wide areas. Inspection times typically exceeded the times achieved by the conventional methods with the exception being thermography and shearography. This is mostly attributed to the increase in initial setup time plus the data analysis associated with the more sophisticated inspection systems. Some methods required multiple shots/images to get full coverage of an inspection area. Special care is needed to ensure that there is sufficient overlap between adjacent images. Laminography's performance would probably improve if there were a larger overlap of inspection images to ensure complete coverage of the panel.
 - Most stiffness-based inspection methods like tap tests, resonance, and MIA performed better on fiberglass than carbon skin. This is because carbon is stiffer than fiberglass so the effect of damage in fiberglass is more pronounced than in carbon-skinned honeycomb. By the same reasoning, the inspection performance declined as the skins of the honeycomb structure became thicker. A defect creates the greatest loss of stiffness in the weakest fiberglass structure, and the effect of similar-sized defects is lessened as the skin thickness increases and the stiffer carbon material is used.
 - Some of the inspection methods included inspector performance levels that were much higher than all of the other inspectors. When the performance outliers were removed from the PoD calculations, the 90% PoD levels could be improved by as much as 30%.

Airlines will need to assess their own inspection personnel to determine where their performance lies amid the scatter of PoD curves shown in this report.

- Effect of inspection rate on PoD – To some degree, PoD can improve as inspection time per area of honeycomb structure increases. Results showed that flaw detection improved (i.e., PoD levels decreased) as the inspector took more time to inspect each panel. Most of the improvements were in the shorter inspection times—increasing the inspection time from 5 to 15 minutes for each 2.25 ft.² panel could reduce the inspection PoD by as much as 60%. The improvement levels off to the point where increased inspection time does not yield better results, so optimum inspection rates determined by this type of data is a coverage of approximately 7 minutes per square foot of inspection region.
- False calls – Overall, the false call rates for most of the NDI methods were deemed to be quite low. For the conventional methods, the Woodpecker device produced the lowest overall false call rate while the Boeing tap hammer produced the highest overall false call rate. For the advanced NDI methods, the lowest number of false calls occurred with the laminography and CATT system while, in general, the number of false calls did not seem to increase as the inspections became more challenging (i.e., thicker skin laminates). The trend analyses did not show any reduction in false call rates as the inspection times were increased. This indicates that the false call rate was much more dependent on individual interpretations than on the rate of making the interpretations. There is no relation between the number of false calls and the resulting PoD values for each composite honeycomb structure category so the false call rate had little effect on PoD values. Note that in certain cases, false call averages were dominated by one or two inspectors with extremely high numbers of false calls. Airlines will need to assess their own inspection personnel to determine where their performance lies amid the variation in false call levels listed in this report.
- Inspection surface coverage – Some inspectors marked grids on their panels to aid in coverage of inspection area. Other inspectors used indexing methods with straight edge and tic marks around the panel perimeter. While most inspectors had good coverage of the inspection surface, it was noted that some followed a random pattern—resulting in the detection of small flaws while some large flaws were missed.
- Setup procedures – Boeing and Airbus inspection procedures were provided for the inspectors to use; however, very few of the inspectors referenced these procedures during their testing. One result is that some of the spacing for the manual tap testing was not as small as the 0.5" recommended in the OEM procedures. It was noted that most of the inspectors used reference standards to set up their equipment and obtain a reference for the expected flaw response.
- Tap testing of composite honeycomb structures – The tap test inspection technique has evolved from a hearing-based manual test into instrumented systems in which the electronic circuits have removed the dependence on the human ear. The mechanized impactors have ensured uniformity of the tapping and increased the inspection throughput while improving flaw detection performance. The tap test will eventually evolve into automated systems capable of imaging and quantitative analysis. However, the enhanced capabilities should not be achieved at the expense of the original advantages of simplicity and ease of field use.

- Amount of overall time spent inspecting composites – The duration of this experiment was longer, and thus more tedious, than what would normally be expected of an inspector. The inspections lasted 2–3 days and involved 99 ft.² of inspection region. When subjected to exceptionally long inspections, it is not unusual for the inspector's attention to wane at times, which increases the possibility of missing a flaw. The recommendation is that wide-area inspections associated with large composite structures be divided into a series of smaller inspection regions to allow for the necessary inspection focus. In addition, some of the more demanding inspections that involve larger regions or complex structure should be inspected using a two-man team. Discussions on signal quality and interpretation between the two inspectors should improve the overall flaw detection performance.
- Lack of exposure to composite honeycomb inspections – While all of the inspectors that participated in this experiment were trained and qualified to inspect composite honeycomb structures, some did not have extensive exposure to such inspections. This is because the commercial fleet does not include a lot of composite honeycomb inspections. Thus, the experiment monitors noted some variation in the inspectors' comfort level in conducting these inspections. Use of the NDI reference standards or NDI feedback specimens, which was provided for unlimited inspector use, helped alleviate this issue. However, it does indicate that additional training and exposure to composite honeycomb inspections—and the unique challenges associated with inspecting composite structures—could help improve these PoD results even further
 - There is a general concern that the lack of routine exposure to composite inspections makes it difficult for the inspectors to maintain the necessary level of expertise. Furthermore, exposure to available flaw specimens is viewed as a method to keep the inspectors ready for when an aircraft needs inspection because of damage. So, in addition to formal composite NDI training classes, aircraft inspectors should conduct routine practice inspections on representative composite structures that contain realistic damage. Such test specimens should be more complex and varied than the existing NDI reference standards and contain known, but non-uniformly spaced, flaw profiles. Industry teams that allow for participation by OEMs, airlines, and MROs should carry out an initiative to develop such test specimens along with specifications for specimen acquisition and use. Added exposure to available flaw specimens is viewed as a way to keep the inspectors ready, well-trained, and current on composite inspections
- Use of aids to ensure proper coverage – The inspection procedures discuss proper coverage of the inspection area and even suggest the use of grids or other methods to ensure that the inspection transducer is moved over the entire surface area. In addition, conformable straight edges and rulers were provided to the inspectors for their use. Some inspectors completed their work using simple freehand (unguided) motion over the entire surface area of each specimen. Some inspectors divided the test specimens into quadrants while still moving the transducer in a freehand motion so that they could better monitor their coverage and transducer movement. Some inspectors used straight edges to guide their transducer movement, while some inspectors also added tick marks to ensure that they moved their straight edge in 0.5" increments along the test specimens. Finally, some

inspectors used straight edges in some regions and freehand in other regions (the percentage of each was not logged, but this combined practice was noted). The inspection results showed a significant improvement in PoD for inspectors that used straight edges. It was similarly observed that the inspection performance decreases when the inspectors attempt to accurately cover the entire inspection area using a freehand method. As the inspection regions become smaller, this effect will start to decrease; however, this does not diminish the value of the finding described here. When inspectors are inspecting large composite honeycomb areas, they should use some form of guides or grids to ensure proper coverage of the inspection area.

- Keys to improving inspection performance – Successful efforts to transition inspectors from “average” to “good” or “outstanding” performance levels will have a significant effect on PoD_[90/95] levels. Overall, the identified, potential measures to improve inspectors’ performance on composite inspections include: increased training, apprenticeships, exposure to representative inspections, enhanced procedures, and inspector teaming and awareness training on inspection obstacles.
- Training – The issues described above can also be addressed via additional personnel training. Some of the training can be in the form of composite awareness training to instruct inspectors on composite materials, composite structure fabrication, and typical aircraft composite construction designs. Other forms of training can stress procedural aspects of the inspections such as the use of NDI deployment aids and the proper use of drawings to assist in signal interpretation.
 - Based on previous Federal Aviation Administration (FAA) Airworthiness Assurance NDI Validation Center (AANC) studies and discussions with airlines, it was determined that a majority of the industry does not have additional, special inspector qualification/certification to qualify personnel for conducting composite inspections. Most companies use the normal qualification program for general NDI inspection as qualification for composite inspection. Specialized certification for aircraft NDI professionals who inspect composite structures should be considered.
 - Airlines and third-party MROs requested additional guidance related to composite NDI training from the OEMs, the FAA, and industry groups in the areas of specific instrument training, specific methods training, repair inspections, composite construction training, and reference standard fabrication and use. Programs supporting the evolution of such training should be initiated and pursued in an industry-wide approach.
 - Some of the specific composite NDI training needs can be addressed by more on-the-job training and apprentice programs. Most airlines and MROs do not place inspectors in their composite shops. An apprentice program could rotate inspectors into composite shops so that they can learn about composite construction while exploring the effects of different construction scenarios on NDI.
- Based on input from the aviation industry, the FAA, working with OEMs and industry groups, should consider publishing an advisory circular (AC) or produce a new aerospace recommended practice (ARP) providing enhanced training guidelines specific to the

inspection of composite structures. The majority of airlines think that additional training should take place for composite inspection, so an AC or ARP outlining enhanced training guidelines could be very useful to the industry. It will be necessary to determine an appropriate way for this to be referenced by existing training standards such as ATA-105, NAS-410, SNT-TC-1A, and EN-4179.

In conclusion, through the cooperative efforts of the FAA-AANC and the aircraft manufacturers, airlines, and repair stations and research organizations, the program described herein represents a successful, harmonized approach by the aviation industry worldwide.

One of the primary technical challenges was to produce the outstanding industry support that allowed this team to successfully conduct the traveling experiment. The end result is a comprehensive assessment of the ability of conventional and emerging NDI techniques to inspect for flaws in composite honeycomb structures. The lessons learned can be used to develop inspection improvements via optimized procedures and practices. These improvements can produce both engineering and economic benefits to aircraft maintenance processes.

Industry-wide performance curves have now been established that determine: 1) how well current inspection techniques are able to reliably find flaws in composite honeycomb structure, and 2) the degree of improvements possible through the integration of more advanced NDI techniques and procedures. This study established the current baseline for the aviation industry. It quantified the performance of conventional NDI techniques that are currently being applied to composites at aircraft maintenance depots and paved the way for improved industry inspections via optimized procedures and practices. In addition, the superior capabilities of a host of advanced NDI techniques were determined. If greater flaw detection sensitivity is needed, advanced NDI methods are available now to address those needs. This investigation quantified NDI performance to show that these NDI methods are ready to be applied to meet the surveillance needs of today's complex composite structures.

9. REFERENCES

1. Roach, D.P., Dorrell, L.R., Kollgaard, J., and Dreher, T., "Improving Aircraft Composite Inspections Using Optimized Reference Standards," SAE Airframe Maintenance and Repair Conference, November 1998, SAE Technical Paper 98AEMR-34.
2. Roach, D. and Rackow, K., "Composite Honeycomb NDI Reference Standards," SAE Aerospace Recommended Practice ARP5606, in conjunction with CACRC Inspection Task Group, March 2001.
3. Roach, D. and Rackow, K., "Solid Composite Laminate NDI Reference Standards," SAE Aerospace Recommended Practice ARP5606, in conjunction with CACRC Inspection Task Group, March 2001.
4. Roach, D., Rice, T., and Rackow, K., "A Quantitative Assessment of Conventional NDI Techniques for Detecting Flaws in Composite Laminate Aircraft Structures," FAA report DOT/FAA/AR-xx/xx, pending FAA publication.

5. Baker, A.A., "Fatigue Studies Related to Certification of Composite Crack Patching for Primary Metallic Aircraft Structure," FAA-NASA Symposium on Continued Airworthiness of Aircraft Structures, FAA report DOT/FAA/AR-97-2, I, July 1997.
6. Fredell, R.S., "Damage Tolerant Repair Techniques for Pressurized Aircraft Fuselages," PhD Dissertation, Delft University of Technology, 1994.
7. Rice, R., Francini, R., Rahman, S., et al., "Effects of Repair on Structural Integrity," FAA report DOT/FAA/CT-93/79, December 1993.
8. Jones, R., Chiu, C., and Paul, J., "Designing for Damage Tolerant Bonded Joints," Composite Structures, Vol. 25, 1993.
9. Chiu, W.K., Rees, D., Chalkley, P., and Jones, R., "Designing for Damage Tolerant Repairs," ARL Aircraft Structures Report 450, August 1992.
10. Boeing Non-Destructive Testing Manual, NDTM ATR 72 Revision 33, Boeing Commercial Aircraft Company.
11. Airbus Non-Destructive Testing Manual, A319/A320/A321, Airbus.
12. Migliore, R., "Investigation and Evaluation of the NDT State of the Art to Improve ATR Aircraft Maintenance," MS Thesis, Universita Degli Studi Di Napoli, May 2007.
13. Armstrong, K.B, Graham, L.B., and Cole, II, W.F., *Care and Repair of Advanced Composites*, 2nd edition, Society of Automotive Engineers, Inc., Warrendale, PA, 2005.
14. Hsu, D., Barnard, D., and Roach, D., ASNT Industry Handbook, *Aerospace NDT*, "Bond Testing," American Society of Nondestructive Testing, Columbus, OH, 2014.
15. Cawley, P., "Low Frequency NDT Techniques for the Detection of Disbonds and Delaminations," *British Journal of NDT*, 1990, pp. 454-461.
16. Newman, J.W., "Holographic and Shearographic Applications in Aerospace Manufacturing," *Materials Evaluation*, 2005, Vol. 63 (7).
17. Thomas, R.L., Favro, L.D., Han, X., and Zhong, O., "Comprehensive Composite Materials," Pergamon/Elsevier Science, Oxford, U.K., 2000, Vol. 5.
18. Bossi, R., Housen, K., and Shepherd, W., "Using Shock Loads to Measure Bond Joint Strength," *Materials Evaluation*, 2002, pp. 1333-1338.
19. Adams, R.D., Allen, A.M., and Cawley, P., "Nondestructive Inspection of Composite Structures by Low Velocity Impact," Rev. Prog. Quantitative Evaluation, Thompson, D.O. and Chimenti, D.E., eds., NY, 1986, pp. 1253-1258.

20. Cawley, P. and Adams, R.D., "Testing of Structures by Impact," U.S. Patent No. 4,542,639, September 24, 1985.
21. Georgeson, G.E., Lea, S., and Hansen, J., "Electronic Tap Hammer for Composite Damage Assessment," Rempt, R.D. and Broz, A.L., eds., Proceedings of the SPIE Conference, Vol. 2945, 1996.
22. Barnard, D., Roach, D., and Hsu, D., "Impact Testing: Evolution of a Long-Standing Technique," *Journal of Materials Evaluation*, July 2009.
23. Georgeson, G.E., Hansen, J.M., Kollgaard, J.R., Lea, S.W., and Bopp, J.R., "Damage Detection Device and Method," U.S. Patent No. 6,748,791, June 15, 2004.
24. Hsu, D.K., Barnard, D.J., Peters, J.J., and Dayal, V., "Physical Basis of Tap Test as a Quantitative Imaging Tool for Composite Structures on Aircraft," Rev. Progress in Quantitative NDE, Vol. 5, American Institute of Physics, Melville, NY, 2000.
25. Boeing Non Destructive Testing Manual, NDTM ATR 72, Revision 33.
26. Peters, J.J., Nielsen, Z.A., and Hsu, D.K., "Comparison of Local Stiffness of Composite Honeycomb Sandwich structures Measured by Tap Test and Mechanical Test," Rev. Progress in Quantitative NDE, Vol. 120, American Institute of Physics, Melville, NY, 2001.
27. Barnard, D.J., Peters, J.J., and Hsu, D.K., "Towards a Generic Manual Scanner for Nondestructive Inspection," Rev. Progress in Quantitative NDE, Vol. 24B, American Institute of Physics, Melville, NY, 2005.
28. Roach, D.P., Moore, D., and Walkington, P., "Nondestructive Inspection of Bonded Composite Doublers for Aircraft," Proceedings of SPIE Conference on Nondestructive Evaluation of Aging Aircraft, December 1996.
29. Roach, D., Beattie, A., and Dahlke, L., et al., "Emerging Nondestructive Inspection Methods for Aging Aircraft," Department of Energy SAND Report 92-2732, March 1994; FAA report DOT/FAA/CT-94/11, October 1994.
30. Palmer, D.D. and Wood, N.O., "Development of MAUS Enhancements for Large Area Wing Inspections," Air Force Structural Integrity Conference, December 1999.
31. Cawley, P. and Adams, R.D., "Testing of Structures by Impact," U.S. Patent No. 4,542,639, September 24, 1985.
32. Mitsuhashi, K., Jyomuta, C., Oka, F., and Nishikawa, H., "Method and Apparatus for Impact-Type Inspection of Structures," U.S. Patent No. 5,048,320, September 17, 1991.

33. Georgeson, G.E., Lea, S., and Hansen, J., "Electronic Tap Hammer for Composite Damage Assessment," Proceedings of SPIE Conference, Vol. 2945, 1996.
34. Georgeson, G.E., Hansen, J.M., Kollgaard, J.R., Lea, S.W., and Bopp, J.R., "Damage Detection Device and Method," U.S. Patent No. 6,748,791, June 15, 2004.
35. Hsu, D.K., Barnard, D.J., Peters, J.J., and Hudelson, N.A., "Nondestructive Inspection and the Display of Inspection Results," U.S. Patent No. 6,327,921, December 11, 2001.
36. Peters, J.J., Nielsen, Z.A., and Hsu, D.K., "Comparison of Local Stiffness of Composite Honeycomb Sandwich structures Measured by Tap Test and Mechanical Test," Rev. Progress in Quantitative NDE, Vol. 120, American Institute of Physics, Melville, NY, 2001.
37. Thomas, R., Favro, L., Han, X. and Zhong, O. "Thermal Methods Used in Composite Inspection," *Comprehensive Composite Materials*, 2000.
38. Favro, L., Han, X., and Thomas, R., "Quantitative Thermal-Wave Measurement of Defects in Composite Aircraft Structures," 44th International SAMPE Symposium and Exhibition, 1999.
39. Cramer, K.E., Winfree, W.P., Reid, D., and Johnson, J., "Thermographic Detection and Quantitative Characterization of Corrosion by Application of Thermal Line Source," SPIE Conference on Nondestructive Evaluation of Utilities and Pipelines III, 277-768, 1999.
40. Cramer, K.E. and Winfree, W.P., "Method and Apparatus for the Portable Identification of Material Thickness and Defects using Spatially Controlled Heat Application," U.S. Patent No. 6000844, 1999.
41. Tarin, M. and Rotolante, R., "NDT in Composite Materials with Flash, Transient, and Lock-in Thermography," FLIR Technical Series, Application Note for Research & Science, 2011.
42. Mayer, T., Scherling, D., and Sun, J., "Shearography Testing on Aerospace CFRP Components," *Journal of Inspection Physics*, June 2002.
43. Stakenborghs, R., "Microwave Inspection Method and Its Application to FRP," Proceedings of MTI AmeriTAC, 2013.
44. Underwood, S., Adams, D., Koester, D., Plumlee, M. and Zwink, B., "Structural Damage Detection in a Sandwich Honeycomb Composite Rotor Blade Material Using Three-Dimensional Laser Velocity Measurements," Proceedings of the American Helicopter Society 65th Annual Forum, 2009.
45. "CT Scans for Airplanes," *Popular Mechanics*, September 2003.

46. Peters, J., Barnard, D., and Hsu, D. "Development of a Fieldable Air-Coupled Ultrasonic Inspection System," Rev. Progress in Quantitative NDE, Vol. 23, American Institute of Physics, Melville, NY, 2004.
47. Roach, D., and Walkington, P., "Hardware and Software Innovations to Improve Ultrasonic Penetration in Highly Attenuative Structures," *Journal of Nondestructive Testing*, November 2006, Presented at European Conference on Nondestructive Testing, September 2006.
48. Hsu, D.K., Kommareddy, V., Barnard, D.J., Peters, J.J., and Dayal, V., "Aerospace NDT Using Piezoceramic Air-Coupled Transducers," Proceedings of the 16th World Conference on NDT, 2004.
49. Kommareddy, V., Peters, J., and Hsu, D., "Air-Coupled Ultrasonic Measurements in Composites," *Microtechnologies for the New Millennium*, International Society for Optics and Photonics, April 2005.
50. Calder, C.A. and Wilcox, W.W., "Noncontact Material Testing Using Laser Energy Deposition and Interferometry," *Materials Evaluation*, 1980.
51. Fiedler, C.J., Ducharme, T., Kwan, J., "The Laser-Ultrasonic Inspection System (LUIS) at the Sacramento Air Logistics Center," Rev. Progress in Quantitative NDE, Vol. 16, American Institute of Physics, Melville, NY, 1997.
52. Dubois, M., Drake, T., and Osterkamp, M., "Low-Cost Ultrasonic Inspection of Composites for Aerospace Applications with LaserUT™ Technologies," *Journal of JSNDI*, Volume 57, Number 1, 2008.
53. Roach, D. and Rackow, K., "Development and Utilization of Composite Honeycomb and Solid Reference Standards for Aircraft Applications," Department of Energy SAND Report SAND2003-2112, June 2004.
54. SAE International, "Composite Honeycomb NDI Reference Standards," Aerospace Recommended Practice 5606, September 2001.
55. SAE International, "Solid Composite Laminate NDI Reference Standards," Aerospace Recommended Practice 5605, September 2001.
56. Roach, D.P., Dorrell, L.R., Kollgaard, J., and Dreher, T., "Improving Aircraft Composite Inspections Using Optimized Reference Standards," SAE Technical Paper 98AEMR-34, SAE Airframe Maintenance and Repair Conference, November 1998.

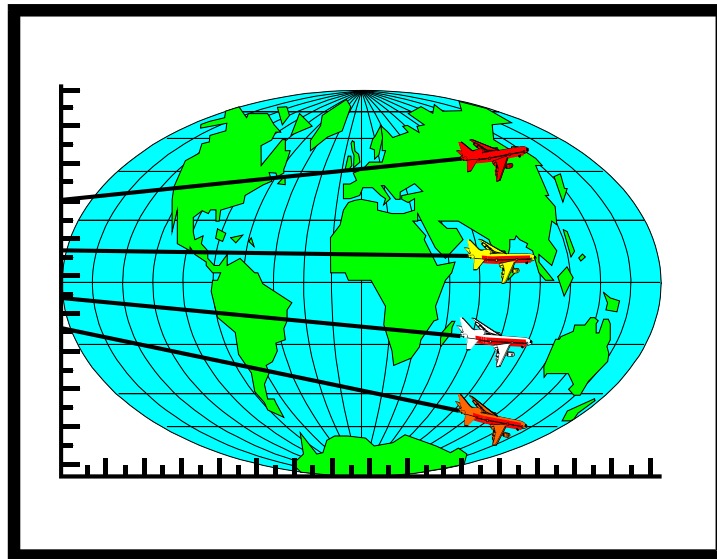


CACRC Inspection Task Group



Detection of Hidden Flaws in Aircraft Composite Honeycomb Structure

EXPERIMENTER BRIEFING AND INFORMATION PACKET



**Experiment Coordinators: D. Roach (505)844-6078
K. Rackow**

**FAA Airworthiness Assurance Center
Sandia National Labs**

III. Experimenter Briefing and Information

The inspection category for evaluation in this experiment is the inspection for representative disbonds, interply delaminations, and impact flaws in composite honeycomb structures. The test articles are modeled after the general range of construction scenarios found on commercial aircraft. The test program is intended to evaluate the technical capability of the inspection procedures and the equipment (i.e. NDI technique). Evaluation of inspector specific or environment specific factors associated with performing this inspection are not the primary objective of this experiment. However, notice will be taken by the experiment monitor if such factors seem to influence results or if unplanned events occur which could impact the results of the inspection. Specific notice will be taken if issues such as deployment or maneuverability adversely affect the outcome of the inspection

For this experiment a set of test specimens containing engineered flaws has been manufactured. The inspections will be conducted on a series of 18" X 18" panels that will be placed on a foam pad to produce uniform boundary conditions across all experimenters. You will be asked to inspect each test specimen and provide any information you can about the presence of applicable flaws. If you determine that flaws are present, you should then provide size and shape information about each detected flaw. The results should be marked directly on the test specimen using markers provided by the experiment monitors. *Inspectors should use any positive indications to find flaws as small as 1/2" in diameter.* Experimenters should work at a pace that is comfortable for them. Although monitors will note start and stop times for your inspection, time to inspect is a secondary variable of the experiment. Inspectors should take whatever time is necessary to assure that any and all flaws in the test specimens are found.

1. Test Specimens and the Flaw Detection Experiment

Engineered Specimens - Engineered specimens have been manufactured that mimic the inspection applications of interest and include realistic flaws found in those structures. Specific information on the construction of the test panels follows. Experimenters will be told the configuration of each panel they inspect.

- **Skin Type** - carbon graphite and fiberglass
- **Skin Thickness** - Panels have 3, 6, and 9 ply skins.
- **Core** - 1" thick Nomex core.
- **Paint** - All panels are painted as per current aircraft specifications.
- **Specimen Deployment** - During testing, panels will be placed on a foam pad to support the entire footprint. (see Figure 5)
- **Flaw Detection** - Inspectors should use any positive indications to find flaws as small as 1/2" in diameter.
- **Tapping Device** - We will provide an array of acceptable tappers (meet Boeing/Airbus specs) and the inspectors will get to choose their tap device. This will eliminate the use of flashlights, washers and other devices that do not meet the size and weight criteria. Some testing with non-standard devices may also be conducted in order to form a basis of comparison with results obtained using recommended taper devices.

Equipment Calibration and Familiarization - Each blind inspection process will be preceded by inspections on appropriate reference standards supplied by the experiment monitors. The inspector will be given information on the manufactured flaws present in the reference standards and will be allowed to use this specimen for check-out of their inspection equipment. The reference standards have the same construction as the blind test specimens and include similar flaws. Thus, they also can be used to allow inspectors to become familiar with an inspection device and learn about a specific equipment's response for various composite structures and flaws within those structures. Figures 2 and 3 show the typical flaw profile found in all of the reference standards. The design is the same for fiberglass and carbon skin and there is a separate specimen for 3 ply, 6 ply, and 9 ply laminates. All of the blind test specimens for this experiment have Nomex honeycomb core so only the bottom, Nomex core portion of each reference standard is needed for equipment set-up. Figure 3 is a cross section of the reference standard showing how the "pillow inserts" are used to simulate interply delaminations and "machined core" regions are used to simulate skin-to-core disbonds. The reference standards will be used as a training tool prior to starting the experiment and will also be used by inspectors during the course of the experiment to set-up their equipment.

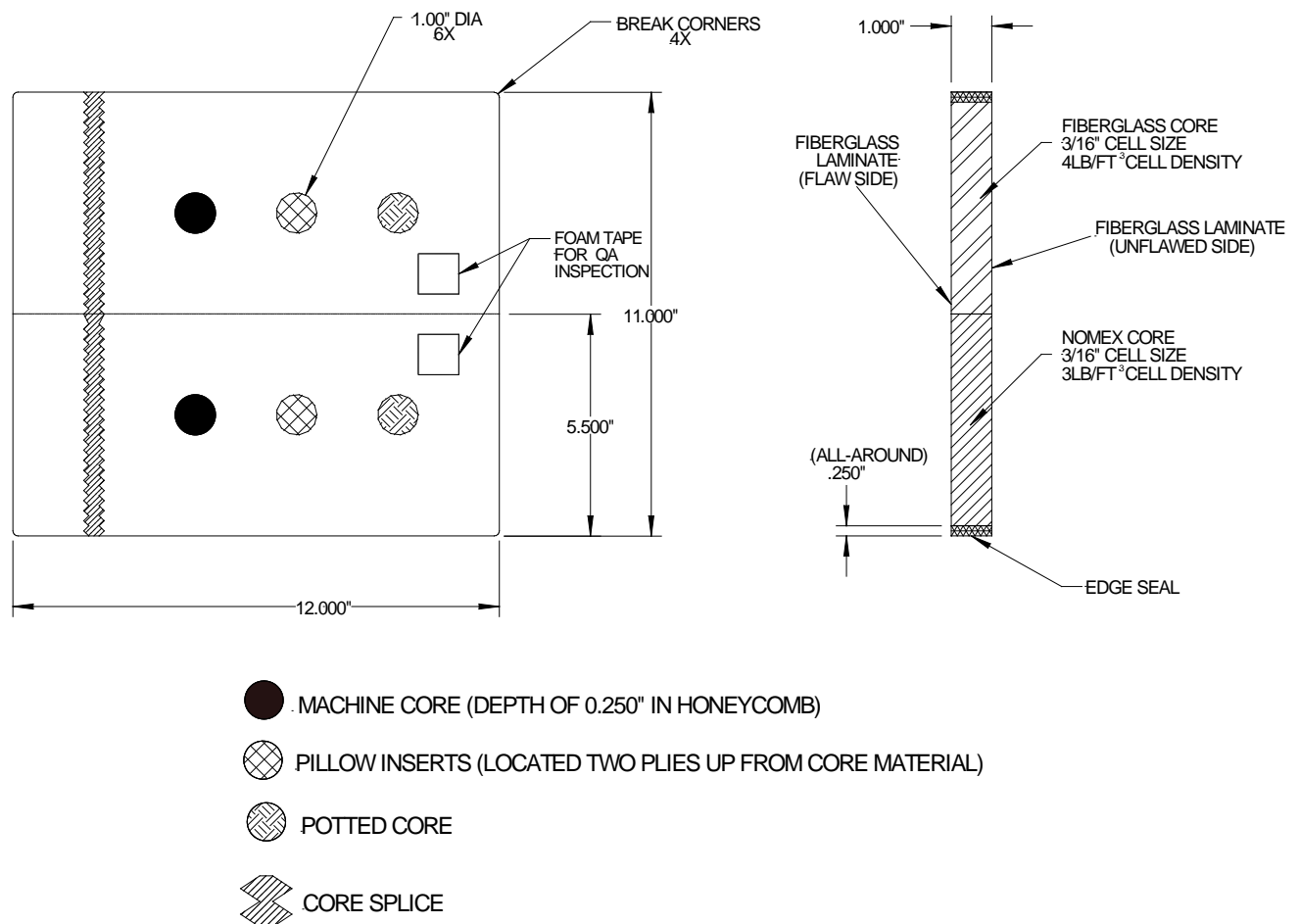


**Figure 2: Final Design of Honeycomb Reference Standards;
(Same Designs for Carbon & Fiberglass Skin and Repeated for 3, 6, 9, and 12 Plies)**

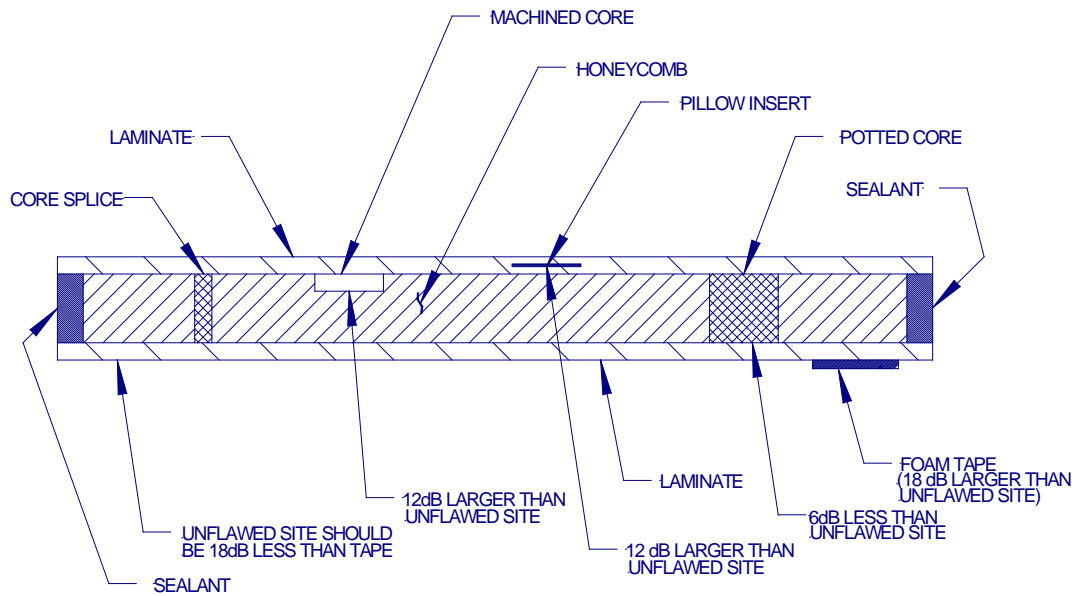


Figure 3: Cross Section of Honeycomb Reference Standard Design

2. Performance Metrics

Multiple performance attributes will be discussed in the final report for this experiment. These are given in the table below and are briefly discussed following the table. Quantitative metrics (standards applied to events that can be numerically counted or quantified) will be applied when appropriate but many of the performance attributes will be discussed using qualitative metrics (standards that rely on human judgments of performance). Where practical, qualitative assessments will be based on predetermined criteria to ensure grading consistency. The intent is to provide useful summaries of the major factors that would influence the user communities' perception of the viability of the technique or specific equipment. Because different users may have different priorities, we will not rank or prioritize the various measures.

Quantitative Metrics - objective standards applied to events that can be numerically counted or quantified.

Qualitative Metrics - subjective standards that rely on human judgments of performance; where practical, qualitative assessments will be based on predetermined criteria to ensure grading consistency.

STRUCTURED EXPERIMENT EVALUATION CRITERIA	
1.	Accuracy and Sensitivity
2.	Data Analysis Capabilities
3.	Versatility
4.	Portability
5.	Complexity
6.	Human Factors
7.	Inspection Time

1. Accuracy and Sensitivity

Accuracy is the ability to **detect** flaws reliably and correctly in composite structures and repairs without overcalling (false calls). Sensitivity is the extent to which the inspection system responds to flaws as a function of size, type, and location (e.g., proximity to repair edges, underlying or adjacent structural elements) in the structure.

Test results will be graded to evaluate the accuracy of quantitative measurements and to assess qualitative measurement parameters. The test results will identify hits (calls with any amount of overlap between the call and the solution), misses (no call for an area of a known flaw), false calls (call with no overlap of a flaw), degree of overlap between experimenter calls and actual flaw areas, and accuracy of quantitative call.

2. Data Analysis Capabilities

Data analysis capabilities define how well the inspection system and process can correctly characterize flaws. Analysis capabilities include, but are not limited to, the ability to identify the flaw size (e.g., lateral extent), flaw location, and flaw type (i.e., distinguish between disbonds and delaminations; backside flaw detection). Quantitative aspects of the data analysis capabilities are provided by evaluating the accuracy and sensitivity as discussed above. Also, the repeatability, reliability, degree of automation, data storage and retrieval capabilities and constraints, and subjective interpretation requirements are considered when assessing the data analysis capabilities.

3. Versatility

Versatility is the capability of the inspection system to be easily adapted for application to varying inspection tasks and conditions (e.g., varying surface conditions, specimen orientations and accessibility). Versatility is primarily assessed using qualitative metrics, such as calibration and equipment reconfiguration requirements to address differing inspection applications (e.g. inspection of fiberglass skin versus carbon skin). Furthermore, variations in system performance due to changes in the surface condition (e.g., paint variations, front and/or back surface contaminants, surface scratches or dents), and specimen configuration (e.g., accessibility and orientation).

4. Portability

Portability is the capability of the inspection system to be easily moved and used in standard aircraft inspection applications. Portability is assessed using qualitative metrics such as the inspection system's size, weight, apparent ease of use in each evaluated inspection application, and inspection restrictions (i.e., limitations created by power requirements, tethering or remote control issues, safety, or other factors that may restrict equipment usage). Equipment storage and shipment requirements will also be considered when evaluating the system portability.

5. Complexity

Complexity is the intricacy of the tasks required to perform the inspections and data analysis. The inspection system should be suitable for use by qualified airline NDI personnel. Also, the inspection process should be efficient, repeatable, and reliable. Complexity is assessed using qualitative metrics, such as: the number of people required to perform the inspection; the number and difficulty of the range of tasks required for the inspection (including setup, calibration, system reconfiguration for changing inspection requirements, data acquisition, and data analysis); the number of simultaneous tasks required; tasks requiring unusual manipulative skills (as compared to traditional inspection needs) or which place the inspector in awkward positions that may be uncomfortable; and tasks that require advanced interpretative skills (including calibration, data acquisition, and data analysis - both qualitative and quantitative).

6. Human Factors

For purposes of this evaluation, human factors include procedures or equipment (hardware or software) related inspection elements that may act as a source of human error. Environmental factors such as temperature, noise, and lighting level will not be considered. The Human Factors criterion is assessed subjectively considering: man-machine interface issues (e.g., data presentation clarity and ease of interpretation, presentation speed, layout and usability of knobs and dials, opportunities for operational or interpretative errors, glare effects, safety to the inspector and others in the surrounding area, etc.); written procedure usability (e.g., clarity, correctness, correlation to tasks actually performed); inspector education, training (initial and recurring) and experience requirements; objective versus subjective calibration, inspection, and analysis processes.

7. Inspection Time

Inspection time is assessed quantitatively. Set up, clean up, inspection, and analysis time will be measured. This includes re-calibration and equipment reconfiguration time to move to differing inspection applications.

3. Experimenter Flaw Calls and Data Logging

The purpose of this experiment is to determine the capability of various inspection methods to detect and measure flaws in composite honeycomb aircraft structure. The Composite Flaw Detection Experiment will travel to airlines, third party maintenance depots, aircraft manufacturers, and NDI developer labs to acquire flaw detection data.

For this experiment a set of test specimens containing engineered flaws has been manufactured. The inspections will be conducted on a series of 18" X 18" panels that will be placed on a foam pad to produce uniform boundary conditions across all experimenters. You will be asked to inspect each test specimen and provide any information you can about the presence of applicable flaws. If you determine that flaws are present, you should then provide size and shape information about each detected flaw. The results should be marked directly on the test specimen using markers provided by the experiment monitors. If instructed by the experiment monitors, inspection results can also be marked on a full-scale sheet of tracing paper. Registration points/lines should be used on the tracing paper to assure location accuracy of the flaws. Also, test specimen numbers should be logged onto each log sheet. Figure 4 shows a sample set of flaw marks on one of the honeycomb test specimens. This study would like to assess performance for flaws as small as 1/2" in diameter. Inspectors should use any positive indications to find flaws as small as 1/2" in diameter. It is not necessary to track small anomalies, such as porosity, that are less than 1/2" in length.

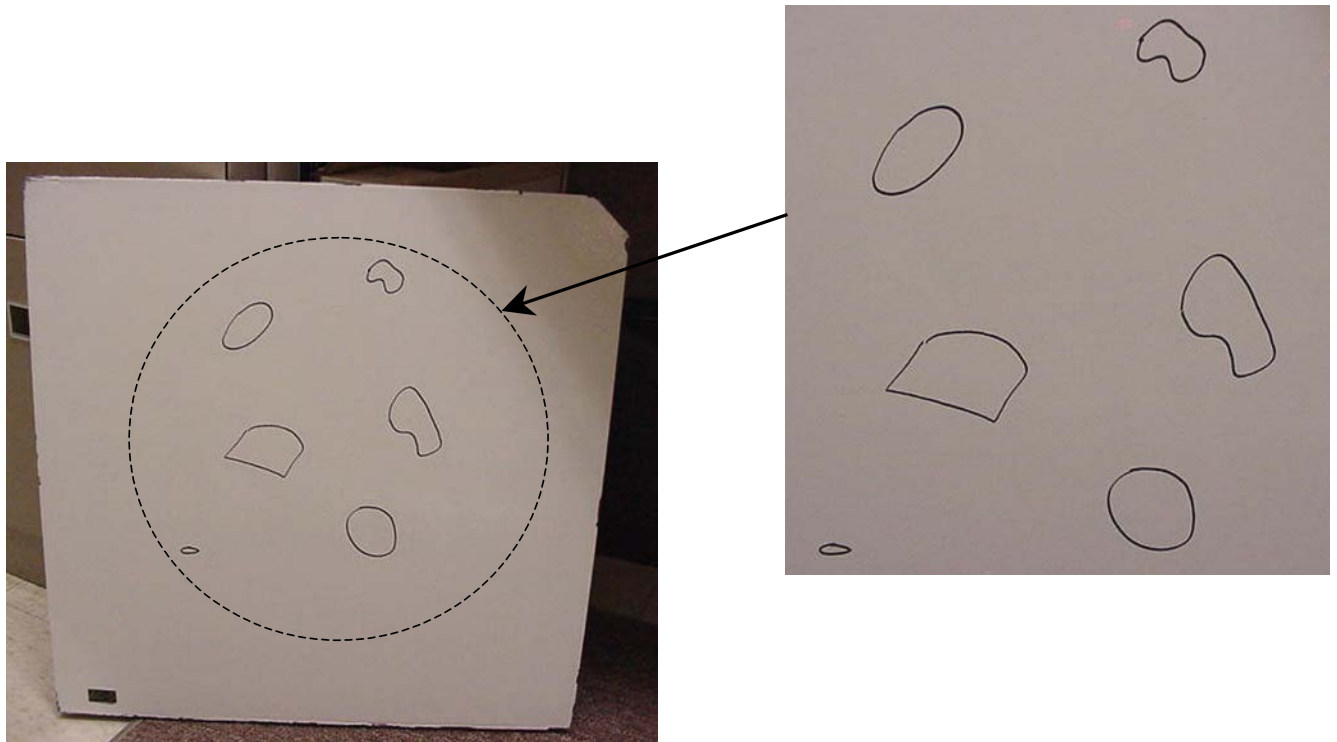


Figure 4: Sample Set of Inspector's Flaw Marks on a Honeycomb Panel

Specimen Deployment -

During the inspections, all panels will be placed on a foam pad to produce uniform boundary conditions across all experimenters. The pad, supplied in the specimen storage cases, should be assembled as per Figure 5 to support the entire perimeter of the test specimen.

The order of inspections will be set forth by the experiment monitors. The inspection order may be varied as far as the 3, 6, or 9 ply specimens, however, once started an inspector will complete

all specimens of a common skin type/thickness continuously before moving on to the next set of specimens. Since the test specimens are painted and the reference standards are unpainted, there may be some very slight differences in equipment response. To accommodate this, each type of test specimen (i.e. 3 ply carbon, 3 ply fiberglass, 6 ply carbon, 6 ply fiberglass, 9 ply carbon, 9 ply fiberglass) will have an unflawed area marked by a square outline. This unflawed region of the specimen can be used by inspectors to confidently null their equipment. Change in equipment responses, corresponding to flaws, can then be observed as per the response variations found on the reference standards.

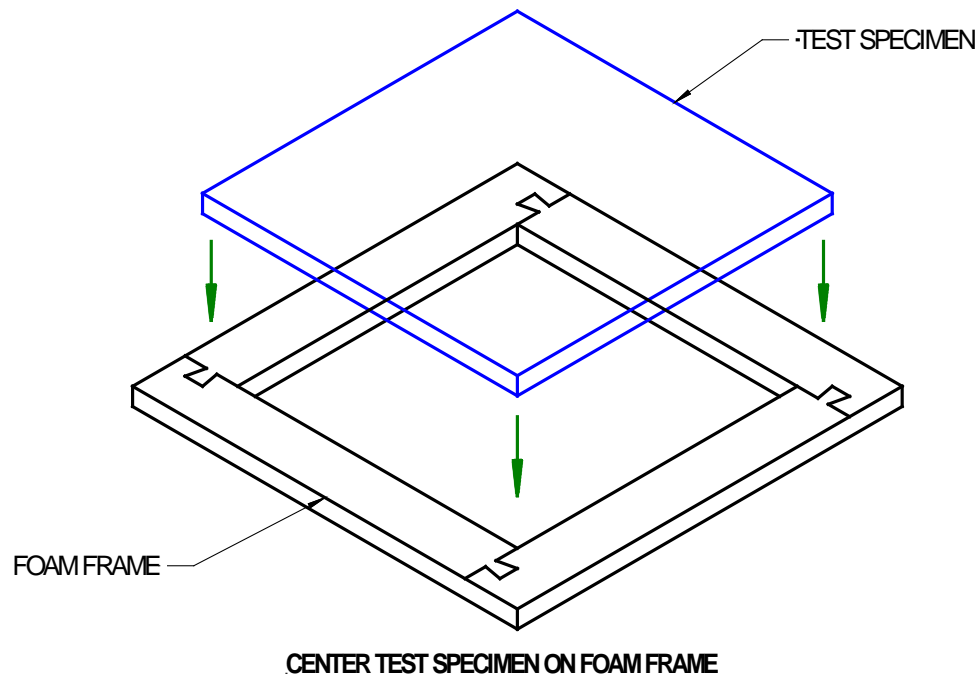


Figure 5: During Inspections, Place Each Panel Such That It Is Supported Around Its Perimeter By a Foam Frame. This Will Provide Uniform Boundary Conditions.

Additional guidance for inspectors performing this experiment are as follows:

- Experimenters should work at a pace that is comfortable for them. Although monitors will note start and stop times for your inspection, time to inspect is a secondary variable of the experiment.
- Applicable procedures from OEM manuals will be provided as a reference tool. Inspectors should use their own judgment as to how to perform the inspection (i.e. a strict procedure will not be enforced).
- Inspection coverage should be 100% of the panel with the exception of a small 1" band around the perimeter of the panels where edge effects may create problems.
- The CACRC Composite Honeycomb Reference Standards, or equivalent, should be used to set-up the equipment. Minor equipment adjustments stemming from in-situ calibration on the parts being inspected are allowed.
- Inspectors should draw the entire size/shape of the flaw (i.e. delineate the edges).

- Reference standards should be used as an aid to determine where to make flaw call edges. This is based on the diameter of the probe and how much of the probe needs to be over the flaw in order to react/detect.
- Inspectors do not need to determine the type of flaw just the location, size, and shape of the suspected anomaly.
- Inspectors should ignore any visual clues (surface anomalies in the paint or small surface marks) and to avoid using these as flaw detection aids. Such anomalies may be intentionally planted to add complexity to the inspection. Inspectors should only make a call on those flaws that are highlighted by their inspection device.

Test results will be graded to evaluate the accuracy of quantitative measurements and to assess qualitative measurement parameters. The test results will identify hits (calls with any amount of overlap between the call and the solution), misses (no call for an area of a known flaw), false calls (call with no overlap of a flaw), and the degree of overlap between experimenter calls and actual flaw areas. Figure 6 is a grading parameter drawing that shows how the hits-misses-false calls results will be graded. Percentage of flaw covered will be another variable of primary interest. Error in lateral extent of flaw and maximum linear extent of overcall are variables of secondary concern and are not currently being considered as part of the grading plan.

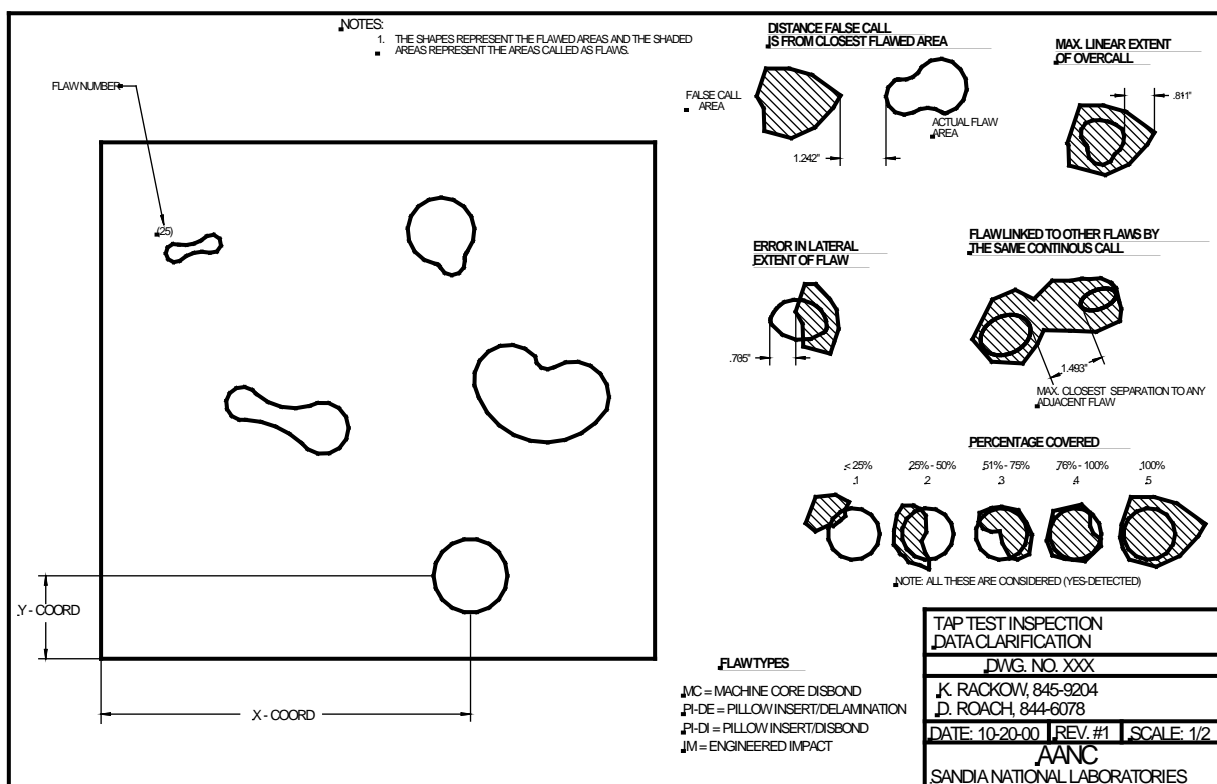


Figure 6: Schematic Showing the Grading Categories Comparing Experimenter Flaw Calls with Actual Flaw Information

4. Sample NDI Procedures for Tap Testing and Ultrasonic Inspection of Composite Honeycomb Structures

Attached are a series of Boeing and Airbus inspection procedures. The procedures are for general deployment of NDT equipment that is relevant to this flaw detection experiment. The NDI procedures are included here as general information to aid inspectors in preparing for the flaw detection experiment. It is not expected that these procedures are sufficient to train an inexperienced inspector. Rather, they provide additional background and guidance to inspectors who are already familiar with the equipment and have experience in performing these type of composite honeycomb inspections. The NDI Reference Standards provided with this experiment can be used in lieu of the standards described in the attached procedures.

APPENDIX B—EXPERIMENT OBSERVATIONS

NDI Exp.	Exp. With Device	Ref. Std used for Set-up	Innovative Procedure or Practice	Accessory Information
10	None	Yes	Formal linescan pattern of inspection at 1/2" increments-rotate panel 90 deg. then repeat. Local sizing done on flaws.	Often spoke with others (while not looking down) & moved woodpecker along the panel. Poss. Cause of some missed flaws.
6.5	?	Yes	Uses hand grid marks to guide coverage. Used larger dia. Side of tool. Initial random scan proc. Over panel by selected areas, later divided panel into 4" squares & tapped zigzag across each sq. in 1/4"-1/2" increment.	When tapping panel edges, panel is moved off of foam frame. 9 Ply panels used greater tapping force to detect defects (taps very hard).
11	?	Yes	Both ends of tool used to tap, mostly small end used. Formal scan zigzag scan pattern of approx. 1-1/2"-2" band.	
6	?	Yes	Initial equipment calibration 30 minutes and after that 5 minutes when changing material or no. of plies.	
8	?	Yes		
1	?	Yes	Used a straight edge for a guide on 9 ply panels. Initial calibration and 9 plies 30 min. and 5 min. or less for others.	Cautioned danger of using excessive gain on 3-ply panel #8 (3F-2). Ref.:B767 NDT manual 51-00-05
12	None	Yes	Lack of good response from woodpecker on 9 ply panels:used yellow indicator for flaw detection here.	Possibly moving device faster than it can acquire averages.
1	?	Yes	Very methodical.	Use of earplugs occasionally to filter out adjacent noise-feels it helps focus on sound & sound anomalies in his panel.
22	Yes	Yes	Difficult to cal & get consistent signal during 9 ply insps. Used area just short of alarm (below 60 but not alarming) to make flaw calls.	Moved probe very fast in sliding motion-possibly to the point of producing false alarms since V-95 will alarm over small poros. Pockets/anomalies if it is moving but meter will slide back to 60-80 if probe is allowed to dwell over the area of interest.
4	Yes	Yes	Unique use of tissue earplugs to filter out extraneous noise & adjacent tapping response.	Fast rapid testing in no set order-coverage could be improved with slower methodical tapping, however this more rapid coverage appears to be typical of tap testing.
16	?	Yes	Grid marked on panel to assist inspection-10mm increments. Inspection carried out using steel rule.	Deaf in one ear. Difficult @ 9 plies especially with adjacent tapping noise. More exception than the rule-very good coverage assured through use rule & grid & careful attention to coverage.

NDI Exp.	Exp. With Device	Ref. Std used for Set-up	Innovative Procedure or Practice	Accessory Information
4	?	Yes	Scans made in random lines across panel & sized as soon as found, using both ends of tool. Tap spacing not as small as recommended 1/2"; dropping tapper rather than using it as an impactor.	Tendency to keep working while talking to others. Inconsistent method of using tool, sometimes just used tool weight to tap & other times used the hand force to ??? The tool.
35	?	Yes	Regular scan line pattern of 1/2" separation. Defects sized when found.	
20	Yes	Yes	Good coverage but possibly moving probe quicker than it can respond-results will tell. Scan made in regular line scan pattern of 1/2" index defects sized as located.	Typical scan speed approx. 12ft/min. on all panels. As a result the alarm would not sound if system was normally set-up on the ref. stds. Dave adjusted his device so that alarm would sound on ref. std. flaws-then did test panels.
15	?	Yes	Panel scanned in lines with approx. 1" between each tap then local sizing of located defects-also random scanning anywhere on panel. Scan mode with large dia. Defect sizing done with large and small diameters.	
5	None	Yes	Marked quadrants on panel to use for inspection coverage aid. Good Coverage	Careful coverage; on 9 ply, set-up equipment using 60% @ flaw rather 80% @ unflawed to increase sensitivity; noted false alarms caused by probe movement & dwelled at each spot to avoid making false calls.
11	None	Yes	Marks area 1" inside of edge & mid-points on panels before starting insp. Moves device with fast pace. Scans to fast for woodpecker to respond properly.	2nd day using device not comfortable with it's capability (just not happy w/it). Getting yellow indication on good areas of ref. Std. Near flaws.
5	None	Yes	He used a 2 x 4 the 1st day only as a guide for tapping along the edge. He paid attention to the digital readout & not the change in pitch of each tap.	He looked at visual indications on impact panels. Covers area regions instead of lines of tapping (last day).
12	?	Yes	2 probe types tried. Wasn't sure which probe was best for this application. Didn't know how attenuator for DTE probe was used. DTE probe didn't seem to work properly w/attenuator.	Switched to Boeing "phase only" calibration @ beginning of 3 ply graphite panels. Orig. cal was per Zetec op manual. Boeing technique is contained in Boeing 747 NDT manual, Part 4, 57-22-01. Noise prob. on panel 26 new instrument produced same results.
7	Yes	Yes	Used milled core to set threshold. He had difficulties calibrating on the 6 ply fiberglass std. Obtained indications between potted core and pillow inserts. Signal to noise was marginal.	Noticed erratic signals part way thru panel 10 (tenth panel) and identified problem with cable. Cable was replaced. Lost signal from probe switched to S-PC-P11 #963927
16	?	Yes	Broke panels into 5 or 6 segments and used raster scan within seg. markings were only at top of panel. After tapping panel insp. would slide hammer across surface to listen for changes in vibration pitch. Did this on some panels - indicated he found some defects he missed with tapping.	Expressed concern about being able to find 1/2" flaws if they were similar to insert flaws on stds. Indicated that he would not normally look for these conditions during in-service inspections. Became very bored during second day of experiment.
7	?	Yes	Spent approx. 1 hour familiarizing himself w/tap hammer & stds. Indicated difficulty in establishing reject threshold. 10% variation was often within noise.	Expressed frustration in using digital hammer. Difficult to watch display while tapping in consistent pattern. Ultimately used tap hammer in convent. manner w/digital data as back-up to evaluate indications. (10% variation from baseline as threshold)

NDI Exp.	Exp. With Device	Ref. Std used for Set-up	Innovative Procedure or Practice	Accessory Information
5.5	?	Yes	Used raster type scan pattern on entire panel. Repeat. inspection twice-once with large end and then small end. Changed scan pattern approx. midway thru -divided panel in left & right halves and did rast. scan on each half.	Spent 1hr 10min. Familiarizing himself w/Boeing & Airbus procedures and evaluated tap hammers.
11	None	Yes	3-ply marked some visual indications before actual woodpecker insp. He looked over manual before starting insps. Marked points for sizing of flaws.	Missed second day of testing due to illness and caught up in final 2 days.
25	None	Yes	Looked for visual clues before scanning panel. Marked cl's on probe to delineate edge of flaw. Somewhat random coverage pattern. 2nd day marked quads. on panel for cov. & seems to be marking with less concern for sizing (No dots for sizing just quick circle on flawed area.)	Didn't read over manual on device just verbal instructions from SNL. 9 ply panels he dropped gain so flaw would alarm on device. (Mach. Core would alarm w/80% setting but not PI) Probe was a lot more sensitive during inspection with this set-up.
24	Yes, 10 yrs.	Yes	Did not use audible alarm, instead used alarm light and variance in meter indication. He used straight line visual coverage to inspect panels. 6 ply stds were difficult to get flaw response from.	Comments: Seems real sensitive to deployment angle of device & more delay in signal response on thicker plies. Somewhat disappointed in equipment. Cal. Date Feb. 7, 99
3	None	Yes	Used a piece of paper to guide and determine coverage of panel (straight edge). Wrote tap values on paper to keep straight what should be called a flaw.	Gets real consistent nos. on readout with each tap. Gave us a very serious effort during inspection.
0	None	Yes	Self-guided testing	
10	Yes	Yes	Has good coverage of panel and serious effort on panels. Originally tried several machines to find the best one. Not happy with set-up but best available.	Noted on ref. Std. signal affected by probe orientation & pressure. Scan speed also an issue and more so on 6 ply than 3 ply. Ran on his own after start up (second shift)
6	None	Yes	Asked about using grid overlay for coverage (uses one on aircraft) but decided not to use on panels. Moves probe a little fast on 3-ply, coverage good. Says not calling small flaws on 6-ply, paint bubbles, etc.	He did not feel equipment was reliable enough or capable of inspecting 9-ply laminates.
17	Yes, tapping in gen.	Yes	Taps panel in halves to insure coverage. Seemed to find pitch change & then hit general area & then mark flaw. (Not real concerned on exact flaw sizing.)	He was distracted some by tapping of Wichitech at same time. Tried and preferred using his own tapper (easier to detect flaws and hear w/his) Only used Ref. Std. For initial set-up of each panel type (never repeated)
13	None	Yes	All plies, listens to several taps, hears different pitch & verifies by looking at digital readout. Has good coverage of panel. Used digital readout more frequently on thicker laminates.	Did a good job of defining edges of flaws.
0	None	Yes	Self-guided testing	

NDI Exp.	Exp. With Device	Ref. Std used for Set-up	Innovative Procedure or Practice	Accessory Information
5	Yes	Yes	Had good coverage of panel, tapped panels in direction (horiz.) then when completed would rotate panel 90 deg. And inspect again.	Uses same design hammer in current work assignment only it was made of brass (heavier). Good conscientious worker.
1.5	None	Yes	Good coverage of panel area. Slight angle of deployment with device but later noted critical to keep device straight. Set-up on std. and sometimes did re-cal on specimens especially if square marked on it.	No previous exp. w/WP. Read user's manual. Did see visual clue but didn't get indication from WP so he did not mark panel. Stated gray panels more difficult to inspect.
7.5	None	Yes	Good coverage of panel area. Read users manual over. Initial set-up (1st few panels) was with gain b/w 80-100 and then changed to 80 after that. Scans panel in one direction & then rotates panel 90 deg. and scans again.	Reviewed user's manual more than once. For 9 ply panels he had to turn gain down to 74-76 in order to get alarm to respond to flaw.
1.5	Yes, 18 mo.	Yes	Good coverage of panel, re-verifies all indications and takes time inspecting panels (note longer insp. times).	Took a fair amount to set-up inspection device for panel configuration.
4	Yes, 7yrs.	Yes	Good coverage of panel, not as concerned with sizing of flaw as finding flaw. Sometimes when scanning would lift front point of probe (3-point probe) off of panel surface.	Took a lot longer to set-up to inspect 6-ply carbon panels versus the 3-ply & says delam and potting much harder to detect in 6-ply, but can easily find disbond on std. Noted gray paint on panels less noise than white paint.
13	Yes, 6yrs.	Yes	Good coverage of panel. After grading results it should be noted that he had a high detection of backside flaws (even called a few PI-D and PI-DEL 1.00"- 2.00" backside on 9 plies fiber.?).	Could not get equipment to alarm on delam of Ref. Std during set-up (3C). I think typical for all construction scenarios. Has used this equip. only a few times, only when S-9R is not available.
5	None	Yes	Good coverage of panel, didn't use audible alarm and initially moved probe at a pretty fast pace. Looked for visual clues at the start of several panels. Had problem with device at end of 6 ply panels.	Definite problem with probe at end of 6 ply panels and constant flaw signal when moving probe over panel. Battery light was coming on a lot even after replacing with a new battery. Noise at probe seems louder.
12	Yes, 6yrs.	Yes	Good coverage of panel, takes time. Used United's S-9R set-up procedure. Looked in our provided book w/procedures, but was not enough information.	Had to switch out initial probe after determination that it was bad. Then changed out probe pitch catch points.
13	None	Yes	Good coverage of panel and did catch problem with 6 ply panel having different response values from std, and it turned out he had wrong panel type for std. (was paying attention to detail)	Used the plus or minus 10% for making calls. Frustrated on 9 ply panels, due to lack of instrument response repeatability.
?	?	Yes	Self-Monitored	
?	?	Yes	Self -Monitored	Backside flaw detection for this advanced technique includes the .75 size.
NDI Exp.	Exp. With Device	Ref. Std used for Set-up	Innovative Procedure or Practice	Accessory Information

3	3 yrs	Yes	Started w/panel #26 on day 2. Because panel has a lot of porosity it was difficult to set device with standard and inspect that particular panel.	Changed from 1/2" to a 1" probe on the second day. Took relatively long to calibrate but then went through panels quickly. 3 yrs. experience using S-9R.
12	3.5 yrs	Yes	Used audio alarm.	Used 1/2" probe for inspections. 3-4 yrs. experience on S-9R. Inspector uses mostly S-9R & TTU devices in his NDT work.
2	None	Yes	Used mylar strip to guide probe on initial pass-then without to draw flaw. Drew lines initially to eliminate edge effect-later panels drew quadrants for coverage - 2nd day (6 ply) drew 8 segments. Very good panel coverage.	No previous exp. w/V-95. Read through manual/worked with device prior to experiment. Noticed improved response after 9v battery was replaced. Stated that manual instructions denoted flashing light meant low battery-battery light on device did not flash, it stayed lit. Noted imperfections in paint surface affected inspection.
6.5	None	Yes	Inspection setting Average 1/4. Good coverage of panels. No previous experience with this device. Tap Hammer and Heatcon coin used mostly by this inspector in his daily work.	Noted that leaning on device gave false results. Considerable improvement in response after changing batteries-battery light was 'on' - wasn't sure it meant low batteries.
11	20	Yes	Looks over panel for visual indications. Uses round side of hammer for most tapping with pointed side used for smaller flaw sizes. Good coverage of panel (at least early on). On 6 ply panels started to use 3"-4" grid pattern on panel like insp. 51.	1st morning hangar background noise <40dB. Moved inspection station away from ventilation system after midday of first day. Says they don't typically tap anything over 3 plies (Boeing does not allow it). He noted difficulty in detecting pitch change of taps late in day. Insp. also A & P split duties.
14	None	Yes	Used good scan speed (not too fast) and good coverage of panels and most of the time scanned 2nd time in 90 deg. direction from first scan. Used two different aids to scan with so woodpecker would stay perpendicular to panel. Re-cal more frequent on 9 plies.	Lead Man. Read over Woodpecker manual before starting inspections. Conscientious about work and results. On 9 ply panels to make a call he would insure it was red signal or if yellow would scan in 90 degree direction to verify consistent repeatable signal. Several times each day people would come talk to him during inspections. Insp. also A & P split duties.

APPENDIX C—DISTRIBUTION LIST FOR DOT DOCUMENT

Frances Abrams
US Air Force
WPAFB, OH

Paul Acres
Lockheed-Martin
Ft Worth, TX

Douglas Adams
Vanderbilt University
Nashville, TN

Tasdiq Ahmed
Thermal Wave Imaging
Ferndale, MI

Aydin Akdeniz
Boeing
Seattle, WA

Dick Alberts
Digiray Corporation
Danville, CA

Nick Amabile
US Navy
Lakehurst, NJ

Jay Amos
Cessna Aircraft Co.
Wichita, KS

Shreyas Ananthan
US Department of Energy
Washington, DC

Paulo Anchieta da Silva
Embraer
São José dos Campos, Brazil

Jim Arnold
United Airlines
Houston, TX

Yoshiaki Asako
Mitsubishi
Addison, TX

Masahiro Asano
Japan Airlines
Tokyo, Japan

Cindy Ashforth
FAA
Seattle, WA

Hesham Azzam
HAHN Spring Ltd
Southampton, United Kingdom

John Bakuckas
FAA WJ Hughes Technical Center
Atlantic City Int'l Airport, NJ

Rocky Ballew
United Airlines
San Francisco, CA

Tom Barber
Delta Airlines
Minneapolis, MN

Dan Barnard
Iowa State Univ – CNDE
Ames, IA

David Barrett
US Navy
Patuxent River MD

Bob Barry
Bell Helicopter
Ft. Worth, TX

Eric Bartoletti
Southwest Airlines
Grapevine, TX

Zachary Bender
Delta Air Lines
Atlanta, GA

Rob Bergman
GE Energy
Schenectady, NY

Phil Berkley
GKN Westland Aerospace
United Kingdom

Malcolm Berner
Delta Air Lines
Atlanta, GA

Blake Bertrand
Boeing
Seattle, WA

Subra Bettadapur
US Navy
Patuxent River, MD

Anne Birt
QinetiQ
Farnborough, United Kingdom

Werner Bischoff
Lufthansa Technik AG
Hamburg, Germany

Wolfgang Bisle
Airbus
Bremen, Germany

James Bitner
Olympus NDT
Kennewick, WA

Sara Black
High Performance Composites
Denver, CO

Kay Blohowiak
Boeing
Seattle, WA

Clemens Bockenheimer
Airbus
Toulouse, France

Bryce Boe
Raytheon Aircraft Co.
Wichita, KS

John Bohler
Delta Air Lines
Atlanta, GA

Christian Boller
Fraunhofer Institute
Saarbrücken, Germany

Mike Borgman
Spirit Aviation
Wichita, KS

Richard Bossi
Boeing
Seattle, WA

Francis Boudreault-Leclerc
Olympus NDT
Québec, Canada

John Brausch
US Air Force
WPAFB, OH

Nick Brinkhoff
Cessna Aircraft Co.
Wichita, KS

Alistair Burns
Air New Zealand
Auckland, New Zealand

Rex Carlton
Delta Airlines
Minneapolis, MN

Charles Buynak
US Air Force
WPAFB, OH

Chris Carella
UTC Aerospace Systems
Vergennes, VT

Sander Carneiro
Agencia Nacional de Aviação Civil
São José dos Campos, Brazil

Christopher Chandler
Delta Airlines
Atlanta, GA

Che-Yin Chang
China Airlines
Taoyuan, Taiwan

Fu-Kuo Chang
Stanford University
Stanford, CA

Randy Chappelle
Delta Air Lines
Atlanta, GA

Carlos Chaves
Embraer
São José dos Campos, Brazil

BoChye Cher
Singapore Air
Singapore

Eric Chesmar
United Airlines
San Francisco, CA

George Clamser
Delta Airlines
Atlanta, GA

Heath Coker
Delta Airlines
Atlanta, GA

Ron Cook
American Airlines
Tulsa, OK

Jeff Cornell
Aviation Technical Services
Seattle, WA

Vicente Cortes
Airbus
Madrid, Spain

Ed Cosgro
Petroleum Helicopters, Inc.
Lafayette, LA

Richard Costantino
UTC Aerospace Systems
Chula Vista, CA

Joe Cotter
UPS
Louisville, KY

Danny Crab
Cargolux Airlines
Luxembourg

Elliott Cramer
NASA - LaRC
Hampton, VA

John Cramer
Kalitta Air
Detroit, MI

Eric Cregger
Boeing
Seattle, WA

Matt Crompton
Dantec Dynamics
Holtsville, NY

Curt Davies
FAA WJ Hughes Technical Center
Atlantic City Int'l Airport, NJ

Mark Davis
Sikorsky Aircraft
Stratford, CT

Paul Davis
Delta Airlines
Atlanta, GA

Russell Day
Kalitta Air
Detroit, MI

Mark Derriso
US Air Force
Wright-Patterson AFB, OH

Mike Derby
US Dept of Energy
Washington, DC

Matt Dill
Nordam
Tulsa, OK

Leo Dominguez
American Airlines/TAESL
Fort Worth, Texas

Fernando Dotta
Embraer
São José dos Campos, Brazil

Steve Douglas
FAA
Washington, DC

Christopher Dragan
Air Force Institute of Technology
Warsaw, Poland

Tommy Drake
iPhoton
Fort Worth, TX

Tom Dreher
Rolls Royce Engine
Indianapolis, IN

Marc Dubois
iPhoton
Fort Worth, TX

Don Duncan
US Airways
Charlotte, NC

Paul Ebert
ST Aerospace
San Antonio, TX

Tom Eischeid
General Electric
Lewistown, PA

Rebeca Elford
United States Air Force
Kirtland AFB, NM

John Ellington
FedEx
Indianapolis, IN

Robert Fabyan
Kalitta Air
Detroit, MI

Tim Fallon
US Navy
Patuxent River, MD

Bennett Feferman
Laser Technology Inc.
Norristown, PA

Luis Fernandes
TAP Portugal
Portugal

Joy Finnegan
Aviation Maintenance
Rockville, MD

Carl Fisher
FedEx
Memphis, TN

Tom Flournoy
FAA WJ Hughes Technical Center
Atlantic City Int'l Airport, NJ

Brian Flinn
University of Washington
Seattle, WA

Rafael Fávaro Foltran
Agencia Nacional de Aviação Civil
São José dos Campos, Brazil

Peter Foote
Cranfield University
Cranfield, United Kingdom

Andrew Freese
Air New Zealand
Aukland, New Zealand

Mark Freisthler
FAA
Renton, WA

Scott Fung
FAA
Renton, WA

Steve Galea
Defence Science and Technology Org
Melbourne, Australia

Yolanda de Frutos Galindo
Airbus
Madrid, Spain

Dave Galella
FAA WJ Hughes Technical Center
Atlantic City Int'l Airport, NJ

Rachel Gayle
United States Air Force
Kirtland AFB, NM

Marc Genest
National Research Council Canada
Ottawa, Canada

Gary Georgeson
Boeing
Seattle, WA

Roger Gibreal
Aviation Technical Services
Seattle, WA

Brad Gilliland
General Electric
Pleasant Hill, MO

Keith Gilmore
United Airlines
San Francisco, CA

Juan Gomez
United Airlines
Orlando, FL

Thomas Gonzales
FedEx
Los Angeles, CA

Steve Goncz
Sky West
Salt Lake City, UT

Grant Gordon
Honeywell
Phoenix, AZ

Nathalie Gouret
Airbus
Blagnac Cedex, France

John Graff
Delta Airlines
Minneapolis, MN

Dennis Granger
US Army
Redstone Arsenal, AL

Robert Grant
FAA
Ft. Worth, TX

Philip Griggs
GE Aviation
Cincinnati, OH

Courtney Guasti
US Army
Redstone Arsenal, AL

Mike Gutierrez
Federal Express
Los Angeles, CA

Fred Guzman
Delta Airlines
Minneapolis, MN

Jason Habermehl
Olympus NDT
Quebec, Canada

Bob Hager
Delta Air Lines
Minneapolis, MN

Colin Hanna
Bombardier
Belfast, United Kingdom

Tim Harris
Boeing
Ft. Lauderdale, FL

Eric Haugse
Boeing
Seattle, WA

Dale Hawkins
FAA
Washington, DC

Pekka Hayrinen
Finnair
Helsinki, Finland

Rudolf Henrich
Airbus
Bremen, Germany

Nick Heminger
Aviation Technical Services
Seattle, WA

Daniel Hebert
Transport Canada
Ottawa, Ontario, Canada

Dirk Heider
University of Delaware
Newark, DE

Scott Herbert
AAR Corp.
Indianapolis, IN

Steve Hicks
Timco
Greensboro, NC

Derek Highet
Cathay Pacific Airlines
Hong Kong, China

Keiji Hirabayashi
All Nippon Airways
Tokyo, Japan

Jim Hofer
Boeing
Huntington Beach, CA

Wolfgang Hoffman
European Aviation Safety Agency
Cologne, Germany

Ed Hohman
Bell Helicopter
Fort Worth, TX

Mike Hoke
ABARIS Training
Reno

Quincy Howard
Boeing
Seattle, WA

Scott Huddleston
US Army
Redstone Arsenal, AL

Jeong-Beom Ihn
Boeing
Seattle, WA

Takahiro Ikeda
Toshiba
Yokohama, Japan

Larry Ilcewicz
FAA
Renton, WA

Yutaka Iwahori
Japan Aerospace Exploration Agency
Tokyo, Japan

Dan Jacobson
San Diego Composites
San Diego, CA

Bill Jappe
Boeing
Huntington Beach, CA

Patrick Johnston
NASA Langley Research Center
Hampton, VA

Kevin Jones
Gulfstream Aerospace Corp.
Savannah, GA

Rusty Jones
FAA
Washington, DC

Ray Kaiser
Delta Air Lines
Minneapolis, MN

Frank Kane
United States Air Force
Kirtland AFB, NM

Hirokuza Karasawa
Toshiba
Yokohama, Japan

Kazunori Kato
Japan Airlines
Tokyo, Japan

Russell Keller
Boeing
Seattle, WA

Seth Kessler
Metis Design Corporation
Cambridge, MA

Hyonny Kim
UC San Diego
La Jolla, CA

Tim Kinsella
Falcon Jet
Little Rock, AR

James Kissel
Delta Airlines
Minneapolis, MN

Rene Klieber
SR Technics
Zurich, Switzerland

Kenneth Knopp
FAA WJ Hughes Technical Center
Atlantic City Int'l Airport, NJ

Hiroshi Kobayashi
All Nippon Airways
Tokyo, Japan

Kendall Koerner
Spirit Aerosystems
Wichita, KS

Alan Koh
Singapore Air
Singapore

Jeff Kollgaard
Boeing
Seattle, WA

Jerzy Komorowski
National Research Council Canada |
Ottawa, ON, Canada

Ajay Koshti
NASA-Johnson Space Center
Houston, TX

Mike Krehbiel
American Airlines
Tulsa, OK

Paul Kulowitch
US Navy
Patuxent River, MD

André Lamarre
Olympus NDT
Québec, Canada

Bob Lasser
Imperium
Beltsville, MD

Francois Landry
Bell Helicopter
Montreal, Canada

Dy Le
US Army
Aberdeen Proving Ground, MD

Ray Leseck
US Airways
Neville Island, PA

Arne Lewis
Boeing
Seattle, WA

Obdulia Ley
Mistras
Princeton, NJ

Marco Liberatoscioli
Alitalia
Rome, Italy

Glenn Light
Southwest Research Institute
San Antonio, TX

Eric Lindgren
US Air Force
WPAFB, OH

John Linn
Boeing
Seattle, WA

Jack Little
Evisive Inc.
Baton Rouge, LA

John Lundeen
US Navy
Patuxent River, MD

Robert Luiten
KLM Airlines
Amsterdam, The Netherlands

John Lundeen
US Navy
Patuxent River, MD

Doug Lutz
General Electric
Lewistown, PA

Renato Maia
Embraer
São José dos Campos, Brazil

Ben Manning
Express Jet
Houston, TX

Carol Martineau
FAA
Washington, DC

Marcias Martinez
Technical University of Delft
Delft, The Netherlands

Ryan Mather
Timco
Macon, GA

Junya Matsuda
Japan Airlines
Tokyo, Japan

Shin Matsumoto
Toshiba
Tokyo, Japan

Jim Mazza
US Air Force
WPAFB, OH

Sergio Mayer
Embraer
San Jose dos Campos, Brazil

Glae McDonald
US Airways
Charlotte, NC

Jim Mcfeat
BAe Systems
Bristol, United Kingdom

Robert Mcquire
FAA
Atlantic City, NJ

Jason Meade
United Airlines
Houston, TX

Alexander Melton
Delta Air Lines
Atlanta, GA

Thomas Mensah
Georgia Aerospace
Atlanta, GA

Steve Micich
AAR Corp.
Indianapolis, IN

Clark Miller
Southwest Airlines
Highland Village, TX

Ronald Miller
Delta Airlines
Minneapolis, MN

Scott Miller
Alaska Airlines
Seattle, WA

Eric Mitchell
American Airlines
Tulsa, OK

Yoichi Mizuma
Japan Airlines
Tokyo, Japan

Elyse Moody
Aviation Week Overhaul & Maintenance
New York, NY

Calvin Moore
US Air Force
Tinker Air Force Base, OK

Tom Moran
US Air Force
WPAFB, OH

Matt Moye
US Air Force
Tinker Air Force Base, OK

Tommy Mullis
US Air Force
Warner Robins, GA

Francois Museux
Airbus
Blagnac, France

Yosuke Nagao
Japan Aerospace Exploration Agency
Tokyo, Japan

Tamotsu Nagasaka
All Nippon Airways
Tokyo, Japan

John Newman
Laser Technology Inc.
Norristown, PA

Bill Nicol
MoviMED
Irvine, CA

Steve Nolet
TPI Composites
Warren, RI

Ronan O'Higgins,
University of Limerick,
Limerick, Republic of Ireland

Toshimichi Ogisu
Fuji Heavy Industries
Tochigi, Japan

Paul Oulton
United Airlines
San Francisco, CA

Christophe Paget
Airbus
Bristol, United Kingdom

Georgios Papageorgiou
Olympic Airways
Athens, Greece

Rob Pappas
FAA
Washington, DC

Mohd. Alamin Pardi
Malaysia Airlines
Selangor, Malaysia

Mick Patino
American Airlines
Tulsa, OK

Kieran Patton
Shannon Aerospace
County Clare, Ireland

Luiz Perin
Embraer
São José dos Campos, Brazil

Dorsey Perkins
Southwest Airlines
Grapevine, TX

Will Perry
General Electric
Lewistown, PA

Hartmut Peters
Lufthansa Technik AG
Hamburg, Germany

Keith Phillips
Airbus
Bristol, United Kingdom

Steve Phillips
Kalitta Air
Detroit, MI

Jérôme Pinsonnault
Bombardier
Montreal, Canada

David Piotrowski
Delta Air Lines
Atlanta, GA

Jan Popp
Lufthansa
Hamburg, Germany

Bill Prosser
NASA Langley Research Center
Hampton, VA

Bernd Rackers
Airbus
Bremen, Germany

Tom Reep
Zetec
Issaquah, WA

Kevin Rees
U.S. Army
Corpus Christi, TX

Jeff Register
General Electric
Minneapolis, MN

Joerg Reinersmann
General Electric
Huerth, Germany

Paul Risso
United Airlines
San Francisco, CA

Kurt Robinson
Delta Air Lines
Atlanta, GA

Ana Rodriguez
Airbus
Madrid, Spain

Raul Rojas
Delta Airlines
Atlanta, GA

Craig Rolfson
Delta Airlines
Minneapolis, MN

Ralph Rotolante
MoviTherm
Boxborough, MA

Jean Rouchon
European Aviation Safety Agency
Toulouse Cedex, France

Ricardo Rulli
Embraer
São José dos Campos, Brazil

Rick Russell
NASA
Kennedy Space Center, FL

Bob Saathoff
Cessna Aircraft Company
Wichita, KS

Patrick Safarian
FAA
Renton, WA

Lamia Salah
Wichita State Univ. - NIAR
Wichita, KS

Liming Salvino
US Navy
Singapore

Fernando Santos
NDT Expert
Toulouse, France

Luis Santos
Embraer
São José dos Campos, Brazil

Jeffery Schaff
Sikorsky Aircraft
Stratford, CT

Carlyn Schlottman
Boeing
Seal Beach, CA

George Schneider
Sikorsky Aircraft
Stratford, CT

Bob Scoble
United Airlines
San Francisco, CA

Dachar Sertpunnuak
Thai Airways International
Bangkok, Thailand

Steve Shepard
Thermal Wave Imaging
Ferndale, MI

Jimmy Shiver
UTC Aerospace Systems
Birmingham, AL

Vilmar da Silva do Valle
Embraer
San Jose dos Campos, Brazil

Walt Sippel
FAA
Renton, WA

Eskil Skoglund
DolphiTech
Raufoss, Norway

Jesse Skramstad
NDT Solutions, Inc.
New Richmond, WI

Duane Slabaugh
Delta Airlines
Atlanta, GA

Art Smith
AAR Corp.
Indianapolis, IN

Scott Smotherman
ST Aerospace Mobile
Mobile, AL

Hideki Soejima
Fuji Heavy Industries
Tochigi, Japan

David Sokol
LSP Technologies
Dublin, OH

Holger Speckmann
Airbus
Bremen, Germany

Giancarlo Spera
Alitalia
Rome, Italy

Reinhardt Spiegel
Airbus
Stade, Germany

Bob Stakenborghs
Evisive, Inc.
Baton Rouge, LA

Raymond Stolarz
JetBlue Airways
Jamaica, NY

Larry Sullivan
UTC Aerospace Systems
Chula Vista, CA

Paul Swindell
FAA WJ Hughes Technical Center
Atlantic City Int'l Airport, NJ

Ralph Sykes
Lockheed Martin
Marietta, GA

Nobuo Takeda
University of Tokyo
Tokyo, Japan

Chinnaphan Thattiyaphong
Thai Airways International
Bangkok, Thailand

Robert Thomason
ST Aerospace
San Antonio, TX

Jeffery Thompson
Boeing
Seattle, WA

Darrell Thornton
UPS
Louisville, KY

Zuhair Tibi
Jet Blue
New York, NY

Sam Tucker
United Airlines
San Francisco, CA

Andrew Vechart
Honeywell Aerospace AT
Golden Valley, MN

Victor Vilents
PK Design
Moscow, Russia

John Vogt
Nordam
Tulsa, OK

Dennis von Seelen
Lufthansa Airlines
Hamburg, Germany

Chinh Vuong
FAA
Ft. Worth, Tx

Simon Waite
European Aviation Safety Agency
Köln, Germany

Rusty Waldrop
US Coast Guard
Elizabeth City, NC

Patrick Walter
Texas Christian University
Ft. Worth, TX

Rick Wampler
Delta Air Lines
Atlanta, GA

Thomas Walz
Dantec Dynamics
Holtsville, NY

Ben Wang
Florida State Univ
Tallahassee, FL

Ed Weinstein
FAA WJ Hughes Technical Center
Atlantic City Int'l Airport, NJ

Lorenz Wenk
Airbus
Hamburg, Germany

Clemens Westerkamp
University of Applied Sciences
Osnabrueck, Germany

Dave Westlund
FAA WJ Hughes Technical Center
Atlantic City Int'l Airport, NJ

Kyle Wetzel
Wetzel Engineering
Lawrence, KS

Al Williams
ST Aerospace Mobile
Mobile, AL

Scott Williams
Southwest Airlines
Grapevine, TX

William Winfree
NASA Langley Research Center
Hampton, VA

Buzz Wincheski
NASA Langley Research Center
Hampton, VA

Ian Won
FAA
Renton, WA

Roy Wong
Bombardier
Montreal, Quebec Canada

Nancy Wood
Boeing
St. Louis, MO

John Vogt
Nordham
Tulsa, OK

Jun Yamanaka
Japan Airlines
Tokyo, Japan

Rick Young
NASA Langley Research Center
Hampton, VA

Lei Yue
Taikoo Xiamen Aircraft Engineering
Xiamen Fujian, China

Sandia National Labs:

1522 Ciji Nelson
1522 David Moore
1522 Kevin Rolfe
1527 Colin McConnell
1833 David Calkins
1833 Michael Kelly
1833 William Miller
6121 David Minster
6121 Joshua Paquette
6122 Daniel Laird
6000 Jim Chavez
6600 Billy Marshall
6610 Jeff Danneels
6620 Roberto Mata
6620 Willy Morse
6620 Dennis Roach
6621 Mark Retter
6622 Robert Baca
6623 Mark Soo Hoo
6625 Barry Boughton
6626 Steve Heffelfinger
6626 Andrea Dorado
6626 Randy Duvall
6626 Stephen Neidigk
6626 Tom Rice
6630 Brad Parks
9532 Recorded Information Management